REFRACTOMETRY STUDIES OF THE OPTICAL PROPERTIES OF POLYMER FILMS AND THE DEVELOPMENT OF POLYMER COATED REFRACTIVE INDEX SENSORS

by

John Edward Saunders

A thesis submitted to the Department of Chemistry

In conformity with the requirements for

the degree of Doctor of Philosophy

Queen's University

Kingston, Ontario Canada

September, 2016

Abstract

Sensors for real-time monitoring of environmental contaminants are essential for protecting ecosystems and human health. Refractive index sensing is a non-selective technique that can be used to measure almost any analyte. Miniaturized refractive index sensors, such as silicon-on-insulator (SOI) microring resonators are one possible platform, but require coatings selective to the analytes of interest.

A homemade prism refractometer is reported and used to characterize the interactions between polymer films and liquid or vapour-phase analytes. A camera was used to capture both Fresnel reflection and total internal reflection within the prism. For thin-films (d = 10 μm - 100 μm), interference fringes were also observed. Fourier analysis of the interferogram allowed for simultaneous extraction of the average refractive index and film thickness with accuracies of Δn = 1-7 $\times 10^{-4}$ and Δd < 3-5%.

The refractive indices of 29 common organic solvents as well as aqueous solutions of sodium chloride, sucrose, ethylene glycol, glycerol, and dimethylsulfoxide were measured at λ = 1550 nm. These measurements will be useful for future calibrations of near-infrared refractive index sensors.

A mathematical model is presented, where the concentration of analyte adsorbed in a film can be calculated from the refractive index and thickness changes during uptake. This model can be used with Fickian diffusion models to measure the diffusion coefficients through the bulk film and at the film-substrate interface.

The diffusion of water and other organic solvents into SU-8 epoxy was explored using refractometry and the diffusion coefficient of water into SU-8 is presented. Exposure of soft baked SU-8 films to acetone, acetonitrile and methanol resulted in rapid delamination. The diffusion of volatile organic compound (VOC) vapours into polydimethylsiloxane and polydimethyl-co-polydiphenylsiloxane polymers was also studied using refractometry. Diffusion and partition coefficients are reported for several analytes.

As a model system, polydimethyl-co-diphenylsiloxane films were coated onto SOI microring resonators. After the development of data acquisition software, coated devices were exposed to VOCs and

the refractive index response was assessed. More studies with other polymers are required to test the viability of this platform for environmental sensing applications.

Co-Authorship

Unless explicitly stated, all the work described in this thesis has been conducted by the author as part of a Ph.D. degree in the Department of Chemistry under the supervision of Dr. Hans-Peter Loock. In all parts of the thesis, the author played a major role in designing and overseeing experiments, analysing the data and preparing manuscripts. Published material has been included in this thesis by expressed permission from all co-authors and publishers.

The original processing technique of the refractometry experiments described in Chapter 4 was co-authored with Mr. Weijian Chen, Dr. Jack Barnes, Dr. Scott Yam and Dr. Hans-Peter Loock and has been previously published in reference [1].

The measurement of near-infrared refractive indices of solvents and solutions in Chapter 5 was co-authored by Mr. Connnor Sanders, Mr. Hao Chen and Dr. Hans-Peter Loock and has been published in reference [2].

The studies on diffusion of liquids into SU-8 film in Chapter 6 were co-authored by Mr. Hao Chen, Mr. Chris Brauer, Mr. McGregor Clayton, Mr. Weijian Chen, Dr. Jack Barnes and Dr. Hans-Peter Loock and have been published in reference [3]

The diffusion of VOCs into siloxane polymers described in Chapter 7 was work with Mr. Hao Chen, Mr. Chris Brauer, Mr. McGregor Clayton, Mr. Weijian Chen, Dr. Jack Barnes and Dr. Hans-Peter Loock. A manuscript on this work is currently in preparation.

1. Chen, W.; Saunders, J. E.; Barnes, J. A.; Yam, S. S.-H.; Loock, H.-P., Monitoring of vapor uptake by refractive index and thickness measurements in thin films. *Optics Letters* **2013,** *38*, 365-367.

2. Saunders, J. E.; Sanders, C.; Chen, H.; Loock, H.-P., Refractive indices of common solvents and solutions at 1550 nm. *Applied Optics* **2016,** *55*, 947-953.

3. Saunders, J. E.; Chen, H.; Brauer, C.; Clayton, M.; Chen, W.; Barnes, J. A.; Loock, H.-P., Quantitative diffusion and swelling kinetic measurements using large-angle interferometric refractometry. *Soft Matter* **2015,** *11*, 8746-8757.

Acknowledgements

I would like to first thank my supervisor Dr. Hans-Peter Loock. Your enthusiasm and passion towards research has been inspiring. You helped push me out of my comfort zone and constantly challenged me to be the best that I can. I am extremely grateful for all of the opportunities you have provided me with over the years. You sent me to many conferences and included me in collaborative research projects both at home and abroad. I feel that I have gained valuable experiences that will help to shape my future career. Your advice and mentorship through graduate school has been instrumental to my success.

I would like to thank my supervisory committee members, Dr. Richard Oleschuk and Dr. Cathleen Crudden, for their ideas and advice toward my project. You have both been very supportive during my time in graduate school. I would also like to thank Dr. Stephen Brown for his technical advice and support and for agreeing to be on my defence committee. You have offered many insightful suggestions and helped me think critically through many details of my work.

I would also like to thank the amazing support staff in the Department of Chemistry. You have all been so helpful and friendly during my time here. I would especially like to thank Annette Keyes and Michelle Boutilier for all of their assistance as Graduate Assistants in the department. All of your organization and knowledge has made everything so much easier over the last few years. I would like to thank Ed Maracle and Robin Roberts for constantly fixing broken computers and instruments in our lab and Kim MacKinder, and the rest of the staff at Science Stores, for keeping everything well stocked and quickly ordering anything we needed.

I would especially like to thank Weijian Chen, who I worked with on many of the refractometer experiments. I am very grateful for all of your help. The analysis techniques that you developed have been essential to my project. I would also like to thank Dr. Jack Barnes for his incredible knowledge and skills, help with constructing experiments, and solving many of our research problems. I would not have been able to make it through graduate school without your help.

I would like to thank the past and present members of the Loock group, and friends from all over the department. You have all been so kind and helpful during my time at Queen's. Whether it was a Friday afternoon at the Grad Club or a BBQ on the weekend, you have always been up for a good time, and have been great friends throughout my time here. Jeff Crouse, Stephen Walker and Nic Andrews, thank you for all of our wine making adventures over the past many years!

I truly value the constant support I have received from my parents Wendy and Jim Saunders, my brothers Jamie and Adam and my sister-in-law Melissa. You have all been so patient and understanding with me and have always been there for me. Your support has made my efforts in graduate school possible. Gillian, your love and constant support has meant so much to me during the past years. You have been my biggest fan and have always watched out for me. I love you very much and am forever grateful for all of your support.

I am thankful for the generous funding from the Natural Sciences and Engineering Research Council of Canada (NSERC), the Ontario Government, Queen's University and the Walter C. Sumner Foundation I received during my time in graduate school.

Statement of Originality

I hereby certify that all of the work described within this thesis is the original work of the author with the following exceptions:

1. The original experimental setup and processing techniques used for the interferometric refractometry sections of this thesis were developed in collaboration with Mr. Weijian Chen, and appeared previously in his M.ASc. thesis.

2. The refractometry data of analytes partitioning into PDMS-PDPS films (Chapter 7.4.4) was collected by Mr. Chris Brauer, and Mr Weijian Chen. A preliminary analysis of this data appeared in both of their M.Sc. and M.ASc. theses. The re-analysis of this data is the original work of the author.

3. The data processing techniques used to filter data prior to Fourier analysis (Chapter 4.4.3) were developed with the assistance of Dr. Raphael Desbiens during an internship at *ABB Canada* in Quebec, QC.

Any published (or unpublished) ideas and/or techniques from the work of others are fully acknowledged in accordance with the standard referencing practices.

John Edward Saunders

September, 2016

Table of Contents

List of Figures

List of Tables

List of Abbreviations

AFM	Atomic force microscopy
ATR	Attenuated total internal reflection
BTEX	Class of contaminants including benzene, toluene, ethylbenzene and xylenes
CCD	Charge coupled device
CMOS	Complementary metal-oxide semiconductor
DMSO	Dimethylsulfoxide
EDTA	Ethylenediaminetetraacetic acid
EDFA	Erbium doped fibre amplifier
FBG	Fibre Bragg grating
FFT	Fast Fourier transform
FSR	Free spectral range
FTIR	Fourier-transform infrared spectroscopy
FWHM	Full width at half maximum
GC	Gas chromatography
HPLC	High performance liquid chromatography
IFFT	Inverse fast Fourier transform
InGaAs	Semiconductor made form indium, gallium and arsenic used in the near-infrared
IR	Infrared
LC	Liquid chromatography
LD	Laser diode
LED	Light emitting diode
LPG	Long period grating
MSE	Mean square error
MZ	Mach-Zehnder (common type of interferometer)

PC	Polarization controller
PCF	Photonic crystal fibre
PDMS	Polydimethylsiloxane
PDMS-PDPS	Poly(dimethyl-co-diphenyl)siloxane
PF	Polarization filter
PGMEA	Propyleneglycol monomethylether acetate
PMMA	Polymethylmethacrylate (Plexiglass)
QCM	Quartz crystal microbalance
Q-factor	Quality factor
RIU	Refractive index unit
SEM	Scanning electron microscopy
SOI	Silicon-on-insulator
SPR	Surface plasmon resonance
SU-8	Common epoxy photoresist available from MicroChem
TE	Transverse electric (s-polarized light)
TEM	Transmission electron microscopy
TM	Transverse magnetic (p-polarized light)
UV	Ultraviolet
VOC	Volatile organic compound
WGM	Whispering gallery mode

Chapter 1

Introduction

In this age of increasing urban population, industrialization and resource exploration, there are many contaminants entering the environment. Exposure to environmental contaminants through poor water or air quality can result in adverse health effects on the population. Some well-known contaminant types include pathogenic organisms, heavy metals, and organic hydrocarbons

Pathogenic contamination of water sources can cause gastrointestinal and other serious health problems, including death.[1] The contamination of the Walkerton, ON, water supply with *Escherichia coli* in the year 2000 resulted in seven deaths and made thousands of people sick.[2] While this was a direct case of negligence, the delay between the contamination event and the availability of water quality test results increased the impact on the community.[2] One way to reduce delays would be to use remote sensors to continually monitor water quality that could alert officials should a contamination event occur.

Heavy metal contamination from lead is a common problem due to corrosion of aging water supply infrastructure.[3] In Canada, lead was commonly used in water pipes until 1975.[3] Recently, a state of emergency was declared in Flint, Michigan due to contamination in their city water supply with lead, which leached out of the municipal water pipes when the water source was switched to the more acidic Flint River in 2014.[4-5] Children are particularly affected by lead toxicity, leading to effects on the nervous system that can result in developmental problems.[3] Contamination of water sources with mercury is also a major problem. Mercury can accumulate in fatty tissues and is known to bio-accumulate in fish stocks, which are often food sources for surrounding communities.[6] Mercury poisoning can cause neurological problems, including vision loss, hearing loss, paralysis, and death.[7] In Ontario, the release of mercury from a chemical plant in Dryden, ON resulted in serious contamination of rivers around the Grassy Narrows and Whitedog First Nations communities between 1962-1970.[8-9] Elevated blood levels, and adverse health effects have been reported from consumption of the contaminated fish stock.[8-9] Remote sensors could be used to perform

routine analysis of the effluents leaving chemical factories, to identify the risk to the environment, and ensure that contaminants leaving industrial sites do not exceed an acceptable level.

Developing nations and newly industrialized societies are particularly affected by environmental contamination, as legislation and/or enforcement have not kept up with emerging threats.[10] For example, there are currently 5 million sites worldwide that have been reported to be contaminated with heavy metals, many of which are located in China.[11] About 800,000 km^2, i.e. 10% of the Chinese Farmland, has been reported to be contaminated with heavy metals including cadmium, mercury and lead due to irrigation with contaminated water.[11-12]

Exposure to organic contaminants can also result in serious health effects over prolonged duration. Oil spills from tankers, off-shore platforms, and pipelines in remote areas can result in major contamination of the environment. Since pipelines often travel long distances between communities, leaks can take a long time to be discovered, causing irreversible damage to some ecosystems. In urban settings, high concentrations of BTEX (benzene, toluene, ethylbenzene, and xylenes) compounds are produced from chemical refineries, power production, transportation, and service stations and can result in serious respiratory problems and increased health risks.[13-16] Many volatile organic compounds are used in the production of polymers and plastics and can accumulate in households from off-gassing of furniture, paints and waxes.[17] The concentration of BTEX compounds in households can be up to 100 times higher than the outdoors.[17] In particular, prolonged exposure to the BTEX class of contaminants have been shown to cause kidney, liver, respiratory, cardiovascular, and neurological effects.[13-16] Sensors could be used to monitor VOC emissions from industrial sources or used to provide a quantitative measure of indoor air quality.

The traditional method for analysing environmental contamination relies on collecting field samples and sending them to certified laboratories for analysis. This process can be very expensive and inefficient. There is also typically a large time delay between sample collection and analysis, which could result in prolonged exposure of populations to contaminants before a problem is identified. This is particularly problematic for remote communities, such as many First Nations communities. Furthermore, since samples are often collected intermittently, this method does not allow for the detection of spikes in

concentrations, and only average concentrations of contaminants are reported. Incorporating remote sensors that are capable of continuously monitoring the levels of contaminants in industrial effluents, or in water sources around pipelines would help identify harmful releases of contaminants into the environment, and minimize the effects from delayed response.

Effective sensors need to be compact, and relatively inexpensive to produce and operate.[18] Additionally they must be selective to a contaminant of known interest and sensitive enough to detect relevant concentrations.[18] Furthermore, typically sensors need to be reversible so that they can continue to be used and not require frequent replacement.[18] They also need to be robust enough to survive in the elements and deal with significant temperature variability. With the increased global connectivity of modern technology, including the internet and cellular phone networks, much of the infrastructure needed for remote sensing may already be in place.[19] Automated sensors could transmit routine reports or warnings when thresholds are reached through phones or the internet to regulatory agencies. This could also allow for measurements over very large geographic regions without requiring a significant number of highly qualified personnel.

While electrochemical[20-21] and gravimetric sensors[22-23] are available, there are many advantages to the use of optical sensors for the detection of different types of analytes.[24-25] They can be constructed using simple components, combining miniaturized light sources (e.g. LEDs) and detectors (e.g. CCD or CMOS chips) that can operate under a wide range of conditions and be powered using batteries. While absorption and fluorescence spectroscopy are highly sensitive methods to quantitatively measure and identify compounds, the interrogation wavelength must overlap with an absorption feature of the target molecule. This can be problematic if there are interferences from other compounds in the matrix having similar absorption spectra. Refractive index sensors are non-selective and can be used to detect target analytes at any wavelength. Since they are even less selective then absorption and fluorescence sensors, it is then necessary to introduce a selective enrichment step, which is specific to the target analyte. Many different platforms exist to detect chemicals through refractive index changes, as will be discussed in Chapter 2. For example, waveguide based interferometers[26] and microring[27] resonators can be reproducibly manufactured

on the wafer level, producing hundreds or thousands of identical devices in a single manufacturing run.[28-29] The resulting low cost and high sensitivity make these refractive index sensors ideal for the purpose of remote environmental sensing. Silicon-on-insulator (SOI) wire microring resonators[27] and interferometers[26] can be coated with siloxane based polymers for the detection of airborne volatile organic hydrocarbons, as will be described in Chapter 8 of this thesis.

One of the major challenges with refractive index sensors is the development of effective coatings and materials for analyte extraction. Materials need to be sensitive to target analytes, have minimal interferences, and be stable over a prolonged period of time.[18] In order to assess the effectiveness of a material, it is important to understand how the optical properties of materials change during exposure to different analytes. Only once this behaviour is known is it possible to correlate the refractive index change of a sensor with the external analyte concentration. Thin-film interferometric refractometry is a technique that will be used in this thesis to characterize the behaviour of polymer films exposed to a range of volatile organic compounds.

The development of remote sensors for monitoring contamination in the environment is essential to ensuring the safety of populations, especially in remote areas. Whether used to monitor the quality of water or air, sensors can help us identify and mitigate risks to society. Additionally, chemical sensors can help to identify contamination when it occurs instead of months or years later. This could help reduce environmental contamination and facilitate more proactive environmental stewardship within our society.

1.1 Thesis Outline

This thesis will begin with a description of the theory relating the refractive index to the electronic and structural properties of molecules in Chapter 2. A detailed review will be provided, discussing the current breadth of refractive index sensors. Optical methods for measuring the thickness and refractive indices of thin transparent films will also be discussed.

In Chapter 3, a model relating the concentration of an analyte adsorbed in a film to simultaneous refractive index and thickness changes is derived. Fickian diffusion models are also presented that are

suitable for fitting to concentration changes in the bulk film and at the film-substrate interface. Approximate diffusion models that are frequently used in the literature are also discussed.

The theory and experimental setup of the interferometric refractometer is presented in Chapter 4. A detailed discussion of the data processing methods used for measuring the refractive indices of both thick and thin liquid and polymer films is also discussed.

Using a prism refractometer, the refractive indices of 29 common organic solvents are studied at 1550 nm in Chapter 5. Refractive indices are also reported for series of aqueous sucrose, sodium chloride, ethylene glycol, glycerol, and dimethylsulfoxide solutions over their full soluble or miscible ranges. Polynomial functions are used to relate the weight fraction of analytes in solution with the solution refractive index to develop correlations that can be used for calibration of near-IR refractive index sensors.

The diffusion of water into SU-8 epoxy films is studied as a model system using the interferometric refractometer in Chapter 6. The chemical compatibility of SU-8 with other organic solvents is also assessed.

The diffusion of vapours of volatile organic compounds (VOCs) into polydimethylsiloxane films and polydimethyl-co-polydiphenylsiloxane copolymer films is studied using interferometric refractometry in Chapter 7. The saturated analyte concentrations within the film are also used to calculate partition coefficients in this chapter.

Siloxane polymers are coated onto silicon-on-insulator Mach-Zehnder interferometers and microring resonators for the purpose of VOC sensing in Chapter 8. This chapter provides a detailed introduction into the scope of miniaturized waveguide refractive index sensing. The sensing of VOC vapours is then presented as a proof of concept of sensing applications on this platform.

A summary of the entire thesis is provided in Chapter 9, with conclusions of the overall progress towards the development of a refractive index sensor for VOC detection. Future experiments and improvements to the refractometer and silicon-on-insulator microresonator setups are also described in detail in this final chapter.

1.2 References

1. Pandey, P. K.; Kass, P. H.; Soupir, M. L.; Biswas, S.; Singh, V. P., Contamination of water resources by pathogenic bacteria. *AMB Express* **2014,** *4* (51), 1-16.

2. Brown, R. S.; Hussain, M., The Walkerton tragedy—issues for water quality monitoring. *The Analyst* **2003,** *128*, 320-322.

3. *Water talk: minimizing exposure to lead from drinking water distribution systems.* Health Canada, 2007, H128-1/07-513E,

4. Fox, M. CDC confirms lead levels shot up in flint kids after water switch. NBC News, http://www.nbcnews.com/storyline/flint-water-crisis/cdc-confirms-lead-levels-shot-flint-kids-after-water-switch-n598496 (accessed Aug, 7, 2016).

5. Hanna-Attisha, M.; LaChance, J.; Sadler, R. C.; Champney Schnepp, A., Elevated blood lead levels in children associated with the flint drinking water crisis: A spatial analysis of risk and public health response. *American Journal of Public Health* **2016,** *106*, 283-290.

6. Baird, C.; Cann, M., *Environmental Chemistry*. 4th Edition, W.H Freeman and Company, New York, NY, 2008.

7. Health effects of exposures to mercury. US Environemental Protection Agency (EPA), https://www.epa.gov/mercury/health-effects-exposures-mercury (accessed Aug. 7, 2016).

8. Porter, J. Mercury levels still rising near Grassy Narrows First Nation, report says. CBC News, http://www.cbc.ca/news/canada/thunder-bay/mercury-levels-still-rising-near-grassy-narrows-first-nation-report-says-1.3109261 (accessed Aug. 7, 2016).

9. Wheatley, B.; Paradis, S., Exposure of Canadian aboriginal peoples to methylmercury. *Water, Air, & Soil Pollution* **1995,** *80*, 3-11.

10. Faure, M. G. *Enforcement Issues for Environmental Legislation in Developping Countries.* United Nations Univeristy, Institute for New Technologies (INTECH), 1995, 1-29.

11. He, Z.; Shentu, J.; Yang, X.; Baligar, V. C.; Zhang, T.; Stoffella, P. F., Heavy metal contamination of soils: sources, indicators, and assessment. *Journal of Environmental Indicators* **2015,** *9*, 17-18.

12. Zhang, X.; Zhong, T.; Liu, L.; Ouyang, X., Impact of soil heavy metal pollution on food safety in China. *PLOS ONE* **2015,** *10*, e0135182, 1-14.

13. *Toxicological Profile for Benzene* Agency for Toxic Substances and Disease Registry, US Department of Health and Human Services, Atlanta, Georgia, 2007,

14. *Draft Toxicological Profile for Toluene.* Agency for Toxic Substances and Disease Registry, US Department of Health and Human Services, Atlanta, Georgia, 2015,

15. *Toxicological Profile for Ethylbenzene.* Agency for Toxic Substances and DIsease Registry, US Department of Health and Human Services, Atlanta, Georgia, 2010,

16. *Toxicological Profile for Xylenes.* Agency for Toxic Substances and Disease Registry, US Department of Health and Human Services, Atlanta, Georgia, 2007,

17. Wheeler, A. J.; Wong, S. L.; Khoury, C.; Zhu, J. *Predictors of indoor BTEX concentrations in Candian residences.* Health, Reports, Statistics Canada, 2013, 24, 11-17.

18. Wolfbeis, O. S., Editorial: probes, sensors, and labels: Why is real progress slow? *Angewandte Chemie International Edition* **2013,** *52*, 9864-9865.

19. Roda, A.; Michelini, E.; Zangheri, M.; Di Fusco, M.; Calabria, D.; Simoni, P., Smartphone-based biosensors: A critical review and perspectives. *TrAC Trends in Analytical Chemistry* **2016,** *79*, 317-325.

20. Bakker, E.; Telting-Diaz, M., Electrochemical sensors. *Analytical Chemistry* **2002,** *74*, 2781-2800.

21. Privett, B. J.; Shin, J. H.; Schoenfisch, M. H., Electrochemical sensors. *Analytical Chemistry* **2008,** *80*, 4499-4517.

22. O'Sullivan, C. K.; Guilbault, G. G., Commercial quartz crystal microbalances – theory and applications. *Biosensors and Bioelectronics* **1999,** *14*, 663-670.

23. Marx, K. A., Quartz crystal microbalance: A useful tool for studying thin polymer films and complex biomolecular systems at the solution−surface interface. *Biomacromolecules* **2003,** *4*, 1099-1120.

24. Wang, X.-D.; Wolfbeis, O. S., Fiber-optic chemical sensors and biosensors (2008–2012). *Analytical Chemistry* **2013,** *85*, 487-508.

25. Wang, X.-d.; Wolfbeis, O. S., Fiber-optic chemical sensors and biosensors (2013–2015). *Analytical Chemistry* **2016,** *88*, 203-227.

26. Densmore, A.; Xu, D.-X.; Janz, S.; Waldron, P.; Mischki, T.; Lopinski, G.; Delâge, A.; Lapointe, J.; Cheben, P.; Lamontagne, B.; Schmid, J. H., Spiral-path high-sensitivity silicon photonic wire molecular sensor with temperature-independent response. *Optics Letters* **2008,** *33*, 596-598.

27. Xu, D. X.; Densmore, A.; Delâge, A.; Waldron, P.; McKinnon, R.; Janz, S.; Lapointe, J.; Lopinski, G.; Mischki, T.; Post, E.; Cheben, P.; Schmid, J. H., Folded cavity SOI microring sensors for high sensitivity and real time measurement of biomolecular binding. *Optics Express* **2008,** *16*, 15137-15148.

28. Densmore, A.; Xu, D.-X.; Waldron, P.; Janz, S.; Lapointe, J.; Mischki, T.; Lopinski, G.; Delage, A.; Cheben, P. Spotter-compatible SOI waveguide devices for biomolecular sensing, *Silicon Photonics III, Proceedings of SPIE 6898*, **2008**, 68981B, 1-8.

29. Carlborg, C. F.; Gylfason, K. B.; Kaźmierczak, A.; Dortu, F.; Bañuls Polo, M. J.; Maquieira Catala, A.; Kresbach, G. M.; Sohlström, H.; Moh, T.; Vivien, L.; Popplewell, J.; Ronan, G.; Barrios, C. A.; Stemme, G.; van der Wijngaart, W., A packaged optical slot-waveguide ring resonator sensor array for multiplex label-free assays in labs-on-chips. *Lab on a Chip* **2010,** *10*, 281-290.

Chapter 2

Literature Review of Refractive Index Sensing

This chapter will begin with an introduction to the theory relating refractive index to the structural and electronic properties of molecules. A detailed literature review will also be presented describing prism-based, optical fibre-based, and chip level waveguide-based refractive index sensors. Several optical methods that can be used for measuring the refractive index and thickness of thin optically transparent films will also be introduced. Several different types of optical coatings will be presented for refractive index sensing of a variety of analytes. Finally, the specific objectives of this thesis will be presented.

2.1 Introduction

Chemical sensing can be performed using a variety of electrochemical, gravimetric, and optical techniques. Electrochemical sensors measure either conductivity, potential, or current to identify changes at the surface of conducting materials.[1-2] Corrosion or degradation of sensor materials can cause significant challenges with electrochemical sensors.[3-4] Additionally, electrical contacts are required, so electrochemical sensors may not be suitable for the detection of flammable or explosive compounds.

Many gravimetric systems measure the change in the resonance frequency of the oscillation of a crystal (e.g. quartz) due to a mass changes in a thin coating material.[5-7] These techniques are highly sensitive but can become complicated when studying thick flexible polymer systems where the coatings can dampen the crystal oscillations and the resonance frequency may no longer depend linearly on mass.[8]

Optical sensors are sensitive non-contact methods useful for measuring the presence of a full range of analytes.[9-10] The absorption spectrum of an analyte is characteristic of specific molecular vibrations or transitions in a molecule. While absorption is sensitive, either a broadband light source must be used, or the interrogation wavelength must be carefully selected to overlap with an absorption feature. Additionally, the absorption of a target species must not overlap with absorption spectra of other molecules in the matrix. For conjugated molecules with significant electron delocalization, fluorescence at wavelengths red-shifted

from the absorption peak can be an additional feature for determining the identity of compounds but is only practical for conjugated systems. For many biosensing applications, fluorescent labels are added. Upon interaction with a target analyte, small fluorescent molecules are cleaved by enzymes and detected.[11-12] This can be synthetically challenging, quite expensive and may also disrupt the way the compounds interact.

Refractive index sensing is a label free method for analysing practically any type of chemical system. [9, 13-16]The refractive index of a sample can be probed at any wavelength, and the change can be monitored for the uptake of any desired analyte. Since refractive index sensors are inherently non-selective, it is important to identify selective interactions of an extraction film or interacting surface that will preferentially bind the desired analyte. Alternatively, a range of different materials can be simultaneously measured and the relative refractive index response used to qualitatively and quantitatively determine the analytes.

An enormous wealth of literature exists around refractive index sensors. Sensing has been demonstrated using prisms[17-19], optical fibre systems[9, 13] and more recently on-chip optical waveguide devices[10, 20]. While the development of novel sensing platforms continues, most are only tested by measuring aqueous sucrose or sodium chloride solutions. To date, little work has been done to incorporate selective chemical coatings with existing refractive index sensors for environmental applications. This project focuses on studying the binding behaviour of analytes in polymer films and on applying polymer coatings to refractometers and microphotonic devices to develop optical sensors for the detection of volatile organic compounds (VOCs).

This chapter will begin with a description of the theory that relates the refractive index of a material to the physical properties of molecules. It will then illustrate different types of refractive index sensing platforms, such as interferometers, prism refractometers, optical fibre sensors, whispering gallery mode sensors, and surface plasmon sensors. Chip-level optical waveguide refractive index sensors will also be introduced. When studying polymer systems, it is important to be able to measure both changes in refractive index and also swelling of materials during exposure to analytes. Some methods of measuring both the refractive index and thickness of thin optically transparent films will also be discussed. Finally, several

different types of optical coatings for refractive index sensors will be presented and an overall research plan of this thesis will be described.

2.1.1 Refractive Index Theory

In order to relate the refractive index of a material to its other electronic and structural properties, some fundamental concepts must first be introduced. In this section we summarize the theory related to refractive index as described in Atkin's Physical Chemistry.[21] In polar molecules, the electron charge is not shared uniformly between the atoms such that partial charges of $+q$, and $-q$ exist around individual atoms.[21] The electric dipole, μ, is related to the magnitude of the partial charges, q and the distance between them, d.[21]

$$\mu = qd \tag{2.1}$$

Some molecules, like CO_2 and CCl_4, carry partial charges on their atoms, but have no permanent dipole due to the cancellation of individual dipoles through molecular symmetry. An instantaneous dipole can also be induced when non-polar molecules are placed in an electric field. The instantaneous dipole, μ^*, is related to the polarizability of a molecule, α, which is a measure of the distortion of the electrons within a molecule in the presence of an electric field with magnitude, E.[21]

$$\mu^* = \alpha E \tag{2.2}$$

Polarizability is usually expressed in units of $C^2m^2J^{-1}$, which can be cumbersome, so often it is simpler to use the polarizability volume, α', in units of m^3 or $Å^3$ ($1\ Å^3 = 1\times10^{-30} m^3$).[21]

$$\alpha' = \frac{\alpha}{4\pi\varepsilon_0} \tag{2.3}$$

Here, ε_0 is the vacuum permittivity ($\varepsilon_0 = 8.854\times10^{-12}\ C^2J^{-1}m^{-1}$). The permittivity of a material (or dielectric constant), ε, is related to the reduction of the potential energy between two charges when immersed in a given medium.[21] For any material, the relative permittivity, ε_r, is related to the absolute permittivity, ε, and the vacuum permittivity, ε_0.[21]

$$\varepsilon_r = \frac{\varepsilon}{\varepsilon_0} \tag{2.4}$$

Additionally, the molar polarization is related to the relative permittivity, the density, ρ, and the molar mass, M through the Debye equation.[21]

$$\frac{\varepsilon_r - 1}{\varepsilon_r + 2} = \frac{\rho P}{M} \tag{2.5}$$

The molar polarization, P, is related to the polarizability of a dielectric material, α. The material may also have a permanent dipole, μ, and contributions from both the induced dipole and temporally averaged permanent dipole govern the polarizability. [21]

$$P = \frac{N_A}{3\varepsilon_0}\left(\alpha + \frac{\mu^2}{kT}\right) \tag{2.6}$$

Here, N_A is Avogadro's number, k is the Boltzmann constant, and T is the temperature in Kelvin.[21] For experiments in the visible or UV region of the spectrum, the frequency of the electric field is high enough that the permanent dipoles are unable to stay aligned with the oscillating electric field and the temporal average of the permanent dipole contribution, i.e. the second term in equation (2.6) can be neglected.[21] Trivially, non-polar molecules do not have a permanent dipole contribution at all temperatures and EM oscillation frequencies.[21] By combining (2.5) with (2.6) at high frequencies corresponding to the visible and UV regions of the spectrum, the Debye equation reduces to the Clausius-Mossotti equation, which relates the polarizability directly to the relative permittivity.[21]

$$\frac{\varepsilon_r - 1}{\varepsilon_r + 2} = \frac{\rho N_A \alpha}{3M\varepsilon_0} \tag{2.7}$$

The refractive index is a factor that describes the delay of light when travelling through a medium that is denser than a vacuum. It is expressed as the ratio of the speed of light in the medium, c, with the speed of light in a vacuum, c_0.

$$n = \frac{c_0}{c} \tag{2.8}$$

The refractive index, *n*, is directly related to the relative permittivity of a compound in the visible or ultraviolet region of the spectrum.[21]

$$n^2 = \varepsilon_r \tag{2.9}$$

The Lorentz-Lorenz equation relates the refractive index of a material to the polarizability of a compound and is analogous to the Clausius-Mossotti equation (eqn. (2.7)).[21]

$$\frac{n^2 - 1}{n^2 + 2} = \frac{\rho N_A \alpha}{3M\varepsilon_0} \tag{2.10}$$

Both the refractive index and relative permittivity are complex properties that are also related to the extinction coefficient of the compound, *k*.

$$\tilde{n} = n + ik \tag{2.11}$$

One way to express the absorbance of a material, *A*, is through the absorption coefficient, α, over a path length, *l*.

$$A = \alpha l \tag{2.12}$$

The absorption coefficient, α, is related to the extinction coefficient, *k*, through the following relation.[22-23]

$$\alpha = \frac{4\pi k}{\lambda} \tag{2.13}$$

The refractive index is discontinuous over large wavelength ranges and passes through regions of anomalous dispersion ($dn/d\lambda > 0$) around absorption lines as is shown in Figure 2.1 for the absorption and refractive index of water in the infrared region of the spectrum.[23] Since the relationship between refractive index and wavelength is not linear, the dispersion of optical glasses and transparent polymers can be modeled using the Cauchy dispersion formula. The Cauchy coefficients, *A*, *B*, and *C* of the expansion series are reported for many materials and liquids.[24-25]

$$n(\lambda) = A + \frac{B}{\lambda^2} + \frac{C}{\lambda^4} \tag{2.14}$$

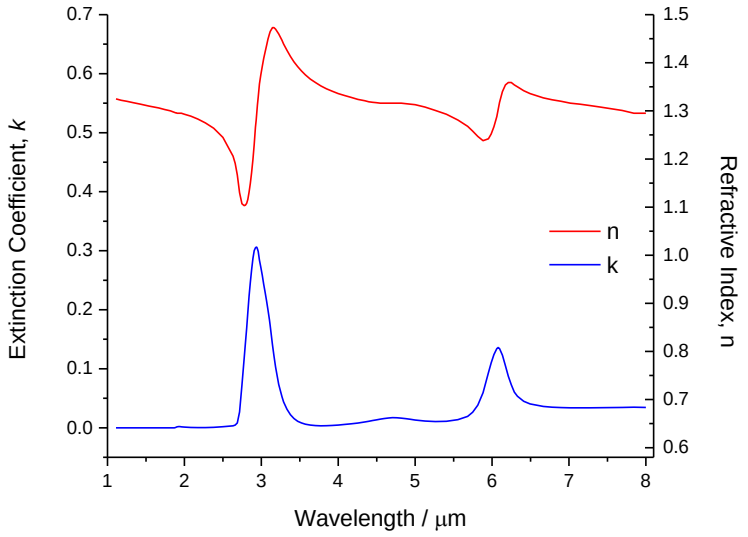

Figure 2.1: The refractive index and absorption of water in the infrared region of the spectrum. The data in this plot was published by J.E. Bertie and coworkers.[23] The refractive index becomes discontinuous and shows anomalous dispersion at the absorption lines around 3 μm and 6 μm.

The Sellmeier relation is more complicated, and often better describes the dispersion shape of optical glasses over larger wavelength ranges.[24] Sellmeier coefficients are often available for optical glasses from commercial glass manufactures.[26-28]

$$n^2(\lambda) = 1 + \frac{B_1\lambda^2}{\lambda^2 - C_1} + \frac{B_2\lambda^2}{\lambda^2 - C_2} + \frac{B_3\lambda^2}{\lambda^2 - C_3} \tag{2.15}$$

The refractive index is not only wavelength dependent, but also depends on temperature. This is due to polarizability changes of the material with temperature as well as thermal expansion of the material.[29-30] This thermal dependence of the refractive index is complicated to model as dn/dT can be either positive or negative depending on the material being studied.[29] Over small temperature ranges thermo-optical coefficients, dn/dT are reported in the literature for many optical materials.[26]

The refractive index can also be approximated from an absorption spectrum using the Kramer-Kronig relationship.[22-23, 31] This function is an example of a Hilbert transform and is an example of an improper integral.[32] The index can be calculated at a desired wavenumber, $\tilde{\nu}_0$, through integration of the absorbance spectrum over all other wavenumbers, $\tilde{\nu}$, within the spectral region. In this relationship, n_∞ is

the limiting refractive index away from the absorption line and C*P* is the Cauchy principal value which is a function that allows the integral to be evaluated when it becomes discontinuous.[31]

$$n(\tilde{\nu}_0) = n_\infty + \frac{2}{\pi} CP \int_0^\infty \frac{\tilde{\nu} k(\tilde{\nu})}{\tilde{\nu}^2 - \tilde{\nu}_0^{\,2}} d\tilde{\nu} \tag{2.16}$$

Now that the theory of refractive index has been discussed, the following sections will give a detailed account of how refractive indices are measured.

2.2 Refractive Index Sensors

Many different types of refractive index sensors have been reported in the literature. Typically their sensitivity is reported from tests with aqueous sucrose or sodium chloride solutions. While they might represent novel methods of measuring refractive indices, only few attempts have been made to demonstrate the sensors for more practical sensing applications. Additionally, many groups report the resolution of their instruments based on the minimum resolution of their detector and do not account for experimental baseline noise when quoting refractive index sensitivity.[33-37] This results in inflated resolutions of $\Delta n = 10^{-5} - 10^{-6}$ are frequently presented as the state-of-the-art in this field.[33-37] In practice, it is very difficult to specify the index of a material with an accuracy of better than $\Delta n = 10^{-4}$. For detection of small refractive index changes, $\Delta n < 10^{-4}$, temperature compensation and stabilisation is required. To give absolute refractive indices, comparison must be made to a reference material, where in many regions of the spectrum, including the near-IR around 1550 nm (the telecom C-band), refractive indices are not accurately known.

2.2.1 Interferometers

When two waves spatially overlap, they can be either constructively mixed, thereby increasing the amplitude of the resulting wave, or destructively mixed where the amplitudes of the two waves cancel each other out. Interferometers are devices where light is split between two arms of different effective lengths (nL) which are recombined to form a beating pattern known as an interferogram. The simplest form of interferometer is the Young interferometer, which is the basis of the double-slit experiment (Figure 2.2).[38] Light leaving two slits spaced apart by a distance, d, interferes on a plane at a distance, L, from the openings.

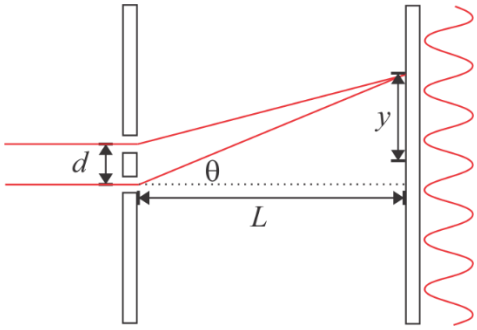

Figure 2.2: Schematic of the Young's double slit experiment. Light is shone from two channels or slits separated by a distance, *d*, and allowed to spatially interfere at a plane of distance, *L*. Typically *L* >> *d*, such that the angle, *θ*, is measured from a point source to the observation plane. The height from the centre of the interferogram is given by, *y*. In modern Young interferometers, the interferogram can be captured using an array detector.

The intensity of the interferogram can be described as

$$I = 4I_0 \cos^2\left(\frac{yd\pi}{L\lambda}\right) \tag{2.17}$$

where d is the separation of the two slits, L is the distance to the observation plane and y is the distance from the centre of the plane.[38] The maxima of the interferogram at the plane a distance, L are related to the wavelength, λ, the spacing between the two slits, d, and the mode order, (m = 0, 1, 2…).[38]

$$\theta_m = \frac{m\lambda}{d} \tag{2.18}$$

The spatial distance between interference maxima, Δy, at the observation plane can be described by:[38]

$$\Delta y = \frac{L}{d}\lambda \tag{2.19}$$

More generally, interferograms can be expressed by the superposition of two wave with complex amplitudes, U.[39]

$$U = \sqrt{I}\exp(i\phi) \tag{2.20}$$

The intensity of the resulting interferogram is defined as the sum of the complex amplitudes of the two waves.[39]

$$I = |U_1 + U_2|^2 \tag{2.21}$$

This expression can be expanded with the complex conjugates of the amplitudes of the two waves.[39]

$$I = I_1 e^{(i\phi_1 - i\phi_1)} + I_2 \, \mathrm{e}^{(i\phi_2 - i\phi_2)} + \sqrt{I_1 I_2}\left[\mathrm{e}^{i(\phi_2 - \phi_1)} + \mathrm{e}^{-i(\phi_2 - \phi_1)} \right] \tag{2.22}$$

Combining the terms and applying Euler's formula yields the general intensity equation that describes most interferometers.[39]

$$I = I_1 + I_2 + 2\sqrt{I_1 I_2}\cos(\Delta\phi) \tag{2.23}$$

If the intensities in the two arms of the interferometer are comparable, then the equation can be expressed as a single intensity, I_0.[39]

$$I = 2I_0\left[1 + \cos(\Delta\phi)\right] \tag{2.24}$$

The relative phase shift of the interferogram, $\Delta\phi$, is related to the wavelength, and the difference of the propagation length of the two arms, Δd. For sensing systems, the propagation length is related to the difference in optical path length between the two arms with refractive index, n, and arm length, L.[39]

$$\Delta\phi = \frac{2\pi\Delta d}{\lambda} = \frac{2\pi}{\lambda}\left(n_1 L_1 - n_2 L_2\right) \tag{2.25}$$

There are many different designs that can be used to build interferometers. Some of the most commonly used interferometer configurations are shown in Figure 2.3 for free space optics.[39] In most cases, analogous configurations can be made using optical fibre or other optical waveguides. Some common uses of each type of interferometer are discussed in the following paragraphs.

Young interferometers are arguably the simplest form of interferometer where light is shone from two slits and allowed to spatially interfere. The interferogram is then detected using a linear array detector or a camera. Changes to the effective path length of either arm will result in a phase shift to the interferogram.

In Michelson interferometers, light is split into two arms of either the same or different lengths which are terminated with mirrors. The light is then recombined at the same splitter into a single output. When one of the mirrors is placed on a translational stage, Michelson interferometers can be used for wavelength multiplexing allowing samples to be probed simultaneously with a broadband light source.[40-41]

Michelson interferometers with a moveable mirror are the operating technique behind Fourier transform infrared (FT-IR) spectrometers.[40]

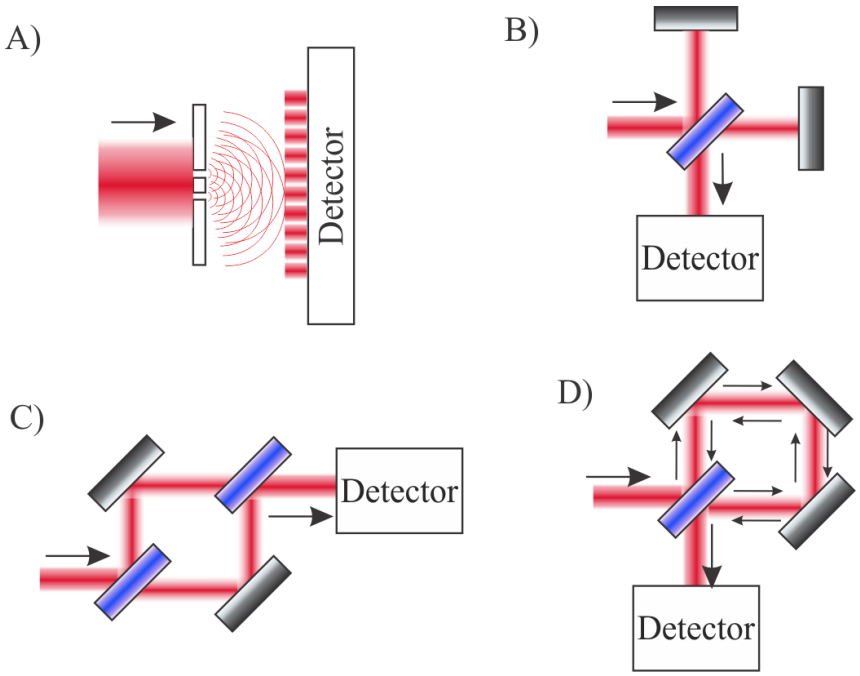

Figure 2.3: Several common geometries of free space interferometers. A) Young interferometers or double-slit interferometers emit light from two slits (or waveguide facets) and the diverging light spatially interferes. B) Michelson interferometers use a beam splitter to split the light into two paths that are reflected off two separate mirrors and then recombined. C) Mach-Zehnder interferometers splits the light into two distinct paths that are later recombined. One arm can pass through a sample while the second arm is used as a reference. D) Sagnac interferometers use a single beam splitter and a series of mirrors such that light simultaneously propagates in a clockwise and counter-clockwise direction within a ring cavity before being recombined.

Mach-Zehnder interferometers split the light into two arms and then recombine the light from the two arms back into a single output at a second splitter. These types of interferometers are useful for external wavelength calibration and optical heterodyne systems where frequency multiplexing is desired.[42-43] They are also commonly used for external intensity modulation of telecom lasers.[44]

In the Sagnac interferometer, light is split into two beams that are counter-propagating within a ring cavity. The resulting path length of the clockwise and counter-clockwise light depends on any external rotation of the cavity. Both free space and fibre based Sagnac interferometers have been shown to be suitable for the construction of gyroscopes to measure the rotation of Earth and other objects.[45-46]

Many other types of interferometers also exist, and this is only a summary of the most common types of interferometers. There are many limitations of free space interferometer for sensing applications, such as alignment stability and contamination of optics. Integrated interferometers that are either based on monolithic platforms or on waveguides have been developed to address these issues. Optical fibre-based and chip-level interferometers will be discussed in Sections 2.2.3 and 2.2.6, respectively, with specific examples of refractive index sensing applications.

2.2.2 Prism-Based Refractometers

Prism refractometers are the simplest and most mature method for measuring refractive indices of liquids and solids. The first prism refractometer, the Abbé refractometer, was introduced more than a century ago. Since then, a variety of geometries have become popular (Figure 2.4). The Abbé-type refractometer (Figure 2.4A) sandwiches liquid samples between two prisms and uses a telescope with an eyepiece or a detector to measure the refractive index based on the angle of refraction through the sample.[18] This method was simplified using the Pulfrich[17, 21, 47] or V-block refractometers[17, 19, 48-49] (Figure 2.4B and C). In the Pulfrich refractometer, light is shone horizontally at the interface between a prism and a sample. The light then refracts into the prism with an angle dependent to the refractive indices of the sample and the prism. With the V-groove refractometer, light is shone into a liquid cell and the angle of refraction is measured directly. Finally, handheld refractometers (Figure 2.4D) are used as quick inexpensive instruments for measuring the refractive index of food stuffs to determine sugar content in juices or alcohol content in beer and wine.[50-51] While handheld refractometers are inexpensive, they usually have poor accuracy of $\Delta n = 0.01 – 0.001$.[52]

More complex refractometers have been reported such as those measuring total internal reflection in dove prisms.[53] Alternatively, small refractive index changes can be measured using differential refractometry, i.e. by simultaneously measuring samples on two adjacent prisms.[54] Some refractometers are also designed to measure the angle of total internal reflection at a prism-sample interface. If a collimated light source is used, then both the light source and detector need to be rotated around the prism to collect

the angular Fresnel reflection and total internal reflection profile related to the refractive index of the sample (Figure 2.5A). This technique was used to measure the refractive index of biological tissues.[55] It was also used with a white light source and a spectrometer to simultaneously measure refractive indices of liquids between 400 - 900 nm.[56]

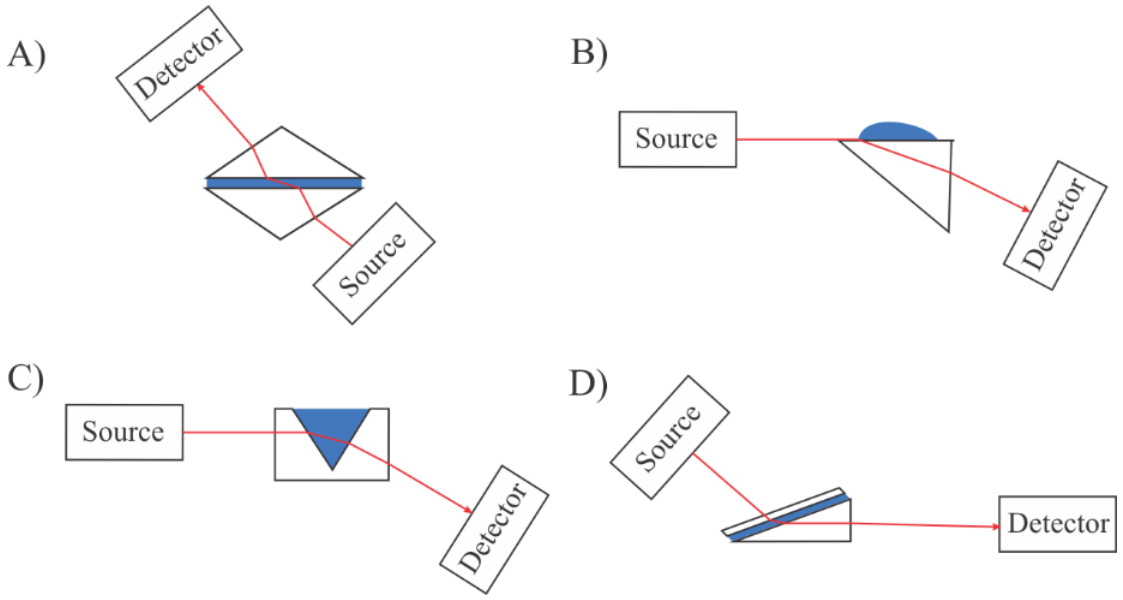

Figure 2.4: Schematic of common prism-based refractometers. In each case, the sample is shown in blue and a telescope would typically be present between the refractometer and the eyepiece or detector. A) in an Abbé refractometer, a liquid sample is sandwiched between an illumination and an analysis prism, and the angle of refraction trough the sample is observed. B) in a Pulfrich refractometer, light is shone parallel to the sample-prism interface and the angle that it couples in to the prism depends on the sample refractive index. C) in a V-block refractometer, light is shone horizontally into a glass prism and is refracted as it passes into a sample. D) in a handheld refractometer a liquid sample is placed between a glass slide and a prism. When it is held up to the light, the angle of refraction at the sample-prism interface is observed.

When laser light is shone directly onto an absorbing liquid, at normal incidence from the top of the prism, the angular intensity of the coupled light can be used to extract both the real and imaginary refractive indices as well as the thickness of thin films.[57] If an expanded beam is focused down to a point or line at the prism-sample interface and a camera is used as the detector, a larger range of angles can be simultaneously measured without having to rotate the source and detector around the prism (Figure 2.5B).[58] For thin transparent samples, this technique can also be used to extract film thickness in addition to their refractive index as will be discussed again in detail in Chapter 4.[58]

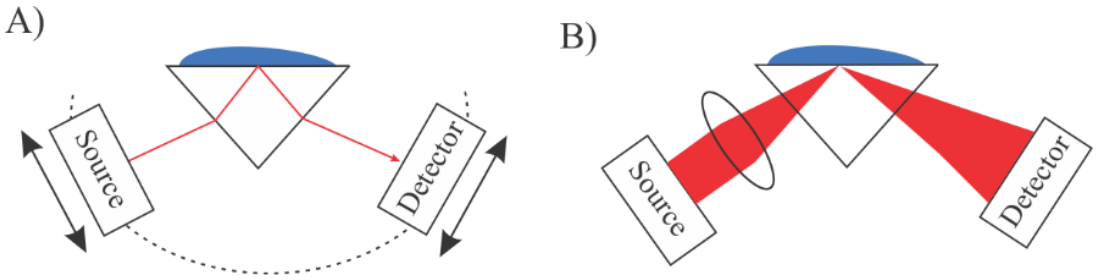

Figure 2.5: Illustrations of total internal reflection prism-based refractometers. The refractive index of a sample can be determined from the critical angle of total internal reflection and the angular Fresnel reflection profile below the critical angle. A) if a collimated source is used, the source and detector need to be rotated around the prism to measure the sample. B) If an expanded beam is focused down using a lens, then a range of incident angles can be simultaneously probed and a static measurement using an array detector can be used to determine the sample refractive index.

When a thin film is present on the total internal reflection prism refractometer, some of the light can be partially guided within the film (Figure 2.6). The resulting thin-film interference results in a series of equally spaced fringes that are indicative of the optical thickness of the film (*nd*). Measurement of the intensity of the first fringe while varying the incidence angle allows for measurement of the sample refractive index, while the fringe spacing allows for the thickness to also be extracted for thin films.[59-61]

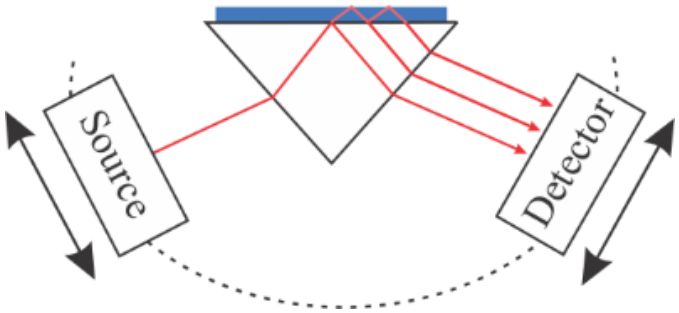

Figure 2.6: Schematic of a total internal reflection refractometer that can simultaneously measure film refractive index and thickness. Light can be quasi-guided within the thin-films resulting in an evenly spaced set of fringes. The fringe spacing is related to the refractive index and thickness of the film. The refractive index can be independently separated from the intensity of the first fringe as the incident angle is varied.

Typical commercial refractometers claim precision and accuracy of $\Delta n = 1\times10^{-4}$ with an accuracy $\Delta n = 1\text{-}2\times10^{-5}$ for temperature controlled models.[62-64] A commercial refractometer also exists using total internal reflection inside of a prism, similar to the one in Figure 2.6, and can measure both film refractive index and thickness at wide range of wavelength with accuracies of $\Delta n = 1\times10^{-4}$.[65]

The prism-based refractometers described in this chapter can easily be adapted to measure refractive indices of samples at any wavelength in the visible and near-IR. Typically, refractive indices are measured at the sodium-D line (λ = 589 nm), though often the refractive index is required at other wavelengths as most materials have substantial refractive index dispersion with wavelength. The refractive index measurements of liquids and solutions will be discussed in detail in Chapter 5 of this thesis. Measurements of solvent refractive indices at 1550 nm will be presented using our refractometer[66], and comparison will be made to other studies in the literature. Fourier analysis of images collected using a prism refractometer similar to the one in Figure 2.5B can be used to simultaneously measure the refractive index and thickness of thin films without needing to scan the incident angle.[58] This method was used to study the diffusion of water into SU-8 epoxy films (Chapter 6), and the diffusion of volatile organic compounds into siloxane polymers (Chapter 7). In the following sections both fibre-based and waveguide-based methods of measuring refractive indices will be briefly described.

2.2.3 Fibre-Based Refractive Index Sensors

There are a wide range of fibre-based refractive index sensors in the literature. Typically, they can be characterized as either grating-based sensors, interferometer-based sensors or reflection-based sensors and will be described in the next three sections. For refractive index sensing, typically, a fibre region will need to be etched, tapered, or polished such that the evanescent field can have a stronger interaction with the surroundings. Several detailed reviews have been published that highlight many chemical and biosensing applications using optical fibre probes.[9, 13]

2.2.3.1 Grating-Based Sensors

Optical refractive index sensors can be made using fibre gratings, where the refractive index of the fibre core is intentionally modified in a periodic fashion. Many useful reviews have been published describing the different types of grating-based fibre sensors.[67-70] Gratings can be permanently written by introducing defects into optical fibres using a phase mask and a high powered femtosecond IR[71-72], or UV excimer laser[73]. An electric arc, for example from a fusion splicer, can also be used with a translation stage

to write gratings.[74] Similarly, femtosecond lasers have been used to write gratings into waveguides.[75] Temporary gratings have also be reported where physical strain is used to compress regions of an optical fibre to generate a long period grating.[76-77] Gratings can be uniformly spaced, made with a varying period or refractive index (chirped gratings)[78] or even tilted relative to the fibre core[68].

There are two main types of fibre gratings, fibre Bragg gratings (FBGs) and long period gratings (LPGs). Fibre Bragg gratings have relatively short periods and act as mirrors reflecting a narrow range of wavelength.[70] Fabry-Perot cavities can be formed by trapping light between two FBGs where the reflection envelope is governed by the reflection spectrum of the first mirror and the cavity fringes obey the standing-wave conditions of the cavity. An illustration showing the reflection and transmission of FBGs and Fabry-Perot cavities is shown in Figure 2.7A and B. FBGs and Fabry-Perot cavities are commonly used as vibration sensors[69, 79-80] but can also be used for chemical sensing if the fibre is tapered or etched around the FBG grating or inside the Fabry-Perot cavity.[81-82]

Long period gratings have longer periodicity than FBGs and instead of acting as mirrors, they couple light into a fiber's cladding modes causing attenuation in the transmission spectrum of the core of the optical fibre. The wavelength of LPG resonance modes are related to the grating periodicity, Λ, and the effective refractive indices of the fibre core and the desired cladding mode, $n_{\text{eff, core}}$ and $n_{\text{eff, clad, i}}$, respectively.[67, 83]

$$\lambda_i = \Lambda\left[n_{eff,core} - n_{eff,clad,i} \right] \tag{2.26}$$

A schematic of LPGs with an illustrative transmission profile is shown in Figure 2.7C. One of the inherent challenges with LPG sensors is that the cladding refractive index must be adjusted such that a resonance will appear within the spectral window of analysis. This can require adding dopants to polymer coatings in order to raise or lower the refractive index of the fibre coating.[81] Additionally, the resonance wavelength response of LPGs is nonlinear with refractive index, which may further complicate their use in chemical sensors.[81]

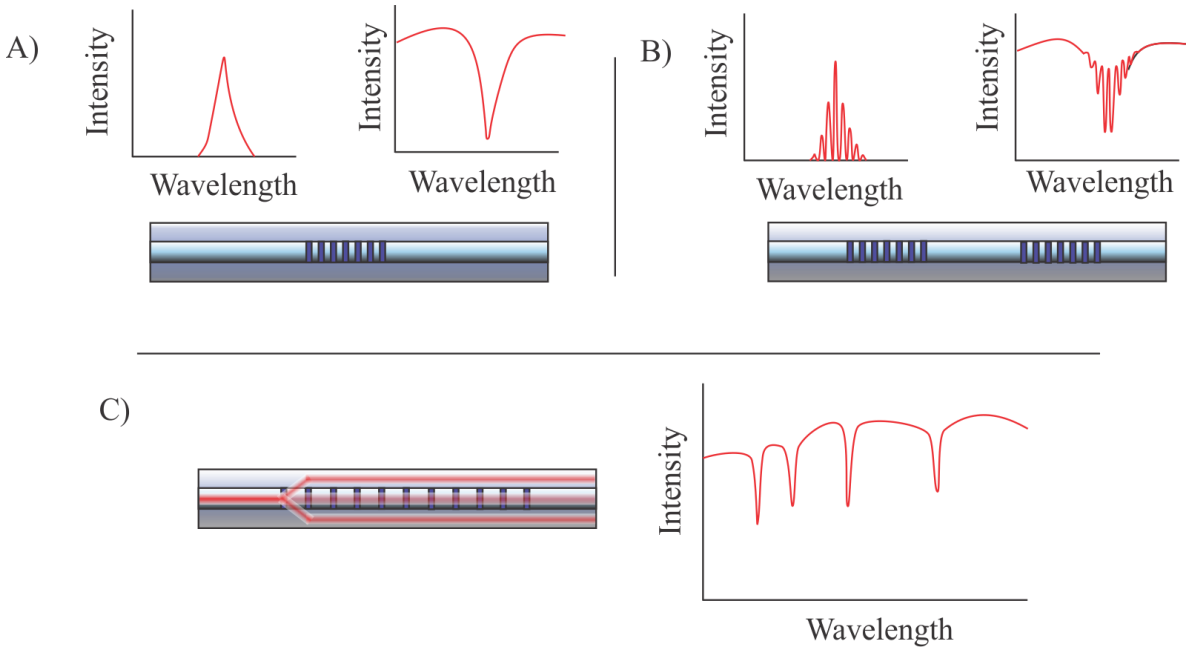

Figure 2.7 Schematics of fibre Bragg gratings, Fabry-Perot cavities of FBGs and long period gratings with illustrative reflection and transmission spectra. A) Fibre Bragg gratings act as mirrors reflecting a narrow range of wavelength. B) Fabry-Perot cavities of FBGs have the same envelope of the single FBG reflection but also contain a series of cavity fringes. C) Long period gratings couple light at specific wavelengths into cladding modes which can be observed as attenuation in the transmission signal.

Despite any potential challenges, several chemical sensing systems have been described using LPGs in the literature. Siloxane polymer coated LPGs have been demonstrated for sensing of volatile organic compounds (VOCs).[81] Calixarene coated LPGs have also been presented for the detection of BTEX (benzene, toluene, ethylbenzene and xylenes) compounds in solution.[84] Sulfide functionalized mesoporous silicate coated LPGs have also been show as suitable materials for detecting lead and other heavy metals in water.[85]

2.2.3.2 Fibre-Based Interferometers

There are many different geometries of optical fibre interferometers presented in the literature.[86-87] Mach-Zehnder (MZ) interferometers can be formed by offsetting the core of a centre optical fibre (Figure 2.8A),[88] and by splicing in a section of multi-mode fibre[35, 89] (Figure 2.8B), thinned-core optical fibre[90] or photonic crystal fibre between two single-mode fibres[36, 91-92]. Similarly, MZ interferometers can be made using two fibre tapers[93-94] or two long period gratings[95] to couple light between core and cladding modes.

The interference in each case is formed from the beating of light travelling in the core and the cladding of optical fibres. A sensing region may be formed either by tapering or etching the waveguide to expose the evanescent field of the cladding mode, increasing the interactions with the surroundings.[36] MZ interferometers have also been reported using two fibre couplers to split the light between two arms and then recombine them back to a single arm (Figure 2.8C).[96-97] In this case, one of the arms is either tapered or etched to expose the evanescent field while the second arm is left as a reference. Similarly, Michelson interferometers have been reported using a fibre coupler terminated with either fibre Bragg gratings or metallic mirrors and an optical circulator is used extract the back-reflected light (Figure 2.8D).[1-2, 69, 87, 98]

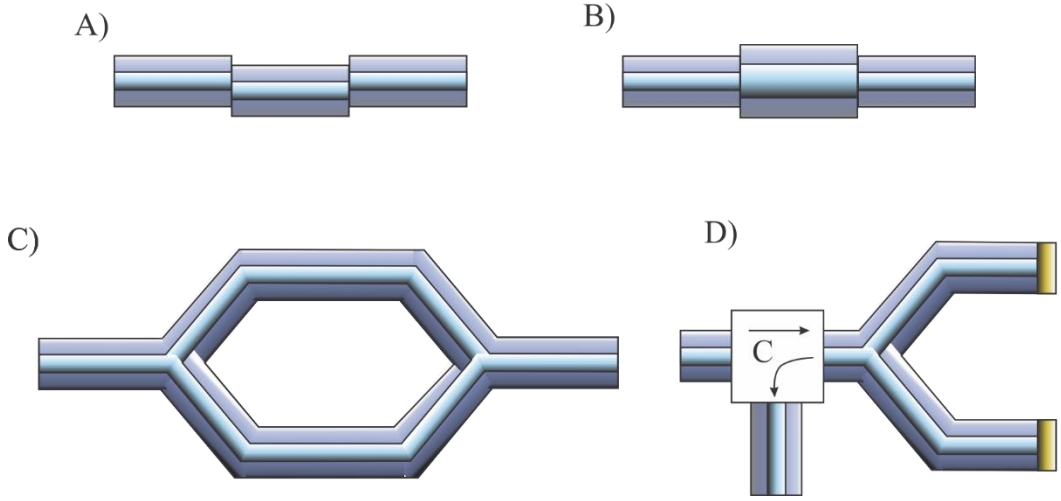

Figure 2.8: Sample geometries of optical fibre interferometers. A) The core of a region of fibre can be offset between two optical fibres causing light to interfere between core and cladding modes. B) MZ interferometers can also be formed by splicing a piece of multi-mode fibre or photonic crystal fibre between two fibres. C) MZ interferometers can be made using optical couplers to split the light into two arms and then recombine them to a single output. D) Michelson interferometers can be constructed using an optical circulator, C, and a fibre coupler where both arms are terminated in an FBG or a mirror.

While the majority of examples of fibre interferometers have only been characterized with sucrose solutions, there are several other sensing examples in the literature. For example, interferometers using PCF fibres have been used by our group and others to measure the refractive indices of gases and vapours of volatile organic compounds.[92, 99 100-101]

2.2.3.3 Reflection-Based Sensors

The refractive index of solutions can also be measured using the Fresnel reflection off the end of an optical fibre. The intensity of the reflected signal, *R*, at normal incidence from one medium into another is related to the refractive indices of the two media, n_1 and n_2.[39]

$$R_{12} = \left(\frac{n_1 - n_2}{n_1 + n_2} \right)^2 \tag{2.27}$$

Intensity measurements are frequently subject to noise from the light source and alignment in experiments. Using the ratio of the reflected intensity from a reference channel and from the sample can help compensate for fluctuations.

$$\frac{R_{reference}}{R_{sample}} = \left[\frac{\left(n_{fibre} - n_{reference} \right) / \left(n_{fibre} + n_{reference} \right)}{\left(n_{fibre} - n_{sample} \right) / \left(n_{fibre} + n_{sample} \right)} \right]^2 \tag{2.28}$$

This equation can be re-arranged to solve for the refractive index of the sample, n_{sample}.

$$n_{sample} = n_{fibre} \frac{\left(1 - \left(n_{fibre} - n_{reference} \right) / \left(n_{fibre} + n_{reference} \right) \sqrt{R_{reference} / R_{sample}} \right)}{\left(1 + \left(n_{fibre} - n_{reference} \right) / \left(n_{fibre} + n_{reference} \right) \sqrt{R_{reference} / R_{sample}} \right)} \tag{2.29}$$

A simple Fresnel reflection setup has been reported where a pulsed laser was shone through a 50/50, 2×2 optical coupler with two different lengths of optical fibre.[102-103] One fibre end was placed in the sample and a second in a reference solution. The light pulses were reflected from the end of each fibre end and, after recombination in a fibre coupler, they were detected with a photodiode. A schematic of this experimental setup is shown in Figure 2.9. While this is a very simple technique for measuring refractive indices, it is difficult to measure samples close to the refractive index of the fibre, which limits measurements to solutions of lower or higher refractive index than $n_{\text{SiO2}} \sim 1.45$.

We have constructed a similar apparatus to measure the refractive indices of cinnamaldehyde (Sigma Aldrich) solutions in 95% ethanol at 1550 nm. A sample oscilloscope trace and the two roots of equation (2.29) for a series of cinnamaldehyde solutions are shown in Figure 2.10. A 1 km fibre spool was

used on the sample arm so that the peaks could be spatially resolved, and an erbium doped fibre amplifier (EDFA) was used to amplify the laser light in the system.

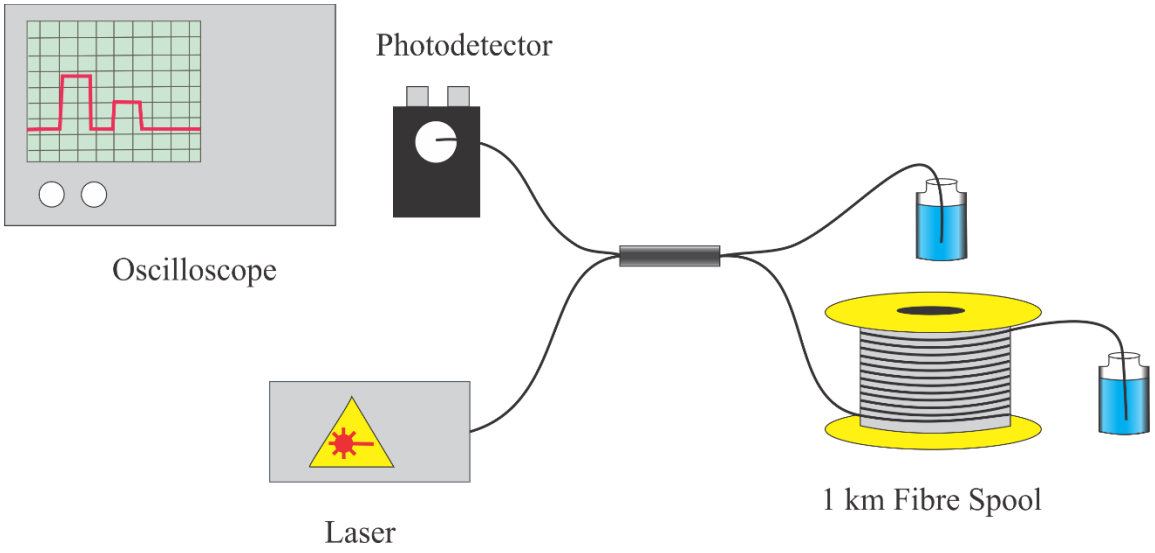

Figure 2.9: Refractive index sensing from Fresnel reflection off the end of an optical fibre immersed in a solution and reference liquid. This figure is based on the experimental setups of Chang and Kim.[102-103] Light from a pulsed source is split into two fibres using a 50/50 2×2 optical coupler with one immersed in a solution and the second in a reference liquid. The Fresnel reflection from the fibre tips was collected with a photodiode and analysed using an oscilloscope. The length of the two arms needed to be different so that the reflections could be temporally resolved.

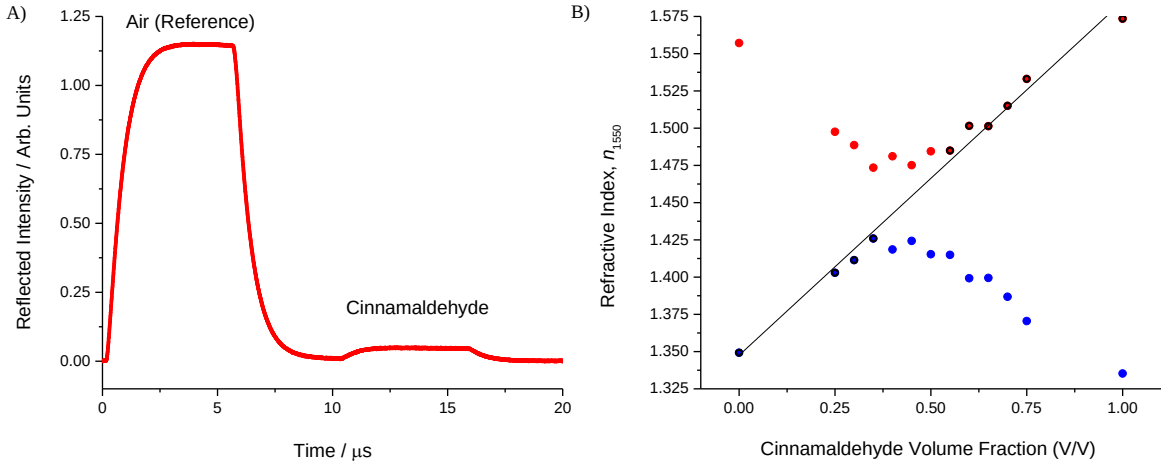

Figure 2.10: Sample data from Fresnel reflection experiments. A) A sample oscilloscope trace shows the reflection off a reference arm in air and a sensing arm in cinnamaldehyde. B) The two roots of equation (2.29) for a series of cinnamaldehyde solutions in 95% ethanol are shown. The points highlighted in black and the linear fit show points where the refractive indices could accurately be measured. The measurements were not reliable for refractive indices that were close to the refractive index of the fibre core.

Alternatively, a continuous-wave laser may be used with the setup in Figure 2.9. The refractive index change of the sample solution can then be observed from either the attenuation or from shifts in the interference pattern due to the phase difference in the Michelson interferometer.[104]

Single channel self-referencing interferometer probes have also been presented to measure solution refractive indices using Fresnel reflection at a fibre-liquid interface. Illustrations of three types of self-referencing fibre probes are shown in Figure 2.11. Reflection probes that can be immersed in solution have been demonstrated using a Fabry-Perot cavity made from two weakly reflecting FBGs[105] (Figure 2.11A), and a Michelson interferometer from splicing a section of multi-mode fibre within the single-mode fibre probe[89] Sengupta and coworkers used a bifurcated fibre probe to measure the refractive index of solutions from the interference between the Fresnel reflection off the fibre probe and the light reflected off a submersed mirror.[106] Similarly, Mudhana and coworkers used a lensed photonic crystal fibre (PCF) and a micro-machined mirror to create a probe for measuring the refractive index of solution (Figure 2.11B).[33] Pevec and Donlagic reported a self-referencing fibre probe created using a series of splicing and etching steps to create two optical cavities within a spliced fibre probe.[107] The first cavity was made by etching defects into the fibre core to measure temperature effects, and the second was made by etching an external cavity into a weakly resistant piece of optical fibre that was later coated with a TiO_2 mirror for refractive index sensing (Figure 2.11C).[107]

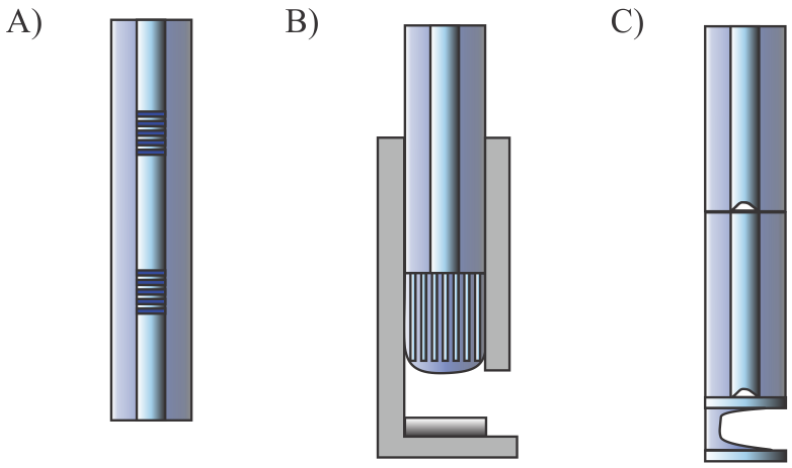

Figure 2.11 Illustration of self-referencing fibre-based reflection probes. Using two separate mirror cavities allows for the simultaneous compensation of temperature effects during experiments. A) A fibre probe can be made using two fibre Bragg gratings where the Fresnel reflection off the end of the fibre can be used for refractive index sensing of solutions.[105] B) A lensed PCF can be spliced onto the end of a standard optical fibre and the refractive index of solution determined from Fresnel reflection off the fibre tip and an external mirror.[33] C) Fibre probes can also be made using a series of etching and splicing steps.[107] Wet etching was used to introduce fibre core defects to create an optical cavity for temperature compensation.[107] A second cavity was generated by etching a weak section of fibre to create a sample reservoir for refractive index sensing of solutions. [107]

2.2.4 Whispering Gallery Mode Sensors

The concept of whispering gallery modes (WGM) is the photonic equivalence of the acoustic phenomena where sound can travel with low loss around the walls of a circular or domed room. Standing waves of whispering gallery modes (i.e. ring-cavity modes) occur at wavelengths that are an integer multiple of the effective mode path (*nL*, approximately the circumference). Light can be coupled into WGM of microring resonators or microsphere resonators using a fibre taper or prism coupler.[108-109] As a consequence of cavity enhancement the light intensity is increased within these optical cavities. The quality factor is a measure of the amount of light within the cavity compared with the round trip loss.[39] Many microsphere and microtoroidal resonators have very low loss with quality factors of $Q = 10^6 – 10^{10}$.[108, 110-111] Most silicon microdisk and microring resonators have much lower quality factors of 10^3-10^5.[112-113] The quality factor depends on the interrogation wavelength, the refractive index and absorption of the resonator material.[114]

WGM in microresonators may be used for chemical sensing, as molecules can accumulate on the surface of microresonators. When molecules bind, the diameter of the resonator increases and the WGM's effective refractive index changes, which – in turn – causes measurable wavelength shifts and changes to the free spectral range (FSR) of the resonances. A number of different geometries exist for whispering gallery mode resonators including microspheres[108, 115-116], microtoroids[110], bottle resonators[117-119], mircodisks[120-121] and microrings[112, 122]. An illustration showing each of these types of resonators is presented in Figure 2.12.

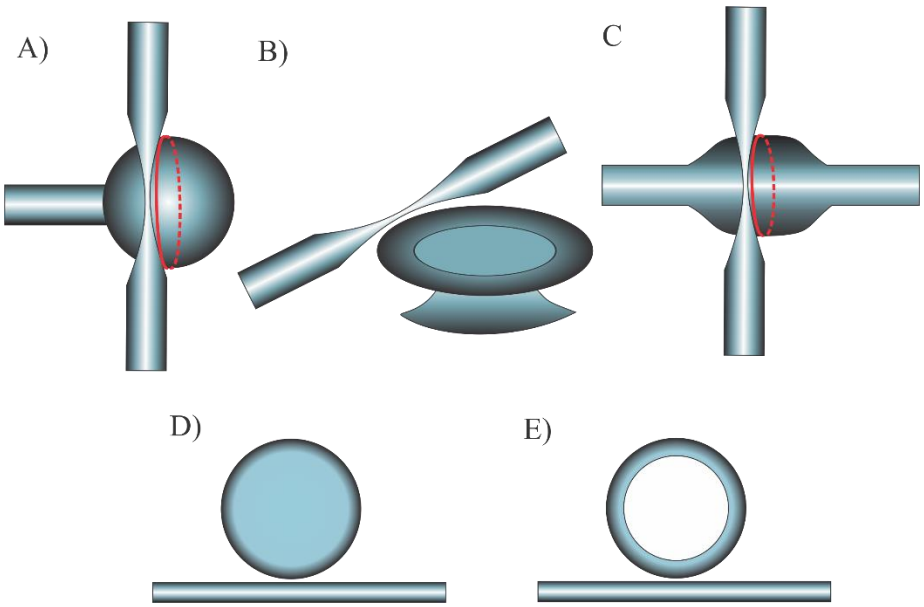

Figure 2.12: Schematic of several common types of whispering gallery mode micro-resonators. A) Microsphere resonators can be made using fusion splicers and high powered lasers. Typically light is coupled into microspheres using either a prism or fibre taper. B) Microtoroid resonators are fabricated directly on a substrate using lithographic and chemical etching processes. C) Bottle resonators can be formed by melting optical fibres. D) Microdisk and, E) microring resonators are fabricated on substrates using standard lithographic procedures.

Whispering gallery mode resonators can be made out of a variety of materials including fused silica[116], quartz[123], silicon[112, 120, 122], silicon nitride[124], silicon carbide[125], sapphire[126-127], titanium dioxide[128], calcium fluoride[111], and many types of polymers[129-130]. Whispering gallery resonances can also be excited around the equator of liquid droplets.[131-133] Since this thesis deals with silicon nanowire microring resonators and their use as refractive index sensor platforms, a detailed discussion of microring resonators with the theory governing their operation will be given in Chapter 8.

2.2.5 Plasmonic Sensors

Surface plasmons are a phenomena of thin metal films (typically gold, silver or aluminum) where the momentum of the incident light causes a delocalized oscillation of the electrons in the metal film to occur.[134] Surface plasmons can be excited by the evanescent field of an incident light beam during total internal reflection within a prism or an optical fibre.[14, 134] They can only be excited by p-polarized light (transverse magnetic, TM), and not by s-polarized light (transverse electric, TE).[134] When the photon momentum in the plane of the metal film is equal to the surface plasmon propagation constant, β, the reflected light at the metal film is attenuated as a surface plasmon resonance (SPR) is excited.[134-135] The propagation constant of the evanescent field of the p-polarized light is related to the wavelength of light, λ, the refractive index of the prism, n_p and the incident angle, θ.[134-135]

$$\beta_{ev} = \frac{2\pi}{\lambda} n_p \sin\theta \tag{2.30}$$

The propagation constant of the surface plasmons, β, depends on the angular frequency of the light, ω, the speed of light, c, and the dielectric constants of the metal, and the surroundings, ε_m and ε_s.[134-135]

$$\beta = \frac{\omega}{c}\sqrt{\frac{\varepsilon_m \varepsilon_s}{\varepsilon_m + \varepsilon_s}} \tag{2.31}$$

A schematic of a prism based SPR instrument using the Kretschmann configuration is shown in Figure 2.13. A series of lenses can be used to simultaneously probe a range of incident angles at the prism-gold interface. In this process, only a narrow range of incident angles will generate plasmon waves. This is indicated by the black line in the reflected light. An SPR spectrometer based on this configuration was constructed by Ms. Amy MacLean and others in our group. Simple and inexpensive SPR instruments can also be constructed using, a collimated laser that can rotated around the prism to collect the same angular reflectance information.[135-136] The inset of Figure 2.13 shows the excitation of a surface plasmon wave from a single angle of incident light.

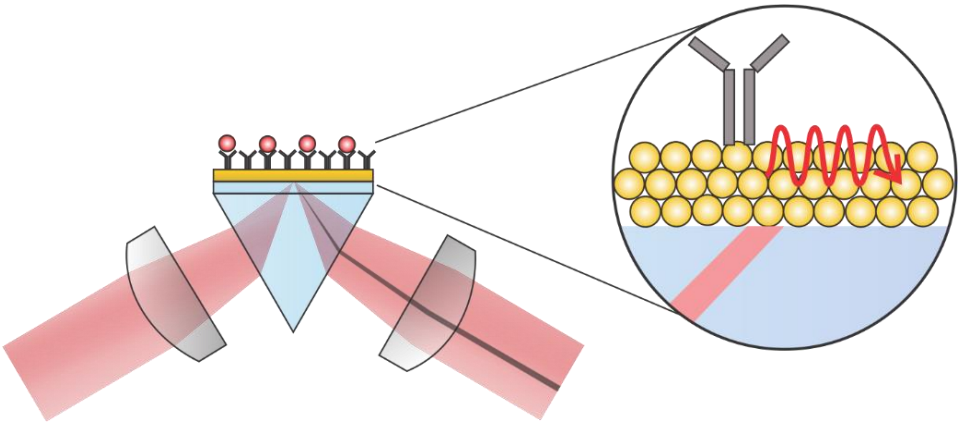

Figure 2.13: Schematic of a simple surface plasmon resonance instrument. An expanded beam is used to probe the prism metal surface from a range of incident angles. Only a narrow range of angles will be able to excite plasmon waves and the reflection will be attenuated. The inset shows a small range of angles exciting a plasmon wave on the metal surface.

Since the momentum of the evanescent field must match the energy needed to excite plasmon modes in the gold surface, the resonances can be probed by varying either the incident angle or wavelength of the light.[14, 134] A schematic showing the shape of a typical SPR resonance is shown in Figure 2.14.

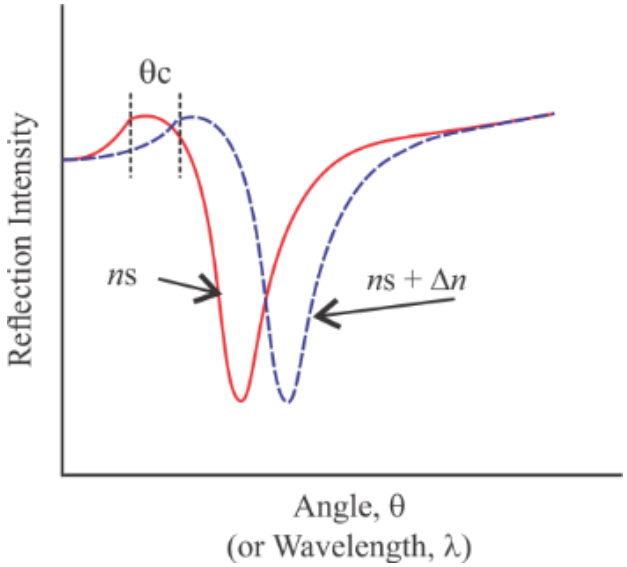

Figure 2.14: Illustration of a typical SPR resonance curve.[14] The reflected intensity will go through a resonance by either scanning the incident angle or the wavelength of the light. The small initial dip marks the critical angle of total internal reflection. The blue curve shows the resonance shift that would occur if the refractive index above the metal film changes by Δn.

While many prism-based SPR instruments are commercially available,[137-138] it is also possible to excite plasmons using metal gratings[139], metal coated optical fibres,[140-142] or metal coated planar waveguide

devices[143]. Fibre-based SPR sensors have also been developed with sensing elements using gold, silver and aluminum in series on the same probe.[144] Localized plasmon resonances can be excited using nanohole arrays and metal nanoparticles.[145-147] Several detailed review articles have been published showing the full ability of SPR for both chemical and biological sensing applications.[14, 148]

SPR is most commonly employed for bio-sensing applications.[15-16] Thiols,[149-151] and more recently carbenes[152] can be used to functionalize gold coatings with organic compounds to allow tethering of antibodies and other proteins to the surface of an SPR slide. These molecules can then react with antigens in solutions flowed over the device, resulting in a refractive index change at the metal layer.

Surface plasmon resonance can be used for other types of chemical sensing[148, 153] and has comparable sensitivities and detection limits with prism-based and waveguide-based refractometers. With commercial scanning instruments, there is a trade-off between angular range of measurement, and angular resolution when monitoring dynamic processes in order to maintain a suitable time resolution.

2.2.6 Chip-Level Sensors

Integration of refractive index sensors into chip-level devices has many advantages over optical fibre sensors. Chip-level optical waveguides can be made out of a variety of materials including silica[154], silicon nitride[124, 155-156], silicon[112, 157]and polymers[158-159]. Devices can be constructed with a high degree of accuracy and repeatability through lithographic and chemical etching processes.[157] In many cases, devices can be made on large wafers producing hundreds of identical sensors in a single fabrication run.[156-157] Since it is not trivial to incorporate light sources and detectors directly on optical waveguide chips, it is often preferred to couple light into optical waveguide chips from external light sources, and use either cameras or optical fibre coupled photodetectors to record transmitted light intensities. This may require high-precision alignment stages or optics.

For many of the previously described fibre-based sensors, chip-level analogues have been presented. For example, on-chip Fabry-Perot cavities have been presented using silicon photonic Bragg gratings that were etched into a chip (Figure 2.15).[160] Here, siloxane polymer coatings were cast into the

mirror cavity, and resonance shifts were observed from the deformation of the silicon gratings from the polymer swelling when exposed to volatile organic compounds.[160]

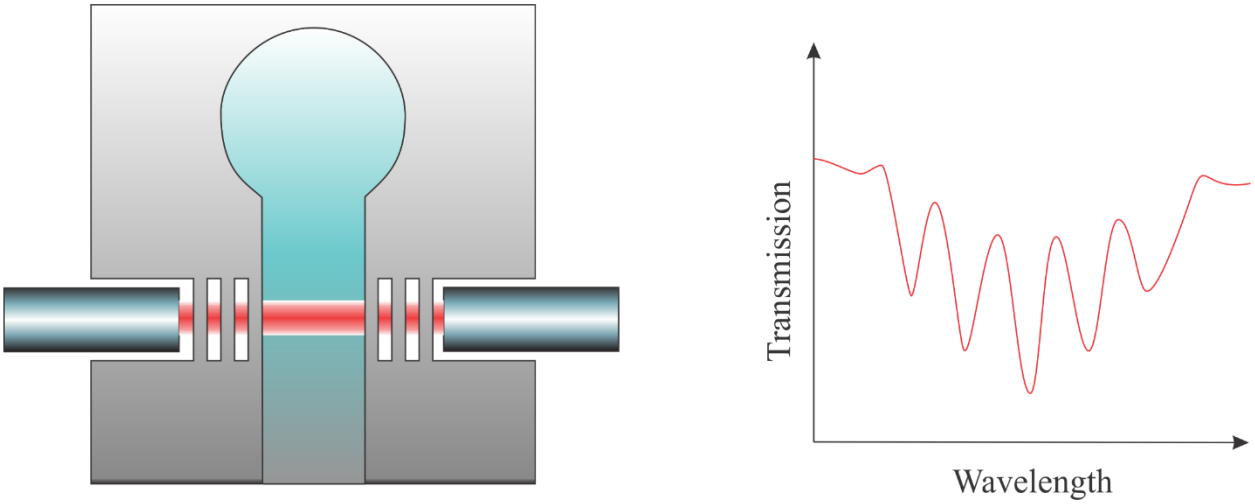

Figure 2.15: Schematic of a chip-based Fabry-Perot cavity formed from two silicon Bragg gratings. The holes forming the mirrors, the well in the centre of the cavity, and the alignment grooves for the optical fibres were all made using deep reactive ion etching. Polymers could be solvent cast into the channel between the Bragg mirrors for analysis. The transmission spectrum will have the overall envelope of the reflection of the first mirror with a series of cavity fringes inside, as is illustrated on the right.

Chip-level interferometers have also been demonstrated. A simple Young interferometer was developed using a set of parallel planar silicon nitride waveguides.[155] A laser was coupled into the waveguides using a grating coupler. One of the channels was left exposed for functionalization while the other channel was buried under a protective layer of silica. The output of the two waveguides coupled out through gratings and the light spatially interfered. The interference pattern was detected using an inexpensive CCD or CMOS camera chip (Figure 2.16). The observed interferogram was the combination of diffraction from the individual waveguides and a two-beam interference. Using this technology, Edmiston and coworkers conducted ppt level detection of the vapours of explosives, including trinitrotoluene, TNT.[155]

Mach-Zehnder interferometers can also be made from optical silicon nanowire waveguides, where one arm is buried under a protective overcoat while the other arm is exposed to the surroundings

for functionalization and chemical sensing.[157] An example of a silicon waveguide MZ interferometer is shown in Figure 2.17A.[157]

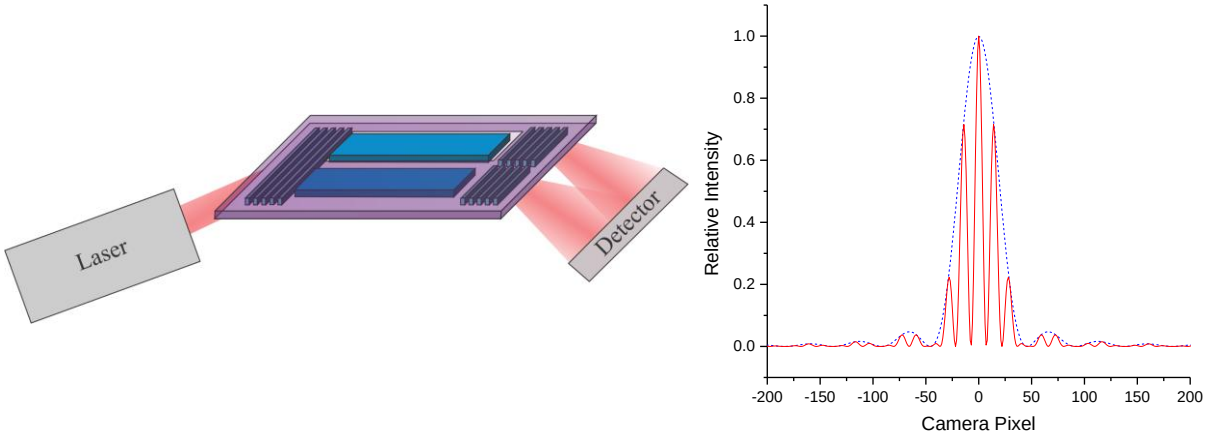

Figure 2.16: Schematic and simulated interferogram of a chip-level Young interferometer. The laser is coupled into and out of both waveguides using grating couplers. The light from the two waveguides is spatially interfered and the pattern is captured using a CCD or CMOS camera. The resulting interferogram is a combination of single slit diffraction (blue dashed line) and two-beam interference. Silicon nitride Young interferometers were previously described by Edmiston and coworkers. [155]

Microring resonators can be also constructed from these optical waveguides. Since the refractive index contrast between the silicon nanowire and the surroundings is very high, photonic wire waveguides can be coiled to reduce the surface area on chips (Figure 2.17B),[112]left as individual rings (Figure 2.17C), [112] or elongated to form race track resonators.[122]

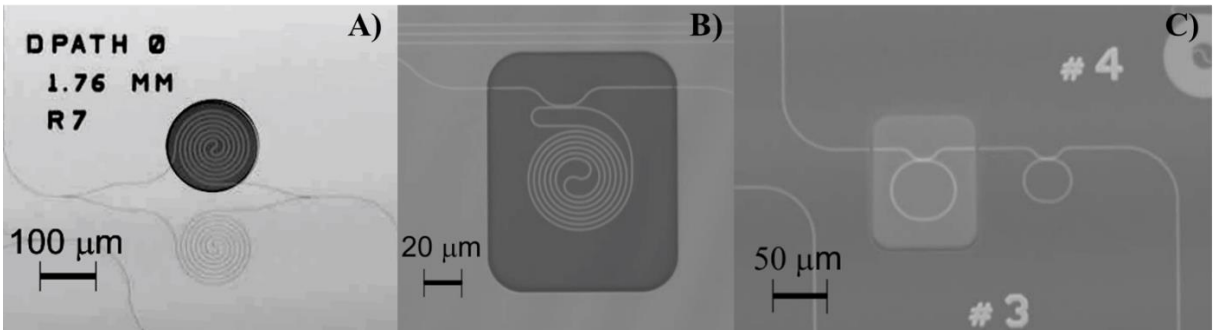

Figure 2.17: Optical profiler images of silicon wire waveguide optical devices. A) A Mach-Zehnder interferometer is shown with coiled arms that are 1.76 mm long. B) A 936 µm long coiled silicon ring resonator. C) A pair of silicon ring resonators 185 µm and 134 µm in circumference.

Many groups have used silicon photonic waveguides for a range of bio-sensing and environmental sensing applications. Carborg and coworkers created a microfluidic chip for simultaneous analysis of 8 silicon nitride microring resonators.[156] Silicon microring technology has been commercialized for simultaneous on-chip test for many different biomolecules in blood samples.[161] Coated silicon microring resonators have also been demonstrated for the detection of ethanol vapour, ammonia and other VOCs.[113, 162-163] A more detailed description of the theory behind different optical devices fabricated out of photonic optical waveguides is presented in Chapter 8.

2.3 Methods of Measuring the Refractive Index and Thickness of Thin Films

It is important to understand the changes in the optical properties of polymers and other coatings when exposed to analytes in order to properly interpret the response of coated microphotonic devices. In this thesis, an independent method to determine both the refractive index and thickness of thin-films is described for this purpose. There are a number of different methods to accurately measure the thickness of thin films, and many of the conventional techniques require expensive and complicated instrumentation. For example, the thickness and surface morphology of samples can be accurately measured using scanning electron microscopy (SEM), and transmission electron microscopy (TEM), but these methods require a great degree of sample preparation, and either sputter coating samples with conducting metals or thinly slicing samples for measurements. This is not practical for dynamic experiments and can be damaging to samples. There are also contact methods including stylus profilometry and atomic force microscopy (AFM) where a cantilever is dragged over or dragged near a sample and the vertical displacement of the cantilever is measured through a change in electrical signal (current or voltage). While these techniques have a very high resolution they do not provide any information about the refractive index of thin films.

For the purpose of this thesis, discussion will focus on optical techniques that can be used to simultaneously measure the refractive index and thickness of thin films. Some of these techniques, including spectroscopic reflectometry and optical microscopy techniques, are only able to measure optical thickness of a material (*nd*). Techniques like neutron reflectometry and spectroscopic ellipsometry are able

to independently resolve both the thickness and refractive index of thin film samples. The thickness and refractive index can be also measured using interferometric refractometry[58] as will be discussed in great detail in this thesis, with the theory discussed in Chapter 4.

2.3.1 Thin-Film Spectroscopic Reflectometry

The intensity of reflected light at normal incidence from a surface, R_{12}, is the square of the reflection coefficient, r_{12}, and is dependent on the refractive indices of the two boundary media, n_1 and n_2 .[164]

$$R_{12} = {r_{12}}^2 = \left(\frac{n_1 - n_2}{n_1 + n_2} \right)^2 \tag{2.32}$$

When light is reflected off of a transparent thin film at normal incidence, it partially reflects from the top and bottom surfaces resulting in thin-film interference fringes. The spacing of the fringes is related to the product of the film's refractive index, n_2, and thickness, d.[164] Here, n_1 is the refractive index of air, n_2 the refractive index of the film and n_3 the refractive index of the substrate beneath the film. The reflection coefficient r_{23} is calculated analogous to r_{12} in equation (2.32).

$$r_{total} = \frac{r_{12} + r_{23} e^{-2i\beta}}{1 + r_{12} r_{23} e^{-2i\beta}} \tag{2.33}$$

The phase delay from reflection within the film is denoted as β.[164]

$$\beta = \frac{2\pi n_2 d}{\lambda_0} \tag{2.34}$$

The reflectance intensity is then the square of equation (2.33) containing the complex conjugates of the imaginary components.[164]

$$R_{total} = \frac{{r_{12}}^2 + {r_{23}}^2 + 2 r_{12} r_{23} \cos(2\beta)}{1 + {r_{12}}^2 {r_{23}}^2 + 2 r_{12} r_{23} \cos(2\beta)} \tag{2.35}$$

This technique can also be used for angles besides normal incidence, in which case, the reflection spectrum will depend on the polarization and the incident angle of the light.

A thin-film spectroscopic reflectometry experiment operated at normal incidence can easily be assembled with a fibre probe, broadband light source and a spectrometer as is shown in Figure 2.18. The

intensity of reflection from a film may be quite weak, so multi-fibre probes can be used to collect more light for the spectrometer. The thin-film reflectance spectrum was calculated using equation (2.35) for a 2 µm thick fused silica film on a high index N-SF11 glass slide, and is also shown in Figure 2.18. The wavelength dependent refractive indices of both materials were calculated from dispersion information available in the literature.[165-166]

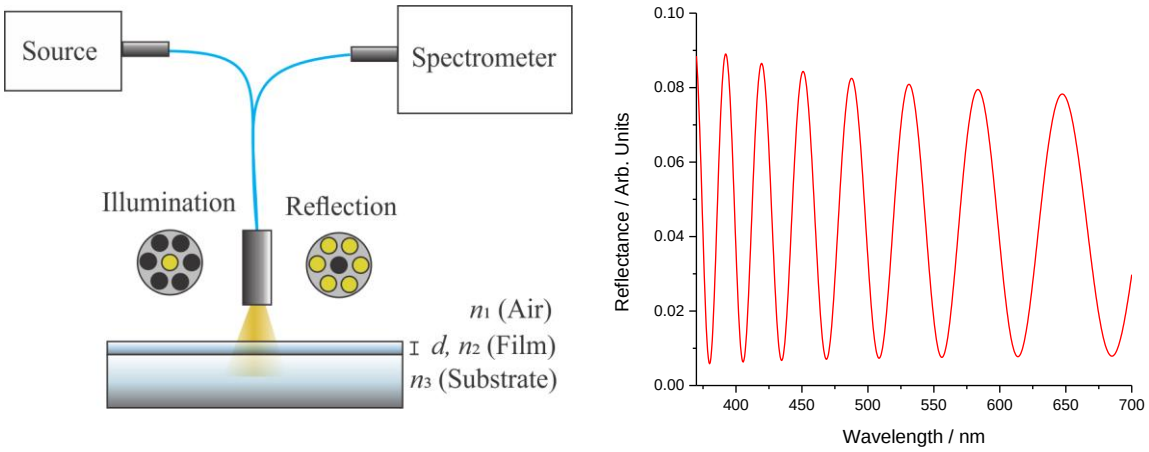

Figure 2.18: Schematic of a simple thin-film reflectance experiment with simulated data using equation (2.35). Typically the reflectance signal will be quite weak, and a multi-fibre probe can be used to collect more reflected light for the spectrometer. A simulated reflectance spectrum is shown for a 2 µm fused silica film on an N-SF11 high index glass substrate, with the wavelength dispersion accounted for using coefficients from the literature.[165-166]

One of the major challenges with spectral thin-film reflectometry is finding the wavelength dispersion information for the refractive indices of the film and the substrate. To effectively account for the dispersion, the refractive index must be calculated for each wavelength using Cauchy or Sellmeier coefficients and these may be difficult to obtain for complicated materials and polymers. The refractive indices of fused silica and Schott N-SF11 high index flint glass are shown in Figure 2.19 between λ = 370-700 nm to highlight this effect.[165-166] The second challenge with thin-film reflectometry is that the refractive index and thickness are intertwined and only the optical thickness can be determined (*nd*). In order to separate these two parameters, either the film identity must be well known so that Sellmeier or Cauchy parameters can be used, or the thickness must be previously well defined. Despite these challenges, several commercial instruments have been developed to measure thin films of thicknesses from 20 nm to several

microns with the specific limits dependent on the transparency and refractive index of the films being studied.[167-169]

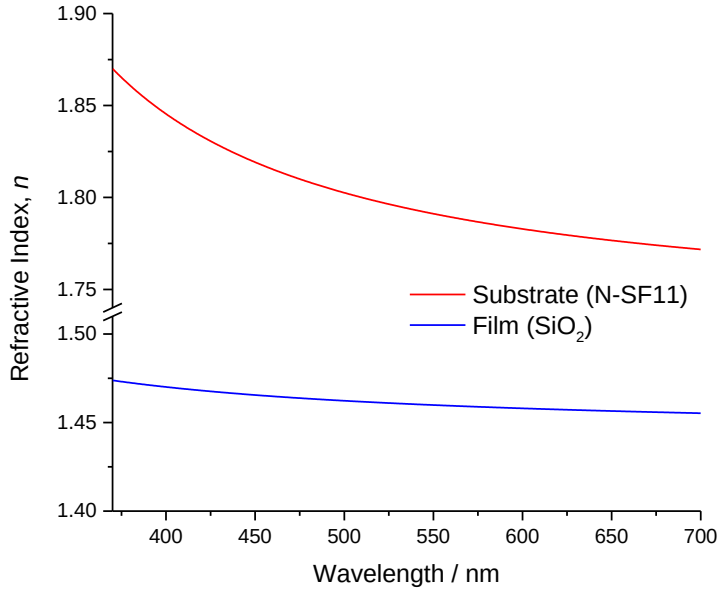

Figure 2.19: Refractive index dispersion for fused silica and Schott N-SF11 high-index glass. The refractive indices were calculated between λ = 370-700 nm from Sellmeier coefficients in the literature. [165-166]

Thin-film reflectometry has been shown to be useful for the in-situ thickness measurement of silicon dioxide layers formed during reactive ion etching of silicon substrates.[170] It has also been demonstrated in conjunction with ellipsometry to study the oxidation of copper films exposure to oxygen gas at high temperatures.[171] Spectroscopic reflection is useful for the measurement of metal and inorganic materials where the composition and thickness are stable and can be well defined. However, using spectroscopic reflectometry to study polymer films is complicated. Polymers may both swell and have refractive index changes when analytes partition within them.

2.3.2 Microscopy Techniques

Besides electron microscopy, there are a couple of modern optical microscopy techniques which are suitable for measuring film thickness and refractive index. Optical microscopy, or optical profilometry, has the added benefit that it can probe the film roughness or thickness over a larger field of view. Both

confocal microscopes and white light interferometric microscopes can be used to measure the morphology of thin films.

Confocal laser scanning microscopes focus an expanded laser beam using a microscope objective onto a sample surface. If the surface is at the focal point of the laser, the light reflects back over the original path, where it is focused down using a lens and passed through a narrow pinhole or slit to be measured by the detector (Figure 2.20).[172-174] If the surface is above or below the focal point of the laser, the light will strike the beam block and will not pass through the slit to the detector (red and blue lines in Figure 2.20).[172-174] When the height is scanned between the objective and the sample, two high intensity peaks will be observed (one from reflection off the top surface of the film and a second from reflection off the substrate at the bottom of the film). A sensitive stepper motor is used to accurately define the optical height (*nd*) of the film with a vertical resolution ~ 2 nm[175], and a lateral resolution of ~200-300 nm.[174]

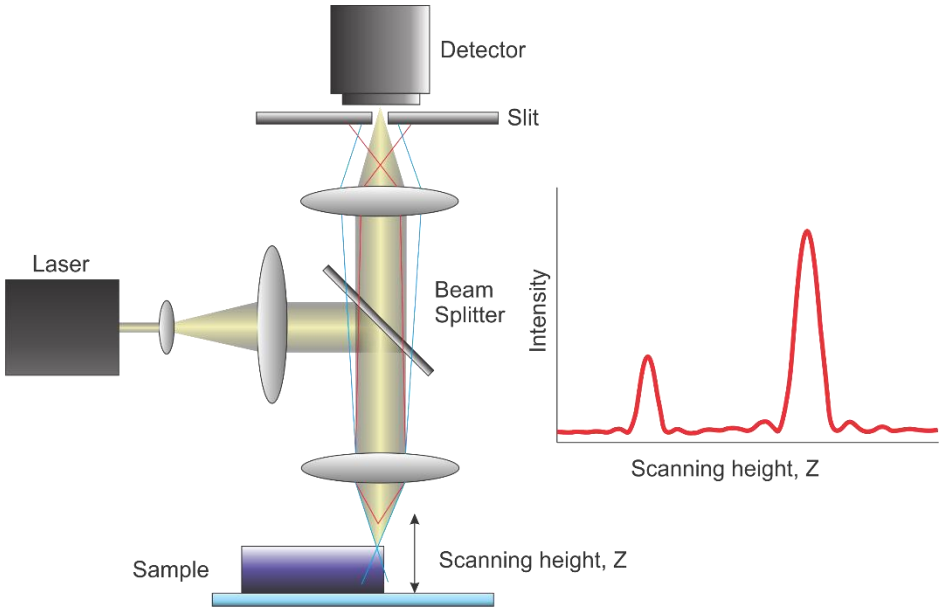

Figure 2.20: Schematic showing the simplified operating principle behind confocal laser microscopy. A laser is first expanded and then focused onto the surface of a sample using an objective. If the sample is at the focal point then the light will reflect back through the original path where it is focused down through a pinhole to the detector. When the sample is above or below the focal point of the laser, then the light will strike the beam block and not reach the detector (red and blue lines). The distance between the objective and the sample is varied and two intense reflection peaks are observed from the top and bottom surfaces of the film.

Confocal microscopes are frequently used for biological sectioning, where a dichroic beam splitter or filter can be used to detect fluorescence at a longer wavelength than the initial excitation source.[173] This allows for greater image resolution of bacteria and other types of cells.[176-177]

White light interference microscopy is another technique that can be used to measure thin-film thickness with high accuracy. In this technique, the light from a white light source (eg. white light LED) is shone onto a surface through a Michelson or Mirau interferometer objective. The interferometer objectives contain a fixed mirror to act as a reference arm, which interferes with the reflected light off the sample. As the height between the sample and the objective is scanned the interferogram is different for each wavelength, and the combined interferogram of the wave packet will pass through a maximum intensity (Figure 2.21). When coupled to a CCD camera, the corresponding interferogram of the sample is measured simultaneously at each pixel over the field of view of the objective. When scanning over transparent films, two maxima are observed in the interference envelope, i.e. from reflections off the top surface and off the substrate below the film. The height difference between these two peaks is related to the optical thickness of the film. Just like confocal microscopy, white light interferometry only measures the optical thickness (*nd*) and knowledge of the material's refractive index is needed to obtain the film thickness and vice versa. When a section of the film is removed to expose the bare substrate, the film thickness can be accurately measured from the step to the substrate. While this does not provide information on the film refractive index, it can be used to calibrate the thickness so that the refractive index can be extracted when measuring an adjacent section of the bulk material.

The next two techniques, neutron reflection and ellipsometry are optical techniques that allow for simultaneous measurement of a film's refractive index and thickness and will be discussed in the following paragraphs.

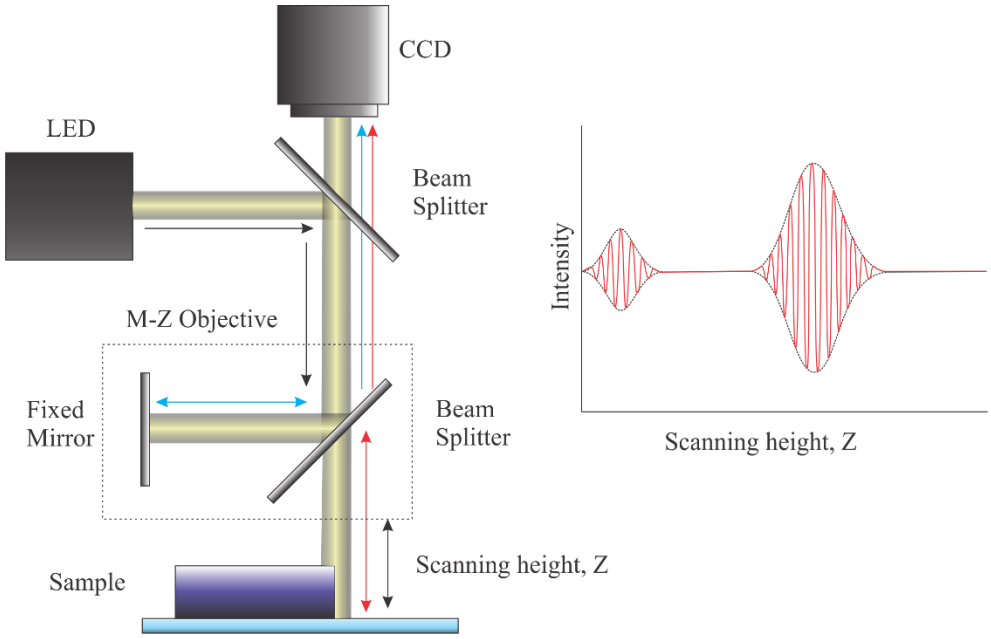

Figure 2.21: Schematic of the operating principle behind scanning white light interferometry. A white light source is shone through a beam splitter so one arm is reflected off the sample (red lines) and a second reference arm is reflected off a stationary mirror (blue lines). The two beams are recombined and the interference intensity is measured using a CCD camera where each pixel represents a different spatial location on the film. The microscope head is lowered using a stepper motor and the height where each pixel passes through an intensity maximum is correlated to the optical thickness of the film.

2.3.3 Neutron Reflection

Similar to light, neutrons can also be used to measure the thickness and refractive index of thin films.[178-180] According to the particle-wave duality, a collimated beam of neutrons will behave similar to light and can undergo both reflection and interference. When neutron beams strike a surface above the critical angle of incidence, they are totally reflected off a surface. At smaller incident angles, similar to light, neutrons undergo Fresnel reflection.[178-180] When neutrons reflect off a thin film, interference fringes are observed in the Fresnel region of reflection.[178-180] This process is similar to x-ray reflection and may be compared to thin-film interferometric refractometry, which will be discussed in Chapter 4.

Neutron reflection has a number of advantages over using photons when characterizing materials. Neutrons interact with the nucleus of the atoms while photons interact with the electrons around atoms.[178,

[180] This means that the scattering distance of neutrons in a material will be different for different atoms and even different isotopes of the same element.[178] Neutron reflection can also be used for film profiling and can measure the change in film composition with depth.[178] This provides a great deal of information that cannot be obtained using light. A clear disadvantage of neutron reflection is that the refractive index is measured at the de Broglie wavelength of the neutron (typically in the wavelength range of x-rays). This index is considerably different from the refractive index at visible and infrared optical frequencies. Additionally, neutron reflection requires specialized equipment. For example, neutron sources require either a nuclear reactor or a particle accelerator. Obviously, these infrastructure costs are prohibitive for research groups interested in examining a large number of samples.

2.3.4 Spectroscopic Ellipsometry

Spectroscopic ellipsometry is a powerful technique for determining the refractive index and thickness of multilayer thin-film systems.[24, 181-182] Many commercial instruments are available that can measure film thicknesses from 0.1 nm to 50 μm while simultaneously measuring the refractive index of each layer.[183] Ellipsometry uses a polarizer to switch between s- and p-polarized light and the ratio, ρ, of the two reflection coefficients r_p and r_s is measured and is related to two angles, ψ and Δ.[24]

$$\rho = \frac{r_p}{r_s} = \tan\psi e^{i\Delta} \tag{2.36}$$

The $\tan\psi$ term is related to the amplitude of the reflection, and Δ is the optical phase difference between the two polarizations of the reflected light.[24] A phase analyser is used to measure the reflected elliptical polarization and a broadband detector measures the intensity of each wavelength in the spectral range of the source.[24] To ensure that the correct solution of the system is found, this process is repeated at a series of different incident angles, θ.[24] Figure 2.22 shows a schematic of the spectroscopic refractometer with a photograph of a commercial device.

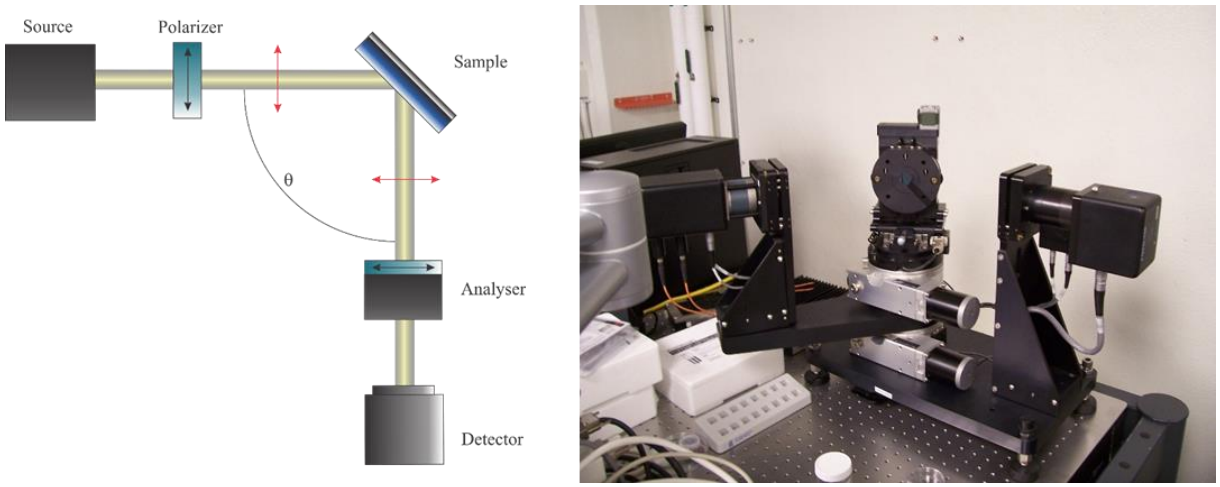

Figure 2.22: Schematic and photograph of a variable angle spectroscopic ellipsometer. A broadband source (240-1700 nm) passes through a polarizer to switch between s and p polarized light. The light is then reflected off a sample and a polarization analyser and a broadband detector is used to measure the amplitude and phase difference of the elliptically polarized reflected light. The photograph shows a commercial variable angle ellipsometer (J.A. Woolam, Lincoln, NE)

Sample spectra of the two angular components of the polarization (ψ and Δ) are show for a 700 nm mesoporous silicate film at four incident angles (θ = 45-60°) in Figure 2.23. The film was prepared by Dr. Xiaowei Wu and the measurement and analysis was performed with Mr. Rodrigo Becerra (Department of Physics, Queen's).

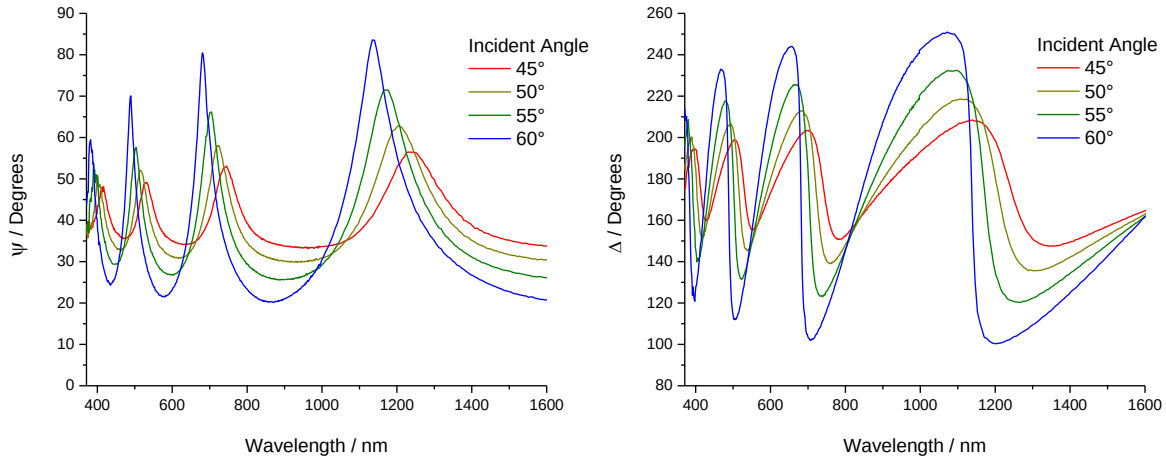

Figure 2.23: Sample spectra of the two angular components of the polarization (ψ and Δ) of a 700 nm silicate film on a silicon substrate for incident angles between 45° and 60°. The fringe structure is related to the optical thickness of the film. The fitting model (not shown) included a 1.7 nm native silicon dioxide layer and a 1 mm silicon substrate.

The experimental collection of data using variable angle spectroscopic ellipsometers is very quick and simple, but the analysis can be very complicated. Once the data is collected a model of the system must be created including the refractive indices, absorption coefficients and thickness of each layer in the system. For each layer in the model, the effects of dispersion must be accounted for and the refractive indices need to be calculated using Cauchy or Sellmeier equations. Once the model is created, the expected angles ψ and Δ are simulated, and the mean squared error, *MSE*, is calculated from the difference between the measured and calculated ellipsometer parameters (ψ and Δ) at each incident angle, θ. Here, $\delta\psi$ and $\delta\Delta$ are the uncertainties on the measured angles and M is the number of incident angles studied.[181]

$$MSE = \frac{1}{2M}\sum_{j=1}^{M}\left[\frac{\left(\psi_j^{Meas} - \psi_j^{Calc}\right)^2}{\delta\psi_j^{\,2}} + \frac{\left(\Delta_j^{Meas} - \Delta_j^{Calc}\right)^2}{\delta\Delta_j^{\,2}}\right] \tag{2.37}$$

The refractive index, absorption coefficient and thickness are all varied for each layer and a least squares fit is used to converge to the solution with the smallest MSE.

While ellipsometry is useful for measurement of static samples, it is difficult to study dynamic systems (e.g. partitioning of an analyte into a polymer film) as the beam path must remain unobstructed between the source and the detector. Additionally, both the refractive index and thickness parameters would have to be independently fit for each measurement taken. Special sample dosing chambers have been presented with windows for the beam to access the sample while allowing analytes to be exposed to a film under study.[184-185] Ellipsometry can also be used to study absorbing films[186] and can be modified to image surfaces[187]

2.4 Chemical Refractive Index Sensing

The challenge with developing suitable chemical sensors on refractive index sensing platforms is overcoming the non-selectivity of the sensing platforms. In order to achieve this, it is essential to find materials that will only interact with, or preferentially interact with a target group of analytes. A number of approaches can be taken depending on the type of analyte being studied. A brief introduction is provided in the next sections to describe what types of materials may be suitable for the detection of volatile

compounds, heavy metals and biomolecules. Two reviews of fibre-based refractive index sensors by Wang and Wolfbeis contain a detailed review of materials that have previously been used for a wide range of target analytes.[9, 13]

2.4.1 Sensing of Volatile Compounds

For small gas molecules, typically metal surfaces are used for refractive index sensing applications. Palladium coatings interact strongly with hydrogen gas and have been shown suitable for leak detection using different types of fibre sensors[188] and SU-8 microdisk resonators[130]. Similarly, ZnO coatings have been shown for the detection of ethanol vapour on microresonators,[113] and the detection of hydrogen sulfide gas (H_2S) using fibre sensors and SPR.[189] A polymethylmethacrylate (PMMA) coating incorporating bromocresol purple, as a pH indicator, has been demonstrated for the detection of ammonia using silicon microring resonators.[162] Ammonia detection was also demonstrated using an optical fibre SPR device coated with a composite polymer of PMMA and a reduced graphene oxide.[142]

Siloxane polymers, for example polydimethylsiloxane, PDMS, are common extraction matrices for non-polar volatile organic hydrocarbons (e.g. hexane, cyclohexane, benzene, toluene, xylenes, etc.).[190-191] Siloxanes are non-selective absorbers of many gases, and need to be functionalized in order to add specificity. For example, polydimethylsiloxane can be functionalized with phenyl or naphthyl containing siloxanes to increase the affinity to aromatic compounds or functionalized with long aliphatic chains or with fluorinated siloxanes.[81, 192-193] Polydiphenylsiloxane doped polydimethylsiloxane films were preciously demonstrated for the detection of m-xylene and cyclohexane vapours using an LPG sensor.[81] A similar polymer was also coated onto a silicon-on-insulator microring resonator.[194] While none of these polymers on their own are entirely selective to individual VOCs, the relative response of a series of different films can be used to determine the identity and the concentration of an exposed analyte.

Molecularly imprinted polymers can be used to detect of larger molecules.[195] A template molecule, similar or identical to the target species, is included within the polymer matrix and removed once the polymer has cured. This leaves voids in the material that are functionalized to have a high affinity to the

target compounds. This technique was used for the trace detection of explosives like dinitrotoluene, DNT, and trinitrotoluene, TNT. Edmiston and coworkers used molecularly imprinted siloxane-based polymers as a sensing layer on a silicon nitride Young interferometer device and detected TNT vapours in the ppt range.[155] Similarly, molecularly imprinted methacrylic acid-divinyl benzene copolymers were also demonstrated for detection of TNT using an optical fibre SPR instrument.[153]

2.4.2 Metal Sensing

Many materials for the sensing of metal ions in solution use porous or cage-forming materials to chelate ions. Since metal ions are positively charged, extraction materials need electronegative elements in order to bind metal ions, such as oxygen, nitrogen or sulfur. For refractive index sensors, ion receptors need to be either covalently bound to the sensor surface or encapsulated inside a polymer coating. Molecules like ethlyenediaminetetraaceticacid (ETDA), have multi-dentate binding centres and have high affinities to metal ions like iron, nickel, copper and cobalt and lead.[196] Porphyrin molecules attached to glass substrates were presented for the detection of lead, mercury, and cadmium through absorption and fluorescence spectroscopy.[197] Cage compounds like crown ethers[198] and calixarenes[199] are also useful for the detection of cationic metal ions, though the relative affinity is related the size of the cavity.[198] Alternatively, heavy metals can be trapped in porous materials like zeolites[200] or mesoporous silicate materials.[85, 201] Tetrasulfide containing mesoporous silicates have been demonstrated for the extraction of lead and mercury ions in solution. These materials have been applied to LPGs[85] and silicon-on-insulator Mach-Zehnder interferometers[163] for the detection of Pb^{2+} and Hg^{2+} ions. Functionalized mesoporous silicates have also been used with UV-Vis spectroscopy to study the uptake of a wide range of heavy metals cations.[202]

2.4.3 Biosensing

There is a large industry and research area related to biosensing. Refractive index sensing is a desirable label-free option for sensing of biological compounds. Biomolecules can easily be attached to refractive index sensors through amines or carboxylic acids groups on functionalised silanes, or thiols in the case of metal SPR slides.[151, 203] Once a protein or other biomolecule is covalently linked to a surface, it

can be used to perform assays with target molecules. Binding sites on biomolecules impart a high degree of selectivity, compensating for the inherent non-selective behavior typical of refractive index sensors.[204] Several review articles have been published with details of a wide range of biosensing applications on fibre-based sensors[9, 13] and surface plasmon-based sensors.[15-16] Commercial instruments have also been developed for sensing of biomolecules (e.g. proteins, aptamers, and DNA) using microring resonators[161] and SPR instruments.[137-138]

2.5 Specific Thesis Objectives

Now that the theory behind refractive index sensors has been described in detail, the specific research objectives related to this thesis will be discussed. Part of this thesis builds upon the previous work of Weijian Chen on interferometric refractometry for characterizing thin films.[205] The aim of this thesis was to develop an optical method for characterizing the interactions of analytes within polymer films. Specifically, interferometric refractometry was used as a method to measure both the changes in refractive index and thickness of polymer films in order to determine the concentration of analytes adsorbed within the material. Through this process robust fitting algorithms were designed to increase the repeatability of the analysis process. Since the eventual goal was to apply chemical coatings to silicon-on-insulator (SOI) microresonator devices, it was important to the study the polymer analyte systems in the near-IR during this process.

In order to model the concentrations of analytes within polymer films, the refractive indices of bulk reagents were needed at λ = 1550 nm. To date, there are very few studies in the literature that accurately report refractive indices of common solvents or solutions at this wavelength. To solve this problem, the refractive indices of many common organic solvents and a series of aqueous solutions were measured.[66] The relationship between analyte concentration and refractive index of aqueous sucrose, sodium chloride, ethylene glycol, glycerol, and dimethylsulfoxide solutions provided alternative calibration solutions for SOI devices and other near-IR refractive index sensors.

Once the refractive indices of the prospective analytes were measured, some model polymer systems were tested. SU-8 is a common photoresist used as a protective overcoat on some of the SOI devices that we planned to study later in this project. Generally speaking, SU-8 is thought to be chemically inert, though for sensitive refractive index studies it was essential to verify this ourselves. The swelling and refractive index change of SU-8 films was studied for the uptake of water and other organic solvents to ensure chemical compatibility of our devices in future SOI experiments.[206]

The uptake of volatile organic compounds (VOCs) into siloxane polymers was used as another model system. Siloxane polymers are commonly used for sensing of VOCs and are employed as materials for solid phase microextraction (SPME). Polydiphenylsiloxane (PDPS) was added to polydimethylsiloxane (PDMS) films in an effort to increase the selectivity of the polymer films to aromatic compounds. The uptake of VOCs into both PDMS and PDMS-PDPS copolymer films were studied to determine the enhancement effect.

Finally, siloxane polymers were coated onto SOI Mach-Zehnder interferometers and microring resonators as a proof of concept for chip-level refractive index sensing. The devices were then exposed to the same VOCs that were previously used in the refractometry experiments. Moreover, these experiments were also performed to ensure that polymer behaviour was reproducible between platforms.

2.6 References

1. Bakker, E.; Telting-Diaz, M., Electrochemical sensors. *Analytical Chemistry* **2002,** *74*, 2781-2800.

2. Privett, B. J.; Shin, J. H.; Schoenfisch, M. H., Electrochemical sensors. *Analytical Chemistry* **2008,** *80*, 4499-4517.

3. Štulík, K., Challenges and promises of electrochemical detection and sensing. *Electroanalysis* **1999,** *11*, 1001-1004.

4. Brett, C. M. A., Electrochemical sensors for environmental monitoring. Strategy and examples. *Pure and Applied Chemistry* **2001,** *73*, 1967-1977.

5. Fanget, S.; Hentz, S.; Puget, P.; Arcamone, J.; Matheron, M.; Colinet, E.; Andreucci, P.; Duraffourg, L.; Myers, E.; Roukes, M. L., Gas sensors based on gravimetric detection—A review. *Sensors and Actuators B: Chemical* **2011,** *160*, 804-821.

6. O'Sullivan, C. K.; Guilbault, G. G., Commercial quartz crystal microbalances – theory and applications. *Biosensors and Bioelectronics* **1999,** *14*, 663-670.

7. Marx, K. A., Quartz crystal microbalance: A useful tool for studying thin polymer films and complex biomolecular systems at the solution−surface interface. *Biomacromolecules* **2003,** *4*, 1099-1120.

8. Johannsmann, D., Viscoelastic, mechanical, and dielectric measurements on complex samples with the quartz crystal microbalance. *Physical Chemistry Chemical Physics* **2008,** *10*, 4516-4534.

9. Wang, X.-d.; Wolfbeis, O. S., Fiber-optic chemical sensors and biosensors (2013–2015). *Analytical Chemistry* **2016,** *88*, 203-227.

10. Lambeck, P. V., Integrated optical sensors for the chemical domain. *Measurement Science and Technology* **2006,** *17*, R93-R116.

11. Leung, A.; Shankar, P. M.; Mutharasan, R., A review of fiber-optic biosensors. *Sensors and Actuators B: Chemical* **2007,** *125*, 688-703.

12. Su, L.; Jia, W.; Hou, C.; Lei, Y., Microbial biosensors: A review. *Biosensors and Bioelectronics* **2011,** *26*, 1788-1799.

13. Wang, X.-D.; Wolfbeis, O. S., Fiber-optic chemical sensors and biosensors (2008–2012). *Analytical Chemistry* **2013,** *85*, 487-508.

14. Roh, S.; Chung, T.; Lee, B., Overview of the characteristics of micro- and nano-structured surface plasmon resonance sensors. *Sensors* **2011,** *11*, 1565-1588.

15. Nguyen, H.; Park, J.; Kang, S.; Kim, M., Surface plasmon resonance: A versatile technique for biosensor applications. *Sensors* **2015,** *15*, 10481-10510.

16. Homola, J., Present and future of surface plasmon resonance biosensors. *Analytical and Bioanalytical Chemistry* **2003,** *377*, 528-539.

17. Moreels, E.; de Greef, C.; Finsy, R., Laser light refractometer. *Applied Optics* **1984,** *23*, 3010-3013.

18. Rheims, J.; Köser, J.; Wriedt, T., Refractive-index measurements in the near-IR using an Abbe refractometer. *Measurement Science and Technology* **1997,** *8*, 601-605.

19. Cooper, P. R., Refractive index measurements of liquids used in conjunction with optical fibers. *Applied Optics* **1983,** *22*, 3070-3072.

20. Washburn, A. L.; Bailey, R. C., Photonics-on-a-chip: recent advances in integrated waveguides as enabling detection elements for real-world, lab-on-a-chip biosensing applications. *The Analyst* **2011,** *136*, 227-236.

21. Atkins, P.; de Paula, J., *Atkins' Physical Chemistry*. 8th Edition, W.H Freeman and Company, New York, NY, 2006.

22. Hale, G. M.; Querry, M. R., Optical constants of water in the 200-nm to 200-μm wavelength region. *Applied Optics* **1973,** *12*, 555-563.

23. Bertie, J. E.; Ahmed, M. K.; Eysel, H. H., Infrared intensities of liquids. 5. Optical and dielectric constants, integrated intensities, and dipole moment derivatives of water and water-d2 at 22.degree.C. *The Journal of Physical Chemistry* **1989,** *93*, 2210-2218.

24. *Handbook of Ellipsometry*. Tompkin, H. G.; Irene, E. A., Eds. William Andrew Inc, Springer-Verlag GmbH & Co., Norwich, NY, 2005.

25. Moutzouris, K.; Papamichael, M.; Betsis, S. C.; Stavrakas, I.; Hloupis, G.; Triantis, D., Refractive, dispersive and thermo-optic properties of twelve organic solvents in the visible and near-infrared. *Applied Physics B* **2014,** *116*, 617-622.

26. Ghosh, G., Sellmeier coefficients and dispersion of thermo-optic coefficients for some optical glasses. *Applied Optics* **1997,** *36*, 1540-1546.

27. Optical Glass Data Sheets. Schott http://www.us.schott.com (accessed July 20, 2016).

28. Optical Glass Dispersion Spreadsheet. Hoya http://www.hoya-opticalworld.com/english/ (accessed July 20, 2016).

29. Waxler, R. M.; Cleek, G. W., The effect of temperature and pressure on the refractive index of some oxide glasses. *Journal of Research of the National Bureau of Standards - A Physics and Chemistry* **1973,** *77A*, 755-763.

30. Kasarova, S. N.; Sultanova, N. G.; Nikolov, I. D., Temperature dependence of refractive characteristics of optical plastics. *Journal of Physics: Conference Series* **2010,** *253*, 012028, 1-6.

31. Bertie, J. E.; Zhang, S. L., Infrared intensities of liquids. IX. The Kramers–Kronig transform, and its approximation by the finite Hilbert transform via fast Fourier transforms. *Canadian Journal of Chemistry* **1992,** *70*, 520-531.

32. Bertie, J. E.; Lan, Z., The refractive index of colorless liquids in the visible and infrared: Contributions from the absorption of infrared and ultraviolet radiation and the electronic molar polarizability below 20 500 cm−1. *The Journal of Chemical Physics* **1995,** *103*, 10152-10161.

33. Mudhana, G.; Park, K. S.; Ryu, S. Y.; Lee, B. H., Fiber-optic probe based on a bifunctional lensed photonic crystal fiber for refractive index measurements of liquids. *IEEE Sensors Journal* **2011,** *11*, 1178-1183.

34. Zhou, J.; Wang, Y.; Liao, C.; Sun, B.; He, J.; Yin, G.; Liu, S.; Li, Z.; Wang, G.; Zhong, X.; Zhao, J., Intensity modulated refractive index sensor based on optical fiber Michelson interferometer. *Sensors and Actuators B: Chemical* **2015,** *208*, 315-319.

35. Wang, P.; Brambilla, G.; Ding, M.; Semenova, Y.; Wu, Q.; Farrell, G., High-sensitivity, evanescent field refractometric sensor based on a tapered, multimode fiber interference. *Optics Letters* **2011,** *36*, 2233-2235.

36. Wu, D.; Zhao, Y.; Li, J., PCF taper-based Mach–Zehnder interferometer for refractive index sensing in a PDMS detection cell. *Sensors and Actuators B: Chemical* **2015,** *213*, 1-4.

37. Ding, M.; Wang, P.; Wang, J.; Brambilla, G., FIB-milled gold-coated singlemode-multimode-singlemode fiber tip refractometer. *IEEE Photonics Technology Letters* **2014,** *26*, 239-241.

38. Hecht, E.; Zajac, A., *Optics*. Addison-Wesley Publishing Company Inc., Don Mills, ON, 1974.

39. Saleh, B. E. A.; Teich, M. C., *Fundamentals of Photonics*. 2nd Edition, John Wiley & Sons, Hoboken, NJ, 2007.

40. Harris, D. C., *Quantitative Chemical Analysis*. Sixth Edition, W. H. Freeman and Company, New York, 2003.

41. Yu, Y.; Lui, L.; Tam, H.; Chung, W., Fiber-laser-based wavelength-division multiplexed fiber Bragg grating sensor system. *IEEE Photonics Technology Letters* **2001,** *13*, 702-704.

42. Feger, T.; Ireland, M. J.; Bento, J.; Bacigalupo, C. A stable and inexpensive wavelength reference for precise wavelength calibration of radial velocity spectrographs, *Ground Based and Airborne Instruments for Astronomy V, Proceedings of SPIE 9147*, Montreal, QC, **2014**, 914780, 1-9.

43. Lin, S.-T.; Cheng, Y.-R., Wavelength shift determination using a dual-path heterodyne Mach–Zehnder interferometer. *Optics Communications* **2006,** *266*, 50-54.

44. 20 GHz Analog Modulator (LN58S-FC). Thorlabs, Inc., http://www.thorlabs.com (accessed Aug. 7, 2016).

45. Macek, W. M.; Davis, D. T. M., Rotation rate sensing with traveling-wave ring lasers. *Applied Physics Letters* **1963,** *2*, 67-68.

46. Culshaw, B., The optical fibre Sagnac interferometer: an overview of its principles and applications. *Measurement Science and Technology* **2006,** *17*, R1-R16.

47. Shenoy, M. R.; Roy, S.; Thyagarajan, K., Simple prism coupling technique to measure the refractive index of a liquid and its variation with temperature. *Review of Scientific Instruments* **1990,** *61*, 1010-1013.

48. Hughes, J. V., A new precision refractometer. *Journal of Scientific Instruments* **1941,** *18*, 234-237.

49. Holmes, J. G., A direct reading refractometer. *Journal of Scientific Instruments* **1945,** *22*, 219-221.

50. Mignani, A. G.; Ciaccheri, L.; Mencaglia, A. A.; Ottevaere, H.; Báca, E. E. S.; Thienpont, H., Optical measurements and pattern-recognition techniques for identifying the characteristics of beer and distinguishing Belgian beers. *Sensors and Actuators B: Chemical* **2013,** *179*, 140-149.

51. Son, H. S.; Hong, Y. S.; Park, W. M.; Yu, M. A.; Lee, C. H., A novel approach for estimating sugar and alcohol concentrations in wines using refractometer and hydrometer. *Journal of Food Science* **2009,** *74*, C106-C111.

52. Handheld Refractometers. Omega Engineering Inc. , http://www.omega.com/ (accessed July 21, 2016).

53. Hsu, C.-C.; Lee, C.-Y.; Chu, K.-H.; Wu, T.-C., Dove prism heterodyne refractometer. *Optics & Laser Technology* **2015,** *73*, 6-11.

54. Johnson, H. W.; Campanile, V. A.; LeFebre, H. A., Low-holdup, reflection-type refractometer for liquid chromatography. *Analytical Chemistry* **1967,** *39*, 32-36.

55. Li, H.; Xie, S., Measurement method of the refractive index of biotissue by total internal reflection. *Applied Optics* **1996,** *35*, 1793-1795.

56. Sánchez-Pérez, C.; García-Valenzuela, A., Spectroscopic refractometer for transparent and absorbing liquids by reflection of white light near the critical angle. *Review of Scientific Instruments* **2012,** *83*, 115102, 1-7.

57. Contreras-Tello, H.; Márquez-Islas, R.; Vázquez-Estrada, O.; Sánchez-Pérez, C.; García-Valenzuela, A., Understanding the performance of Abbe-type refractometers with optically absorbing fluids. *Measurement Science and Technology* **2014,** *25*, 075201, 1-7.

58. Chen, W.; Saunders, J. E.; Barnes, J. A.; Yam, S. S.-H.; Loock, H.-P., Monitoring of vapor uptake by refractive index and thickness measurements in thin films. *Optics Letters* **2013,** *38*, 365-367.

59. Ulrich, R.; Torge, R., Measurement of thin film parameters with a prism coupler. *Applied Optics* **1973,** *12*, 2901-2908.

60. Ding, T.-N.; Garmire, E., Measuring refractive index and thickness of thin films: a new technique. *Applied Optics* **1983,** *22*, 3177-3181.

61. Taya, S. A.; El-Agez, T. M., Optical sensors based on Fabry–Perot resonator and fringes of equal thickness structure. *Optik - International Journal for Light and Electron Optics* **2012,** *123*, 417-421.

62. Refractometers, Totally reflecting everything. Mettler Toledo, http://www.mt.com/ca/en/home/ (accessed July 21, 2016).

63. Refractometers for food, beverage, chemical, petroleum, and pharmaceutical labs. Rudolph Research Analytical, http://rudolphresearch.com/products/refractometers/ (accessed July 21, 2016).

64. Refractometer, Choose one measure everything. Anton Paar, http://www.anton-paar.com/ca-en/ (accessed July 21, 2016).

65. Metricon's Model 2010/M Refractometer. Metricon Corporation, http://www.metricon.com/ (accessed July 21, 2016).

66. Saunders, J. E.; Sanders, C.; Chen, H.; Loock, H.-P., Refractive indices of common solvents and solutions at 1550 nm. *Applied Optics* **2016,** *55*, 947-953.

67. James, S. W.; Tatam, R. P., Optical fibre long-period grating sensors: characteristics and application. *Measurement Science and Technology* **2003,** *14*, R49-R61.

68. Albert, J.; Shao, L.-Y.; Caucheteur, C., Tilted fiber Bragg grating sensors. *Laser & Photonics Reviews* **2013,** *7*, 83-108.

69. Gangopadhyay, T. K., Prospects for fibre Bragg gratings and Fabry-Perot interferometers in fibre-optic vibration sensing. *Sensors and Actuators A: Physical* **2004,** *113*, 20-38.

70. Mihailov, S. J., Fiber Bragg grating sensors for harsh environments. *Sensors* **2012,** *12*, 1898-1918.

71. Fang, X.; Liao, C. R.; Wang, D. N., Femtosecond laser fabricated fiber Bragg grating in microfiber for refractive index sensing. *Optics Letters* **2010,** *35*, 1007-1009.

72. Liao, C. R.; Wang, D. N., Review of femtosecond laser fabricated fiber Bragg gratings for high temperature sensing. *Photonic Sensors* **2013,** *3*, 97-101.

73. Ran, Y.; Tan, Y.-N.; Sun, L.-P.; Gao, S.; Li, J.; Jin, L.; Guan, B.-O., 193 nm excimer laser inscribed Bragg gratings in microfibers for refractive index sensing. *Optics Express* **2011,** *19*, 18577-18583.

74. Palai, P.; Satyanarayan, M. N.; Das, M.; Thyagarajan, K.; Pal, B. P., Characterization and simulation of long period gratings fabricated using electric discharge. *Optics Communications* **2001,** *193*, 181-185.

75. Grenier, J. R.; Fernandes, L. A.; Aitchison, J. S.; Marques, P. V. S.; Herman, P. R., Femtosecond laser fabrication of phase-shifted Bragg grating waveguides in fused silica. *Optics Letters* **2012,** *37*, 2289-2291.

76. Savin, S.; Digonnet, M. J. F.; Kino, G. S.; Shaw, H. J., Tunable mechanically induced long-period fiber gratings. *Optics Letters* **2000,** *25*, 710-712.

77. Lin, C.-H.; Li, Q.; Au, A. A.; Jiang, Y.; Wu, E.; Lee, H. P., Strain-induced thermally tuned long-period fiber gratings fabricated on a periodically corrugated substrate. *Journal of Lightwave Technology* **2004,** *22*, 1818-1827.

78. Kersey, A. D.; Davis, M. A. Interferometric fiber sensor with a chirped Bragg grating sensing element, *10th International Conference on Optical Fibre Sensors* Glasgow, UK, **1994**, 319-322.

79. Avino, S.; Barnes, J. A.; Gagliardi, G.; Gu, X.; Gutstein, D.; Mester, J. R.; Nicholaou, C.; Loock, H.-P., Musical instrument pickup based on a laser locked to an optical fiber resonator. *Optics Express* **2011,** *19*, 25057-25065.

80. MacLean, A. G.; Schneider, L. T.; Freytag, A. I.; Gribble, A.; Barnes, J. A.; Loock, H.-P., Cavity-enhanced photoacoustic detection using acoustic and fiber-optic resonators. *Applied Physics B* **2015,** *119*, 11-19.

81. Barnes, J.; Dreher, M.; Plett, K.; Brown, R. S.; Crudden, C. M.; Loock, H.-P., Chemical sensor based on a long-period fibre grating modified by a functionalized polydimethylsiloxane coating. *The Analyst* **2008,** *133*, 1541-1549.

82. Zhang, J.; Sun, Q.; Liang, R.; Wo, J.; Liu, D.; Shum, P., Microfiber Fabry–Perot interferometer fabricated by taper-drawing technique and its application as a radio frequency interrogated refractive index sensor. *Optics Letters* **2012,** *37*, 2925-2927.

83. Barnes, J. A.; Brown, R. S.; Cheung, A. H.; Dreher, M. A.; Mackey, G.; Loock, H.-P., Chemical sensing using a polymer coated long-period fiber grating interrogated by ring-down spectroscopy. *Sensors and Actuators B: Chemical* **2010,** *148*, 221-226.

84. Partridge, M.; Wong, R.; James, S. W.; Davis, F.; Higson, S. P. J.; Tatam, R. P., Long period grating based toluene sensor for use with water contamination. *Sensors and Actuators B: Chemical* **2014,** *203*, 621-625.

85. Du, J.; Cipot-Wechsler, J.; Lobez, J. M.; Loock, H.-P.; Crudden, C. M., Periodic mesoporous organosilica films: Key components of fiber-optic-based heavy-metal sensors. *Small* **2010,** *6*, 1168-1172.

86. Zhu, T.; Wu, D.; Liu, M.; Duan, D.-W., In-line fiber optic interferometric sensors in single-mode fibers. *Sensors* **2012,** *12*, 10430-10449.

87. Lee, B. H.; Kim, Y. H.; Park, K. S.; Eom, J. B.; Kim, M. J.; Rho, B. S.; Choi, H. Y., Interferometric fiber optic sensors. *Sensors* **2012,** *12*, 2467-2486.

88. Tian, Z.; Yam, S. S.-H.; Loock, H.-P., Single-mode fiber refractive index sensor based on core-offset attenuators. *IEEE Photonics Technology Letters* **2008,** *20*, 1387-1389.

89. Zhao, Y.; Cai, L.; Li, X.-G., High sensitive modal interferometer for temperature and refractive index measurement. *IEEE Photonics Technology Letters* **2015,** *27*, 1341-1344.

90. Li, L.; Xia, L.; Xie, Z.; Liu, D., All-fiber Mach-Zehnder interferometers for sensing applications. *Optics Express* **2012,** *20*, 11109-11120.

91. Jha, R.; Villatoro, J.; Badenes, G.; Pruneri, V., Refractometry based on a photonic crystal fiber interferometer. *Optics Letters* **2009,** *34*, 617-619.

92. Villatoro, J.; Finazzi, V.; Badenes, G.; Pruneri, V., Highly sensitive sensors based on photonic crystal fiber modal interferometers. *Journal of Sensors* **2009,** *2009*, 1-11.

93. Tian, Z.; Yam, S. S.-H.; Barnes, J.; Bock, W.; Greig, P.; Fraser, J. M.; Loock, H.-P.; Oleschuk, R. D., Refractive index sensing with Mach-Zehnder interferometer based on concatenating two single-mode fiber tapers. *IEEE Photonics Technology Letters* **2008,** *20*, 626-628.

94. Lu, P.; Men, L.; Sooley, K.; Chen, Q., Tapered fiber Mach–Zehnder interferometer for simultaneous measurement of refractive index and temperature. *Applied Physics Letters* **2009,** *94*, 131110, 1-3.

95. Allsop, T.; Reeves, R.; Webb, D. J.; Bennion, I.; Neal, R., A high sensitivity refractometer based upon a long period grating Mach–Zehnder interferometer. *Review of Scientific Instruments* **2002,** *73*, 1702-1705.

96. Shipley, S. P.; Georgiou, G.; Boucouvalas, A. C., Compact all-fibre Mach-Zehnder devices. *IEE Proceedings Journal - Optoelectronics* **1987,** *134*, 203-207.

97. Félix, M.; Salazar, D.; Castro, J.; Márquez, H., Experimental measurement of fused fiber coupler and M-Z interferometer performance as WDM devices. *Fiber and Integrated Optics* **2007,** *26*, 187-200.

98. Kashyap, R.; Nayar, B., An all single-mode fiber Michelson interferometer sensor. *Journal of Lightwave Technology* **1983,** *1*, 619-624.

99. Andrews, N. L. P.; Ross, R.; Munzke, D.; van Hoorn, C.; Brzezinski, A.; Barnes, J. A.; Reich, O.; Loock, H.-P., In-fiber Mach-Zehnder interferometer for gas refractive index measurements based on a hollow-core photonic crystal fiber. *Optics Express* **2016,** *24*, 14086-14099.

100. Rogers, K. R.; Poziomek, E. J., Fiber optic sensors for environmental monitoring. *Chemosphere* **1996,** *33*, 1151-1174.

101. Lee, B., Review of the present status of optical fiber sensors. *Optical Fiber Technology* **2003,** *9*, 57-79.

102. Chang, K.-A.; Lim, H.-J.; Su, C. B., A fibre optic Fresnel ratio meter for measurements of solute concentration and refractive index change in fluids. *Measurement Science and Technology* **2002,** *13*, 1962-1965.

103. Kim, C.-B.; Su, C. B., Measurement of the refractive index of liquids at 1.3 and 1.5 micron using a fibre optic Fresnel ratio meter. *Measurement Science and Technology* **2004,** *15*, 1683-1686.

104. Meng, H.; Shen, W.; Zhang, G.; Wu, X.; Wang, W.; Tan, C.; Huang, X., Michelson interferometer-based fiber-optic sensing of liquid refractive index. *Sensors and Actuators B: Chemical* **2011,** *160*, 720-723.

105. Shlyagin, M. G.; Martínez Manuel, R.; Esteban, ó., Optical-fiber self-referred refractometer based on Fresnel reflection at the fiber tip. *Sensors and Actuators B: Chemical* **2013,** *178*, 263-269.

106. Sengupta, D.; Sai Shankar, M.; Reddy, P. S.; Sai Prasad, R. L. N.; Srimannarayana, K., A low cost fiber optic refractive index sensor. *Optoelectronics and Advanced Materials - Rapid Communications* **2010,** *4*, 128-131.

107. Pevec, S.; Donlagic, D., High resolution, all-fiber, micro-machined sensor for simultaneous measurement of refractive index and temperature. *Optics Express* **2014,** *22*, 16241-16253.

108. Barnes, J. A.; Gagliardi, G.; Loock, H.-P., Phase-shift cavity ring-down spectroscopy on a microsphere resonator by Rayleigh backscattering. *Physical Review A* **2013,** *87*, 053843, 1-5.

109. Hanumegowda, N. M.; White, I. M.; Fan, X., Aqueous mercuric ion detection with microsphere optical ring resonator sensors. *Sensors and Actuators B: Chemical* **2006,** *120*, 207-212.

110. Armani, D. K.; Kippenberg, T. J.; Spillane, S. M.; Vahala, K. J., Ultra-high-Q toroid microcavity on a chip. *Nature* **2003,** *421*, 925-928.

111. Savchenkov, A. A.; Matsko, A. B.; Ilchenko, V. S.; Maleki, L., Optical resonators with ten million finesse. *Optics Express* **2007,** *15*, 6768-6773.

112. Xu, D. X.; Densmore, A.; Delâge, A.; Waldron, P.; McKinnon, R.; Janz, S.; Lapointe, J.; Lopinski, G.; Mischki, T.; Post, E.; Cheben, P.; Schmid, J. H., Folded cavity SOI microring sensors for high sensitivity and real time measurement of biomolecular binding. *Optics Express* **2008,** *16*, 15137-15148.

113. Yebo, N. A.; Lommens, P.; Hens, Z.; Baets, R., An integrated optic ethanol vapor sensor based on a silicon-on-insulator microring resonator coated with a porous ZnO film. *Optics Express* **2010,** *18*, 11859-11866.

114. Ilchenko, V. S.; Savchenkov, A. A.; Matsko, A. B.; Maleki, L. Crystalline whispering gallery mode resonators: in search of the optimal material, *Laser Resonators, Microresonators, and Beam Control XVI, Proceedings of SPIE 8960*, San Francisco, CA, **2014**, 896013, 1-10.

115. Vollmer, F.; Arnold, S., Whispering-gallery-mode biosensing: label-free detection down to single molecules. *Nature Methods* **2008,** *5*, 591-596.

116. Barnes, J. A.; Gagliardi, G.; Loock, H.-P., Absolute absorption cross-section measurement of a submonolayer film on a silica microresonator. *Optica* **2014,** *1*, 75-83.

117. Louyer, Y.; Meschede, D.; Rauschenbeutel, A., Tunable whispering-gallery-mode resonators for cavity quantum electrodynamics. *Physical Review A* **2005,** *72*, 031801, 1-4.

118. Senthil Murugan, G.; Wilkinson, J. S.; Zervas, M. N., Selective excitation of whispering gallery modes in a novel bottle microresonator. *Optics Express* **2009,** *17*, 11916-11925.

119. Lu, Q.; Wu, X.; Liu, L.; Xu, L., Mode-selective lasing in high-Q polymer micro bottle resonators. *Optics Express* **2015,** *23*, 22740-22745.

120. Soltani, M.; Yegnanarayanan, S.; Adibi, A., Ultra-high Q planar silicon microdisk resonators for chip-scale silicon photonics. *Optics Express* **2007,** *15*, 4694-4704.

121. Kippenberg, T. J.; Spillane, S. M.; Armani, D. K.; Vahala, K. J., Fabrication and coupling to planar high-Q silica disk microcavities. *Applied Physics Letters* **2003,** *83*, 797-799.

122. De Vos, K.; Bartolozzi, I.; Schacht, E.; Bienstman, P.; Baets, R., Silicon-on-Insulator microring resonator for sensitive and label-free biosensing. *Optics Express* **2007,** *15*, 7610-7615.

123. Vernooy, D. W.; Ilchenko, V. S.; Mabuchi, H.; Streed, E. W.; Kimble, H. J., High-Q measurements of fused-silica microspheres in the near infrared. *Optics Letters* **1998,** *23*, 247-249.

124. Moss, D. J.; Morandotti, R.; Gaeta, A. L.; Lipson, M., New CMOS-compatible platforms based on silicon nitride and Hydex for nonlinear optics. *Nature Photonics* **2013,** *7*, 597-607.

125. Cardenas, J.; Zhang, M.; Phare, C. T.; Shah, S. Y.; Poitras, C. B.; Guha, B.; Lipson, M., High Q SiC microresonators. *Optics Express* **2013,** *21*, 16882.

126. Ichikawa, K.; Mori, T.; Kitano, H.; Fukuda, M.; Mochizuki, A.; Tanaka, M., Fourier transform infrared study on the sorption of water to various kinds of polymer thin films. *Journal of Polymer Science Part B: Polymer Physics* **2001,** *39*, 2175-2182.

127. Ilchenko, V. S.; Savchenkov, A. A.; Matsko, A. B.; Maleki, L., Generation of Kerr frequency combs in a sapphire whispering gallery mode microresonator. *Optical Engineering* **2014,** *53*, 122607, 1-8.

128. Park, J.; Ozdemir, S. K.; Monifi, F.; Chadha, T.; Huang, S. H.; Biswas, P.; Yang, L., Titanium dioxide whispering gallery microcavities. *Advanced Optical Materials* **2014,** *2*, 711-717.

129. Martin, A. L.; Armani, D. K.; Yang, L.; Vahala, K. J., Replica-molded high-Q polymer microresonators. *Optics Letters* **2004,** *29*, 533-535.

130. Eryürek, M.; Karadag, Y.; Taşaltın, N.; Kılınç, N.; Kiraz, A., Optical sensor for hydrogen gas based on a palladium-coated polymer microresonator. *Sensors and Actuators B: Chemical* **2015,** *212*, 78-83.

131. Huston, A. L.; Lin, H.-B.; Eversole, J. D.; Campillo, A. J., Effect of bubble formation on microdroplet cavity quality factors. *Journal of the Optical Society of America B* **1996,** *13*, 521-531.

132. Avino, S.; Krause, A.; Zullo, R.; Giorgini, A.; Malara, P.; De Natale, P.; Loock, H. P.; Gagliardi, G., Direct sensing in liquids using whispering-gallery-mode droplet resonators. *Advanced Optical Materials* **2014,** *2*, 1155-1159.

133. Attar, S. T.; Shuvayev, V.; Deych, L.; Martin, L. L.; Carmon, T., Level-crossing and modal structure in microdroplet resonators. *Optics Express* **2016,** *24*, 13134-13141.

134. Maier, S. A., Surface Plasmon Polaritons at Metal / Insulator Interfaces. In *Plasmonics: Fundamentals and Applications*, Springer Science + Business Media LLC: New York, NY, 2007.

135. Tang, Y.; Zeng, X.; Liang, J., Surface plasmon resonance: An introduction to a surface spectroscopy technique. *Journal of Chemical Education* **2010,** *87*, 742-746.

136. Lavine, B. K.; Westover, D. J.; Oxenford, L.; Mirjankar, N.; Kaval, N., Construction of an inexpensive surface plasmon resonance instrument for use in teaching and research. *Microchemical Journal* **2007,** *86*, 147-155.

137. BioNavis: excellence in surface plasmon resonance. BioNavis, http://www.bionavis.com/ (accessed July 25, 2016).

138. Biacore: label free interaction analysis. Biacore Life Sciences, https://www.biacore.com/lifesciences/index.html (accessed July 25, 2016).

139. Kvasnička, P.; Chadt, K.; Vala, M.; Bocková, M.; Homola, J., Toward single-molecule detection with sensors based on propagating surface plasmons. *Optics Letters* **2012,** *37*, 163-165.

140. Sharma, A. K.; Gupta, B. D., Fiber optic sensor based on surface plasmon resonance with nanoparticle films. *Photonics and Nanostructures - Fundamentals and Applications* **2005,** *3*, 30-37.

141. Sharma, A. K.; Jha, R.; Gupta, B. D., Fiber-optic sensors based on surface plasmon resonance: A comprehensive review. *IEEE Sensors Journal* **2007,** *7*, 1118-1129.

142. Mishra, S. K.; Tripathi, S. N.; Choudhary, V.; Gupta, B. D., SPR based fibre optic ammonia gas sensor utilizing nanocomposite film of PMMA/reduced graphene oxide prepared by in situ polymerization. *Sensors and Actuators B: Chemical* **2014,** *199*, 190-200.

143. Li, H.; Noh, J. W.; Chen, Y.; Li, M., Enhanced optical forces in integrated hybrid plasmonic waveguides. *Optics Express* **2013,** *21*, 11839-11851.

144. Verma, R.; Gupta, B. D. SPR based three channels fiber optic sensor for aqueous environment, *Photonic Instrumentation Engineering, Proceedings of SPIE 8992*, **2014**, 899209, 1-8.

145. Willets, K. A.; Van Duyne, R. P., Localized surface plasmon resonance spectroscopy and sensing. *Annual Review of Physical Chemistry* **2007,** *58*, 267-297.

146. Artar, A.; Yanik, A. A.; Altug, H., Fabry–Pérot nanocavities in multilayered plasmonic crystals for enhanced biosensing. *Applied Physics Letters* **2009,** *95*, 051105, 1-3.

147. Mayer, K. M.; Hafner, J. H., Localized surface plasmon resonance sensors. *Chemical Reviews* **2011,** *111*, 3828-3857.

148. Ince, R.; Narayanaswamy, R., Analysis of the performance of interferometry, surface plasmon resonance and luminescence as biosensors and chemosensors. *Analytica Chimica Acta* **2006,** *569*, 1-20.

149. Nuzzo, R. G.; Allara, D. L., Adsorption of bifunctional organic disulfides on gold surfaces. *Journal of the American Chemical Society* **1983,** *105*, 4481-4483.

150. Bain, C. D.; Troughton, E. B.; Tao, Y. T.; Evall, J.; Whitesides, G. M.; Nuzzo, R. G., Formation of monolayer films by the spontaneous assembly of organic thiols from solution onto gold. *Journal of the American Chemical Society* **1989,** *111*, 321-335.

151. Love, J. C.; Estroff, L. A.; Kriebel, J. K.; Nuzzo, R. G.; Whitesides, G. M., Self-assembled monolayers of thiolates on metals as a form of nanotechnology. *Chemical Reviews* **2005,** *105*, 1103-1170.

152. Crudden, C. M.; Horton, J. H.; Ebralidze, I. I.; Zenkina, O. V.; McLean, A. B.; Drevniok, B.; She, Z.; Kraatz, H.-B.; Mosey, N. J.; Seki, T.; Keske, E. C.; Leake, J. D.; Rousina-Webb, A.; Wu, G., Ultra stable self-assembled monolayers of N-heterocyclic carbenes on gold. *Nature Chemistry* **2014,** *6*, 409-414.

153. Cennamo, N.; D'Agostino, G.; Galatus, R.; Bibbò, L.; Pesavento, M.; Zeni, L., Sensors based on surface plasmon resonance in a plastic optical fiber for the detection of trinitrotoluene. *Sensors and Actuators B: Chemical* **2013,** *188*, 221-226.

154. Politi, A.; Cryan, M. J.; Rarity, J. G.; Yu, S.; O'Brien, J. L., Silica-on-silicon waveguide quantum circuits. *Science* **2008,** *320*, 646-649.

155. Edmiston, P. L.; Campbell, D. P.; Gottfried, D. S.; Baughman, J.; Timmers, M. M., Detection of vapor phase trinitrotoluene in the parts-per-trillion range using waveguide interferometry. *Sensors and Actuators B: Chemical* **2010,** *143*, 574-582.

156. Carlborg, C. F.; Gylfason, K. B.; Kaźmierczak, A.; Dortu, F.; Bañuls Polo, M. J.; Maquieira Catala, A.; Kresbach, G. M.; Sohlström, H.; Moh, T.; Vivien, L.; Popplewell, J.; Ronan, G.; Barrios, C. A.; Stemme, G.; van der Wijngaart, W., A packaged optical slot-waveguide ring resonator sensor array for multiplex label-free assays in labs-on-chips. *Lab on a Chip* **2010,** *10*, 281-290.

157. Densmore, A.; Xu, D.-X.; Waldron, P.; Janz, S.; Lapointe, J.; Mischki, T.; Lopinski, G.; Delage, A.; Cheben, P. Spotter-compatible SOI waveguide devices for biomolecular sensing, *Silicon Photonics III, Proceedings of SPIE 6898*, **2008**, 68981B, 1-8.

158. Yeniay, A.; Gao, R.; Takayama, K.; Gao, R.; Garito, A. F., Ultra-low-loss polymer waveguides. *Journal of Lightwave Technology* **2004,** *22*, 154-158.

159. Zhao, Y.-G.; Lu, W.-K.; Ma, Y.; Kim, S.-S.; Ho, S. T.; Marks, T. J., Polymer waveguides useful over a very wide wavelength range from the ultraviolet to infrared. *Applied Physics Letters* **2000,** *77*, 2961-2963.

160. St-Gelais, R.; Mackey, G.; Saunders, J.; Zhou, J.; Leblanc-Hotte, A.; Poulin, A.; Barnes, J. A.; Loock, H.-P.; Brown, R. S.; Peter, Y.-A., Gas sensing using polymer-functionalized deformable Fabry–Perot interferometers. *Sensors and Actuators B: Chemical* **2013,** *182*, 45-52.

161. The Maverick Detection System. Genalyte, http://www.genalyte.com/ (accessed July 25, 2016).

162. Passaro, V. M. N.; Dell'Olio, F.; De Leonardis, F., Ammonia optical sensing by microring resonators. *Sensors* **2007,** *7*, 2741-2749.

163. Saunders, J.; Dreher, M. A.; Barnes, J. A.; Crudden, C. M.; Du, J.; Loock, H.-P.; Xu, D.-X.; Densmore, A.; Ma, R.; Janz, S.; Vachon, M.; Lapointe, J.; Delage, A.; Schmid, J.; Cheb, P. Detection of lead contamination of water and VOC contamination of air using SOI micro-optical devices, *IEEE Conference on Group IV Photonics*, Beijing, China, **2010**, 177-179.

164. Born, M.; Wolf, E., *Principles of Optics: Electomagnetic Theory of Propagation, Interference and Diffraction of Light*. 4th Edition, Pergamon Press, Toronto, Canada, 1970.

165. Malitson, I. H., Interspecimen comparison of the refractive index of fused silica. *Journal of the Optical Society of America* **1965,** *55*, 1205-1209.

166. *N-SF11 Glass Data Sheet.* Schott, 2015, 785257.322,

167. NanoCalc thin film reflectometry system. Ocean Optics, http://oceanoptics.com/product/nanocalc/ (accessed July 13, 2016).

168. F3 Series Reflectometers. Filmetrics, http://www.filmetrics.com/thicknessmeasurement/f3 (accessed July 13, 2016).

169. Spectroscopic Reflectometer SR Series. Angstrom Sun Technologies, http://www.angstec.com/products/Spectroscopic%20Reflectometer%20SR%20Series (accessed July 13, 2016).

170. Benson, T. E.; Kamlet, L. I.; Klimecky, P.; Terry, F. L., In-situ spectroscopic reflectometry for polycrystalline silicon thin film etch rate determination during reactive ion etchinc. *Journal of Electronic Materials* **1996,** *25*, 955-964.

171. Hu, Y. Z.; Sharangpani, R.; Tay, S.-P., Kinetic investigation of copper film oxidation by spectroscopic ellipsometry and reflectometry. *Journal of Vacuum Science & Technology A: Vacuum, Surfaces, and Films* **2000,** *18*, 2527-2532.

172. *Basic Confocal Microscopy*. Price, R. L.; Jerome, W. G., Eds. Springer Science + Business Media, LLC, New York, NY, 2011.

173. *Confocal Microscopy Methods and Protocols* 2nd Edition, Paddock, S. W., Ed. Springer Science + Business Media, New York, NY, 2014.

174. Semwogerere, D.; Weeks, E. R., Confocal Microscopy. In *Encyclopedia of Biomaterials and Biomedical Engineering*, Taylor & Francis: 2005; pp 1-10.

175. Leica DCM8 3D Optical Surface Metrology System Leica Microsystems, http://www.leica-microsystems.com/home/ (accessed July 23, 2016).

176. Caldwell, D. E.; Korber, D. R.; Lawrence, J. R., Imaging of bacterial cells by fluorescence exclusion using scanning confocal laser microscopy. *Journal of Microbiological Methods* **1992,** *15*, 249-261.

177. Amos, W. B.; White, J. G., How the confocal laser scanning microscope entered biological research. *Biology of the Cell* **2003,** *95*, 335-342.

178. Russell, T. P., X-ray and neutron reflectivity for the investigation of polymers. *Materials Science Reports* **1990,** *5*, 171-271.

179. Müller-Buschbaum, P.; Bauer, E.; Maurer, E.; Nelson, A.; Cubitt, R., In-situ neutron reflectometry probing competitive swelling and de-swelling of thin polystyrene films. *Physica Status Solidi (RRL) – Rapid Research Letters* **2007,** *1*, R68-R70.

180. Mukherjee, M.; Singh, A.; Daillant, J.; Menelle, A.; Cousin, F., Effect of solvent−polymer interaction in swelling dynamics of ultrathin polyacrylamide films: A neutron and X-ray reflectivity study. *Macromolecules* **2007,** *40*, 1073-1080.

181. Tolmachev, V. A., Adsorption-ellipsometry method of studying the optical profile, thickness, and porosity of thin films. *Journal of Optical Technology* **1999,** *66*, 596-607.

182. Ogieglo, W.; Wormeester, H.; Eichhorn, K.-J.; Wessling, M.; Benes, N. E., In situ ellipsometry studies on swelling of thin polymer films: A review. *Progress in Polymer Science* **2015,** *42*, 42-78.

183. Variable angle spectroscopic ellipsometers. J. A. Woolam Co., https://www.jawoollam.com/ (accessed July 24, 2016).

184. Sirard, S. M.; Green, P. F.; Johnston, K. P., Spectroscopic ellipsometry investigation of the swelling of poly(dimethylsiloxane) thin films with high pressure carbon dioxide. *The Journal of Physical Chemistry B* **2001,** *105*, 766-772.

185. Chen, W.-L.; Shull, K. R.; Papatheodorou, T.; Styrkas, D. A.; Keddie, J. L., Equilibrium swelling of hydrophilic polyacrylates in humid environments. *Macromolecules* **1999,** *32*, 136-144.

186. Hilfiker, J. N.; Singh, N.; Tiwald, T.; Convey, D.; Smith, S. M.; Baker, J. H.; Tompkins, H. G., Survey of methods to characterize thin absorbing films with spectroscopic ellipsometry. *Thin Solid Films* **2008,** *516*, 7979-7989.

187. Chou, C.; Teng, H.-K.; Yu, C.-J.; Huang, H.-S., Polarization modulation imaging ellipsometry for thin film thickness measurement. *Optics Communications* **2007,** *273*, 74-83.

188. Javahiraly, N.; Perrotton, C. Hydrogen leak detection: a comparison between fiber optic sensors based on different designs, *Photonics Applications for Aviation, Aerospace, Commercial and Harsh Environments, Proceedings of SPIE 9202*, San Diego, CA, **2014**, 920206, 1-17.

189. Usha, S. P.; Mishra, S. K.; Gupta, B. D., Fiber optic hydrogen sulfide gas sensors utilizing ZnO thin film/ZnO nanoparticles: A comparison of surface plasmon resonance and lossy mode resonance. *Sensors and Actuators B: Chemical* **2015,** *218*, 196-204.

190. Pawliszyn, J., *Solid Phase Microextraction Theory and Practice*. John Wiley & Sons Ltd., New York, NY, 1997.

191. Pawliszyn, J., Theory of solid-phase microextraction. *Journal of Chromatographic Science* **2000,** *38*, 270-278.

192. Plett, K. L. *Development and Characterization of Polysiloxane Polymer Films for Use in Optical Sensor Technology*. Ph.D. Thesis, Queen's University, 2008.

193. Mackey, G. *Synthesis, Modification, and Application of Siloxane Materials for Environmental Sensing*. Ph.D. Thesis, Queen's University, 2016.

194. Saunders, J.; Dreher, M. A.; Barnes, J. A.; Crudden, C. M.; Brown, R. S.; Loock, H.-P.; Xu, D.-X. Detection of volatile organic compounds with functionalized long-period gratings and micro-ring resonators, *ICO International Conference on Information Photonics (IP)*, Ottawa, ON, **2011**, 1-2.

195. Vasapollo, G.; Sole, R. D.; Mergola, L.; Lazzoi, M. R.; Scardino, A.; Scorrano, S.; Mele, G., Molecularly imprinted polymers: Present and future prospective. *International Journal of Molecular Sciences* **2011,** *12*, 5908-5945.

196. Nowack, B.; Sigg, L., Adsorption of EDTA and metal–EDTA complexes onto goethite. *Journal of Colloid and Interface Science* **1996,** *177*, 106-121.

197. Delmarre, D.; Méallet, R.; Bied-Charreton, C.; Pansu, R. B., Heavy metal ions detection in solution, in sol–gel and with grafted porphyrin monolayers. *Journal of Photochemistry and Photobiology A: Chemistry* **1999,** *124*, 23-28.

198. Gokel, G. W.; Leevy, W. M.; Weber, M. E., Crown ethers: Sensors for ions and molecular scaffolds for materials and biological models. *Chemical Reviews* **2004,** *104*, 2723-2750.

199. Benounis, M.; Jaffrezic-Renault, N.; Halouani, H.; Lamartine, R.; Dumazet-Bonnamour, I., Detection of heavy metals by an optical fiber sensor with a sensitive cladding including a new chromogenic calix[4]arene molecule. *Materials Science and Engineering: C* **2006,** *26*, 364-368.

200. Erdem, E.; Karapinar, N.; Donat, R., The removal of heavy metal cations by natural zeolites. *Journal of Colloid and Interface Science* **2004,** *280*, 309-314.

201. Zhang, L.; Zhang, W.; Shi, J.; Hua, Z.; Li, Y.; Yan, J., A new thioether functionalized organic–inorganic mesoporous composite as a highly selective and capacious Hg2+ adsorbent. *Chemical Communications* **2003**, 210-211.

202. Liu, T.; Li, G.; Zhang, N.; Chen, Y., An inorganic–organic hybrid optical sensor for heavy metal ion detection based on immobilizing 4-(2-pyridylazo)-resorcinol on functionalized HMS. *Journal of Hazardous Materials* **2012,** *201-202*, 155-161.

203. Goddard, J. M.; Hotchkiss, J. H., Polymer surface modification for the attachment of bioactive compounds. *Progress in Polymer Science* **2007,** *32*, 698-725.

204. Justino, C. I. L.; Freitas, A. C.; Pereira, R.; Duarte, A. C.; Rocha Santos, T. A. P., Recent developments in recognition elements for chemical sensors and biosensors. *TrAC Trends in Analytical Chemistry* **2015,** *68*, 2-17.

205. Chen, W. *Chemical Detection and Sensing Using Optical Interferometry*. M.A.Sc Thesis, Queen's University, 2013.

206. Saunders, J. E.; Chen, H.; Brauer, C.; Clayton, M.; Chen, W.; Barnes, J. A.; Loock, H.-P., Quantitative diffusion and swelling kinetic measurements using large-angle interferometric refractometry. *Soft Matter* **2015,** *11*, 8746-8757.

Chapter 3

Analyte Concentrations in Films and Diffusion Processes

This chapter describes the theory used to determine analyte concentrations within polymer films from refractive index changes and film swelling during chemical uptake. We present equations that can be applied to interferometric refractometry and other miniaturized refractive index sensors including photonic wire micro-resonators and interferometers. The kinetics describing the concentration changes within films can then be related to diffusion. The theory behind diffusion and the mathematics that govern Fickian systems are described in detail. In a brief introduction, several experimental techniques that can be used for measuring diffusion are described. Concentration measurements can also be used at equilibrium to determine partition coefficients, as will be shown below.

Our models are readily transferrable to different films, coatings, and varnishes. For example, solid phase microextraction (SPME) is a sample preparation technique that takes advantage of partitioning of analytes with a polymer film at equilibrium. Combining SPME coatings directly with refractive index sensors is a useful method to understand chemical systems as is later discussed in Chapter 7. Once characterized, SPME coatings can be applied to miniaturized refractive index systems for the development of chemical sensors as discussed in Chapters 8.

3.1 Introduction

The absolute analyte concentration in a polymer film can be difficult to measure. For films with comparably large volume and surface area, it is easiest to simply measure the mass change of the system upon exposure to an analyte.[1-2] However, sample introduction in gravimetric experiments can be challenging, and balances may be subject to drift and instability over long periods of time. An alternative approach is to periodically weigh a sample material during its exposure to an analyte.[3] This may result in increased noise, and limited temporal resolution of the uptake or release process. In some cases, thickness changes due to swelling can be used as an approximation of the film concentration. For example, the swelling of an SU-8 cantilever when exposed to water[4] or the swelling of a hydrogel when exposed to

water[5] was used as a proxy for the analyte concentration in the solid matrix. Unfortunately, when partitioning occurs into a film, a substantial density change may also occur and in an extreme case of a rigid porous film, a large amount of analyte may be partitioned into the film without any measurable thickness change. The concentration of a sorbent in a film can be determined much more accurately by measuring both the thickness and refractive index changes. The refractive index is not expected to change linearly with analyte concentration, as only the polarizabilities of the components should be additive. This is expected by the additivity of the Lorentz-Lorenz equation.[6] In this chapter, I will develop a mathematical model to relate refractive index and thickness changes to the concentration of an analyte within a film. The determination of refractive index and thickness of polymer films using a large angle interferometric refractometer is discussed in Chapter 4.

3.2 Determining Analyte Concentrations in Films

The polarizability of molecules is related to the strength of their induced dipole within the presence of an electric field,[7] as was discussed in Chapter 2. Classically, the induced dipole may be understood as a measure of how easily the electrons can be moved around within a molecule. The molar polarization of a compound, P, is related to the polarizability of individual molecules.[7]

$$P = \frac{N_A \alpha}{3\varepsilon_0} \tag{3.1}$$

Here, N_A is Avogadro's number, α is the polarizability of a molecule, and ε_0 is the vacuum permittivity. The polarizability, α ,is a tensor, and can be anisotropic, i.e. the distortion of the electrons depends on the direction of the electric field.[6] In our case of a large assembly of disordered molecules, we treat the average polarizability as an isotropic (scalar) molecular property. The polarization can be related to the bulk properties of a material such as refractive index, n, density, ρ, and molar mass, M.[7]

$$P = \frac{n^2 - 1}{n^2 + 2}\frac{M}{\rho} \tag{3.2}$$

The combination of these two equations gives the Lorentz-Lorenz equation relating the polarizability, α, of a material to its refractive index, n.[7]

$$\frac{n^2-1}{n^2+2}=\frac{N_A\alpha}{3\varepsilon_0} \tag{3.3}$$

The overall refractive index of a mixture of compounds does not change linearly with the relative quantity of each substance. However, the polarization contributions are additive, such that the polarization of a mixture, P_{mix}, can be determined from the polarizations of the two components weighted by the respective mole fractions, X. In our specific case of a binary mixture with an analyte and a polymer matrix the two contributions are given subscripts A and P, respectively.

$$\begin{aligned} P_{mix} &= X_A P_A + X_p P_p \\ P_{mix} &= X_A P_A + \left(1-X_A\right) P_p \end{aligned} \tag{3.4}$$

With equation (3.2), the polarization of the mixture can be related to its refractive index and density.

$$\begin{aligned} P_{mix} &= \frac{{n_{mix}}^2-1}{{n_{mix}}^2+2}\frac{M_{mix}}{\rho_{mix}} \\ P_{mix} &= \frac{{n_{mix}}^2-1}{{n_{mix}}^2+2}\frac{X_A M_A+\left(1-X_A\right)M_p}{\rho_{mix}} \end{aligned} \tag{3.5}$$

Equating equation (3.5) to equation (3.4) allows for the derivation of the relationship between the analyte concentration within a film and molar polarization.

$$\left(\frac{{n_{mix}}^2-1}{{n_{mix}}^2+1}\right)\frac{X_A M_A+\left(1-X_A\right)M_P}{\rho_{mix}} = X_A P_A+\left(1-X_A\right)P_P \tag{3.6}$$

Equation (3.6) can be expanded so it is easier for future rearrangement.

$$\left(\frac{{n_{mix}}^2-1}{{n_{mix}}^2+2}\right)\left(\frac{X_A M_A - X_A M_P}{\rho_{mix}}\right)+\left(\frac{{n_{mix}}^2-1}{{n_{mix}}^2+2}\right)\left(\frac{M_P}{\rho_{mix}}\right) = X_A P_A - X_A P_P + P_P \tag{3.7}$$

This expanded equation can be rearranged to solve for X_{A}.

$$X_A = \frac{P_P - \left(\frac{n_{mix}{}^2 - 1}{n_{mix}{}^2 + 2}\right)\frac{M_P}{\rho_{mix}}}{\left[\left(\frac{n_{mix}{}^2 - 1}{n_{mix}{}^2 + 2}\right)\left(\frac{M_A - M_P}{\rho_{mix}}\right) - \left(P_A - P_P\right)\right]} \tag{3.8}$$

It is often not possible to measure the density of the mixture ρ_{mix}, so an expression must be derived and substituted for this term. Let us first consider the equation for the mole fraction, where the masses and molar masses are expressed as *m* and *M* respectively.

$$X_A = \frac{\frac{m_A}{M_A}}{\frac{m_A}{M_A} + \frac{m_P}{M_P}} \tag{3.9}$$

Equation (3.9) can be re-arranged to give an expression for ratio of the two masses.

$$\frac{m_A}{m_P} = \left(\frac{X_A}{1 - X_A}\right)\frac{M_A}{M_P} \tag{3.10}$$

The ratio of the density of the mixture, ρ_{mix}, and the density of the polymer material, ρ_P, can be described based on the initial thickness, *d*, the thickness of the mixture, $d + \Delta d$, and the respective masses of each component, m_a and m_p. This equation assumes that the swelling during partitioning of an analyte into a film occurs in one dimension such that the film's footprint area, *A*, remains constant.

$$\begin{aligned} \frac{\rho_{mix}}{\rho_P} &= \frac{\frac{m_A + m_P}{(d + \Delta d)A}}{\frac{m_P}{dA}} \\ \frac{\rho_{mix}}{\rho_P} &= \left(\frac{m_A + m_P}{m_p}\right)\left(\frac{d}{d + \Delta d}\right) \end{aligned} \tag{3.11}$$

This can be simplified and re-arranged to derive an equation for the density of the mixture.

$$\rho_{mix} = \rho_P \frac{\left(1 + \frac{m_A}{m_P}\right)}{\left(1 + \frac{\Delta d}{d}\right)} \tag{3.12}$$

Substituting equation (3.10) into equation (3.12) gives an expression for the density of the mixture where the terms are either known constants (molar masses, M) or measurable properties (d and Δd).

$$\rho_{mix} = \rho_P \frac{\left(1+\left(\frac{X_A}{1-X_A}\right)\frac{M_A}{M_P}\right)}{\left(1+\frac{\Delta d}{d}\right)} \tag{3.13}$$

Substituting equation (3.13) into equation (3.8) gives an expression that uses only constants and measurable properties.

$$X_A = \frac{P_P - \left(\frac{{n_{mix}}^2-1}{{n_{mix}}^2+2}\right)\frac{M_P\left(1+\frac{\Delta d}{d}\right)}{\rho_P\left(1+\left(\frac{X_A}{1-X_A}\right)\frac{M_A}{M_P}\right)}}{\frac{{n_{mix}}^2-1}{{n_{mix}}^2+2}\frac{\left(M_A-M_P\right)\left(1+\frac{\Delta d}{d}\right)}{\rho_P\left(1+\left(\frac{X_A}{1-X_A}\right)\frac{M_A}{M_P}\right)} + P_p - P_A} \tag{3.14}$$

This resulting equation appears unnecessarily complicated. We simplify the equation by removing a factor of $\left[1+\left(\frac{X_A}{1-X_A}\right)\frac{M_A}{M_P}\right]^{-1}$ from both the numerator and denominator.

$$X_A = \frac{P_P\left(1+\left(\frac{X_A}{1-X_A}\right)\frac{M_A}{M_P}\right) - \left(\frac{{n_{mix}}^2-1}{{n_{mix}}^2+2}\right)\frac{M_P}{\rho_P}\left(1+\frac{\Delta d}{d}\right)}{\left(\frac{{n_{mix}}^2-1}{{n_{mix}}^2+2}\right)\left(\frac{M_A-M_P}{\rho_P}\right)\left(1+\frac{\Delta d}{d}\right) + \left(P_P-P_A\right)\left(1+\left(\frac{X_A}{1-X_A}\right)\frac{M_A}{M_P}\right)} \tag{3.15}$$

The molar polarization of the polymer film (equation (3.2)) is then rearranged.

$$\frac{M_P}{\rho_P} = P_P\left(\frac{{n_P}^2+2}{{n_P}^2-1}\right) \tag{3.16}$$

Substitution of equation (3.16) into (3.15) brings us closer to the final equation.

$$X_A = \frac{P_P\left(1+\left(\frac{X_A}{1-X_A}\right)\frac{M_A}{M_P}\right) - P_P\left(\frac{{n_{mix}}^2-1}{{n_{mix}}^2+2}\right)\left(\frac{{n_P}^2+2}{{n_P}^2-1}\right)\left(1+\frac{\Delta d}{d}\right)}{\left(\frac{{n_{mix}}^2-1}{{n_{mix}}^2+2}\right)\left(\frac{M_A}{\rho_P}\right)\left(1+\frac{\Delta d}{d}\right) - P_P\left(\frac{{n_{mix}}^2-1}{{n_{mix}}^2+2}\right)\left(\frac{{n_P}^2+2}{{n_P}^2-1}\right)\left(1+\frac{\Delta d}{d}\right) + \left(P_P - P_A\right)\left(1+\left(\frac{X_A}{1-X_A}\right)\frac{M_A}{M_P}\right)} \tag{3.17}$$

After re-arrangement of equation (3.17), an expression is derived to relate the analyte concentration within the film, X_A, to the film refractive index and thickness changes.

$$X_A = \frac{P_P - P_P\left(\frac{{n_{mix}}^2-1}{{n_{mix}}^2+2}\right)\left(\frac{{n_p}^2+2}{{n_p}^2-1}\right)\left(1+\frac{\Delta d}{d}\right)}{P_P - P_P\left(\frac{{n_{mix}}^2-1}{{n_{mix}}^2+2}\right)\left(\frac{{n_p}^2+2}{{n_p}^2-1}\right)\left(1+\frac{\Delta d}{d}\right) - P_A} \tag{3.18}$$

Where the refractive indices of the original polymer and mixture, n_P and n_{mix}, initial film thickness, d, and thickness change, Δd, are experimentally obtained. The molar polarizations of the polymer and analyte are calculated using equation (3.2) from literature values of density and refractive index. For polymers, the molar mass, M_P, is assumed to be the molar mass of a monomer unit of the polymer. The full rearrangement between equations (3.17) and (3.18) is described in Appendix 3.1.

The dynamic analyte concentration within a film during chemical partitioning will often be diffusion controlled. The basic theory and mathematics behind Fickian diffusion are described in the following section.

3.3 Diffusion Coefficients

Polymers can exist in two distinct states: a rigid or glassy state, and at higher temperatures, a flexible rubbery state.[8] The temperature change between these two states is known as the glass transition temperature.[8] The migration of an analyte into a polymer can be described by Fickian diffusion at temperatures above the glass transition temperature of the material.[9] Rubbery polymers are flexible and easily allow analyte permeation and mobility within a film.[9] The glass transition temperature of PDMS is T_g = -123°C,[10] which means that analyte diffusion at room temperature is expected to be Fickian. Films below the glass transition tend to be rigid and the polymer chain relaxation rate is either comparable or slower than the analyte diffusion.[9] These materials can be modeled using other non-Fickian models.[9] The

glass transition temperature for SU-8 2000 epoxy photoresist is T_g = 210°C,[11] suggesting that diffusion at room temperature should be non-Fickian. For tracer diffusion at low concentration and at early times, the diffusion of water and other analytes into SU-8 has been shown to behave Fickian in the literature.[4, 12-13] Fickian diffusion will be used to describe the theory behind diffusion and provide suitable diffusion models that will be used later in this thesis.

3.3.1 Theory of Diffusion in Polymer Systems

Diffusion is typically explained as the migration of molecules from an area of high concentration to an area of lower concentration through a "random walk" motion. The mathematics used to explain diffusion were developed by Fick and are analogous to the equations previously derived by Fourier to describe heat conduction.[14] The flux, *F*, i.e. the rate of molecule transfer per unit area, is described by Fick's First Law and is related to a diffusion constant, *D*, and the concentration gradient in the medium, $\delta C/\delta x$.[7]

$$F = -D\frac{\delta C}{\delta x} \tag{3.19}$$

In many applications flux may be difficult to measure, so it becomes more practical to measure diffusion through changes in concentration over time, $\delta C/\delta t$, as it is expressed in Fick's Second Law for one dimensional diffusion.[7]

$$\frac{\delta C}{\delta t} = D\frac{\delta^2 C}{\delta x^2} \tag{3.20}$$

Here, the concentration change is related to a diffusion constant, *D*, and a second order differential equation with respect to position, *x*. While solutions to these equations are not trivial and depend on the boundary conditions that are applied, equation (3.20) has been rigorously solved for a variety of different conditions by Crank.[14]

For the diffusion into a film of thickness, *d*, that is attached to an impermeable boundary at $x = 0$ (i.e. a glass substrate), the boundary conditions include a constant analyte concentration above the film, C_∞, an initial analyte concentration in the film of zero, and assume that the bottom of the film is constantly impermeable.[14]

$$\begin{aligned} C &= C_\infty, & x &= d, & t &\geq 0 \\ C &= 0, & x &= 0, & t &\geq 0 \\ C &= 0, & 0 < x &< d, & t &= 0 \end{aligned} \tag{3.21}$$

The solution for diffusion into a film attached to an impermeable boundary at $x = 0$ with coordinates of $0 < x < d$ is identical to the symmetrical diffusion from both sides into a film of twice the thickness ($d < x < d$) and can be expressed as an infinite sum of exponentials.[14]

$$C(x,t) = C_\infty \left[1 - \frac{4}{\pi} \sum_{n=0}^{\infty} \frac{(-1)^n}{2n+1} \exp\left(-D(2n+1)^2 \frac{\pi^2 t}{4d^2} \right) \times \cos\left((2n+1) \frac{\pi x}{2d} \right) \right] \tag{3.22}$$

Where C_∞, is the limiting concentration as $t \to \infty$. This equation agrees best over moderate and large times.[15] For short times, the concentration profile is better expressed by a sum of complementary error functions.[15]

$$C(x,t) = C_\infty \left[\sum_{n=0}^{\infty} (-1)^n \operatorname{erfc}\left(\frac{(2n+1)d - x}{2\sqrt{Dt}} \right) + \sum_{n=0}^{\infty} (-1)^n \operatorname{erfc}\left(\frac{(2n+1)d + x}{2\sqrt{Dt}} \right) \right] \tag{3.23}$$

For those who are unfamiliar with error functions, a brief primer has been included in Appendix 3.2.[16]

When diffusion is assumed to occur from both sides of the polymer, the diffusion equations (eqns. (3.22) and (3.23)) will differ by a factor of 2 on d, as a result of a difference in the coordinate system.[17] This is also true for the integrated version of this equation which is used to determine the average concentration within a film.[18-19] This difference in coordinate system is described in Figure 3.1. When deriving diffusion expressions it is important to use the correct coordinate system in order to arrive at the appropriate model for the system. The equations for symmetrical diffusion are analogous to the equations presented in this chapter and are well summarized in the literature.[20-21]

The time-dependent concentration profiles for a film with a thickness of $d = 40$ μm and a diffusion constant of $D = 1.00 \times 10^{-8}$ cm^2/s were calculated using equations (3.22) and (3.23). The resulting profiles are shown in Figure 3.2. All the red curves were calculated using a sum of 10 exponential functions and all of the dashed black lines using a sum of 10 complementary error functions.

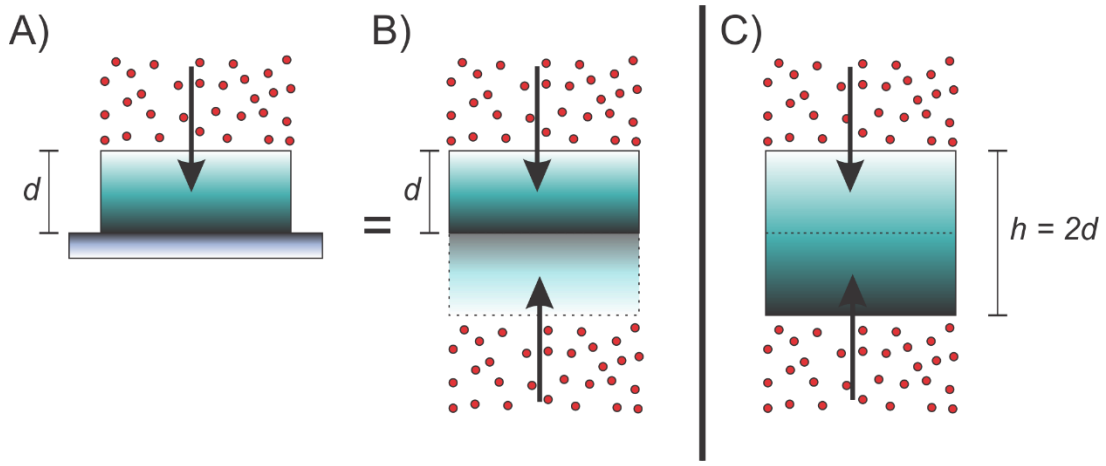

Figure 3.1: Graphical representation of different film coordinate systems used for the derivation of diffusion equations. A) Diffusion through a film of thickness, *d*, that is mounted on an impermeable boundary such that diffusion only occurs from the top surface of the film. The solution to the diffusion in A) is the same as that of B). B) Symmetrical diffusion into a film of thickness 2*d*. C) Typically symmetrical diffusion is expressed with a total film thickness h, which will differ by a factor of 2 or 4 on *d* and d^2 respectively in all diffusion equations.

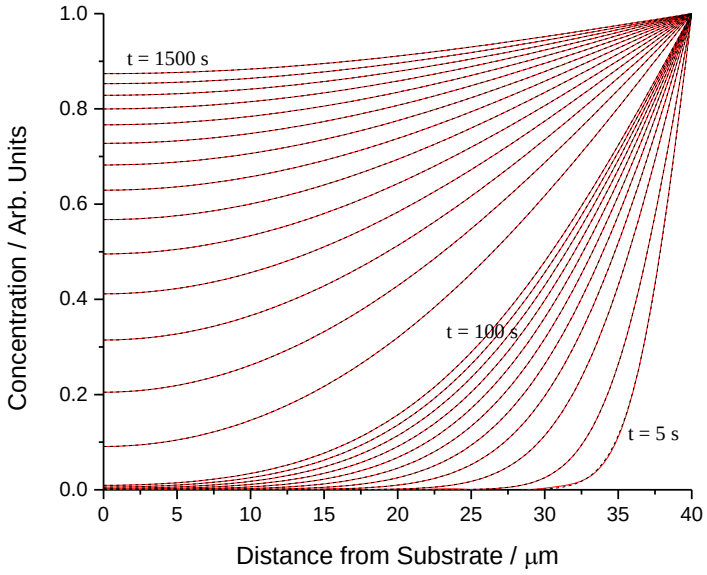

Figure 3.2: Concentration profiles for diffusion of an analyte into a 40 μm thick film with a diffusion coefficient of $D = 1.00\times10^{-8}$ cm^2/s. The top of the film $x = 40$ μm is where the analyte is exposed to the top of the film and the bottom at $x = 0$ μm represents an impermeable boundary at the film-substrate interface. Curves are shown from right to left for $t = 5$ s, for $t = 10$-100 s in 10 second intervals, and for $t = 100$-1500 s in 100 second intervals. In each case, the red lines show a sum of 10 exponential functions (equation (3.22)) and the black dashed lines a sum of 10 complementary error functions (equation (3.23)).

The sum of exponential functions model the concentration profile well at medium to late times but at early times many terms are needed to accurately model the concentration profile. To demonstrate this effect, the concentration profiles were modeled using equation (3.22) with 1, 3, 5, 7 and 10 terms respectively at t = 5 s, t =100 s and t =1000 s and are shown in Figure 3.3. It is quite noticeable that at t =5 s, the model requires more than 7 terms before the oscillations in the concentration profile disappear. At t = 100 s it only takes 3 terms to effectively model the profile and at later times of t = 1000 s a single exponential term is sufficient for modeling the concentration profile.

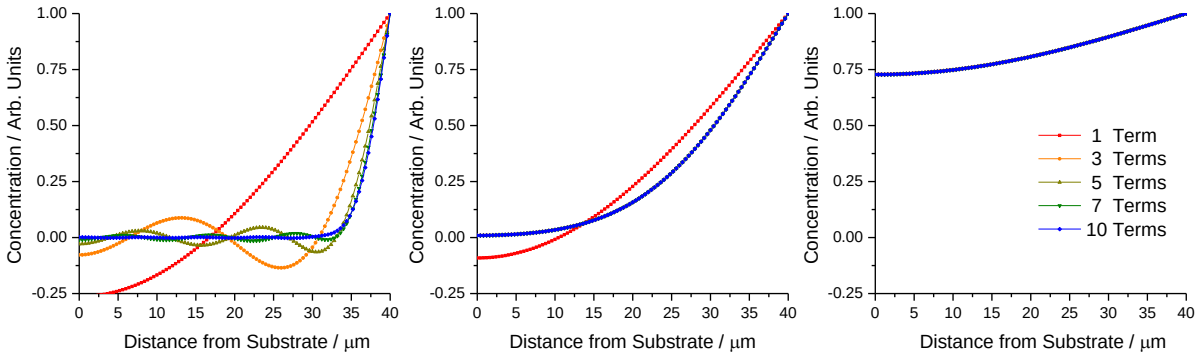

Figure 3.3: Modelling of concentration profiles using a sum of exponential functions at early, medium and late times. Concentration profiles were calculated at t = 5 s, t = 100 s, and t = 1000 s using 1, 3, 5, 7 and 10 exponential terms. At early times (t = 5s), more than 7 exponential terms are needed to suitably model the diffusion profile. Less than 7 terms results in oscillations in the concentration profiles. At medium times (t = 100s) only 3 terms are needed, and at later times (t = 1000s) only a single term is needed to give an accurate concentration profile.

At early times, a sum of error functions can also be used to determine the concentration profile within a material. The concentration was modelled using the same number of terms and at the same times as shown for the exponential functions in Figure 3.3. The resulting curves are shown in Figure 3.4. For the ease of computation, a ten-term exponential fit is likely the simplest method for reliable analysis. It is important to emphasize that adding additional terms does not increase the number of fitting parameters even though it improves the model of the system.

Experimentally, it is not easy to measure concentration profiles within a film. The concentration can be probed at the film-substrate interface, e.g. using microresonators, long period gratings or attenuated total internal reflection spectroscopy (ATR).

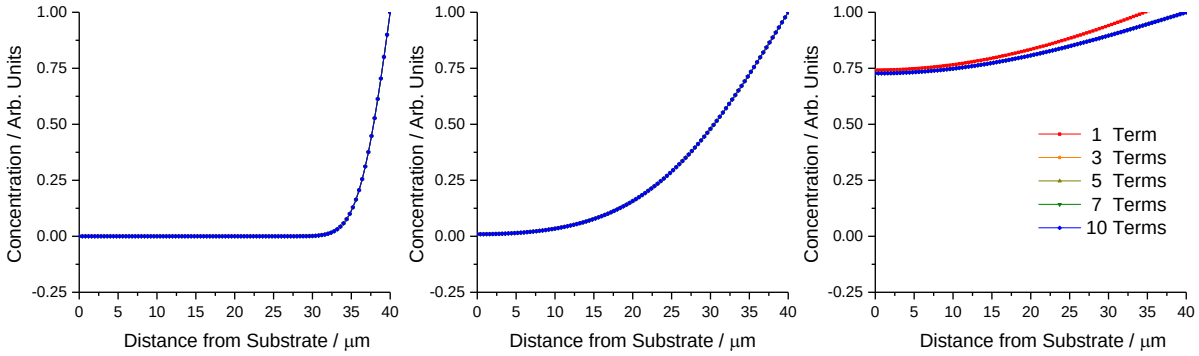

Figure 3.4: Modelling of concentration profiles using a sum of complementary error functions (erfc) at early, medium and late times. Concentration profiles were calculated at *t* = 5 s, *t* = 100 s, and *t* = 1000 s using 1, 3, 5, 7 and 10 erfc terms. At early and medium times (*t* = 5 s, 100 s), only a single term was needed to model the diffusion profile. At later times (*t* = 1000 s), three terms were required to effectively model the concentration within the film. Moving further to later times will require even more terms to properly model the concentration.

Alternatively, the average concentration throughout the bulk film can be measured gravimetrically or through mass spectrometry. When studying the concentration at a film-substrate interface, equation (3.22) can be solved at $x = 0$, causing the cosine function to go to unity.

$$C\left(x=0,t\right)=C_{\infty}\left[1-\frac{4}{\pi}\sum_{n=0}^{\infty}\frac{\left(-1\right)^{n}}{2n+1}\exp\left(-D\left(2n+1\right)^{2}\frac{\pi^{2}t}{4d^{2}}\right)\right] \tag{3.24}$$

A similar equation can be derived to describe the average concentration in a film by integrating equation (3.22).

$$\begin{aligned}\bar{C}\left(t\right)&=\frac{1}{d}\int_{x=0}^{d}C_{\infty}\left[1-\frac{4}{\pi}\sum_{n=0}^{\infty}\frac{\left(-1\right)^{n}}{2n+1}\exp\left(-D\left(2n+1\right)^{2}\frac{\pi^{2}t}{4d^{2}}\right)\times\cos\left(\left(2n+1\right)\frac{\pi x}{2d}\right)\right]dx\\ \bar{C}\left(t\right)&=C_{\infty}\left[1-\frac{8}{\pi^{2}}\sum_{n=0}^{\infty}\frac{\left(-1\right)^{n}}{\left(2n+1\right)^{2}}\exp\left(-D\left(2n+1\right)^{2}\frac{\pi^{2}t}{4d^{2}}\right)\times\sin\left(\left(2n+1\right)\frac{\pi}{2}\right)\right]\end{aligned} \tag{3.25}$$

The sine function produces odd multiples of $\frac{\pi}{2}$ so it can be replaced with:

$$\sin\left(\frac{\left(2n+1\right)\pi}{2}\right)=\left(-1\right)^{n} \tag{3.26}$$

This yields the final equation for the average analyte concentration in the film.

$$\bar{C}(t) = C_{\infty}\left[1 - \frac{8}{\pi^2}\sum_{n=0}^{\infty}\frac{1}{(2n+1)^2}\exp\left(-D(2n+1)^2\frac{\pi^2 t}{4d^2}\right)\right] \tag{3.27}$$

The concentration at the film-substrate interface is delayed relative to the bulk as it takes time for the sorbate to diffuse to the bottom of the film before a response can be observed. This initial time lag is shown in Figure 3.5 for a modeled diffusion with a rate of $D = 1.00\times10^{-8}$ cm^2/s through a 40 µm thick film. The two curves were calculated using ten term approximations of equations (3.24) and (3.27).

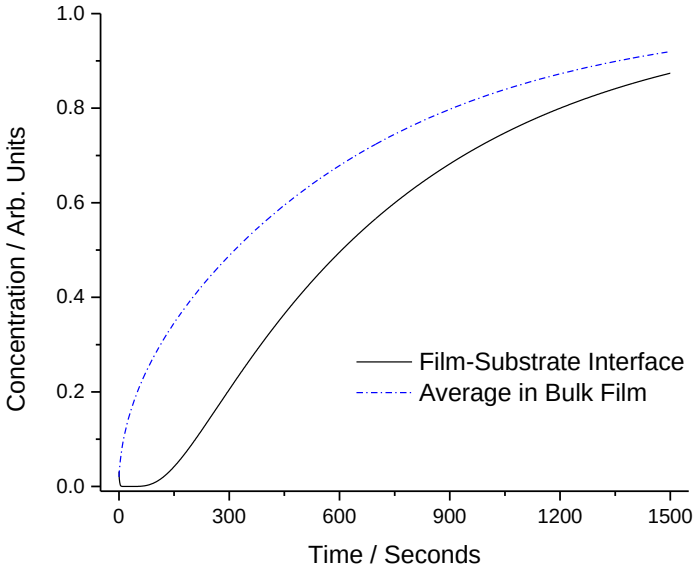

Figure 3.5: Modeled diffusion curves of concentration changes in the bulk film and at the film-substrate interface of a 40 µm film with a diffusion rate of $D = 1.00\times10^{-8}$ cm^2/s. The dashed blue line shows the average concentration in the film calculated using 10 terms with equation (3.27). The solid black line shows the concentration at the film-substrate interface calculated using 10 terms with equation (3.24).

It is also possible to calculate the diffusion coefficient from the average concentration changes at early times using a complex sum of complementary error functions.[14]

$$\bar{C}(t) = 2C_{\infty}\left(\frac{Dt}{d^2}\right)^{1/2}\left[\frac{1}{\sqrt{\pi}} + 2\sum_{n=1}^{\infty}(-1)^n \,\mathrm{ierfc}\left(\frac{nd}{\sqrt{Dt}}\right)\right] \tag{3.28}$$

To improve the fitting at both early and late times, Balik described a blended model that fits to equations analogous to (3.27) and (3.28) using a Fermi function to weight between the two equations as a function of time.[20]

$$\frac{C(t)}{C_\infty} = \phi(x)\, f(x) + \left[1 - \phi(x)\right] g(x) \tag{3.29}$$

Here, f(x) and g(x) represents the two functions and ϕ is the Fermi function that weights between the two functions with time. A number of approximations are often used based on equation (3.27) to simplify determination of diffusion coefficients. Balik illustrated several different methods for extracting diffusion coefficients from gravimetric data of sorption in thin polymer films.[20] The different approximations are explained and evaluated using the simulated data from Figure 3.5 in the following section.

3.3.2 Approximations for Estimating Diffusion Coefficients

The equations in the previous section are solutions for a film of thickness, d, with an impermeable membrane at $x = 0$. A number of different approximations based on the diffusion equations are used in the literature when solving diffusion coefficients. In the following section we compare these approaches, briefly explain the assumptions and test the methods with the modelled diffusion through a 40 μm film with a diffusion coefficient of 1.00×10^{-8} cm^2/s. In each case the equations have been modified to agree with our reference frame as was discussed in the previous section. It can be quite challenging to accurately determine the saturated analyte concentration in the film, C_∞. The robustness of the various models and the resulting uncertainty of the diffusion constants was therefore tested by varying the asymptotic (equilibrium) concentration, C_∞, by ± 10%. The diffusion coefficients obtained using all of the different models will be summarized at the end.

If the analyte concentration in the saturated film is well defined, the diffusion coefficient can be determined from the time of half concentration ($t_{0.5}$), where $C/C_\infty = 0.5$. Taking a two term approximation of equation (3.27) gives the following relationship.[15, 20-21]

$$D = \frac{0.19675 d^2}{t_{0.5}} \tag{3.30}$$

For the model diffusion into a 40 μm thick film with a diffusion coefficient of $D = 1.00\times10^{-8}$ cm^2/s (Figure 3.5), the half-concentration time was found to be $t_{0.5}$ = 315 s. This corresponded to a diffusion coefficient of $D = 0.99\times10^{-8}$ cm^2/s. If the saturated concentration was higher or lower by 10%, then $t_{0.5}$ = 260-390 s, which yielded diffusion coefficients $D = 0.81\text{-}1.21\times10^{-8}$ cm^2/s.

Alternatively, diffusion rates may be determined from the initial uptake rate. The relative concentration C/C_∞ forms a straight line when graphed against $t^{1/2}$ using a single term approximation of equation (3.28) (Figure 3.6).[20-21] At early times, the complementary error function is negligibly small and the first part of the equation will be dominant.

$$\frac{C}{C_\infty} = \frac{2}{d}\left(\frac{Dt}{\pi}\right)^{0.5} \tag{3.31}$$

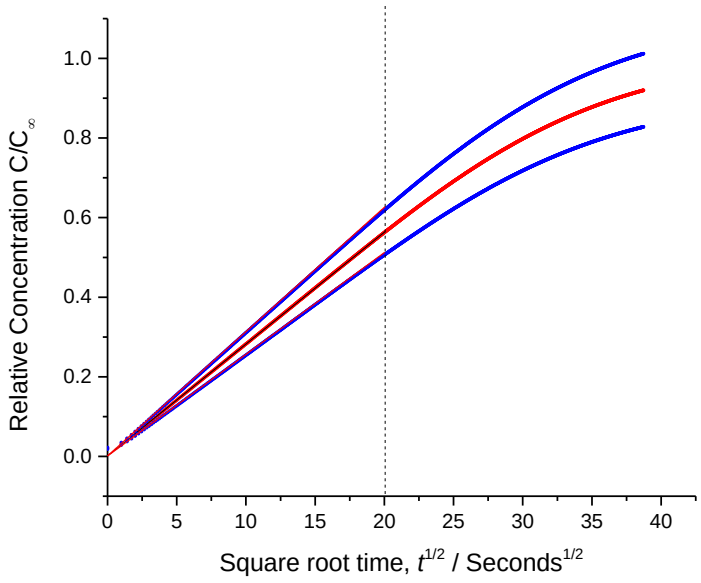

Figure 3.6: Estimation of the diffusion coefficient from the initial slope of the relative concentration with the square root of time. The red curve shows the relative concentration assuming no errors in the saturated concentration. The two blue curves show the fits if the saturated concentration was different by ± 10%. Each curve was fit from *t* = 0-400 s.

The linear slope from the correctly modeled data yielded a diffusion coefficient of $D = 0.99\times10^{-8}$ cm^2/s. If there was a 10% error in the saturated concentration, the diffusion coefficient ranged from $D = 0.82\text{-}1.23\times10^{-8}$ cm^2/s.

Diffusion coefficients can also be obtained from the limiting slope at later times from a plot of $\ln(1\text{-}C/C_\infty)$ vs t (Figure 3.7). This equation is derived from a single term of equation (3.27).[20-21]

$$\ln\left(1-\frac{C}{C_\infty}\right)=\ln\left(\frac{8}{\pi^2}\right)-\frac{\pi^2 Dt}{4d^2} \tag{3.32}$$

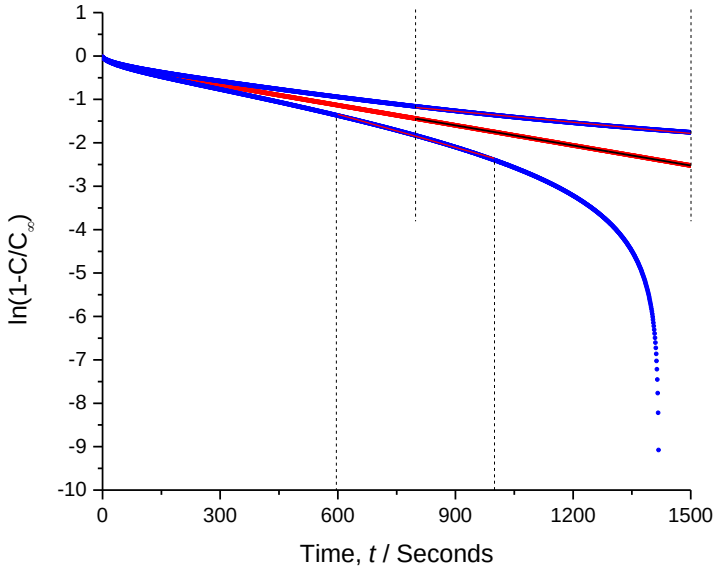

Figure 3.7: Estimation of the diffusion coefficient from the limiting slope at late time of $\ln(1\text{-}C/C_\infty)$ versus time. When the saturated concentration is underestimated the curve deviates from linearity at late times, as C/C_∞ becomes greater than 1. In this case, the linear function was fit to data from t = 600-1000 s. For the actual data and the overestimated saturated concentration, the linear fit was taken from t = 800-1500 s. The fitting regions are shown by the dashed lines.

If the saturated concentration is underestimated by 10%, the curve is no longer linear and will not give a good approximation of the diffusion coefficient. When there is no error in the saturated concentration, the correct diffusion coefficient was determined as $D = 1.00\times10^{-8}$ cm^2/s. When the concentration was different by ±10% the diffusion coefficient ranged from $D = 0.55\text{-}1.65\times10^{-8}$ cm^2/s.

When the saturated film concentration, C_∞, is not well known, the diffusion constant can be calculated from the derivative of a single term of equation (3.27).[20-21]

$$\ln\left(\frac{d\bar{C}(t)}{dt}\right) = \ln\left(\frac{2DC_\infty}{d^2}\right) - \frac{\pi^2 Dt}{4d^2} \tag{3.33}$$

At long times, the slope can be taken of a plot of ln(dC/dt) versus *t* as is shown in Figure 3.8.

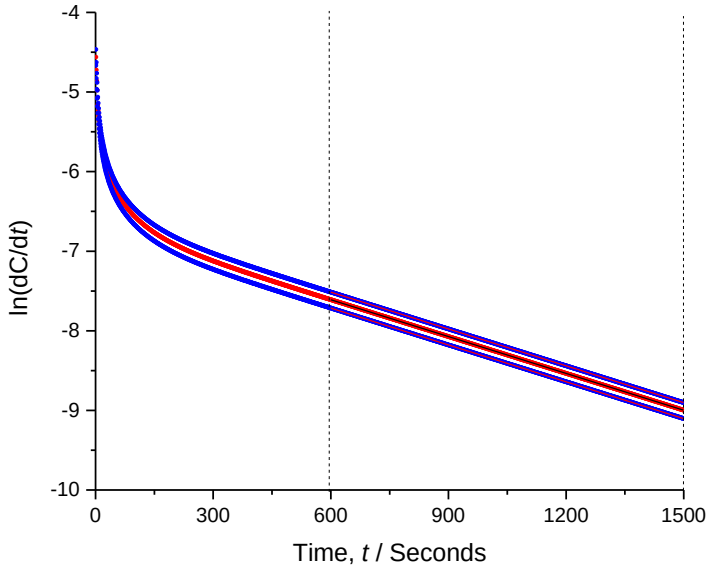

Figure 3.8: Estimation of the diffusion coefficient from the limiting slope at late times of the logarithm of the derivative versus time. This model does not require the saturated concentration to be known, as this will only affect the *y*-intercept and not the slope. The red curve shows the actual saturated concentration and the two blue curves show ±10% error on the saturation concentration. In each case the linear fits from *t* = 600-1500 s yielded diffusion coefficients of *D* = 1.00×10^{-8} cm^2/s.

This method is independent of the saturation concentration and yielded diffusion of $D = 1.00\times10^{-8}$ cm^2/s from the linear fits in all three curves.

A final method determines diffusion coefficients from the full dataset by first integrating over the full sorption isotherm to calculate the sorption moment, τ_s.[20-21]

$$\tau_s = \int_0^\infty \left[1 - \frac{C(t)}{C_\infty}\right] dt \tag{3.34}$$

Equation (3.34) can be equated to the integral of the remaining portion of a single term of equation (3.27) to relate the sorption moment to the diffusion coefficient.

$$\tau_s = \int_0^{\infty} \frac{8}{\pi^2} \exp\left(\frac{-\pi^2 Dt}{4d^2}\right) dt \tag{3.35}$$

After integration and rearrangement, the diffusion coefficient can be calculated from the following relation, which is often further approximated with an integer in the literature.[20-21]

$$D = \frac{32d^2}{\pi^4 \tau_s} \approx \frac{d^2}{3\tau_s} \tag{3.36}$$

A plot of 1-C/C$_\infty$ versus time is presented in Figure 3.9, with the sorption moment of the actual concentration indicated by the hatched region below the red curve.

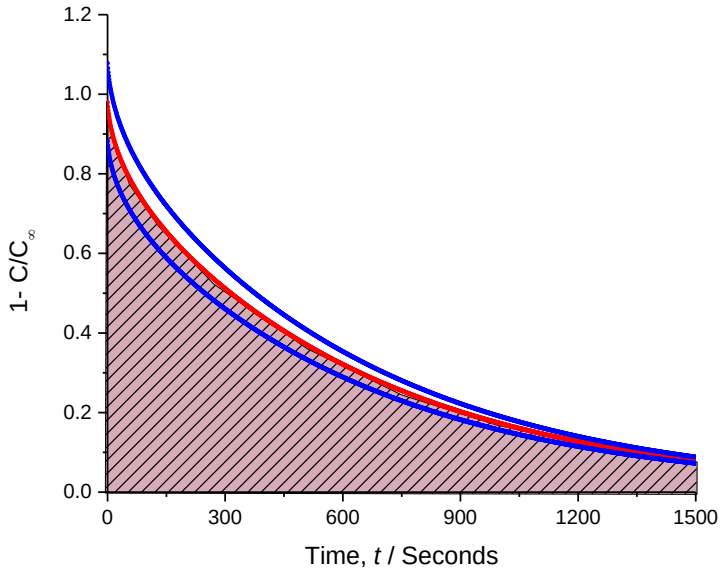

Figure 3.9: The sorption moment is calculated by integrating under the curve of 1-C/C$_\infty$ with time. The red curve shows the diffusion when the correct saturation concentration is used, with the pink hatched area indicating the sorption moment. The two blue curves show an under and over estimation of the saturated concentration by 10%.

The sorption moment was calculated as τ_s = 481.3 from the correct saturation concentration which yielded a diffusion coefficient of D = 1.09×10^{-8} cm^2/s. When the saturation concentration was off by ±10% the sorption moment was τ_s = 379.4-583.2, resulting in diffusion coefficients of D = 0.90-1.39×10^{-8} cm^2/s.

While most of the above methods are approximations based on a single exponential term in equation (3.27), they still adequately determine the diffusion constant when the saturation concentration is well defined. This parameter is often very difficult to determine accurately, so the 10% error on the saturation concentration used to assess the different techniques is realistic, especially with slow diffusion rates where it takes a long time for saturation to be achieved.

The most reliable method for determining the diffusion coefficients is to work directly with the solution of the true diffusion equation (eq.(3.27)). The fits using a single term approximation and a 10 term approximation are given in Figure 3.10. The inset shows that the single term approximate agrees well for t > 200s, and deviates greatly at early time. The ten term approximation should fit exactly as the simulated data was already generated using the ten term diffusion equation. The validity of a ten term approximation was already demonstrated in Figure 3.3. It is important to emphasize that the additional exponential terms does not add any additional fitting parameters and thus does not substantially increase the computational power required for the fit.

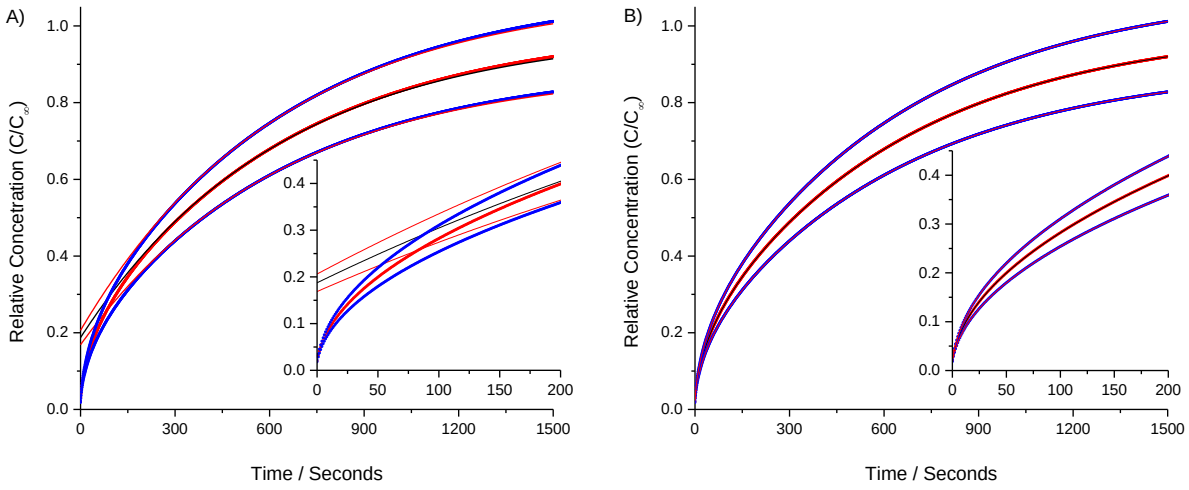

Figure 3.10: Comparison between a single-term and ten-term exponential fit to the simulated diffusion through a 40 μm film with a diffusion coefficient of D =1.00×10^{-8} cm^2/s. The inset shows that at early time (t < 200s) the single term approximation (A) deviates substantially from the data. The ten term approximation (B) shows great agreement with the data throughout the entire fit.

We have shown several methods that are used in the literature for approximating diffusion coefficients in systems. While many of these methods are simple and require minimal computation power,

most require the saturation concentration to be well known. A 10% error in the saturation concentration can result in a 20% error in diffusion coefficients calculated using the half concentration time ($t_{0.5}$), or the initial slope of the relative concentration versus square root time. When using the limiting slope of $\ln(1-C/C_\infty)$ versus time, the diffusion coefficients can deviate even more by 45-65%. Using the sorption moment can result in deviation of 10-39%. The safest methods of determining diffusion coefficients is to take the limiting slope of the derivative or fitting with the exponential solution to the diffusion equation. As was shown in this section, even a single-term approximation only deviated by 2%, with the majority of the error at shorter times. Switching to a ten-term fit may be a bit more complicated to set up initially, but does not require any additional computation power to calculate. The ten-term diffusion fit was used for the studies presented in the rest of this thesis. The diffusion coefficients calculated using all of the methods described above are presented in Table 3.1 for comparison.

Table 3.1: Comparison of diffusion coefficients calculated using a series of different methods. With each method, the diffusion coefficient was also calculated when simulating a ±10% error on the saturation concentration. The safest methods to calculate diffusion coefficients when the saturated concentration is not well defined is to use the limiting slope of the derivative or to fit the data with a sum of 10 exponential terms of equation (3.27).

Method	**Diffusion Coefficients ($\times 10^{-8}$ cm^2/s)**		
	***D* (No Error on C_∞)**	***D* (-10% Error on C_∞)**	***D* (+10% Error on C_∞)**
Half-Concentration ($t_{0.5}$)	1.00	0.81	1.21
Initial slope (C/C_∞ vs $t^{1/2}$)	0.99	0.80	1.20
Limiting slope ($\ln(1-C/C_\infty)$ vs t)	1.00	1.65	0.55
Limiting slope (ln(dC/dt) vs t)	1.00	1.00	1.00
Sorption Moment (τ_S)	1.09	1.39	0.90
Single Exponential Fit (Equation (3.25))	1.02	1.02	1.02
10 Exponential Fit (Equation (3.25))	1.00	1.00	1.00

3.4 Experimental Methods for Measuring Diffusion

Diffusion coefficients can be studied in a variety of ways both in real-time and through sampling materials exposed to an analyte for different amounts of time. In all cases, care must be taken to ensure that the temperature is consistent and that a uniform analyte concentration is available for dosing. Depending on the methods, this may also involve ensuring a gas-tight system around the material being studied such that no unwanted contamination or leaks occur. Sample papers from the literature are used to illustrate the range of different methods that diffusion coefficients can be measured.

Diffusion can be measured through the mass change of a film during the uptake of an exposed analyte. When measuring mass changes, the average film concentration is probed over time and the diffusion should follow equation (3.27). Blume and coworkers used an apparatus to generate saturated solvent vapours and then flowed the vapours over a PDMS film hanging inside of gas cell that was suspended from a balance.[1] Using this apparatus, they measured the diffusion of several gases, water, ethanol, chloroform and toluene into PDMS.[1] In a similar experimental setup, Kaltenecker-Commerçon and coworkers measured the diffusion of water vapour into a polyimide-polydimethylsiloxane copolymer.[2] Lue and coworkers showed that the same studies can also be performed using microbalances to measure changes in thinner PDMS films when exposed to benzene, toluene and cyclohexane.[21] Gravimetric measurements can also be made by sampling a material after different exposure times to an analyte. In the blot and weigh technique, a polymer sample is immersed within a liquid for different amounts of time, blotted dry and then weighed immediately.[3] Cocchi and coworkers used this approach to measure the diffusion of aliphatic hydrocarbons, alcohols and food oils into PDMS.[3] This technique is far less accurate as there may be adsorbed liquid still on the surface of the film and molecules will begin to diffuse out of the polymer as it is being measured. Gravimetric methods are very sensitive for determining the absolute amount of analyte in a film over time. Unfortunately, as we found experimentally, balances may be susceptible to drift and instability over long periods of time, and can be affected by vibrations and air movement in a lab. The results of our gravimetric experiments were inconclusive and are not included in this thesis.

Another way to measure the mass uptake within a film is with a quartz crystal microbalance (QCM) or alternatively known as a thickness shear-mode resonator. This technique works by measuring the change in resonance frequency of a polymer coated quartz crystal as analyte diffuses into a film. For example, Hossenlopp and coworkers used a QCM to measure the diffusion of water into SU-8 photoresist.[12] This technique works best for measuring diffusion in film with a thickness $d < 100$ nm, and can be complicated when studying flexible polymer films as damping terms need to be included to properly model the system.[22]

Several groups have also incorporated polymer membranes at the inlets to different types of mass spectrometers for analysis. Lapack and coworkers studied the diffusion of dichloromethane, acetone and chlorobenzene through a PDMS tube at the inlet of a quadrupole mass spectrometer.[23] Similarly, Boscaini and coworkers studied the diffusion of a series of BTEX compounds, alcohols and ketones through a PDMS tube at the inlet with a proton transfer mass-spectrometer.[24] Oh and coworkers used a polymer sheet membrane at the inlet of a time of flight mass spectrometer to study the diffusion of aromatic compounds, alcohols and fluorinated or iodated aromatic compounds through PDMS.[25] While mass spectrometers allow for quantitative measurements of analyte concentration after calibration, they require high-vacuum systems and expensive equipment. While the results may be very useful, mass spectrometry is generally not a practical method for measuring diffusion coefficients.

Diffusion coefficients can also be measured using standard SPME where samples are collected with an SPME fibre and detected using GC or HPLC.[17, 26] This technique requires repeated sampling over a range of exposure times resulting in sparse diffusion curves with more noise than real-time measurements. Repeated sampling is impractical for determining the diffusion in a system. The major strength of standard SPME is in measuring equilibrium concentration and partition coefficients of film-analyte systems.

Several optical techniques can also be used to measure diffusion into polymer films. Linossier and coworkers used attenuated total internal reflection Fourier transform infrared spectroscopy (ATR-FTIR) to measure the diffusion of water into polymethylmethacrylate (PMMA). This was observed my measuring the IR O-H stretch.[27] Similarly, Balik and Xu used ATR-FTIR to measure the diffusion of water into latex paint.[28] ATR spectroscopy is a quantitative technique for measuring concentrations at the bottom interface

of a film. The resulting diffusion can be fit with equation (3.24). A major limitation of this technique is that it is only suitable for systems where the target analyte has a distinct absorption peak that does not interfere with the polymer film. This can be problematic for measuring C-H stretches of non-polar compounds in organic polymers. This technique can however be quite useful when measuring hydroxyl, amine and carbonyl stretches of analytes absorbed in polymers.

An alternate optical approach to studying diffusion of analytes into polymer systems is through measurement of polymer refractive index changes. Refractive index is a non-specific property and can be used to study most polymer-analyte systems. The disadvantage is that refractive index measurements are non-selective and many different analytes may cause a change in a polymer refractive index. Many highly sensitive refractive index sensors exist and are practical for systems that are very well known and are free of interferences or if functionality can be added to the polymer film to enhance the selectivity. Refractive index sensors can be developed using highly precise lithographic procedures that are capable for mass production of optical chips with silicon wire waveguide microresonators[29-32], silicon Bragg reflectors[33] and silicon nitride waveguide interferometers[34]. Refractive index sensing can also be performed using fibre sensors[35-36], fibre tapers[37-38], long period gratings (LPGs)[39-41], and photonic crystal fibres[42-44]. Additionally, Podgorsek and Franke showed that surface plasmon resonance can be used to study the diffusion of benzene and toluene into a Teflon AF coating.[45] We have studied the diffusion of liquid water into SU-8 photoresist using an interferometric refractometer as will be discussed in Chapter 6 and the diffusion of vapours of volatile hydrocarbons into siloxane polymers as will be discussed in Chapter 7.

Interferometric refractometry is a versatile technique that can used to quantify the uptake of almost any analyte-film pair. Under controlled laboratory conditions it is one of the easiest methods for determining diffusion coefficients benefiting from simultaneously measuring the film thickness and refractive index. Unfortunately, it is currently not practical for field measurements, and is not able to identify complex analyte matrices. Complex analyte matrices may be studied by fingerprint analysis using a series of different polymer films where the relative response can be used to determine the identity and quantity of analytes exposed to a sensor. The understanding of film behaviour gained using our

characterization method can be applied to polymer-coated array sensors on micro-resonator chips for the development of more selective gas-phase analyte sensors.

3.5 Partition Coefficients and Solid Phase Microextraction (SPME)

A common property that can be measured in systems at equilibrium is the partition coefficient. The partition coefficient is the ratio of the equilibrium concentrations within two phases. This provides a measurement of the concentration magnification within one phase over another. For example, we can consider the volatility of a molecule which can be expressed by Henry's Law, where the Henry's Law constant, k_H, is related to the vapour pressure of an analyte in the gas phase, $P_{analyte}$, above an aqueous solution with an analyte concentration of C_{Water}.[46]

$$k_H = \frac{P_{analyte}}{C_{water}} \tag{3.37}$$

The Henry's law constant can used to define the air-water partition coefficient of an analyte, K_{aw}.[47]

$$K_{aw} = \frac{C_{air}}{C_{water}} = \frac{k_H}{RT} \tag{3.38}$$

Here, the analyte concentration in air and water are denoted by C_{air} and C_{water} respectively, R is the ideal gas constant and T is the temperature in Kelvin. A compound with a large K_{aw} (> 1) has a higher concentration in air while a compound with a small K_{aw} (< 1) has a higher concentration in the aqueous phase.

Partition coefficients for an analyte into non-polar organic compounds (for example into a polymer film) are often unavailable, but can be approximated by the partition coefficient of the analyte into octanol.[48] Octanol-water partition coefficients are useful for predicting partitioning of a compound into soil or into fatty tissues in organisms.[49] This give rise to three partition coefficients between air, water and octanol.

$$K_{aw} = \frac{C_{\text{air}}}{C_{\text{water}}} \qquad K_{ow} = \frac{C_{\text{octanol}}}{C_{\text{water}}} \qquad K_{oa} = \frac{C_{\text{octanol}}}{C_{\text{air}}} \tag{3.39}$$

Compounds that have a large K_{ow} tend to bio-accumulate within organisms[49] which can result in bio-magnification within organisms of higher trophic levels.[49] Partition coefficients are essential for predicting

the fate of contaminates in the environment, and can help determine if they will accumulate in water, soil or air.[48]

Alternatively, the partition coefficients can be used to determine the concentration magnification within a polymer film, with subscript, *f*. Here three partition coefficients between air, water and a polymer film can be expressed.

$$K_{aw} = \frac{C_{air}}{C_{water}} \qquad K_{fw} = \frac{C_{film}}{C_{water}} \qquad K_{fa} = \frac{C_{film}}{C_{air}} \tag{3.40}$$

If a material has a large K_{fw} or K_{fa} it can be used to concentrate the analyte of interest making it easier for sensing. This pre-concentration technique is known as solid-phase microextraction (SPME).[47]

Solid-phase microextraction (SPME) has been developed as a solvent free sample preparation technique for the analysis of many volatiles compounds. A large wealth of literature has been published on this technique.[47, 50] The most common device for SPME uses a gas tight syringe with a polymer-coated silica fibre that is used to extract target analytes.[47] The syringe is inserted into a septum-sealed sample container filled with an aqueous solution or into the air headspace above a solution or a solid sample. The polymer coated fibre is then exposed and left to equilibrate with the surroundings before being retracted back into the gas syringe and sealed for later chromatographic analysis. The film concentration will be the result of either a two or three phase equilibrium as is shown in Figure 3.11. Alternatively, polymer coated stirring bars can be used to stir and extract target analytes from aqueous solutions.[51] A list of common materials that are used in commercially available SPME fibres is provided in Table 3.2.

The concentration at equilibrium in the film, air, and water (C_f^∞, C_a^∞ and C_w^∞) is related to the initial solution concentration, C_0.[47]

$$C_0 V_w = C_f^\infty V_f + C_a^\infty V_a + C_w^\infty V_w \tag{3.41}$$

This equation can be re-arranged and solved for the moles or mass within the fibre coating at equilibrium, depending on the units of the concentrations used $\left(n = C_f^\infty V_f\right)$.[47]

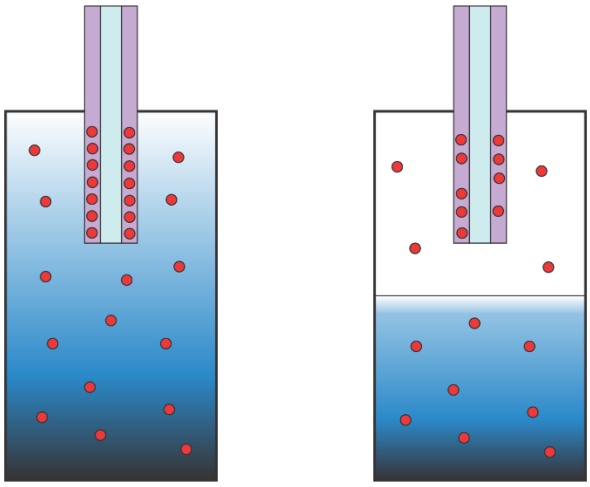

Figure 3.11: Schematic drawing showing liquid phase extraction and headspace extraction using an SPME fibre. The optical fibre is shown in light blue with the polymer extraction coating shown in purple. In the first case, there is an equilibrium between the concentration in the polymer coating and the aqueous solution. In the second case, there is a three-phase equilibrium between the head-space air, the solution and the polymer coating. Once extraction is completed the fibre is retracted inside a gas syringe and sealed for later chromatographic analysis.

Table 3.2: Summary of common commercially available SPME fibres indicating potential target analytes.[52] Many custom functionalized materials have also been reported in the literature.[53-54]

SPME Material	Target Analytes
Polydimethylsiloxane	Non-polar and aromatic hydrocarbons.
Carbowax (Polyethyleneglycol)	Alcohols and other polar compounds
Poly(acrylate) or Poly(acrylic acid)	Phenols and other polar compounds
Polydimethylsiloxane - Divinylbenzene	Amines and nitroaromatics

The partition coefficients were previously expressed in equation (3.40).

$$n = \frac{K_{fw} V_f C_0 V_w}{K_{fw} V_f + K_{aw} V_a + V_w} \tag{3.42}$$

When working with heterogeneous materials, it is also possible that there could be additional equilibria in the system so the amount of analyte in the film at equilibrium can be instead expressed by a sum of the partition coefficients of phase, i, with water.[47]

$$n = \frac{K_{fw} V_f C_0 V_w}{K_{fw} V_f + \sum_{i=1}^{n} K_{iw} V_i + V_w} \tag{3.43}$$

Typically, SPME fibres are inserted into the inlet of a gas chromatograph (GC) or high-performance liquid chromatograph (HPLC) for desorption of the analytes and concentration analysis.[47, 50] While these methods are highly sensitive after an appropriate calibration, GCs and HPLCs are large instruments and are only practical for laboratory based analysis. Thus traditional SPME is not practical for field analysis. There has been development of mobile GCs and LCs though they lack the sensitivity of conventional lab instruments.[55-56] Measurements of equilibrated samples only gives information of the average concentration during exposure and will not provide any information about time-dependent concentration spikes.

Integration of the sample extraction (SPME) element directly with a transduction element is essential for the development of portable sensors for measuring volatile organics and other compounds that affect air quality. One method to achieve time-resolved measurements is through determining the refractive index and thickness changes within a film during the partitioning of volatile compounds. Polydimethylsiloxane was chosen as a sample material, as it is commercially available, reproducible, highly stable and well characterized in the literature. The analysis of the diffusion of organic compounds and partition coefficients into PDMS is described in detail in Chapter 7. Once the refractive index response was well characterized, other miniaturized refractive index sensors, e.g. silicon-on-insulator (SOI) micro-resonators were used to quantify the partitioning into polymer films. Experiments using siloxane polymer-coated SOI microring resonators and Mach-Zehnder interferometers are discussed in Chapter 8.

3.6 Conclusions

The analyte concentration in a polymer film can be determined from the refractive index and thickness changes when dosed with a target analyte. Equations have been derived to calculate film analyte concentration using the data from interferometric refractometry. These equations can be applied to other refractive index sensing platforms including fibre-based sensors, waveguide interferometers and micro-resonators. Using the change in analyte concentration, Fickian diffusion equations have also been

derived based on equations by Crank. Using a sum of exponential functions, diffusion coefficients can be extracted from the average concentration in a bulk film or at the film-substrate interface. A series of approximations on diffusion curves have been presented in the literature and the accuracy of each method has also been assessed. At equilibrium, refractive index sensing technologies can also be used to determine partition coefficients and are useful as transduction elements for Solid-phase microextraction (SPME). Polymer coatings on miniaturized refractive index sensors, such a wire waveguide microresonators, show promise for the development of fingerprint sensors for the detection of volatile organic compounds in air.

3.7 Acknowledgements

I would like to acknowledge Mr. Chris Brauer, Mr. Weijian Chen, Dr. Jack Barnes and Dr. Hans-Peter Loock for their collaborative efforts in helping to develop the film analyte concentration equations in Section 3.2. I would also like to thank Dr. Jack Barnes and Dr. Hans-Peter Loock for their assistance in the derivation of the diffusion equations from the previous derivations by Crank (Section 3.3.1).

3.8 References

1. Blume, I.; Schwering, P. J. F.; Mulder, M. H. V.; Smolders, C. A., Vapour sorption and permeation properties of poly (dimethylsiloxane) films. *Journal of Membrane Science* **1991,** *61*, 85-97.

2. Kaltenecker-Commerçon, J. M.; Ward, T. C.; Gungor, A.; McGrath, J. E., Water resistance of poly(imide-siloxane) adhesives: Diffusion coefficients by gravimetric sorption. *The Journal of Adhesion* **1994,** *44*, 85-102.

3. Cocchi, G.; De Angelis, M. G.; Doghieri, F., Solubility and diffusivity of liquids for food and pharmaceutical applications in crosslinked polydimethylsiloxane (PDMS) films: I. Experimental data on pure organic components and vegetable oil. *Journal of Membrane Science* **2015,** *492*, 600-611.

4. Liu, C.; Liu, Y.; Sokuler, M.; Fell, D.; Keller, S.; Boisen, A.; Butt, H.-J.; Auernhammer, G. K.; Bonaccurso, E., Diffusion of water into SU-8 microcantilevers. *Physical Chemistry Chemical Physics* **2010,** *12*, 10577-10583.

5. Smiley-Wiens, J.; Serpe, M. J., Solvent exchange kinetics in poly(N-isopropylacrylamide) microgel-based etalons. *Colloid and Polymer Science* **2013,** *291*, 971-979.

6. Born, M.; Wolf, E., *Principles of Optics: Electomagnetic Theory of Propagation, Interference and Diffraction of Light*. 4th Edition, Pergamon Press, Toronto, Canada, 1970.

7. Atkins, P.; de Paula, J., *Atkins' Physical Chemistry*. 8th Edition, W.H Freeman and Company, New York, NY, 2006.

8. Ebewele, R. O., *Poymer Science and Technology*. CRC Press LLC, Boca Raton, FL, 2000.

9. Masaro, L.; Zhu, X. X., Physical models of diffusion for polymer solutions, gels and solids. *Progress in Polymer Science* **1999,** *24*, 731-775.

10. *Sylgard 184 Elastomer Product Information* Dow Corning, 2014, 11-3184B-01,

11. *SU-8 2000 Permanent Epoxy Negative Photoresist Datasheet.* Microchem, 2016,

12. Hossenlopp, J.; Jiang, L.; Cernosek, R.; Josse, F., Characterization of epoxy resin (SU-8) film using thickness-shear mode (TSM) resonator under various conditions. *Journal of Polymer Science Part B: Polymer Physics* **2004,** *42*, 2373-2384.

13. Vanlandingham, M. R.; Eduljee, R. F.; Gillespie, J. W., Moisture diffusion in epoxy systems. *Journal of Applied Polymer Science* **1999,** *71*, 787-798.

14. Crank, J., *The Mathmatics of Diffusion*. First Edition, Oxford University Press, London, UK, 1956.

15. *Diffusion in Polymers*. Crank, J.; Park, G. S., Eds. Academic Press Inc. , New York, NY, 1968.

16. Gautschi, W., Error Function and Fresnel Integrals. In *Handbook of Mathematical Functions, Graphs, and Mathematical Tables*, 10th Printing; Abramowitz, M.; Stegun, I. A., Eds. U.S. Department of Commerce, NIST: Washington, DC, 1972.

17. Chao, K.-P.; Wang, V.-S.; Yang, H.-W.; Wang, C.-I., Estimation of effective diffusion coefficients for benzene and toluene in PDMS for direct solid phase microextraction. *Polymer Testing* **2011,** *30*, 501-508.

18. Brazel, C. S.; Peppas, N. A., Mechanisms of solute and drug transport in relaxing, swellable, hydrophilic glassy polymers. *Polymer* **1999,** *40*, 3383-3398.

19. Lin, C.-C.; Metters, A. T., Hydrogels in controlled release formulations: Network design and mathematical modeling. *Advanced Drug Delivery Reviews* **2006,** *58*, 1379-1408.

20. Balik, C. M., On the extraction of diffusion coefficients from gravimetric data for sorption of small molecules by polymer thin films. *Macromolecules* **1996,** *29*, 3025-3029.

21. Lue, S. J.; Wang, S. F.; Wang, L. D.; Chen, W. W.; Du, K.-M.; Wu, S. Y., Diffusion of multicomponent vapors in a poly(dimethyl siloxane) membrane. *Desalination* **2008,** *233*, 277-285.

22. Johannsmann, D., Viscoelastic, mechanical, and dielectric measurements on complex samples with the quartz crystal microbalance. *Physical Chemistry Chemical Physics* **2008,** *10*, 4516-4534.

23. LaPack, M. A.; Tou, J. C.; McGuffin, V. L.; Enke, C. G., The correlation of membrane permselectivity with Hildebrand solubility parameters. *Journal of Membrane Science* **1994,** *86*, 263-280.

24. Boscaini, E.; Alexander, M. L.; Prazeller, P.; Märk, T. D., Investigation of fundamental physical properties of a polydimethylsiloxane (PDMS) membrane using a proton transfer reaction mass spectrometer (PTRMS). *International Journal of Mass Spectrometry* **2004,** *239*, 179-186.

25. Oh, K.-S.; Koo, Y.-M.; Jung, K.-W., Characterization of a sheet membrane interface for sample introduction into a time-of-flight mass spectrometer. *International Journal of Mass Spectrometry* **2006,** *253*, 65-70.

26. Louch, D.; Motlagh, S.; Pawliszyn, J., Dynamics of organic compound extraction from water using liquid-coated fused silica fibers. *Analytical Chemistry* **1992,** *64*, 1187-1199.

27. Linossier, I.; Gaillard, F.; Romand, M.; Feller, J. F., Measuring water diffusion in polymer films on the substrate by internal reflection fourier transform infrared spectroscopy. *Journal of Applied Polymer Science* **1997,** *66*, 2465-2473.

28. Balik, C. M.; Xu, J. R., Simultaneous measurement of water diffusion, swelling, and calcium carbonate removal in a latex paint using FTIR–ATR. *Journal of Applied Polymer Science* **1994,** *52*, 975-983.

29. Lambeck, P. V., Integrated optical sensors for the chemical domain. *Measurement Science and Technology* **2006,** *17*, R93-R116.

30. Xu, D. X.; Densmore, A.; Delâge, A.; Waldron, P.; McKinnon, R.; Janz, S.; Lapointe, J.; Lopinski, G.; Mischki, T.; Post, E.; Cheben, P.; Schmid, J. H., Folded cavity SOI microring sensors for high sensitivity and real time measurement of biomolecular binding. *Optics Express* **2008,** *16*, 15137-15148.

31. Densmore, A.; Xu, D.-X.; Waldron, P.; Janz, S.; Lapointe, J.; Mischki, T.; Lopinski, G.; Delage, A.; Cheben, P. Spotter-compatible SOI waveguide devices for biomolecular sensing, *Silicon Photonics III, Proceedings of SPIE 6898*, **2008**, 68981B, 1-8.

32. Yebo, N. A.; Lommens, P.; Hens, Z.; Baets, R., An integrated optic ethanol vapor sensor based on a silicon-on-insulator microring resonator coated with a porous ZnO film. *Optics Express* **2010,** *18*, 11859-11866.

33. St-Gelais, R.; Mackey, G.; Saunders, J.; Zhou, J.; Leblanc-Hotte, A.; Poulin, A.; Barnes, J. A.; Loock, H.-P.; Brown, R. S.; Peter, Y.-A., Gas sensing using polymer-functionalized deformable Fabry–Perot interferometers. *Sensors and Actuators B: Chemical* **2013,** *182*, 45-52.

34. Edmiston, P. L.; Campbell, D. P.; Gottfried, D. S.; Baughman, J.; Timmers, M. M., Detection of vapor phase trinitrotoluene in the parts-per-trillion range using waveguide interferometry. *Sensors and Actuators B: Chemical* **2010,** *143*, 574-582.

35. Wang, X.-D.; Wolfbeis, O. S., Fiber-optic chemical sensors and biosensors (2008–2012). *Analytical Chemistry* **2013,** *85*, 487-508.

36. Wang, X.-d.; Wolfbeis, O. S., Fiber-optic chemical sensors and biosensors (2013–2015). *Analytical Chemistry* **2016,** *88*, 203-227.

37. Tian, Z.; Yam, S. S.-H.; Barnes, J.; Bock, W.; Greig, P.; Fraser, J. M.; Loock, H.-P.; Oleschuk, R. D., Refractive index sensing with Mach-Zehnder interferometer based on concatenating two single-mode fiber tapers. *IEEE Photonics Technology Letters* **2008,** *20*, 626-628.

38. Lu, P.; Men, L.; Sooley, K.; Chen, Q., Tapered fiber Mach–Zehnder interferometer for simultaneous measurement of refractive index and temperature. *Applied Physics Letters* **2009,** *94*, 131110, 1-3.

39. Du, J.; Cipot-Wechsler, J.; Lobez, J. M.; Loock, H.-P.; Crudden, C. M., Periodic mesoporous organosilica films: Key components of fiber-optic-based heavy-metal sensors. *Small* **2010,** *6*, 1168-1172.

40. Barnes, J.; Dreher, M.; Plett, K.; Brown, R. S.; Crudden, C. M.; Loock, H.-P., Chemical sensor based on a long-period fibre grating modified by a functionalized polydimethylsiloxane coating. *The Analyst* **2008,** *133*, 1541-1549.

41. Barnes, J. A.; Brown, R. S.; Cheung, A. H.; Dreher, M. A.; Mackey, G.; Loock, H.-P., Chemical sensing using a polymer coated long-period fiber grating interrogated by ring-down spectroscopy. *Sensors and Actuators B: Chemical* **2010,** *148*, 221-226.

42. Jha, R.; Villatoro, J.; Badenes, G.; Pruneri, V., Refractometry based on a photonic crystal fiber interferometer. *Optics Letters* **2009,** *34*, 617-619.

43. Mudhana, G.; Park, K. S.; Ryu, S. Y.; Lee, B. H., Fiber-optic probe based on a bifunctional lensed photonic crystal fiber for refractive index measurements of liquids. *IEEE Sensors Journal* **2011,** *11*, 1178-1183.

44. Andrews, N. L. P.; Ross, R.; Munzke, D.; van Hoorn, C.; Brzezinski, A.; Barnes, J. A.; Reich, O.; Loock, H.-P., In-fiber Mach-Zehnder interferometer for gas refractive index measurements based on a hollow-core photonic crystal fiber. *Optics Express* **2016,** *24*, 14086-14099.

45. Podgorsek, R. P.; Franke, H., Optical determination of molecule diffusion coefficients in polymer films. *Applied Physics Letters* **1998,** *73*, 2887-2889.

46. Aqueous Solubility and Henry's Law Constants of Organic Compounds. In *CRC Handbook of Chemistry and Physics*, 96th Edition (Internet Version 2016); Haynes, W. M., Ed. CRC Press / Taylor and Francis: Boca Rafton, FL, 2016.

47. Pawliszyn, J., *Solid Phase Microextraction Theory and Practice*. John Wiley & Sons Ltd., New York, NY, 1997.

48. *Transport and Fate of Chemicals in the Environment*. Gulliver, J. S., Ed. Springer Science + Business Media, New York, NY, 2012.

49. Baird, C.; Cann, M., *Environmental Chemistry*. 4th Edition, W.H Freeman and Company, New York, NY, 2008.

50. Pawliszyn, J., Theory of solid-phase microextraction. *Journal of Chromatographic Science* **2000,** *38*, 270-278.

51. Sánchez-Rojas, F.; Bosch-Ojeda, C.; Cano-Pavón, J. M., A review of stir bar sorptive extraction. *Chromatographia* **2009,** *69*, 79-94.

52. SPME Fiber Selection Guide. Supelco, Sigma-Aldrich, http://www.sigmaaldrich.com/technical-documents/articles/analytical/selecting-spme-fibers.html (accessed July 30, 2016).

53. Dietz, C.; Sanz, J.; Cámara, C., Recent developments in solid-phase microextraction coatings and related techniques. *Journal of Chromatography A* **2006,** *1103*, 183-192.

54. Kumar, A.; Gaurav; Malik, A. K.; Tewary, D. K.; Singh, B., A review on development of solid phase microextraction fibers by sol–gel methods and their applications. *Analytica Chimica Acta* **2008,** *610*, 1-14.

55. Contreras, J.; Murray, J.; Tolley, S.; Oliphant, J.; Tolley, H.; Lammert, S.; Lee, E.; Later, D.; Lee, M., Hand-portable gas chromatograph-toroidal ion trap mass spectrometer (GC-TMS) for detection of hazardous compounds. *Journal of the American Society for Mass Spectrometry* **2008,** *19*, 1425-1434.

56. Sharma, S.; Plistil, A.; Simpson, R. S.; Liu, K.; Farnsworth, P. B.; Stearns, S. D.; Lee, M. L., Instrumentation for hand-portable liquid chromatography. *Journal of Chromatography A* **2014,** *1327*, 80-89.

Chapter 4

Theory of Interferometric Refractometry

This chapter describes the theory behind interferometric refractometry and provides detailed information about the optical setup and analysis techniques. The methods described in this chapter were used during the data analysis in three different experimental studies presented in this thesis. The determination of near-infrared refractive indices of common solvents and solutions is presented in Chapter 5.[1] The diffusion of liquids into thin-films of SU-8 photoresist is discussed in detail Chapter 6.[2] Lastly, the diffusion of solvent vapours into thin-films of polydimethylsiloxane (PDMS) is described in Chapter 7. Many aspects of this chapter are found in three articles that were published together with other researchers in the Loock group.[1-3] First I will discuss the theoretical background of refractometry and interferometry. Then I will describe the instrument we developed and the analysis and interpretation of the data it produces.

4.1 Introduction

The theory behind refractometry and interferometry will be discussed in detail and used to derive all necessary equations to describe the optical phenomena observed when studying both thick and thin films of liquids and polymers using a large-angle interferometric refractometer. Selected experimental data is also presented to complement the theoretical discussion with actual images and data. Detailed methods for optimizing the accuracy and reproducibility of refractometer experiments are also presented. The accuracies of both the refractive index and thickness measurements obtained by Fourier analysis of thin-films are validated with additional experiments. Finally, future improvements to simplify the refractometer alignment and increase the robustness of the instrument are discussed.

4.1.1 Theory of Refractometry

When light passes from one medium into a second medium with a different refractive index, it is refracted according to Snell's law.

$$n_1 \sin\theta_i = n_2 \sin\theta_t \tag{4.1}$$

Here, n_1 and n_2 represent the refractive indices of the two media and θ_i and θ_t are the incident and refracted angles, respectively. When light passes into a medium with a lower refractive index, there is a threshold incident angle where Snell's law becomes undefined, and the light is completely reflected. This angle is known as the critical angle of total internal reflection, θ_C, and can be easily determined from the two refractive indices.

$$\sin\theta_C = \frac{n_2}{n_1} \tag{4.2}$$

For incident angles smaller than the critical angle, some of the light will be reflected in a process known as Fresnel reflection. The intensity of Fresnel reflection is different for *s*-polarized and *p*-polarized light, R_s and R_p, and can be expressed using the Fresnel equations.[4]

$$\begin{aligned} R_s &= r_s{}^2 = \left(\frac{n_1 \cos\theta_i - n_2 \cos\theta_t}{n_1 \cos\theta_i + n_2 \cos\theta_t} \right)^2 \\ R_p &= r_p{}^2 = \left(\frac{n_2 \cos\theta_i - n_1 \cos\theta_t}{n_2 \cos\theta_i + n_1 \cos\theta_t} \right)^2 \end{aligned} \tag{4.3}$$

The corresponding reflection amplitudes of the electromagnetic field in the absence of absorption are expressed as r_s and r_p.[4] The reflection intensity profiles for *s*-polarized and *p*-polarized light when n_1 = 1.7434 and n_2 = 1.4000 were simulated for the entire range of incidence angles (0-90°) in Figure 4.1. At the Brewster angle, θ_B, p-polarized light experiences no Fresnel reflection, and the numerator of equation (4.3) is exactly zero. The Brewster angle can be easily calculated for a given system.[4]

$$\theta_B = \arctan\left(\frac{n_2}{n_1} \right) \tag{4.3}$$

Experimentally, the angular range probed in the refractometer experiments in this thesis is small (~4°) and close enough to the critical angle such that the Brewster angle was not observed.

Refractometry combines angle-resolved measurements of Fresnel reflection and total internal reflection within a calibrated system in order to measure the refractive indices of unknown samples. This

can be accomplished using prisms[3, 5-9], optical fibres,[10-13] gratings[14-15] and micro-optical devices.[16-19] A detailed review of different types of refractometers has already been presented in Chapter 2.

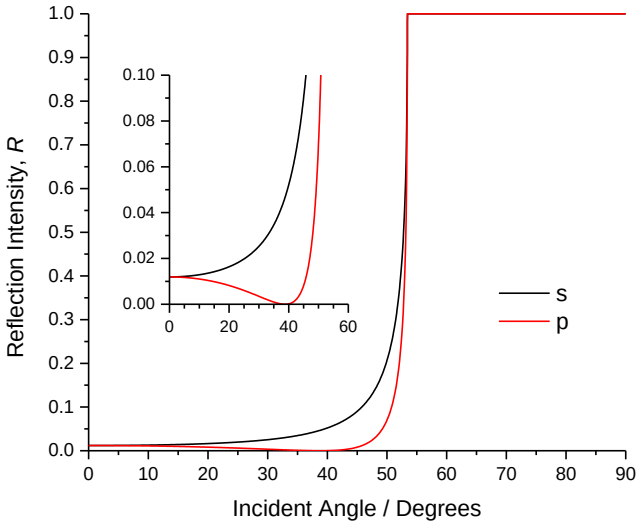

Figure 4.1: Simulation of the intensity profile for the reflection of *s*-polarized and *p*-polarized light. The refractive indices of the two media were set to n_1 = 1.7434 and n_2 = 1.4000.The *s*-polarized reflection is shown in black and the p polarized light is shown in red. The regions of total internal reflection (above the critical angle) were set to 1, as the Fresnel equations were undefined. The inset shows that the reflected intensity of *p*-polarized light at the Brewster angle $\theta_B \approx 40°$ is exactly zero.

4.1.2 Thin Film Interference

Interference is the effect from the superposition of two waves of light that have been spatially offset so that there is a phase difference between them, $\Delta\phi$ (Figure 4.2). Depending on the phase difference between the two waves, they can be added constructively resulting in an overall enhancement of the amplitude of the resulting wave, or destructively where an overall reduction of the amplitude is observed. When studying thin films, interference can result from the superposition of light reflected from the bottom and top surfaces of a thin film. At different incident angles, the phase difference between the two waves differs and an interferogram is observed. The simplest model to describe our system is a two-beam interference model based on the reflection of light at the prism-film and film-air interfaces. This model had been originally developed by former M.Sc. Candidate Weijian Chen, and was used to describe the thin-film

refractometer.[3, 20] His derivation is presented in an annotated version below to provide a complete discussion of the underlying principles behind the interferometric refractometer.

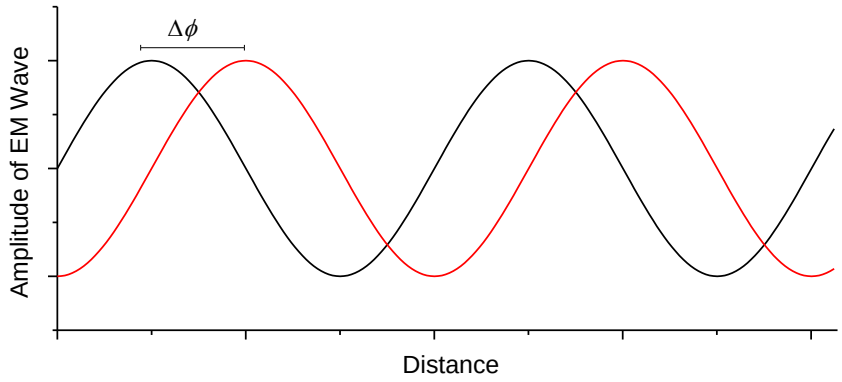

Figure 4.2: Schematic showing a π/2 phase shift, Δφ, between two waves. The tick marks on the bottom axis show π/2 spacing of the sine waves.

A schematic drawing showing the reflection from the bottom and top surfaces of a film placed on a prism is presented in Figure 4.3. The coordinates labeled as *A*-*D* are given as reference points for the derivation of two-beam interference equations.

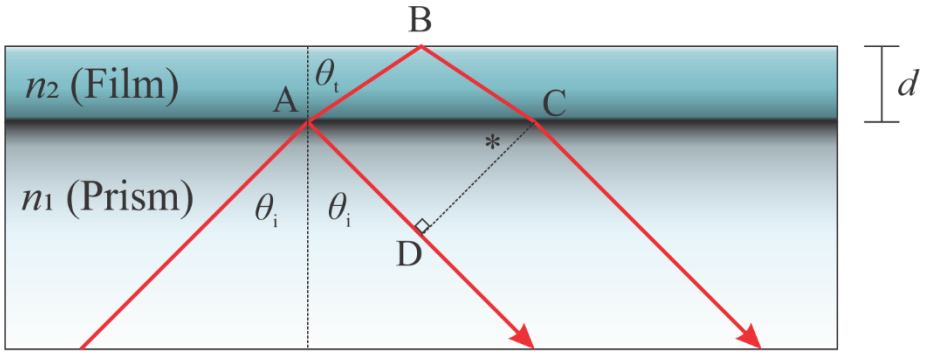

Figure 4.3: Schematic showing reflection from the bottom and top surfaces of a thin film placed on top of a prism. The coordinates *A*-*D* are given as reference points for the derivation of interference equations. The angle indicated by the asterisk is equivalent to θ_i.

The optical path length difference between the two waves, ΔL, can be expressed based on the coordinates labeled as *A*-*D*.

$$\Delta L = n_2\left(\overline{AB} + \overline{BC}\right) - n_1\left(\overline{AD}\right) \tag{4.4}$$

The lines $\overline{AB}$ and $\overline{BC}$ can be expressed in terms of the transmitted angle, θ_t, and the film thickness, *d*.

$$\overline{AB} = \overline{BC} = \frac{d}{\cos\theta_t} \tag{4.5}$$

Using trigonometry, an expression can also be derived for the line $\overline{AC}$.

$$\overline{AC} = 2d\tan\theta_t \tag{4.6}$$

The angle with the asterisk in Figure 4.3, is the same as θ_i which and can be used to define the line $\overline{AD}$.

$$\begin{aligned} \sin\theta_i &= \frac{\overline{AD}}{\overline{AC}} \\ \overline{AD} &= 2d\tan\theta_t \sin\theta_i \end{aligned} \tag{4.7}$$

Substituting equations (4.5)-(4.7) into equation (4.4) gives an expression for the optical displacement related to the film thickness, the incident angle, and the transmitted angle.

$$\Delta L = n_2\left(\frac{2d}{\cos\theta_t}\right) - n_1\left(2d\tan\theta_t\sin\theta_i\right) \tag{4.8}$$

This expression can be re-written with respect to only the transmitted angle using Snell's law.

$$\begin{aligned} \Delta L &= n_2\left(\frac{2d}{\cos\theta_t}\right) - n_1\left(2d\tan\theta_t\frac{n_2}{n_1}\sin\theta_t\right) \\ \Delta L &= n_2\left(\frac{2d}{\cos\theta_t}\right) - n_2\left(\frac{2d}{\cos\theta_t}\right)\sin^2\theta_t \end{aligned} \tag{4.9}$$

It can then be simplified by collecting the terms to yield:

$$\Delta L = \left(\frac{2n_2 d}{\cos\theta_t}\right)\left(1-\sin^2\theta_t\right) \tag{4.10}$$

This can be further simplified using the trigonometric identity $\left(1=\sin^2\theta+\cos^2\theta\right)$.

$$\Delta L = 2n_2 d\cos\theta_t \tag{4.11}$$

For each integer number of wavelength that is optically displaced between the two beams, a 2π phase shift occurred. The phase difference, $\Delta\phi$, is related to the optical path length difference, ΔL, and the wavelength of light, λ.[4]

$$\Delta\phi = \frac{2\pi\Delta L}{\lambda} = \frac{4\pi n_2 d\cos\theta_t}{\lambda} \tag{4.12}$$

This expression can be re-written in terms of the incident angle using first a trigonometric identity to express the angle as a sine function and then substitution with Snell's law.

$$\Delta\phi = \frac{4\pi n_2 d}{\lambda}\left(\sqrt{1-\sin^2\theta_t}\right)$$
$$\Delta\phi = \frac{4\pi n_2 d}{\lambda}\left(\sqrt{1-\left(\frac{n_1}{n_2}\sin\theta_i\right)^2}\right) \tag{4.13}$$

Alternatively, the phase difference, $\Delta\phi$, can be expressed as $(\phi - \phi_0)$, where ϕ_0 represents a constant phase offset and ϕ represents the phase as a function of incident angle. Squaring both sides of the equation will remove the square root from the equation.

$$(\phi-\phi_0)^2 = \left(\frac{4\pi n_2 d}{\lambda}\right)^2\left[1-\left(\frac{n_1}{n_2}\sin\theta_i\right)^2\right] \tag{4.14}$$

The n_2 terms can be consolidated to simplify the equation.

$$(\phi-\phi_0)^2 = \left(\frac{4\pi d}{\lambda}\right)^2\left[n_2{}^2 - n_1{}^2\sin^2\theta_i\right] \tag{4.15}$$

Expansion of all the terms and re-arrangement gives rise to the final expression relating the phase to the incident angle, and the refractive indices of both the prism and our samples n_1 and n_2, respectively.[3, 20]

$$n_1\sin^2\theta_i = -\left(\frac{\lambda}{4\pi d}\right)^2\phi^2 + 2\left(\frac{\lambda}{4\pi d}\right)^2\phi\phi_0 - \left(\frac{\lambda}{4\pi d}\right)^2\phi_0{}^2 + n_2{}^2 \tag{4.16}$$

By consolidating all terms that do not depend on phase into constants, we obtain a quadratic function that can be used to fit to the measured phase.

$$n_1{}^2\sin^2\theta_i = a\phi^2 + b\phi + c \tag{4.17}$$

Here, the film thickness, d, and refractive index, n_2, can be extracted independently from a quadratic fit to the phase data.[3]

$$d = \frac{\lambda}{4\pi\sqrt{-a}} \qquad n_2 = \sqrt{c - \frac{b^2}{4a}} \tag{4.18}$$

4.1.3 Interferometric Refractometry

When probing a thin-film with a narrow range of incident angles near the critical angle, a thin-film interferogram can be overlaid with the Fresnel reflection below the critical angle. If this interferogram can be spatially resolved, e.g. with a camera, it can then be used to extract the average film refractive index, $\bar{n}_{film}$, and thickness, *d*, through Fourier analysis of the phase data. At the same time, the film refractive index at the prism-film interface, n_{FS}, can also be extracted from the position of the critical angle of total internal reflection. The following sections describe the experimental setup and the data processing technique used with our homemade interferometric refractometer. Experimental results showing measurements of thick liquid samples, and thin polymer films are presented in Chapters 5-7.

4.2 Experimental Optical Setup

The large-angle interferometric refractometer was constructed using a 1550 nm laser diode (LD) (Thorlabs LPS-1550-FC, 1.5 mW) as a high-coherence-length light source. A three-paddle fibre polarization controller (PC) and polarization filter (PF) were used to first rotate the polarization and to then select only p-polarized light. Two lenses, L1 and L2, were used as a Galilean beam expander to increase the laser beam diameter to approximately 1 cm. A folding aluminum mirror was used to reflect the light upward where the light was focused onto the top surface of a 25 mm high-density flint glass equilateral prism (Schott N-SF11, n_{1550} = 1.7434) using a cylindrical lens, L3 (f = 2.50 cm). A second cylindrical lens, L4 (f = 5.00 cm), was used to collimate the light reflected within the prism towards the near-IR CCD camera (Edmund Optics, NIR Camera # 56-567). This lens also focused parallel beams from multiple reflections within the film onto the same line of the camera. A schematic drawing of the entire optical setup is shown in Figure 4.4 with similar figures previously reported.[3] Cylindrical lenses are preferred over spherical lenses to reduce aberration of the fringes in the images. Earlier versions of this optical setup used spherical lenses for L3 and L4 with f = 2.54 cm and f = 5.00 cm respectively.

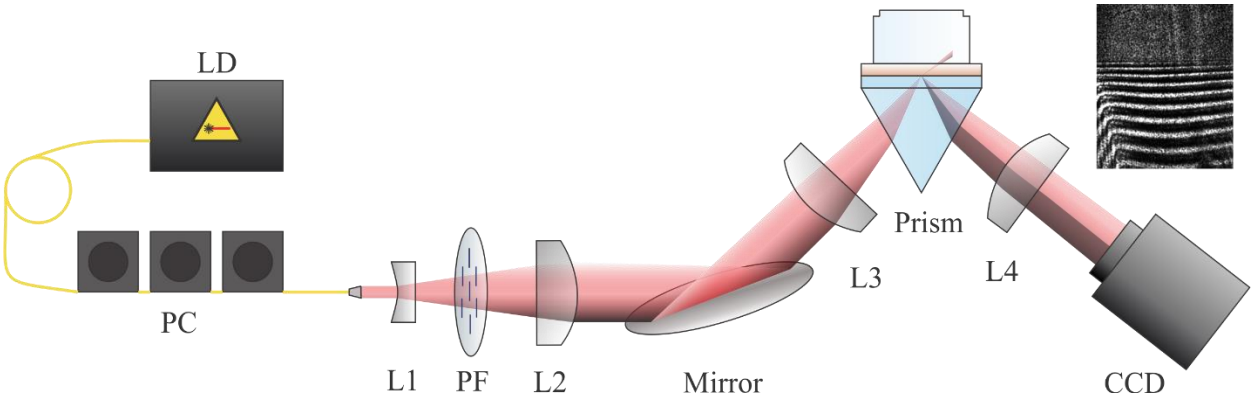

Figure 4.4: Schematic of a homemade interferometric refractometer. A fibre-coupled 1.5 mW 1550 nm laser diode (LD) was coupled to a 3-paddle polarization controller (PC). The beam was expanded to approximately 1 cm using a Galilean beam expander (L1 and L2). A linear polarized filter (PF) was used to select only vertically, p-polarized light. A cylindrical lens (L3) was used to focus the light to a line on the top surface of a high-index (N-SF11) prism so that a range of incident angles probed the samples. For convenience, samples were coated on N-SF11 slides that were index matched to the prism. Some of the light was total internally reflected within the prism/slide while light at smaller incident angles was partially refracted into the film. The final lens, L4, was used to collimate the diverging light towards a near-IR CCD camera. This lens was also used to focus down parallel beams from multiple reflections within the film onto the same line of the camera giving rise to the interference fringes in the sample camera image.

For convenience and to avoid damaging the prism between samples, all films and liquids were placed on top of an N-SF11 glass slide (1 mm thick) that was index-matched to the prism using a refractive index standard (Cargille Labs) with n_D = 1.7250 (n_{1550} = 1.6884). Cargille liquids closer to the refractive index of the prism contained sulfur that frequently crystalized making the fluids difficult to work with. A glass cap was attached to the top of the slide or film using either a bead of polydimethylsiloxane for gas sensing experiments or commercial "5-minute" epoxy for liquid sensing with organic solvents.

When L3 and L4 were spherical lenses, there was significant aberration from focussing in the horizontal direction. This caused curvature in the fringe pattern of the thin-film interference. Once we switched to cylindrical lenses, there was no longer any horizontal focussing and the fringes became much straighter and sharper. This improvement is shown in Figure 4.5 for two SU-8 films measured using the two different optical setups.

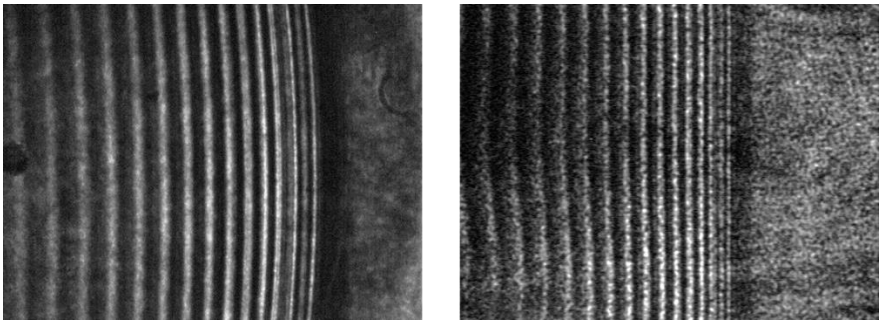

Figure 4.5: Comparison between images of SU-8 films taken using spherical and cylindrical optics. The left image shows the thin-film interference for a 35 μm thick SU-8 film captured with spherical lenses. The curvature of the fringes near the interface is quite substantial. The right image shows a 43 μm thick SU-8 film captured using cylindrical lenses. In this case, the fringes are no longer curved. In both cases there is a dark band without fringes that borders the bright region of total internal reflection.

One observation that can be made from Figure 4.5 is that the interference fringes do not extend all the way to the region of total internal reflection. For angles close to the critical angle, a large lateral displacement occurs, which can be described by the line $\overline{AC}$ (equation (4.6)) in Figure 4.3. If this displacement is large enough, the two beams are no longer able to spatially overlap. This effect is discussed in more detail in Section 4.4.1.

The camera used in the near-IR refractometer experiments contained a phosphor-coated silicon CCD array. Silicon photodiodes can only be used to detect photons with more energy than the silicon bandgap (1.1 eV),[21] λ = 200-1100 nm.[21-22] At 1550 nm, a phosphor coating was needed to absorb light through a multiphoton absorption, which was re-emitted at a visible wavelength that could be detected using the standard silicon CCD array. This phosphor-coated silicon CCD can only operate from λ = 1400-1600 nm and does not have a flat response over the full wavelength range. The intensity reported by the camera depends on the absorption spectrum of the phosphor coating which absorbs strongest near 1550 nm.[23] An alternative approach would be to use a CCD camera with a semiconductor material that absorbs directly in the near-IR (e.g. InGaAs). InGaAs cameras have relatively uniform response of greater than 70% efficiency over the entire wavelength range from λ = 900-1700 nm. Unfortunately, this technology is currently being marketed for surveillance and military purposes and is prohibitively expensive to be practical for a refractometer instrument.

4.2.1 Alignment Techniques

One of the major challenges with the interferometric refractometer is changing the alignment when measuring samples with very different refractive indices, i.e. different critical angles. There are a variety of ways to align the current setup, though it is always best to use a systematic approach. The alignment procedure used in our experiments is detailed in this section as it may be useful for future students working with similar instruments. Possible improvements to the optical setup to improve the ease and robustness of alignment were explored during a brief internship at *ABB Canada* in Quebec City. A few suggested improvements resulting from this experience will be presented in the future work (Section 4.6).

When aligning optical setups containing lasers, it is important that all necessary precautions are observed. High power laser systems require the use of eye protection and caution needs to be taken blocking the beam path when adding additional optics to avoid stray reflections. Index cards can be useful to observe the laser beam because no one should ever look directly into a laser. The specific procedures for laser safety are device and group specific and it is important to take time to inform oneself on all safety procedures prior working with lasers or aligning any optical systems.

In order to effectively align the refractometer, it is important to know the refractive index range of the samples to be studied. Once the sample range is known, it is easiest to work back from the desired critical angle in the prism to determine the required angle of the folding mirror. Using the desired refractive index, the critical angle of total internal reflection, θ_c, can be calculated. An equilateral prism was used for the refractometry experiments, so all the internal angles were known to be 60°. Using Snell's Law, it is possible to determine the amount of refraction that has occurred within the prism (i.e. the incident and transmitted angles, θ_t and θ_i, that occur when light enters the prism from air). Using the incident angle, the angle of the light relative to the vertical axis, θ_V, can be calculated.

$$\theta_V = 60° - \theta_i \tag{4.19}$$

The angle of the reflected light beam from the horizontal, θ_H, is twice the angle of rotation of the folding mirror, θ_{mirror}. This angle can be calculated once θ_V is known.

$$\theta_H = 90° - \theta_V \tag{4.20}$$

$$\theta_{\text{mirror}} = \frac{\theta_H}{2} = \frac{1}{2}(90° - \theta_V) \tag{4.21}$$

All of the angles described above are shown in Figure 4.6 with the mirror and the prism as reference points. The initial laser beam was horizontal prior to reflecting off the folding mirror which was mounted in an optical rotation mount with a resolution of 2° allowing for precise control of the mirror angle.

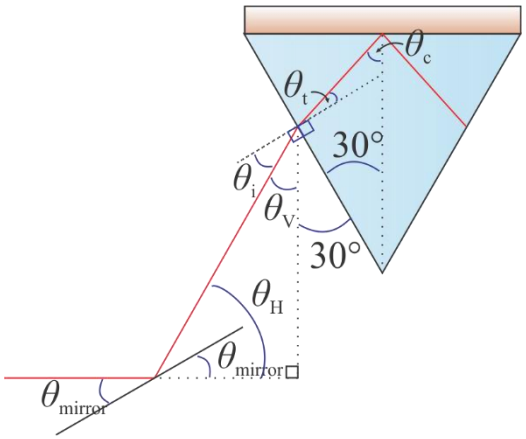

Figure 4.6: Schematic showing the reflection geometry in the optical refractometer setup. All the angles used when calculating the angle of the folding mirror are indicated. The critical angle, θ_c can be calculated from n_{prism} and n_{sample}. The transmitted angle, θ_t, can be determined using trigonometry and the incident angle, θ_i can be calculated with Snell's law. The angles θ_V, θ_H and θ_{mirror} are all calculated using trigonometry.

A fibre-coupled red diode laser (λ ~ 630 nm) was used during the alignment of the refractometer. While it is possible to use IR detection cards with the near-IR lasers, it can be very difficult to see when the light becomes diffuse, so using a visible laser makes the initial alignment easier.

It is best to first align are laser, the mirror, the prism and the camera. This is easiest to do without any lenses of filters so that the collimated beam passes through the centre of each optical component. The mirror is set to the desired angle, and the prism inserted such that total internal reflection is observed and the laser is reflected. A liquid or film sample of the desired index must be placed on top of the prism in order to observe the correct angular range of total internal reflection. Once the prism is aligned, the camera can be placed such that the laser beam is centred with the camera. It is best to cover the camera with the

lens cap or use a diffuser to prevent the highly collimated laser light from damaging individual pixels on the camera.

Next, lenses L1-L4 are added one at a time using an index card to ensure that the light passes through the centre of each lens and that each lens is perpendicular to the beam path. Aberration may be observed if the light does not pass perpendicularly through the centre of the optics. The distance between L1 and L2 should be set to the sum of the two focal lengths in order for the output of the second lens to be properly collimated. L3 must be placed such that the focal point is at the prism-sample interface, and L4 must be placed such that the camera is at the focal length of the final lens. L3 was mounted on a linear translation stage to allow for fine tuning of the focal point with the prism.

Once the optical setup was aligned with the visible laser, it was replaced with the near-IR laser. Some minor adjustments were still typically required with the lens positions, mirror angle and prism height to optimize the refractive index range of the system. The lenses were all purchased with near-IR anti-reflective coatings and dispersed visible light differently than near-IR light. When making small alignment adjustments to the refractive index range, the mirror, prism, and camera could often be adjusted without having to follow the full alignment procedures outlined above. It is important to also rotate L3 and L4 to ensure that they are always normal to the beam path. Once the system is fully aligned, it is necessary to run a refractive index calibration with known standards.

4.2.2 Calibration Techniques

Refractive index calibration solutions were purchased from Cargille Labs (Cedar Grove, NJ). The refractive indices were provided for each solution at 1550 nm from the supplier. Through communication with Cargille Labs, we learned that the refractive indices were obtain by extrapolation from measurements at visible wavelengths, giving the near-IR refractive indices an accuracy of $\delta n = \pm 0.005$. This was the largest source of error in our refractive index measurements, which can only be improved using better defined calibration standards, should they be available. Cargille refractive index liquids are available from $n_D = 1.3000\text{-}2.11$ in step sizes of $\Delta n = 0.0002\text{-}0.0015$ depending on the refractive index range.[24] Each

solution is a mixture of different compounds; for example low refractive index liquids (n_D = 1.3000-1.4000) typically contain several fluorinated hydrocarbons.[24] Liquids for n_D = 1.4000-1.5700 contain mixtures of silicone, aliphatic and aromatic hydrocarbons.[24] For refractive indices between n_D = 1.572-1.640, brominated aromatic hydrocarbons, such as bromonaphthalene, are added to raise the solution refractive index.[24] At even higher refractive indices, the brominated compounds are replaced with diiodomethane and sulfur (n_D = 1.7000-1.8000).[24]

In its current configuration, the large-angle refractometer probes a 4° range of incident angles. This requires re-alignment and calibration each time a different refractive index range is studied. For each range a series of 4-6 Cargille liquids were measured in triplicate to calibrate the system. The refractive indices of aqueous solutions of sucrose, sodium chloride, dimethylsulfoxide, ethylene glycol and glycerol were measured using the calibrated refractometer and the refractive index has been determined as a function of analyte weight fraction (Chapter 5).[1] These aqueous solutions can now be used for calibration of the refractometer or other optical devices and are not oily like Cargille liquids, so they will be easier to remove. For higher refractive index calibration ranges, solutions of cinnamaldehyde (n_{1550} = 1.5767) were previously prepared in ethanol.[20] It can be difficult to find a single liquid reagent with such a high refractive index, so cinnamaldehyde can be very effective for higher index calibration. However, care must be taken to make fresh calibration solutions as the ethanol is very volatile causing solution concentrations to change over time. Also, cinnamaldehyde reacts with moisture producing an insoluble precipitate and will degrade overtime. Cinnamaldehyde solutions have been previously characterized and will not be discussed in any more detail here.[20]

When placing different Cargille liquids on the refractometer, the angle between Fresnel reflection and total internal reflection, i.e. the critical angle, shifts. A composite image of six calibration liquids from n_{1550} = 1.3154-1.3730 is presented in Figure 4.7 to demonstrate this effect.

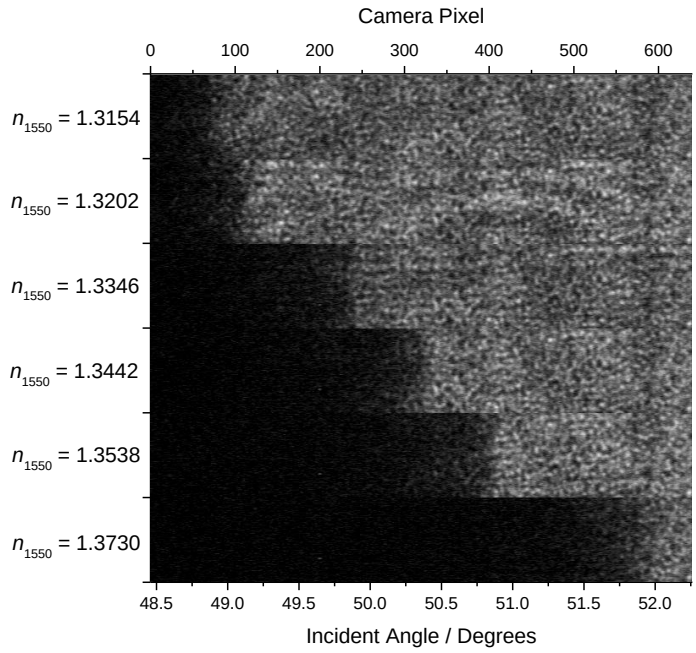

Figure 4.7: Composite image of six Cargille refractive index liquids used to calibrate the refractometer. The interface between Fresnel reflection (dark regions) and total internal reflection (bright regions) shifts to higher incident angle for higher refractive indices. For each solution, the refractive index is given at 1550 nm.

The critical angle for each solution was determined by fitting the profile data with the Fresnel equation for the reflection of *p*-polarized light (equation (4.3). The full fitting procedure for determining the refractive index of thick liquid films is discussed in Section 4.3 and Chapter 5. The known refractive indices of Cargille liquids were plotted against the camera pixel at the critical angle, to calibrate the system (Figure 4.8). Originally, a linear fit was used to relate the camera pixels to solution refractive index in earlier experiments (Figure 4.8A) (for example, studying the solvent uptake into SU-8 photoresist in Chapter 6).[2] A quadratic fit was found to give an improved fit and calibration (Figure 4.8B). In each plot, the fit is shown as a black line, with 99% confidence intervals given by blue lines above and below the fits. The fit residuals are also given below each fit. It is quite apparent from the structure of the residual from the linear fit that a polynomial function is needed to compensate for the curvature in the calibration.

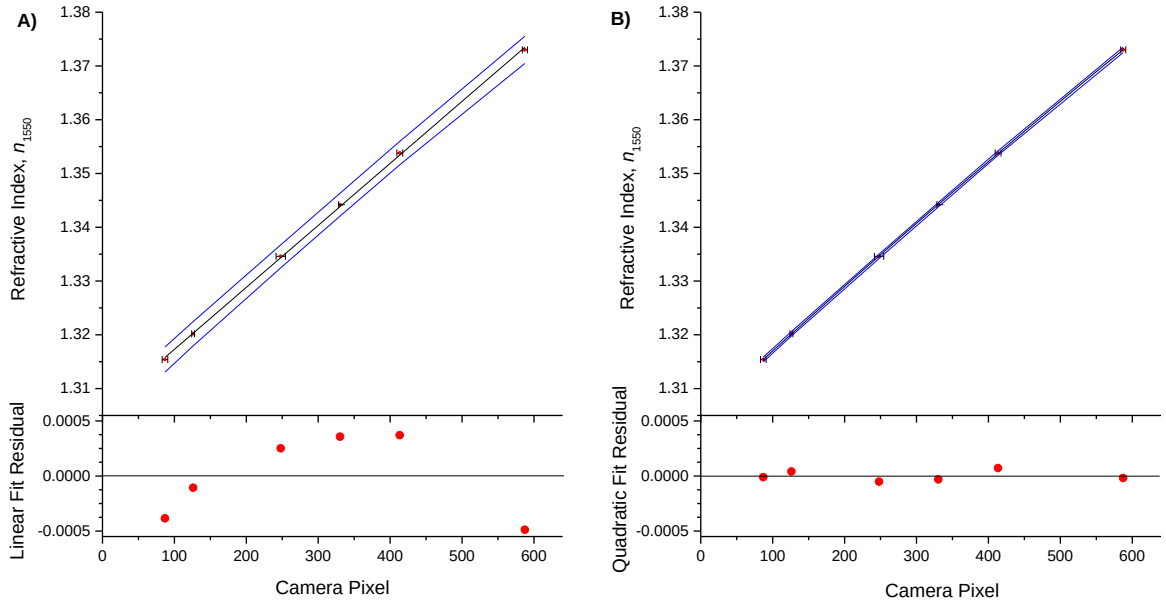

Figure 4.8: Comparison of refractometer calibrations using linear and quadratic fits. A) The linear fit to the calibration points shows structure in the residual indicating that it does not properly fit the data. The 99% confidence intervals are shown as blue traces above and below the fit (δn = ± 2.1-2.5×10^{-3}). B) A quadratic function fits the data better and gives a smaller, randomly dispersed residual. The 99% confidence intervals were calculated using Matlab™ and are shown as blue traces above and below the fit (δn = ± 4-5×10^{-4}).

The refractive indices of Cargille liquids were provided by the supplier at 1550 nm with an accuracy of δn = ± 5×10^{-3}. All the values were extrapolated from refractive index measurements at visible wavelengths, resulting in a rather conservative value for the accuracy. Experimentally, as will be discussed in Chapter 5, the accuracy of refractive index measurements of pure solvents when compared with literature values was found to be between δn = ± 1-20×10^{-4}.[1] When compared with literature values, our refractive indices for small polar compounds (acetontrile,1-propanol, methanol, ethanol and 1,4-dioxane) only deviated by δn = ± 1-3×10^{-4}. For halogenated and aromatic compounds (chloroform, toluene and benzene) larger deviations of δn = ± 10-23×10^{-4} were observed. The precision of repeated measurements ranged from δn = ± 1-19×10^{-4} with typical values of δn = ± 5×10^{-4}.[1] The overall accuracy of this system can be improved with the availability of more accurate calibration standards, such as optical glasses for example.

4.3 Refractometry of Thick Films (Thicker than 100 µm)

The large angle refractometer can be used to accurately measure the refractive indices of thick polymer or liquid films. The angular Fresnel reflection at a prism-film interface can be accurately described using the Fresnel equation for p-polarized light. This section describes the data collection and analysis methods when studying thick films. The refractive index measurements of thick liquid films of common solvents and solutions are described in Chapter 5.[1]

4.3.1 Fresnel Reflection

The reflection profile for thick films is governed by the Fresnel equation for p-polarized light, equation (4.3).[4] Using Snell's law, the equation can be re-written as a function of the incident angle, θ_i.

$$R_p(\theta_i) = \left(\frac{n_1\sqrt{1-\left[(n_1/n_2)\sin\theta_i\right]^2} - n_2\cos\theta_i}{n_1\sqrt{1-\left[(n_1/n_2)\sin\theta_i\right]^2} + n_2\cos\theta_i} \right)^2 \tag{4.22}$$

Some of incident angles are refracted into the liquid film and others are total internally reflected within the prism. A schematic showing this effect with a sample image and profile are presented in Figure 4.9.

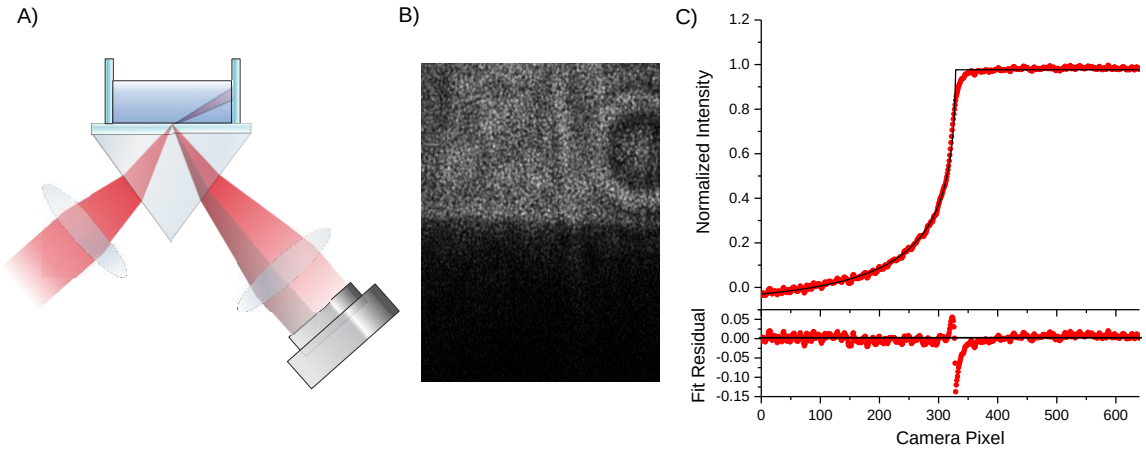

Figure 4.9: Schematic drawing showing Fresnel reflection and total internal reflection of a thick film on the refractometer. A) Some of the incident angles are refracted into the sample; this corresponds to the darker region representing the Fresnel Reflection. The bright region of the reflection shows total internal reflection. B) A sample image is given for a Cargille liquid where n_{1550} = 1.3442. The corresponding profile is shown in C) with the fit to the Fresnel equation and the fit residual.

Since our camera relies on a phosphor coated silicon CCD chip, it has some interferences from background visible light. A sample liquid (25% w/w glycerol in water) was measured on the refractometer when the overhead room lights were both on and off (Figure 4.10A). It is apparent that the room light has a strong effect on the camera signal and the refractometer setup needed to be protected with a dark box to prevent stray room light during measurements. Additionally, the camera gain was found to be too low to collect the low intensity portion of the Fresnel reflection (camera pixels 1-300). Without this part of the curve it was impossible to fit the data properly with the Fresnel equation. The software gain of the camera was increased to find an optimal level in order to capture the full Fresnel curve (Figure 4.10B). The numbers in Figure 4.10B are an arbitrary brightness scale used in the National Instruments™ (Austin, TX) Automation Explorer software. Figure 4.10B showed that a gain of 10 set to the brightness scale was sufficient for collecting the entire Fresnel curve. Increasing the gain higher provided no additional benefit and increased the amount of pixel noise.

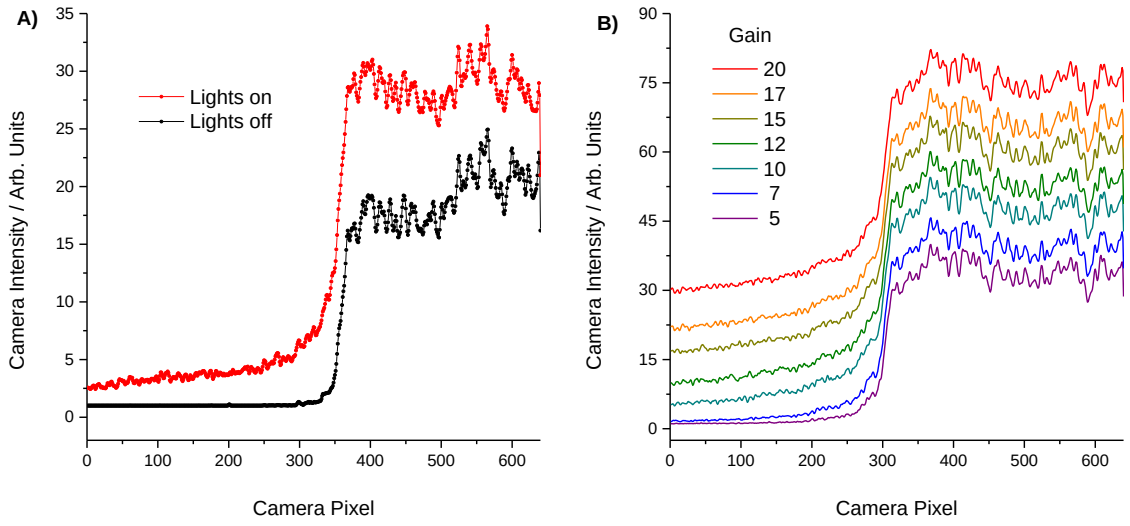

Figure 4.10: Experiments to determine the optimal camera conditions for the near-IR phosphor coated CCD. A) The profiles are shown for a solution of 25% w/w glycerol in water with the overhead lights both on and off in the room. When the lights were off the signal was much weaker and the camera gain was not strong enough to collect the weaker portion of the Fresnel reflection. B) With the room lights off, the camera brightness gain was adjusted for a solution of 25% w/w ethylene glycol in water to find the optimal setting to capture the whole Fresnel reflection. The optimal brightness intensity was found when the gain was set to 10.

The response of the near-IR camera was not linear, and camera signal, S, scaled with the light intensity, I, such that $S = I^{1.41}$.[23] In order to fit the data with the Fresnel equation, the camera intensity had to be first rescaled linearly. The fits could be additionally improved by first normalizing the data using the profile from a fully bright image to remove the optical defects in the system and a fully dark image to remove the intensity offset of the camera.

$$I_{\text{Normalized}} = \frac{\left(I_{\text{Sample}} - I_{\text{Dark}}\right)}{\left(I_{\text{Background}} - I_{\text{Dark}}\right)} \tag{4.23}$$

When fitting the raw data to the Fresnel equation, a reasonable estimate of the critical angle can be made but the function does not fit the curve well (Figure 4.11A). Once the data was linearized and normalized, it fit very well to the Fresnel equation (Figure 4.11B). An amplitude and a y-offset term, A and Y_0, were included in each fit.

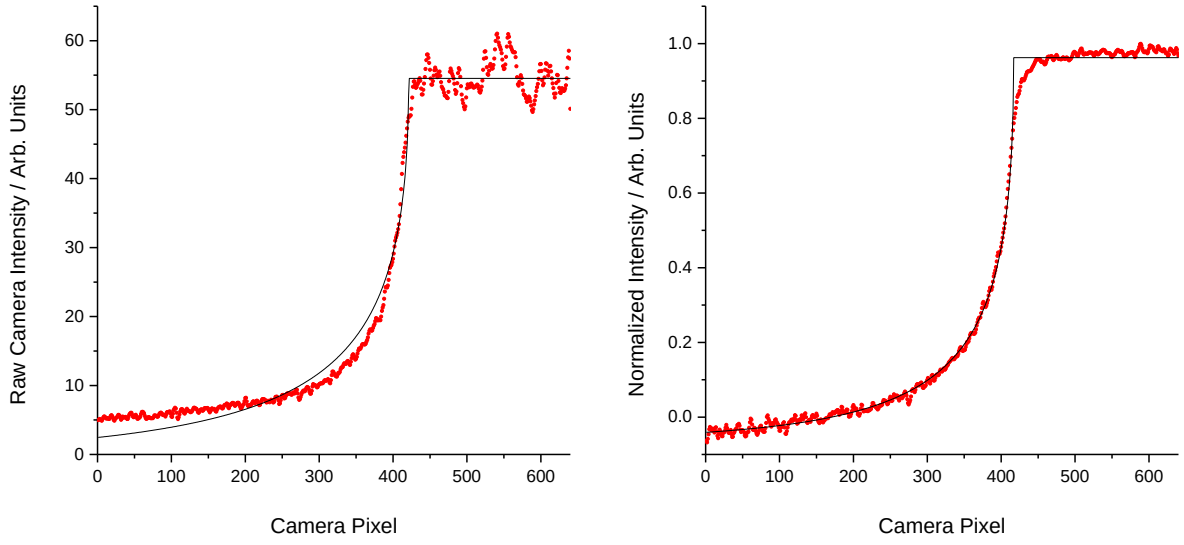

Figure 4.11: Comparison of Fresnel fits to a raw refractometer profile and a normalized linear profile. A) The raw intensity profile is shown for a Cargille liquid, n_{1550} = 1.3442. The Fresnel function did not describe the shape of the reflection well because the camera signal was non-linear with light intensity. B) The same profile, once linearized and normalized, fit remarkably well to the Fresnel equation.

The data analysis was originally implemented through excel macros and was later recoded using Matlab™. The full discussion of the fitting technique is described in the next section.

4.3.2 Fitting Methods

Two different procedures were used for fitting the Fresnel equation to experimental data: one where the solution refractive index was known (e.g. calibration samples) and a second when determining the refractive index of an unknown sample.

During calibrations, a least squares algorithm was used to find the optimal Fresnel fit to the data. In this case, since the angular range was unknown, it was replaced with a linear approximation.

$$\theta_i = \left(a \times \text{Pixel} + b\right) \tag{4.24}$$

When substituted into the Fresnel equation, the revised fitting algorithm fit to a, b, A and $Y_{0,}$. The refractive indices n_1 and n_2 were both known and set as constants.

$$Y\left(\text{Pixel}\right) = A\left(\frac{n_1\sqrt{1-\left[\left(n_1/n_2\right)\sin\left(a\times\text{Pixel}+b\right)\right]^2} - n_2\cos\left(a\times\text{Pixel}+b\right)}{n_1\sqrt{1-\left[\left(n_1/n_2\right)\sin\left(a\times\text{Pixel}+b\right)\right]^2} + n_2\cos\left(a\times\text{Pixel}+b\right)}\right)^2 - Y_0 \tag{4.25}$$

In the region of total internal reflection ($\theta_i > \theta_C$), equation (4.25) becomes undefined so it is fit instead to a constant.

$$Y\left(Pixel\right) = A - Y_0 \tag{4.26}$$

Using a least squares algorithm, a piecewise function of equations (4.25) and (4.26) was used to determine the camera pixel at the critical angle. The camera "critical pixel" was plotted against the known refractive index to calibrate the system (Figure 4.8). A set of sample Fresnel fits are shown for a full series of Cargille refractive index liquids in Figure 4.12 spanning the range from n_{1550} = 1.3154-1.3730.

When measuring solutions with an unknown refractive index, a two-step process was needed to accurately fit the Fresnel reflection. The critical angle of each calibration solution was calculated using Snell's law and a quadratic fit was used to correlate the camera pixel to incident angle from the calibration data (Figure 4.13).

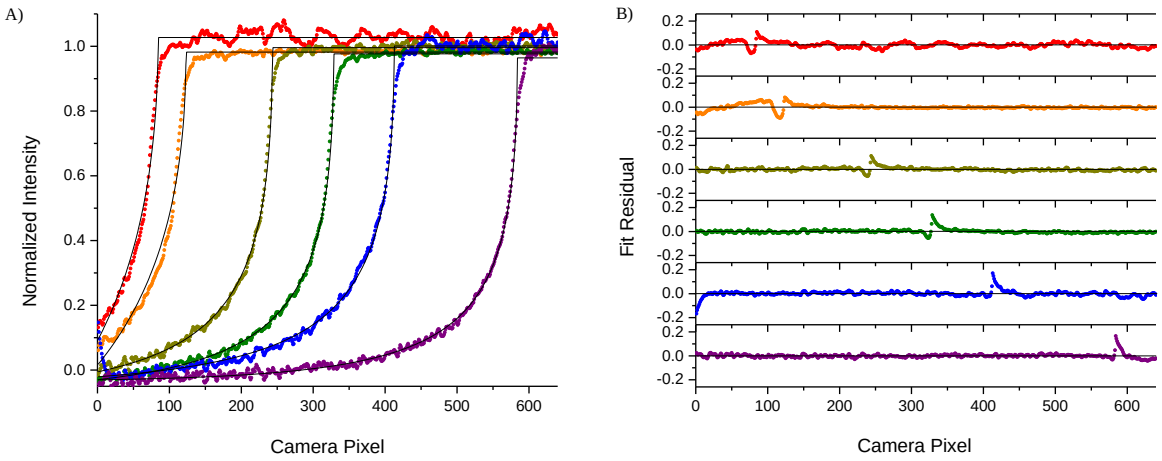

Figure 4.12: Fresnel fits to a series of Cargille liquids with known refractive indices. A) Cargille liquids with n_{1550} = 1.3154, 1.3202, 1.3346, 1.3442, 1.3538, 1.3730 are shown from left to right. The camera pixel at the critical angle was used for the calibration of the system (Figure 4.8). The corresponding fit residuals are shown in B).

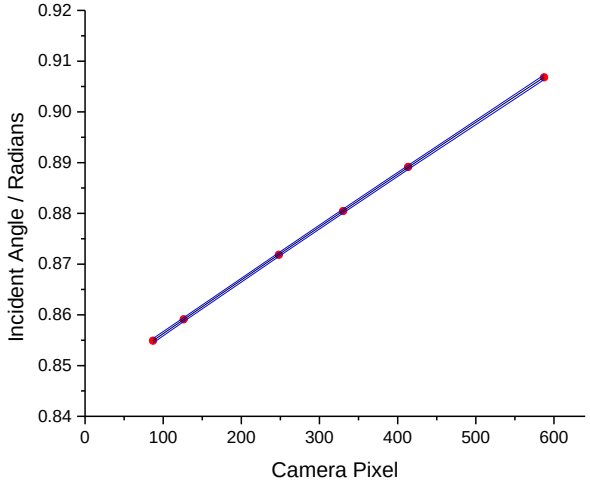

Figure 4.13: A quadratic fit was used to correlate the camera pixel to incident angle from the calibration solutions. The critical angle was calculated using Snell's law and the known refractive indices of the solutions. The 99% confidence interval of the fi is shown with blue lines and the correlation between pixel and incident angle was: $\theta = -5.15\times10^{-9}(\text{Pixel})^2 + 1.07\times10^{-4}(\text{Pixel}) + 0.846$.

Once the incident angle was mapped onto the camera pixels, a least squares fit to the Fresnel equation (equation (4.27)) was used to determine the refractive indices of unknown samples, n_2, and fitting parameters A, and Y_0. The refractive index of the prism and glass slide (N-SF11) was $n_1 = 1.7434$.[25]

$$Y(\theta_i) = A\left(\frac{n_1\sqrt{1-\left[(n_1/n_2)\sin(\theta_i)\right]^2} - n_2\cos(\theta_i)}{n_1\sqrt{1-\left[(n_1/n_2)\sin(\theta_i)\right]^2} + n_2\cos(\theta_i)}\right)^2 - Y_0 \quad (4.27)$$

Once n_2 was determined, the data was fit a second time using the refractive index as a constant and replacing the incident angle with a linear approximation in the same method previously used with the calibration solutions. This two-step process was needed to ensure that the pixel corresponding to the critical angle was accurately defined. The solution refractive index was then calculated from the critical pixel and the quadratic fit to the Cargille calibration data. In principle, it should be possible to determine the refractive index using a single fit. However, it was found that the Fresnel equation did not fit the data well when the angular range was set by the calibration (Figure 4.14A). After the second fit, the critical angle was more accurately determined (Figure 4.14B).

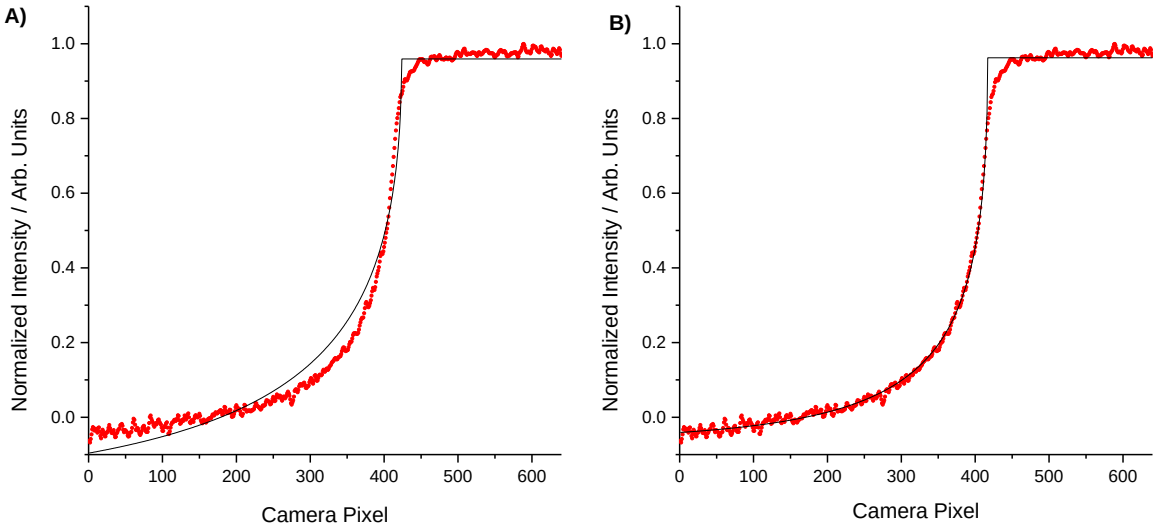

Figure 4.14: A two-step fitting algorithm was used to accurately define the critical angle of samples with unknown refractive indices. A) The refractive index of a sample of 24% w/w aqueous sucrose was measured. In the first fit, the camera pixel was converted to incident angle using the previous calibration with Cargille liquids. B) The second fit used the refractive index fit, n_2, from A) as a constant. The x-axis was replaced with a linear extrapolation ($\theta_i = a\times$Pixel $+b$) as was done previously when fitting the calibration solutions. The "critical pixel" was then converted to the sample refractive index using a quadratic calibration fit (e.g. Figure 4.8B).

A full study was performed to determine the refractive indices of common solvents and a several series of aqueous solutions at 1550 nm and is described in Chapter 5. Prior to our study, most of the solvent and

solution refractive indices were unavailable at 1550 nm. Many groups used the refractive index at the sodium d line, n_D (589 nm), as a stand-in when calibrating sensors in the near-IR.[26-30]

4.4 Refractometry of Thin Films (Films 10-100 μm thick)

When the refractometer samples are sufficiently thin, Fresnel reflection at the film-substrate and film-air interfaces can be superimposed resulting in thin film interference. This is observed for films 10-100 μm thick. Unlike many other interference techniques, it is possible to extract the thickness and the average refractive index independently from the interferogram. This can be achieved using Fourier analysis of the image profiles as will be discussed in the following section. Experiments studying the uptake of liquids and solvent vapours into polymer films are discussed in detail in Chapter 6 and Chapter 7 of this thesis. This chapter focuses on the fitting techniques and optimization of the refractometer for thin-film analysis.

4.4.1 Thin-Film Interference Refractometry

The full optical setup of the interferometric refractometer was previously shown in Figure 4.4. When a film is sufficiently thin, the light reflected from the bottom surface (substrate-film) and top surface (film-air) interfaces will result in thin film interference. A schematic drawing showing multiple reflections within a polymer film is given in Figure 4.15A. The second lens serves two purposes: to collimate the divergent light cone and to focus parallel beams down to the same location on the camera resulting in the interferogram. The image in Figure 4.15B was obtained for a 43 μm thick SU-8 photoresist film. The intensity of the image profile is shown in Figure 4.15C.[2] In Figure 4.15B and Figure 4.15C there is a noticeable dark band where the fringes do not extend fully to the critical angle of total internal reflection. This band occurs because there is a large enough lateral displacement such that the beams can no longer interfere with each other. The lateral displacement between the Fresnel reflection and first reflection within the film ($\overline{AC}$) was calculated for the 43 μm SU-8 film (Figure 4.15B and C) and is shown in Figure 4.16.

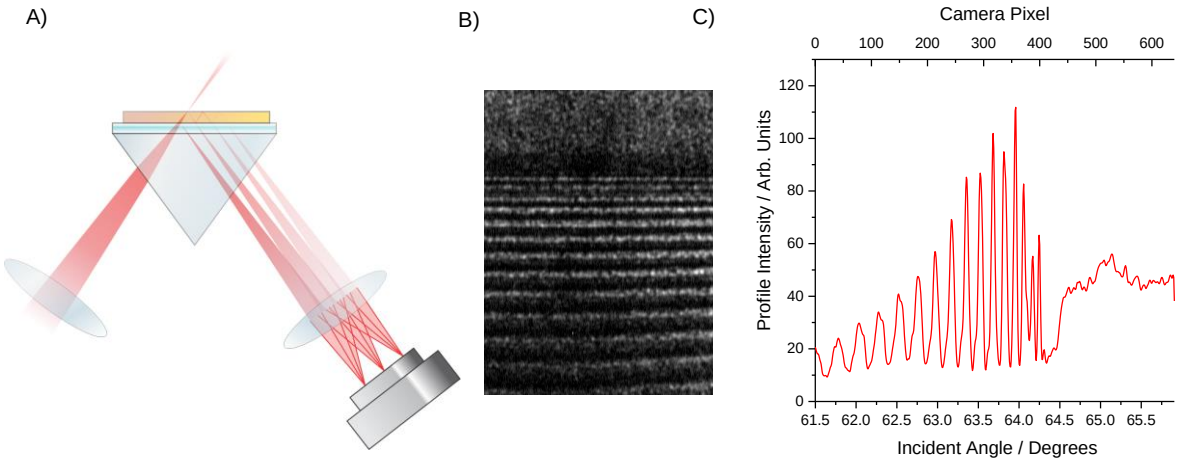

Figure 4.15: Schematic and sample data for the analysis of thin films using the large-angle interferometric refractometer. A) The light transmitted through the film can be refracted into the air or reflected back into the film. Each beam reflected in the film will give rise to a parallel beam that can interfere with the first Fresnel reflection at the bottom surface of the film. The second lens is used to focus the parallel beams down to the same line of the CCD camera resulting in the interferogram. B) A sample interference image for a 43 µm thick SU-8 film with the respective intensity profile shown in C).

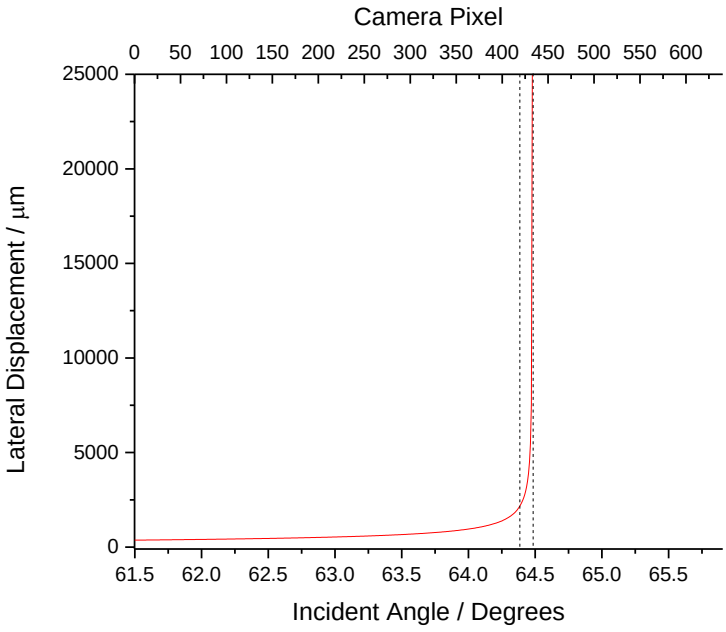

Figure 4.16: The lateral displacement between Fresnel reflection and a single reflection within the film. Light that has undergone multiple reflections within the film, will be further displaced. The first dashed line is used to indicate the position where the fringes end in Figure 4.15C, and the second dashed line the critical angle for a 43 µm SU-8 film assuming an interface refractive index, n_{1550} = 1.5733.

The fringes disappear when the displacement is greater than 2 mm between the two beams. The width of this dark band becomes smaller for thinner films or for materials with a lower refractive index.

4.4.2 Fourier Analysis of Image Profiles

The Fourier analysis procedure of our interferometric refractometer was originally developed by Weijian Chen and is described in great detail in his thesis and publication.[3, 20] The derivation will be discussed again here to provide the theory that complements the characterization methods used with the experimental data.[3, 20]

Interference can be descried from the superposition of two waves, which have intensities of I_1 and I_2 respectively and have a delay distance of ΔL.[4]

$$I = I_1 + I_2 + 2\sqrt{I_1 I_2}\cos\left(\frac{2\pi}{\lambda}\Delta L\right) \tag{4.28}$$

If the two waves have the same intensity it will simplify to the following relationship:[4]

$$I = 2I_0 + 2I_0\cos\left(\frac{2\pi}{\lambda}\Delta L\right) \tag{4.29}$$

This can be expressed as the phase difference between the two waves by substitution with equation (4.12).

$$I = 2I_0 + 2I_0\cos\left(\Delta\phi\right) \tag{4.30}$$

If we apply Euler's formula, we can express the cosine function as a sum of complex exponentials.

$$I = 2I_0 + I_0 e^{i\Delta\phi} + I_0 e^{-i\Delta\phi} \tag{4.31}$$

The Fourier transform is a useful technique for converting data in the position or time domain into the frequency domain and, vice versa. Mathematically Fourier transforms can be expressed as the integral of the opposite function.[4]

$$\begin{aligned} F(\omega) &= \int_{-\infty}^{\infty} f(x) e^{-2\pi i\omega x} dx \\ f(x) &= \int_{-\infty}^{\infty} F(\omega) e^{2\pi i\omega x} d\omega \end{aligned} \tag{4.32}$$

When working with discrete data sets it is not easy to manually calculate Fourier transforms, and instead discrete Fast Fourier Transform (FFT) algorithms are used. These algorithms are included in most advanced

data processing software (e.g. Igor Professional, Maple™, and Matlab™). If the FFT is taken of equation (4.31), the following expression arises.

$$F(\omega) = FFT\{2I_0\} + FFT\left\{I_0 e^{i\Delta\phi}\right\} + FFT\left\{I_0 e^{-i\Delta\phi}\right\} \tag{4.33}$$

In the Fourier transform, the expression $FFT\left\{I_0 e^{i\Delta\phi}\right\}$ corresponds the positive frequencies components. The expression $FFT\left\{I_0 e^{-i\Delta\phi}\right\}$ represents the mirror image at negative frequencies and the final term $FFT\{2I_0\}$ contains all non-periodic information, including the background offset, at 0 Hz. If the data is filtered in the frequency domain to remove all information at negative frequencies and around 0 Hz, the single positive term can be isolated. When the inverse Fourier transform (IFFT) is taken of the filtered data, the phase can be extracted from the complex position values.

$$IFFT\left\{F(\omega)\right\} = f(x) = I_0 e^{i\Delta\phi} \tag{4.34}$$

The argument of the exponential is the phase, $\Delta\phi$, which can be determined from the imaginary and real components of the Fourier filtered data.

$$\Delta\phi = \arctan\left(\frac{\mathrm{Im}\left[f(x)\right]}{\mathrm{Re}\left[f(x)\right]}\right) \tag{4.35}$$

Experimentally, the same analysis was performed on the profile data of the 43 μm SU-8 film shown in Figure 4.15B. The profile is shown again in Figure 4.17A with the magnitude of the Fourier transform in Figure 4.17B. The FFT has been magnified to show the symmetry, as the height of the Dirac delta peak reaches 25000 counts. As expected, there are three components to the FFT: a positive frequency region, a mirrored negative frequency region and a large Dirac delta peak. The data was filtered such that all data outside of the blue square was set to 0. After Fourier filtering in the frequency domain, the data was transformed back to the position domain and the phase was extracted from the complex values according to equation (4.35). The arctan function is discontinuous at π and - π, so the data needs to be "unwrapped" (i.e. an integer value of 2π is added each time a discontinuity is reached). The raw and unwrapped phase are shown in Figure 4.18.

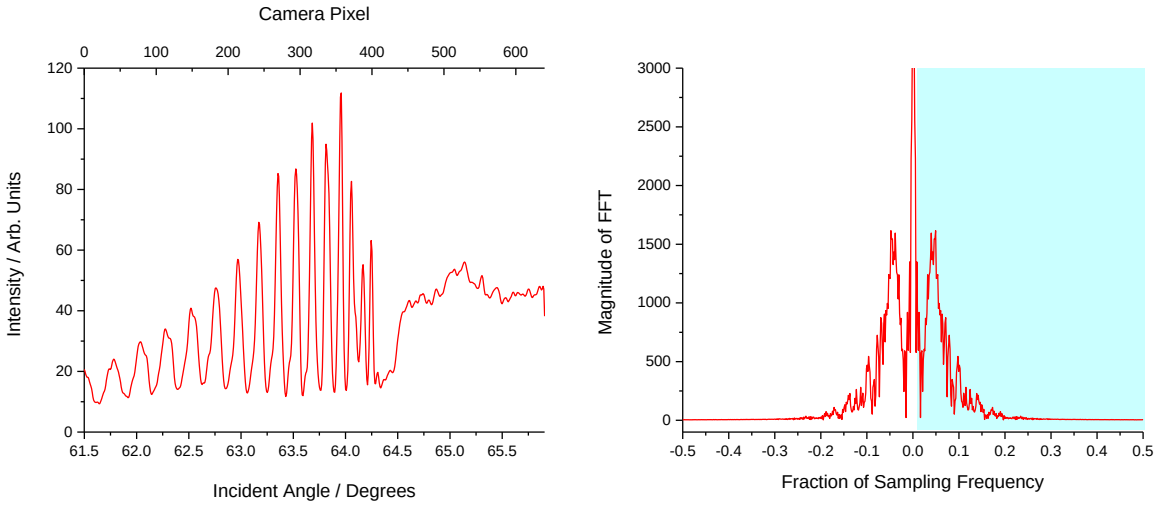

Figure 4.17: Intensity profile and Fourier transform of the profile data for a 43 µm SU-8 film. The FFT shows three regions: a positive frequency region, a negative frequency region and a Dirac delta peak at 0 Hz. This experimental data agrees with what is predicted in equation (4.33). The region highlighted in blue shows the data of interest, all other regions were set to 0 before applying an inverse Fourier transform back to the position domain.

In each plot the y-axis corresponds to $n_1^2\sin^2\theta_i$ which is determined from the refractive index calibration of the camera pixels. A quadratic fit was used to determine the refractive index and thickness information from the phase according to equations (4.16)-(4.18).

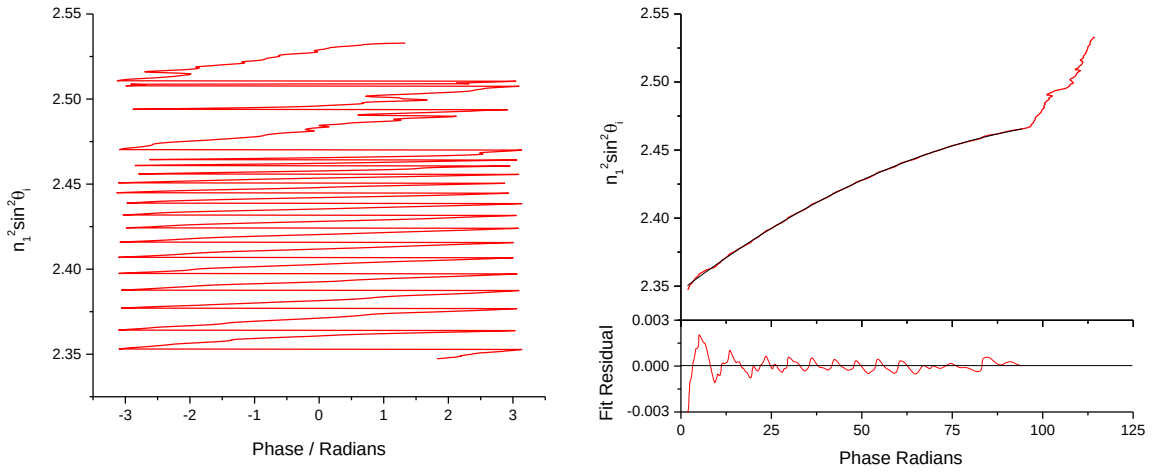

Figure 4.18: Raw and unwrapped phase from the measurement of an SU-8 film. A) The raw phase has discontinuities at π and $-\pi$ resulting from the arctan function. B) The phase was unwrapped by adding an integer number of 2 π at each discontinuity. The unwrapped phase was fit with a quadratic function with the fitting parameters a = -8.186×10^{-6}, b = 2.03×10^{-3}, c = 2.3468 yielding a thickness of d = 43.1 µm and an average refractive index of $\bar{n}_{film} = 1.5725$.

SU-8 films were used to study the diffusion and uptake of liquid reagents into a polymer film. The full study is described in detail in Chapter 6.[2] The fitting protocol was further optimized to reduce noise and increase the reproducibility, which is discussed in the following sections.

4.4.3 Profile Processing for Improved Analysis

One of the major sources of noise comes from the high background (non-periodic) intensity in the images. Reducing this background before performing the Fourier filtering can help clean up the Fourier transform. This section focuses on different techniques that can be used to help process the images prior to Fourier filtering to remove noise. These techniques were introduced to use by Dr. Raphael Desbiens during an internship at *ABB Canada*. Methods to enhance the precision and reproducibility when performing multiple measurements are described in Section 4.4.4.

The non-periodic signal (background brightness) in the region of total internal reflection will broaden the delta peak and increase the noise in the FFT. Since this region does not contain any useful interference information, it can be set to 0. Next, the fringe region can be fit with a polynomial function to remove the offset light intensity (Figure 4.19B) and make the fringes symmetrical around Y = 0. Once the quadratic fit is subtracted, the data can be multiplied with a cosine function to ensure that the ends of the fringe envelope go through zero and that there are no discontinuities at the ends of the fringe region (Figure 4.19C). Processing the data in this method before taking the Fourier transform reduces the intensity of the delta peak as can be observed in Figure 4.20.

While the profile processing resulted in only minor improvements to the phase data, (not shown here) it did not remove the oscillations in the phase (see residual in Figure 4.18B). These oscillations are the result of higher order harmonic frequencies in the Fourier transform. It is not possible to resolve the harmonic frequencies in Figure 4.20 due to peak broadening in the FFT as a result of unevenly spaced fringes in the original images. The peak broadening can be minimized by first evenly respacing the fringes by resampling the data prior to taking the FFT. The following paragraph discusses this process.

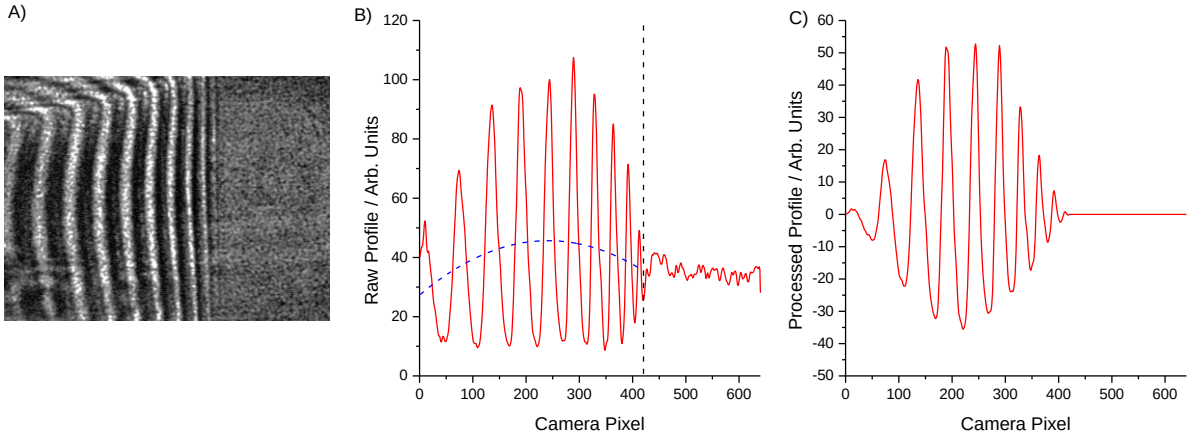

Figure 4.19: Processing of images to remove background noise prior to Fourier filtering. B) The profile is shown for a 25 µm polydimethylsiloxane (PDMS) film. The region of total internal reflection at camera pixels above 412 are set to 0, and the rest of the profile is fit with a quadratic function to subtract the baseline light intensity (blue fit). C) The quadratic baseline was subtracted from the data so that the fringes were evenly distributed around an intensity of Y = 0. This data was also multiplied with a cosine function with the same periodicity as the fringe envelope to ensure that the ends go to zero and are not discontinuous.

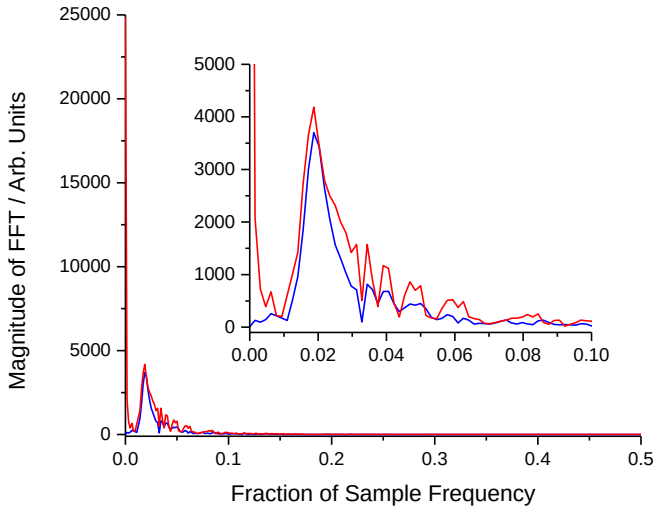

Figure 4.20: Comparison between the Fourier transforms before and after background intensity processing. The red trace shows the FFT of the raw data for the PDMS film. The blue curve shows that the delta peak is almost completely removed by subtracting out the non-periodic background signal before Fourier processing the data. The inset is provided to show that the processed data maintains the same structures in the FFT.

A 1-D interpolation function (interp1) in Matlab™ was used to rescale the (x, y) data such that the fringes were evenly spaced with respect to the new x-axis index number. The output phase (Figure 4.18B) was

plotted against camera pixel and fit with a quadratic function to get a smooth curve over the fringe region of the data. A newly spaced phase axis was made from the original phase fit where the points were evenly spaced in increments of $\Delta\phi$ = 0.05 over the full fringe region. Using the newly spaced phase axis, the corresponding camera pixel axis was resampled from the original pixel and phase data. The data still maintained the same (x, y) coordinates, but now the x -spacing was different between points. Once the pixel axis was resampled, the camera intensity was resampled to give the corresponding y-values for the new x-coordinates, interpolated from the original intensity data and camera pixel axis. If the processed data and the resampled data are both plotted by their (x, y) coordinates, they overlap completely indicating that that the data has not been changed (Figure 4.21A). However, if the resampled intensity is plotted against the data point index the fringes are now evenly spaced (Figure 4.21B).

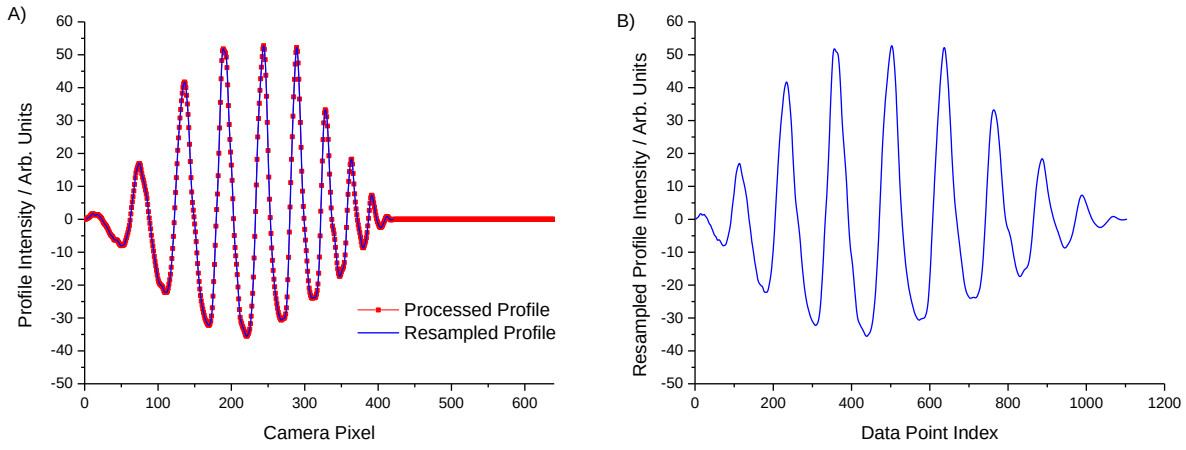

Figure 4.21: Resampling of the data can be used to rescale the pixel axis so that the fringes are evenly spaced with data point index. A) The processed and resampled profile data are plotted with their respective (x, y) coordinates to show that they still overlap and the data information has remained intact. B) When the resampled data is plotted by data point index it is apparent that the fringes are now evenly spaced prior to Fourier analysis.

The Fourier transform of the resampled data shows structure with clearly resolvable peaks (Figure 4.22). Filtering the FFT to remove all the data other than the major peak, removes all the information contained in the harmonic frequencies. The IFFT is then used to return the data back to the position domain, which is then resampled back to the original pixel coordinates. Finally, the phase is extracted as previously discussed

from the resampled Fourier processed data. Filtering out the harmonic peaks greatly improves the quality of the phase and removes most of the oscillations previously observed (Figure 4.23).

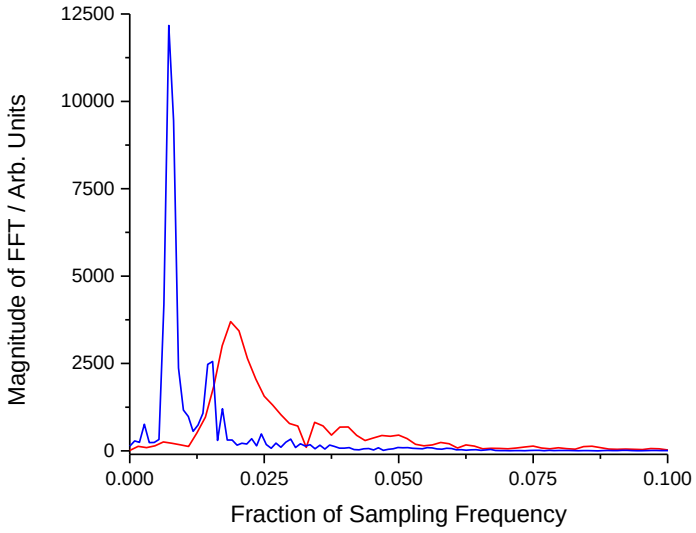

Figure 4.22: Improvement of the peak resolution in the Fourier transform when resampling the original data so the fringes are evenly spaced prior to Fourier processing. The red curve shows the FFT of the background subtracted data from Figure 4.20, while the blue curve shows the FFT of the resampled data. After resampling the data, it is possible to separate the main frequency peak from higher order harmonics. The peak position has changed because the number of data points of the resampled data is much larger than the original data and the spacing between points (sampling frequency) has also changed.

While this process vastly improves the phase data for a single measurement, it is challenging to use with a dynamic system where the refractive index and thickness are changing with time. After resampling the data each data set will have a different number of points and a different sampling frequency. Also the range over which the fringe data exists will change from image to image. It is therefore easier to reduce uncertainty by running multiple fits to different regions of the same phase output and then averaging the results to incorporate the resampling procedure into a dynamic analysis. Future work may be done to optimize this routine such that it is more suitable for dynamic systems.

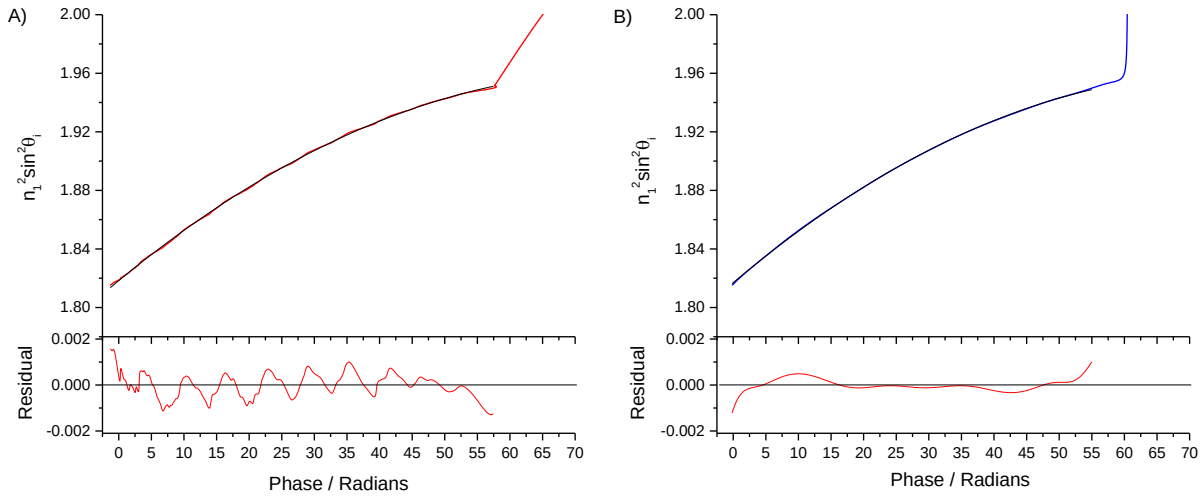

Figure 4.23: Comparison between the phases of Fourier filtered image profiles of a 25 µm PDMS film before and after resampling the fringe data to a uniform spacing. A) The original data has an oscillation pattern that can be seen in the fit residual due to interference from higher order harmonic frequencies. B) Resampling the data allows for a much cleaner filter in the frequency domain in order to remove all of the higher order harmonics. This results in a much smoother phase which will provide more consistent refractive index and thickness values for all fitting regions on the curve. The refractive index and thickness values were comparable between the fits shown in A) and B) within in the measurement error (n = 1.4002, n = 1.3999) and (d = 25.4 µm, d = 24.8 µm) respectively.

4.4.4 Improvements on Reproducibility

There are many useful applications for studying dynamic systems using the interferometric refractometer. Diffusion of analytes into films can be accompanied by swelling and refractive index changes resulting from liquids or vapours partitioning into a polymer film. This diffusion of water into SU-8 epoxy is described in Chapter 6 and the diffusion of VOCs into siloxane polymers are discussed in Chapter 7. Additionally, the refractometer could be used to study the drying or curing of a transparent coating or the corrosion of a surface over time. One challenge with analysing dynamic systems is that the interference fringes move as the film thickness and refractive index changes. This is shown for the uptake of 160 Pa of m-xylene vapours into a 25 µm PDMS film (Figure 4.24). The interference profile of a single image is shown on the left which is converted to a column of pixels and when repeated with the profiles of an entire data set, can be used to make a composite image of the changes in the fringe pattern over a period of time.

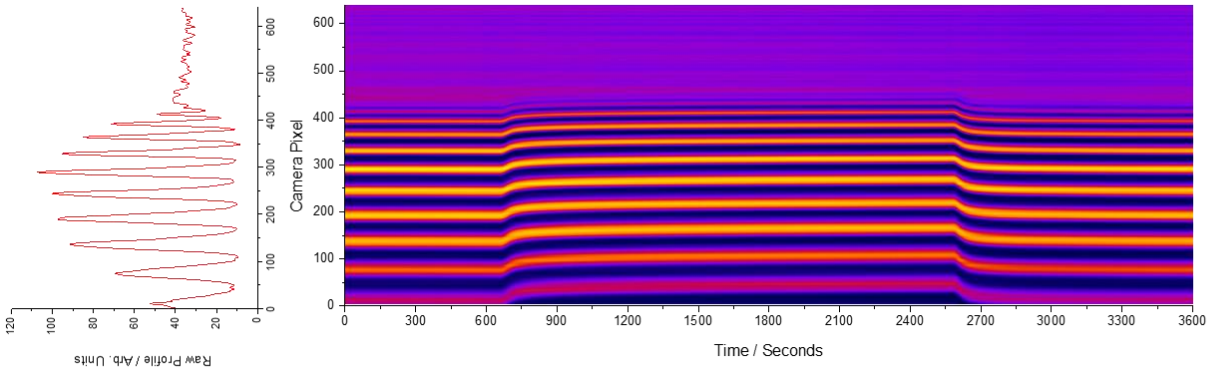

Figure 4.24: The change in interference fringes during the uptake and release of 160 Pa of m-xylene vapours within a 25 µm PDMS film. The vertical axis shows the profile intensity as a function of camera pixel. The profiles have been compiled from a series of 3594 images collected at a time scale of 1 second and are plotted as an image to illustrate the fringe movement during the uptake and release processes. As is evident from the fringe motion a dynamic system is needed to determine the end of the fringe region before the data can be reliably processed.

One of the easiest ways to develop a reliable process for removing the non-periodic noise from the total internal reflection is to track the position of a single peak or valley by fitting each profile with a Lorentzian function to determine the change in the feature position. The Lorentzian fit is shown to the valley near pixel 420 of a single image in Figure 4.25A. This fit was repeated to track the movement of the valley through an entire data set (Figure 4.25B).The valley movement during analyte uptake and release was fit using a bi-exponential rise and decay function to smooth the transitions as much as possible (Figure 4.25B). The region before the uptake was either fit using a linear function or a polynomial function depending on the degree or curvature during the stabilization of the instrument. It was found that this method was suitable for tracking a single valley or peak and overlapped well with the same feature in the fringe image (Figure 4.26). The fits to the fringe valley was rounded to the nearest integer and any discontinuities when switching between fitting functions were manually smoothed. This integer dataset was then used as the upper boundary, where any camera pixels above this point were set to 0. The profiles for the entire uptake and release procedure were processed simultaneously in an array using a custom written Matlab™ algorithm. The end regions of the profiles from the upper limit to pixel 640 were set to zero, and the fringe patterns were pre-processed using the techniques discussed in Section 4.4.3. The FFT, frequency filtering and IFFT

were then applied simultaneously on the entire array to maximize the amount of simultaneous calculations taking advantage of multiple processor cores when calculating the FFTs. This was substantially faster than performing the operations sequentially with each profile being processed in turn, as was the case with previous analysis algorithms written in Igor Professional (Wavemetrics, Lake Oswego, OR).

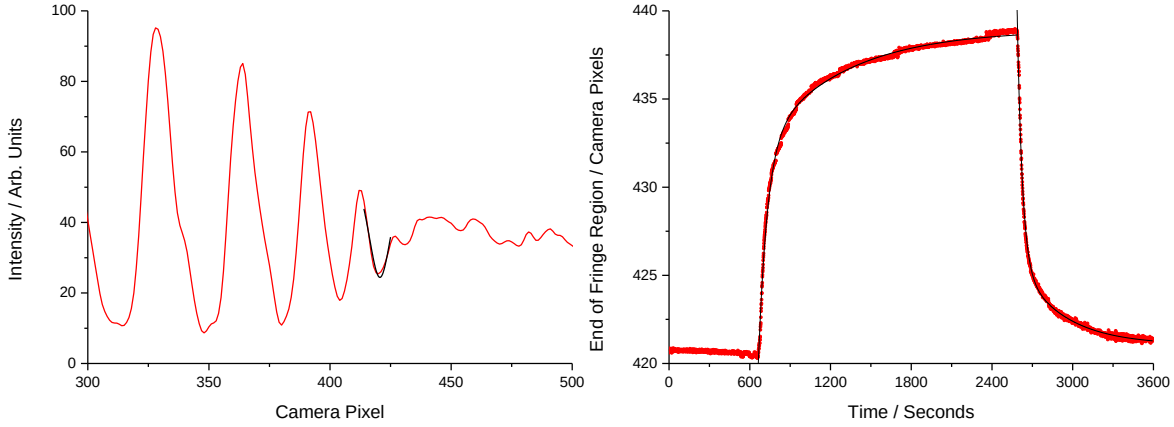

Figure 4.25: The position of a single valley can be tracked by fitting each profile with a Lorentzian function. The fringe shift can then be fit with a bi-exponential rise and decay function (shown with black lines) to smooth the fringe transition. The initial region is either fit to a linear or polynomial function to approximate the fringe change before the analyte was added.

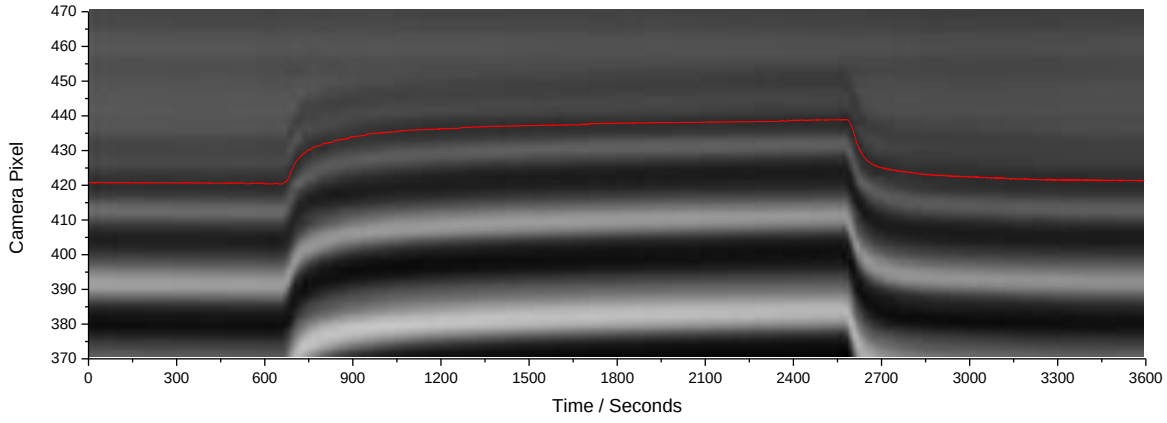

Figure 4.26: The peak fitting algorithm was compared with the composite fringe image to assess the quality of fringe tracking. The fringe position, as was shown in Figure 4.25B, was overlaid with an enlarged portion of the uptake profile from Figure 4.24. From this image it is clear that the algorithm accurately tracked the same valley during the uptake and release of m-xylene.

Once the phase was extracted and unwrapped for each profile, each image was fit 100 times with different fitting ranges starting at pixel (1-100) and ending at the upper limit (previously defined by the fit

to the valley near pixel 420). Averaging the 100 fits was an alternative method to resampling the data in order to reduce the errors caused by the oscillations in the phase data. The starting window is indicated by the blue square in Figure 4.27 with the upper limit for the first image indicated by the solid black line.

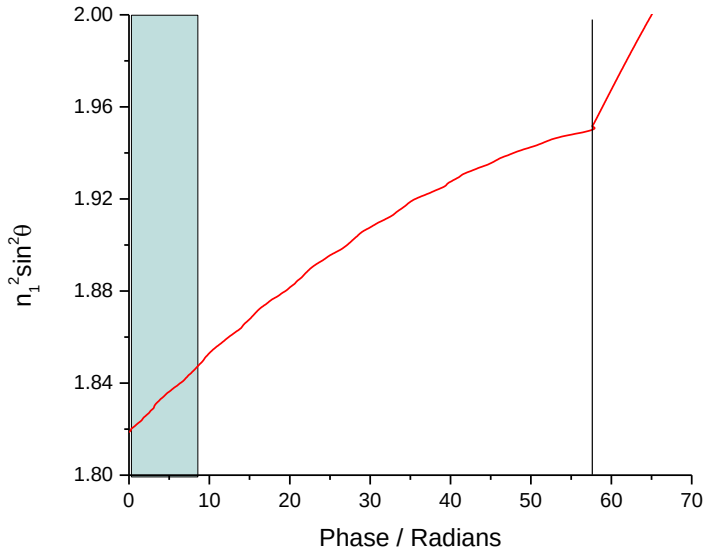

Figure 4.27: Quadratic fitting ranges for a sample profile during the uptake and release of 160 Pa of m-xylene within a 25 µm PDMS film. The lower limit of the fit ranged from camera pixel 1-100 (shown by the blue square in the image) and ended at the valley around pixel 420 shown by the solid black line. In total 100 different fits were made to each curve to remove variability from the phase oscillations caused by higher order harmonic frequencies in the Fourier transform.

The refractive index and thickness was then reported for each image as the average of all 100 fits with the error on each value presented as the standard deviation. The deviation of refractive index and thickness over the 100 fits to the phase in Figure 4.27 is shown in Figure 4.28. The average values of refractive index and thickness for the uptake and release of m-xylene into the 25 µm thick PDMS film are shown in Figure 4.29 to show the quality of data possible when studying dynamic systems. The analyte concentration within the film can be calculated using the refractive index and thickness changes as a function of time. The concentration profile then allows for extraction of uptake, release kinetics and partition coefficients of analytes within polymer films. The detailed analysis of the uptake and release of volatile organic hydrocarbons (VOCs) within siloxane films is described in Chapter 7.

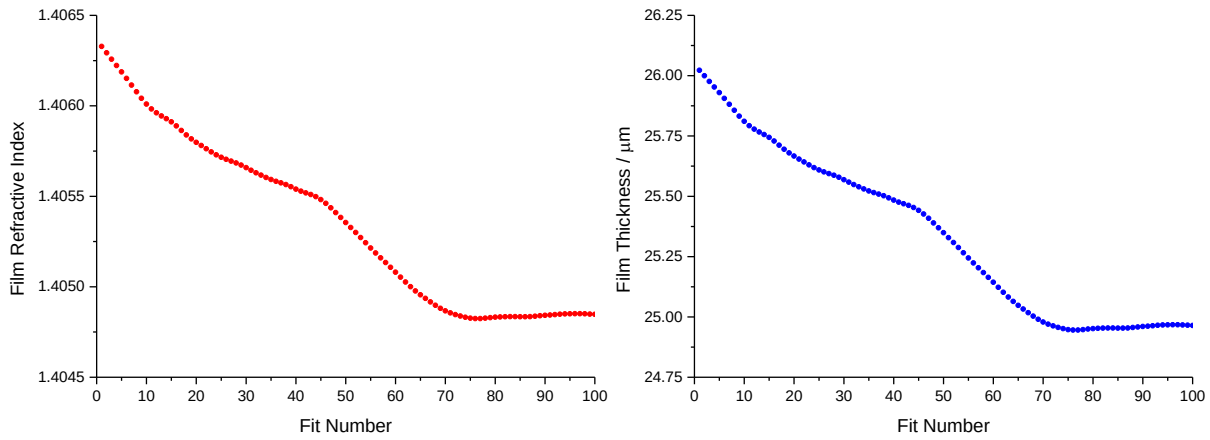

Figure 4.28: The fitting deviation of refractive index and thickness from 100 fits to the phase in Figure 4.27. The refractive index and thickness deviate substantially from different fitting windows and can deviate by as much as $\Delta n = 15\times10^{-4}$ and $\Delta d = 1.1$ µm. The average values were n = 1.4053, d = 25.3 µm with standard deviations of $\sigma_n = 5\times10^{-4}$ and $\sigma_d = 0.3$ µm.

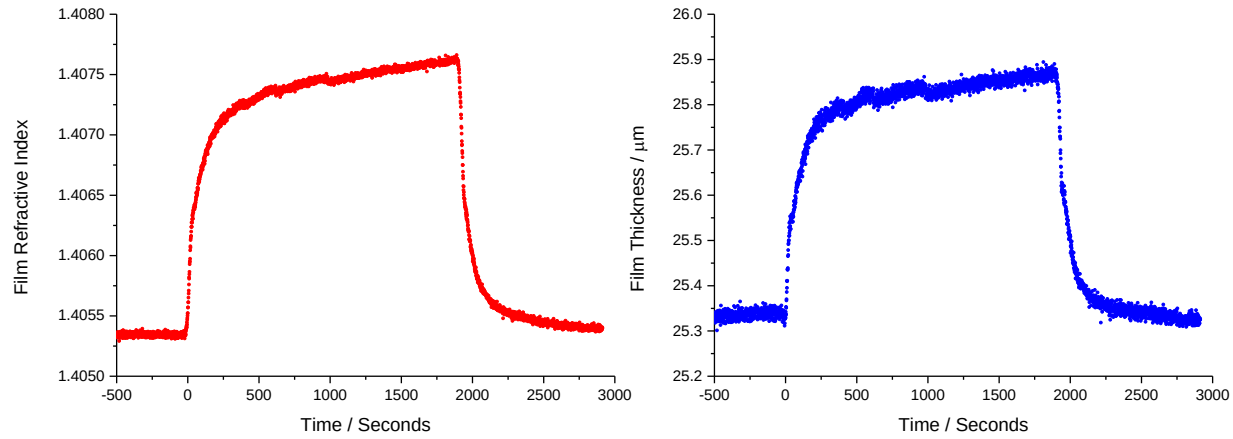

Figure 4.29: The change in average film refractive index and thickness of a 25 µm PDMS film exposed to 160 Pa m-xylene and then dry nitrogen over a period of 3594 seconds. The interferometric refractometer is a useful technique for measuring refractive index changes in dynamic systems.

4.4.5Accuracy of Refractive Index Measurements

In order to validate the techniques using the interferometric refractometer, accuracy experiments were run to ensure the quality of both the film refractive index and thickness measurements. The simplest way to assess the quality of the refractive index measurements was to compare the analysis of a thin liquid film with that of a thick liquid film. A solvent film has a uniform refractive index throughout and will not

possess gradients that might exist within polymers if multiple domains were present. Thin liquid films were created by placing a few drops of liquid in the refractometer, and removing some of the liquid using a tissue until fringes were observed on the camera image. The profiles of a thin and thick film of 1-propanol are shown in Figure 4.30. As would be expected, the critical angle of total internal reflection was the same for both samples.

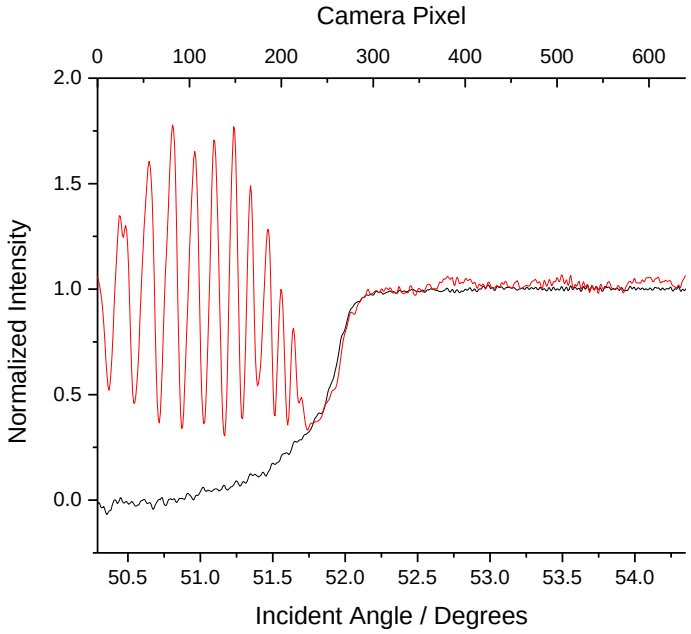

Figure 4.30: Normalized intensity profiles of both a thin film and thick film of 1-propanol. The refractive index of three independent measurements of thick films was found to give n_{1550} = 1.3737(2). The thin film was processed following the protocol in Sections 4.4.2-4.4.4 and yielded n_{1550} = 1.3736(3), d = 46.7(5) µm from the average of 50 different fits to the phase curve.

The quality of the fit at different film thicknesses was also assessed by capturing images of a 1-propanol film as it evaporated. For very thick films (> 100 µm) there was not enough resolution of the fringes to accurately perform Fourier analysis on the films. For 6 different 1-propanol films, a 100 pixel sample was taken from each image and was made into a composite image (Figure 4.31). The first three images were too thick for measurement using Fourier analysis and are assumed as being thicker than 100 µm. The bottom three images were all analyzable and the film thicknesses are reported with the relative time reference between measurements. It is notable that the critical angle of total internal reflection is constant for all samples as would be expected and is denoted by the dashed red line in Figure 4.31. Also, the fringes move

closer to the critical angle as the film decreases in thickness, which supports our hypothesis that the rays reflecting from the top surface of the film near the critical angle are laterally displaced too far to be able to interfere with Fresnel reflection at the substrate-film interface. As the film becomes thinner the angular range over which this effect occurs will decrease as the lateral displacement (equation (4.6)) is a function of film thickness.

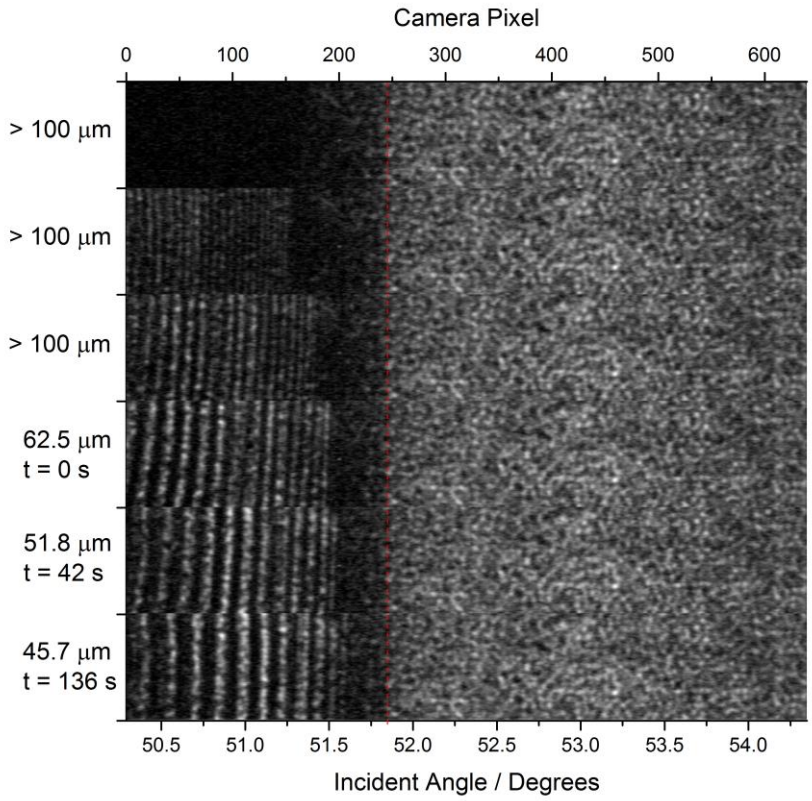

Figure 4.31: Composite image of 6 different thickness films of 1-propanol as the film evaporated. The top three films did not have suitable fringe resolution for accurate Fourier analysis and are assumed as > 100 μm thick. The bottom three films were all measureable and the film thickness and relative time are indicated. The critical angle of total internal reflection is indicated by the dashed red line. The fringe regions extend closer to the critical angle as the film becomes thinner.

Fourteen images were analysed as the 1-propanol film evaporated and the resulting average refractive index and thickness are shown in Figure 4.32. The vertical error bars indicate the standard deviation from the average of 50 different fits to each phase curve. The bottom three images in Figure 4.31 are represented by the data points at t = 0, 42 s and 136 s respectively in Figure 4.32. The average refractive

index from the 14 measurements of the 1-propanol film was found to be n_{1550} = 1.3735(7) over a thickness range of d = 45.7-62.4 µm.

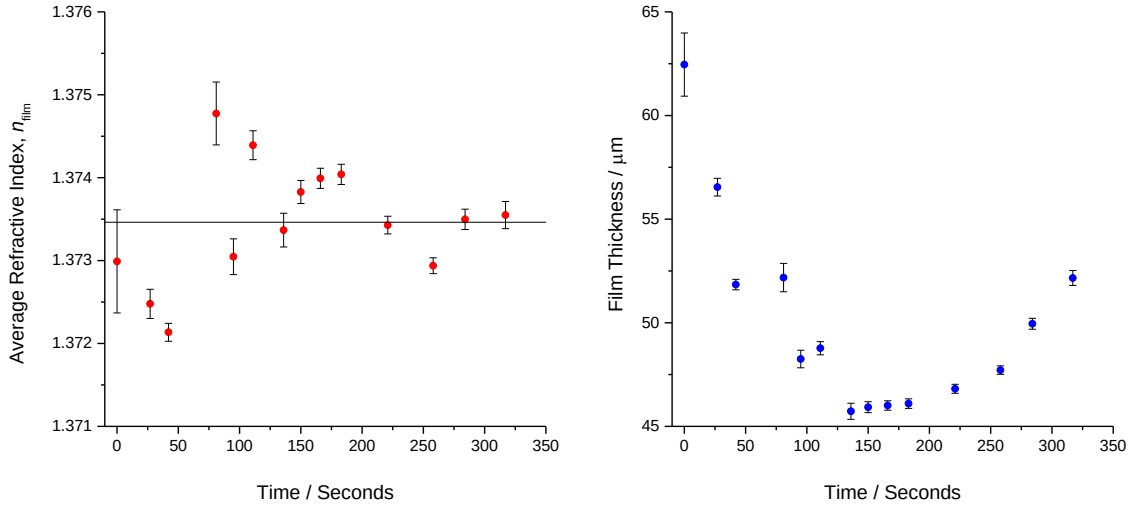

Figure 4.32: The refractive index and thickness measurements from 14 images during the evaporation of a 1-propanol film. The thickness of the film initially decreased and then slowly increased again as it evaporated. The average refractive index, n_{1550} = 1.3735(7), was measured for films d = 45.7-62.4 µm thick. The images are shown for the data from t = 0s, 42 s and 136 s in Figure 4.31.

The increase in thickness as the film evaporated was likely due to contraction of the solvent drop, causing the location of the centre of the droplet to change relative to point of observation. Alternatively, it might have been due to coalescence of multiple droplets into a single droplet during this process.

As was demonstrated in this section, the refractive index measurements using Fourier analysis are comparable to those using the Fresnel reflection of thicker films. The results were found to be within in the error of thick film measurements, though showed more scatter from repeated measurements than the thick film analysis. This suggests that when very accurate measurements of refractive index are needed, it is more reliable to make thicker films and measure the Fresnel reflection. The accuracy of the thickness measurement can be assessed by comparing the thickness of the same film on additional instruments, which is discussed in Section 4.4.6.

4.4.6 Accuracy of Thickness Measurements

The accuracy of the thickness measurements from the interferometric refractometer needed to also to be assessed. The easiest was to verify the thickness information was to measure the same film on the refractometer and on other types of optical profilometers. For measuring the film thickness using stylus and optical profilometers, a portion of the film was scratched off to produce a ridge down to the bare substrate.

An SU-8 film was measured on the interferometric refractometer in the process described in Sections 4.4.3 and 4.4.4. The background subtracted image profile is given in Figure 4.33A with the extracted unwrapped phased plotted with a quadratic fit in Figure 4.33B. The analysis of the film yielded a refractive index of n_{1550} = 1.5705(2) with a film thickness of d = 34.2(1) μm.

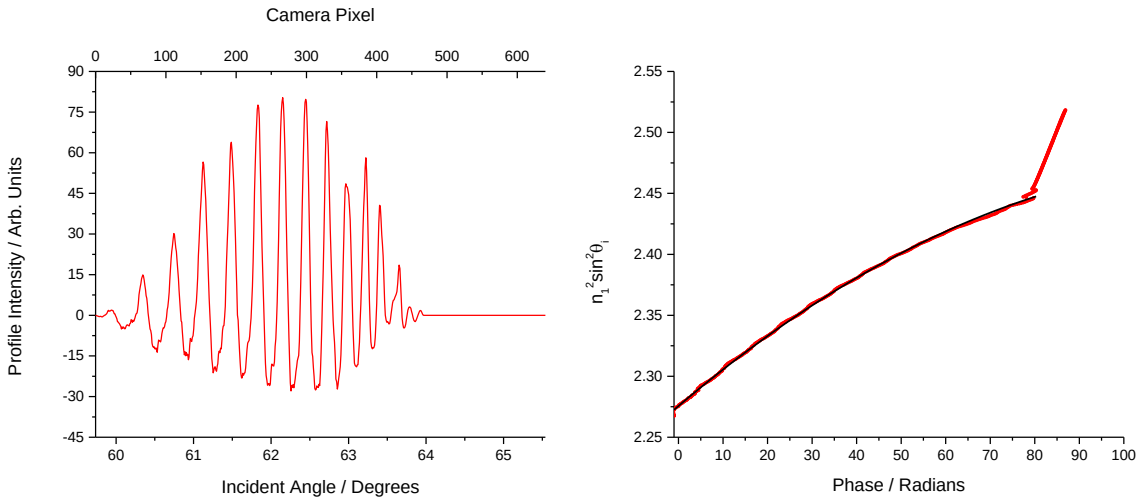

Figure 4.33: Background subtracted profile and phase fit for a 34 μm SU-8 film. The refractive index and thickness were both determined from 100 quadratic fits to the phase data. The results for the quadratic fit shown were n_{1550} = 1.5701 and d = 33.8 μm. The average values from the 100 different fits yielded n_{1550} =1.5705(2) and d =34.2(1) μm.

Stylus profilometers work similar to an AFM where a stylus tip is dragged over a sample and the height variations are measured through an electrical response related to the stylus height. A Vecco Dektak 8 stylus profiler (Tucson, AZ) was used to probe the edge of an SU-8 photoresist film over a 100 μm × 2.00 mm area with step sizes of δX = 1 μm and δY = 0.1 μm. The film was scanned from the top of the film and ended at the substrate to avoid tearing the film. A 3D surface plot of the SU-8 film is given in Figure 4.34

where the average thickness was determined as d = 34.21(9) µm in nearly perfect agreement with the optical measurement. A sample profile is also shown in Figure 4.34.

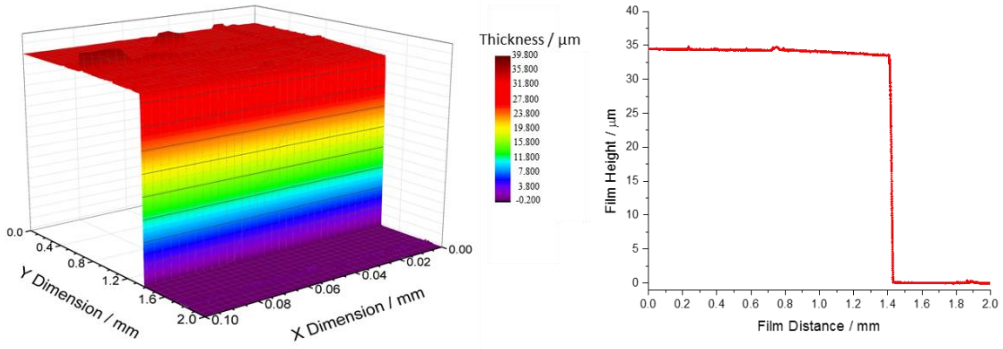

Figure 4.34: 3D surface plot of an SU-8 film using a stylus profilometer. The stylus profiler probed a 2 mm distance of the film in 0.1 µm steps (δY). The stylus probed in total 98 lines (~100 µm) in 1 µm steps (δX). A sample profile is given on the right. The average film thickness was d = 34.21(9) µm.

Stylus profilometers drag a stylus over a sample which can tear soft samples or cause chemical contamination. To avoid these problems, film thickness can be measured using non-contact optical approaches. Many different types of optical profilers exist including confocal microscopy[31-33], microscopy using structured light and vertical scanning white light interferometry (VSI)[34-36]. These devices can measure an entire focal region simultaneously and do not need to be scanned across a sample. The same film previously measured with a stylus profilometer was also studied using a Bruker Contour GT-K optical profiler (Tucson, AZ). The optical profiler used a 5× Mach-Zehnder (M-Z) interferometric objective with a 1× magnification tube and a 640×480 pixel camera was used to collect the data. The theory behind white light interferometers was previously discussed in Chapter 2.3.2. Light was reflected off of a sample and interfered with light reflecting off a stationary mirror inside the M-Z objective. The intensity of the interferogram was measured at each pixel using a CCD camera as the microscope head was lowered in the Z direction using a high-precision stepper motor. At a certain height, Z, the interference intensity between the two beams reached a maximum and was used to define the film height at a given pixel. The same SU-

8 film measured in Figure 4.34 was measured using the optical profilometer. The 3D surface plot and a sample profile are presented in Figure 4.35.

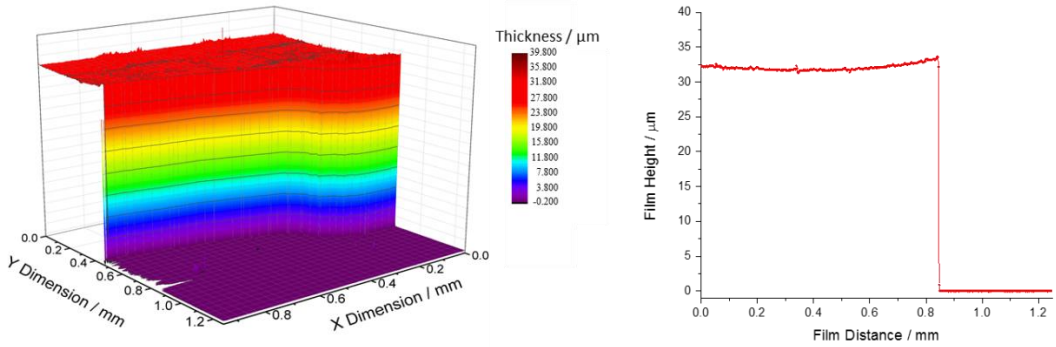

Figure 4.35: 3D surface plot of an SU-8 film using an optical profilometer. The microscope probed a 0.9456×1.2608 mm region of the film with a pixel resolution of 1.97 µm (δX = δY). A sample profile is given on the right. The film thickness was d = 31.90(4) µm.

While the refractometer and stylus profiler thickness measurements were in very close agreement, the thickness from the optical profilometer deviated by 6.7%. It was not possible to ensure that the same region of the film was probed in each experiment, so it is likely that the main difference in the measured thicknesses were a result of thickness variations across the film. From these measurements, we are quite confident that the refractometer can accurately probe the thickness to within 7%. Considering the accuracy observed with the refractive index measurements it is more likely the accuracy is actually better than 3-5% of the total thickness. Additional experiments with highly accurate thickness standards are needed in order to fully quantify the thickness accuracy.

4.5 Summary

The theory behind the operation of the optical refractometer when measuring both thick and thin films has been discussed with the derivation of all necessary equations and fitting routines. The typical methods used to increase the reliability and automation of data analysis for both measurement modes were also reported in detail. For thin-film measurements, the accuracy of the refractive index obtained through Fourier analysis was found to be within $\delta n = 2\times10^{-4}$, though the scatter of repeated measurements was found

at least 3 times higher than with thick films. The thickness accuracy was also studied with comparison made using both stylus and optical profilometers. In each case, the thickness did not deviate by more than 7%, it is likely though the accuracy is actually within 3-5% and most of the differences were the result of inhomogeneity in the film.

The thick-film refractometry methods described in this chapter were used to study the refractive index of common solvents and solutions in the near-IR and are discussed in detail in Chapter 5.[1] The diffusion of liquid solvents into SU-8 photoresist was quantified through Fourier analysis of thin films in Chapter 6.[2] Finally, the diffusion of solvent vapours into thin films of highly flexible PDMS is described through Fourier analysis in Chapter 7.

4.6 Future Work

During a research internship at *ABB Canada* in Quebec City, we worked on different methods to improve the optical setup of the refractometer. The goal was to increase the robustness of the optical alignment in order to create a more user friendly product. The discussions were incredibly insightful and a few of the ideas from this experience are described in this section as future work.

The equilateral prism can be easily replaced with a cylindrical prism where every incident angle will now enter the prism at 90° and will not be diffracted within the prism. This will greatly simplify the alignment as the distance from the focusing lens to the centre of the prism will be same for every incident angle (i.e. radii on the same circle). The focusing lens could then be fixed at a constant distance and pivot with respect to the centre of the cylindrical prism (Figure 4.36).

An additional improvement could be made by switching to a polarization maintaining (PM) fibre-coupled polarized diode laser. This would remove the need for polarization optics (controller and filter). The laser could be then coupled in line with the beam expanding optics and focusing lens. A folding mirror would no longer be needed, and the whole optical arm could pivot around the centre of the prism. A second arm could have the final collimating lens and the camera at fixed distances from the focal point of the prism. The proposed optical configuration is shown in Figure 4.37.

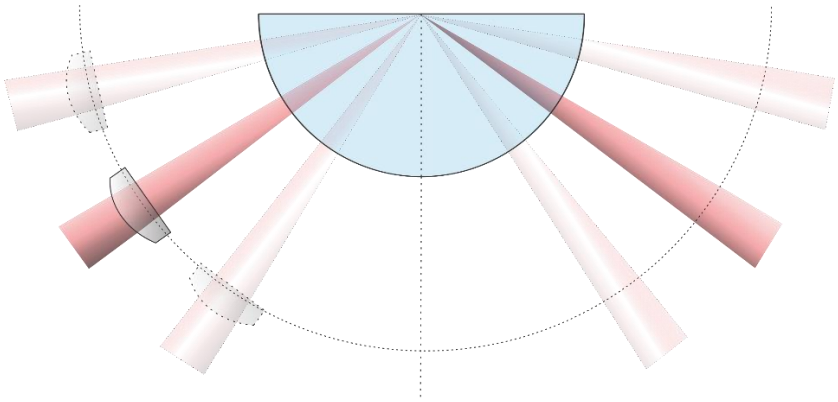

Figure 4.36: Schematic showing the focusing of light into a cylindrical prism. The light will always have an incident angle of 90° with the prism so there will not be any diffraction. This means that the focusing lens could be fixed on a pivot around the centre of the prism and will always have the same focal point inside the prism.

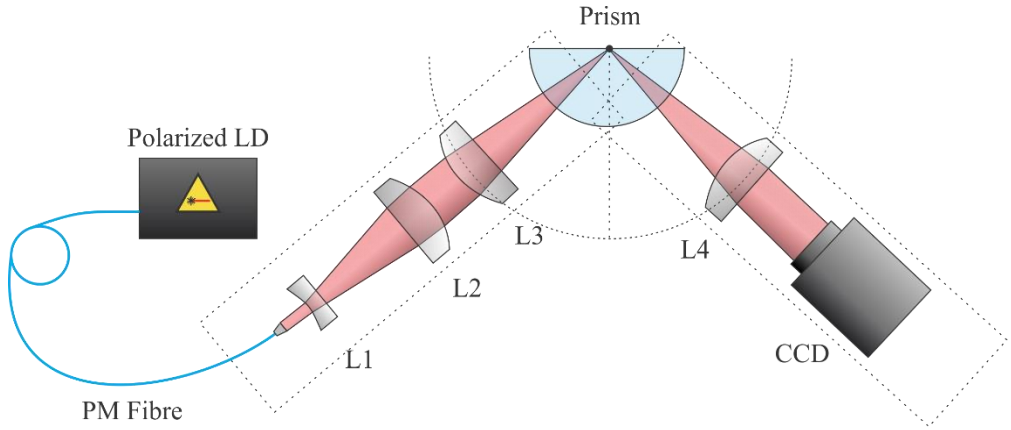

Figure 4.37: Proposed optical configuration for a future refractometer design. Replacing the laser diode with a PM fibre-coupled polarized laser removes the need for any polarization optics. The laser can then be mounted on the same arm with the Galilean beam expander (L1 and L2) and the focussing lens, L3. The final collimating lens L4 and the CCD camera could be fixed on a second arm such that both arms pivot around the centre of the cylindrical prism.

Finally, designing a mechanism to move both arms so that they always maintain the same angle relative to the prism would allow for a very robust system that could be adjusted to different refractive index ranges through a crank or stepper motor. This could allow for studying systems where the refractive index changes so drastically that a single calibration cannot capture the results from a full experiment. The refractometer could then be used to easily study the curing of paints, varnishes or adhesive films, where large refractive index changes are expected as the solvents evaporate.

4.7 Acknowledgements

I would like to acknowledge all of the assistance from the employees at *ABB Canada* for working with us on optimizing and modelling the optical refractometer. I would like to thank Dr. Frédéric Grandmont, Mr. Martin Gagné and Mr. François Tanguay for their discussions on possible improvements to the refractometer design that I discussed in Section 4.6. I would also like to thank Mr. François Tanguay, Dr. Sogol Borjian and Mr. Hao Chen for their assistance modelling our optical setups for both thin and thick films using Zemax OpticStudio™ 2015. I would also like to thank Dr. Raphael Desbiens for his assistance working on the Matlab™ code, and teaching us about the Fourier filtering techniques discussed in Section 4.4.3. I would like to acknowledge CMC microsystems for their access to Zemax OpticStudio™ 2015 through a designer subscription. I would also like to thank Mr. Nakkiran Arulmozhi and Dr. Jerkiewickz for their assistance in film measurement using the Veeco stylus profiler. Finally, I would like to thank Mr. Weijian (Jason) Chen for his work on developing the theory and original refractometer code which made these experiments possible.

4.8 References

1. Saunders, J. E.; Sanders, C.; Chen, H.; Loock, H.-P., Refractive indices of common solvents and solutions at 1550 nm. *Applied Optics* **2016,** *55*, 947-953.

2. Saunders, J. E.; Chen, H.; Brauer, C.; Clayton, M.; Chen, W.; Barnes, J. A.; Loock, H.-P., Quantitative diffusion and swelling kinetic measurements using large-angle interferometric refractometry. *Soft Matter* **2015,** *11*, 8746-8757.

3. Chen, W.; Saunders, J. E.; Barnes, J. A.; Yam, S. S.-H.; Loock, H.-P., Monitoring of vapor uptake by refractive index and thickness measurements in thin films. *Optics Letters* **2013,** *38*, 365-367.

4. Saleh, B. E. A.; Teich, M. C., *Fundamentals of Photonics*. 2nd Edition, John Wiley & Sons, Hoboken, NJ, 2007.

5. Rheims, J.; Köser, J.; Wriedt, T., Refractive-index measurements in the near-IR using an Abbe refractometer. *Measurement Science and Technology* **1997,** *8*, 601-605.

6. Moreels, E.; de Greef, C.; Finsy, R., Laser light refractometer. *Applied Optics* **1984,** *23*, 3010-3013.

7. Cooper, P. R., Refractive index measurements of liquids used in conjunction with optical fibers. *Applied Optics* **1983,** *22*, 3070-3072.

8. Li, H.; Xie, S., Measurement method of the refractive index of biotissue by total internal reflection. *Applied Optics* **1996,** *35*, 1793-1795.

9. Sánchez-Pérez, C.; García-Valenzuela, A., Spectroscopic refractometer for transparent and absorbing liquids by reflection of white light near the critical angle. *Review of Scientific Instruments* **2012,** *83*, 115102, 1-7.

10. Wang, X.-D.; Wolfbeis, O. S., Fiber-optic chemical sensors and biosensors (2008–2012). *Analytical Chemistry* **2013,** *85*, 487-508.

11. Wang, X.-d.; Wolfbeis, O. S., Fiber-optic chemical sensors and biosensors (2013–2015). *Analytical Chemistry* **2016,** *88*, 203-227.

12. Tian, Z.; Yam, S. S.-H.; Loock, H.-P., Single-mode fiber refractive index sensor based on core-offset attenuators. *IEEE Photonics Technology Letters* **2008,** *20*, 1387-1389.

13. Tian, Z.; Yam, S. S.-H.; Barnes, J.; Bock, W.; Greig, P.; Fraser, J. M.; Loock, H.-P.; Oleschuk, R. D., Refractive index sensing with Mach-Zehnder interferometer based on concatenating two single-mode fiber tapers. *IEEE Photonics Technology Letters* **2008,** *20*, 626-628.

14. Albert, J.; Shao, L.-Y.; Caucheteur, C., Tilted fiber Bragg grating sensors. *Laser & Photonics Reviews* **2013,** *7*, 83-108.

15. Barnes, J.; Dreher, M.; Plett, K.; Brown, R. S.; Crudden, C. M.; Loock, H.-P., Chemical sensor based on a long-period fibre grating modified by a functionalized polydimethylsiloxane coating. *The Analyst* **2008,** *133*, 1541-1549.

16. Lambeck, P. V., Integrated optical sensors for the chemical domain. *Measurement Science and Technology* **2006,** *17*, R93-R116.

17. Washburn, A. L.; Bailey, R. C., Photonics-on-a-chip: recent advances in integrated waveguides as enabling detection elements for real-world, lab-on-a-chip biosensing applications. *The Analyst* **2011,** *136*, 227-236.

18. Xu, D. X.; Densmore, A.; Delâge, A.; Waldron, P.; McKinnon, R.; Janz, S.; Lapointe, J.; Lopinski, G.; Mischki, T.; Post, E.; Cheben, P.; Schmid, J. H., Folded cavity SOI microring sensors for high sensitivity and real time measurement of biomolecular binding. *Optics Express* **2008,** *16*, 15137-15148.

19. Densmore, A.; Xu, D.-X.; Waldron, P.; Janz, S.; Lapointe, J.; Mischki, T.; Lopinski, G.; Delage, A.; Cheben, P. Spotter-compatible SOI waveguide devices for biomolecular sensing, *Silicon Photonics III, Proceedings of SPIE 6898*, **2008**, 68981B, 1-8.

20. Chen, W. *Chemical Detection and Sensing Using Optical Interferometry*. M.A.Sc Thesis, Queen's University, 2013.

21. Jalali, B., Can silicon change photonics? *Physica Status Solidi A* **2008,** *205*, 213-224.

22. DET10A High Speed Photodetector. Thorlabs, http://www.thorlabs.com (accessed July 31, 2016).

23. CamIR1550 Notes for Operation. Applied Scintillation Technologies, Harlow, UK, www.appscintech.com (accessed July 31, 2016).

24. Refractive Index (Matching) Liquids. Cargille-Sacher Laboratories Inc. , http://www.cargille.com/refractivestandards.shtml (accessed July 31, 2016).

25. *N-SF11 Glass Data Sheet.* Schott, 2015, 785257.322,

26. Jha, R.; Villatoro, J.; Badenes, G.; Pruneri, V., Refractometry based on a photonic crystal fiber interferometer. *Optics Letters* **2009,** *34*, 617-619.

27. Li, L.; Xia, L.; Xie, Z.; Liu, D., All-fiber Mach-Zehnder interferometers for sensing applications. *Optics Express* **2012,** *20*, 11109-11120.

28. Lu, P.; Men, L.; Sooley, K.; Chen, Q., Tapered fiber Mach–Zehnder interferometer for simultaneous measurement of refractive index and temperature. *Applied Physics Letters* **2009,** *94*, 131110, 1-3.

29. Guo, T.; Tam, H.-Y.; Krug, P. A.; Albert, J., Reflective tilted fiber Bragg grating refractometer based on strong cladding to core recoupling. *Optics Express* **2009,** *17*, 5736-5742.

30. Sun, A.; Wu, Z., A hybrid LPG/CFBG for highly sensitive refractive index measurements. *Sensors* **2012,** *12*, 7318-7325.

31. *Basic Confocal Microscopy*. Price, R. L.; Jerome, W. G., Eds. Springer Science + Business Media, LLC, New York, NY, 2011.

32. *Confocal Microscopy Methods and Protocols* 2nd Edition, Paddock, S. W., Ed. Springer Science + Business Media, New York, NY, 2014.

33. Semwogerere, D.; Weeks, E. R., Confocal Microscopy. In *Encyclopedia of Biomaterials and Biomedical Engineering*, Taylor & Francis: 2005; pp 1-10.

34. Wyant, J. C. White light interferometry, *Holography: A Tribute to Yuri Denisyuk and Emmett Leith*, **2002**, 98-107.

35. Kumar, U. P.; Haifeng, W.; Mohan, N. K.; Kothiyal, M. P., White light interferometry for surface profiling with a colour CCD. *Optics and Lasers in Engineering* **2012,** *50*, 1084-1088.

36. Pavliček, P.; Michálek, V., White-light interferometry—Envelope detection by Hilbert transform and influence of noise. *Optics and Lasers in Engineering* **2012,** *50*, 1063-1068.

Chapter 5

Refractive Indices of Common Solvents and Solutions at 1550 nm

A large portion of the material presented in this chapter has been previously published in "The refractive index of common solvents and solutions at 1550 nm", Applied Optics **2016**, *55*, (4) 947-953.[1] All figures and sections have been used with permission of the co-authors and through permission obtained from the Optical Society of America (OSA).

This chapter includes the refractive index measurements (λ = 1550 nm) of a series of 29 common organic solvents. The refractive indices of aqueous solutions of sucrose, sodium chloride, ethylene glycol, glycerol and dimethylsulfoxide were also measured over the full soluble/miscible range. Polynomial fits of the refractive index versus analyte weight fraction are provided, and can be used when preparing calibration solutions for other near-IR refractive index sensors.

5.1 Introduction

It can be difficult to obtain reliable refractive indices of even common organic solvents in the near-infrared region of the spectrum. These values are frequently required to calibrate new refractive index sensors for, e.g., food processing, environmental monitoring and chemical detection. Fiber-optic refractive index sensors and microphotonic sensors based on silicon-on-insulator technology operate typically in the C-band region of the telecom spectrum from 1530 to 1565 nm. In this wavelength range, the attenuation of silica fibers is minimized ($\leq$ 0.18 dB/km),[2] and the attenuation of silicon waveguides is also comparably low (0.3-0.5 dB/cm).[3-4]

Fortunately, several groups have already used refractometry and interferometric methods to determine the refractive indices of some organic solvents, which one can use to validate new measurements and new instruments.[5-7] Rheims and coworkers presented an Abbé refractometer measuring the refractive indices of solvents sandwiched between two prisms at λ = 830 nm.[5] Moutzouris and coworkers used a commercially available refractometer to collect refractive indices of 12 organic solvents at five different wavelengths between 450 nm and 1551 nm at 300K.[6] Also, Samoc and coworkers consolidated a wealth of

refractive index values from the literature for four solvents at wavelengths in the visible and infrared and obtained Sellmeier and Cauchy parameters for these refractive indices between 270 nm and 2190 nm.[7] In their study, they emphasize the discrepancy of many solvent refractive index values currently presented in the literature, especially those in the near-IR.[7]

In this chapter, new measurements of refractive indices of several common solvents as well as five series of solutions that may be used to calibrate new sensors are reported. All measurements were made at λ = 1550 nm and at approximately 298K. The refractive indices of 29 solvents were determined using a large-angle refractometer described previously.[8-9] The measured refractive indices of aqueous sucrose and sodium chloride solutions over the full solubility range are presented. Refractive indices of aqueous mixtures of dimethylsulfoxide (DMSO), ethylene glycol and glycerol are given over the entire miscible range. The concentration dependence of the refractive indices are modelled using 3rd order polynomial fits. The reported fit parameters can now be used to produce calibration solutions of any refractive index between n_{1550} = 1.3164 and 1.4631.

5.2 Experimental Setup for Thick Film Measurements

The experimental setup and methods for studying thick films (d > 100 μm) on the refractometer are described in this section. The details of the optical setup are provided in Section 5.2.1. Some basic theory and analysis techniques used for measuring refractive indices of liquid samples are discussed in Section 5.2.3. Finally, the calibration methods used with this instrument are discussed in Section 5.2.4

5.2.1 Optical Experimental Setup

The refractometer setup has been previously described in Chapter 4.2.[8-9] Briefly, the instrument was constructed using a λ = 1550 nm diode laser (Thorlabs LPS-1550-FC, 1.5 mW). A Galileo-type beam expander was used to expand the laser beam to approximately 1 cm, where a fibre polarization controller and polarization filter were used to select p-polarized light. The light was then focused onto the top surface of a 25 mm high-density flint glass equilateral prism (Schott N-SF11, n_{1550} =1.7434) using a f = 2.50 cm cylindrical lens. This produced a 4° range of incidence angles at the sample-substrate interface. Some angles

were total internally reflected inside the prism and others were refracted into the liquid sample depending on its refractive index. This is illustrated in Figure 5.1A with a sample image in Figure 5.1B. A second cylindrical lens with $f = 5.00$ cm was used to collimate the reflected light onto a near-IR CCD camera (Edmund Optics, NIR Camera # 56-567). Cylindrical lenses are preferred over spherical lenses to reduce aberration in the images. A glass cap was glued onto an N-SF11 slide using commercially available "5 minute" epoxy and was used as a liquid sample well. Approximately 2-3 mL of each sample was pipetted into the sample well and was measured in triplicate, or averaged from six measurements when the refractive index overlapped between two calibrations ranges.

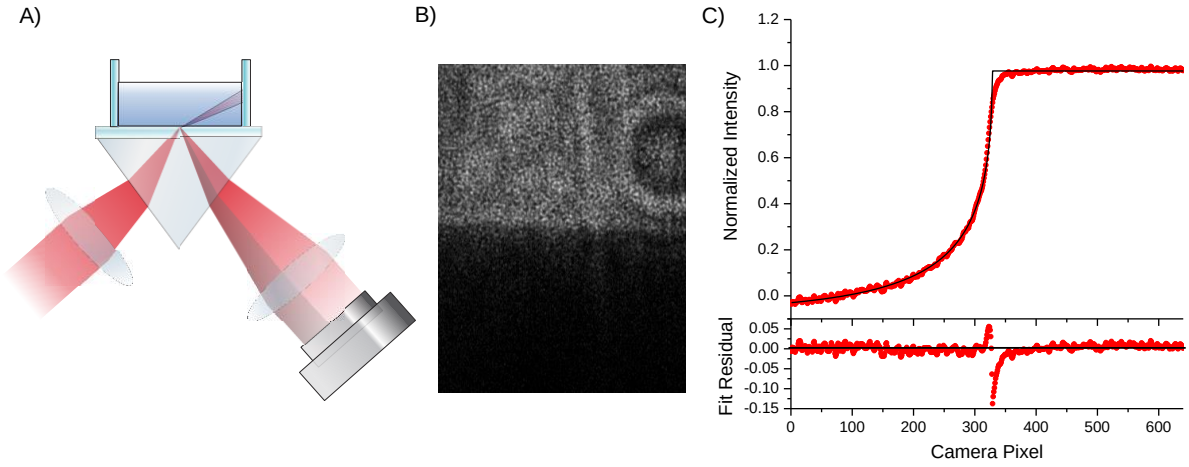

Figure 5.1: Schematic demonstrating Fresnel and total internal reflection at a slide liquid interface by refractometry. A) Light is focused down using a lens to generate a range of incident angles at the substrate-sample interface. On top of the prism, an N-SF11 slide was attached using index matching liquid n_{1550} = 1.6884. A glass cap was glued onto the slide using commercial 5 minute epoxy to make a well for measuring liquids samples. Depending on the refractive index of the sample, the angles of light total internally reflected (shown in light red) and those that undergo Fresnel reflection (shown in dark red) will change. The Fresnel region will appear darker on the near-IR camera as some of the light will be refracted into the sample. B) A sample image of a Cargille refractive index solution (n_{1550} = 1.3442). The bright part at the top of the image shows total internal reflection and the dark portion the Fresnel reflection below the critical angle. C) Piecewise Fresnel fit to the image profile from B).

The residual of the fit in Figure 5.1 shows that most of the error occurs when switching between functions describing Fresnel reflection and total internal reflection. Curvature in this region may be increased when studying absorbing or scattering samples.[10-11] This curvature may also be influenced by variations in the interface pixel across the camera image due to tilted optical elements. The overall noise in the image is due

to laser speckle, which is a commonly observed effect from diffuse reflection of coherent light sources off rough surfaces.[12] This is a major limitation to the pixel resolution and the sharpness of our images. In order to remove this effect a less coherent source could be used, but would result in less resolution of interference fringes when studying thin films. Overall however, the fit agrees quite well with the data and can only be improved by accounting for other optical effects.

5.2.2 Chemical Information

All reagents and solvents were obtained as reagent grade or higher purity from commercial suppliers. Reagents were used as supplied without any additional purification. A detailed list of the suppliers and purity of each reagent is listed in Appendix 5.1.

5.2.3 Analysis of Fresnel Reflection

The near-IR camera (Edmund Optics #56-567) used for the refractometry experiments was a phosphorous coated CCD array. This camera works through a non-linear two-photon absorption process, where the absorption of two infrared photons results in the emission of a visible photon that can be detected by a standard silicon CCD array. The response of the camera, *S*, is related non-linearly to the light intensity, *I*, through a scaling exponent of 1.41 $\left(S = I^{1.41}\right)$.[13] In our experiments, a dark box was placed above the refractometer to reduce the amount of stray visible light reaching the CCD during experiments. The camera gain was enhanced, in the software, prior to running experiments in order to capture the low intensity end of the Fresnel reflection.

For each measurement, three images were taken: (1) a dark image using a high-index liquid to determine the brightness offset of the camera, (2) a blank image showing any defects in the system such as optical artifacts or contamination on optical components, and (3) the image of each sample. The blank (bright) image was obtained by placing a low-index liquid on the prism such that light at all angles were totally internally reflected.

The profile of each image was taken by averaging over all rows and then returned to a linear scale by taking the 1.41th root of the intensity. The data profiles were then normalized using a custom Matlab script according to equation (5.1).

$$I_{Normalized} = \frac{\left(I_{Sample} - I_{Dark}\right)}{\left(I_{Blank} - I_{Dark}\right)} \tag{5.1}$$

The normalization process removed the noise from the raw camera images as is demonstrated in Figure 5.2.

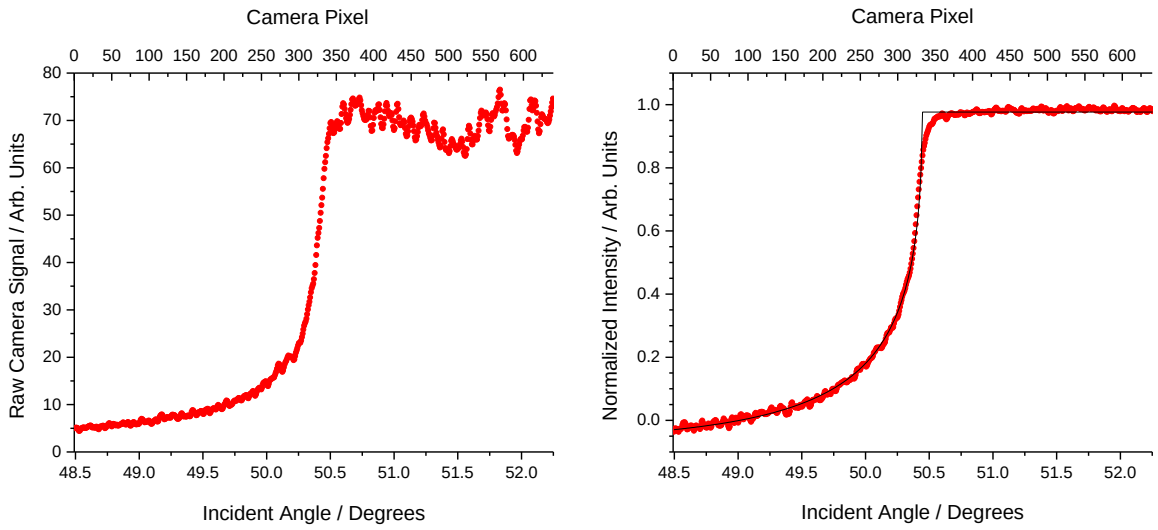

Figure 5.2: Comparison between raw and normalized camera profiles for a Cargille refractive index solution n_D = 1.3500 (n_{1550} = 1.3442). A) The raw data has not yet been linearized and shows substantial noise in the region of total internal reflection above 50.5°. B) The normalized curve now agrees very closely with the Fresnel reflection of p polarized light (shown by the black fit line).

For incident angles below the critical angle of total internal reflection, the intensity of the reflected light at the film-substrate interface is governed by Fresnel reflection, which behaves differently for s- and p-polarized light.

$$R_s = r_s^{\,2} = \left(\frac{n_1 \cos\theta_i - n_2 \cos\theta_t}{n_1 \cos\theta_i + n_2 \cos\theta_t}\right)^2 \tag{5.2}$$

$$R_p = r_p^{\,2} = \left(\frac{n_1 \cos\theta_t - n_2 \cos\theta_i}{n_1 \cos\theta_t + n_2 \cos\theta_i}\right)^2 \tag{5.3}$$

Here, the subscripts 1 and 2 represent the prism and sample respectively, while *i* and *t* represent the incident and transmitted angle. Equations (5.2) and (5.3) can be substituted with Snell's law to express the reflected light intensity using only the incident angle, θ_i.

$$R_s = \left(\frac{n_1 \cos\theta_i - n_2 \sqrt{1 - \left[(n_1/n_2) \sin\theta_i \right]^2}}{n_1 \cos\theta_i + n_2 \sqrt{1 - \left[(n_1/n_2) \sin\theta_i \right]^2}} \right)^2 \tag{5.4}$$

$$R_p = \left(\frac{n_1 \sqrt{1 - \left[(n_1/n_2) \sin\theta_i \right]^2} - n_2 \cos\theta_i}{n_1 \sqrt{1 - \left[(n_1/n_2) \sin\theta_i \right]^2} + n_2 \cos\theta} \right)^2 \tag{5.5}$$

For the purpose of these experiments, a polarization filter and polarization controller were used to select only the vertically p-polarized light. All further equations expressing reflection, *R*, will be assumed as the reflection of p-polarized light, R_P. In principle, either polarization could be used to make measurements, though it is important to know which equation is required as the two polarizations have different reflection curves (Figure 5.3).

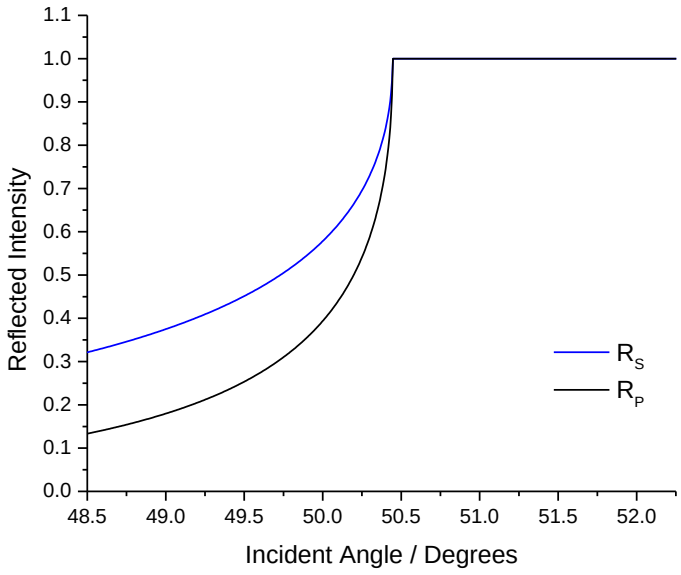

Figure 5.3: Simulated s- and p-polarized reflection profiles for a solution of n_{1550} = 1.3442. The angular range shown here is the same as in Figure 5.2.

Two additional fitting parameters $A \approx 1$ and $Y_0 \approx 0$ are used when fitting real data for amplitude scaling and a y-offset.

$$R = A * \left[\frac{n_1 \sqrt{1 - \left(\frac{n_1}{n_2} \sin\theta_i \right)^2} - n_2 \cos\theta_i}{n_1 \sqrt{1 - \left(\frac{n_1}{n_2} \sin\theta_i \right)^2} + n_2 \cos\theta_i} \right]^2 - Y_0 \tag{5.6}$$

Above the critical angle, $(n_1/n_2)\sin\theta_i \geq 1$, equation (5.6) becomes undefined and the intensity is fit to a constant.

$$R = A - Y_0 \tag{5.7}$$

A piecewise function was fit to the angular reflection profile using a least squares algorithm in Matlab™ (Mathworks, Natick, MA). During calibration, the camera angular range was unknown so the angle, θ, was replaced with a linear approximation $aP + b$, where P was the pixel column on the image, and a and b were both fitting parameters. A representative fit to a refractive index solution with n_{1550} = 1.3442 (Cargille Laboratories, Cedar Grove, NJ) (Figure 5.1B) was shown in Figure 5.1C. The refractometer was then calibrated in five different angular ranges in order to measure refractive indices of solvents and solutions between 1.3049 and 1.4895, i.e. between θ_i = 48.46 and 58.69°. This calibration process is described in greater detail in the following section.

5.2.4 Refractive Index Calibration

In its current configuration, the refractometer probes a 4° range of incident angles, corresponding to a refractive index range of approximately dn = 0.07. In order to probe a wider range of samples, the refractometer had to be calibrated in 5 different angular ranges. The calibration was performed using a series of 18 Cargille refractive index liquids (Cargille Laboratories, Cedar Grove, NJ) ranging from n_{1550} = 1.3154 to 1.4856, with a minimum of 5 liquids per range. Cargille Laboratories provided refractive index values at 1550 nm through extrapolation using Cauchy equations from measurements at shorter wavelength. The accuracy of the extrapolation is quoted as ± 0.005, and is the dominant limitation of the accuracy of

our refractive index measurements. The environmental conditions in the lab were recorded using a temperature and humidity monitor (Omega, OM-EL-USB-RT), with an accuracy of ± 0.2°C when compared with a standard ethanol thermometer. The temperature during experiments ranged between 24.0°C and 26.7°C, averaging approximately 25.6°C. At least three measurements were taken of each calibration solution and solvent. In each case, the normalized reflection profile was fit using a piecewise function of Fresnel reflection and total internal reflection described by equations (5.6) and (5.7) as was shown in Figure 5.1C. The critical angle was found to follow a quadratic relation with respect to camera pixel and could be approximated by a linear function over a small angular range. The 5 different calibration ranges are shown in Figure 5.4 with x-error bars showing 1σ standard deviation of the averages from 3-6 measurements of each solution. The quadratic fits are shown as red lines and the 99.7% (3σ) confidence intervals are shown as dashed blue lines above and below the fits.

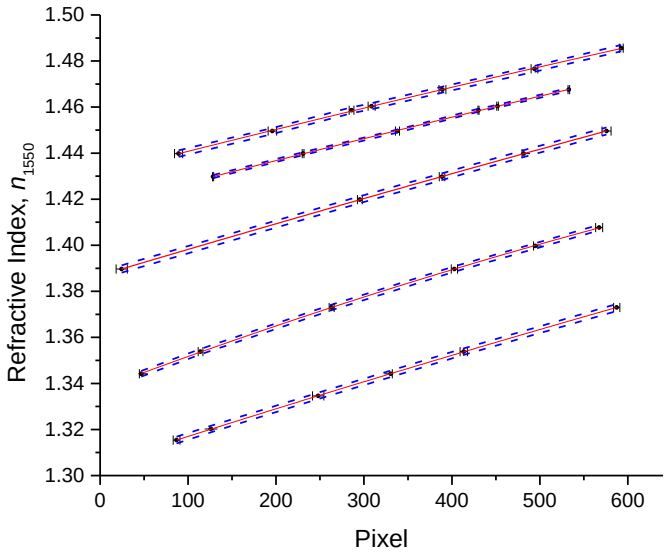

Figure 5.4: Refractive index calibrations with Cargille refractive index solutions. The refractometer probes a 4° range of incident angles, so five different calibrations with Cargille refractive index solutions were needed to measure the full range of refractive indices. For each range a quadratic fit was used to correlate the refractive index to the camera pixel at the critical angle for each sample (red lines). The upper and lower 99.7% (3σ) confidence intervals were calculated from the fits and are shown as dashed blue lines for each range.

A series of 29 common solvents were then measured in triplicate (or 6 times when they overlapped between two calibration ranges). An image compilation showing 100 pixel cross-sections of all of the solvent

measurements is presented in Figure 5.5. The numbers in the image correspond to the solvent indices in Table 5.1 of Section 5.3. The bright regions show total internal reflection and the dark regions show the Fresnel reflection below the critical angle, i.e. when some of the light is refracted into the sample. The boundary region gives the critical angle for each solvent.

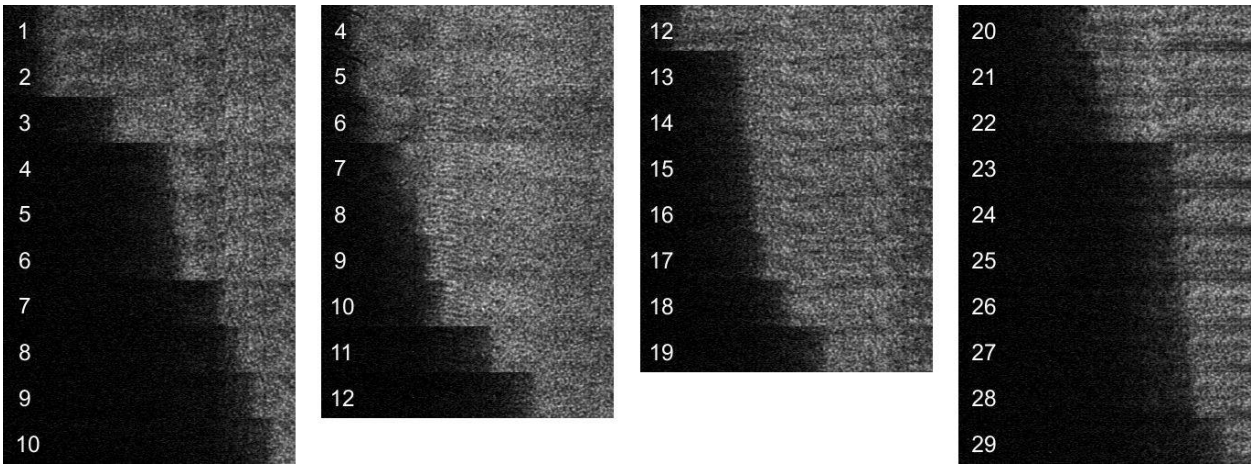

Figure 5.5: Compilation of images of all the organic solvents measured from 4 of the 5 calibration ranges. Range 1 (n_{1550} = 1.3049-1.3787) shows solvents 1-10. Range 2 (n_{1550} = 1.3379-1.4148) shows solvents 4-12. Range 3 (n_{1550} = 1.3870-1.4563) shows solvents 12-19 and Range 5 (n_{1550} = 1.4312-1.4895) shows solvents 20-29. The numbers refer to the refractive indices in Table 5.1.

5.3 Refractive Indices of Common Solvents

The refractive indices of 29 common organic solvents were measured in triplicate for each calibration range. When possible, solvents were measured in two different calibration ranges and were then averaged from a total of six measurements. The average refractive indices and the experimental standard deviations are given in Table 5.1. Comparison is made to literature values where available. The literature values for *n* (589 nm) have also been included for comparison. It was quite challenging to find literature refractive indices at λ = 1550 nm for most organic solvents. Frequently, refractive indices at λ = 589 nm are used in the literature as substitutes when calibrating fibre-based refractive index sensors operating in the near-IR.[14-18] While these calibrations may provide similar values for the sensitivity of the sensor, such

practice clearly results in errors in the absolute accuracy of near-IR refractive index sensors and should be avoided.

The solvent refractive indices reported here for deionized water, methanol, acetonitrile, 1-propanol and 1,4-dioxane were in very close agreement to values previously reported in the literature, differing by only Δn = 1-3 $\times 10^{-4}$. The index of chloroform was found to be Δn = 1.3-1.5 $\times 10^{-3}$ lower than previously reported. A wide range of refractive indices have been reported for toluene and benzene spanning 3-4$\times 10^{-3}$ refractive index units. In both cases, however, our values fall within the ranges previously reported in the literature.

Table 5.1: Refractive indices of 29 organic solvents at 1550nm. The infrared refractive indices reported in this study are given with 1σ standard deviation of 3-6 measurements in brackets. The literature values are provided at 589 nm and at 1550 nm from the literature where available. The temperature of literature values are also shown in brackets.

Index	Solvent	*n* (589 nm) from [19]	*n* (1550 nm) at 298 K	n (1550 nm) from literature
1	Deionized Water	1.33336 (293K)	1.3164(2)	1.3154 (293K) [20] 1.3180 (298K) [21]
2	Methanol	1.3288 (293K)	1.3174(1)	1.3172 (300K) [6]
3	Acetonitrile	1.3442 (303K)	1.3348(2)	1.3345 (300K) [6]
4	Acetone	1.3588 (293K)	1.3483(2)	
5	Anhydrous Ethanol	1.3611 (293K)	1.3503(3)	1.3520 (293K)* [20]
6	95% Ethanol	---	1.3522(5)	1.3520 (293K)* [20]
7	Formaldehyde Solution 37%	1.3765 (293K)	1.3616(7)	
8	2-Propanol (Isopropanol)	1.3776 (293K)	1.3661(3)	
9	Hexanes (Mixture of Isomers)	1.3727 (298K)**	1.3695(4)	
10	1-Propanol	1.3850 (293K)	1.3737(4)	1.3738 (300K) [6]
11	2-Butanol	1.3978 (293K)	1.3864(1)	
12	Tetrahydrofuran	1.4050 (298K)	1.3969(3)	
13	Dichloromethane	1.4224 (293K)	1.4124(2)	
14	1,4-Dioxane	1.4242 (293K)	1.4127(5)	1.4124 (300K) [6]

15	Cyclohexane	1.4235 (298K)	1.4147(1)	
16	N,N-Dimethylformamide	1.4305 (293K)	1.4153(1)	
17	Ethylene Glycol	1.4318 (293K)	1.4176(2)	
18	N,N-Dimethylacetamide	1.4341 (298K)	1.4235(4)	
19	Chloroform	1.4459 (293K)	1.4321(1)	1.4334 (293K) [20] 1.43367 (293K) [7]
20	Glycerol	1.4746 (293K)	1.4571(7)	
21	Trichloroethylene	1.4773 (293K)	1.4601(3)	
22	Dimethylsulfoxide (DMSO)	1.4793 (293K)	1.4631(2)	
23	p-Xylene	1.4929 (293K)	1.4753(1)	
24	Ethylbenzene	1.4930 (298K)	1.4759(1)	
25	Toluene	1.4941 (298K)	1.4760(2)	1.4737 (300K) [6] 1.4778 (293K) [20]
26	m-Xylene	1.4944 (298K)	1.4769(2)	
27	Xylenes (Mixture of Isomers and Ethylbenzene)	---	1.4778(2)	
28	Benzene	1.5011 (293K)	1.4789(3)	1.4769 (300K) [6] 1.47986 (293K) [7]
29	o-Xylene	1.5018 (298K)	1.4846(2)	

* Reference [6] does not indicate whether 95% or anhydrous ethanol was measured
** Literature value was reported for n-hexane as a stand-in for the mixture of hexanes.

5.4 Refractive Indices of Aqueous Solutions

The refractive indices of five common series of aqueous solutions were measured including sodium chloride, sucrose, dimethylsulfoxide (DMSO), glycerol, and ethylene glycol. The solutions were prepared using deionized water (Fisher Scientific) and reagent grade or higher purity reagents (Sigma Aldrich). The mass fraction, *W*, was accurately determined from the masses of water and reagents measured on an analytical balance (Sartorius BL120S) to ± 0.1 mg accuracy. This provided a mass fraction uncertainty of

δW = 4-8×10^{-6}. The refractive index as a function of the mass fraction of each solute was fit with a 3rd order polynomial function.

$$n(W) = AW^3 + BW^2 + CW + D \tag{5.8}$$

The polynomial fits and fit residuals for the five series are shown in Figure 5.6. The four terms of the polynomial fits of equation (5.8) are given in Table 5.2, over the calculated range of mass fraction, *W*. The raw data for each series are provided in Appendix 5.2.

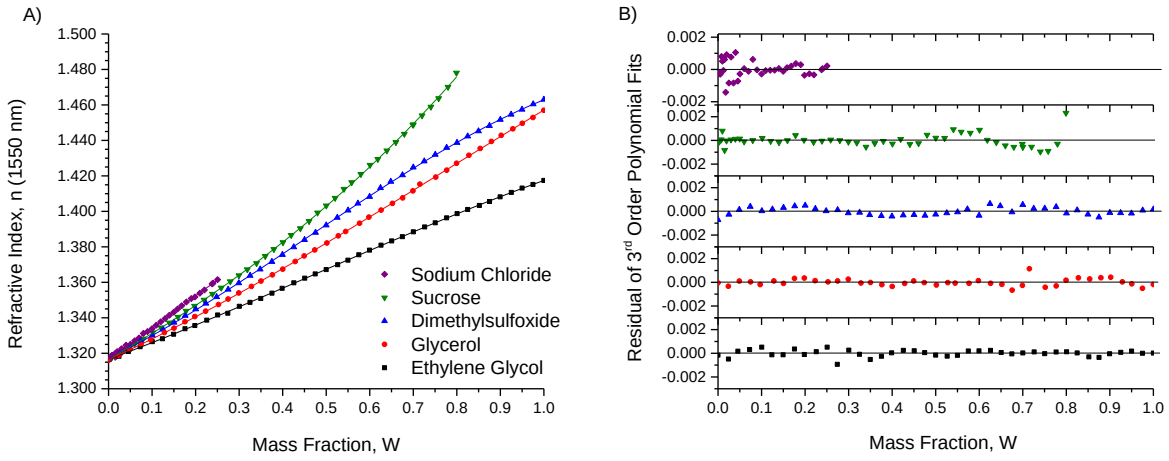

Figure 5.6: The refractive indices of aqueous solutions of sodium chloride, sucrose, dimethylsulfoxide, glycerol and ethylene glycol as a function of analyte mass fraction, *W*. Each solution was run in triplicate with the average values plotted in A). All the curves were fit with a 3rd order polynomial function (equation (5.8)) and the fit residuals are shown in B)

While a 3rd order polynomial function was used, the fit may be improved by adding additional terms. One method of assessing whether additional terms will improve the fit is to compute the autocorrelation function of the residuals. If the periodic dependencies decrease when additional parameters are added, then the fit has been improved.

Table 5.2: Fitting parameters from 3rd-order polynomial fits of refractive indices (n_{1550}) as a function of mass fraction for five series of aqueous solutions. The suitable calculation range of each equation is given as a range of mass fraction, *W*. Ethylene glycol, glycerol and DMSO are fully miscible in water and fits were over the entire concentration range from 0-100% w/w. Cells labeled *A*-*D* are the fit parameters to equation (5.8).

Analyte	NaCl	Sucrose	Ethylene Glycol	Glycerol	DMSO
W	0-0.25	0-0.80	0-1.00	0-1.00	0-1.00
A	-0.0800	0.0330	-0.0223	-0.0216	-0.0730
B	0.0740	0.0456	0.0321	0.0512	0.0998
C	0.1620	0.1416	0.0910	0.1110	0.1189
D	1.3162	1.3166	1.3166	1.3165	1.3172

34 aqueous sodium chloride solutions were prepared from 0-25% (w/w), limited by the solubility of sodium chloride in water at room temperature. These solutions spanned a refractive index range of n_{1550} = 1.3164 to 1.3599. In the case of sucrose, we refer to the commonly used BRIX scale as a calibration system, where 1 degree BRIX corresponds to 1 g of sucrose in 100 g of aqueous sample. The refractive indices (589 nm) and densities of sucrose solutions have been accurately measured and are available in the literature.[22] We prepared 48 sucrose solutions ranging from 0-80 % (w/w) – again, limited by the solubility of sucrose in water. For solutions greater than 68 % (w/w), supersaturated solutions were prepared by heating the solutions in a boiling water bath and subsequent cooling to 298K, if left to stand too long, solutions would begin to recrystallize. The refractive indices spanned all five calibration regions from n_{1550} = 1.3164-1.4781 (Figure 5.6).

Dimethylsulfoxide (DMSO) was measured from a series of 40 aqueous mixtures ranging from 0-100 % (w/w) in 2.5 % increments. DMSO is quite convenient for calibration solutions as it benefits from a very low volatility and reasonably high refractive index, and can be used to calibrate over a wide index range. The solutions ranged from n_{1550} = 1.3164-1.4631 (Figure 5.6). Ethylene Glycol is a highly viscous

polar compound that is fully miscible in water yielding solutions between n_{1550} = 1.3164-1.4174. In total 40 solutions were prepared from 0-100 % (w/w) in 2.5 % increments and are also shown in Figure 5.6.

Glycerol, alternatively known as glycerin or glycerine, is a viscous polar liquid that is commonly used in the food, cosmetics and pharmaceutical industries. Similar to ethylene glycol it is fully miscible in water and can be used to prepare solutions ranging from n_{1550} = 1.3164-1.4569. 40 Solutions were made from 0-100% (w/w) in 2.5 % increments and were shown in Figure 5.6.

5.5 Polarizabilities of Aqueous Mixtures

From comparison with literature values, the accuracy of refractive indices appears to be greater than the rather conservative estimate of the Cargille refractive index liquids (δn = ±0.005) (Cargille Laboratories). For example, our refractive index measurements of methanol, acetonitrile, 1-propanol and 1,4-dioxane were within $\Delta n = \pm 3\times10^{-4}$ of values previously reported.[6] Also, the quadratic fits to the nominal refractive indices of the calibration standards were within Δn = ± 2-5 $\times10^{-4}$, indicating the that values provided by the manufacturer were more precise than the company allowed for. Whenever possible, measurements were taken in the overlapped region between two calibration ranges and were averaged from six measurements instead of three. The precision was found to be between δn = 0.0001-0.0019 for replicate measurements with typical standard deviations of $\sigma_n \sim 0.0005$. The accuracy error for calculations using the polynomial functions of equation (5.8) with the parameters in Table 5.2 did not exceed σ_n = ±0.0023 (for the most concentrated sucrose solution), and was typically $\sigma_n < 0.0003$ (residuals in Figure 5.6B).

The refractive indices of the three series of binary solvent mixtures can be used to test the validity of the Lorentz-Lorenz equation. The refractive indices of solvent mixtures are not expected to scale linearly with the mole fraction of the respective solvent. Instead, the total polarizabilities of the solutions are expected to be a weighted sum of the electronic polarizabilities of the two constituents.

$$\alpha_{LL}(X) = \sum_i X_i \alpha_i \tag{5.9}$$

The electronic polarizability, α, is related to the refractive index through the Lorentz-Lorenz equation,[23] which is analogous to the Clausius-Mossotti equation which equates the polarizability to the relative permittivity, ε_r.[24]

$$\alpha_i = \left(\frac{n_i^2 - 1}{n_i^2 + 2} \right) \frac{3\varepsilon_0 M_i}{N_A \rho_i} \tag{5.10}$$

The polarizability has units of $C^2m^2J^{-1}$, which can be cumbersome, so polarizabilities are often expressed in the literature as polarizability volumes, α', in units of m^3.[24]

$$\alpha' = \frac{\alpha}{4\pi\varepsilon_0} \tag{5.11}$$

Combining equations (5.9) and (5.10), the refractive index of the mixture, $n(X)$, can be related to the refractive indices of the pure components (given subscripts 1 and 2). The concentrations of the two components are given as mole fractions X_1 and X_2 respectively. This expression assumes, based on the Lorentz-Lorenz equation, that the polarizabilities are strictly additive.[23]

$$\begin{aligned} &\left(\frac{n(X)^2 - 1}{n(X)^2 + 2} \right) \frac{3\varepsilon_0}{N_A \rho(X)} \left(X_1 M_1 + X_2 M_2 \right) \\ &\qquad = \left(\frac{n_1^2 - 1}{n_1^2 + 2} \right) \frac{3\varepsilon_0 M_1}{N_A \rho_1} (X_1) + \left(\frac{n_2^2 - 1}{n_2^2 + 2} \right) \frac{3\varepsilon_0 M_2}{N_A \rho_2} (X_2) \end{aligned} \tag{5.12}$$

This equation uses the measured density of the mixture $\rho(X)$ and those of the pure components ρ_1 and ρ_2. It also weights the molar mass of the mixture based on the molar masses of M_1 and M_2 respectively. The constants ε_0 and N_A, are the vacuum permittivity and Avogadro's number.

The densities of aqueous solutions containing polar molecules are far from linear, which can be explained by the presence of intermolecular forces, such as hydrogen bonding between molecules. The densities of the aqueous mixtures of sodium chloride, glycerol, dimethylsulfoxide and ethylene glycol have been reported in the literature at 25°C, literature values for sucrose solutions were also available but at 20°C. [22, 25-28] The literature values of each series was fit with a 2nd - 5th order polynomial function depending on the degree of curvature.

$$\rho(W) = AW^5 + BW^4 + CW^3 + DW^2 + EW + F \tag{5.13}$$

The polynomial fits and fitting residuals are shown in Figure 5.7, with the Fitting Parameters given in Table 5.3.

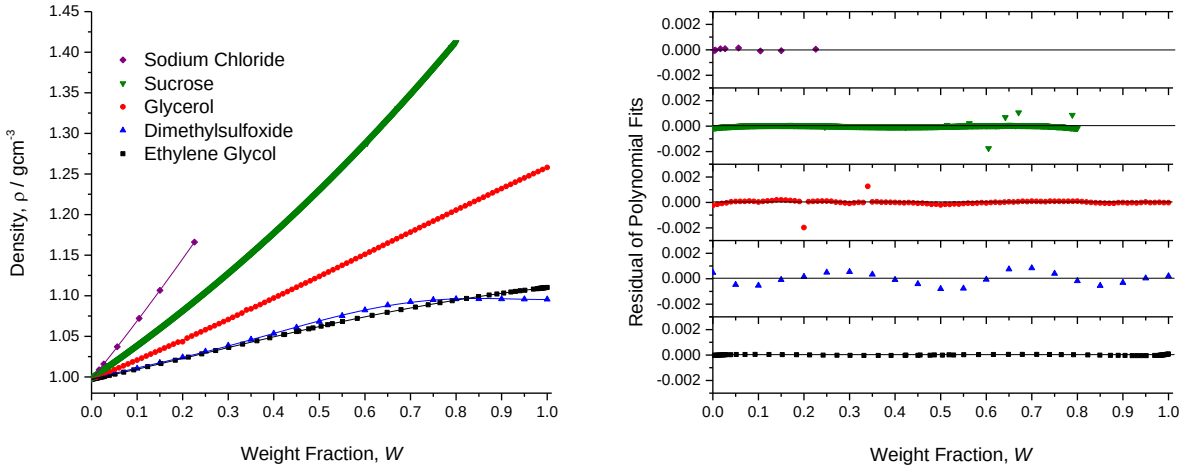

Figure 5.7: Literature densities of aqueous solutions of sodium chloride, sucrose, glycerol, dimethylsulfoxide and ethylene glycol.[22, 25-28] The sodium chloride data was fit with a 2nd order polynomial function, the sucrose and glycerol data sets were fit with 3rd order polynomial functions, the ethylene glycol and DMSO data were fit with a 4th and 5th order polynomial function respectively. The fitting residuals are shown in B) with the fitting parameters listed in Table 5.3.

Table 5.3: Polynomial fit parameters to the literature densities of aqueous solutions of sodium chloride, sucrose, glycerol, dimethylsulfoxide and ethylene glycol as shown in Figure 5.7.[22, 25-28] The fits ranged from a 2nd order fit for sodium chloride to a 5th order fit to the DMSO data with the parameters *A*-*F* corresponding to equation (5.13).

	A	***B***	***C***	***D***	***E***	***F***	**Ref.**
Sodium Chloride	---	---	---	0.2385	0.6940	0.9971	[25]
Sucrose*	---	---	0.0263	0.1476	0.3826	0.9984	[22]
Glycerol	---	---	-0.0385	0.0726	0.2265	0.9973	[26]
Dimethyl-sulfoxide	0.6703	-1.6403	1.2350	-0.3359	0.1669	0.9966	[27]
Ethylene Glycol	---	0.0256	-0.0933	0.0613	0.1194	0.9971	[28]

* The sucrose densities were reported at 20°C. All others were obtained at 25°C

The density is non-linear with concentration for solutions with strong intermolecular forces, e.g. dipole-dipole and hydrogen-bonding interactions.[29] The deviation of the density from additivity is the result

of the difference between the total volume and the additive volume of the two solutions (i.e. the excess molar volume). The excess molar volume can be readily calculated from the molar masses, M_i, the masses of the components added to the solution, m_i, and the densities of the mixture and individual components, $\rho(X)$ and ρ_i.

$$V_{exc}(X) = \frac{1}{\Sigma(m_i/M_i)}\left[\frac{\Sigma m_i}{\rho(X)} - \Sigma\left(\frac{m_i}{\rho_i}\right)\right] \tag{5.14}$$

The excess molar volumes for the binary aqueous solutions of ethylene glycol, glycerol and dimethylsulfoxide are shown in Figure 5.8 to emphasize that the solution volume cannot be assumed to be additive. The concentration dependent density must be taken into account when applying the Lorentz-Lorenz equation.

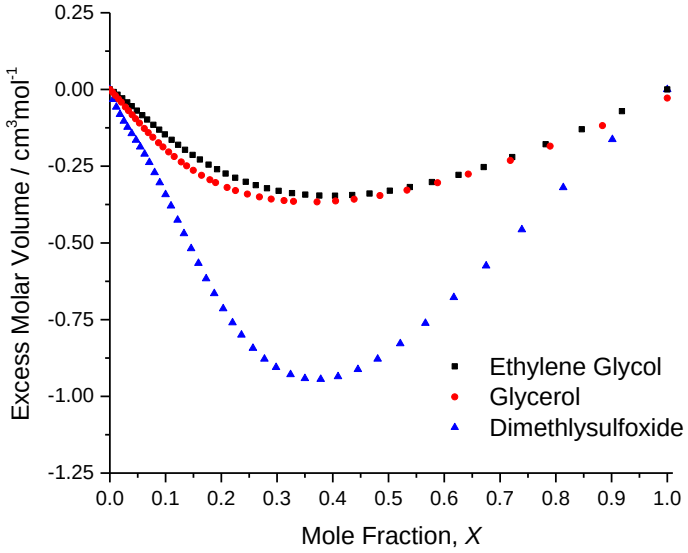

Figure 5.8: Excess molar volume by concentration of ethylene glycol and dimethylsulfoxide in aqueous solutions.[26-28] Each curve passes through a minimum between X = 0.35-0.45, indicating that the intermolecular forces between water and the analyte (A-B) are stronger than the forces in the bulk reagents (A-A and B-B).

The average polarizability of all molecules in solution may be calculated from experimental values of $n(X)$ and $\rho(X)$. The density, $\rho(X)$, was calculated from the polynomial fits to equation (5.13), where the fit parameters are listed in Table 5.3.

$$\bar{\alpha}_{\exp}(X) = \left(\frac{n(X)^2 - 1}{n(X)^2 + 2} \right) \frac{3\varepsilon_0}{N_A \rho(X)} \sum_i X_i M_i \tag{5.15}$$

The polarizabilities of the aqueous solutions show a linear relationship and are indeed additive ($\alpha_{LL}(X) \approx \alpha_{exp}(X)$) within 1% of the values (Figure 5.9).

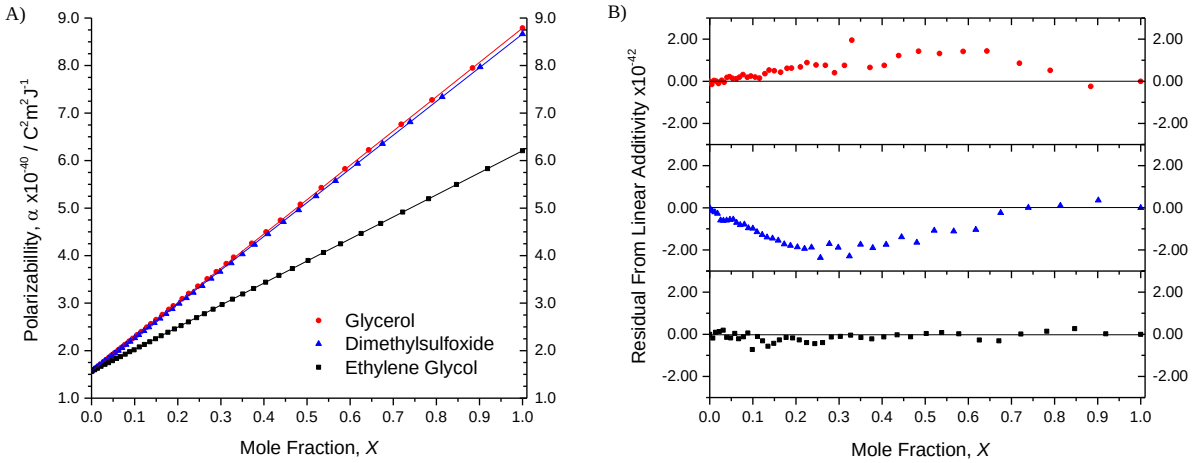

Figure 5.9: Polarizability of aqueous glycerol, dimethylsulfoxide and ethylene glycol solutions. A) The scatter points show the experimentally calculated polarizabilities, α_{exp}, from equation (5.15). The linear lines show the expected value assuming complete additivity of the Lorentz-Lorenz equation, α_{LL}, with the residual from linearity shown in B).

Strictly speaking these observations do not directly validate the Lorentz-Lorenz equation, since this equation is also used to determine the polarizabilities of the neat compounds. Instead, we demonstrated here that the polarizabilities calculated using the Lorentz-Lorenz equation are largely additive as is expected. The electronic polarizabilities of water, dimethylsulfoxide, ethylene glycol and glycerol were calculated from the refractive indices and densities of the pure compounds and are listed in Table 5.4. The polarizabilities of sucrose and sodium chloride were estimated from a linear fit of the experimental polarizabilities over the full solubility range at 298K (Table 5.4). Polarizabilities were calculated using the literature densities and refractive indices at 589 nm for comparison.[19, 30-31]

Table 5.4: Electronic polarizabilities of water, dimethylsulfoxide, ethylene glycol, glycerol, sucrose and sodium chloride. The electronic polarizabilities and polarizability volumes were calculated from experimental data using equations (5.10) and (5.11). The polarizabilities for sucrose and sodium chloride were extrapolated from the linear fit to the measured polarizabilities at lower concentrations. For each liquid reagent, the polarizability volumes were also calculated using literature values of refractive index at 589 nm and density at either 20°C or 25°C depending on availability. [19, 30-31]

Reagent	Electronic Polarizability α ($\times 10^{-40}$ C^2m^2/J)	Polarizability Volume α' ($\times 10^{-30}$ m^3)	Literature Polarizability Volume α' ($\times 10^{-30}$ m^3)
Water	1.5649(9)	1.4065(8)	1.47 [30-31], 1.48 [24]
Dimethylsulfoxide	8.665(4)	7.788(4)	7.98 [19]
Ethylene Glycol	6.207(2)	5.579(2)	5.73 [19]
Glycerol	8.80(1)	7.91(1)	8.14 [19]
Sucrose	30.28(1)	27.21(1)	---
Sodium Chloride	3.981(4)	3.578(4)	---

The polarizability measurements shown in this study and those calculated from literature values deviate because the refractive index in the infrared region of the spectrum is substantially lower than in the visible region. The refractive index of, for example, water decreases from n_D = 1.33336[31] to n_{1550} =1.3164[1]. The polarizabilities, however, do show the same trend in the infrared as in the visible.

The small deviation from additivity is intriguing. The residual in Figure 5.9B, i.e. the "excess polarizability", $\Delta\alpha$, shows clear trends for the water-DMSO and the water-glycerol mixtures. The average polarizability of a binary mixture of compounds can deviate from the simple weighted sum (equation (5.12)) if there are intermolecular contributions to the polarizability that change with the composition of the mixture.[32-33] In aqueous solutions these intermolecular contributions are likely a consequence of the extensive hydrogen-bonding network as well as the mobility of the protons in these solutions. DMSO and other aprotic solvents disrupt this network and we would expect a reduction of the polarizability term, i.e. negative excess polarizability. The largest negative deviation occurs around X = 0.35 corresponding to a 2:1 ratio of water to DMSO molecules, i.e. when a water molecule has on average one DMSO (for every two water molecules) in its first coordination sphere.

In the case of glycerol, a positive excess polarizability could indicate an enhancement of the hydrogen-bonding network from the presence of the 3 hydroxyl groups. This maximum in the excess polarizability occurs around $X = 0.50$ where the ratio of water to glycerol is close to 1:1.

An alternative explanation for the trends in excess polarizability may be the concentration-dependent shifts in the near-IR absorption peaks.[34] For example, it was previously observed that the $2\nu_1$ O-H overtone stretch of water, at around 1450 nm, shifted to longer wavelengths when water was mixed with acetone.[35] Since water was used in all three series, it is quite possible that the overtone absorption peaks for our binary mixtures would be affected. This could result in changes to the refractive index and therefore the calculated polarizabilities. Without further experiments it is currently not possible to fully explain the trends in the excess polarizability.

5.6 Conclusions

The refractive indices of 29 common solvents were measured at 1550 nm using a homemade refractometer. Selected solvents were chosen as examples of aliphatic, aromatic, cyclic and halogenated hydrocarbons. Molecules containing alcohols, ethers, aldehydes, ketones, and amides were also studied. For most of these solvents, refractive indices were not previously available in the near-infrared. The refractive indices were also measured for aqueous solutions of sodium chloride, sucrose, ethylene glycol, glycerol and dimethylsulfoxide over their full solubility range and fit with 3rd order polynomial functions. Using the coefficients provided in this chapter, refractive index calibration solutions can be prepared between $n_{1550} = 1.3164$ and 1.4781. These aqueous solutions are suitable for the calibration of many types of near-infrared sensors including long period gratings, fibre interferometers and silicon photonic devices.

In the measurements of binary aqueous mixtures containing ethylene glycol, glycerol and dimethylsulfoxide (DMSO) it was found that the polarizability and therefore the refractive index could be calculated from the mole fraction of analyte and the polarizabilities of the neat compounds. The additivity of the Lorentz-Lorenz equation agrees within a 1% accuracy of the experimentally measured solutions. It

is believed that the small deviations observed are a result of either changes in intermolecular interactions of hydrogen-bonding networks, or from concentration dependent solvent effects on the overtone absorption wavelength of water.

5.7 Acknowledgements

I would like to acknowledge Mr. Connor Sanders, a summer research student, for preparing and measuring the solvents and solutions presented in this chapter. I would like to thank both Connor and Dr. Hans-Peter Loock for their initial work designing excel macros for data analysis in this section. Preliminary solvent experiments were conducted by Mr. Weijian (Jason) Chen and Mr. Hao (Sean) Chen, two M.Sc. Candidates in our group. I would also like to acknowledge Mr. Lyndsay Hull for proving samples of o-Xylene and p-Xylene to expand the scope of reagents in this study. Finally, I would like to acknowledge Mr. Weijian Chen's assistance in the design of the refractometer optical setup and data acquisition software.

5.8 References

1. Saunders, J. E.; Sanders, C.; Chen, H.; Loock, H.-P., Refractive indices of common solvents and solutions at 1550 nm. *Applied Optics* **2016,** *55*, 947-953.

2. *Corning SMF-28 Ultra Optical FIber Product Information*; Corning, NY, November 2014.

3. Cardenas, J.; Poitras, C. B.; Robinson, J. T.; Preston, K.; Chen, L.; Lipson, M., Low loss etchless silicon photonic waveguides. *Optics Express* **2009,** *17*, 4752-4757.

4. Ye, W. N.; Xiong, Y., Review of silicon photonics: history and recent advances. *Journal of Modern Optics* **2013,** *60*, 1299-1320.

5. Rheims, J.; Köser, J.; Wriedt, T., Refractive-index measurements in the near-IR using an Abbe refractometer. *Measurement Science and Technology* **1997,** *8*, 601-605.

6. Moutzouris, K.; Papamichael, M.; Betsis, S. C.; Stavrakas, I.; Hloupis, G.; Triantis, D., Refractive, dispersive and thermo-optic properties of twelve organic solvents in the visible and near-infrared. *Applied Physics B* **2014,** *116*, 617-622.

7. Samoc, A., Dispersion of refractive properties of solvents: Chloroform, toluene, benzene, and carbon disulfide in ultraviolet, visible, and near-infrared. *Journal of Applied Physics* **2003,** *94*, 6167-6174.

8. Chen, W.; Saunders, J. E.; Barnes, J. A.; Yam, S. S.-H.; Loock, H.-P., Monitoring of vapor uptake by refractive index and thickness measurements in thin films. *Optics Letters* **2013,** *38*, 365-367.

9. Saunders, J. E.; Chen, H.; Brauer, C.; Clayton, M.; Chen, W.; Barnes, J. A.; Loock, H.-P., Quantitative diffusion and swelling kinetic measurements using large-angle interferometric refractometry. *Soft Matter* **2015,** *11*, 8746-8757.

10. García-Valenzuela, A.; Barrera, R. G.; Sánchez-Pérez, C.; Reyes-Coronado, A.; Méndez, E. R., Coherent reflection of light from a turbid suspension of particles in an internal-reflection configuration: Theory versus experiment. *Optics Express* **2005,** *13*, 6723.

11. Sánchez-Pérez, C.; García-Valenzuela, A., Spectroscopic refractometer for transparent and absorbing liquids by reflection of white light near the critical angle. *Review of Scientific Instruments* **2012,** *83*, 115102, 1-7.

12. *Topics in Applied Physics Vol.9 Laser Speckle and Related Phenomena*. Springer-Verlag, New York, NY, 1975.

13. CamIR1550 Notes for Operation. Applied Scintillation Technologies, Harlow, UK, www.appscintech.com (accessed July 31, 2016).

14. Jha, R.; Villatoro, J.; Badenes, G.; Pruneri, V., Refractometry based on a photonic crystal fiber interferometer. *Optics Letters* **2009,** *34*, 617-619.

15. Li, L.; Xia, L.; Xie, Z.; Liu, D., All-fiber Mach-Zehnder interferometers for sensing applications. *Optics Express* **2012,** *20*, 11109-11120.

16. Lu, P.; Men, L.; Sooley, K.; Chen, Q., Tapered fiber Mach–Zehnder interferometer for simultaneous measurement of refractive index and temperature. *Applied Physics Letters* **2009,** *94*, 131110, 1-3.

17. Guo, T.; Tam, H.-Y.; Krug, P. A.; Albert, J., Reflective tilted fiber Bragg grating refractometer based on strong cladding to core recoupling. *Optics Express* **2009,** *17*, 5736-5742.

18. Sun, A.; Wu, Z., A hybrid LPG/CFBG for highly sensitive refractive index measurements. *Sensors* **2012,** *12*, 7318-7325.

19. Physical Constants of Organic Compounds. In *CRC Handbook of Chemistry and Physics*, 96th Edition (Internet Version 2016); Haynes, W. M., Ed. CRC Press / Taylor and Francis: Boca Rafton, FL, 2016.

20. Kedenburg, S.; Vieweg, M.; Gissibl, T.; Giessen, H., Linear refractive index and absorption measurements of nonlinear optical liquids in the visible and near-infrared spectral region. *Optical Materials Express* **2012,** *2*, 1588-1611.

21. Hale, G. M.; Querry, M. R., Optical constants of water in the 200-nm to 200-μm wavelength region. *Applied Optics* **1973,** *12*, 555-563.

22. U.S.D.A. *Sucrose Conversion Table*; (United States Department of Agriculture), 1981.

23. Born, M.; Wolf, E., *Principles of Optics: Electomagnetic Theory of Propagation, Interference and Diffraction of Light*. 4th Edition, Pergamon Press, Toronto, Canada, 1970.

24. Atkins, P.; de Paula, J., *Atkins' Physical Chemistry*. 8th Edition, W.H Freeman and Company, New York, NY, 2006.

25. Gates, J. A.; Wood, R. H., Densities of aqueous solutions of sodium chloride, magnesium chloride, potassium chloride, sodium bromide, lithium chloride, and calcium chloride from 0.05 to 5.0 mol kg-1 and 0.1013 to 40 MPa at 298.15 K. *Journal of Chemical & Engineering Data* **1985,** *30*, 44-49.

26. *Physical Properties of Glycerine and Its Solutions*; (Glycerine Producers' Association), 1963.

27. LeBel, R. G.; Goring, D. A. I., Density, viscosity, refractive index, and hygroscopicity of mixtures of water and dimethylsulfoxide. *Journal of Chemical & Engineering Data* **1962,** *7*, 100-101.

28. Sakurai, M., Partial molar volumes of ethylene glycol and water in their mixtures. *Journal of Chemical & Engineering Data* **1991,** *36*, 424-427.

29. Aminabhavi, T. M.; Gopalakrishna, B., Density, viscosity, refractive index, and speed of sound in aqueous mixtures of N,N-dimethylformamide, dimethylsulfoxide, N,N-dimethylacetamide, acetonitrile, ethylene glycol, diethylene glycol, 1,4-dioxane, tetrahydrofuran, 2-methoxyethanol, and 2-ethoxyethanol at 298.15 K. *Journal of Chemical & Engineering Data* **1995,** *40*, 856-861.

30. Physical Constants of Inorganic Compounds. In *CRC Handbook of Chemistry and Physics*, 96th Edition (Internet Version 2016); Haynes, W. M., Ed. CRC Press / Taylor and Francis: Boca Rafton, FL, 2016.

31. Index of Refraction of Inorganic Liquids. In *CRC Handbook of Chemistry and Physics*, 96th Edition (Internet Version 2016); Haynes, W. M., Ed. CRC Press / Taylor and Francis: Boca Rafton, FL, 2016.

32. Alvarardo, Y. J.; Labarca, P. H.; Cubillan, N.; Osorio, E.; Karam, A., Solvent effect on the exlectronic polarizability of benzonitrile. *Zeitschrift für Naturforschung A* **2003,** *58*, 68-74.

33. Onsager, L., Electric moments of molecules in liquids. *Journal of the American Chemical Society* **1936,** *58*, 1486-1493.

34. Bertie, J. E.; Lan, Z., The refractive index of colorless liquids in the visible and infrared: Contributions from the absorption of infrared and ultraviolet radiation and the electronic molar polarizability below 20 500 cm−1. *The Journal of Chemical Physics* **1995,** *103*, 10152-10161.

35. Andrews, N. L. P.; MacLean, A. G.; Saunders, J. E.; Barnes, J. A.; Loock, H.-P.; Saad, M.; Jia, C.; Ramaswamy, K.; Chen, L. R., Quantification of different water species in acetone using a NIR-triple-wavelength fiber laser. *Optics Express* **2014,** *22*, 19337-19347.

Chapter 6

Refractometer Diffusion Studies of Liquids into SU-8 Epoxy

A large portion of the material presented in this chapter has been previously published in "Quantitative diffusion and swelling kinetic measurements using large-angle interferometric refractometry", Soft Matter **2015**, *11*, 8746-8757.[1] All figures and text excerpts in this chapter have been used with permission of the co-authors and in accordance with the acceptable usage policy by the Royal Society of Chemistry.

This chapter studies the diffusion of water and other liquids into SU-8 epoxy films. SU-8 is a common photoresist used in protective overcoats on many chip-based refractive index sensors. SU-8 films are exposed to water and other organic solvents (Section 6.3.1 and 6.3.3) and interferometric refractometry is used to simultaneously measure the refractive index and thickness changes of thin films. A more detailed description of the general operation of this device was provided in Chapter 4. The mole fraction of water in the SU-8 film is then calculated using an equation derived from the Lorenz-Lorentz and Clausius-Mossotti equations as was discussed in Chapter 3.2. Comprehensive models for the diffusion kinetics through the bulk film and film-substrate interface are also described in Section 6.3.1. The interactions of SU-8 with other solvents including methanol, isopropanol, acetone, acetonitrile and m-xylene will be described in Section 6.3.3. Comparison is made with Hansen solubility parameters in Section 6.3.4 to justify our results.

6.1 Introduction

Understanding the diffusion of liquids and gases out of thin polymer films is of important concern for many industrial processes. This includes, for example, the application and curing of paints and coatings and of protective layers for electronic components. Diffusion of gases and solvents *into* polymer films affects the chemical resistance of materials and is similarly important. In analytical chemistry applications analyte diffusion into thin films governs solid phase microextraction (SPME) (Chapter 3.5). It also governs the partitioning of the analytes between mobile and stationary phases in chromatographic separations The

uptake and release of sorbates can frequently be modelled using Fick's laws of diffusion with the appropriate boundary conditions.[2] In this chapter, we model our system with an impermeable substrate on one side of the film and an infinite, homogenous supply (or sink) on the other.[2] Many different methods and approximations are used when measuring diffusion coefficients and were discussed in full detail in Chapter 3.3.

Briefly, diffusion coefficients can be calculated from changes in mass or film thickness during the uptake or release of an analyte. For example, the resonance frequency can be measured using quartz crystal microbalances (QCM) or thickness shear mode resonators to measure changes to the effective film mass.[3-4] This works best for thin films (< 100 nm) and requires correction terms to account for elasticity and damping of thicker films.[5]

Diffusion coefficients can also be determined from optical properties of films such as absorption, bulk refractive index and fluorescence. These changes are related to the average concentrations of analytes within the film. For example, using attenuated total-internal reflection Fourier transform infrared spectroscopy (ATR-FTIR), diffusion coefficients can be measured in real time from the absorption lines characteristic of the diffusing target species.[6-8] The refractive index is arguably the most universal optical property of a film that changes with analyte uptake. It can be measured over a very large wavelength range, but provides the least information about the identity of the molecule. The specificity can be recovered by synthesizing coating materials that are selective to a target group of analytes. Refractive indices are often measured using Abbé-type refractometers, where a sample is placed between an illumination and a refraction prism.[9] A detailed introduction to different types of refractometry was provided in Chapter 2.2. Refractive index measurements on their own are often not sufficient for characterizing the uptake or release of compounds into thin films. For example, the uptake of an analyte into a film frequently leads to a refractive index increase, but if the film also swells upon analyte uptake, and the analyte refractive index is lower than that of the film, then the refractive index of the system may actually decrease.

Variable angle spectroscopic ellipsometry is usually the preferred technique for the simultaneous measurement of refractive index and thickness of thin films (d = 10 nm - 1 μm).[10-11] While it is difficult to

beat the resolution and accuracy offered by this technique, it can be complicated to measure the film's refractive index and thickness *in situ*, since ellipsometry typically requires unobstructed optical access to the top surface of the film.[12-13] In this regard, "conventional" refractometry has demonstrated potential for determining the *in situ* refractive index of liquids and films.[9, 14-15] Typically, thin-film interference cannot be used to independently measurement the thickness and refractive index but can only measure the optical path length, i.e. the product of these two values. Hence, it remains difficult to use these measurements for accurate uptake analysis.

Alternatively, film thickness, surface roughness, density and refractive index profiles can be measured for thin films (d = 1-500 nm) using either X-ray or neutron reflectometry.[16-19] Collimated X-ray or neutron beams are reflected by a film at glancing angles and the film profile is extracted from the angular or spectral reflection pattern. Neutron reflection has the added advantage that it is sensitive to the nuclear mass, allowing it to distinguish between different isotopes contained in either the films or the diffusing analytes.[16] These techniques have been used to study the swelling of polyacrylamide[18-19] and polystyrene[17] polymers. While both reflectometry techniques provide better than nanometer resolution, they require highly specialized and expensive equipment. Both techniques are conceptually quite similar to the optical method presented in this chapter.

Here, we demonstrate the use of our large-angle interferometric refractometer for *independent* measurements of (a) the film's thickness, (b) its bulk refractive index and (c) the refractive index at the film-substrate interface. The instrument permits measurements at a rate that is currently limited by the frame rate of our camera (1 Hz), with a refractive index resolution of $\Delta n < 5 \times 10^{-4}$ and a thickness resolution of $\Delta d < 1\%$ on a 40 μm thick film. This technique is suitable for characterization of smooth, and homogeneous, transparent films with a thickness in the range of d = 15-150 μm. In a letter and in Chapter 7, we described the application of this method for measuring gas diffusion into a siloxane polymers.[20] In this chapter the technique is validated by observing the time-resolved diffusion of water into SU-8 photoresist films (d = 40-45 μm). The uptake of methanol, isopropanol and other solvents into SU-8 is also described.

6.1.1 SU-8 and Other Epoxy-Based Photoresists

SU-8 is a popular photoresist for electronic and photonic circuitry and for micromechanical and microelectro-mechanical systems (MEMS). Photo-activated resists, including SU-8, Novolac™ and EPON™ resins, are commonly used as templates for high aspect ratio structures.[21-22] Using photolithography, SU-8 can be made into complex structures including pillars, microcantilevers, microfluidic channels and micromechanical valves in lab-on-a-chip applications.[23-24] The structure of SU-8 is a tetramer glycidylether of a Bisphenol A Novolac resin shown with the structures of Novolac™ and EPON™ resists for comparison in Figure 6.1.[25-26] Some of the common trade names of these resists have also been included.

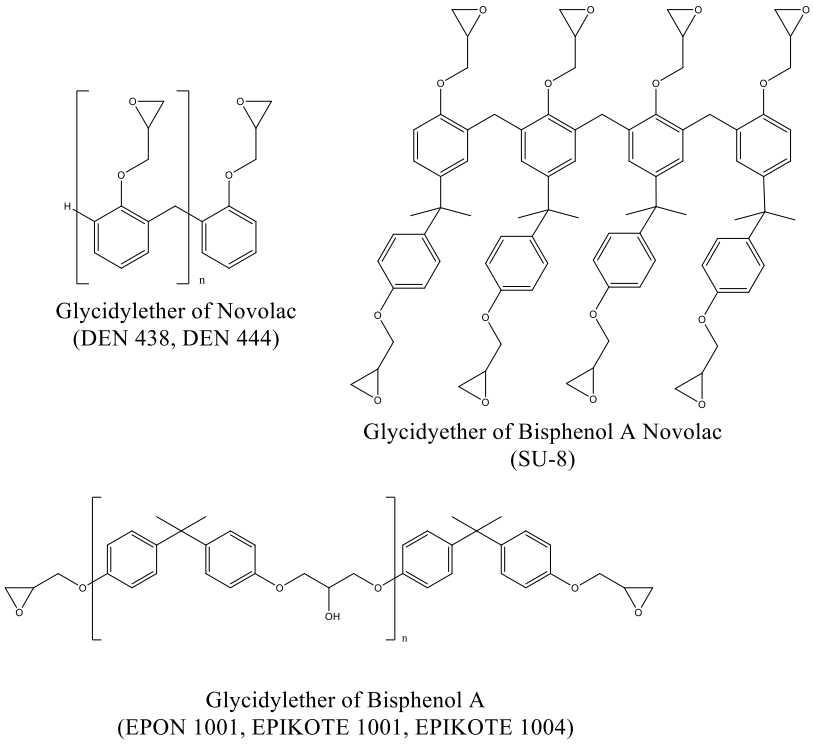

Figure 6.1: Chemical structures of common Novolac™, EPON™ and SU-8 photoresists. In each structure, the epoxy groups ring open to form ether bridges during photo-acid catalyzed cross-linking of the material. Common trade names are provided, for example, DEN stands for Dow Epoxy Novolac.[25-26]

SU-8 is also used in the fabrication of microfluidics on top of optical nanodevices (e.g. silicon, silicon nitride and silica photonic devices), and as a protective overcoat for photonic and electronic chips.[27-29] In these applications, it is important to understand the diffusion of water and other solvents through SU-8.

Previous studies on water diffusion into photoresist films found that water caused SU-8 and other photoresists to swell slightly.[4, 30-33] Exposure to other solvents can also result in film cracking, delamination and damage to microstructures.[34-37]

SU-8 was selected as a test material because of the extensive literature and well-understood physical properties of this photoresist. In this study, we use interferometric refractometry at large incident angles to demonstrate real-time kinetic measurements of the refractive index and thickness of films. The diffusion of water and other solvents into SU-8 photoresist is used to highlight the sensitivity and accuracy of the technique. Comprehensive models for both the diffusion kinetics and the quantification of the water mole fraction and mass fraction in the film complete the study.

This chapter provides first a brief review of the interferometric refractometer, its operating principle and a data analysis procedure. A more detailed description of the general operation of this device is given in Chapter 4. The change in thickness and refractive index of a thin SU-8 film during the uptake of water is presented. The mole fraction of water in the SU-8 film is then calculated using an equation derived from the Lorenz-Lorentz and Clausius-Mossotti equations as discussed in Chapter 3.2. The average bulk refractive index, and the refractive index near the film-substrate interface are both used to obtain the diffusion coefficients of water from a simple, but accurate, kinetic model based on Fick's laws of diffusion. The interactions of SU-8 with other solvents including methanol, isopropanol, acetone, acetonitrile and m-xylene are also described.

6.1.2 Goos-Hänchen Effect

When light is totally internally reflected at a surface (i.e. the angle of incidence is larger than the critical angle), some of the wave energy interacts with the surrounding medium, with refractive index n_2, through the evanescent field. This evanescent field or evanescent wave is localized at the surface and decays exponentially with depth. When the wavelength of light matches the absorption spectrum of molecules in the vicinity of the evanescent field of an optical fibre or waveguide sensor, attenuation of the propagating light will be observed, allowing for evanescent absorption spectroscopy.[38-40] Also, when light couples into

the evanescent field, a phase delay will occur compared with the reflected light. As the result of the conservation of energy, the reflected beam is laterally translated, through an effect known as the Goos-Hänchen effect as shown in Figure 6.2.[41-42] This effect has been observed experimentally with different shifts observed for the reflection of s- and p-polarized light at a gold surface.[42] Merano and coworkers have described the displacement of the shift, L_{GH}, using the phase of the complex reflection, δ, as a function of incident angle, θ, and the wavelength of light, λ.[42]

$$L_{GH} = \frac{\lambda}{2\pi}\frac{d\delta(\theta)}{d\theta} \tag{6.1}$$

The complex reflection can be described using Fresnel's equations for s and p polarized light.[43] The theory behind this effect has been worked on by many groups to obtain a mathematical solution for this effect.[41-42, 44]

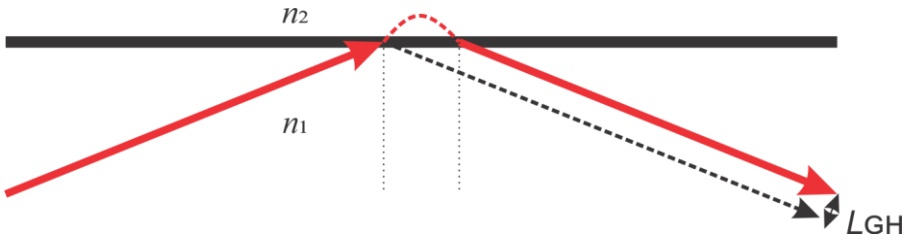

Figure 6.2: Ray diagram demonstrating the Goos-Hänchen effect during total internal reflection. Light is coupled into the evanescent field during total internal reflection and experiences a phase shift. In order to conserve energy in the system this results in a lateral translation of the reflected beam. The original expected beam is indicated by the dashed black arrow, and the displacement is indicated by L_{GH}.

In the optical experiments discussed in this chapter the Goos-Hänchen effect is expected at the film-slide interface, but the respective displacement, L_{GH}, should be constant as the relative refractive index change in the film is very small. On the top surface of the film, however, the "ray displacement" will change dramatically as water is placed on the film. Initially, the surroundings are occupied by air, $n_{1550} \sim 1.00$, and are replaced with water, $n_{1550} = 1.3164$, or other solvents. This change in refractive index will cause sudden changes in the evanescent field penetration depth and the magnitude of the Goos-Hächen effect of light reflected from the top surface of the film. Experimentally, as will be discussed in Section 6.3, a sudden jump in refractive index and thickness was observed upon the addition of the liquid above SU-8 films. The

Goos-Hänchen effect was not quantified in this study, and was removed by correcting the data before Fourier analysis of the results. The sudden changes were not related to any diffusion or binding process but were due to the Goos-Hänchen effect, i.e. an artifact of the experiment. These effects were not observed when dosing gaseous analytes over siloxane films since the refractive index change of the surroundings would not differ substantially, as was presented in Chapter 7.

6.2 Experimental Setup and Methods

The large-angle interferometric refractometer and Fourier transform-based data analysis were briefly described in a letter.[20] Both are described in full detail in Sections 4.2-4.3 and in the literature.[1, 45] A brief introduction providing information about the specific optical setup and analysis used in the SU-8 sensing experiments are provided in Sections 6.2.1-6.2.3. The preparation of SU-8 films is then described in detail in Section 6.2.4.

6.2.1 Optical Experimental Setup

The refractometer experimental setup was described in full detail in Chapter 4.2. Cylindrical lenses were used directly before and after the prism in this study. Preliminary experiments on diffusion into SU-8 were run with spherical lenses and showed significant curvature of the fringes due to optical aberrations (Figure 4.5).

For thin film measurements (10 μm < d < 100 μm), interference fringes were overlaid with the Fresnel reflection at angles below the critical angle of total internal reflection. Below the critical angle, the Fresnel reflection from the bottom surface of the film interfered with light reflected from the top surface of the film, which resulted in a fringe pattern (Figure 6.3). One would expect this fringe pattern to extend all the way to the angle of total internal reflection, but instead a dark band is observed at glancing angles that are very close to the critical angle. At these angles, the light is reflected over considerable lengths within the film and is then spatially separated from the reflection at the bottom of the film (Section 4.4.1). Angles above the critical angle, contained no interference fringes and are seen as the bright region on the right third of the image (Figure 6.3).

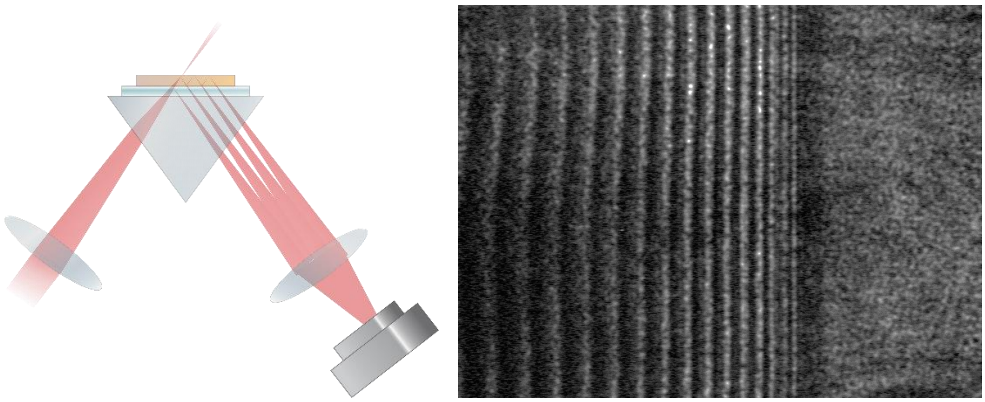

Figure 6.3: Thin-film interference and total internal reflection of a 43 µm SU-8 film. Left: Schematic showing multiple reflections of the incident light within a thin film. The second lens focuses parallel displaced beams resulting from multiple internal reflections inside the film onto the same line of the CCD camera. Right: The interference fringes from a 43 µm thick SU-8 film as recorded by the camera. The right third of the image shows a region of total internal reflection that borders on a dark band corresponding to the Fresnel reflection from the film-substrate interface. The boundary line between regions of Fresnel reflection and total internal reflection gives the critical angle and therefore the refractive index at the film-substrate interface.

6.2.2 Extracting the Film Thickness and Average Refractive Index

The cross-sections of the images were obtained by averaging the intensities of each pixel column using a custom Matlab™ protocol (Figure 6.4A). Occasionally, sections of the images were omitted due to air bubbles in the index matching liquid below the film, or defects in the optical system (e.g. dust, smudges, or scratches). Fourier analysis was performed directly on the cross-sections to extract the associated phase, ϕ, as was previously described by Weijian Chen.[20, 46] Pre-processing of the images was found to remove noise in the phase but was not implemented until later experiments (Chapter 7). After "unwrapping" the phase (Figure 6.4B), the average refractive index of the film, $\bar{n}_F$, and its thickness, *d*, were extracted using a quadratic two-beam interference fit to the data as was previously discussed in Section 4.1.2.[20]

$$n_S^2 \sin^2\theta_i = \left(\frac{\lambda_0}{4\pi d}\right)^2 \left[-\phi^2 + 2\phi\phi_0 - \phi_0^2\right] + \bar{n}_F^2$$
$$n_S^2 \sin^2\theta_i = a\phi^2 + b\phi + c \qquad (6.2)$$

The fitting parameters *a*, *b*, and *c*, are used to obtain the film thickness, *d*, and the average refractive index, $\bar{n}_F$.

$$d = \frac{\lambda}{4\pi\sqrt{-a}} \qquad \text{and} \qquad \bar{n}_F = \sqrt{c - \frac{b^2}{4a}} \tag{6.3}$$

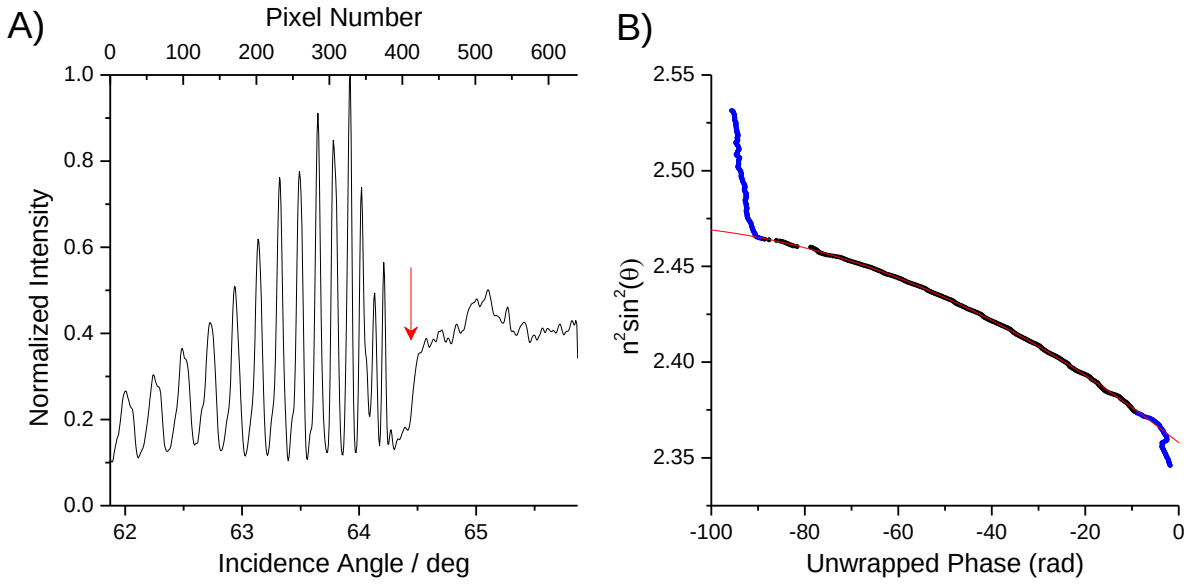

Figure 6.4 Cross-section of the interferogram and phase of a 43 µm SU-8 film. A) The cross-section is shown for the image in Figure 6.3B. The fringes are due to thin film interference whereas the step marks the transition to total internal reflection. The critical angle was determined from a Gaussian fit to the derivative of this curve and is marked by an arrow. B) The unwrapped phase was obtained after Fourier analysis of the left graph. A selection of the phase data that correspond to the fringe region (black dots) were fit with equation (6.2) (red line). This fit yielded a film thickness of d = 43.41 µm and an average refractive index of $\bar{n}_F$ = 1.5722 .

To increase the robustness of our measurements, the refractive index and thickness values were obtained by averaging 600 fits using slightly different fitting windows on the phase curve to compensate for any image anomalies.

6.2.3 Extracting the Refractive Index at the Film Substrate Interface

The critical angle, θ_C, depends on the refractive index at the film-substrate interface, n_{FS}, and can be obtained directly from the images and the cross-sections as the transition between the "dark" regions of Fresnel reflection and the brighter total internal reflection (Figure 6.3 and Figure 6.4).

$$\theta_c = \sin^{-1}\left(\frac{n_{FS}}{n_S}\right) \tag{6.4}$$

The relationship between the pixel column number and the sample refractive index values, n_{FS}, is almost linear, but was found to be more accurately fit with a 2nd order polynomial function in later experiments. Calibration was performed using liquid samples including Cargille refractive index matching oils (Cargille Labs, Cedar Grove, NJ) and solutions of cinnamaldehyde (Sigma Aldrich, Oakville, ON) in ethanol (Figure 6.5). Cinnamaldehyde was more challenging to work with due to its degradation into crystalline by-products in the presence of high lab humidity.

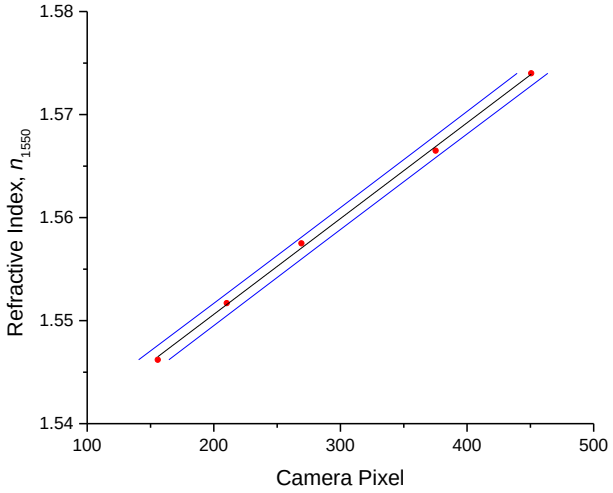

Figure 6.5: Linear refractive index calibration for SU-8 films. Each solution was run in triplicate with the average values shown. The points at camera pixel 210 and 450 were for Cargille refractive index fluids n_d = 1.574 and n_d = 1.600 respectively. The other three points were for solutions of 85%, 90% and 95% v/v cinnamaldehyde in 95% ethanol. The linear fit gave n (pixel) = 9.295×10^{-5} (pixel) + 1.5320. The two blue lines show the 3σ confidence intervals of the fit.

To visualize the uptake of the solvents, the image ross-sections, obtained as in Figure 6.4A, were stacked as columns to produce a composite image (Figure 6.6A). This composite image was then Fourier filtered (Figure 6.6B) using Image-J[47] to remove noise from periodic features smaller than 10 pixels and larger than 640 pixels. Fourier filtering also removed vertical stripes, which were attributed to intensity fluctuations between images. Finally, an edge-finding algorithm, based on the first derivative, was used to determine the critical angle, and n_{FS} (Figure 6.6C). The critical angle was extracted by fitting a Gaussian function to the highlighted band (arrow in Figure 6.6C).

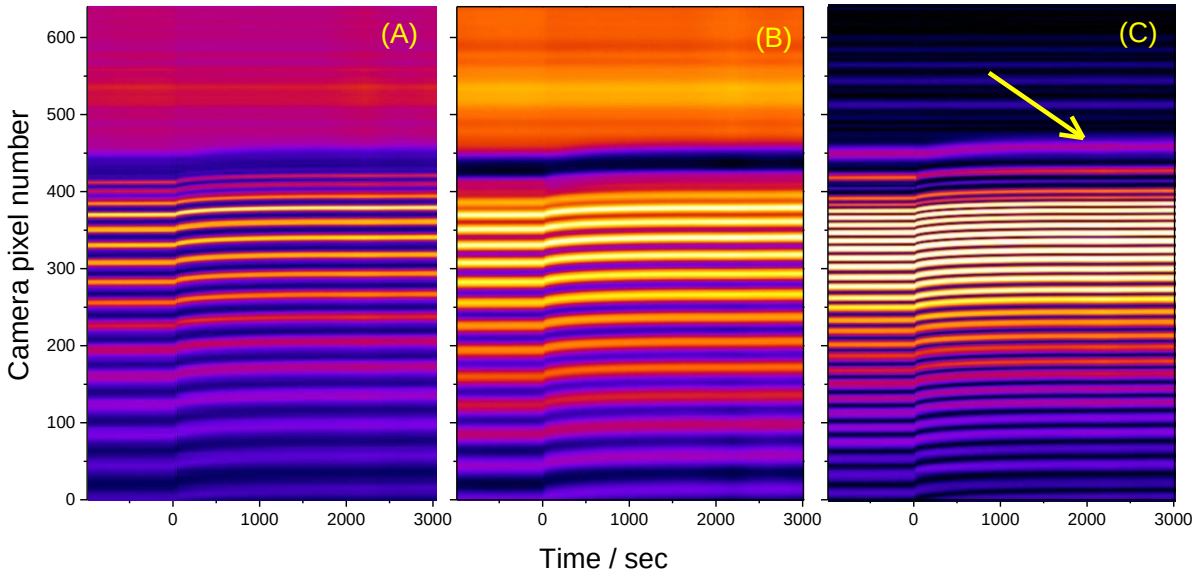

Figure 6.6: Composite images from image cross-sections showing the uptake of water into a 43 µm SU-8 film. A) 4000 image cross-sections similar to Figure 6.4A were taken in 1s intervals and stacked as pixel columns. At *t* = 0 s water was placed above the SU-8 film B) A Fourier filter was applied to the image to reduce the noise. C) An edge finding routine was used to help locate the critical angle (arrow). This image has been contrast-enhanced to emphasize the interface position.

6.2.4 Film Synthesis and Coating Procedures

Five SU-8 films were prepared using SU-8 50 resin (Microchem, Newton, MA), which was spin-coated onto high density flint glass slides (Schott Glass N-SF11, thickness ~1 mm; $n_{1550} = 1.7434$) according to the manufacturer's instructions. The slides were cleaned with isopropanol, dried using compressed air and then heated to 65ºC. To obtain films with thicknesses between 30 to 45 µm, the slides were spin coated at 500 rpm for 15 seconds with an acceleration of ~50 rpm/s to uniformly spread the resin on the substrate, then at 3000 rpm for 35 seconds with an acceleration of ~250 rpm/s to achieve the desired thickness. The films were then prebaked at 65ºC for 5 minutes followed by a soft bake at 95ºC for 15 minutes. Three of the slides were exposed to UV light (P = 10mW/cm^2, λ = 350nm) for 40 seconds. The other two slides were exposed for an additional 2 minutes and 20 seconds (total: 3 minutes) to test whether the UV curing time affected the film properties. After the curing step, the slides were post-baked at 65ºC for 1 minute and then at 95ºC for 4 minutes. The slides were left on the hot plate for 15 minutes as the hot

plate cooled down to prevent cracking from rapid cooling. Between experiments, the slides were stored in a vacuum desiccator containing activated Drierite (Sigma Aldrich). The desiccator was evacuated using an oil-free membrane pump. While the lab was climate controlled, there are seasonal humidity fluctuations which may affect experiments. In order to fully ensure water and other solvents have been removed from the film it would need to be heated up above the glass transition temperature and annealed to remove the last of the solvents. This was avoided for fear of altering the mechanical properties of the film between experiments. To contain the liquid solvents on top of the films, a glass cylinder was glued to the top of the SU-8 films using commercially available "5-minute" epoxy adhesive. The coated slides were then placed on top of the prism using refractive index matching liquid (n_d = 1.7250, Cargille Labs).

6.3 Analyte Uptake into SU-8 Photoresist

Typically, SU-8 is known to have a strong chemical resistance,[21, 48] though previous experiments with SOI micro-resonators suggested that there is some affinity to water and to organic solvents (Chapter 8). For all analyte experiments, baseline measurements of the stable film was taken for 20 minutes before approximately 5 mL of water or other solvents were pipetted on top of the SU-8 film. The results for the water experiments are discussed in Section 6.3.1 and other solvents in Section 6.3.2.

6.3.1 Uptake of Water into SU-8 Photoresist

The diffusion of water through an SU-8 film was recorded by taking images of the interference patterns in one-second intervals. Fourier analysis was performed on each image profile to extract the film thickness and average refractive index. A sudden jump in the average film refractive index was observed when water was deposited on top of the films (Figure 6.7). This step was followed by a much slower change in thickness and refractive index, which is consistent with the expected diffusion dynamics.

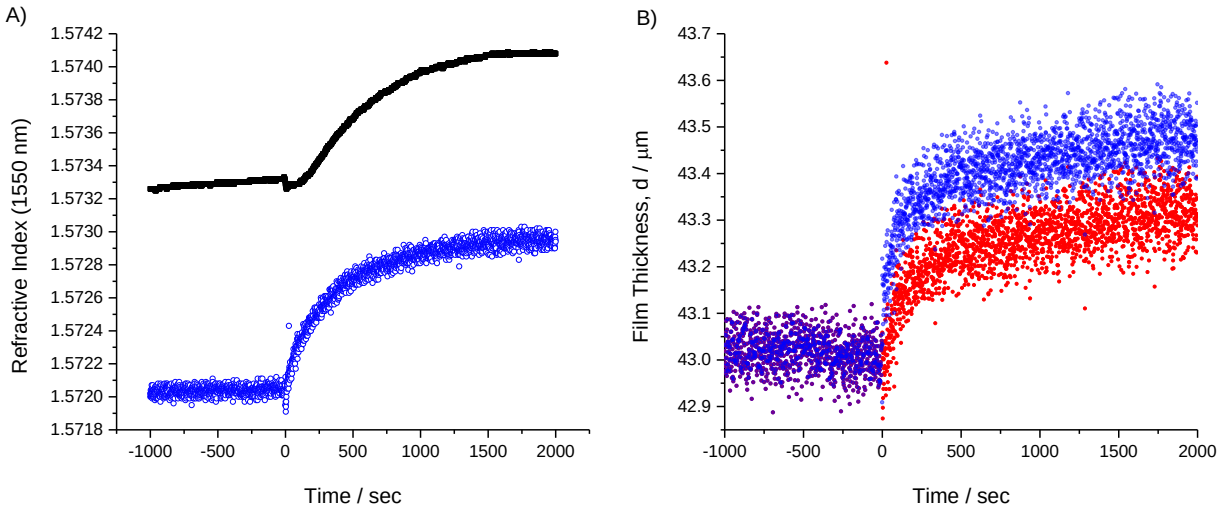

Figure 6.7 Refractive index and thickness change during water uptake into an SU-8 film. A) The average refractive index, $\bar{n}_{film}$, obtained by fitting the unwrapped phase with equation (6.2) (blue open circles) and the refractive index near the film-substrate interface, n_{FS} , (black dots) during the uptake of water. The refractive index near the film-substrate interface, n_{FS} , is obtained from the critical angle (Figure 6.6). The Goos-Hänchen effect caused only a small step in the bulk refractive index curve, $\bar{n}_{film}$. B) Thickness of an SU-8 film obtained by fitting the unwrapped phase with equation (6.2) (blue empty circles). The much larger Goos-Hänchen effect in the thickness measurement was corrected by subtracting 160 nm from all measurements after t = 0 (red dots).

The initial step observed during the uptake of water is attributed to the Goos-Hänchen effect (Section 6.1.2). The optical environment above the film changed rapidly from air to water resulting in a sudden extension of the evanescent field's permeation depth, and an increase of the effective index of the film. For large incident angles, this caused a small spatial shift of the reflected beam. Since the shift occured between two consecutive images (Δt = 1s) it can be assumed that it is not a result of diffusion into the film and can be subtracted from the data set. After subtraction of the Goos-Hänchen effect, both the bulk (average) refractive index and the film's thickness were found to increase immediately. Conversely, the Goos-Hänchen effect is not observed at the film-substrate interface (critical angle) as the surrounding environment, the bulk film, did not change significantly. Instead, we observed a delayed response since analytes needed to first diffuse through the film to the film-substrate interface before they were observed (Figure 6.7). The large data set allows for an estimate of the precision of the relative refractive index and

thickness measurements as $\delta n_{FS} = 1.6 \times 10^{-5}$, $\delta \bar{n}_F = 2.6 \times 10^{-5}$ and δd = 0.04 μm based on the standard deviations of the 900s before the uptake experiment.

The analyte mole fraction concentration within the film, X, can be calculated from the refractive index and thickness changes in the film. The full derivation of this equation was given in Chapter 3.2.

$$X = \frac{P_{SU-8} - P_{SU-8}\left(\frac{n_{SU-8}^{\ 2}+2}{n_{SU-8}^{\ 2}-1}\right)\left(\frac{n_{mix}^{\ 2}-1}{n_{mix}^{\ 2}+2}\right)\left(1+\frac{\Delta d}{d}\right)}{P_{SU-8} - P_{SU-8}\left(\frac{n_{SU-8}^{\ 2}+2}{n_{SU-8}^{\ 2}-1}\right)\left(\frac{n_{mix}^{\ 2}-1}{n_{mix}^{\ 2}+2}\right)\left(1+\frac{\Delta d}{d}\right) - P_{Analyte}} \tag{6.5}$$

In certain situations, it may be more desirable to express the concentration as a mass fraction, Y. This is straightforward as long as the molar masses of the analyte and the film material are known.

$$Y = \frac{XM_{Analyte}}{XM_{Analyte} + (1-X)M_{Film}} \tag{6.6}$$

In this case, $n_{SU\text{-}8}$ and n_{mix} are the initial refractive index of the SU-8 film and the film refractive index at time, t, respectively. Equation (6.5) was used to calculate the concentration at the interface, X_{FS}, and the average concentration in the film, $\bar{X}_{film}$, by using either n_{FS} or $\bar{n}_{film}$ as $n_{mix.}$ The molar polarization, $P_{SU\text{-}8}$ and $P_{Analyte}$, are calculated from the refractive index, n_i, molar mass, M_i, and density, ρ_i, of the respective substances.

$$P_i = \left(\frac{n_i^{\ 2}-1}{n_i^{\ 2}+2}\right)\frac{M_i}{\rho_i} \tag{6.7}$$

In the calculation of the water mole fraction, the molar mass of a single tetramer unit of SU-8, $M_{SU\text{-}8}$ = 1399.7 g/mol, as well as M_{H2O} = 18.0153 g/mol, $\rho_{SU\text{-}8}$ =1.19 g/mL,[49] and ρ_{H2O} = 0.99704 g/mL were used. The refractive index of SU-8 was taken from the initial data before an analyte was added, and varied slightly between experiments depending on the location of the film that was probed. The refractive indices of water and other solvents were measured using the interferometric refractometer as was discussed in Chapter 5.[45]

The time-dependent concentration in a film can be expressed as a function of the distance from the bottom substrate, *y*, as a sum of exponential functions.[2] The full discussion about diffusion coefficients and the derivation of diffusion equations was given in Chapter 3.3.

$$X(y,t) = X_\infty \left[1 - \frac{4}{\pi} \sum_{n=0}^{\infty} \frac{(-1)^n}{2n+1} \exp\left(-D(2n+1)^2 \frac{\pi^2 t}{4d^2} \right) \times \cos\left((2n+1) \frac{\pi y}{2d} \right) \right] \tag{6.8}$$

Here, X_∞ is the saturated film concentration, *D* is the diffusion coefficient, *t* is time in seconds, and *d* is the film thickness in cm. The diffusion rate of analytes into SU-8 can be determined from either the concentration changes at the film-substrate interface, X_{FS} , or average changes in the bulk film, $\bar{X}_{film}$. When using the interface data, the concentration is expressed by equation (6.8) evaluated at *y* = 0 (the film-substrate interface).

$$X(0,t) = X_\infty \left[1 - \frac{4}{\pi} \sum_{n=0}^{\infty} \frac{(-1)^n}{2n+1} \exp\left(-D(2n+1)^2 \frac{\pi^2 t}{4d^2} \right) \right] \tag{6.9}$$

When calculating the concentrations from the bulk refractive index, $\bar{n}_{film}$, the average film concentration is related to the integral of equation (6.8).

$$\bar{X}(t) = X_\infty \left[1 - \frac{8}{\pi^2} \sum_{n=0}^{\infty} \frac{1}{(2n+1)^2} \exp\left(-D(2n+1)^2 \frac{\pi^2 t}{4d^2} \right) \right] \tag{6.10}$$

The mole and mass fractions, *X* and *Y*, were calculated assuming a constant film thickness, *d*, from both interface and average bulk refractive indices of the film (Figure 6.8A). As, predicted in Section 3.3.1, there is a delay in the response at the film-substrate interface as analyte must first diffuse through the bulk of the film before a response is observed. The fits to equations (6.10) and (6.9) (the bulk and interface data respectively) are shown as red lines in Figure 6.8A. While it is reasonable to exclude the swelling information for the film-substrate interface calculations, where the density of the material will not change substantially, it should not be excluded when considering the bulk film. The concentration was calculated

as a function of both the average film refractive index, $\bar{n}_{film}(t)$, and film thickness, $d(t)$ and is shown in Figure 6.8B.

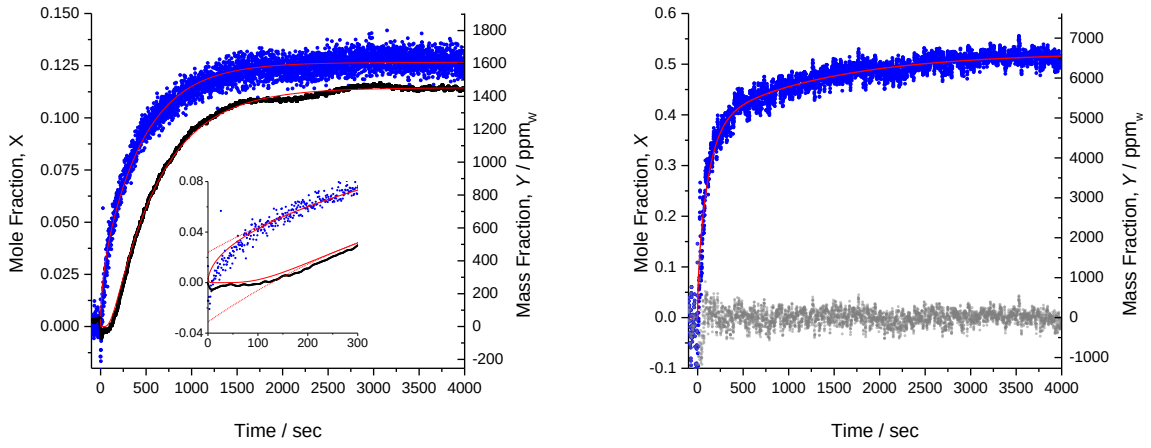

Figure 6.8: Water concentration in the bulk film and at the film-substrate interface during diffusion into an SU-8 film. The mole fraction of water in SU-8 is calculated using the data in Figure 6.7 and equation (6.5). A) The uptake was calculated at a constant thickness, *d*, ignoring the film swelling. The uptake through the bulk film, $\bar{X}(t)$, (blue circles) occurred immediately after water was added to the film. The response at the film interface, X_{FS}, (black circles) was delayed, compared to the bulk, as time was needed for the water to first diffuse through the film. The bulk film and interface data were fit to 10 term exponential fits of equations (6.10) and (6.9) respectively. The inset shows that at short times a single exponential fit does not accurately agree with the data (dashed red line). B) If the thickness change information is included with the change in bulk refractive index, the uptake can be fit to a sum of two diffusion uptake curves each described by equation (6.10). The fit residual is shown as grey points.

When neglecting the change of density entirely, i.e. setting $\Delta d = 0$ in equation (6.5), the film-substrate data, X_{FS} (black circles), and the bulk film data, $\bar{X}(t)$ (blue circles), both fit well to 1-D Fickian diffusion models (Figure 6.8A). The diffusion coefficient obtained by fitting the film-substrate data, X_{FS}, to equation (6.9) was found to be D = 13.98(2)×10^{-9} cm^2/s, with a limiting value of X_∞ = 0.11440(4) (Y_∞ = 1452.2 ppm$_w$). The uncertainty in the last digit reflects the fit error. The fit of equation (6.10) to the bulk concentration data yielded fitting parameters of D = 16.42(8)×10^{-9} cm^2/s, and X_∞ = 0.12656(9) (Y_∞ = 1606.5 ppm$_w$). The diffusion coefficients determined from both the film-substrate interface, through changes in the critical angle, and from the bulk concentration data, through Fourier analysis of the images, are in very close agreement.

When the swelling was included, the data could not be fit using a simple 1-D diffusion model, but instead reflects showed contributions from two diffusion processes with different rates. The data was fit using a sum of two uptake curves, as in equation (6.10), each having ten exponential terms in the sum. The fit agrees remarkably well with the data and yields two diffusion coefficients, D_1 and D_2, with two limiting values, $X_{\infty,1}$ and $X_{\infty,2}$ respectively. The fits gave $D_1 = 5.67\times10^{-9}$ cm^2/s, $X_{\infty,1} = 0.176$ for the slower process and $D_2 = 61.2\times10^{-9}$ cm^2/s, $X_{\infty,2} = 0.348$ for the faster process. The respective mass fractions were also calculated using equation (6.6) as $Y_\infty = 2230$ ppm$_w$ and 4420 ppm$_w$, respectively. A mole fraction of 0.176 (0.348) implies that on average there is approximately one water molecule per 5.7 (2.8) SU-8 tetramer units (Figure 6.1). The similarity of D_1 and $X_{\infty,1}$ to the fits from Figure 6.8A suggests that the slow process is related to diffusion of adsorbed water through the film. This lends support to the hypothesis that the density of the lower portion of the films does not change as much the overall film thickness changes would suggest, and, that the thickness change is largely a surface phenomenon.

We speculate that the fast "diffusion" process is related to the rapid change in thickness that was observed (Figure 6.7). This is likely due to a restructuring of the SU-8 surface layers and is therefore a local phenomenon. The bulk density and the local density at the film-substrate interface would then be much less affected. Liu *et al*. made a similar qualitative observation when they found that water predominantly absorbed in the uppermost part of a 5.6 μm thick cantilever.[30] The slow diffusion process was then responsible for the changes to the refractive index below the surface of the film and was observable in critical angle measurements. The two diffusion coefficients may also be the result of clustering of water near the surface of the film. This was experimentally observed by Liu and coworkers who showed that the uneven swelling of SU-8 micro-cantilevers caused the beams to bend when exposed to water.[30] This effect could be verified using neutron reflectometry as was shown by Tanchak and coworkers for water clustering in polyelectrolyte films.[50] The two values may also suggest that the model is deviating from Fickian behaviour. If water acts as a plasticizer, it may reduce the glass transition temperature of the SU-8, affecting the uptake rates.[51] This effect could be verified using differential scanning calorimetry. The SU-8 films were prepared by spin coating and might also show birefringence which may complicate our analysis. The

films were tested for birefringence by observing the films between two cross polarizers and no interferences were observed. We believe that our films can therefore be treated as isotropic.

Diffusion coefficients are often calculated from similar data but with only using a single exponential term in the series in equation (6.10).[52] While this assumption is adequate at late times in the diffusion process or for sparse data sets[53] the fits may deviate substantially at early times of the uptake curve (inset in Figure 6.8A). When fitting only the early data, the diffusion coefficient from a single exponential fit differs by a factor of two compared to the fit including ten exponential terms. Of course, the additional terms in equation (6.10) do not introduce extra fitting parameters and therefore do not complicate the fit.

6.3.2 Comparison of Results with Literature

The preparation of SU-8 is a multistep process involving spin coating, a two-step soft bake, exposure to light (UV or X-ray), a two-step post-bake, development to remove the uncured resist, and an optional hard-bake for added stability of complex structures. There are a large number of parameters that may be adjusted, and, accordingly, the properties of SU-8 films can vary drastically depending on the protocol used.

In our experiments, the diffusion constant for the slow process ($D = 5.67\times10^{-9}$ cm^2/s), which we attribute to diffusion through the bulk, was larger by a factor of 2 than the literature values ($D = 1.25\text{-}3.00\times10^{-9}$ cm^2/s).[4, 30-31] This is not unexpected as our SU-8 curing conditions were different from those reported by other groups. Diffusion of water through EPON 828, a closely related material, has similarly been shown to exhibit a large range of diffusion rates ($D = 4\times10^{-10}$ - 1×10^{-8} cm^2/s).[32] The large range of diffusion coefficients is a result of mechanical differences from the preparation procedures of the epoxies. For example, high concentrations of solvents, gamma-butyrolactone in SU-8, or cyclopentanone in SU-8 2000, at the time of UV irradiation allows for enhanced diffusion of photo-acids generated within the film.[31, 54] This results in denser cross-linked materials that form stronger films, with less internal stress and cracking during film preparation.[31, 54] If the concentration of solvent is too high, photo-acids may diffuse into unexposed portions of the SU-8 causing unwanted cross-linking and defects in complex structures.[55]

As the degree of cross-linking increases, the affinity to water decreases due to the increased rigidity of the material.[56] In the present work, the SU-8 films were not optimized to increase their resistance to water and others solvents, and it is therefore not surprising that the measured diffusion rate was found to be higher than the previously reported rates.[4, 30-31]

Finally, two of the previously reported methods calculated diffusion rates from swelling of SU-8, and ignored any density effects from the incorporation of water within the film. This would lead to an underestimate of the diffusion coefficients.[30-31] Especially for porous films, the diffusion rates would be underestimated at early times, as analytes may fill pores but not necessarily swell the film. Refractive index measurements would be more appropriate in this situation.

In any case, the affinity of SU-8 to water and the swelling that can occur during the uptake of water may represent substantial challenges when using SU-8 for microfluidic applications or photonic sensor overcoats. In these types of applications, care must be taken when establishing SU-8 coating protocols to ensure that highly cross-linked films are produced, which are more resistant to water and humidity.

6.3.3 Uptake of Other Solvents into SU-8 Photoresist

To further understand the chemical compatibility of SU-8, the uptake and swelling of the SU-8 films when exposed to other common organic solvents was explored. Using the same procedure outlined above, the change of refractive index and thickness was measured as the film was exposed to six different solvents. In none of the cases was it possible to accurately determine diffusion rates from the data. Instead, uptake experiments were allowed to proceed to equilibrium, if the film remained intact, or were terminated when the film disintegrated.

When the SU-8 films were exposed to isopropanol and m-xylene, the thickness and refractive index changes were too small to reliably calculate diffusion coefficients. After these experiments, the SU-8 films were dried in a vacuum desiccator with activated Drierite (Sigma Aldrich) to minimize moisture uptake into the film.

When small polar solvents (methanol, acetone and acetonitrile) were placed on top of SU-8 films, rapid dissolution and eventual delamination of the SU-8 polymer was observed. It is expected that SU-8 curing conditions can be optimized to prevent dissolution and delamination, although significant swelling might still be expected. Partitioning of methanol vapour into SU-8 was also observed using SU-8 clad Silicon-on-Insulator (SOI) micro-photonic interferometers and ring resonators (Chapter 8).

In the case of methanol, one of the SU-8 films that was UV-cured for 40 seconds began to dissolve almost instantaneously. This was observed by the appearance of a second set of interference fringes. The fringes of the emerging layer at low incident angles became more closely spaced as time proceeded, indicating that the new layer was becoming thicker (Figure 6.9). The fringes at larger incident angles and the position of the critical angle remain unaffected until approximately 1600 seconds into the experiment, suggesting that the new layer was formed on the top surface of the film – likely due to top-down dissolution of SU-8 by methanol.

Additionally, the boundary between the SU-8 film and the new layer rapidly shifted to larger angles of incidence, indicating that the refractive index of this new layer increased as more of the SU-8 was dissolved. The original fringes of the film spread out as the remaining SU-8 film became thinner, until it delaminated from the substrate at around t = 2000 s. Delamination was also observed with SU-8 films that were exposed to UV light for 3 minutes, although on a much slower time scale. From these experiments it is apparent that SU-8 had a strong affinity to methanol. The films used in our experiments were not hard baked, so it is possible that they were not fully cross-linked. Hard baking is essential when fabricating complex structures out of SU-8, and would also have provided additional chemical resistance. The results seen in this section can be rationalized by considering theoretical interactions between the solvents and similar polymers through solubility parameters as are described in Section 6.3.4.

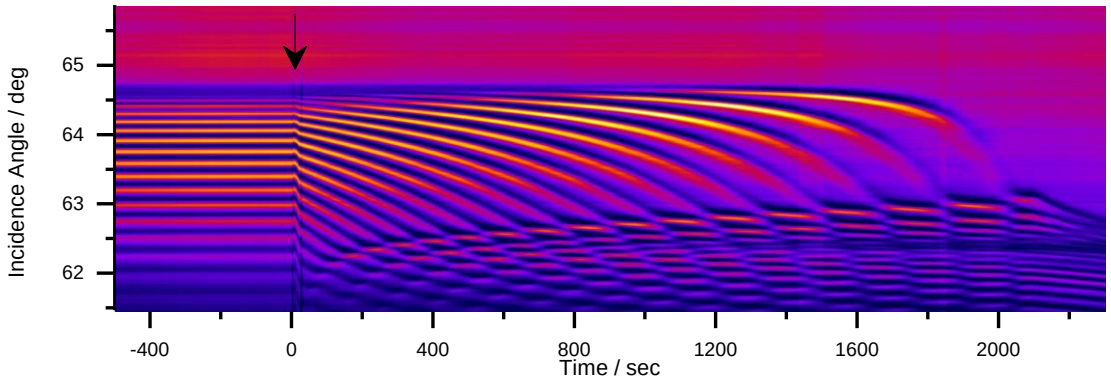

Figure 6.9: Uptake of methanol into SU-8 over 2300 seconds. Adding methanol onto the film's surface resulted in a Goos-Hänchen shift denoted by the arrow on the figure. Almost immediately, the film dissolved and a second set of fringes from a topmost solution layer began to appear at smaller incident angles. The spread of the fringes to higher incident angles indicated that the film was thinning as it dissolved until it was delaminated from the substrate at around *t* = 2000 seconds. This image has been coloured using a lookup table for enhanced effect.

6.3.4 Using Solubility Parameters to Predict Polymer Film Compatibility with Solvents

Using the solubility parameters of solvents and polymers, it is possible to rationalize the interactions between sorbates and polymers. The Hildebrand solubility parameter describes a material based on its cohesive energy (the energy required to vaporize a liquid into isolated molecules), U, and its molar volume, V_m.[57]

$$\delta = \sqrt{U / V_m} \tag{6.11}$$

At temperatures far below a liquid's boiling point, the vaporization enthalpy of solvents may instead be used as an approximation.[57]

$$\delta = \sqrt{\frac{\Delta H_{vap} - RT}{V_m}} \tag{6.12}$$

Substances with similar solubility parameters are expected to interact strongly and have the greatest mutual solubility, while those with very different values are usually immiscible. The cohesion parameter is

analogous to the solubility parameter and is used to describe non-liquids.[58] Optimal solubility of a polymer in a solvent is expected when the cohesion parameter of the polymer is close to the solubility parameter of a solvent. When the two parameters are mismatched, one should expect less pronounced swelling of the polymer.

More refined approaches, such as those of Hansen, distinguish the different intermolecular contributions to the solubility and cohesion parameters (such as dispersion, polar (electrostatic), and hydrogen-bonding contributions).[59]

$$\delta^2 = \delta_D{}^2 + \delta_P{}^2 + \delta_H{}^2 \tag{6.13}$$

The interaction strength between a given solvent (1) and polymer (2) can be described using the distance between the solvent solubility coordinates and the centre of the polymers' cohesion sphere, R_a.[59]

$$R_a = \sqrt{4\left(\delta_{D2} - \delta_{D1}\right)^2 + \left(\delta_{P2} - \delta_{P1}\right)^2 + \left(\delta_{H2} - \delta_{H1}\right)^2} \tag{6.14}$$

The closer the three solvent parameters are to the centre of the polymer's solubility sphere, the larger is the affinity of the polymer to this solvent. One can now experimentally define an interaction radius, $R_{0,}$ of the polymer at which the solvents show only marginal interactions with the polymer. It represents the boundary between solvents that will dissolve a polymer material and those that will have no interaction, i.e. only when $R_a/R_0 < 1$ is a polymer expected to be soluble in a given solvent.[59] Typically, processing solvents for polymers are chosen where a strong solubility is expected. Tables of solubility parameters are readily available in the literature for most common organic solvents and for many polymers.[58, 60] Literature Hansen solubility parameters for some common organic solvents are listed in Table 6.1 to support the discussion of the solvent interactions with SU-8.[58, 60]

Table 6.1: Literature Hansen Solubility Parameters for selected organic solvents. Solvents are sorted based on similar functionality. The three Hansen parameters are given in units of root pressure and the molar volumes are given in units of L/mol.[58, 60]

Index	Solvent	δ_D ($MPa^{1/2}$)	δ_P ($MPa^{1/2}$)	δ_H ($MPa^{1/2}$)	V_m ($Lmol^{-1}$)
1	n-Butane	14.1	0.0	0.0	101.4
2	n-Pentane	14.5	0.0	0.0	116.2
3	n-Hexane	14.9	0.0	0.0	131.6
4	n-Heptane	15.3	0.0	0.0	147.4
5	n-Octane	15.5	0.0	0.0	163.5
6	n-Decane	15.7	0.0	0.0	195.9
7	Cyclopentane	16.4	0.0	1.8	94.9
8	Cyclohexane	16.8	0.0	0.2	108.7
9	Benzene	18.4	0.0	2.0	89.4
10	Toluene	18.0	1.4	2.0	106.8
11	Ethylbenzene	17.8	0.6	1.4	123.1
12	o-Xylene	17.8	1.0	3.1	121.2
13	p-Xylene	17.6	1.0	3.1	123.3
14	Naphthalene	19.2	2.0	5.9	111.5
15	Chlorobenzene	19.0	4.3	2.0	102.1
16	Aniline	19.4	5.1	10.2	91.5
17	Benzaldehyde	19.4	7.4	5.3	101.5
18	Phenol	18.0	5.9	14.9	87.5
19	Anisole	17.8	4.1	6.7	119.1
20	Bisphenol-A	19.2	5.9	13.8	207.5
21	Chloromethane	15.3	6.1	3.9	55.4
22	Dichloromethane	18.2	6.3	6.1	63.9
23	Chloroform	17.8	3.1	5.7	80.7

24	Carbon Tetrachloride	17.8	0.0	0.6	97.1
25	Trichloroethylene	18.0	3.1	5.3	90.2
26	Methanol	15.1	12.3	22.3	40.7
27	Ethanol	15.8	8.8	19.4	58.5
28	1-Propanol	16.0	6.8	17.4	75.2
29	2-Propanol	15.8	6.1	16.4	76.8
30	1-Butanol	16.0	5.7	15.8	91.5
31	Tertbutyl Alcohol	15.2	5.1	14.7	95.8
32	Ethylene Glycol	17.0	11.0	26.0	55.8
33	Glycerol	17.4	12.1	29.3	73.3
34	Water	15.5	16.0	42.3	18.0
35	Dimethyl Ether	15.2	6.1	5.7	63.2
36	Diethyl Ether	14.5	2.9	5.1	104.8
37	Methylethyl Ether	14.7	4.9	6.2	84.1
38	Tetrahydrofuran	16.8	5.7	8.0	81.7
39	1,4 Dioxane	19.0	1.8	7.4	85.7
40	Ammonia	13.7	15.7	17.8	20.8
41	Methylamine	13.0	7.3	17.3	44.4
42	Ethylamine	15.0	5.6	10.7	65.6
43	Dimethylamine	15.3	4.8	11.2	66.2
44	Diethylamine	14.9	2.3	6.1	103.2
45	Ethylenediamine	16.6	8.8	17.0	67.3
46	Acetonitrile	15.3	18.0	6.1	52.6
47	Formaldehyde	12.8	14.4	15.4	36.8
48	Acetone	15.5	10.4	7.0	74.0

49	Acetic Acid	14.5	8.0	13.5	57.1
50	Acetylchloride	16.2	11.2	5.8	71.4
51	Ethylacetate	15.8	5.3	7.2	98.5
52	Acetic Anhydride	16.0	11.7	10.2	94.5
53	Acrylylchloride	16.2	11.6	5.4	81.3
54	Cyclopentanone	17.9	11.9	5.2	89.1
55	Gamma-butyrolactone	19.0	16.6	7.4	76.8
56	PGMEA*	15.6	5.6	9.8	137.1
57	Acetamide	17.3	18.7	22.4	60.8
58	N,N Dimethylformamide	17.4	13.7	11.3	77.0
59	N,N Dimethylacetamide	16.8	11.5	10.2	92.5
60	Dimethylsulfoxide	18.4	16.4	10.2	71.3

*Propylene Glycol Monomethyl Ether Acetate

The cohesion parameters for many commercial polymers have been reported in the literature.[58, 60] Neither the Hildebrand nor the Hansen solubility parameters are readily available for any formulation of SU-8 photoresist, so similar epoxy photoresists such as EPON 1001, have been previously used as stand-ins in the literature.[61] SU-8 is a glycidyl ether of Bisphenol A Novolac (Figure 6.1) and is very similar in structure to other glycidyl ethers of Bisphenol A resin, (such as many EPON and EPIKOTE resins) or to glycidyl ether of Novolacs such as the Dow Epoxy Novolac (DEN) resins.[25-26] The cohesion parameters for EPON 1001, EPIKOTE 1001, EPIKOTE 1004, DEN 438 and DEN 444 are listed in Table 6.2.[60]

While the structures in Figure 6.1 appear similar to SU-8, the degree of crosslinking is much higher in SU-8 compared with the other epoxy resins. This should offer SU-8 enhanced chemical resistance and a smaller interaction radius compared to other epoxies. To relate the solubility parameters of the solvents to those of the epoxy polymers, the interaction spheres of three representative polymers with small interaction radii (EPON 1001, EPIKOTE 1004 and DEN 444) are shown in Figure 6.10 and Figure 6.11.

Table 6.2: The cohesion parameters of polymers similar to SU-8. The three Hansen parameters for dispersion, polar and hydrogen bonding interactions are presented in units of root pressures. The interaction radius of each polymer, R_o, is also given. All values were reported by Hansen.[60]

Polymer	δ_D (MPa$^{1/2}$)	δ_P (MPa$^{1/2}$)	δ_H (MPa$^{1/2}$)	R_0 (MPa$^{1/2}$)
EPON 1001	17.0	9.6	7.8	7.1
EPIKOTE 1001	20.00	10.32	10.11	10.02
EPIKOTE 1001 (10%)	18.1	11.4	9.0	9.1
EPIKOTE 1004	17.4	10.5	9.0	7.9
DEN 438	20.3	15.4	5.3	15.1
DEN 444	19.5	11.6	9.3	10.0

For example, in both Figure 6.10 and Figure 6.11, the solvents that are expected to interact with EPON 1001 are many chlorinated hydrocarbons, a series of ethers, amines, ketones and carboxylic acids. Gamma-butyrolactone (55) is the solvent used with SU-8 resists and is found close to the interaction boundary in Figure 6.10 and Figure 6.11. Cyclopentanone is the solvent for SU-8 2000 series (54) and PGMEA is the developer used during SU-8 processing (56). Both were found within the solubility limits of EPON 1001.

By comparison, in our experiments, SU-8 films were exposed to several solvents and the interaction was monitored qualitatively. The relative interaction strength, R_a/R_0, was calculated from the above Hansen solubility parameters of EPON 1001, EPIKOTE 1004 and DEN444 (Table 6.3). It is apparent that the Hansen model is not able to reproduce the strong interaction of SU-8 with methanol (and the weaker interactions with water) while predicting stronger than observed – and comparable interactions – of the epoxy with 2-propanol and m-xylene.

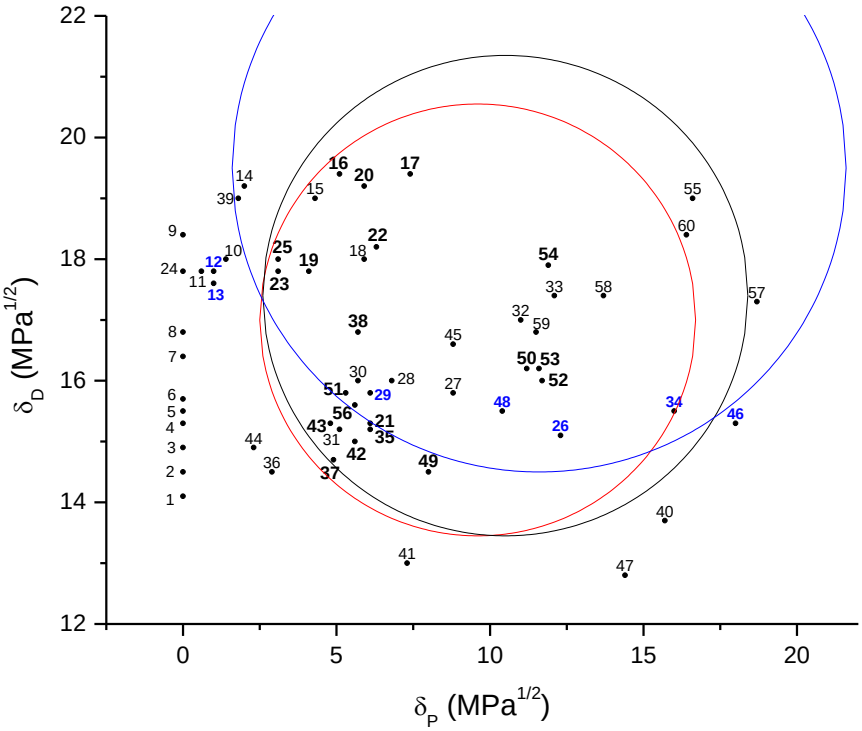

Figure 6.10: Hansen Solubility of 60 common organic solvents in the plane of dispersion and polar forces compared with the interaction radii of three different epoxies. The bold numbers indicate solvents that are also within the solubility radii of EPON 1001 in the Dispersion/Polar and Hydrogen bonding/Polar plane. The solvents in blue indicate solvents that were exposed to SU-8 in this study. The red circle, black circle and blue circle are the interaction radii of EPON 1001, EPIKOTE 1004 and DEN 444, respectively.

The shortcomings of the Hansen solubility model are well known. The model fails to appropriately account for the influence of the solvent molar volume and the polymer's molecular weight.[60] This is especially problematic when working with high molecular weight polymers, which are often less soluble than predicted. Additionally, polymers are often more soluble in solvents with small molar volumes (V_m < 100) than would otherwise be expected.[60]

Our experimental results agree with those of Ford, who found that SU-8 was soluble in eight different solvents including acetone, acetonitrile, ethyl acetate, tetrahydrofuran and dioxane.[61] Ford and coworkers showed that SU-8 has a strong affinity to small polar molecules containing carbonyl groups and ethers.[61] It is then not surprising to see a weak response to water and alcohols as well.

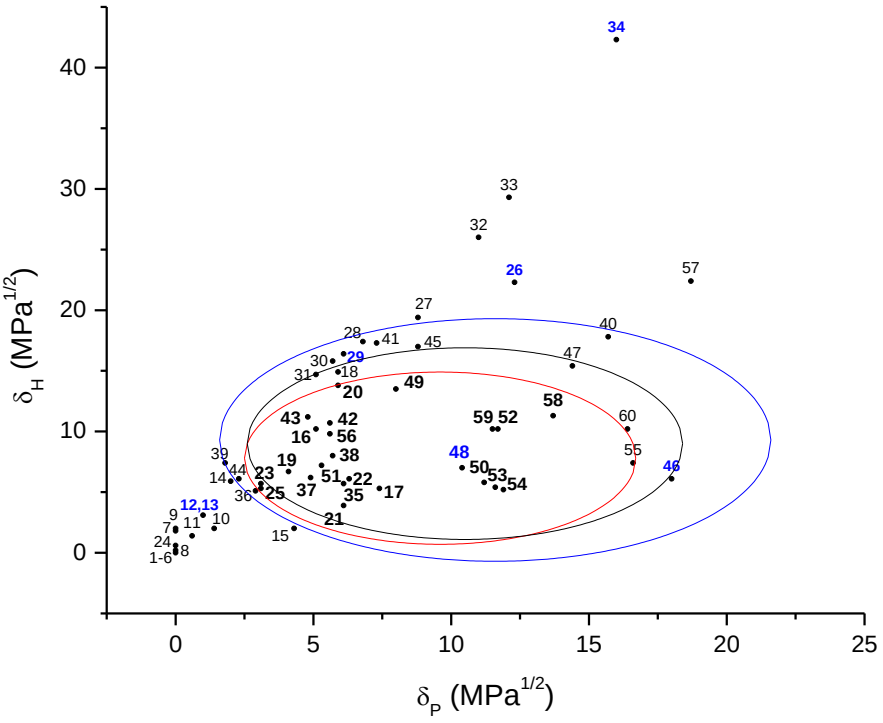

Figure 6.11: Hansen Solubility of 60 common organic solvents in the plane of hydrogen bonding and polar forces compared with the interaction radii of three types of epoxies. The bold numbers indicate solvents that are also within the solubility radii of EPON1001 in the Dispersion/Polar and Hydrogen bonding/Polar plane. The solvents in blue indicate solvents that were exposed to SU-8 in this study. The red circle, black circle and blue circle are the interaction radii of EPON 1001, EPIKOTE 1004 and DEN 444, respectively.

Of course, the solubility constants reported in the literature are specific to the preparation of the epoxies. The concentration of polymer in solution, and the solvent used at the time of casting can have significant effects on the degree of crosslinking in the material.[60] This could greatly change the physical behaviour and solubility of a material. Additionally, solubility constants are temperature-dependent.[60] Moreover, since we do not have any solubility parameters of SU-8 we can only use stand-in epoxies that are presented in the literature. Considering all these limitations, our experimental results agree well with the observation made by Ford *et al*. on the dissolution in acetone and acetonitrile.[61] The extension from dissolution in small ethers presented by Ford *et al.*[61] to small alcohols in this study also seems plausible.

The stronger than expected interactions of SU-8 with acetonitrile, methanol and water are likely due to the small molar volumes of these three solvents.

Table 6.3: Comparison of the observed solvent interactions with SU-8 against the predicted interaction strength from Hansen solubility parameters. For methanol, acetone and acetonitrile, the films swelled rapidly and were delaminated after a few minutes. Swelling was observed for water and isopropanol. No swelling or any other effect was observed for exposure to m-xylene. The interaction strength R_a/R_0 is given for each solvent – epoxy pair. Values of $R_a/R_0 < 1$ indicate strong interactions and predicted high solubility.

Index	Solvent	SU-8 film response	R_a/R_0		
			EPON 1001	EPIKOTE 1004	DEN 444
48	Acetone	Dissolved	0.45	0.58	0.84
46	Acetonitrile	Dissolved	1.30	1.23	1.10
26	Methanol	Dissolved	2.14	1.92	1.57
34	Water	Swelling	4.96	4.59	3.42
29	2-Propanol	Minor Swelling	1.35	1.24	1.16
12/13	m-Xylene	No Swelling	1.39	1.51	1.29

6.4 Conclusions and Future Work

Using Fourier analysis of images taken using a large-angle interferometric refractometer, it is possible to simultaneously extract the changes in average refractive index, $\bar{n}_{film}$, and thickness, d, of thin transparent films (d = 15-150 μm). Additionally, from changes in the critical angle of total internal reflection, the refractive index at the film-substrate interface, n_{FS}, was extracted. An expression was derived relating the mole fraction of an analyte within a film to both the refractive index and thickness changes during chemical uptake.

Diffusion expressions derived from those presented by Crank[2] were used to model the changes of both the average concentration and the film-interface concentration during the uptake process. Despite its simplicity, the model described the experimental data very well. One might have anticipated complications, as concentration and refractive index gradients are present within the film prior to reaching equilibrium, as

was previously discussed in Chapter 3.3. In our analysis, however, these effects were not apparent and the data was fit remarkably well (Figure 6.8). The data is of such high quality that two parallel uptake processes can be readily distinguished and quantified. While our model agrees well with the data, it does not account for surface roughness, absorption, scattering or birefringence of the film. Parameters could be included in the future to address these properties and develop a more complete model.

Using ~40 μm thick spin-coated SU-8 50 photoresist films as a model system, the uptake of common solvents was measured. Diffusion of water into SU-8 was accompanied by changes in $\bar{n}_{film}$ and n_{FS} of Δn = 0.0009 and 0.0008 respectively and a thickness change of 0.7%. Kinetic analysis of the average bulk film concentration, $\bar{X}_{Film}$, gave two diffusion processes that occurred at different rates ($D_1 = 5.67\times10^{-9}$ cm^2/s and $D_2 = 61.2\times10^{-9}$ cm^2/s) with equilibrium mole fractions of $X_{\infty,1}$ = 0.176, (mass fraction, Y = 2230 ppm$_w$) and $X_{\infty,2}$ = 0.348 (Y = 4420 ppm$_w$). As was suggested previously,[30] the surface of an SU-8 film has a stronger affinity to water than the bulk of the film. We propose that the faster process corresponds to restructuring of the top layers of the SU-8 film and the slower process corresponds to the diffusion of water throughout the entire film. Since the second process is accompanied by only a very small change of density, the slower diffusion process can also be quantified using refractive index changes at the film-substrate interface when neglecting density changes. The constants $D = 1.398(2)\times10^{-8}$ cm^2/s, X_∞ = 0.11440(4); Y = 1452 ppm$_w$ are consistent with a lower permeability of the bulk film compared to the surface. The diffusion constants reported here are higher than those in the literature for the SU-8 2000 series, firstly because the two materials are prepared from precursors in different solvents and may have different physical properties and secondly, because some of the previous reported values measure diffusion constants from only the swelling of the SU-8 film and neglect solvent contributions to density changes.

Thickness or refractive index changes were not measurable when SU-8 was exposed to isopropanol and m-xylene, but rapid film dissolution and delamination was observed when SU-8 was exposed to acetone, acetonitrile and methanol. This suggests that SU-8 has a strong affinity to polar solvents. The chemical resistance of SU-8 films can likely be increased by more strongly cross-linking the polymer. Since

SU-8 fabrication involves a multi-step process, the mechanical properties of SU-8 are substantially altered for different fabrication protocols. Ultimately, care must be taken to optimize the fabrication conditions when using SU-8 as overcoats for photonic sensors and for microfluidic applications to reduce analyte partitioning and swelling within films.

The optical measurements described in this report provide rapid, high-quality, non-contact information about the diffusion of a mobile phase into a film of finite thickness. One application could be to analyse the output from chromatographic separations if the solution layer is thick enough. The instrument developed in our lab permits measurements of film thickness with a resolutions of $d < 1\%$ resolution and is thus sensitive to swelling of the film. The thickness range is currently limited to d = 10-100 μm by the number of fringes visible in the image and may be changed by either recording images with higher resolution or by changing the distance between the prism and the camera. In addition, the refractive index is simultaneously measured both in the bulk film and near the film-substrate interface. The refractive index range is fundamentally limited by the requirement of total internal reflection at the film-substrate interface. When using a flint glass substrate, this is limited to film refractive indices $n_{1550} < 1.74$. Other substrates that exhibit transparency at the interrogation wavelength can also be used. For low index polymers, regular soda-lime glass microscope slides (n_{1550} = 1.5070)[62] and a matching prism would be sufficient. Silicon (n_{1550} = 3.4777)[63] may be used as a substrate for very high index films. In combination with the Lorentz-Lorenz model and a Fickian diffusion model, all three measurements allow for the precise calculation of the average analyte mole fraction and mass fraction within a film at a high time resolution.

This technique was also applied to study the faster partitioning of volatile compounds into siloxane-based polymers. It is also well suited for quantitatively measuring uptake concentrations, and partition coefficients from much larger refractive index and thickness changes. These experiments will be discussed in detail in Chapter 7.

6.5 Acknowledgements

I would like to thank Dr. Robert Knobel (Department of Physics, Queen's) and members of the Kingston Nano-Fabrication Lab (KNFL) for access to their facility and their assistance in the preparation of the SU-8 films used in this study. An initial set of experiments not shown in this chapter were run by Mr. McGregor Clayton during a summer work term with our group, and was the basis of this study. I would like to acknowledge Mr. Weijian (Jason) Chen for his assistance with the construction of the optical setup and data processing techniques used in this study. Without his ground work, this study would not have been possible. Additionally, I thank Mr. Chris Brauer, Dr. Jack Barnes, and Dr. Hans-Peter Loock for their assistance with the derivation of the mole fraction and diffusion equations presented in this chapter. Finally, I would like to thank Mr. Jeff Crouse for help in Fortran programming used to speed up the lengthy data analysis in this study.

6.6 References

1. Saunders, J. E.; Chen, H.; Brauer, C.; Clayton, M.; Chen, W.; Barnes, J. A.; Loock, H.-P., Quantitative diffusion and swelling kinetic measurements using large-angle interferometric refractometry. *Soft Matter* **2015,** *11*, 8746-8757.

2. Crank, J., *The Mathmatics of Diffusion*. First Edition, Oxford University Press, London, UK, 1956.

3. Patel, R.; Zhou, R.; Zinszer, K.; Josse, F.; Cernosek, R., Real-time detection of organic compounds in liquid environments using polymer-coated thickness shear mode quartz resonators. *Analytical Chemistry* **2000,** *72*, 4888-4898.

4. Hossenlopp, J.; Jiang, L.; Cernosek, R.; Josse, F., Characterization of epoxy resin (SU-8) film using thickness-shear mode (TSM) resonator under various conditions. *Journal of Polymer Science Part B: Polymer Physics* **2004,** *42*, 2373-2384.

5. Johannsmann, D., Viscoelastic, mechanical, and dielectric measurements on complex samples with the quartz crystal microbalance. *Physical Chemistry Chemical Physics* **2008,** *10*, 4516-4534.

6. Linossier, I.; Gaillard, F.; Romand, M.; Feller, J. F., Measuring water diffusion in polymer films on the substrate by internal reflection fourier transform infrared spectroscopy. *Journal of Applied Polymer Science* **1997,** *66*, 2465-2473.

7. Ichikawa, K.; Mori, T.; Kitano, H.; Fukuda, M.; Mochizuki, A.; Tanaka, M., Fourier transform infrared study on the sorption of water to various kinds of polymer thin films. *Journal of Polymer Science Part B: Polymer Physics* **2001,** *39*, 2175-2182.

8. Skourlis, T. P.; McCullough, R. L., Measurement of diffusivity of a liquid diamine in solid epoxies using attenuated total reflectance infrared spectroscopy (FTIR-ATR). *Journal of Applied Polymer Science* **1994,** *52*, 1241-1248.

9. Rheims, J.; Köser, J.; Wriedt, T., Refractive-index measurements in the near-IR using an Abbe refractometer. *Measurement Science and Technology* **1997,** *8*, 601-605.

10. Tolmachev, V. A., Adsorption-ellipsometry method of studying the optical profile, thickness, and porosity of thin films. *Journal of Optical Technology* **1999,** *66*, 596-607.

11. *Handbook of Ellipsometry*. Tompkin, H. G.; Irene, E. A., Eds. William Andrew Inc, Springer-Verlag GmbH & Co., Norwich, NY, 2005.

12. Elbs, H.; Krausch, G., Ellipsometric determination of Flory-Huggins interaction parameters in solution. *Polymer* **2004,** *45*, 7935-7942.

13. Chen, W.-L.; Shull, K. R.; Papatheodorou, T.; Styrkas, D. A.; Keddie, J. L., Equilibrium swelling of hydrophilic polyacrylates in humid environments. *Macromolecules* **1999,** *32*, 136-144.

14. Kedenburg, S.; Vieweg, M.; Gissibl, T.; Giessen, H., Linear refractive index and absorption measurements of nonlinear optical liquids in the visible and near-infrared spectral region. *Optical Materials Express* **2012,** *2*, 1588-1611.

15. Moutzouris, K.; Papamichael, M.; Betsis, S. C.; Stavrakas, I.; Hloupis, G.; Triantis, D., Refractive, dispersive and thermo-optic properties of twelve organic solvents in the visible and near-infrared. *Applied Physics B* **2014,** *116*, 617-622.

16. Russell, T. P., X-ray and neutron reflectivity for the investigation of polymers. *Materials Science Reports* **1990,** *5*, 171-271.

17. Müller-Buschbaum, P.; Bauer, E.; Maurer, E.; Nelson, A.; Cubitt, R., In-situ neutron reflectometry probing competitive swelling and de-swelling of thin polystyrene films. *Physica Status Solidi (RRL) – Rapid Research Letters* **2007,** *1*, R68-R70.

18. Wang, W.; Kaune, G.; Perlich, J.; Papadakis, C. M.; Bivigou Koumba, A. M.; Laschewsky, A.; Schlage, K.; Röhlsberger, R.; Roth, S. V.; Cubitt, R.; Müller-Buschbaum, P., Swelling and switching kinetics of gold coated end-capped poly(N-isopropylacrylamide) thin films. *Macromolecules* **2010,** *43*, 2444-2452.

19. Mukherjee, M.; Singh, A.; Daillant, J.; Menelle, A.; Cousin, F., Effect of solvent−polymer interaction in swelling dynamics of ultrathin polyacrylamide films: A neutron and X-ray reflectivity study. *Macromolecules* **2007,** *40*, 1073-1080.

20. Chen, W.; Saunders, J. E.; Barnes, J. A.; Yam, S. S.-H.; Loock, H.-P., Monitoring of vapor uptake by refractive index and thickness measurements in thin films. *Optics Letters* **2013,** *38*, 365-367.

21. Lorenz, H.; Despont, M.; Fahrni, N.; LaBianca, N.; Renaud, P.; Vettiger, P., SU-8: a low-cost negative resist for MEMS. *Journal of Micromechanics and Microengineering* **1997,** *7*, 121-124.

22. Shaw, J. M.; Gelorme, J. D.; LaBianca, N. C.; Conley, W. E.; Holmes, S. J., Negative photoresists for optical lithography. *IBM Journal of Research and Development* **1997,** *41*, 81-94.

23. Balslev, S.; Jorgensen, A. M.; Bilenberg, B.; Mogensen, K. B.; Snakenborg, D.; Geschke, O.; Kutter, J. P.; Kristensen, A., Lab-on-a-chip with integrated optical transducers. *Lab on a Chip* **2006,** *6*, 213-217.

24. Abgrall, P.; Conedera, V.; Camon, H.; Gue, A.-M.; Nguyen, N.-T., SU-8 as a structural material for labs-on-chips and microelectromechanical systems. *Electrophoresis* **2007,** *28*, 4539-4551.

25. *Epoxy Resins: Chemistry and Technology*. 2nd Edition, May, C. A., Ed. Marcel Dekker, New York, NY, 1988.

26. *Physical Properties of Polymers Handbook*. 2nd Edition, Mark, J. E., Ed. Springer Science + Business Media, LLC, New York, NY, 2007.

27. Xu, D. X.; Densmore, A.; Delâge, A.; Waldron, P.; McKinnon, R.; Janz, S.; Lapointe, J.; Lopinski, G.; Mischki, T.; Post, E.; Cheben, P.; Schmid, J. H., Folded cavity SOI microring sensors for high sensitivity and real time measurement of biomolecular binding. *Optics Express* **2008,** *16*, 15137-15148.

28. Schmid, J. H.; Bock, P. J.; Cheben, P.; Sinclair, W.; García, J.; Janz, S.; Lapointe, J.; Aers, G. C.; Poitras, D.; Li, Y.; Lopinski, G.; Delâge, A.; Densmore, A.; Lamontagne, B.; Ma, R.; Xu, D.-X. Applications of subwavelength grating structures in silicon-on-insulator waveguides, *Silicon Photonics V, Proceedings of SPIE 7606*, **2010**, 76060F, 1-9.

29. Duval, D.; González-Guerrero, A. B.; Dante, S.; Osmond, J.; Monge, R.; Fernández, L. J.; Zinoviev, K. E.; Domínguez, C.; Lechuga, L. M., Nanophotonic lab-on-a-chip platforms including novel bimodal interferometers, microfluidics and grating couplers. *Lab on a Chip* **2012,** *12*, 1987-1994.

30. Liu, C.; Liu, Y.; Sokuler, M.; Fell, D.; Keller, S.; Boisen, A.; Butt, H.-J.; Auernhammer, G. K.; Bonaccurso, E., Diffusion of water into SU-8 microcantilevers. *Physical Chemistry Chemical Physics* **2010,** *12*, 10577-10583.

31. Wouters, K.; Puers, R., Diffusing and swelling in SU-8: insight in material properties and processing. *Journal of Micromechanics and Microengineering* **2010,** *20*, 095013, 1-10.

32. Vanlandingham, M. R.; Eduljee, R. F.; Gillespie, J. W., Moisture diffusion in epoxy systems. *Journal of Applied Polymer Science* **1999,** *71*, 787-798.

33. Diamant, Y.; Marom, G.; Broutman, L. J., The effect of network structure on moisture absorption of epoxy resins. *Journal of Applied Polymer Science* **1981,** *26*, 3015-3025.

34. Berger, C. M.; Henderson, C. L., The effect of humidity on water sorption in photoresist polymer thin films. *Polymer* **2003,** *44*, 2101-2108.

35. Blanco Carballo, V. M.; Melai, J.; Salm, C.; Schmitz, J., Moisture resistance of SU-8 and KMPR as structural material. *Microelectronic Engineering* **2009,** *86*, 765-768.

36. Park, J.; Shin, D.-S., Application of epoxy-based photosensitive polymers for optical MEMS and subsequent reliability evaluation. *Materials Chemistry and Physics* **2006,** *98*, 309-315.

37. Yi, L.; Xiaodong, W.; Chong, L.; Zhifeng, L.; Denan, C.; Dehui, Y., Swelling of SU-8 structure in Ni mold fabrication by UV-LIGA technique. *Microsystem Technologies* **2005,** *11*, 1272-1275.

38. Messica, A.; Greenstein, A.; Katzir, A., Theory of fiber-optic, evanescent-wave spectroscopy and sensors. *Applied Optics* **1996,** *35*, 2274-2284.

39. Loock, H., Ring-down absorption spectroscopy for analytical microdevices. *TrAC Trends in Analytical Chemistry* **2006,** *25*, 655-664.

40. van der Sneppen, L.; Ariese, F.; Gooijer, C.; Ubachs, W., Liquid-phase and evanescent-wave cavity ring-down spectroscopy in analytical chemistry. *Annual Review of Analytical Chemistry* **2009,** *2*, 13-35.

41. Renard, R. H., Total reflection: A new evaluation of the Goos–Hänchen shift. *Journal of the Optical Society of America* **1964,** *54*, 1190-1197.

42. Merano, M.; Aiello, A.; 't Hooft, G. W.; van Exter, M. P.; Eliel, E. R.; Woerdman, J. P., Observation of Goos-Hänchen shifts in metallic reflection. *Optics Express* **2007,** *15*, 15928-15934.

43. Saleh, B. E. A.; Teich, M. C., *Fundamentals of Photonics*. 2nd Edition, John Wiley & Sons, Hoboken, NJ, 2007.

44. Pillon, F.; Gilles, H.; Girard, S.; Laroche, M.; Kaiser, R.; Gazibegovic, A., Goos-Hänchen and Imbert-Fedorov shifts for leaky guided modes. *Journal of the Optical Society of America B* **2005,** *22*, 1290-1299.

45. Saunders, J. E.; Sanders, C.; Chen, H.; Loock, H.-P., Refractive indices of common solvents and solutions at 1550 nm. *Applied Optics* **2016,** *55*, 947-953.

46. Chen, W. *Chemical Detection and Sensing Using Optical Interferometry*. M.A.Sc Thesis, Queen's University, 2013.

47. Schneider, C. A.; Rasband, W. S.; Eliceiri, K. W., NIH Image to ImageJ: 25 years of image analysis. *Nature Methods* **2012,** *9*, 671-675.

48. Rodríguez-Ruiz, I.; Llobera, A.; Vila-Planas, J.; Johnson, D. W.; Gómez-Morales, J.; García-Ruiz, J. M., Analysis of the structural integrity of SU-8-based optofluidic systems for small-molecule crystallization studies. *Analytical Chemistry* **2013,** *85*, 9678-9685.

49. Roch, I.; Bidaud, P.; Collard, D.; Buchaillot, L., Fabrication and characterization of an SU-8 gripper actuated by a shape memory alloy thin film. *Journal of Micromechanics and Microengineering* **2003,** *13*, 330-336.

50. Tanchak, O. M.; Yager, K. G.; Fritzsche, H.; Harroun, T.; Katsaras, J.; Barrett, C. J., Ion distribution in multilayers of weak polyelectrolytes: A neutron reflectometry study. *The Journal of Chemical Physics* **2008,** *129*, 084901.

51. Ebewele, R. O., *Polymer Science and Technology*. CRC Press Ltd., Boca Raton, FL, 2000.

52. Carter, M. C. D.; Sorrell, C. D.; Serpe, M. J., Deswelling kinetics of color tunable poly(*N-i*sopropylacrylamide) microgel-based etalons. *The Journal of Physical Chemistry B* **2011,** *115*, 14359-14368.

53. Brazel, C. S.; Peppas, N. A., Mechanisms of solute and drug transport in relaxing, swellable, hydrophilic glassy polymers. *Polymer* **1999,** *40*, 3383-3398.

54. Keller, S.; Blagoi, G.; Lillemose, M.; Haefliger, D.; Boisen, A., Processing of thin SU-8 films. *Journal of Micromechanics and Microengineering* **2008,** *18*, 125020, 1-10.

55. Becnel, C.; Desta, Y.; Kelly, K., Ultra-deep x-ray lithography of densely packed SU-8 features: II. Process performance as a function of dose, feature height and post exposure bake temperature. *Journal of Micromechanics and Microengineering* **2005,** *15*, 1249-1259.

56. Feng, R.; Farris, R. J., Influence of processing conditions on the thermal and mechanical properties of SU8 negative photoresist coatings. *Journal of Micromechanics and Microengineering* **2003,** *13*, 80-88.

57. Barton, A. F. M., Solubility parameters. *Chemical Reviews* **1975,** *75*, 731-753.

58. Barton, A. F. M., *CRC Handbook of Solubility Parameters and Other Cohesion Parameters*. 2nd Edition, CRC Press, Inc., Boca Raton, FL, 1991.

59. Hansen, C. M., The three dimensional solubility parameter - Key to paint component affinities I - Solvents, plasticizers, polymers, and resins. *Journal of Paint Technology* **1967,** *39* (505), 104-117.

60. Hansen, C. M., *Hansen Solubility Parameters: A User's Handbook*. 2nd Edition, CRC Press, Taylor & Francis Group, Boca Raton, FL, 2007.

61. Ford, J.; Marder, S. R.; Yang, S., Growing "nanofruit" textures on photo-crosslinked SU-8 surfaces through layer-by-layer grafting of hyperbranched poly(ethyleneimine). *Chemistry of Materials* **2009,** *21*, 476-483.

62. Rubin, M., Optical properties of soda lime silica glasses. *Solar Energy Materials* **1985,** *12*, 275-288.

63. Salzberg, C. D.; Villa, J. J., Infrared refractive indexes of silicon, germanium and modified selenium glass. *Journal of the Optical Society of America* **1957,** *47*, 244-246.

Chapter 7

Diffusion of Volatile Organic Compounds into Siloxane Polymers

In this chapter, the use of siloxane polymers as an extraction matrix for the detection of VOCs including BTEX, cyclohexane, acetone, methanol and isopropanol will be explored. Both refractive index and thickness changes will be measured using optical refractometry to quantify the uptake of VOC vapours into PDMS and PDMS-PDPS copolymer films. The analyte concentration within the film will be used to estimate diffusion rates and equilibrium partition coefficients. This chapter will begin with an introduction to siloxane chemistry in Section 7.2, and describe the synthesis of our films in Section 7.3. The results from refractometer studies on the exposure of thin siloxane films to VOCs will be described in Section 7.4.

7.1 Introduction

There is a well-established industry surrounding siloxane polymers. Siloxanes are employed as sealants in bathrooms, kitchens, and aquariums, in household silicone cookware and utensils, and even in skin care products. Polydimethylsiloxane (PDMS) has many useful physical properties making it an ideal polymer for many scientific applications. It can be easily shaped using moulds and templates, and will maintain its shape once cured. PDMS is optically transparent in the visible and into the UV from λ = 230-800 nm[1-2] making it suitable for optical components including contact lenses, micro-lenses[2-5] and gratings for spectroscopic sensor applications.[2, 6] The optical focusing properties of PDMS lenses can be tuned by mechanically distorting the material.[2, 4] PDMS is a very elastic material and can be easily contact-sealed to glass and silicon surfaces for microfluidic applications. It can also be permanently bonded through formation of Si – O – Si bonds if both surfaces are treated with an oxygen plasma prior to contact. [1, 7-8] PDMS is hydrophobic and does not swell significantly upon exposure to common polar solvents, such as water and methanol,[1, 9] which are commonly required for biological systems, environmental sensing and many other applications. PDMS microfluidics can be readily used for sample introduction over optical waveguide refractive index sensing elements[7, 10] and other transduction elements to produce real-time sensors. PDMS is known to be biocompatible with cells, is impermeable to water and permeable to gases,

making it a useful material for studying biological systems.[1, 9] It is even suitable for biological implants and as scaffolding in tissue engineering for bone growth.[11-12] Through soft lithography using templates, PDMS can be used to make valves, [13] and mixers[7, 14] in microfluidic channels for lab-on-a-chip applications. It can also be used for microfluidics on disposable immunoassay sensor chips for antibodies [15] and bacteria.[16] However, being hydrophobic, PDMS microfluidics can be particularly prone to forming air bubbles and absorbing non-polar analytes (e.g. fluorescent tag molecules, proteins and cells), which may complicate experiments.[1, 17]

The diffusion of compounds into elastomers can cause substantial swelling which will complicate the relationship between film analyte concentration and refractive index. Changes in a film's density upon swelling are difficult to predict, but can be inferred from both film thickness and refractive index changes in order to accurately calculate the concentration of an analyte within a film. Many studies calculate uptake from only the change in volume (swelling) and do not account for any partitioning into micro-pores or cavities within the film[18-20] The swelling of PDMS when exposed to VOCs has been studied in great detail and swelling parameters are readily available for common organic solvents in the literature.[21-22] In these studies, pieces of PDMS were either immersed in solvent for 24 hours, or exposed to solvent vapours for 72 hours with the swelling determined by measuring the length changes in all dimensions. The most significant swelling occurs when PDMS was exposed to amines, ethers, and small non-polar molecules such as pentane and benzene.[21-22] This strong affinity to non-polar molecules makes PDMS a useful extraction matrix and is the reason why PDMS is one of the most widely used materials in solid-phase microextraction (SPME).[23-25] For example, PDMS is a useful extraction matrix for polycyclic aromatic hydrocarbons (PAHs) from air, particulates, and soil samples. [26-27] In the food industry, PDMS-based SPME is used in a wide range of applications from the analysis of edible vegetable oils[28] to the detection of hormones in chicken and pork.[29] It has also been shown to be useful for the extraction of a wide range of compounds in coffee, milk, honey, vegetables and meat products.[30] In SPME, a PDMS (or other polymer) coated silica fibre is inserted into the air headspace above a solution, or directly into an aqueous solution to extract non-polar compounds.[25] Once equilibrium is reached, the fibre is retracted back into a gas tight

syringe and stored until the sample can be analysed. The syringe is then inserted into a gas chromatograph, where the analytes are desorbed and quantified using common detectors (e.g. flame ion detection (GC-FID), thermal conductivity, or mass spectrometry).[24-25] While the SPME extraction layer is usually coated on a fibre, PDMS may alternatively be coated on a magnetic stir bar, used as the walls of a sample vessel, or as a membrane on the bottom of the vessel when interfaced with online detection.[24] Many groups have studied the uptake of volatile organic compounds (VOCs) into PDMS and have calculated both diffusion constants[31-37] and partition coefficients[38-43] for their systems. SPME, followed by laboratory instrumental analysis, is a commonly used method for quantification of the BTEX (benzene, toluene, ethylbenzene, xylenes) class of organic contaminants in both air[44] and in aqueous solutions.[23] Sensing of BTEX compounds is of particular interest as all the compounds are listed by the United States Environmental Protection Agency (EPA) as part of 187 controlled hazardous air contaminants enacted after the Clean Air Act in 1990. [45]

BTEX compounds are naturally occurring and are a major component in crude oil and other fossil fuels.[46-49] The main exposure to humans is through the combustion of coal and oil in industrial processes, transportation, and heating.[46-49] They are also present from evaporation at petroleum fuel stations, in cigarette smoke, volcanic emissions, and smoke from forest fires.[46-49] BTEX compounds are commonly used as solvents in pharmaceutical production, in chemical production of adhesives, paints, waxes, and paint thinners and for use as precursors in the production of polymers and other molecules.[46-49] Exposure can occur through the off-gassing of many objects in our surroundings making levels inside residential locations up to 100-times higher than outdoors.[44] Additionally, BTEX compounds are used as additives in commercial gasoline as anti-knock compounds.[46-49] Long-term exposure to high levels of BTEX compounds is known to cause chronic problems with the kidneys, liver, respiratory, and cardiovascular systems as well as neurological effects and leukemia in the case of benzene.[46-49] One of the conventional methods for detecting BTEX contamination involves placing extraction cartridges near the sample area and waiting for it to equilibrate with the surroundings.[44] The cartridge is then sealed and sent to a laboratory for later analysis through gas chromatography.[44] This passive method does not provide any information about

concentration spikes, or give any temporal information about the analyte concentration in the environment. Incorporation of extraction matrices with other transduction devices, like refractive index sensors can allow for the development of real-time remote sensors.

In this chapter, the use of PDMS as an SPME material for the extraction and detection of VOCs including BTEX, cyclohexane, acetone, methanol and isopropanol will be explored. Both refractive index and thickness changes will be observed using optical refractometry to quantify the uptake of VOC vapours into PDMS films. The refractometer is a simple and useful instrument for the screening of materials to determine relative uptake of various chemical species. Once a suitable database is constructed, a series of different films can be applied to miniature refractive index sensing platforms, including photonic waveguide devices, to develop a reversible chemical sensor for VOCs based on the relative response to the analytes of interest. This chapter will begin with an introduction to siloxane chemistry in Section 7.2, including the detailed synthetic information of the reagents used in the synthesis of our films in Section 7.3. The chapter will progress to the results from refractometer studies on the exposure of thin siloxane films to VOCs in Section 7.4.

7.2 Chemistry of Siloxane Polymers

There are a number of different ways to make siloxane polymers depending on the desired functionality, chain length and degree of cross linking. The most commonly used siloxane is polydimethylsiloxane (PDMS) which is available from a variety of commercial sources in, typically, a two-part system of an oligomer base and a crosslinking additive. One of the most inexpensive and commonly used kits is Sylgard 184 from Dow Corning, which was used to make the PDMS films described in this study. A hydrosilylation reaction polymerizes the oligomer units in most commercial PDMS kits, including Sylgard 184. When designing custom materials and copolymers it is often easier to instead use monomer units with silanol groups to form oligomer chains through a condensation reaction. These chains can then be crosslinked with metal particles, such as titanium.[50]

7.2.1 Synthesis of Siloxanes Through Hydrosilylation Reactions

The exact composition of many commercially available siloxane products is a patented secret. Many polymers contain additives to enhance the physical properties of the materials, for example plasticizers can be added to lower the glass transition temperature, fillers can be added to help re-inforce polymers and reduce cost, and compounds can be added to reduce the oxidative and UV degradation of polymers.[51] Most commercial PDMS comes in a two-part kit containing a siloxane base and a curing agent. The base consists of a mixture of vinyl-terminated polydimethylsiloxane and branched siloxanes in order to generate a 3-dimensionally crosslinked structure (Figure 7.1).[52-53] Additionally, vinyl-terminated silica particles are present as filler in these kits.

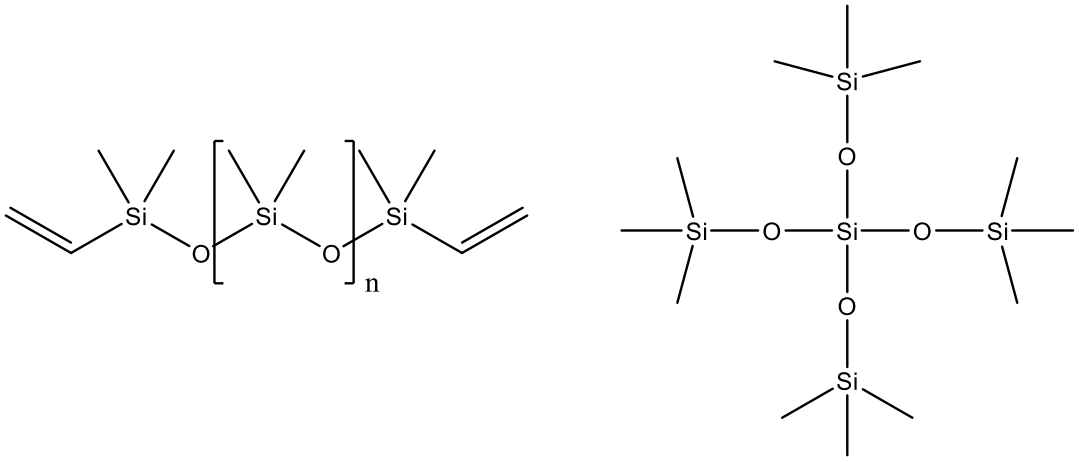

Figure 7.1: Sample chemical structures of siloxane base compounds in most commercial PDMS kits. Left: vinyl terminated polydimethylsiloxane forms Si-C bonds through hydrosilylation. Right: tetra(trimethylsilyl)siloxane is a sample branched siloxane compound.

The curing agent contains additional compounds including methylhydrogensiloxanes, cyclic vinyl terminated siloxanes (Figure 7.2) and a platinum based catalyst similar to Karstedt's catalyst (Figure 7.3).[52-53]

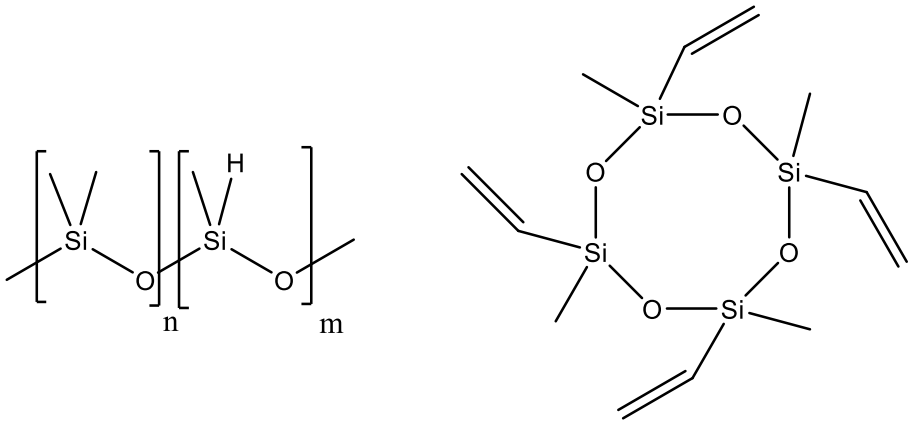

Figure 7.2: Sample chemical structures of siloxane compounds in the curing agents of most commercial PDMS kits. Left: poly(dimethyl-co-methylhydrogen)siloxane provides attachment points for vinyl-functionalized siloxanes. Right: tetramethyltetravinylcyclotetrasiloxane is used to facilitate the 3-dimensional crosslinking of the material.

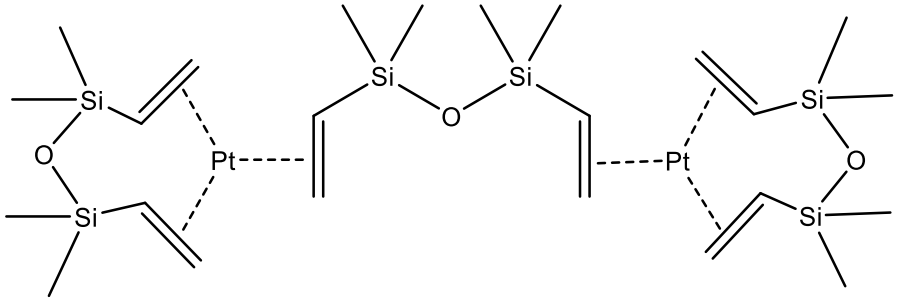

Figure 7.3: Chemical structure of Karstedt's Catalyst. Karstedt's catalyst, or similar platinum catalysts, crosslink PDMS through carbon-silicon bond formations during hydrosilylation.

A platinum-based catalyst facilitates the hydrosilylation reaction, which crosslinks the siloxane material. The precise mechanism of the reaction has not been confirmed, but multiple schemes have been suggested.[54-56] Shown in Figure 7.4 is a proposed reaction scheme with a simple platinum catalyst to illustrate the reaction cycle. The ligands on platinum and its oxidation state will differ depending on the catalyst being used. The proposed mechanism consists of four steps: 1) the vinyl group of one of the siloxanes first coordinates to the platinum catalyst in a ligand exchange with a leaving group, 2) one of the methylhydrogensiloxane molecules undergoes oxidative addition to the platinum catalyst, oxidizing the Pt(II) to Pt(IV), 3) a proton then transfers to the coordinated vinyl group, 4) and the product undergoes reductive elimination reducing the Pt(IV) back to Pt(II), restarting the catalytic cycle.

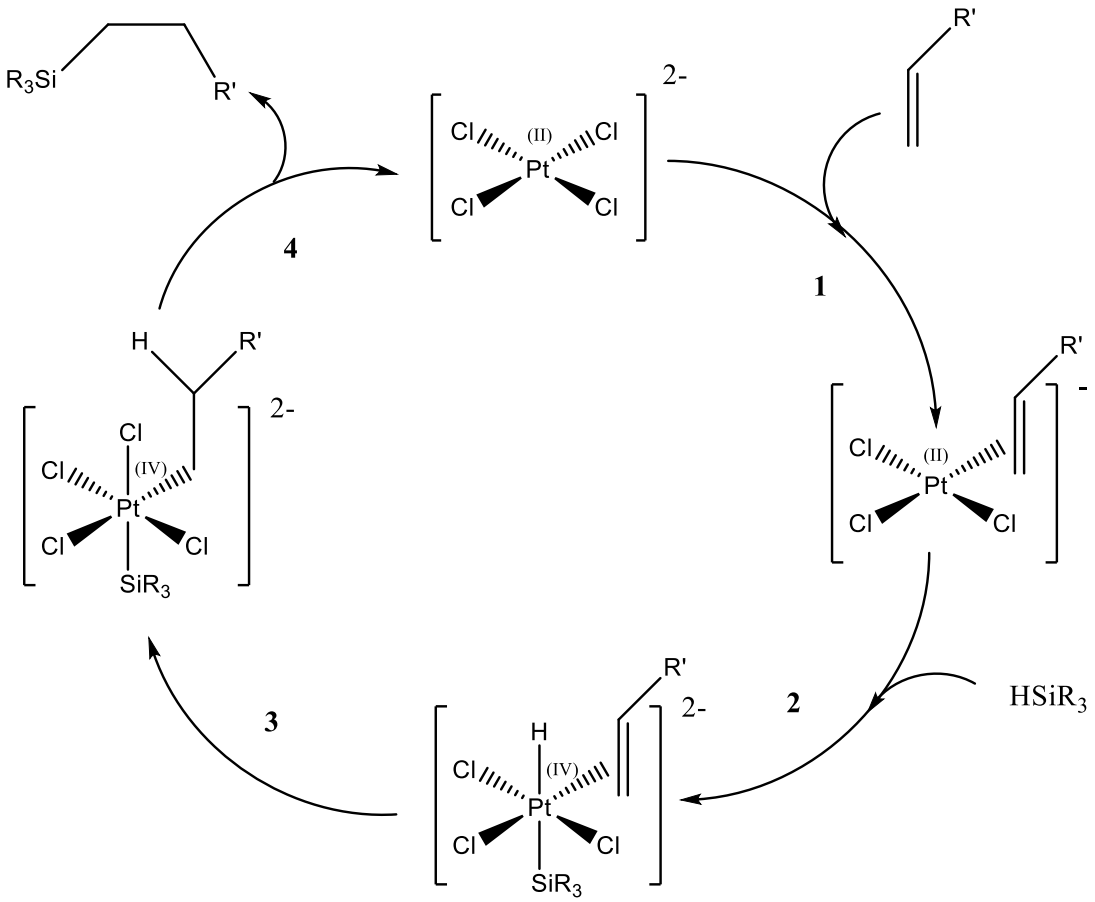

Figure 7.4: Sample catalytic cycle of the hydrosilylation of a vinyl functionalized silane and a silicon hydride-containing molecule using a platinum catalyst. Depending on the catalyst used, the ligands and the oxidation states of platinum may differ. Here, a simple platinum catalyst is shown to demonstrate the mechanism. The exact order of steps in this mechanism is debated in the literature. 1) A vinyl-terminated molecule first coordinates to the Pt catalyst. 2) A silicon hydride-containing molecule undergoes oxidative addition to the Pt catalyst. 3) A proton shifts to the vinyl group. 4) The molecule undergoes reductive elimination to produce the product and the cycle restarts.[52]

The properties of siloxane polymers can be modified by making copolymers with different monomers, and has been studied extensively at Queen's by former graduate students.[57-59] The replacement of some of the methyl groups in PDMS with phenyl groups was proposed to increase the material's affinity to aromatic hydrocarbons including BTEX compounds.[60] When synthesizing the functionalized copolymers, if the relevant monomers are readily available, it is easier to synthesize oligomer chains through condensation reactions as opposed to hydrosilylation. This procedure will be discussed in section 7.2.2. The syntheses of polydimethylsiloxane and poly(dimethyl-co-diphenyl)siloxane copolymer films are described in detail in sections 7.3.1 and 7.3.2.

7.2.2 Synthesis of Siloxanes by Alcoholysis, Hydrolysis and Condensation Reactions

Siloxane polymers can be rapidly synthesized from chloro-terminated or alkoxy-terminated silanes that undergo hydrolysis in water to produce intermediates terminated with silanol groups (Si-OH), which then condense to form siloxanes.[61] Since many of the starting reagents, such as chlorosilanes, are very reactive in the presence of water, silanols are quickly produced and rapid polymerization occurs causing oligomers to become insoluble.[61]

Alternatively, siloxane polymers can be synthesized in a more controlled fashion by generating alkoxy-terminated intermediates in a solution containing only trace amounts of water (in the air or solvent), allowing the condensation polymerization to occur slowly. Using alcohols as a solvent instead of water converts chlorosilanes to dialkoxysilanes, which are less reactive than silanols.[57, 61-62] The alcoholysis competes with hydrolysis, reducing the number of reactive sites so that a slower but controlled condensation reaction occurs.[61] The synthesis in the presence of alcohols is more suitable for the synthesis of copolymer mixtures from multiple precursors. The methanolysis and hydrolysis reactions of the two precursors used in the formation of a poly(dimethyl-co-diphenyl)siloxane copolymer are shown in Figure 7.5.

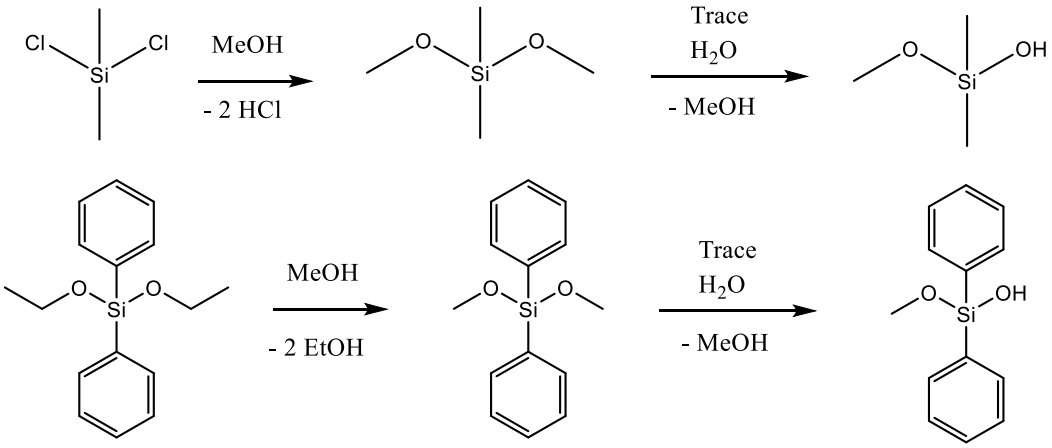

Figure 7.5: Methanolysis and hydrolysis reactions of dichlorodimethylsilane and diethoxydiphenylsilane. The majority of reactive sites in the polymer are blocked by methoxy groups to slow down the condensation of the polymer, trace water from the air and in the solvents will hydrolyse end sites which will condense to form polymer oligomers.

Once sufficient amounts of hydrolysed materials are present in the reaction, the mixture begins to condense forming the Si – O backbone of the oligomers (Figure 7.6).

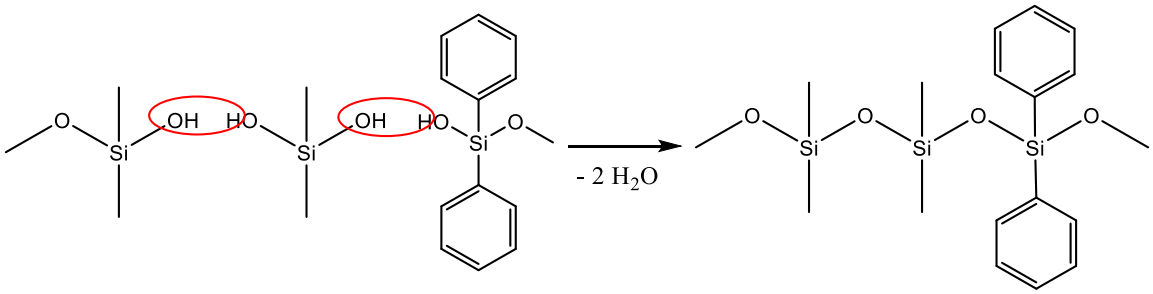

Figure 7.6: Condensation reaction of hydrolysed dimethyl and diphenyl silanes to form siloxane oligomers. In principle, if reagents are added alternating between precursors, the oligomers should have a random distribution of the two precursors.

After the condensation reaction is completed, the oligomers can be crosslinked by adding titanium (IV) isopropoxide dissolved in hexanes.[50] The crosslinking mechanism is not fully understood but is believed to involve the formation of Ti – O – Si bonds to TiO_2 nanoparticles incorporated within the structure of the material (Figure 7.7).[50]

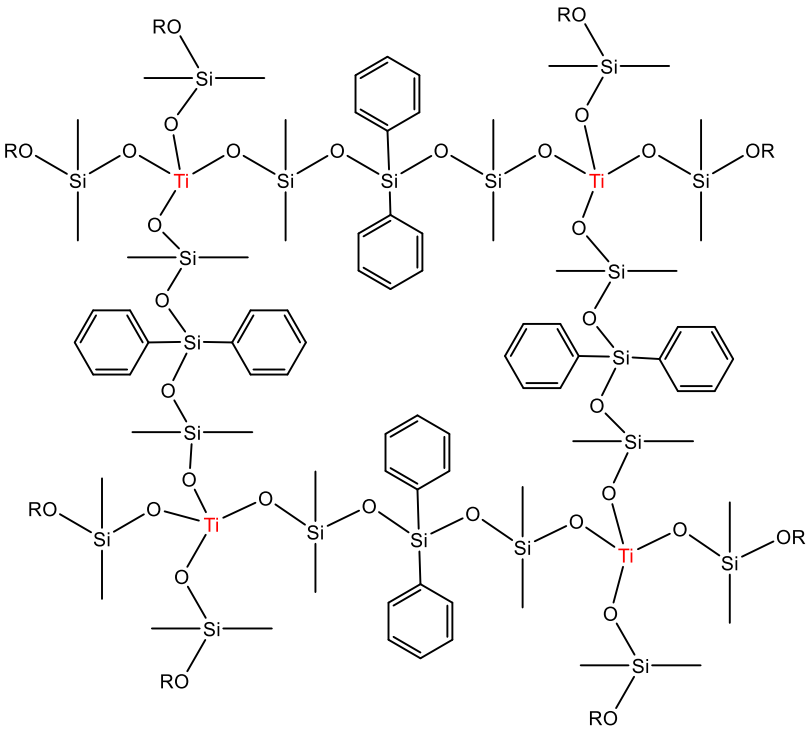

Figure 7.7: Proposed crosslinking mechanism of siloxane oligomers using titanium (IV) isopropoxide.[57] The exact mechanism is unknown but may also form Ti-O-Si bonds to titanium nanoparticles within polymer films.[50] These particles may also have electrostatic interactions with other chains that are not covalently bound to the nanoparticles.[50]

The specific conditions and synthetic procedures used to prepare PDMS-PDPS copolymer films are discussed in Section 7.3.2.

7.3 Experimental Setup and Methods

For vapour phase experiments, saturated solvent vapours were generated by bubbling nitrogen gas through a gas wash bottle containing approximately 100 mL of the desired solvent. These vapours were then further diluted with nitrogen gas using a two-channel flowmeter gas blender (Advanced Specialty Gas Equipment, Middlesex, NJ) to a range of concentrations between 5-30 % of the saturated vapour pressure.

To create an extraction volume of constant partial gas pressure, a small glass dome was placed over the film. This dome was made from the top portion of a glass vial cut using a diamond mill bit. The cell was placed above the cured siloxane films and additional PDMS was used to seal around the outside of the cell. Once cured, two syringe needles were inserted into the vial lid, one connected to the gas dosing setup and a second to allow the vapour to vent out of the room. The gas-dosing interferometric refractometry setup is shown in Figure 7.8. The full optical experimental setup was previously shown in Chapter 4.2.

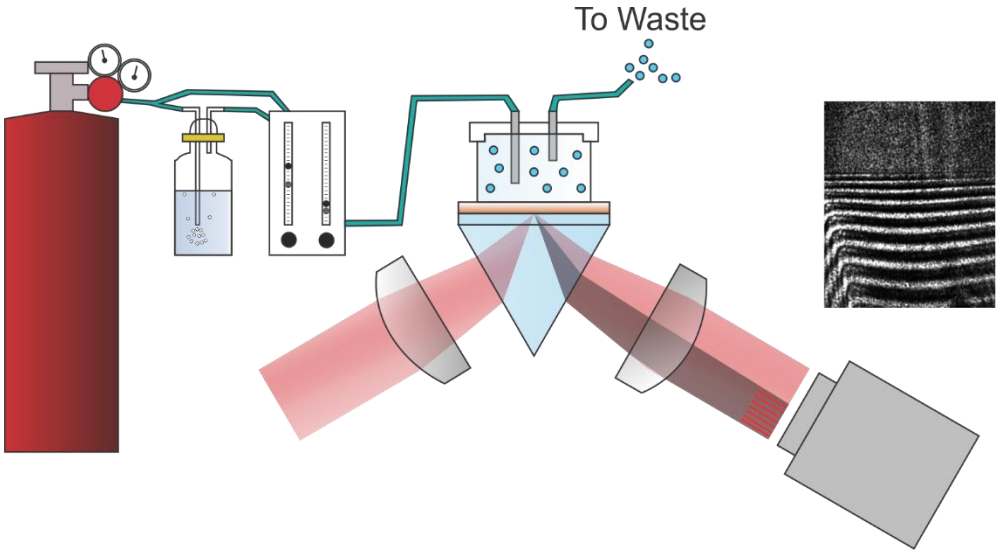

Figure 7.8: **Gas sensing experimental setup with the interferometric refractometer. Solvent vapours were generated by bubbling nitrogen through neat solvent in a gas wash bottle to generate saturated solvent vapours that were further diluted with additional nitrogen using a two-channel flowmeter gas blender to a range of different partial pressures. The vapours were flowed into a glass gas cell secured on top of the polymer film and an output channel was used to constantly vent the vapours out of the room. A sample refractometer image is also provided of a 25 µm PDMS film.**

The optical setup for the PDMS experiments, used cylindrical lenses (f = 20 mm) before the prism and (f = 50 mm) after the prism to focus down the fringes and collimate the divergent light. Previously run experiments with PDMS-PDPS copolymer films (Section 7.4.4) used spherical lenses (f = 25.4 mm) and (f = 50 mm) in the experimental setup. The spherical lenses caused aberration effects and distorted the images, causing curvature in the fringes due to focussing along the horizontal plane. Two images are shown for comparison to emphasize this effect in Figure 7.9.

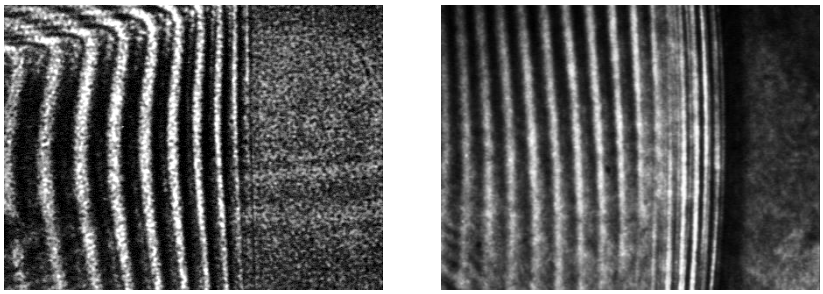

Figure 7.9: Comparison of images taken with cylindrical and spherical lenses in the optical setup. Left: An image of a 25 μm PDMS film taken using cylindrical lenses (f = 20 mm and f = 50 mm). The curvature in the fringes is due to film roughness and is not from optical distortion. Right: An image of a 25 μm PDMS-PDPS copolymer film taken using spherical lenses (f = 25.4 mm, f = 50 mm). Both the fringes and interface of total internal reflection are curved due to optical distortion from focusing in the horizontal direction.

7.3.1 Preparation of Polydimethylsiloxane (PDMS) Films

The PDMS films were prepared using a commercially available product, Dow Corning Sylgard 184 (Paisley Products of Canada, Scarborough, ON). The material was prepared by mixing 1.0 g of the PDMS base with 100 mg of the curing agent. Once sufficiently mixed, this was dissolved into 10 mL of hexanes and then approximately 150-200 μL was solvent cast onto 25 mm x 25 mm N-SF11 high index glass slides. After the solvent had evaporated, the films were cured in an oven at 70-80ºC for at least two hours. The resulting films were approximately 20-25 μm thick. The thickness could be increased by casting additional layers or increasing the polymer to hexane ratio. The film thickness could be decreased by further diluting the polymer solution or by spin coating the solution onto slides. The thickness of spin coated films will be

affected by the viscosity of the solution and the spin speed. The concentration of the precursor in the solvent dilution may be optimized to get the desired film thickness.

7.3.2 Preparation of Poly(dimethyl-co-diphenyl)siloxane (PDMS-PDPS) Films

A diphenyl functional group was added to PDMS to increase the affinity of the resulting polymer to aromatic compounds, i.e. BTEX class of volatile organic compounds. The PDMS-PDPS copolymer was synthesized by the acid-catalysed co-condensation of dichlorodimethylsilane (Sigma Aldrich, Oakville ON) and diethoxydiphenylsilane (Alfa Aesar, Ward Hill, MA) added at a 4:1 molar ratio. First, 4.0 mL (33 mmol) of dichlorodimethylsilane and 2.2 mL (8 mmol) diethoxydiphenylsilane were added dropwise alternating between the two reagents to a 20 mL vial containing 2.3 mL of glacial acetic acid and 1.9 mL of methanol while stirring. Caution needs to be taken as this reaction evolves corrosive HCl gas and needs to be performed in a fume hood. The precursors were slowly hydrolysed by moisture in the air and traces of water in methanol and subsequently condensed in solution to form oligomer chains.[61-62] The competing methanolysis slowed the polymerization and helped prevent the oligomers from gelling out of solution due to rapid hydrolysis with water.[61] After one hour of stirring, the oligomer solution was gently boiled to evaporate volatile components for one hour. Additional volatile compounds where removed subsequently using a stream of nitrogen gas for at least two hours. After condensation of the oligomers, 85.9 mg of PDMS/PDPS polymer was dissolved in 986 μL of hexanes and mixed with 12.7 μL of 10% v/v titanium (IV) isopropoxide (Sigma Aldrich, Oakville, ON) solution in hexanes. Approximately 150-200 μL of the mixture was solvent cast onto glass slides for the refractometry experiments as described in Section 7.4.4. Experimentally, white particle precipitates (likely TiO_2) were observed in the polymer films after solvent casting onto slides which agrees with the crosslinking mechanism suggested in Section 7.2.2. In the experiments on polymer coated silicon-on-insulator (SOI) devices (Chapter 8) the solution was spin coated at 2000 – 3000 rpm onto SOI devices. In both cases, the films were cured in an oven at 70 - 80°C for ~ 12 hours with more time given when necessary as the films often remaining partially tacky. The quality

problem was only observed with high loadings of polydiphenylsiloxane and was less problematic when the amount of PDPS was less than 20 mole percent of the polymer.[57]

7.3.3 Gas Flow Concentration and Uncertainty Calculations

The gas blender contained two flow channels each with a 150 mm graduated glass tube containing both a glass and stainless steel float that could be used for different flow rate ranges. The gas flow rate was not proportional to the float height and the values provided by the manufacturer followed a 3rd order polynomial relationship with the float readings as is shown in Figure 7.10A. The accuracy of the gas blender was quoted by the manufacturer as ± 5% of the full scale (±7.5 mm) which is shown as the blue lines on either side of the flow measurement in Figure 7.10A. Using the uncertainty on each channel, the error in gas concentrations can be approximated was calculated and is shown in Figure 7.10B for m-xylene, ethylbenzene, toluene, benzene and cyclohexane between 5-30% of the saturated vapour pressure. This error can be reduced if the flow meter is properly calibrated.

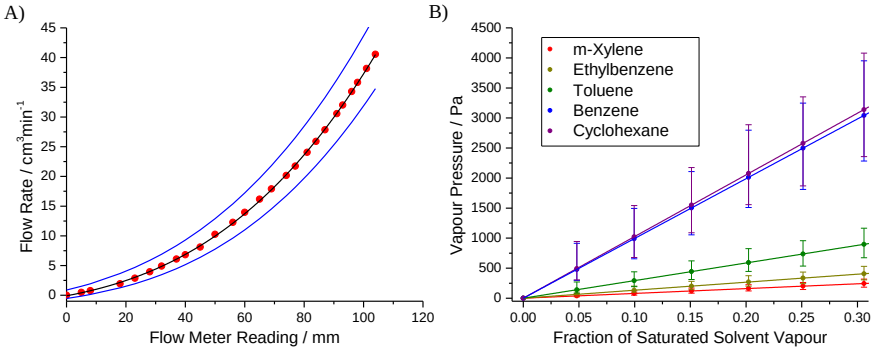

Figure 7.10: Flow rate correlation with glass float reading and uncertainties of non-polar vapour concentrations. A) The flow rate is fit with a 3rd order polynomial function (black line) with upper and lower uncertainties in the flow rate accuracy (± 7.5 mm) shown in blue. B): The uncertainty in vapour pressure for BTEX and cyclohexane solvents from 5-30% of the saturated vapour pressures.

The concentrations as partial pressures, $P°$, were calculated from the analyte fraction of the total flow rate, X_{Analyte} and the saturated vapour pressure, $P°_{\text{Sat}}$, at 20°C for the respective analytes.

$$P° = P°_{Sat}\left(\frac{Flow_{Analyte}}{Flow_{Analyte} + Flow_{N_2}}\right) = P°_{Sat}\,X_{Analyte} \tag{7.1}$$

The uncertainty of the concentration can be calculated from the uncertainties in the two flow rates, where the error in partial pressure concentration is related to the error in the fraction of analyte flow, X_{Analyte}.

$$\partial P° = P°\left(\frac{\partial X_{Analyte}}{X_{Analyte}}\right) \tag{7.2}$$

This can be estimated from the errors on the analyte flow rate and total flow rate respectively.

$$\left(\frac{\partial X_{Analyte}}{X_{Analyte}}\right)^2 = \left(\frac{\partial Flow_{Analyte}}{Flow_{Analyte}}\right)^2 + \left(\frac{\partial Flow_{Total}}{Flow_{Total}}\right)^2 \tag{7.3}$$

The total flow rate error is then easily obtained from the error in the analyte flow and nitrogen flow.

$$\partial Flow_{Total}{}^2 = \partial Flow_{Analyte}{}^2 + \partial Flow_{N_2}{}^2 \tag{7.4}$$

Since the flow rates are not linear with the scale on the channels, the upper error bars will be significantly larger than the lower error bars at each concentration. The estimate of errors on the BTEX concentrations are given in Table 7.1. A complete table giving the uncertainties in concentration of solvent vapours from X = 0.05-0.95 is provided in Appendix 7.1.

Table 7.1: Sample uncertainties of BTEX vapour pressures from X = 0.05-0.30. The two values in the error represent the lower and upper errors on the concentrations, i.e. 40 (-15, +35) implies that the pressure can range from 25 to 75 Pa. The saturated vapour pressures were used as provided by the chemical suppliers at 20°C.

X Analyte	$P°$ Benzene (Pa)	$P°$ Toluene (Pa)	$P°$ Ethylbenzene (Pa)	$P°$ m-Xylene (Pa)
0.05	480 (-180, +440)	140 (-54, +130)	64 (-24, +58)	40 (-15, +35)
0.10	990 (-330, +500)	290 (-100, +150)	130 (-40, +70)	80 (-27, +41)
0.15	1500 (-400, +600)	440 (-130, +180)	200 (-60, +80)	120 (-40, +50)
0.20	2000 (-500, +800)	590 (-150, +230)	270 (-70, +100)	160 (-40, +60)
0.25	2500 (-700, +700)	740 (-200, +220)	340 (-90, +100)	200 (-60, +60)
0.30	3000 (-800, +900)	900 (-220, +270)	410 (-100, +120)	240 (-60, +70)

7.3.4 Theory and Analysis Methods

The amount of analyte absorbed within a film can be calculated from the refractive index and thickness changes during exposure to an analyte, but requires the molar polarization of both the analyte and the polymer to be known. The molar polarizations for a series of solvents, P_i, were calculated using the measured refractive indices presented in Chapter 5,[63] n_i, the molar mass, M_i, and the density, ρ_i, as provided by the chemical suppliers.[64] The molar polarization of PDMS, and PDMS-PDPS copolymer films were calculated from experimentally obtained refractive indices, weighted molar masses from a single silicon containing unit, and the literature density of PDMS.[65] As was shown in Chapter 2, the molar polarization can be expressed as:

$$P_i = \frac{N_A \alpha_i}{3\varepsilon_0} = \left(\frac{n_i^2 - 1}{n_i^2 + 2} \right) \frac{M_i}{\rho_i} \tag{7.5}$$

Here, α_i is the electronic polarizability, N_A is Avogadro's number, and ε_0 is the vacuum permittivity. The parameters and the molar polarization for the reagents used in this chapter are given in Table 7.2. A typical image for a 25 μm thick PDMS film, solvent cast from Sylgard 184, is shown in Figure 7.11 along with a background subtracted and scaled image profile. The background subtraction processing techniques have been previously discussed in detail in Chapter 4.4.3.

The mole fraction concentration of an analyte within a film can be calculated from the refractive index and thickness changes of the film determined from Fourier analysis of the image profiles over time.

$$X(t) = \frac{P_{PDMS} - P_{PDMS}\left(\frac{n_{PDMS}^2 + 2}{n_{PDMS}^2 - 1} \right)\left(\frac{n_{mix}^2(t) - 1}{n_{mix}^2(t) + 2} \right)\left(1 + \frac{\Delta d(t)}{d_0} \right)}{P_{PDMS} - P_{PDMS}\left(\frac{n_{PDMS}^2 + 2}{n_{PDMS}^2 - 1} \right)\left(\frac{n_{mix}^2(t) - 1}{n_{mix}^2(t) + 2} \right)\left(1 + \frac{\Delta d(t)}{d_0} \right) - P_{Analyte}} \tag{7.6}$$

The concentration as a function of time, $X(t)$, is related to the refractive index of the mixture, n_{mix}, and the film thickness change, Δd, at a given time, t. The molar polarizations (P_{PDMS} and $P_{Analyte}$), initial film refractive index n_{PDMS} and thickness d_0 at $t = 0$ are also required. The derivation of this equation and processing method was previously shown in Chapter 3.2. The rate of concentration change in the bulk film

is governed by Fickian diffusion (Chapter 3.3) and can be fit with the following functions originally derived by Crank: [66]

$$X(t)_{uptake} = X_{\infty}\left[1-\frac{8}{\pi^2}\sum_{n=0}^{\infty}\frac{1}{(2n+1)^2}\exp\left(-\frac{(2n+1)^2 D\pi^2 (t-t_0)}{4d^2}\right)\right]$$
$$X(t)_{release} = X_{\infty}\left[\frac{8}{\pi^2}\sum_{n=0}^{\infty}\frac{1}{(2n+1)^2}\exp\left(-\frac{(2n+1)^2 D\pi^2 (t-t_0)}{4d^2}\right)\right] \quad (7.7)$$

Table 7.2: Refractive indices, molar mass, densities and molar polarizabilities of selected organic solvents, PDMS and PDMS-PDPS copolymer. The molar polarizations were calculated using equation (7.5). The refractive indices were presented in Chapter 5,[63] unless otherwise specified. The solvent densities were used as provided by the supplier.

Material	Refractive Index n_{1550} [63]	Molar Mass, M (g/mol)	Density, ρ (g/cm^3)[64]	Molar Polarization, P (cm^3/mol)
Benzene	1.4789	78.11	0.874 (298 K)	25.3
Toluene	1.4760	92.14	0.865 (298 K)	30.0
Ethylbenzene	1.4759	106.17	0.867 (298 K)	34.5
m-Xylene	1.4769	106.17	0.868 (298 K)	34.6
Cyclohexane	1.4147	84.16	0.779 (298 K)	27.0
Acetone	1.3483	58.08	0.791 (298K)	15.7
Methanol	1.3174	32.04	0.791 (298K)	7.98
2-Propanol	1.3661	60.10	0.785 (298K)	17.2
PDMS	1.3997 (1554nm) [65]	74.15*	1.03 [65]	17.4
PDMS-PDPS	1.4586	98.98**	1.03 [65]†	26.2

* Molar mass of PDMS is given as one repeating unit of PDMS, $Si(CH_3)_2O$.
** Molar mass of PDMS-PDPS is given as the weighted average silicon containing unit in the polymer.
† The density of PDMS-PDPS copolymer was unavailable so the density of PDMS is used as an estimate.

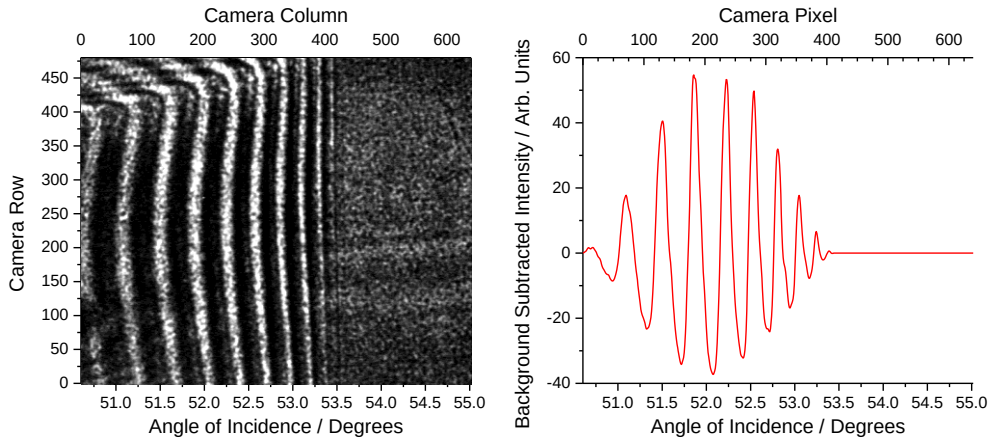

Figure 7.11: Refractometer image and background subtracted profile for a 25 µm PDMS film. The left region of the image shows thin film interference in the Fresnel reflection portion of the image and the bright region on the right shows total internal reflection in the prism above the critical angle with the film. The profile has been processed to remove the non-periodic noise above the critical angle, the fringes have been background subtracted and multiplied with a cosine function to remove intensity discontinuities on the limits prior to Fourier processing.

For this system, the quality of the fit improves substantially when fitting to a two-rate diffusion model instead of a single-rate diffusion as in equation (7.7).

$$X(t)_{uptake} = X_1\left[1-\frac{8}{\pi^2}\sum_{n=0}^{\infty}\frac{1}{(2n+1)^2}\exp\left(-\frac{(2n+1)^2 D_1\pi^2(t-t_0)}{4d^2}\right)\right] + X_2\left[1-\frac{8}{\pi^2}\sum_{n=0}^{\infty}\frac{1}{(2n+1)^2}\exp\left(-\frac{(2n+1)^2 D_2\pi^2(t-t_0)}{4d^2}\right)\right] \quad (7.8)$$

This may be the result of the complexity of the PDMS matrix, which contains silica nanoparticles and cross-linked oligomers. Diffusion into different domains in the material may then occur on different time scales. Alternatively, one rate may be related to restructuring of the surface layers of the film and the second rate related to diffusion through the bulk. The fit to a single-rate diffusion process (equation (7.7)) and two-rate diffusion process (equation (7.8)) are shown in Figure 7.12 for the uptake and release of 200 Pa m-xylene into PDMS. It is clear from the residual of the fits that the model involving a two-rate diffusion process agrees better with our data. The fitting parameters for the fits in Figure 7.12 are given in Table 7.3.

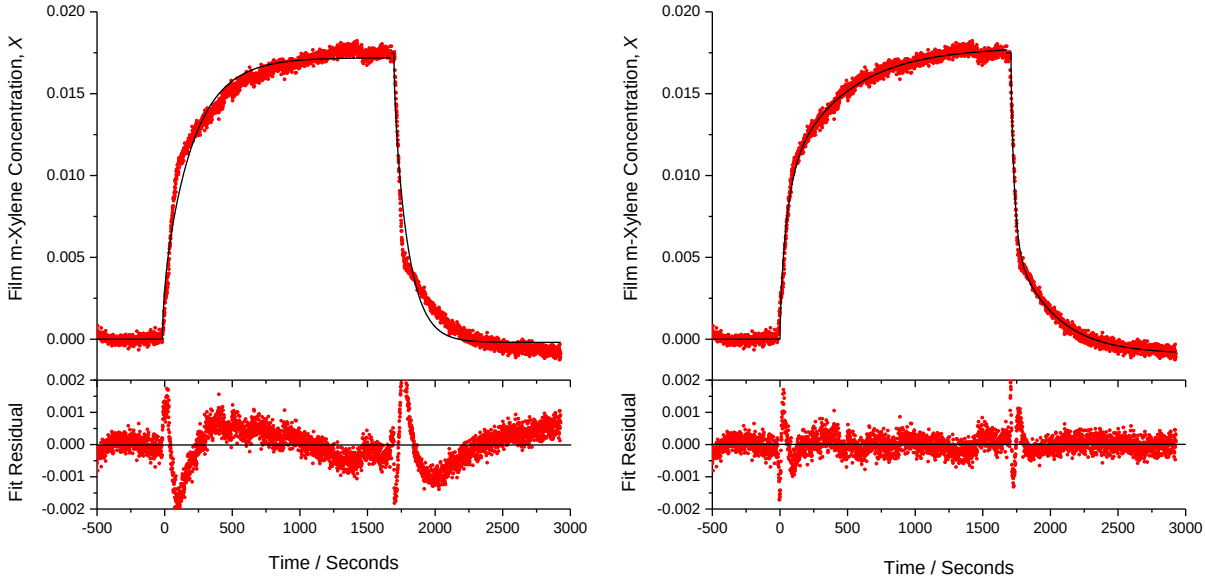

Figure 7.12: Comparison between single-rate and two-rate diffusion processes for the uptake and release of 200 Pa m-xylene within a 25 µm PDMS film. (Left) The fit to a single diffusion process (eqn. (7.7)) is shown with the residual plotted in the bottom panel. The fit clearly deviates from the data in multiple places. (Right) A two-rate diffusion fit (eqn. (7.8)) is shown with the residual indicated below. The fit from a two-rate process agrees more closely with the experimental data.

The spikes in the residuals of Figure 7.12 show the error in the curvature from the fitting models. The error is magnified in the steeper portions of the curve and is strongly affected by the time (t = 0) used to switch between fitting functions. These spikes indicate that there may be additional affects that are not treated with our model and should be explored in future work. For example, it is possible there is uneven portioning of analyte at the top surface of the film which changes the concentration profile of the system. Also currently there are no parameters to deal with surface roughness or birefringence, both of which are expected with polymer systems. The birefringence of the solvent cast siloxane films was tested by observing the films between cross polarizers and no interferences were observed. We believe that our films can therefore be treated as isotropic. Autocorrelation functions can be used to assess the improvement when adding additional parameters to the fitting function.

To account for variability of the diffusion fits and any improper local minima being captured during least squares curve fitting, the diffusion coefficients, D_1, and D_2, are reported from the average of a minimum of five different absorption and release experiments with different vapour concentrations. The

average diffusion rates are reported in Section 7.4 with 1σ standard deviation of the values. When necessary, Grubb's test was used to remove a single statistical outlier prior to calculating the average value. The resulting diffusion coefficients are presented for non-polar and polar molecules in the following result section.

Table 7.3: Fitting parameters for a single and two-rate diffusion fit to the uptake of 200 Pa m-xylene into PDMS (Figure 7.12). Here, the fitting parameters are presented for the fits shown in Figure 7.12, more accurate diffusion coefficients are presented in the results sections and are averaged from multiple experiments.

	Uptake (Single Fit)	**Release (Single Fit)**	**Uptake (Double Fit)**	**Release (Double Fit)**
X_1	0.0172	0.0177	0.0079	0.0104
D_1 ($\times 10^{-8}$ cm^2/s)	1.22	2.35	4.70	9.53
X_2	---	---	0.0100	0.0080
D_2 ($\times 10^{-8}$ cm^2/s)	---	---	0.620	0.852

7.4 Results of Sorption Experiments into Siloxane Films

The results for the sorption of non-polar and polar compounds into PDMS and PDMS-PDPS films are described in the following sections. For each set of experiments, the refractive index and thickness changes are first presented from equilibrium measurements to demonstrate the trend upon exposure to each analyte. For each sorption experiment, the analyte concentration within the film is calculated from the refractive index and thickness data using equation (7.6) during both the uptake and release processes (e.g. Figure 7.12). The uptake and release processes are then fit with a two-rate diffusion equation (eq. (7.8)) and the overall equilibrium limiting concentrations (X_{total}) are plotted by vapour concentration. The diffusion coefficients are then averaged from the fits to at least five different concentrations and are compared with literature values. Finally, the partition coefficients are calculated from the equilibrium analyte concentrations within the film.

7.4.1 Sorption of Non-Polar Molecules into PDMS

Polydimethylsiloxane is known to have a strong affinity to many non-polar molecules, including aliphatic, cyclic, aromatic, and polyaromatic hydrocarbons.[23-27] The BTEX class of volatile contaminants (benzene, toluene, ethylbenzene and xylenes) are of particular interest in sensing applications as they are frequently released in industrial processes and pose many health hazards from both ingestion and inhalation.[46-49] The uptake of BTEX vapours into a PDMS film was studied at a variety of concentrations from 5-30% of the saturated vapour pressures. The same film was also exposed to cyclohexane for comparison with a non-aromatic cyclic hydrocarbon. In each case, the refractive index and relative thickness changes, Δn and $\Delta d/d_0$, were calculated from the average of at least 100 points once equilibrium was reached between the film and the analyte (Figure 7.13).

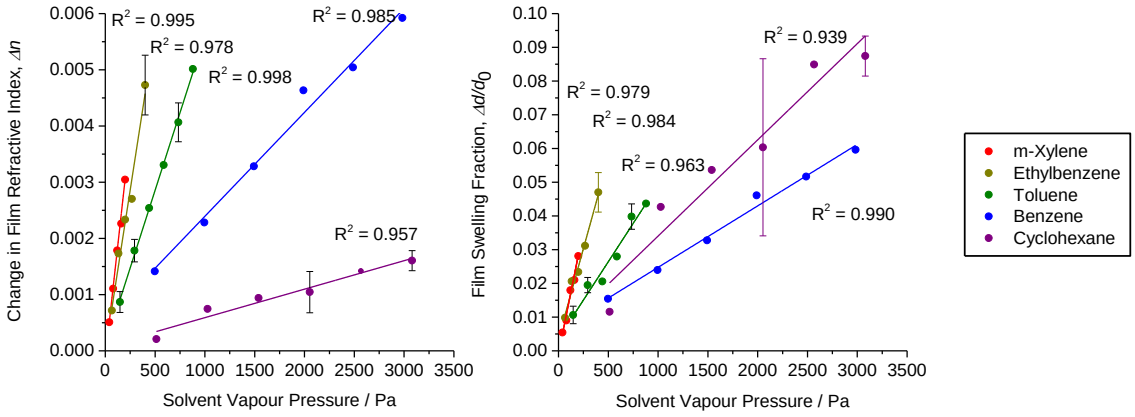

Figure 7.13: Refractive index and relative thickness change during the uptake of BTEX and cyclohexane vapours into PDMS. The vapour pressures are plotted from 5-30% of the saturated vapour pressures for each solvent and error bars (1σ standard deviation) are given for experiments where a single concentration was tested three or more times.

The refractive index and thickness changes showed strong linearity with Pearson's correlation coefficients ranging from R^2 = 0.939-0.998. The large error bar in the swelling data from cyclohexane was the result of a spike in one of the three values at this concentration and was likely due instability of the gas dosing setup. The other error bars are more representative of the typical 1σ standard deviations during measurements.

The refractive index and thickness changes were used to calculate the mole fraction of sorbent within the polymer film as a function of time according to equation (7.6). The uptake profiles showed

similar trends for the different gas concentrations, and could all be fit well with a sum of two diffusion processes, with each converging to a different asymptotic value, X_{Total}. The fits to the uptake and release profiles of m-xylene at partial pressures from 40 to 200 Pa into PDMS are shown in Figure 7.14 and Figure 7.15 with the respective fit residuals.

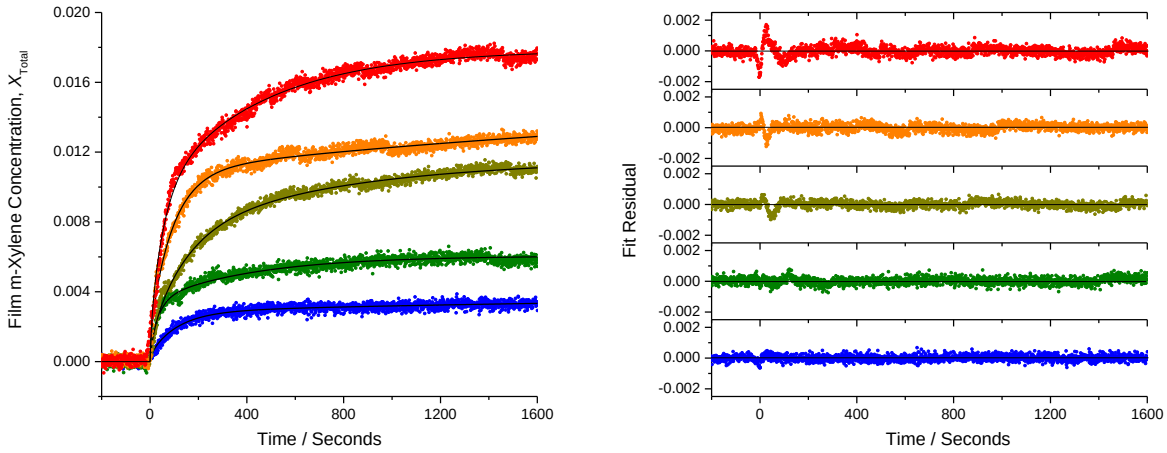

Figure 7.14: Uptake profiles for the exposure of PDMS to 40-200 Pa of m-xylene vapour. The plot shows the uptake during exposure to 40, 80, 120, 160, and 200 Pa (blue to red traces respectively) with the two-rate diffusion process fits shown as black solid lines. For time before t = 0 s the data is fit to 0, as the function is not defined. The respective fit residuals are shown in the right panel.

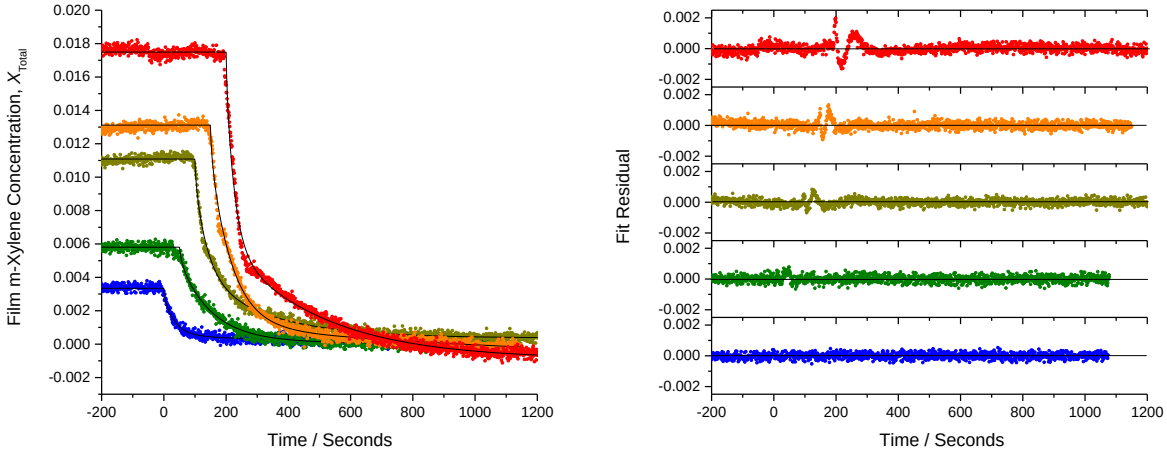

Figure 7.15: Release profiles for the exposure of PDMS to 40-200 Pa of m-xylene vapour. The plot shows the release after exposure to 40, 80, 120, 160, and 200 Pa (blue to red traces respectively) with the two-rate diffusion process fits shown as black solid lines. The respective fit residuals are shown in the right panel. Each dataset has been artificially offset by 50 seconds from the lower traces to better illustrate the trends with concentration. For time before t = 0 s, the data is fit to the sum of $X_1 + X_2$, as the function is not defined.

In Figure 7.15, the release curves were artificially offset by 50 seconds to make the trends more apparent. The residuals in Figure 7.14 and Figure 7.15 were randomly dispersed indicating that the function fit well to the data. It is notable that there are spikes at the beginning of the uptake and release for higher concentrations but this was not observed at lower pressures. These errors are partly the result of experimental noise and inaccuracy in the start time, t_0, as the fit switches from a constant value to the fitting curve.

The asymptotic mole fraction, X_{Total}, was calculated from the sum of the two amplitude terms, X_1 and X_2, obtained by fitting the data from each solvent concentration to equation (7.8). In certain cases, the film may not have fully reached equilibrium, and the fits of the uptake and release data converged to different values of X_{Total}, so the trends were assessed separately. The asymptotic saturated mole fractions as a function of vapour partial pressure are shown in Figure 7.16 for BTEX compounds and cyclohexane. At some vapour concentrations, experiments were run in triplicate and the 1σ standard deviations were given as error bars on these values. The uncertainty on the other points was expected to be comparable.

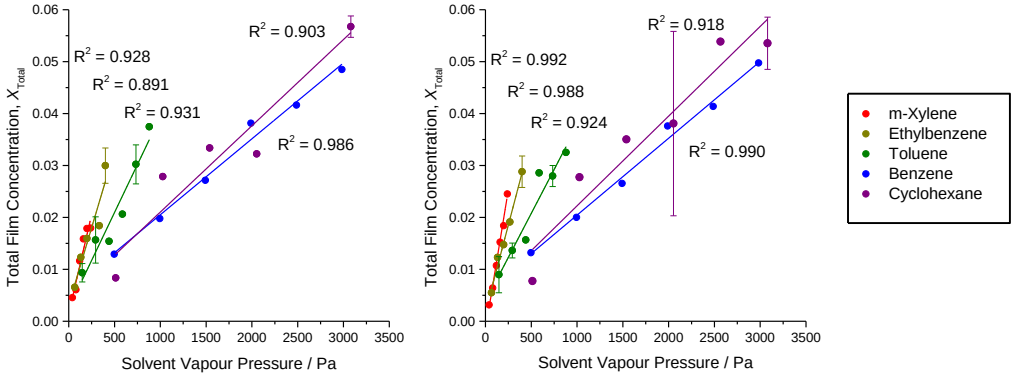

Figure 7.16: The equilibrated concentration, X_{Total}, of non-polar analytes within the PDMS film as a function of ambient vapour concentration. The left graph shows X_{Total} calculated from the asymptotic mole fraction of the uptake data and the right graph shows the corresponding values from the release fits. The trends of the uptake and release data are comparable, but the fits converged to different saturated film concentrations. Error bars show 1σ standard deviation on measurements that were run in triplicate.

The vapour pressure ranges in Figure 7.16 for benzene and cyclohexane are much larger than the other BTEX compounds as their saturated vapour pressures (9900 Pa and 10 000 Pa)[64] are five to ten times larger those of m-xylene, ethylbenzene and toluene (800, 1300 and 2900 Pa respectively)[64].

When quantifying the affinity of a polymer to an analyte, both the refractive index and thickness changes are required. If only one of the two parameters is used, incorrect conclusions may be drawn. For example, from the refractive index data (Figure 7.13), it appears that PDMS does not have a high affinity to cyclohexane, although the uptake resulted in close to 10% swelling of PDMS under the larger vapour concentrations. The low refractive index sensitivity for cyclohexane is a result of the similarity in refractive index of cyclohexane, n_{1550} = 1.4147[63], to that of PDMS, n_{1554} = 1.3999[65]. The BTEX solvents have much higher refractive indices, n_{1550} = 1.4759-1.4789[63], and thus have a larger contrast with PDMS. The film may appear to have a stronger affinity to BTEX than cyclohexane, even though the equilibrium concentrations of the analytes in the film were comparable.

The diffusion coefficients, D_1 and D_2, from the uptake fits were averaged from the measurements at different vapour concentrations. Occasionally, if one of the fit values failed Grubbs' test for statistical outliers, it was removed before calculating the average and the 1σ standard deviation. The average diffusion rates with errors of 1σ standard deviation are reported for BTEX and cyclohexane uptake into PDMS in Table 7.4.

The 1σ standard deviation of the averaged values of D_1 and D_2 in Table 7.4 are much larger than the uncertainty of the fit parameters. This may be due to the temperature dependence of the diffusion coefficients. While the experiments were run at room temperature, 21-23°C, the room temperature was not well controlled and, at times, may have drifted over a 2-3°C range due to chiller and ventilation cycling in the instrument room. Other factors, including fluctuations in vapour flow rate, may have also been responsible for the deviations. While there are some deviations in diffusion rates between the uptake and release data, they should be identical, if the process was purely diffusion controlled. Any other processes – including restructuring of the polymer, binding and release from particular binding sites and delamination of the polymer – would result in a hysteresis with different rates for the forward and reverse reactions. The

remarkable agreement between uptake and release diffusion constants supports our hypothesis that the uptake and release are diffusion controlled processes.

Table 7.4: The average diffusion rates determined from the uptake and release data of BTEX and cyclohexane into a 25 µm PDMS film. The average is calculated from at least 5 values at different concentrations with the errors given as 1σ standard deviation. The corresponding asymptotic mole fractions were previously shown in Figure 7.16.

	Uptake		Release	
Solvent	D_1 **(×10^{-8} cm^2/s)**	D_2 **(×10^{-8} cm^2/s)**	D_1 **(×10^{-8} cm^2/s)**	D_2 **(×10^{-8} cm^2/s)**
Benzene	5 (1)	0.3 (1)	10 (2)	1.3 (3)
Toluene	6 (3)	0.1 (1)	6 (2)	0.4 (3)
Ethylbenzene	5 (1)	0.09 (6)	4 (2)	0.4 (1)
m-Xylene	3 (1)	0.4 (3)	6 (2)	0.5 (5)
Cyclohexane	13 (6)	0.7 (6)	14 (5)	0.5 (4)

We found that a fit to two-rate diffusion process gave much better agreement with our data. Typically, literature on PDMS only gives one diffusion coefficient. Since our method is an optical method, we could be detecting both penetration into the uppermost layers of the film from air and diffusion through the film that may be occurring with different time scales. This model is similar to what has been proposed for SU-8 photoresist films (Chapter 6).[20, 67] Sylgard 184 has a significant amount of silica nanoparticle filler in the precursor, and the two diffusion coefficients may also represent partitioning into different domains of the material. Finally, it is possible that one of the processes is due to a slow and reversible restructuring of the film following analyte uptake. In order to fully understand this diffusion process, additional experiments on related polymers with and without silica filler and possibly with different morphologies are needed. These experiments will not be discussed here but could be performed as future work on this project.

There are many different ways diffusion coefficients are calculated in the literature, as was discussed previously in Section 3.3.2. Not surprisingly, we therefore find a large range of reported values for a given system as was shown by Lue and coworkers where they report the diffusion of saturated benzene

vapour through PDMS as D = 4.67 - 9.97 $\times 10^{-7}$ cm^2/s depending on the calculation method used.[33] The diffusion of analytes into polymers from aqueous solutions is typically slower compared with diffusion from air, and has been reported to differ by a factor of 10.[34] A compilation of literature diffusion values for solvent vapours through PDMS are shown in Table 7.5.

Table 7.5: Experimental and literature diffusion coefficients for BTEX and cyclohexane vapours into PDMS films. References [31-32, 35-36] had PDMS materials in-line with different forms of mass spectrometry to detect diffusion through PDMS membranes, while reference [33] calculated diffusion rates using gravimetric data and reference [34] used an SPME syringe with GC/FID. This table shows D_1 and D_2 from the two-rate diffusion fits averaged from both the uptake and release data.

Solvent	This Work D ($\times 10^{-6}$ cm^2/s)	Literature
Benzene	0.08(3), 0.009(8)	0.467 – 0.997 [33], 1.01 [34], 1.34 [32], 2.2 [35], 2.8 [37, 39], 4.8 [31], 4.9 [36]
Toluene	0.06(2), 0.003(2)	0.177-0.320 [33], 0.44 [34], 1.15 [32], 1.8 [35], 3.5 [36], 4.0 [31]
Ethylbenzene	0.06(4), 0.004(4)	0.47 [32], 1.7 [36]
m-Xylene	0.05(2), 0.005(4)	0.51 [32], 1.2* [35]
Cyclohexane	0.13(5), 0.009(9)	0.18 – 0.761 [33]

* Value is for o-Xylene

The values of diffusion coefficients that we report for PDMS are lower by one order of magnitude compared to many literature values. It is plausible that differences in the composition of the PDMS studied in this experiment were responsible for the slower diffusion rates we observed. None of the literature studies made measurements on Sylgard 184; several groups studied Sylastic PDMS, and precursors from other manufacturers. The difference in degree of crosslinking and filler material may substantially affect the rate of diffusion of vapours through polymers and could explain these differences. Also, as was discussed in Chapter 3.2.2, depending on the methods that were used to determine the diffusion coefficients, there may be substantial error in some of the literature values.

The partition coefficients were also calculated from the saturated film concentrations and film thickness data and will be discussed together with those for polar compounds in Section 7.4.3. Comparison to the uptake of analytes into PDMS-PDPS copolymer films will also be discussed in Section 7.4.4.

7.4.2 Sorption of Polar Molecules into PDMS

The diffusion of three polar molecules, methanol, isopropanol, and acetone, into PDMS was also studied. Since PDMS is hydrophobic, it is expected that there would be only a weak affinity to any of these solvents. This was definitely true for both alcohols tested, as neither showed a significant change in the film's refractive index and caused less than 1% relative swelling (Figure 7.17). Exposure to acetone caused the film to swell by $\Delta d/d$ = 1-3 % and the film refractive index to decrease by Δn = 2-8×10^{-4}. Although these are larger changes than were observed with either methanol or isopropanol, it is still a much smaller response when compared to the non-polar analytes discussed in the previous section. Since the film swells, the decrease in refractive index is not surprising, as the refractive indices of acetone (n_{1550} = 1.3483), methanol (n_{1550} = 1.3174) and isopropanol (n_{1550} = 1.3661) are all much lower than that of PDMS.[63]

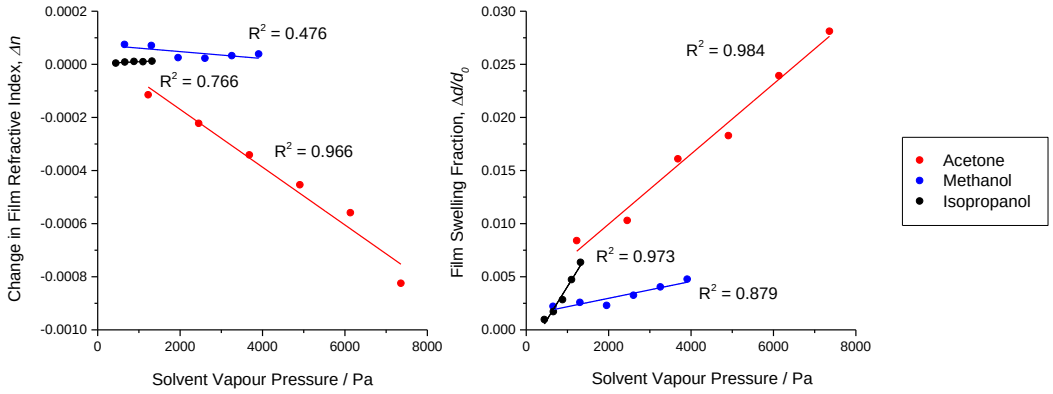

Figure 7.17: The refractive index change and relative swelling of PDMS from the uptake of acetone, methanol, and isopropanol. No significant refractive index changes were observed when PDMS was exposed to methanol or isopropanol, which was accompanied by only minor swelling, < 1%. The film decreased in refractive index and swelled up to 3% when exposed to acetone vapours.

Similar to the previous section, the analyte concentration within the film was calculated using equation (7.6) and the saturated concentrations and diffusion coefficients were determined from fits to equation (7.8). The equilibrium analyte concentrations, X_{Total}, as a function of ambient vapour concentration are shown in Figure 7.18. As before, the analyte concentrations within the film were comparable between both the uptake and release data.

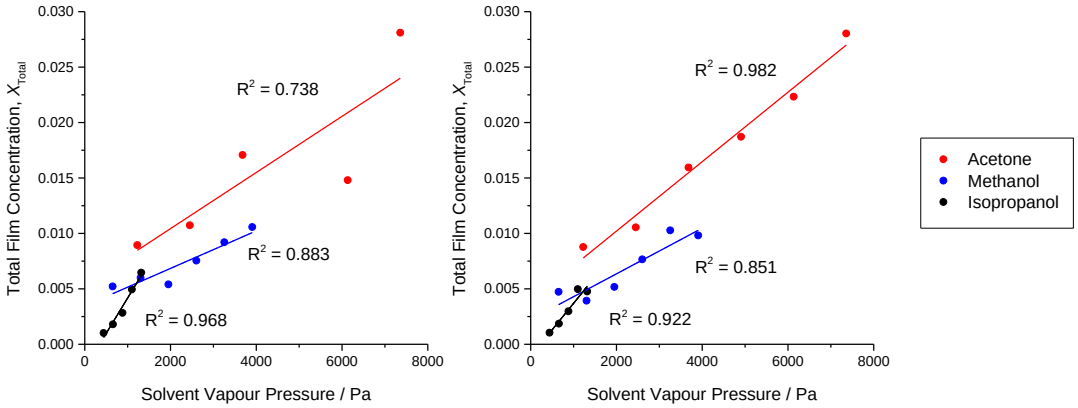

Figure 7.18: The saturated film concentrations (X_{Total}) determined from exposure of PDMS to a range of concentrations of acetone, methanol, and isopropanol vapours. The left trace shows the limiting mole fraction from the uptake fits and the right trace shows the same from the release fits.

It is important to note the much higher solvent vapour pressures in Figure 7.18, as the sensitivities (slopes) of each of the analytes shown in Figure 7.18 were much smaller than all of the non-polar analytes discussed in Section 7.4.1. The diffusion coefficients for methanol, isopropanol, and acetone were averaged from the different uptake experiments and some interesting trends were observed. The resulting diffusion coefficients are given in Table 7.6.

Table 7.6: Average diffusion coefficients, D_1 and D_2, for the uptake and release of acetone, methanol, and isopropanol into PDMS. It was not possible to calculate diffusion coefficients from the uptake data of methanol due to irregularities in the data. The uptake into isopropanol fit to a single diffusion process, so D_2 was left blank. The equilibrium analyte concentrations in the film were previously shown in Figure 7.18.

	Uptake Data		Release Data	
Solvent	**D_1 ($\times 10^{-8}$ cm^2/s)**	**D_2 ($\times 10^{-8}$ cm^2/s)**	**D_1 ($\times 10^{-8}$ cm^2/s)**	**D_2 ($\times 10^{-8}$ cm^2/s)**
Acetone	25 (9)	1 (1)	34 (14)	2.3 (4)
Methanol	---	---	13 (7)	1.1 (8)
Isopropanol	14 (4)	---	24 (6)	---

When exposing the films to isopropanol, the uptake and release were much faster than previously observed with the non-polar BTEX and cyclohexane vapour. This would be expected as methanol, acetone,

and isopropanol are smaller molecules than BTEX and cyclohexane. Additionally, given that PDMS is non-polar, the polar solvents will not have strong interactions within the polymer, allowing the molecules to travel more quickly through the film. The uptake and release of isopropanol fit to a single diffusion process and no values of D_2 were obtained for this system. A sample fit to the uptake and release of 880 Pa isopropanol exposed to PDMS is shown in Figure 7.19A. Additionally, during the experiments with methanol, the concentration seemed to reach a maximum value and then decreased to an equilibrated value as time progressed. This made it impossible to extract diffusion coefficients from the uptake data (Figure 7.19B). However, since each experiment approached an asymptotic value, it was still possible to determine the saturated film concentrations X_{Total} from the uptake data by fitting to the data before the uptake began and the data around equilibrium. The effect observed during the uptake of methanol may be the result of film restructuring, where the saturated concentration after restructuring is slightly lower than what was originally able to diffuse into the film over a short time scale, causing some of the analyte to partition back out of the film. More experiments are required to fully understand this effect.

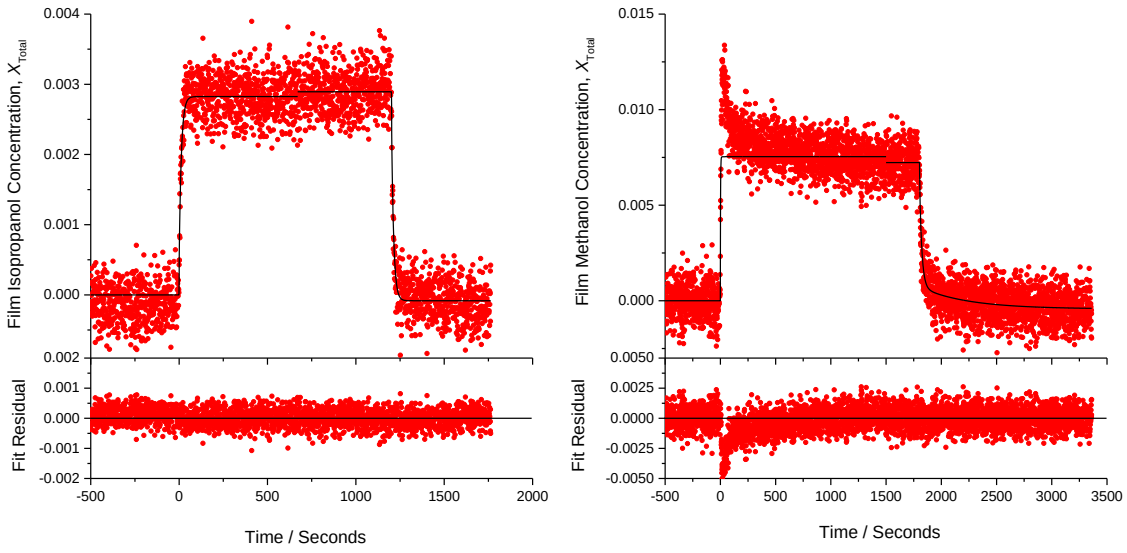

Figure 7.19: Uptake and release of 880 Pa isopropanol and 2600 Pa methanol vapour within a PDMS film. Left: The uptake and release of isopropanol was fit to a single diffusion coefficient, with the fit residual shown in the bottom panel. Right: The exposure to methanol was fit to a two-rate diffusion model, though it was not possible to extract diffusion coefficients from the uptake dataset. The limiting mole fraction was still estimated from the data set from both the uptake and release data.

The uncertainties on the diffusion coefficients for these analytes were very large, which is a result of the high noise level and the lower saturation concentrations compared with the non-polar molecules. For example, the response to 5% saturated isopropanol (220 Pa) was well below the detection limit and was not included in the analysis. The average diffusion coefficients from the uptake and release data of acetone, methanol, and isopropanol are given in Table 7.7. Literature values are provided for comparison.

Table 7.7: Experimental and literature diffusion coefficients for acetone, methanol, and isopropanol into PDMS. Reference [32] measured diffusion through PDMS in-line with a mass spectrometer and reference [33] used gravimetric methods to determine diffusion rates. Our work lists an average of the diffusion coefficients for the uptake and release processes D_1 and D_2 where applicable.

Solvent	This work D_1 and D_2 ($\times 10^{-6}$ cm^2/s)	Literature
Acetone	0.3(1), 0.02(1)	0.10 [32]
Methanol	0.13(7), 0.011(8)*	0.30 [32], 7.09 [33]
Isopropanol	0.19(7)**	---

* Values reported only from release data

** Isopropanol data was fit to a single diffusion process.

There were not many values reported in the literature for the diffusion of polar molecules into PDMS. Since PDMS is quite hydrophobic, the partitioning of polar compounds was very small. For SPME of polar molecules, a polar extraction matrix like polyacrylate (PA) is often used.[25, 68-69] The large diffusion coefficients reported here for acetone and methanol of 3×10^{-7} cm^2/s and 1×10^{-7} cm^2/s are in close agreement to the diffusion coefficients reported by Boscaini and coworkers of 1×10^{-7} cm^2/s and 3×10^{-7} cm^2/s respectively.[32] The value reported by Lue and coworkers for diffusion of methanol through PDMS was faster by almost two orders of magnitude compared to our values reported here.[33] Due to the small amount of partitioning of polar compounds into PDMS, it is not surprising that there would be a larger deviation in reported values. Experiments with polar compounds will likely have a higher noise level compared to those with non-polar compounds, causing a larger uncertainty on calculated diffusion coefficients. We were unable to locate a literature value for the diffusion of isopropanol into PDMS, though it is expected to be comparable to both acetone and methanol. Using the saturated mole fraction and swelling data, it is possible

to determine the partition coefficients of analytes within the polymer matrix relative to air. A method allowing us to determine partition coefficients from the data presented in the last two sections will be discussed in the Section 7.4.3.

7.4.3 Determination of Partition Coefficients into PDMS

The process of using polymer materials to extract analytes from air or aqueous solution is known as solid phase microextraction (SPME).[24-25] This technique was described in detail with a discussion of the theory behind partition coefficients in Chapter 3.5. The basic theory behind calculating partition coefficients will be discussed here for analytes adsorbed into PDMS films.

The sorption data previously discussed can be used to estimate partition coefficients, K_{fa}, between PDMS and air for different analytes. In order to calculate partition coefficients, the concentration in both phases must be expressed in similar units (e.g. mol/L), since mole fraction concentrations within the film and in air are not directly comparable. The film volume is calculated from the area of the glass gas cell (A = 2.60 cm^2) and the film thickness at the time of equilibrium, $d(t \rightarrow \infty)$. The initial amount of polymer, N_{PDMS} (in moles) was calculated from the initial thickness at t = 0 seconds, the density of cured PDMS, ρ_{PDMS} = 1.03 g/cm^3,[65] and the molar mass of a monomer unit is M_{PDMS} = 74.15 g/mol.

$$N_{PDMS} = \frac{\pi r^2 d\left(t=0\right)\rho_{PDMS}}{M_{PDMS}} \tag{7.9}$$

It then becomes straightforward to use the saturated mole fraction to calculate the moles of analyte in the polymer, and thus the concentration in mol/L. Rearranging

$$X_{analyte} = \frac{N_{analyte}}{N_{analyte} + N_{PDMS}} \tag{7.10}$$

we obtain an expression for $N_{analyte}$.

$$N_{analyte} = \frac{N_{PDMS} X_{analyte}}{\left(1 - X_{analyte}\right)} \tag{7.11}$$

The concentration of the analyte in the film can then be calculated in units of mol/L.

$$C_{film} = \frac{N_{analyte}}{\pi r^2 d\left(t \to \infty\right)} \frac{1000\,cm^3}{L} \tag{7.12}$$

The concentration of an analyte in air can be calculated from the analyte partial pressure using the ideal gas law, assuming a temperature of 298K.

$$C_{air} = \frac{N_{analyte}}{V} = \frac{P_{analyte}}{RT} \tag{7.13}$$

The film-air partition coefficient, K_{fa}, is defined as:

$$K_{fa} = \frac{C_{film}}{C_{air}} \tag{7.14}$$

The partition coefficients were calculated for a range of analytes using the saturated film concentrations described in Sections 7.4.1 and 7.4.2 and equations (7.9)-(7.14). The K_{fa} values were calculated from the analyte concentration in the film under several different ambient vapour concentrations and the average values are shown in Table 7.8. Where available, literature values are presented for direct comparison. Sprunger and coworkers have compiled a detailed review of literature values of K_{fa} into PDMS.[70]

Table 7.8: Comparison between experimental and literature film-air partition coefficients for a range of VOCs in PDMS. Literature values were provided where available for comparison, and experimental values were calculated from equations (7.9)-(7.14). The uncertainties were given as 1σ standard deviation.

Solvent	This work, K_{fa}	Literature, K_{fa}
m-Xylene	3100 ± 400	2200 [38], 3200 [40], 3962 [39]
Ethylbenzene	2600 ± 400	2000 [38], 3266 [39]
Toluene	1600 ± 500	800 [38], 1006 [41], 1200 [40], 1322 [39]
Benzene	700 ± 100	300 [38], 400 [40], 419 [41], 493 [39]
Cyclohexane	700 ± 200	420 [40]
Acetone	160 ± 50	90 [40], 101 [42], 130 [43]
Methanol	100 ± 20	
Isopropanol	120 ± 30	100 [40]

The partition coefficients that we report in Table 7.8 are averaged from both the uptake and release data at a minimum of 5 different gas concentrations. In a few cases, a single point was determined as a statistical outlier using Grubbs' test and was removed prior to calculating the average and 1σ standard deviation. The values we report are in close agreement with those previously cited in the literature. The Student's t-test was used and determined that the partition coefficients reported for m-xylene, ethylbenzene and isopropanol were not significantly different from the average literature values at a 95% confidence level. All other values were found to be systematically higher then literature values at a 95% confidence level. This is most likely due to differences in the PDMS composition from different commercial brands being interrogated. Conventionally, K_{fa} values are calculated offline using an SPME fibre inside a gas syringe to collect analyte from a solution or the headspace above an aqueous sample. After equilibrium has been reached, the fibre is retracted and then stored until it can be injected into a gas chromatograph for quantification.[25] Here, we show the ability to calculate similar values through optical methods, in a process that is suitable for in situ measurements with a comparable degree of accuracy.

7.4.4 Sorption of Solvent Vapour Molecules into Poly(dimethyl-co-diphenyl)siloxane Films

To increase the affinity of the PDMS films to aromatic compounds including the BTEX class of contaminants, copolymer films were made using a mole ratio of 20% polydiphenylsiloxane and 80% polydimethylsiloxane precursors. The synthesis of PDMS-PDPS films was previously discussed in Section 7.3.2. The PDMS-PDPS films were solvent cast onto glass slides (originally soda lime glass slides, n_{1550} = 1.507 [71]) in the same procedure used with the PDMS films. When studying thin films 10-15 µm thick, there were regions that did not contain any interference information and had to be removed before Fourier processing. This may have been the result of poorly aligned optical components in the setup. Reflections from additional interfaces were also observed in the refractometer images at larger incidence angles since the refractive index of PDMS-PDPS copolymer, n_{1550} = 1.4586(9), was close to that of the soda lime glass, and consequently close to the critical angle between the slide and prism. These additional fringes

were not observed with the higher index N-SF11 slides, which were used in later experiments. These two effects are demonstrated in Figure 7.20.

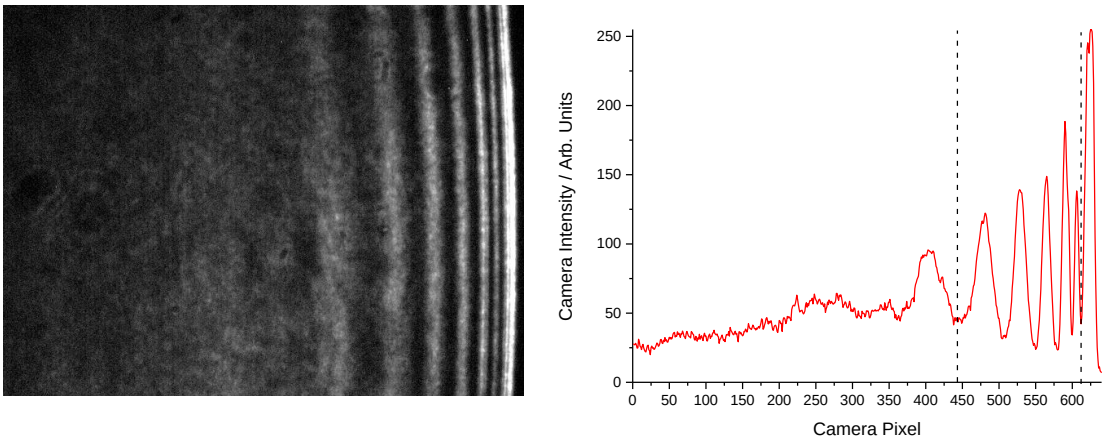

Figure 7.20: Interferogram and cross-section of a 12.9(7) µm PDMS-PDPS copolymer film, n_{1550} = 1.4586(9). The region outside the two dashed lines was excluded prior to Fourier processing to reduce the noise from non-periodic information. The dark band on the right is the result of an extra interface observed between the prism and the relatively low refractive index soda lime glass. This dark band was not observed when using higher index N-SF11 slides.

Thin films of PDMS-PDPS copolymer were exposed to solvent vapours of aromatic BTEX compounds, and cyclohexane. The experiments were conducted with a time resolution of 15-30 seconds between images and did not contain enough information for estimating diffusion coefficients. Instead, only the images taken near equilibrium at an exposure time of 900 seconds were processed. The film refractive index changes and swelling ratios were observed during exposure to a range of solvent vapour pressures of BTEX compounds and cyclohexane (Figure 7.21). Each experiment was conducted in triplicate with error bars showing the 1σ standard deviation on each point. The analyte mole fraction in the film at equilibrium was calculated using equations (7.5) and (7.6). The density of PDMS-PDPS copolymer films was unknown and was estimated to be the same as PDMS (ρ = 1.03 g/cm^3).[65] The molar mass was taken as the weighted average of a single silicon containing unit (80% PDMS and 20% PDPS), M = 98.98 g/mol. In each experiment, the refractive index of PDMS-PDPS films was taken from the initial exposure to nitrogen gas. The analyte concentrations within the film as a function of the ambient vapour pressure of BTEX and cyclohexane are shown in Figure 7.16.

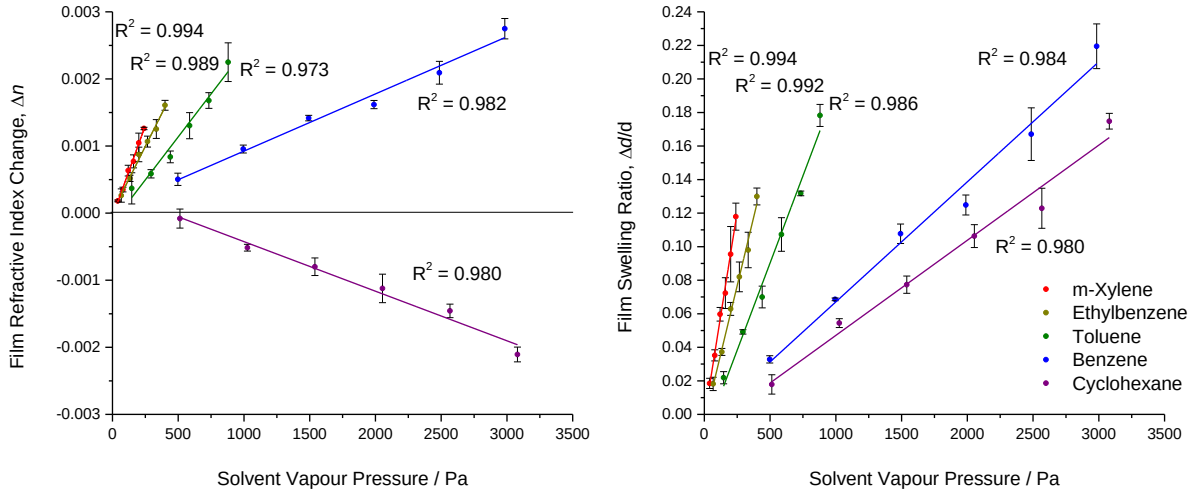

Figure 7.21: PDMS-PDPS copolymer refractive index and thickness changes during exposure to BTEX and cyclohexane vapours. All experiments were run in triplicate with 1σ standard deviation shown as error bars on each point. The refractive index of the PDMS-PDPS film increased with exposure to all BTEX compounds, but decreased during the uptake of cyclohexane, which had a lower refractive index (n_{1550} = 1.4147).[63] The film swelled when exposed to all solvents and exhibited a linear response. Swelling of more than 20% was observed during the exposure to 3000 Pa benzene vapour.

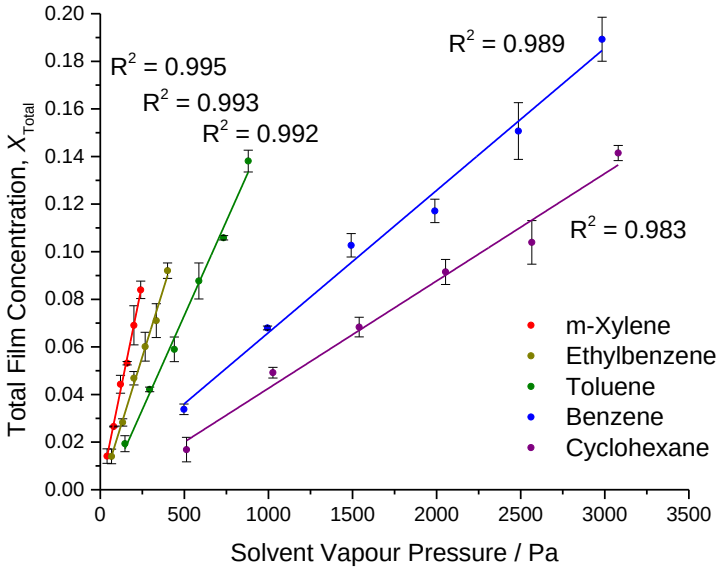

Figure 7.22: Equilibrium BTEX and cyclohexane concentrations within PDMS-PDPS films as a function of solvent vapour pressure. The film analyte concentration increased linearly with solvent vapour pressure of BTEX and cyclohexane vapour. The highest sensitivity was observed for m-xylene, ethylbenzene and toluene, all of which exhibited a similar trend with the PDMS films (Figure 7.16). The error bars show 1σ standard deviation of each point.

The analyte concentrations in the film and air were calculated, as was discussed in Section 7.4.3. These concentrations were used to calculate the film-air partition coefficients, K_{fa}, which are presented in Table 7.9 with the partition coefficients for PDMS (Table 7.8) for comparison. Since this is a custom material, it was not possible to compare with partition coefficients from the literature.

Table 7.9: Partition coefficients, K_{fa}, of BTEX and cyclohexane in PDMS-PDPS copolymer films. The partition coefficients for PDMS (Table 7.8) have been included for comparison. Adding PDPS to the film resulted in an extraction enhancement of 2-3 times compared with commercial PDMS. The enhancement was slightly smaller for cyclohexane, suggesting that the film selectivity was altered. In each case the uncertainty represents a 1σ standard deviation.

Solvent	K_{fa}	
	PDMS-PDPS	PDMS
m-Xylene	9500 ± 1000	3100 ± 400
Ethylbenzene	6000 ± 700	2900 ± 900
Toluene	4000 ± 500	1500 ± 400
Benzene	1900 ± 100	700 ± 100
Cyclohexane	1300 ± 300	700 ± 100
Hexanes	500 ± 150	---

The addition of PDPS to PDMS films was found to increase the affinity to BTEX compounds. Using the Student's t-test, the enhancement was found to be statistically more than a factor of 2 for all of the BTEX compounds at a 95% confidence level. The enhancement to cyclohexane was found to be statistically relevant but was not more than a factor of two when tested at a 95% confidence level. This showed that adding PDPS to the film imparted some added selectivity to aromatic compounds. Additionally, since the polymer had a higher refractive index, not all analytes resulted in positive refractive index changes during partitioning. Analytes such as cyclohexane, hexanes, and alcohols will cause the refractive index to decrease as the polymer film swells to accommodate the sorbate in the film. This results in a decrease of the polarizability of the film. The direction of the refractive index change is another property that can be used to help identify compounds in an unknown sample through fingerprint detection. While a reliable trend was observed, all equilibrium measurements were taken after only 900 seconds of exposure

to the respective analytes, and may underestimate the total sorbent concentration in the film. Unfortunately, these experiments were not run with a fast enough camera frame rate to measure diffusion processes in the PDMS-PDPS copolymer films, and would need to be repeated to provide additional information. Future experiments would be helpful in validating the partition coefficients presented in this chapter and are essential for fully understanding the differences of analyte partitioning inside of copolymer materials. Repeating the experiment with a range of PDMS to PDPS doping ratios would also clarify the effect that PDPS has on the films.

Ultimately, since refractive index sensors are non-selective, a series of different materials could be used to distinguish a range of volatile organic compounds and a suitable combination of materials may be used to develop an "artificial nose" type of sensor.

7.5 Conclusions

In this chapter, the basic mechanisms of siloxane chemistry used in the synthesis of commercial siloxane polymers and custom made siloxane copolymers was discussed. Interferometric refractometry was used to study the diffusion kinetics from the uptake and release of vapours of volatile organic solvents within siloxane polymers. This included studies with a commercial polydimethylsiloxane (PDMS), Sylgard 184, and a poly(dimethyl-co-diphenyl)siloxane copolymer film. The diffusion into PDMS fit best to a two-rate diffusion process which may be explained by the presence of different domains in the polymer from a complex mixture of additives and silica nanoparticle filler. The diffusion rates we report are an order of magnitude slower than values previously reported in the literature. We expect this is the result of differences in film properties from materials with different amounts of crosslinking and polymer additives. Many of the literature values may also have substantial uncertainty as they were calculated using simplified models where the saturation concentration was required. The errors in diffusion coefficients from under/over estimating the saturated equilibrium concentrations can be quite substantial (>20%) as was previously discussed in Chapter 3. Using the equilibrated concentrations of analytes in the films from both the uptake and release data, the partition coefficients of PDMS to BTEX compounds, cyclohexane, acetone, methanol

and isopropanol were determined. All partition coefficients were in reasonable agreement with literature values.

Adding diphenyl functionality to a siloxane polymer was expected to help increase the affinity to aromatic hydrocarbons. Poly(dimethyl-co-diphenyl)siloxane (PDMS-PDPS) films were synthesized using a condensation reaction to produce materials with approximately 20% diphenyl and 80% dimethyl functionalized siloxanes by mole. The original PDMS-PDPS data was very noisy and was collected with a slow camera frame rate between 15-30 seconds per image. Due to the slow image collection rate, diffusion kinetics could not be calculated, instead, images obtained at equilibrium were processed to determine the saturated analyte concentrations in the film after 900 seconds of exposure to each solvent vapour. Additional filtering techniques were introduced and film thickness and refractive index were extracted from the very noisy data. The partition coefficients were calculated for vapours of BTEX, cyclohexane and a commercial mixture of hexane isomers. The refractive index and thickness changes during exposure to polar compounds were too small to be distinguished over the large noise level with this data. The PDMS-PDPS film showed an enhancements of 2-3 times to aromatic BTEX compounds and showed a smaller enhancement with non-aromatic hydrocarbons. Additionally, adding diphenyl groups to the polymer increased the film refractive index to $n_{1550} = 1.4586(9)$, which meant that decreases in refractive index were now observed when exposed to cyclohexane, and hexanes. When exposed to the higher refractive index BTEX compounds, the film's refractive index still increased. This suggests that not only the affinity but also the selectivity of the polymer film was enhanced by adding the diphenyl functionality.

The methods outlined in this chapter show how the analyte response to polymer films can be quantified. Creating a large enough database with different types of polymers could allow for the development of multichannel refractive index sensors where the quantity and identity of volatile organic compounds could be assessed from the differential response of a series of uniquely functionalised polymers. PDMS and PDMS-PDPS films were also coated onto silicon-on-insulator (SOI) wire waveguide interferometers and micro-ring resonators as a proof of concept for miniaturized detection schemes. The results of these experiments will be discussed in detail in Chapter 8.

7.6 Acknowledgements

I would like to acknowledge Mr. Hao Chen for collecting the PDMS experimental data presented in Section 7.4. I would also like to thank Mr. Chris Brauer and Mr. Weijian Chen for the collection of the PDMS-PDPS data in Section 7.5. A preliminary analysis of the same data appeared previously in both of their theses.[72-73] Additionally, I would like to acknowledge the contributions from Mr. McGregor Clayton on repeating earlier PDMS-PDPS experiments. I would like to thank Dr.. Gillian Mackey, in Dr. Stephen Brown's group for all her assistance with the PDMS-PDPS copolymer synthesis. Finally, I would like to thank Dr. Raphael Desbiens at *ABB Canada* in Quebec City for his assistance with data filtering techniques which made the reanalysis of previously collected data possible.

7.7 References

1. Sia, S. K.; Whitesides, G. M., Microfluidic devices fabricated in poly(dimethylsiloxane) for biological studies. *Electrophoresis* **2003,** *24*, 3563-3576.

2. Wilbur, J. L.; Jackman, R. J.; Whitesides, G. M.; Cheung, E. L.; Lee, L. K.; Prentiss, M. G., Elastomeric optics. *Chemistry of Materials* **1996,** *8*, 1380-1385.

3. Cadarso, V. J.; Llobera, A.; Villanueva, G.; Dominguez, C.; Plaza, J. A., 3-D modulable PDMS-based microlens system. *Optics Express* **2008,** *16*, 4918-4929.

4. Yu, H.; Zhou, G.; Chau, F. S.; Lee, F., Fabrication and characterization of PDMS microlenses based on elastomeric molding technology. *Optics Letters* **2009,** *34*, 3454-3456.

5. Wang, Y.-C.; Tsai, Y.-C.; Shih, W.-P., Flexible PDMS micro-lens array with programmable focus gradient fabricated by dielectrophoresis force. *Microelectronic Engineering* **2011,** *88*, 2748-2750.

6. Azmayesh-Fard, S. M.; Lam, L.; Melnyk, A.; DeCorby, R. G., Design and fabrication of a planar PDMS transmission grating microspectrometer. *Optics Express* **2013,** *21*, 11889-11900.

7. Fürjes, P.; Holczer, E. G.; Tóth, E.; Iván, K.; Fekete, Z.; Bernier, D.; Dortu, F.; Giannone, D., PDMS microfluidics developed for polymer based photonic biosensors. *Microsystem Technologies* **2015,** *21*, 581-590.

8. McDonald, J. C.; Duffy, D. C.; Anderson, J. R.; Chiu, D. T.; Wu, H.; Schueller, O. J. A.; Whitesides, G. M., Fabrication of microfluidic systems in poly(dimethylsiloxane). *Electrophoresis* **2000,** *21*, 27-40.

9. Whitesides, G. M.; Ostuni, E.; Takayama, S.; Jiang, X.; Ingber, D. E., Soft lithography in biology and biochemistry. *Annual Review of Biomedical Engineering* **2001,** *3*, 335-373.

10. Xu, D. X.; Densmore, A.; Delâge, A.; Waldron, P.; McKinnon, R.; Janz, S.; Lapointe, J.; Lopinski, G.; Mischki, T.; Post, E.; Cheben, P.; Schmid, J. H., Folded cavity SOI microring sensors for high

sensitivity and real time measurement of biomolecular binding. *Optics Express* **2008,** *16*, 15137-15148.

11. Almeida, J. C.; Castro, A. G. B.; Lancastre, J. J. H.; Miranda Salvado, I. M.; Margaça, F. M. A.; Fernandes, M. H. V.; Ferreira, L. M.; Casimiro, M. H., Structural characterization of PDMS–TEOS–CaO–TiO2 hybrid materials obtained by sol–gel. *Materials Chemistry and Physics* **2014,** *143*, 557-563.

12. Sánchez-Téllez, D. A.; Téllez-Jurado, L.; Rodríguez-Lorenzo, L. M., Optimization of the CaO and P2O5 contents on PDMS–SiO2–CaO–P2O5 hybrids intended for bone regeneration. *Journal of Materials Science* **2015,** *50*, 5993-6006.

13. Ismagilov, R. F.; Rosmarin, D.; Kenis, P. J. A.; Chiu, D. T.; Zhang, W.; Stone, H. A.; Whitesides, G. M., Pressure-driven laminar flow in tangential microchannels: an elastomeric microfluidic switch. *Analytical Chemistry* **2001,** *73*, 4682-4687.

14. Stroock, A. D., Chaotic mixer for microchannels. *Science* **2002,** *295*, 647-651.

15. Linder, V.; Verpoorte, E.; de Rooij, N. F.; Sigrist, H.; Thormann, W., Application of surface biopassivated disposable poly(dimethylsiloxane)/glass chips to a heterogeneous competitive human serum immunoglobulin G immunoassay with incorporated internal standard. *Electrophoresis* **2002,** *23*, 740-749.

16. Kim, G.; Moon, J.-H.; Moh, C.-Y.; Lim, J.-g., A microfluidic nano-biosensor for the detection of pathogenic Salmonella. *Biosensors and Bioelectronics* **2015,** *67*, 243-247.

17. Wang, J. D.; Douville, N. J.; Takayama, S.; ElSayed, M., Quantitative analysis of molecular absorption into PDMS microfluidic channels. *Annals of Biomedical Engineering* **2012,** *40*, 1862-1873.

18. St-Gelais, R.; Mackey, G.; Saunders, J.; Zhou, J.; Leblanc-Hotte, A.; Poulin, A.; Barnes, J. A.; Loock, H.-P.; Brown, R. S.; Peter, Y.-A., Gas sensing using polymer-functionalized deformable Fabry–Perot interferometers. *Sensors and Actuators B: Chemical* **2013,** *182*, 45-52.

19. Smiley-Wiens, J.; Serpe, M. J., Solvent exchange kinetics in poly(N-isopropylacrylamide) microgel-based etalons. *Colloid and Polymer Science* **2013,** *291*, 971-979.

20. Liu, C.; Liu, Y.; Sokuler, M.; Fell, D.; Keller, S.; Boisen, A.; Butt, H.-J.; Auernhammer, G. K.; Bonaccurso, E., Diffusion of water into SU-8 microcantilevers. *Physical Chemistry Chemical Physics* **2010,** *12*, 10577-10583.

21. Lee, J. N.; Park, C.; Whitesides, G. M., Solvent compatibility of poly(dimethylsiloxane)-based microfluidic devices. *Analytical Chemistry* **2003,** *75*, 6544-6554.

22. Rumens, C. V.; Ziai, M. A.; Belsey, K. E.; Batchelor, J. C.; Holder, S. J., Swelling of PDMS networks in solvent vapours; applications for passive RFID wireless sensors. *Journal of Materials Chemistry C* **2015,** *3*, 10091-10098.

23. Louch, D.; Motlagh, S.; Pawliszyn, J., Dynamics of organic compound extraction from water using liquid-coated fused silica fibers. *Analytical Chemistry* **1992,** *64*, 1187-1199.

24. Pawliszyn, J., Theory of solid-phase microextraction. *Journal of Chromatographic Science* **2000,** *38*, 270-278.

25. Pawliszyn, J., *Solid Phase Microextraction Theory and Practice*. John Wiley & Sons Ltd., New York, NY, 1997.

26. Menezes, H. C.; de Lourdes Cardeal, Z., Determination of polycyclic aromatic hydrocarbons from ambient air particulate matter using a cold fiber solid phase microextraction gas chromatography–mass spectrometry method. *Journal of Chromatography A* **2011,** *1218*, 3300-3305.

27. Martendal, E.; Carasek, E., A new approach based on a combination of direct and headspace cold-fiber solid-phase microextraction modes in the same procedure for the determination of polycyclic aromatic hydrocarbons and phthalate esters in soil samples. *Journal of Chromatography A* **2011,** *1218*, 1707-1714.

28. Cocchi, G.; De Angelis, M. G.; Doghieri, F., Solubility and diffusivity of liquids for food and pharmaceutical applications in crosslinked polydimethylsiloxane (PDMS) films: I. Experimental data on pure organic components and vegetable oil. *Journal of Membrane Science* **2015,** *492*, 600-611.

29. Hu, C.; He, M.; Chen, B.; Hu, B., Determination of estrogens in pork and chicken samples by stir bar sorptive extraction combined with high-performance liquid chromatography–ultraviolet detection. *Journal of Agricultural and Food Chemistry* **2012,** *60*, 10494-10500.

30. Kawaguchi, M.; Takatsu, A.; Ito, R.; Nakazawa, H., Applications of stir-bar sorptive extraction to food analysis. *TrAC Trends in Analytical Chemistry* **2013,** *45*, 280-293.

31. Sysoev, A. A.; Ketola, R. A.; Mattila, I.; Tarkiaine, V.; Kotiaho, T., Application of the numerical model describing analyte permeation through hollow fiber membranes into vacuum for determination of permeation parameters of organic compounds in a silicone membrane. *International Journal of Mass Spectrometry* **2001,** *212*, 205-217.

32. Boscaini, E.; Alexander, M. L.; Prazeller, P.; Märk, T. D., Investigation of fundamental physical properties of a polydimethylsiloxane (PDMS) membrane using a proton transfer reaction mass spectrometer (PTRMS). *International Journal of Mass Spectrometry* **2004,** *239*, 179-186.

33. Lue, S. J.; Wang, S. F.; Wang, L. D.; Chen, W. W.; Du, K.-M.; Wu, S. Y., Diffusion of multicomponent vapors in a poly(dimethyl siloxane) membrane. *Desalination* **2008,** *233*, 277-285.

34. Chao, K.-P.; Wang, V.-S.; Yang, H.-W.; Wang, C.-I., Estimation of effective diffusion coefficients for benzene and toluene in PDMS for direct solid phase microextraction. *Polymer Testing* **2011,** *30*, 501-508.

35. Oh, K.-S.; Koo, Y.-M.; Jung, K.-W., Characterization of a sheet membrane interface for sample introduction into a time-of-flight mass spectrometer. *International Journal of Mass Spectrometry* **2006,** *253*, 65-70.

36. LaPack, M. A.; Tou, J. C.; McGuffin, V. L.; Enke, C. G., The correlation of membrane permselectivity with Hildebrand solubility parameters. *Journal of Membrane Science* **1994,** *86*, 263-280.

37. Newns, A. C.; Park, G. S., The diffusion coefficient of benzene in a variety of elastomeric polymers. *Journal of Polymer Science Part C: Polymer Symposia* **1969,** *22*, 927-937.

38. Isidorov, V. A.; Vinogorova, V. T., Experimental determination and calculation of distribution coefficients between air and fiber with polydimethylsiloxane coating for some groups of organic compounds. *Journal of Chromatography A* **2005,** *1077*, 195-201.

39. Zhang, Z.; Pawliszyn, J., Headspace solid-phase microextraction. *Analytical Chemistry* **1993,** *65*, 1843-1852.

40. Hierlemann, A.; Zellers, E. T.; Ricco, A. J., Use of linear solvation energy relationships for modeling responses from polymer-coated acoustic-wave vapor sensors. *Analytical Chemistry* **2001,** *73*, 3458-3466.

41. Baltussen, E.; David, F.; Sandra, P.; Janssen, H.-G.; Cramers, C., Equilibrium sorptive enrichment on poly(dimethylsiloxane) particles for trace analysis of volatile compounds in gaseous samples. *Analytical Chemistry* **1999,** *71*, 5193-5198.

42. Grote, C.; Pawliszyn, J., Solid-phase microextraction for the analysis of human breath. *Analytical Chemistry* **1997,** *69*, 587-596.

43. Nilsson, T.; Larsen, T. O.; Montanarella, L.; Madsen, J. ø., Application of head-space solid-phase microextraction for the analysis of volatile metabolites emitted by Penicillium species. *Journal of Microbiological Methods* **1996,** *25*, 245-255.

44. Wheeler, A. J.; Wong, S. L.; Khoury, C.; Zhu, J. *Predictors of indoor BTEX concentrations in Candian residences.* Health, Reports, Statistics Canada, 2013, 24, 11-17.

45. Original list of hazardous air pollutants, United States Environmental Protection Agency (EPA), 1990. https://www3.epa.gov/airtoxics/orig189.html (accessed Apr. 2, 2016).

46. *Toxicological Profile for Benzene* Agency for Toxic Substances and Disease Registry, US Department of Health and Human Services, Atlanta, Georgia, 2007,

47. *Toxicological Profile for Xylenes.* Agency for Toxic Substances and Disease Registry, US Department of Health and Human Services, Atlanta, Georgia, 2007,

48. *Toxicological Profile for Ethylbenzene.* Agency for Toxic Substances and DIsease Registry, US Department of Health and Human Services, Atlanta, Georgia, 2010,

49. *Draft Toxicological Profile for Toluene.* Agency for Toxic Substances and Disease Registry, US Department of Health and Human Services, Atlanta, Georgia, 2015,

50. Diré, S.; Babonneau, F.; Carturan, G.; Livage, J., Synthesis and characterization of siloxane-titania materials. *Journal of Non-Crystalline Solids* **1992,** *147-148*, 62-66.

51. Ebewele, R. O., *Poymer Science and Technology*. CRC Press LLC, Boca Raton, FL, 2000.

52. Ortiz-Acosta, D. *Sylgard Cure Inhibition Characterization*; LA-UR-12-25325, 1053123; Los Alamos National Laboratory: 2012.

53. Lisensky, G. C.; Campbell, D. J.; Beckman, K. J.; Calderon, C. E.; Doolan, P. W.; Ottosen, R. M.; Ellis, A. B., Replication and compression of surface structures with polydimethylsiloxane elastomer. *Journal of Chemical Education* **1999,** *76*, 537-541.

54. Chalk, A. J.; Harrod, J. F., Homogeneous catalysis. II. The mechanism of the hydrosilation of olefins catalyzed by group VIII metal complexes. *Journal of the American Chemical Society* **1965,** *87*, 16-21.

55. Stein, J.; Lewis, L. N.; Gao, Y.; Scott, R. A., In situ determination of the active catalyst in hydrosilylation reactions using highly reactive Pt(0) catalyst precursors. *Journal of the American Chemical Society* **1999,** *121*, 3693-3703.

56. Marciniec, B., Catalysis of hydrosilylation of carbon-carbon multiple bonds: Recent progress. *Silicon Chemistry* **2002,** *1*, 155-174.

57. Plett, K. L. *Development and Characterization of Polysiloxane Polymer Films for Use in Optical Sensor Technology*. Ph.D. Thesis, Queen's University, 2008.

58. Little, J. R. L. *Tunable and High Refractive Index Polydimethylsiloxane Polymers for Label-Free Optical Sensing*. M.Sc Thesis, Queen's University, 2013.

59. Mackey, G. *Synthesis, Modification, and Application of Siloxane Materials for Environmental Sensing*. Ph.D. Thesis, Queen's University, 2016.

60. Barnes, J.; Dreher, M.; Plett, K.; Brown, R. S.; Crudden, C. M.; Loock, H.-P., Chemical sensor based on a long-period fibre grating modified by a functionalized polydimethylsiloxane coating. *The Analyst* **2008,** *133*, 1541-1549.

61. Noll, W., *Chemistry and Technology of Silicones*. English Translation of 2nd Edition, Academic Press Inc. , London, UK, 1968.

62. Zimmermann, B.; Bürck, J.; Ache, H.-J., Studies on siloxane polymers for NIR-evanescent wave absorbance sensors. *Sensors and Actuators B: Chemical* **1997,** *41*, 45-54.

63. Saunders, J. E.; Sanders, C.; Chen, H.; Loock, H.-P., Refractive indices of common solvents and solutions at 1550 nm. *Applied Optics* **2016,** *55*, 947-953.

64. Sigma-Aldrich, Chemical Information and MSDS. Sigma-Aldrich Co. LLC, https://www.sigmaaldrich.com/canada-english.html (accessed Aug. 6, 2016).

65. *Sylgard 184 Elastomer Product Information* Dow Corning, 2014, 11-3184B-01,

66. Crank, J., *The Mathmatics of Diffusion*. First Edition, Oxford University Press, London, UK, 1956.

67. Saunders, J. E.; Chen, H.; Brauer, C.; Clayton, M.; Chen, W.; Barnes, J. A.; Loock, H.-P., Quantitative diffusion and swelling kinetic measurements using large-angle interferometric refractometry. *Soft Matter* **2015,** *11*, 8746-8757.

68. Möder, M.; Schrader, S.; Franck, U.; Popp, P., Determination of phenolic compounds in waste water by solid-phase micro extraction. *Fresenius Journal of Analytical Chemistry* **1997,** *357*, 326-332.

69. Haftka, J. J.-H.; Scherpenisse, P.; Jonker, M. T. O.; Hermens, J. L. M., Using polyacrylate-coated SPME fibers to quantify sorption of polar and ionic organic contaminants to dissolved organic carbon. *Environmental Science & Technology* **2013,** *47*, 4455-4462.

70. Sprunger, L.; Proctor, A.; Acree, W. E.; Abraham, M. H., Characterization of the sorption of gaseous and organic solutes onto polydimethylsiloxane solid-phase microextraction surfaces using the Abraham model. *Journal of Chromatography A* **2007,** *1175*, 162-173.

71. Rubin, M., Optical properties of soda lime silica glasses. *Solar Energy Materials* **1985,** *12*, 275-288.

72. Chen, W. *Chemical Detection and Sensing Using Optical Interferometry*. M.A.Sc Thesis, Queen's University, 2013.

73. Brauer, C. *Charachterization of Thin Films and Their Responses to Contaminants Using Real-Time Refractometry*. M.Sc. Thesis, Universität Potsdam, 2013.

Chapter 8

Refractive Index Sensing Using Polymer Coated Silicon-on-Insulator Devices

This chapter begins with a discussion about optical waveguides in Section 8.1.1 and the theory related to silicon-on-insulator microring resonators and Mach-Zehnder interferometers in Section 8.1.3. The optical setup is described in Section 8.2.1 and the development of data acquisition software is discussed in detail in Section 8.2.3. Initially, PDMS is coated onto a silicon-on-insulator MZ interferometer and the response to saturated m-xylene vapours was assessed (Section 8.3.1). Later, a PDMS-PDPS copolymer was coated onto tandem ring resonators and was exposed to a full range of VOCs (Section 0). Finally, the results obtained using the SOI platform are compared with the refractometer results from Chapter 7 in Section 2.5.

8.1 Introduction

This chapter describes some of the theory behind optical waveguides and micro-optical devices constructed from silicon. Silicon photonic devices can be made using standard lithographic processes already developed for the manufacturing of silicon electronics, and can be easily scaled up to produce thousands of identical devices on a single wafer.[1-2] Using silicon as a platform for both light and electron conduction allows for the integration of photonic and electronic components within a single chip.[3-4]

Silicon-on-insulator (SOI) devices can be made from subwavelength dimensioned silicon waveguides on top of an insulating layer of silica. The combination of small size and large refractive index contrast causes the evanescent field to interact strongly with the first few hundred nanometers around the waveguides. Silicon waveguide Mach-Zehnder interferometers and microring resonators can therefore be used to measure changes in ambient refractive index, above uncoated and coated devices, with sensitivities on the order of $\Delta n = 10^{-4}$.

The SOI chips used in this work were designed, manufactured and provided to us by the National Research Council (Ottawa, ON). The SOI chips were covered with either a protective overcoat of SU-8 epoxy photoresist, or a layer of silica depending on the fabrication batch. Regions over selected sensing interferometer arms or microrings were left unprotected for later functionalization with polymers and other

materials for refractive index sensing. The uptake of volatile organic compounds (VOCs) onto uncoated and siloxane-coated devices was explored. Comparison is made with the refractometry results described in the previous chapter.

8.1.1 Waveguides

Many different types of optical waveguides exist for on-chip optical devices. Typically, waveguides are made from high refractive index materials such as silicon nitride[2, 5-6] (Si_3N_4, n_D = 2.017)[7] and silicon[1, 8] (n_D = 3.9622)[9], but they can also be made from silica[10] (SiO_2, n_D = 1.4584)[11] or even polymers[12-13]. While silicon nitride waveguides have a lower refractive index than silicon, they are optically transparent within the visible region of the spectrum and can be interrogated using much cheaper silicon photodetectors and cameras. Silicon nitride waveguides can be made into on-chip microring resonators[2, 6, 14] and interferometers[5]. Silicon waveguides have a much higher refractive index contrast with silica and other substrates. They have typical losses of 3-6 dB/cm[1, 8, 15] and can be made into small footprint devices with tight bend radii while still only having optical losses of about 10 dB/cm[1]. Silicon has a bandgap of 1.1eV[16] and is suitable for photodetectors from λ = 200-1100 nm.[16] For photons with energies below the bandgap, silicon is transparent in much of the infrared region of the spectrum from λ = 1.2-7 μm.[17] One of the major benefits of silicon photonics is its compatibility with the C (1530-1565nm) and L (1565-1625nm) wavelength bands used in telecommunication technology. Silicon optical resonators, multiplexers and other on-chip devices can operate at much faster speeds than conventional electronics and are heavily researched for telecommunications and computing applications.[18-19]

Silicon waveguides can be designed in a variety of geometries with the simplest being slab waveguides, which have a very large width (assumed to be infinite in simulations) relative to their finite height. Rectangular or ridge waveguides have finite widths, and the dimensions are optimized for the desired propagating modes.[20-21] Changing the dimensions of the rib region of ridge waveguides can allow for propagation of either TE or TM polarized modes.[21-22] Other forms of waveguides include, slot waveguides[21, 23], grating waveguides[24-26] and photonic crystal waveguides[27-29]. In these final types of

waveguides, refractive index sensing can also occur directly within spaces in the waveguides as opposed to relying solely on evanescent field interactions.[30-31] Figure 8.1 shows an overview of common waveguide geometries.

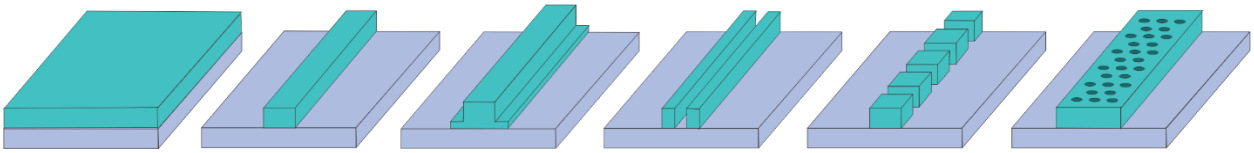

Figure 8.1 Summary of common waveguide geometries. Shown from left to right are illustrations of slab waveguides, ridge waveguides, rib waveguides, slot waveguides, grating waveguides and photonic crystal waveguides. Optical devices using silicon and silicon-nitride waveguides of various geometries have been reported in the literature.[2, 5, 8, 32] The refractive index of the guided mode in waveguides with air gaps will typically be lower than for the solid waveguides.

When light is guided in a waveguide, some of the energy interacts with the surroundings through the evanescent field. Using a common approximation, the decay length of the evanescent field, d_{EF}, depends on the incident angle, θ_i, the effective refractive index of the waveguide, n_{eff}, and the refractive index of the cladding layer, n_c.[33-34]

$$d_{EF} = \frac{\lambda_0}{2\pi\sqrt{n_{eff}^{\,2}\sin^2\theta_i - n_c^{\,2}}} \tag{8.1}$$

For multiple layer systems when the waveguide has a finite thickness, the effective index of the waveguide will be affected by the waveguide dimensions and the refractive indices of the substrate and overcoat layers. The evanescent field of slab waveguides can be calculated from solutions to Maxwell's equations using the appropriate boundary conditions.[3, 35] Using mode equations from the literature,[3, 35] the evanescent field was calculated for a 260 nm silicon slab waveguide ($n_{Si,\ 1550}$ = 3.4777)[36] with a silica substrate ($n_{SiO2,\ 1550}$ = 1.444)[11] and a PDMS overcoat ($n_{PDMS,\ 1550}$ = 1.3999)[37]. The approximation of the silicon ridge waveguide as a two-dimensional slab waveguide is justified only when TM modes are calculated. The resulting evanescent field was normalized so the three segments of the graph had an equal area and is shown in Figure 8.2.

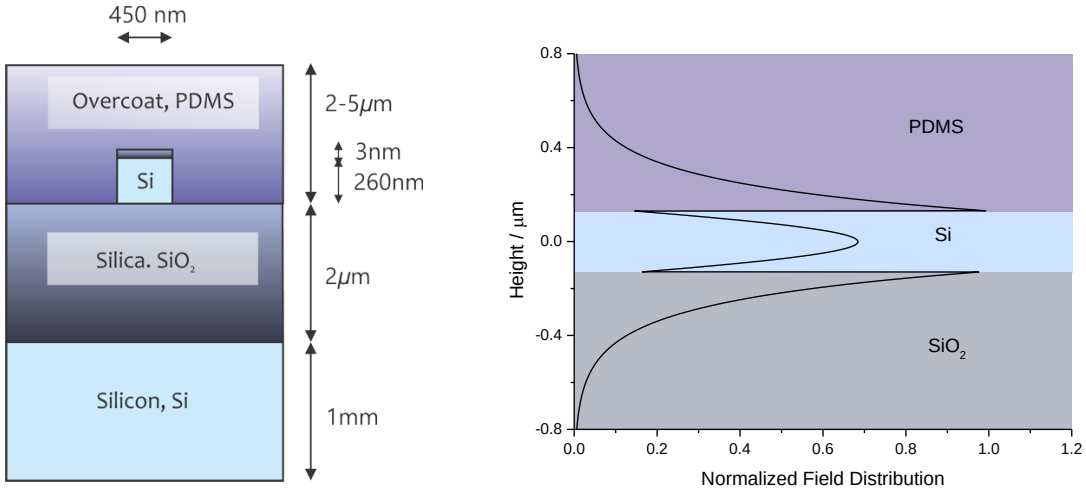

Figure 8.2: Cross-section and evanescent field profile for a typical silicon-on-insulator waveguide. The silicon waveguides of the devices studied in this chapter have dimensions of 260 nm × 450 nm with a 3 nm thin layer of silica as a cladding over the waveguides. The right figure shows the normalized field intensity of the TM mode in a 260 nm thick slab waveguide as a function of distance from the centre of the silicon waveguide.[3, 35] Each portion of this curve has been normalized to the same area.

The resulting evanescent field distribution of the slab waveguide was in very close agreement with fields modelled previously for silicon-on-insulator ridge waveguides with similar heights.[20, 38] While this calculation was comparable for the TM mode, it is expected to poorly model TE modes, where the waveguide width will play a larger effect.

One particular challenge with the use of silicon waveguides is to get light into and out of the optical chips. The high refractive index of silicon causes a considerable amount of loss due to Fresnel reflections at the air-silicon (or silica-silicon) interface when light is coupled into the waveguides using optical fibres with external light sources and detectors. Alternatively, one can generate and detect light directly on the chip using microfabricated sources and detectors. Many groups are currently working on developing on-chip lasers and detectors but they are very complicated to make requiring multistep lithographic processes.[39] Silicon is an indirect bandgap material and is not suitable for the development of efficient light sources and lasers.[40] Additionally, in the near-infrared, the photons do not have enough energy to excite electrons over the bandgap, so silicon can also not be used in photodetectors. Of course, the lack of interactions of silicon with 1.5 μm light makes the use of silicon as a waveguide material possible in the first place.

Lasers integrated with silicon photonics have been produced using germanium as a gain medium. These lasers require very high currents to overcome the lasing thresholds and their efficiency is still poor as germanium is also an indirect bandgap material.[41-42] More efficient lasers can be produced from the direct bandgap of mixtures of group III and V semiconductors, for example, InP, GaAs, InGaAs, InGaAsP.[39, 43-44] Similarly, on-chip photodetectors have also been demonstrated for near-infrared detection of SOI waveguides using germanium[45-46] and with group III-V semiconductors[47-49].

On-chip laser and detectors are not yet well established, so for lab scale experiments it is more practical to couple light into and out of silicon photonic chips for use with tuneable external cavity diode lasers and photodiode detectors. The following section will discuss different methods of coupling light into and out of optical waveguides and the benefits and challenges of each method will be discussed.

8.1.2 Coupling Light Into Optical Waveguides

For lab-based SOI experiments, it is practical to couple light into silicon waveguides from an external light source. Light can be coupled into these waveguides using optical grating couplers[50-51], prism couplers[52-53] , or edge-on from an optical fibre.[54-55] These three coupling methods are illustrated in Figure 8.3.

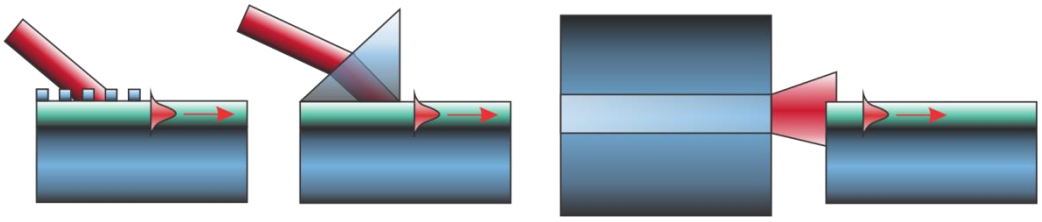

Figure 8.3: Schematic of coupling methods to get light into photonic waveguides. Light can be coupled into optical waveguides using surface relief gratings, prisms or edge-on from an optical fibre.

A major challenge with edge-on coupling into waveguides is the significant loss due to mode mismatch between the larger optical fibre and the waveguide. The acceptance mode of the waveguide can be enlarged by tapering down the facet of the waveguide[54] or terminating the waveguide with a partial grating that develops into an increasingly spaced full grating[56]. These two methods can also be combined to form

tapered gratings at the end of waveguides that are less sensitive to misalignment and exhibit a reduced polarization dependence.[57] Illustrations of the inverse taper and waveguide grating are shown in Figure 8.4.

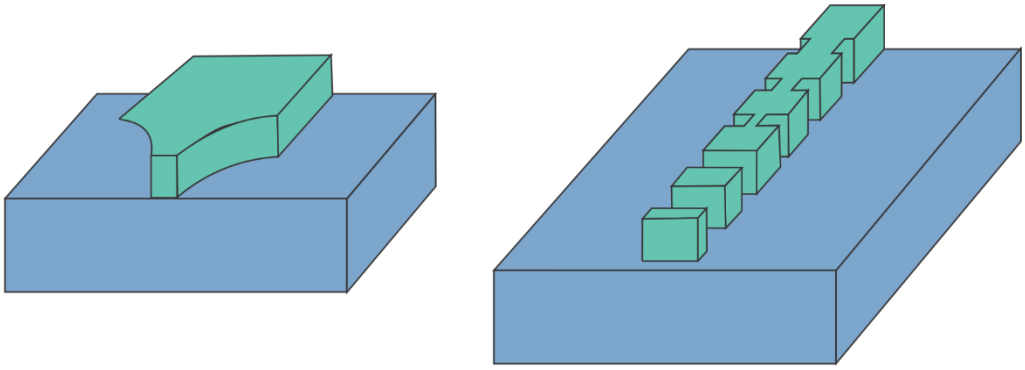

Figure 8.4: Schematic showing two methods of enlarging the mode field at the end of optical waveguides for increased edge-on coupling efficiency with optical fibres. A) an inverse taper can be used to increase the mode volume at the edge of an SOI chip.[54] B) a partial grating that blends into an increasingly spaced full grating gradually decreases the effective refractive index of the waveguide enlarging the mode volume at the edge of the chip.[56]

For initial lab-based experiments with SOI devices, edge-on coupling is the simplest method for alignment to optical devices. Furthermore, if the top surface of the chip is not required for coupling in light, it is easier to functionalize devices with coatings for refractive index sensing applications. However, high-precision alignments stages are needed since the alignment of the optical fibres to the SOI devices can be highly sensitive and subject to mechanical drift. Both prisms and surface relief gratings can be used to decrease the alignment sensitivity but may complicate the application of functionalized coatings or microfluidics needed for sensing experiments. The simplified alignment of grating-coupled and prism-coupled devices makes them more suitable for eventually packaged sensor probe designs. Edge-on coupling can also be used when making packaged sensors, though typically V-groove assemblies are used to secure the optical fibres at the same pitch as the optical waveguides on SOI chips.[58-59] All the channels are aligned together and then permanently bonded to the chip.[58-59]

A brief summary of the theory behind on-chip interferometers and microresonators is presented in Section 8.1.3.

8.1.3 Silicon-on-Insulator Devices

As was discussed in Section 8.1.1, silicon waveguides on an insulating layer of silica (SOI) have a very large refractive index contrast with their surroundings and can be used to fabricate highly sensitive refractive index sensors. This section describes the theory behind SOI refractive index sensors including Mach-Zehnder interferometers and microring resonators.

Silicon has a very large dispersion in the near-infrared, meaning that its refractive index depends strongly on the wavelength of interrogation. For silicon optical waveguides, the group index, n_g, is often more convenient to work with as it is corrected for the dispersion of the effective refractive index of the waveguide, n_{eff}.

$$n_g = n_{eff} - \lambda\left(\frac{dn_{eff}}{d\lambda}\right) \tag{8.2}$$

The effective refractive index, n_{eff}, is related to the phase velocity through a medium, V, and the speed of light in a vacuum, c_0.

$$n_{eff} = \frac{c_0}{V} \tag{8.3}$$

The group index is similar to the effective index but is related to the propagation velocity of the envelope of the wave packet through a medium, known as the group velocity, V_g.

$$n_g = \frac{c_0}{V_g} \tag{8.4}$$

The equations presented in the coming sections relate to either the effective refractive index or group index of SOI waveguides and will be used to explain the theory behind interferometers and microring resonators.

8.1.3.1 Mach-Zehnder Interferometers

The silicon-on-insulator chips were provided by the National Research Council (Ottawa, ON) and contained Mach-Zehnder interferometers with arm lengths ranging from 1.76 mm to ~8.1 mm. To efficiently use the space on wafers, and to allow for localized refractive index sensing of small samples, the

interferometer arms were coiled up in double spirals as is shown in Figure 8.5.[60-61] A benefit of balanced Mach-Zehnder (MZ) interferometers, is the built-in temperature compensation as changes in ambient temperature will cause nearly identical refractive index changes to both arms of the interferometer. In practice, since the effective refractive indices of the waveguides are different for the two arms, additional compensation is needed to fully account for temperature drifts.

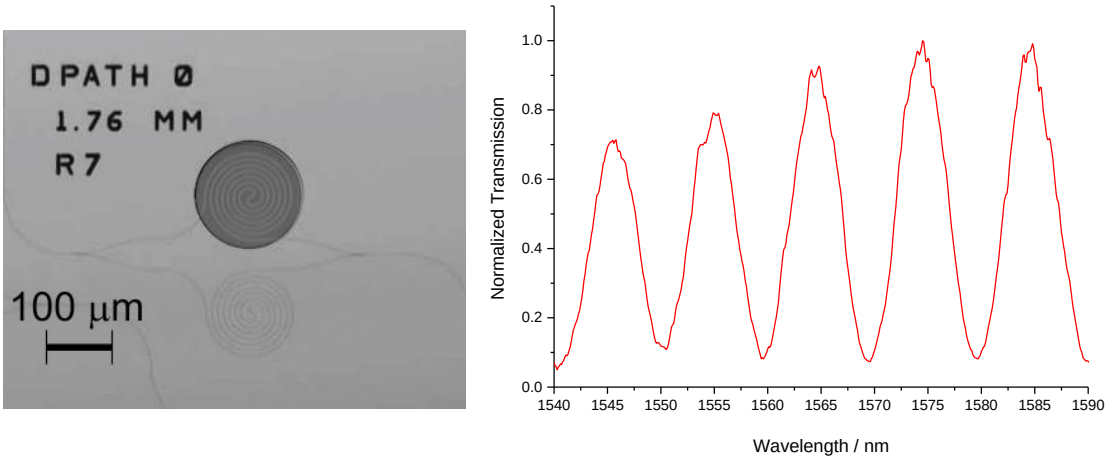

Figure 8.5: Optical profilometer image and transmission spectrum of a Mach-Zehnder interferometer with arm lengths of 1.76 mm. The dark disk on the top ring of the interferometer shows an exposed region of waveguide for refractive index sensing. The rest of the device is buried under a protective overcoat to act as a reference arm. The spectral range of the fringes of the interferometer was $\Delta\lambda = 9.8$ nm, with a fringe width of $\delta\lambda \sim 5$ nm.

Similar to other interferometers discussed in Chapter 2.2, the intensity of the Mach-Zehnder interferometer is governed by a sinusoidal function.[1, 62]

$$I = \frac{I_0}{2}\left[1+\cos\left(\frac{2\pi}{\lambda}\left(n_{eff,sen}L_{sen} - n_{eff,ref}L_{ref}\right)\right)\right] \tag{8.5}$$

Here, $n_{\text{eff,sen}}$ and $n_{\text{eff,ref}}$ are the effective refractive indices of the sensing and reference arm and L_{sen} and L_{ref} are the length of the respective interferometer arms.[1]

The spectral resonance shift of an MZ interferometer, $\Delta\lambda$, is related to the change in effective index of the sensing arm, $\delta n_{\text{eff,sen}}$, and is independent of the interferometer arm length in a balanced interferometer when $L_{\text{sen}} = L_{\text{ref}}$.[50]

$$\Delta\lambda = \frac{\lambda L_{sen}\delta n_{eff,sen}}{n_{g,sen}L_{sen} - n_{g,ref}L_{ref}} \tag{8.6}$$

The width of the interference fringes, $\delta\lambda$, is however directly related to arm length of the interferometer.[50]

$$\delta\lambda = \frac{\lambda^2}{2\left(n_{g,sen}L_{sen} - n_{g,ref}L_{ref}\right)} \tag{8.7}$$

The phase shift of the interferometer, $\Delta\phi$, is related to the ratio of the spectral resonance shifts, $\Delta\lambda$, and the fringe width, $\delta\lambda$. This can be simplified, to show that the phase shift is related to the product of the effective refractive index change and the length of the sensing arm, L_{sen}.[50]

$$\Delta\phi = \pi\frac{\Delta\lambda}{\delta\lambda} = \frac{2\pi L_{sen}\delta n_{eff,sen}}{\lambda} \tag{8.8}$$

Initially, refractive index experiments were performed using Mach-Zehnder interferometers to study the uptake of solvent vapours into siloxane based films (Section 8.3.1). These experiments were performed at a constant wavelength while monitoring the transmission intensity as the interferogram shifted in wavelength. While this was simple, it was greatly affected by intensity fluctuations from the laser and mechanical drift of the alignment optical fibres. This problem was later resolved by stepping or scanning over a spectral window of at least one fringe period to accurately define the wavelength of each fringe.

Moreover, the interferometer measurements only provide the relative refractive index difference between the two arms. In some of our experiments, the SU-8 overcoat, which was used to protect the rest of the chip, also adsorbed analyte and the SU-8's refractive index would consequently change. The unwanted uptake of analytes into the overcoat was later quantified using microring resonators, and allowed for independent measurement of both the absolute refractive index change of our polymer coatings and the protective overcoat during chemical uptake. (Section 8.3.2).

8.1.3.2 Microring Resonators

An alternate approach to refractive index sensing is with microring resonators adjacent to optical waveguides on SOI chips. Light can couple strongly into microresonators when the wavelength can form a standing wave within the ring (i.e., an integer number of wavelength will fit around the circumference of

the resonator). The wavelength of a resonance of mode, *m*, is related to the effective refractive index and length (or circumference) of the resonator, n_{eff} and L respectively.

$$m\lambda_{resonance} = n_{eff} L \tag{8.9}$$

When this resonance condition is met, light intensity builds up inside of the ring and with each round trip, some of the light couples back out and destructively interferes with the light in the bus waveguide, resulting in attenuation of the transmission spectrum on resonance. Alternatively, due to ring roughness and scattering centres in the waveguide, some of the light will couple into counter-propagating modes and can be observed as peaks in the back reflection in the original waveguide. If a second drop waveguide is coupled to the top of the ring, peaks can be observed on resonance with comparable intensity to the attenuation observed in the transmission spectrum. All three of these phenomena are illustrated in Figure 8.6.

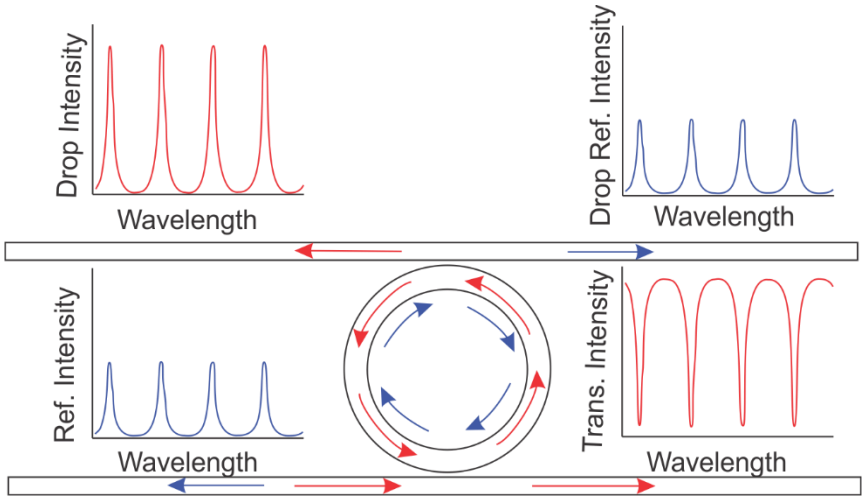

Figure 8.6: Schematic showing transmission, back reflection and cross-coupling spectra for a ring resonator. In the transmission spectrum, light coupling back out of the ring destructively interferes with light in the bus waveguide causing attenuation on resonance. In the back reflected spectrum, some of the light is scattered within the ring into counter-propagating modes. Peaks can be observed in the back reflected spectrum as counter-propagating light couples back into the original waveguide (blue). If a second waveguide is adjacent to the ring, light can couple out of the ring into the second waveguide and peaks are observed on resonance. The back reflected light can also couple into the opposite direction of the drop waveguide.

The resonances of a given ring resonator can be predicted using equation (8.9) as long as the cavity length and effective refractive index are known. The first 5000 resonance modes were calculated for a resonator with a ring length of L = 1.27 mm ring resonator and an effective refractive index of n_{eff} = 4.66

(Figure 8.7). An inset is included to show the resonance modes within the near-infrared C-band wavelength range. For the purpose of this calculation, the dispersion of the effective refractive index was ignored, in practice, n_{eff} will be different for each wavelength and will greatly complicate the prediction of the actual resonance modes. From this calculation, it is obvious that the resonance modes do not have a uniform wavelength spacing or a common free spectral range. However, in a narrow wavelength range in the near-infrared, the free spectral range can be approximated as constant. This is shown by the linear fit (black line) in the inset of Figure 8.7.

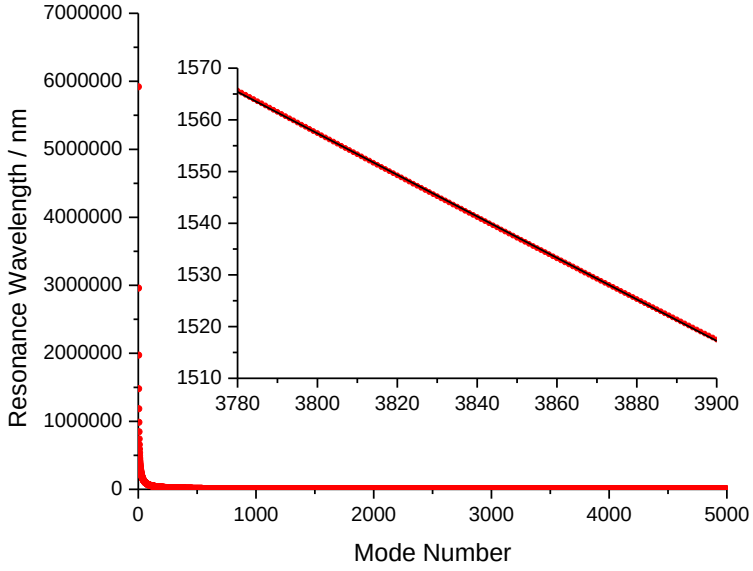

Figure 8.7: The wavelength of the first 5000 resonances for an L = 1.27 mm ring resonator with an effective index of n_{eff} = 4.66. The mode number, m. is the integer number of wavelength that fit around the ring (equation (8.9)). The wavelength spacing between resonances is not consistent over the full wavelength range, but can be assumed as constant over a narrow wavelength range with higher order modes. The inset shows the resonances in the near-infrared C-band with a linear fit (black line) showing that the free spectral range between these resonances is relatively constant.

The free spectral range of the resonances at a specific wavelength, λ_0, can be predicted from the group index, n_g, and resonator length, L.[8]

$$\Delta\lambda_{FSR} = \frac{\lambda_0^{\,2}}{n_g L} \tag{8.10}$$

For example, for a 1.27 mm resonator with a group index of n_g = 4.66, $\Delta\lambda_{FSR}$(1520 nm) = 390 pm and $\Delta\lambda_{FSR}$(1560 nm) = 411 pm.

The simplest resonator is a Fabry-Perot cavity between two highly reflective mirrors. In this case, the higher the reflectivity of the mirrors, the more intensity that will build up in the cavity. The magnification of the light intensity within an optical cavity is described by the quality factor, or Q-factor and is a ratio of the energy stored in the cavity with the loss of light for each round trip in the cavity.[62]

$$Q = 2\pi \frac{Stored\ Energy\ in\ Cavity}{Energy\ Loss\ \ per\ Round\ Trip} \tag{8.11}$$

The more reflective the mirrors, or the lower the loss in a ring resonator cavity, the higher the Q-factor and the narrower the cavity fringes will be. The fringe broadness is described as the width of the peak at half of the maximum intensity, or the "full width half maximum" (FWHM). This is related to the losses in the cavity, α_r, and the speed of light in a vacuum, c_0.[62]

$$\delta\nu_{FWHM} = \frac{c_0\alpha_r}{2\pi} \tag{8.12}$$

The Q-factor is also related to the FWHM, $\delta\nu_{FWHM}$, at a given frequency, ν_0, which is approximately the same as the FWHM, $\delta\lambda_{FWHM}$, for narrow resonances at a given wavelength, λ_0.[8, 62]

$$Q = \frac{\nu_0}{\delta\nu_{FWHM}} \approx \frac{\lambda_0}{\delta\lambda_{FWHM}} \tag{8.13}$$

An alternative method of describing the strength of an optical cavity is known as the cavity finesse, F, which is a ratio of the free spectral range ($\Delta\nu_{FSR}$) and the full width half maximum ($\delta\nu_{FWHM}$). Again, this can be approximated by the wavelength equivalents ($\Delta\lambda_{FSR}$, $\delta\lambda_{FWHM}$).[62]

$$F = \frac{\Delta\nu_{FSR}}{\delta\nu_{FWHM}} \approx \frac{\Delta\lambda_{FSR}}{\delta\lambda_{FWHM}} \tag{8.14}$$

The Q-factor can easily be used to calculate the cavity finesse and vice versa.[62]

$$Q \approx \frac{\nu_0}{\Delta\nu_{FSR}} F \approx \frac{\lambda_0}{\Delta\lambda_{FSR}} F \tag{8.15}$$

The spectrum of a 936 μm long silicon spiral ring resonator on a silica substrate with water as the cladding layer is shown in Figure 8.8. The resonances can be fit with a Lorentzian function to determine the resonance location, λ_0, and width, $\delta\lambda_{FWHM}$.

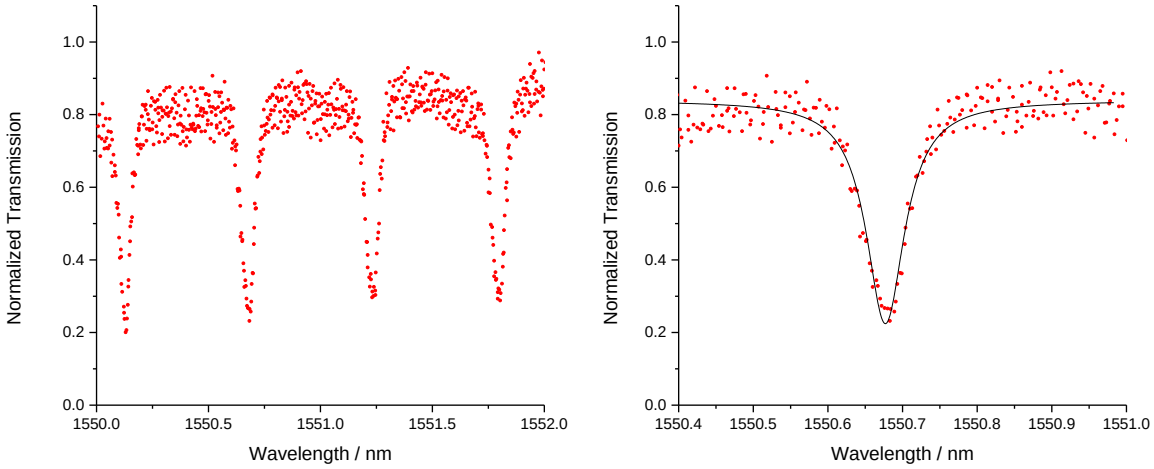

Figure 8.8: Spectrum of a 936 μm long silicon spiral ring resonator exposed to water. The Lorentzian fit to the second resonance is shown on the right. The width was calculated as $\delta\lambda_{FWHM}$ = 62 pm with a free spectral range of $\Delta\lambda_{FSR}$ = 552 pm. The Q-factor and cavity finesse were calculated as Q = 24 000 ± 3 000 and F = 9 ± 1. This yielded a group index of n_g = 4.59 which was comparable to previously reported values for these devices exposed to water.[63]

The cavity finesse and Q-factor can also be expressed by the losses in the optical resonator which can be described by the cavity absorption and scattering loss, α, and the coupling coefficient, t.[8]

$$F = \frac{\pi\sqrt{\alpha t}}{1-\alpha t} \tag{8.16}$$

$$Q \cong \frac{\pi n_g L}{\lambda_0}\frac{\sqrt{\alpha t}}{1-\alpha t} \tag{8.17}$$

The cavity resonance spectrum can be modeled using the cavity loss and coupling coefficients.[8]

$$I = \frac{\left[\alpha^2 - 2\alpha t\cos\phi + t^2\right]}{\left[1-2\alpha t\cos\phi + \alpha^2 t^2\right]} \tag{8.18}$$

Where the angle, ϕ, (in radians) is related to the effective index of the waveguide, n_{eff}, resonator length, L, and wavelength of light, λ_0.[8]

$$\phi = \frac{2\pi n_{eff} L}{\lambda_0} \tag{8.19}$$

The shift in resonance wavelength can be directly correlated to changes in the effective index of the waveguide, which is related to the changes in the ambient refractive index surrounding the sensing region of a ring resonator.[8]

$$\frac{\Delta\lambda}{\lambda_0} = \frac{\Delta n_{eff}}{n_g} \tag{8.20}$$

The resonance spectrum of a 936 μm long ring resonator when exposed to water is shown in Figure 8.9 and was fit with equation (8.18) to determine loss and coupling coefficients.

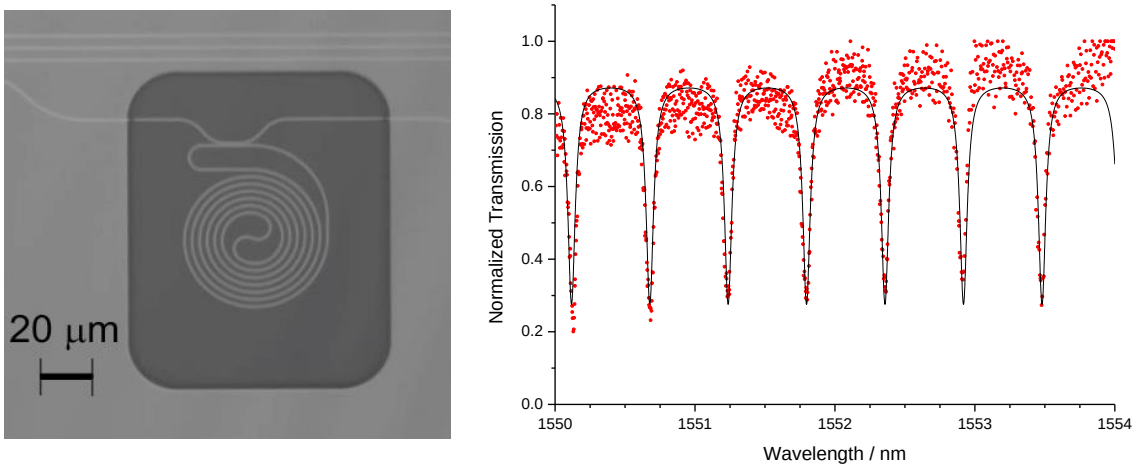

Figure 8.9: Optical profilometer image and resonance spectrum of a 936 μm long spiral ring resonator. The spectral resonances were fit with equation (8.18) (black line) including an amplitude scaling term and y-offset. The loss and coupling coefficients were determined as *α*, *t* = (0.93, 0.75), and the effective waveguide index was calculated as n_{eff} = 4.59.

The effective index calculated in Figure 8.9, n_{eff} = 4.59, was comparable to the group index of n_g = 4.55 previously reported when silica clad devices were exposed to water.[63] The loss and coupling coefficients were determined as *a*, *t* = (0.93, 0.75) from the transmission spectrum in Figure 8.9. It is apparent from equations (8.16) - (8.18) that *α* and *t* are interchangeable and while the two values can be determined it is not certain which value corresponds to which coefficient.

It is possible to extract the two values independently as was previously described in the literature.[64] In order to do this, the extinction coefficient, ε, must first be calculated, which is related to the maximum and minimum transmission intensity around a resonance.

$$\varepsilon = \frac{T_{Max}}{T_{Min}} \tag{8.21}$$

Using the information from the cavity finesse and the extinction coefficient, two values, A and B can be calculated.[64]

$$A = \frac{\cos(\pi/F)}{1+\sin(\pi/F)} \tag{8.22}$$

$$B = 1 - \left[\frac{1-\cos(\pi/F)}{1+\cos(\pi/F)}\right]\frac{1}{\varepsilon} \tag{8.23}$$

Where the values of the cavity attenuation and the coupling constant can be solved as the two roots of the following expression.[64]

$$(\alpha, t) = \left(\frac{A}{B}\right)^{1/2} \pm \left(\frac{A}{B} - A\right)^{1/2} \tag{8.24}$$

Again, it is not inherent which of the two roots is related to the cavity attenuation or the coupling constant, though in many situations, the coupling constant will show a much stronger wavelength dependence than the cavity attenuation allowing for assignment of the parameters when solved over a large enough spectral window.[64] This method is problematic when the losses are very small and the two terms are close to 1.[64] The two coefficients were calculated from the cavity resonances shown in Figure 8.9, and were in close agreement with the values previously determined from the fit to equation (8.18). The wavelength dependent values of α and t are shown in Figure 8.10. In this figure, the smaller coefficient showed slightly more variation with wavelength so it is most likely the coupling coefficient, t.

A major challenge with refractive index sensing is the temperature dependence of refractive index, which can result in resonance shifts of 50-60 pm/°C.[63] The thermo-optic coefficient for silicon, has been reported in the literature as $dn/dT = 1.8\times10^{-4}$ K^{-1} at 300 K and λ = 1550 nm.[65] Temperature changes can

also cause thermal expansion of the silicon substrate increasing the cavity dimension, L, though this will be a minor effect as the coefficient of expansion (2.56×10^{-6} K^{-1} at 293 K) is two orders of magnitude smaller than the thermo-optic coefficient.[66]

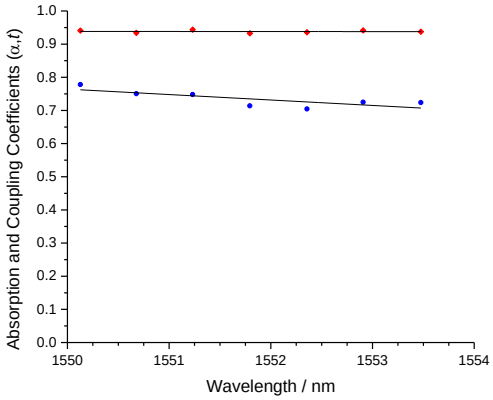

Figure 8.10: Wavelength dependence of cavity loss and coupling coefficients (α,t). The loss and coupling coefficients were calculated for the resonances in Figure 8.9 using equations (8.22)-(8.24). The black lines show the linear fit to the points for the two parameters. The coefficient around 0.75 (blue circles) appears to have a slightly stronger wavelength dependence and is likely the coupling coefficient, *t*, and the top coefficient around 0.93 (red diamonds), is likely the cavity loss coefficient, α.

When studying a single microring resonator, it is impossible to disentangle temperature effects from sensing experiments. One method to resolve this problem is to use a tandem pair of microring resonators with different cavity lengths. One of the rings is used as a temperature reference and is covered with a protective overcoat of SiO_2 or SU-8. In theory, the resonances of the reference ring will only shift with changes in temperature and can be used to remove temperature related shifts in the sensing ring signal. An optical profilometer image and a transmission spectrum of a tandem ring resonator, with sensing ring and reference ring circumferences of 185 μm and 134 μm respectively, are shown in Figure 8.11. The Q-factor of the sensing rings and reference rings were found as Q_{sens} = 30 000 ± 4 000 and Q_{ref} = 32 000 ± 3 000, respectively.

For the development of multi-parameter sensors, arrays of identical ring resonators can be simultaneously probed using a single input waveguide. Some of the devices can be used for temperature compensation while others can be functionalized with different materials and measured simultaneously

using a near-infrared linear array detector or camera. A microscope image showing a 16 ring resonator array is presented in Figure 8.12 with 15 sensing rings and 1 reference ring for temperature compensation.

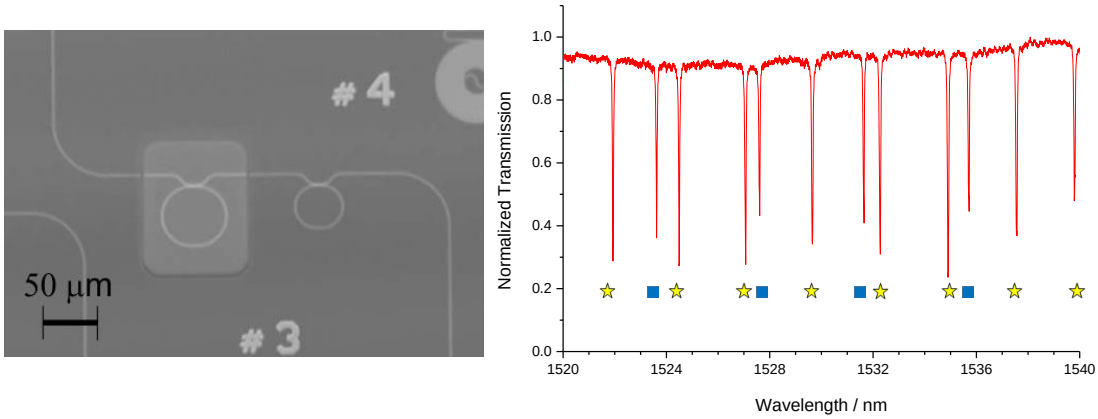

Figure 8.11: Optical profilometer image and transmission spectrum of a tandem ring resonator with sensing ring and reference ring circumferences of 185 µm and 134 µm, respectively. The resonances of the two rings can be separated as they have different free spectral ranges ($\Delta\lambda_{FSR}$). Here the free spectral range of the sensing and reference rings are $\Delta\lambda_{FSR}$ = 2.5 nm, 4.0 nm respectively. The sensing resonances are denoted by the yellow stars and the reference resonances with blue squares.

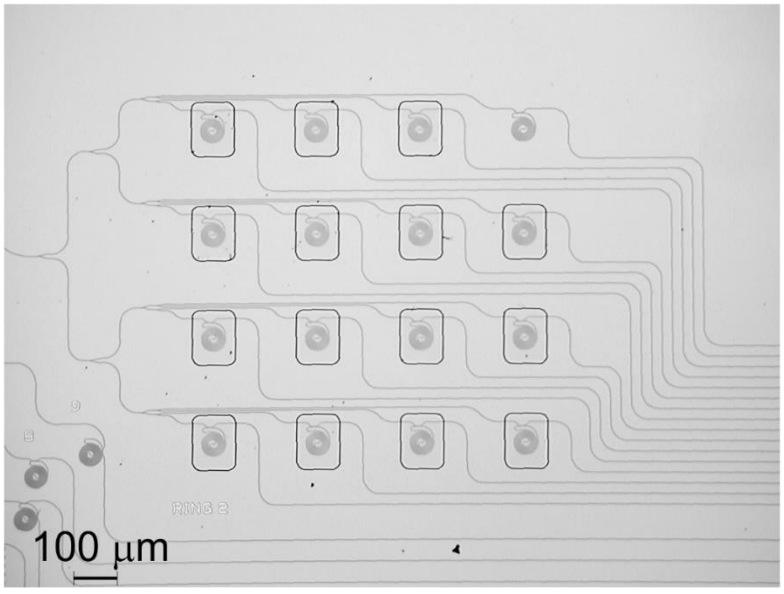

Figure 8.12: Optical microscope image of a 16 array of microring resonators. 15 rings can be coated with materials for refractive index sensing while one ring is buried under a protective over coat to compensate for temperature effects. Each ring is excited from a single input channel with 16 individual output channels to allow for simultaneous detection using a linear array detector or camera. An enlarged image of one of these ring resonators was shown previously in Figure 8.9.

8.2 Experimental Setup and Methods

This section outlines details of the experimental setup used to interrogate refractive index sensors in our group. Detailed information is provided about the optical components and experimental methods used for both gas and liquid sensing with SOI devices. A large portion of this project involved the development of code for data acquisition and interfacing of multiple components. Several different methods were tried during the development of the current code and are described in this section. Finally, refractive index calibration and the temperature correction of devices are also discussed.

8.2.1 Optical Experimental Setup

An Ando tuneable external cavity diode laser (AQ4320D) was used to scan across resonances and interferograms between λ = 1520-1620 nm. The laser diode was most stable when set to a power of 0.5-1.0 mW. It was internally chopped at a frequency of 300 kHz for all experiments and was used on the narrow linewidth setting. A three-paddle fibre polarizer (two quarter wave plates, and one half wave plate) was used to rotate the polarization of the light to couple into vertically polarized TM modes of the SOI waveguides. While the exact polarization could not be measured, the wave plates were optimized to produce the cleanest spectrum possible. A conically tapered single-mode optical fibre was used to couple light into the chip and was mounted on a 3-axis precision positioning stage (ULTRAlign Newport, Franklin, MA). Light from the output facet was collected using a precision-mounted straight-cleaved multi-mode optical fibre (100/140μm for the core and cladding diameters respectively). A CCD camera with a 70× telescope objective was mounted above the setup and used to align the fibres with the waveguide facets. The output light intensity was detected using an InGaAs photodiode detector (DET10C Thorlabs, Newton, NJ), and the signal was retrieved using a lock in amplifier (SRS 844RF Stanford Research Systems, Sunnyvale, CA). The detector intensity at the laser modulation frequency was collected alongside with the laser ramp voltage using a 16-bit analogue-to-digital converter (A/D) (USB-1608-FS Measurement Computing, Norton, MA), connected to the computer through a USB interface. The data acquisition was performed using custom LabView™ virtual instruments (VIs) incorporating drivers available from Measurement Computing to

access the A/D converter. The development of data acquisition software is discussed in detail in Section 8.2.3. A schematic of the experimental setup is shown in Figure 8.13. A photograph of the sensitive optical alignment, requiring high-precision positioning stages to couple light into and off of the SOI chips, is shown in Figure 8.14. This experimental setup was modified slightly for dosing gaseous and liquid samples over the SOI devices as will be discussed in Section 8.2.2.

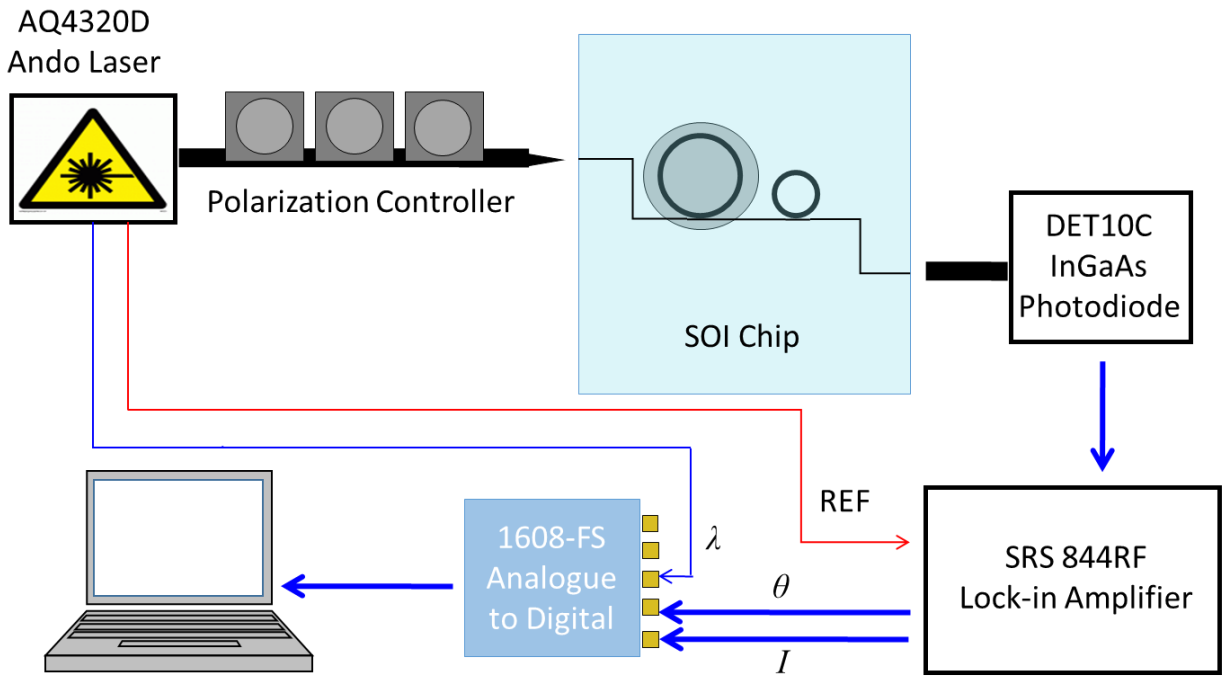

Figure 8.13: Schematic of the experimental setup for interrogating silicon-on-insulator devices. A tuneable external cavity diode laser (λ = 1520-1620 nm) was coupled to a fibre polarization controller to rotate the light to vertically polarized light in order to couple into TM modes on the SOI waveguides. A tapered single-mode optical fibre was used to couple into the SOI chip and a multi-mode optical fibre (100/140µm) collected the light leaving the chip, which was detected using an InGaAs photodetector. The signal was extracted using a lock-in amplifier and read by the computer using an A/D converter.

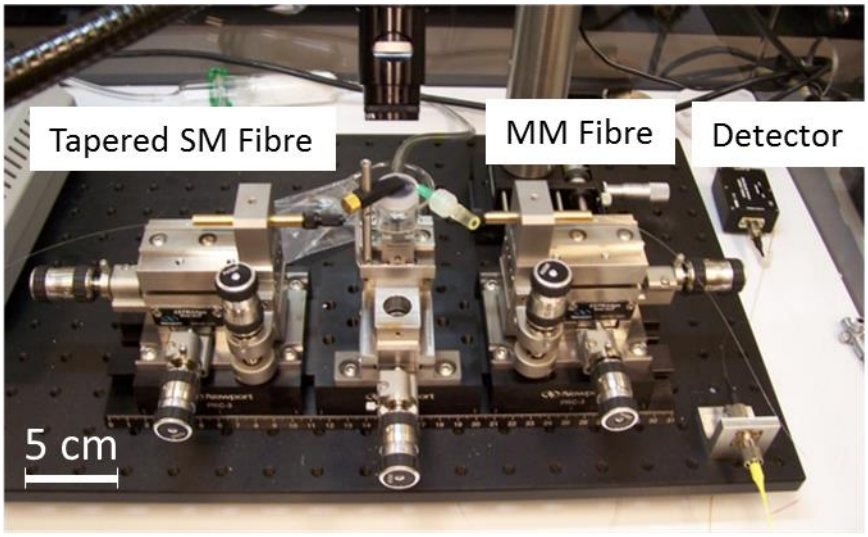

Figure 8.14: Photograph demonstrating the sensitive alignment needed to couple into SOI devices. The left precision stage holds a tapered single-mode optical fibre and the right precision stage holds the multi-mode collection optical fibre. The SOI device is under the glass dome on the central stage. The alignment microscope camera can be seen in the top of the image and the InGaAs photodiode in the top right corner.

8.2.2 Gas and Liquid Dosing Systems

For dosing SOI devices with solvent vapour, dry nitrogen was bubbled through a gas wash bottle to generate saturated solvent vapours that were further diluted with additional dry nitrogen using a two-channel flowmeter gas blender. The output of the flowmeter was then connected to a glass dome that was clamped above the SOI device. Holes were cut out of the glass dome to avoid putting pressure on the SOI chips or optical fibres. This system was used for generating vapour concentrations from 0.3% to 100% of the saturation pressure and is shown in Figure 8.15. The total flow rate was typically ~40 cubic centimetres per minute (ccm) and needed to be maintained relatively constant to reduce experimental noise and drift.

Flowing liquid samples over SOI devices was more challenging as any leaks disrupted the fibre alignment and interrupted experiments. Additionally, air bubbles often caused sudden changes in refractive index over sensors and complicated data analysis during liquid dosing experiments. Two different approaches for flowing liquids over SOI devices were explored. The first approach was to clamp a machined polymethylmethacrylate (PMMA) cap on top of the SOI devices. Glass capillaries were epoxied on either

end of the liquid cap and solutions were pumped through the system using a syringe pump (Harvard Apparatus 11 Plus, St. Laurent, QC). The waste was collected into a beaker behind the optical setup.

A) B)

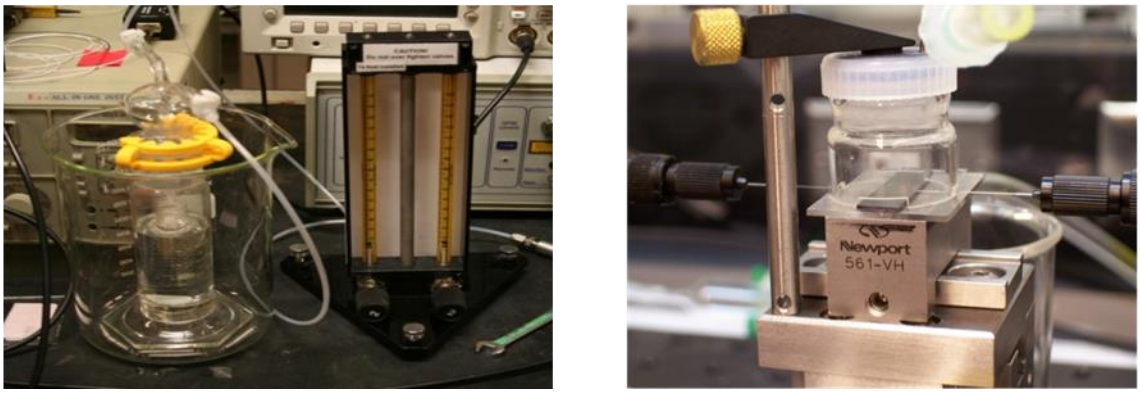

Figure 8.15: Solvent vapour generation and dosing system for polymer coated silicon-on-insulator experiments. A) Nitrogen gas was bubbled through liquid solvents in a gas wash bottle to generate saturated solvent vapours. These vapours were then further diluted with additional nitrogen down to concentrations from 0.3% - 100% of the saturated vapour pressure using a two-channel flowmeter gas blender. B) The solvent vapours were flowed into a glass dome over the SOI devices with holes cut out for the optical fibres and the SOI chip.

The second approach was to make microfluidics using soft lithography. Polydimethylsiloxane was cast onto a template (e.g., silicon wafer or glass slide) with a negative of the desired fluidics, and then peeled off once cured. This method was used to make both curved and straight channels depending on the template used. Holes could then be punched into the PDMS and syringe needles were inserted into the holes to flow liquid in and out of the PDMS fluidics. It was important to ensure that the fluidics were transparent so that the channels could be properly aligned relative to the desired SOI devices.

When using the PDMS fluidics, the syringe pump was used in reverse, sucking liquid from an open vial through the fluidics into the syringe. This generated a weak vacuum inside the fluidics and helps adhere the PDMS channels to the SOI chip without requiring clamping from above. When the fluidic channels were narrow, air bubbles were more frequent and complicated experiments. Simple wide channel microfluidics could be prepared using negatives prepared from transparent tape on glass slides.[67-68] Figure 8.16 shows the two different approaches of flowing liquids over SOI devices. These methods were used when calibrating the refractive index response of SOI devices, as will be discussed in Section 8.2.3.

A) B)

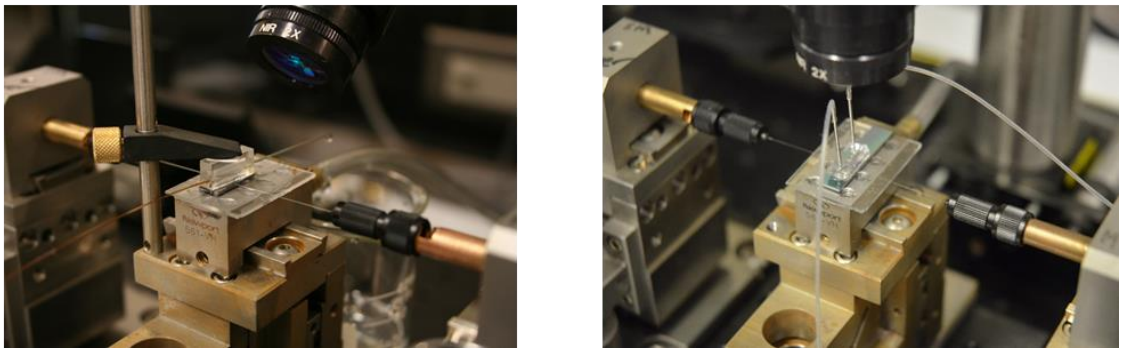

Figure 8.16: Methods for dosing liquid samples over Silicon-on-Insulator devices. A) A machined polymethylmethacrylate cap was clamped on top of the SOI chip and liquid was pumped through glass capillaries using a syringe pump. B) Polydimethylsiloxane fluidics were made using soft lithography and samples were sucked through the fluidics into a syringe pump. These fluidics were held on the chip by electrostatic forces and through a weak vacuum generated by the syringe pump.

8.2.3 Data Collection Methods and Programming

To conduct silicon-on-insulator experiments in our lab, communication was required between various components including a tuneable laser, photodetector, lock-in amplifier, and an analogue-to-digital converter. A significant part of this project was the initial development of algorithms for data acquisition. The data collection progressed through a series of three different methods that are described in the following sections. Initially, experiments were conducted with Mach-Zehnder interferometers, where the laser was held at a single wavelength and the intensity was monitored over time. This was used to track the phase shift as interference fringes moved through the observation wavelength as the refractive index over the sensing arm changed. The second method involved stepping the laser wavelength across a spectral window. The final, and currently used program, continuously scanned the laser and simultaneously collected the data over a fixed spectral window.

8.2.3.1 Fixed Wavelength Method

The initial interferometer experiments, required manually setting the laser wavelength and power, and used a proprietary program for data collection, TracerDAQ® (Measurement Computing). The data

collection was later replaced with custom National Instruments LabView™ VIs incorporating Measurement Computing drivers to read out the lock-in amplifier signal from the A/D converter over time. The fixed wavelength method allowed for quick data collection (50-100 Hz). This method is demonstrated with a refractive index calibration of a Mach-Zehnder interferometer using 5 aqueous sucrose solutions in Figure 8.17.

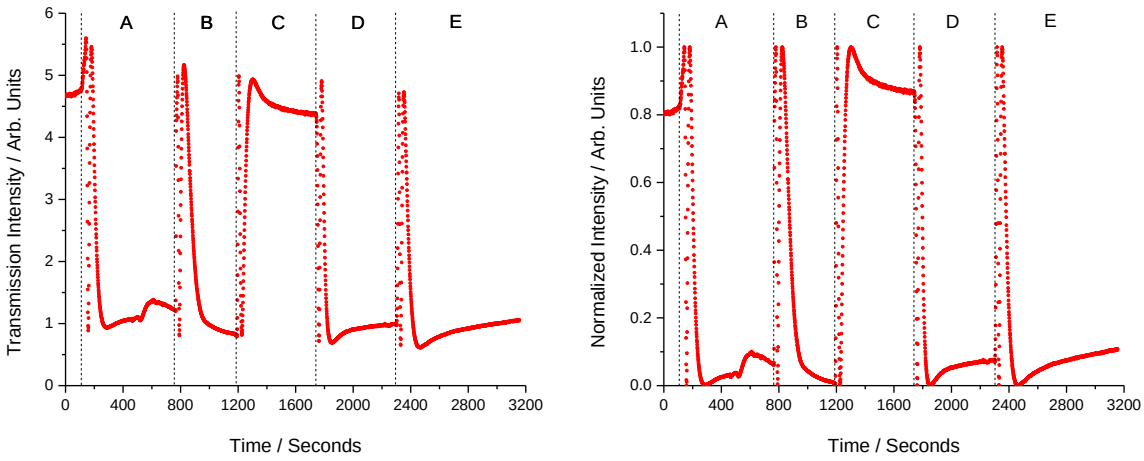

Figure 8.17: Signal intensity at a constant wavelength of λ = 1523 nm for an *L* = 8.1 mm Mach-Zehnder interferometer exposed to a series of sucrose solutions. The solutions A-E are of increasing sucrose concentrations with refractive indices n_{1550} = 1.3195-1.3308. A) The transmission intensity of the interference fringes drifted by more than 15% due to experimental drift. B) The signal was offset subtracted and normalized to more accurately determine the phase shift over time.

Unfortunately, measuring refractive index changes at a fixed wavelength made the experiment highly susceptible to any laser fluctuations or mechanical drift of the coupling alignment. These measurement errors were later reduced by stepping or scanning the laser over a small spectral window to collect a series of interference fringes where the phase shift was directly observed from the interferograms.

8.2.3.2 Stepped Wavelength Method

The first data acquisition program to collect ring resonator and interferometer spectra was written in LabView™ to manually step the laser over a spectral window. This was the most robust method for accurate wavelength measurements and produced the most consistent data.

While there is code to automatically step the laser with a constant wavelength step, it was very difficult to properly sync the data collection from the A/D converter to the laser step. To get around this problem, a for-loop was used in LabView™ to manually change the laser wavelength, and then a data point was sampled. Repeatedly sending commands to the laser caused delays in response and made this method very slow. The speed could be improved by increasing the step size, but only at a loss of resolution. The spectra for a ring resonator stepped from λ = 1520-1525 nm in steps of Δλ = 10 pm, 5 pm and 1 pm are shown in Figure 8.18.

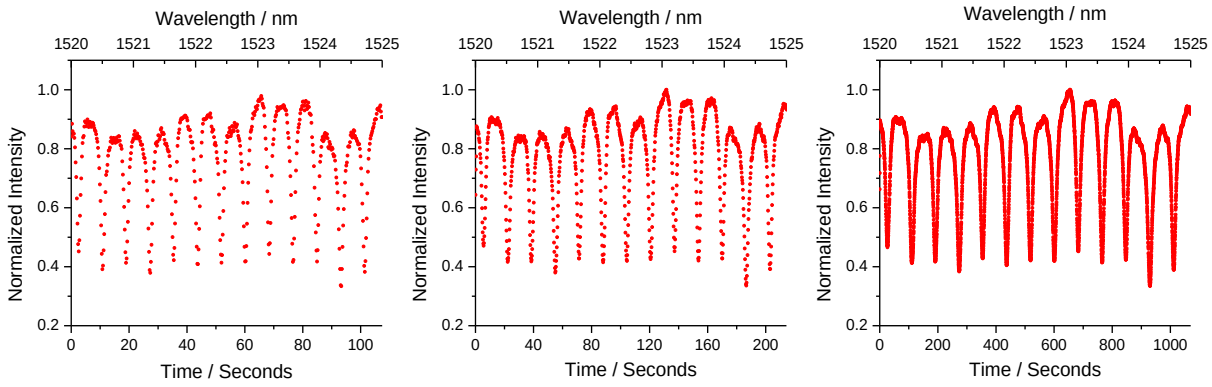

Figure 8.18 Comparison between low, medium, and high resolution wavelength spectra of an *L* = 1.27 mm microring resonator when the laser was stepped from λ = 1520-1525 nm. The laser was stepped in wavelength intervals of 10 pm, 5pm and 1 pm respectively shown from left to right. This required 20, 40 or, 200 s/nm of spectral window being measured.

While this method was effective for accurately acquiring spectra of ring resonators and interferometers it was quite slow and was later replaced by continually scanning the laser, as will be discussed in Section 8.2.3.3.

8.2.3.3 Scanned Wavelength Method

The final program iteration used internal commands to continually scan the laser while independently collecting the intensity information from the photodetector. The start wavelength, end wavelength and scan time were initialized with commands send to the laser in LabView™. Once all of the parameters were set and the data output file initialized, a command was send to the laser to begin a continuous scan. In this mode, the laser generated a linear voltage ramp to indicate the progress within the

scan window. This ramp ran from 0 to 2.3V at 0% and 100% of the scan window respectively. A sample voltage ramp for a 15 second scan is shown in Figure 8.19.

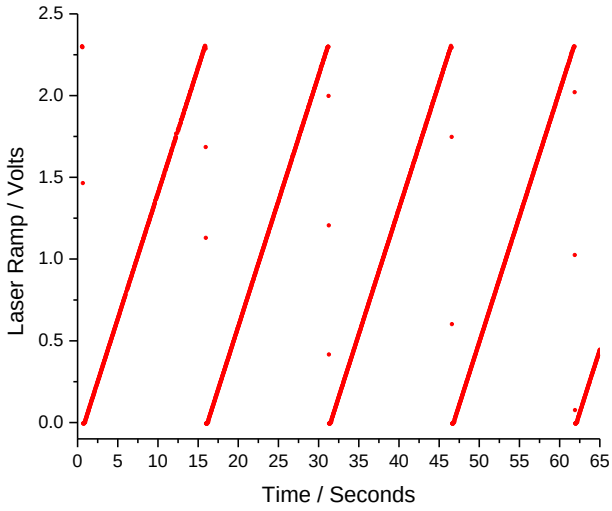

Figure 8.19: Sample voltage ramp from the Ando laser when run on the continuous wavelength scan mode. The laser ramp ranges from 0 V to 2.3 V as a function of progress through the scan window. There is a brief delay between scans as the grating needed to reset to the original position before the next scan could begin.

The laser wavelength was automatically assigned in the LabView™ code using the input wavelength parameters and the laser ramp voltage. The laser ramp had some jitter, which resulted in jitter of the wavelength assignment saved during experiments. Calculating the wavelength on the fly allowed for the live spectrum to be plotted on the screen during experiments. The data acquisition VI stored the time, the laser ramp voltage and photodetector signal for each point, since the A/D converter had 8 input channels it was also possible to simultaneously record the phase shift from the laser reference. Post experiment, the laser wavelength could be reassigned either as a function of time or from a linear fit to the laser ramp to remove the jitter.

The data collection rate was limited by the averaging time of the lock-in amplifier. Typically the best performance was observed with a minimum time constant of 3 ms on the lock-in amplifier which gave a maximum reliable data collection rate of 10 ms (100 Hz). At faster averaging, the noise level increased substantially. It is important that the data collection rate be at least a factor of 2-3 times slower than the

lock-in averaging to avoid oversampling the data. The resolution of a device transmission spectrum was now limited only by the laser scan time and the size of the spectral window. The required time resolution was assessed by scanning from λ = 1520-1540 nm with scan times of 15 s, 30 s, 60 s, 100 s, 200 s, 400 s respectively. The resulting spectra between λ = 1520-1525 nm are shown in Figure 8.20.

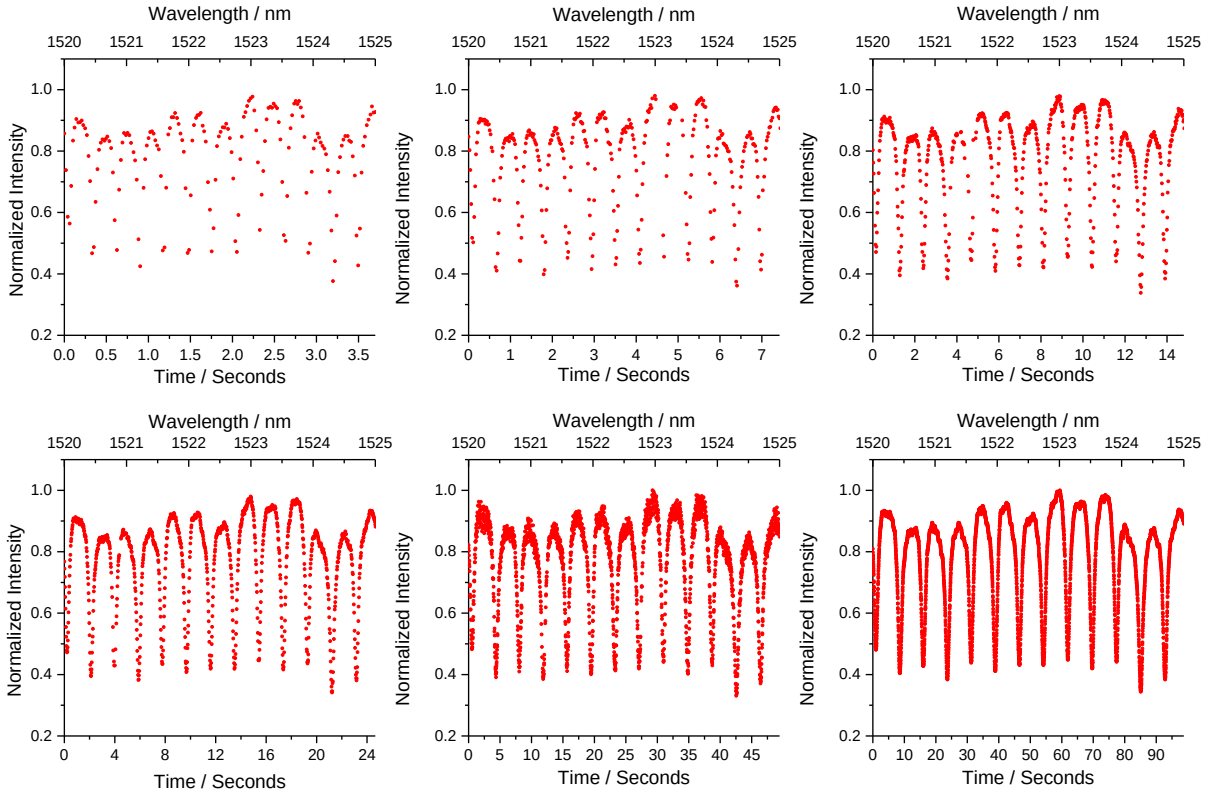

Figure 8.20: Comparison of the spectral resolution as a function of laser scan rate over a fixed spectral window. The top row shows spectra when the laser was scanned at rates of 1.3 s/nm, 2.0 s/nm, and 4.0 s/nm. The bottom row shows spectra at rates of 6.7 s/nm, 13.3 s/nm and 26.6 s/nm. The minimum resolution for accurate measurements depends on the FWHM of the resonances. For the *L* = 1.27 mm ring resonator in this figure, the minimum laser scan rate was 3 s/nm, where each resonance was described by a minimum of 20 points.

The recommended minimum resolution for acquiring ring resonator spectrum using this code occurred at laser scan rates of 3-5 s/nm. When high-resolution spectra were required, the recommended scan rates were closer to 20 s/nm. This is a factor of ten times faster than the stepped wavelength code described in the previous section, where a low-resolution scan needed 20 s/nm and a high-resolution scan > 200 s/nm.

The initial scanning code saved all of the data in the same channels and plotted all the scans as the experiment progressed. It was essential to observe a live spectrum in order to recognize problems from air

bubbles (in liquid experiments) or loss of signal from alignment drifts in the setup. Unfortunately, when every scan was plotted, the computer slowed down substantially as the number of data points increased in the graph, and the data acquisition rate slowed reducing the resolution of later scans. The loss of spectral resolution is demonstrated by the left two spectra in Figure 8.21 for scans at t = 15 s and t = 1965 s respectively.

A simple algorithm was added to the data acquisition program to separate the data between scans and to refresh the graph to show only the live feed of the current laser scan. The algorithm assumed that the data set was complete when the derivative of the last three values of the laser ramp was less than -0.01, indicating the downward slope at the end of the laser ramp. A new data set was then started once the derivative and the voltage ramp were both positive again. In the event of laser ramp fluctuations around 0 V, any data set that contained less than 20 points was assumed to be an error and automatically deleted. This algorithm allowed the graphs to be continually refreshed and improved the consistency of the spectral resolution between scans, as is shown with the two right spectra in Figure 8.21 at t = 15 s and t = 1965 s.

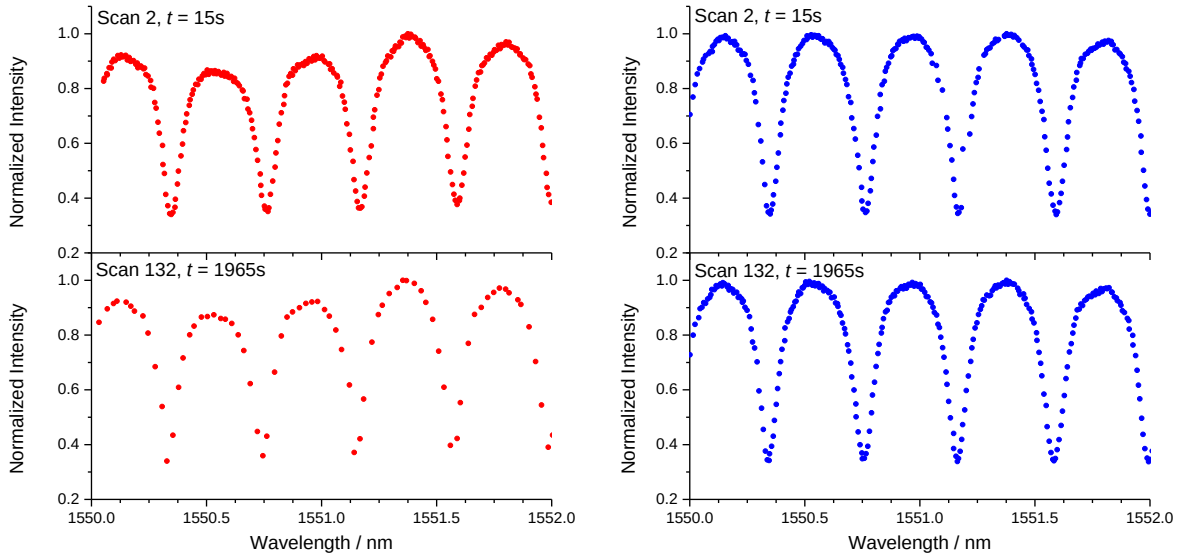

Figure 8.21: Comparison between the loss in spectral resolution when plotting all scans or when refreshing to only show the current laser scan in LabView™. The two left traces show the loss of resolution that occurs when plotting all the data on a single graph in the data acquisition software. When the data was automatically separated into individual scans the number of data points remained almost unchanged over the full time of the experiment, as is seen in the two traces on the right.

The number of data points using both modes shown in Figure 8.21 as a function of experiment time and scan number are shown in Figure 8.22. The number of data points when plotting all data sets decayed exponentially while the number of data points remained constant when plotting only the current laser scan.

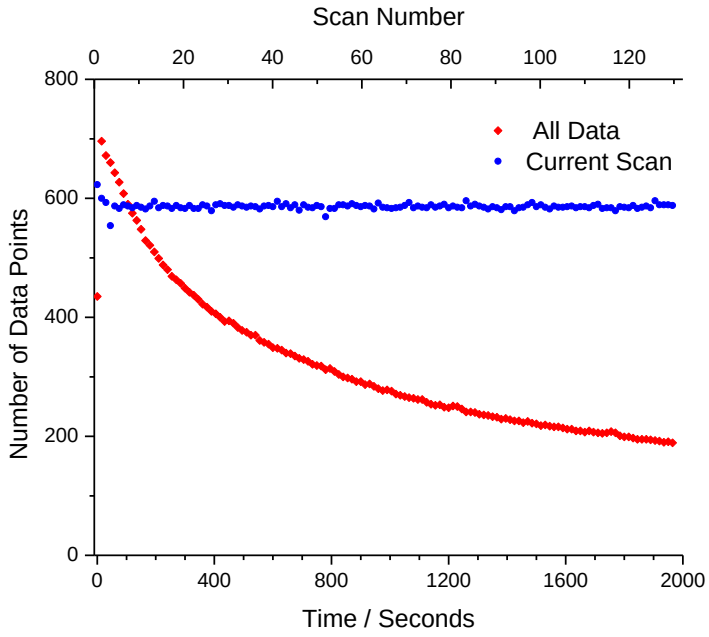

Figure 8.22: The number of data points as a function of scan number and experiment time when plotting all data and only the current laser scan. The number of data point decayed exponentially when plotting all the data as the experiment progressed. When automatically separating the data into individual scans and only plotting the current laser scan, the spectral resolution remained almost constant.

While the automation of separating the data into individual scans helped with data consistency between scans, it was a not easy to write the algorithm as it had to be robust enough to not incorrectly separate the data. Especially since any data acquisition errors could not be repaired post-experiment. The final data acquisition program used this algorithm and even included an initial attempt at on-the-fly peak resonance fitting and tracking. Unfortunately, LabView™ only provides a very cumbersome method for conducting non-linear curve fitting and does not have any built-in Lorentzian fitting functions making on-the-fly analysis difficult. Post-experimental data analysis using for example, Igor Professional (Wavemetrics, Portland, OR), or Matlab™ (Mathworks, Natick, MA) was much more reliable and our preferred method to analyse data. The final acquisition program had a user friendly front end and allowed

the user to record all essential experimental parameters and notes directly within the data files. The user inputs and data outputs from the front panel of the LabView™ code are described in Appendix 8.2.

The data acquisition code was also adapted for the interrogation of microsphere resonators in a different project.[69] For this purpose, additional input channels were added to read the corresponding signal from a quartz crystal microbalance (QCM), using the RS232 serial port, and the signal from a second lock-in amplifier. This program was used to simultaneously measure both the intensity and phase from the transmission and back-reflected spectra collected using two different photodetectors.

The experimental results achieved using SOI MZ interferometers and ring resonators are discussed in Section 8.3, and were typically obtained using the stepped laser program.

8.2.4 Refractive Index Calibration

The refractive index sensitivity of interferometers and microring resonators was determined by calibration with aqueous sucrose solutions. In principle, other aqueous solutions with sodium chloride, ethylene glycol, dimethylsulfoxide or glycerol could also be used for calibrations.

The first experiments using MZ interferometers were run at a constant laser wavelength. In this case, the intensity was recorded as a function of time and the phase shift was calculated from the normalized data. Once the intensity offset was subtracted and the data was normalized so that the fringes spanned between I = 0 - 1, the phase shift could be extracted from the arccosine of the processed signal.

$$\phi = \cos^{-1}\left[2\times\left(I-\frac{1}{2}\right)\right] \tag{8.25}$$

The total phase shift was tracked for a series of aqueous sucrose solutions with increasing concentration. The resulting linear calibration of an 8.1 mm MZ interferometer yielded a sensitivity of $\Delta\phi/\Delta n$ = 3900 radians/RIU and a resolution of $\Delta n = 2.0\times10^{-3}$, as is shown in Figure 8.23. The original intensity data from this experiment was previously shown in Figure 8.17.

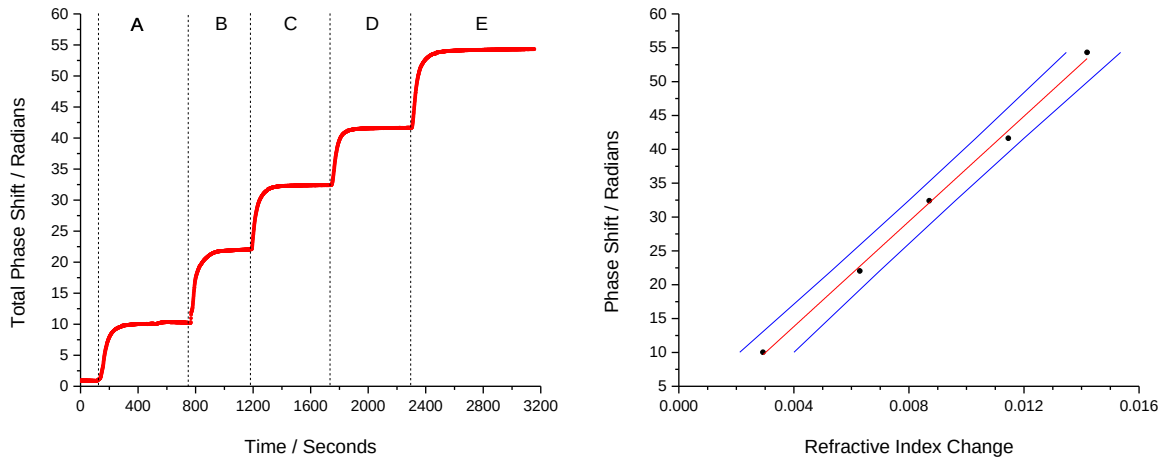

Figure 8.23: Refractive index calibration of an 8.1 mm Mach-Zehnder interferometer at a fixed wavelength, λ = 1523 nm. The solutions A-E are aqueous sucrose solutions with refractive indices of n_{1550} = 1.3195, 1.3229, 1.3253, 1.3281 and 1.3308 respectively. The total phase shift was extracted from the normalized intensity data in Figure 8.17. The phase shifts for the five solutions are shown in the right figure with 1σ confidence intervals shown in blue on either side of the linear fit. The device sensitivity was determined as $\Delta\phi/\Delta n$ = 3900 radians/refractive index unit (RIU) and the resolution was estimated as $\Delta n = 2.0\times10^{-3}$.

After the laser stepping program was developed (Section 8.2.3.2), the phase shift was calculated from the peak wavelength displacement using equation (8.8). The calibration of an L = 3.017 mm MZ interferometer is shown in Figure 8.24. The sensitivity for the MZ interferometer was found to be $\Delta\phi/\Delta n$ = 3200 radians/RIU and the resolution was estimated from spread of the calibration as $\Delta n = 2\times10^{-4}$. Since a larger spectral region was now used, less processing was needed when normalizing and analyzing the data.

Using the same wavelength stepping program, an L = 936 μm coiled microring resonator was also calibrated using sucrose solutions with n_{1550} = 1.3173-1.3210. A sample transmission spectrum is shown in Figure 8.25 with the change in a single resonance peak over time. In this experiment, the device was flushed with water between each solution. The wavelength shift from each solution was averaged using two of the resonances, as the third resonance moved out of the scan window when measuring the higher refractive index solutions. The resulting calibration gave a sensitivity of $\Delta\lambda/\Delta n$ = 115 nm/RIU with a detection limit of $\Delta n = 2\times10^{-4}$ (Figure 8.26).

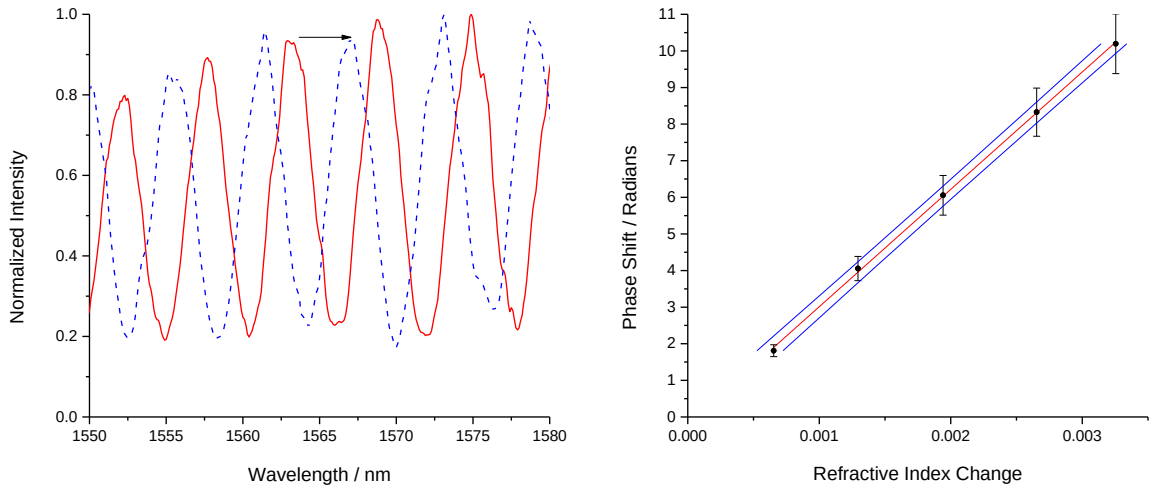

Figure 8.24: Spectrum and linear refractive index calibration of an L = 3.017 mm Mach-Zehnder interferometer. A) The spectrum of water (n_{1550} = 1.3164) and 0.9 % w/w sucrose solution (n_{1550} = 1.3179) over the MZ interferometer is shown by the solid red and dashed blue curves, respectively. The spectral shift, and the fringe spacing was used to determine the phase shift. B) The phase shift was recorded for solutions of n_{1550} = 1.3173-1.3199, and the calibration yielded a sensitivity of $\Delta\phi/\Delta n$ = 3200 radians/RIU with a resolution of $\Delta n = 2\times10^{-4}$. The red line shows the linear fit with the two blue lines showing ± 95% confidence intervals. The error bars show the standard deviation calculated from the shifts of three different fringes.

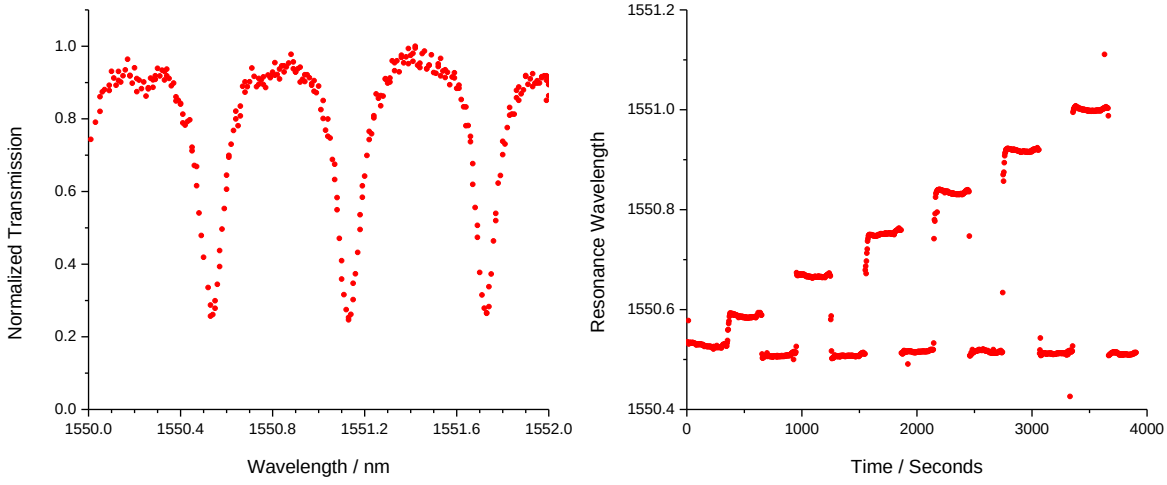

Figure 8.25: Sample transmission spectrum of an L = 936 µm microring resonator and the change in a single resonance peak position during a refractive index calibration with sucrose solutions. A) The transmission spectrum shows three resonance peaks with a width of $\delta\lambda_{FWHM}$ = 0.116 ± 0.011 nm and spacing of $\Delta\lambda_{FSR}$ = 0.596 nm. This resonator had a Q-factor of Q = 13 000 ± 1 000 and a finesse of F = 5.2 ± 0.5. B) The wavelength shift of the first resonance is shown during exposure to sucrose solutions of 0.5-3% w/w in 0.5% steps (n_{1550} = 1.3173-1.3201). The device was washed with water between calibration solutions.

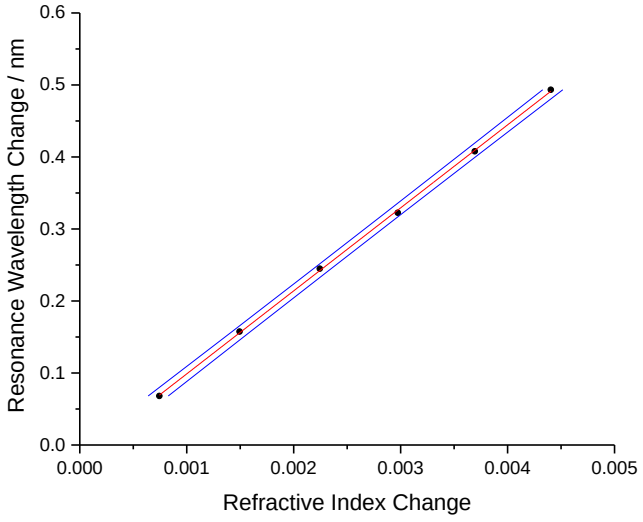

Figure 8.26: Linear fit to the sucrose calibration for an L = 936 µm microring resonator from Figure 8.25. The red line shows the linear fit and the blue lines show ± 95% confidence intervals of the fit. The slope gave a sensitivity of $\Delta\lambda/\Delta n$ = 115 nm/RIU with a detection limit of $\Delta n = 2\times10^{-4}$.

The stepped wavelength method was also used to calibrate a pair of tandem ring resonators with circumferences of L = 185 µm and L = 134 µm for the sensing and reference rings respectively. The transmission spectrum of the tandem ring when exposed to water and sucrose solutions from 2.3-9.3 %w/w (n_{1550} = 1.3164-1.3303) in shown in Figure 8.27. A Lorentzian function was fit to the data to determine the peak location for the refractive index calibration (Figure 8.27). The tandem ring resonators contain a reference ring that can be used to compensate for temperature related resonance shifts, as will be discussed in the following section. It is apparent in Figure 8.27, that the reference ring position remains unchanged between solutions. The calibration of the tandem ring resonators yielded a sensitivity of $\Delta\lambda/\Delta n$ = 71.8 nm/RIU with a resolution of $\Delta n = 1.2\times10^{-3}$. More recent calibrations of tandem ring resonators on similar chips yielded sensitivities of up to $\Delta\lambda/\Delta n$ = 140 nm/RIU with estimated detection limits of $\Delta n = 3\times10^{-4}$.

During long experiments, temperature fluctuations can add a large amount of noise to resonance shifts, and can make analyzing results challenging. To compensate for temperature effects, either the ambient temperature must be accurately recorded, or experiments must be restricted to tandem ring resonators where temperature induced resonance shifts can be inferred from the wavelength shifts of a

reference ring. The methods of temperature compensation using a reference ring are described in Section 2.2.5.

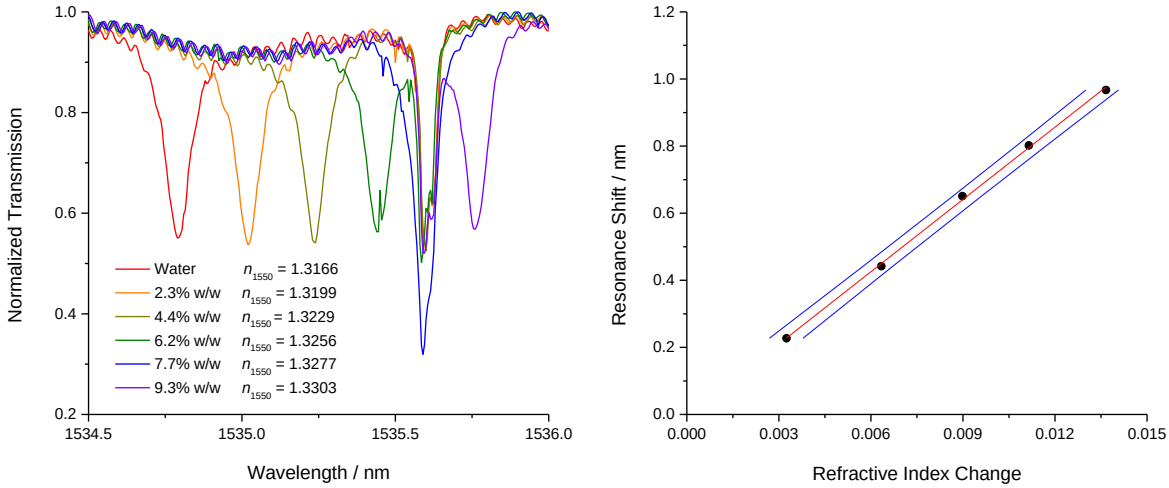

Figure 8.27: Refractive index calibration of a pair of tandem ring resonators with circumferences of L = 185 µm and L = 134 µm for the sensing and reference rings. A) The reference peak was present at a constant wavelength of 1535.6 nm and had a Q-factor of Q = 28 000, while the sensing ring had a Q-factor of Q = 16 000 and shifted with each solution. B) The sensitivity of the linear fit was found as $\Delta\lambda/\Delta n$ = 71.8 nm/RIU with 1σ confidence intervals shown with blue lines. The fit gave an expected detection limit of $\Delta n = 1.2\times10^{-3}$.

8.2.5 Temperature Compensation

The advantage of using a pair of tandem ring resonators, is the ability to correct for wavelength shifts resulting from temperature fluctuations observed by a reference ring during experiments. This can be especially helpful for long uptake experiments where substantial temperature drifts may be present. The temperature response of the resonator depends on the thermo-optic coefficients of the waveguide and surrounding media, i.e., it is related to the change in effective refractive index of the waveguide.[63]

$$\frac{\delta\lambda}{\delta T} = \frac{\lambda}{n_g}\frac{\delta n_{eff}}{\delta T} \tag{8.26}$$

The temperature resonance shifts for silica clad ring resonators have been previously reported as 62.1 pm/°C, while sensing rings covered in air or water have resonance shifts of 60.6 pm/°C and 48.9 pm/°C

respectively.[63] For SU-8 clad devices, the temperature induced resonance shifts of the reference rings are different depending on whether they are under air or water with shifts of 29.7 pm/°C and 36.6 pm/°C, respectively. Similarly, the sensing rings on the SU-8 clad devices shift by 52.6 pm/°C under air and 35.1 pm/°C when under water.[63]

An example of the benefits of temperature compensation is shown with recent experimental data collected by Mr. Hao Chen studying the uptake of lead (II) ions into a tetrasulfide functionalized mesoporous silica coated SOI device. In his experiment, the resonance changes during the uptake and release of 1 ppm Pb (II) are almost entirely obscured by the temperature effects caused by a 1°C oscillation in the ambient temperature. The sensing ring and reference ring resonance positions are shown for a 1.5 hour period (Figure 8.28A). The temperature effects observed by the reference ring can be subtracted out of the sensing ring data to compensate for temperature fluctuations (Figure 8.28B). In this experiment, the coating was only a few hundred nanometers thick so the temperature response of the sensing ring should be comparable to uncoated ring exposed to water.

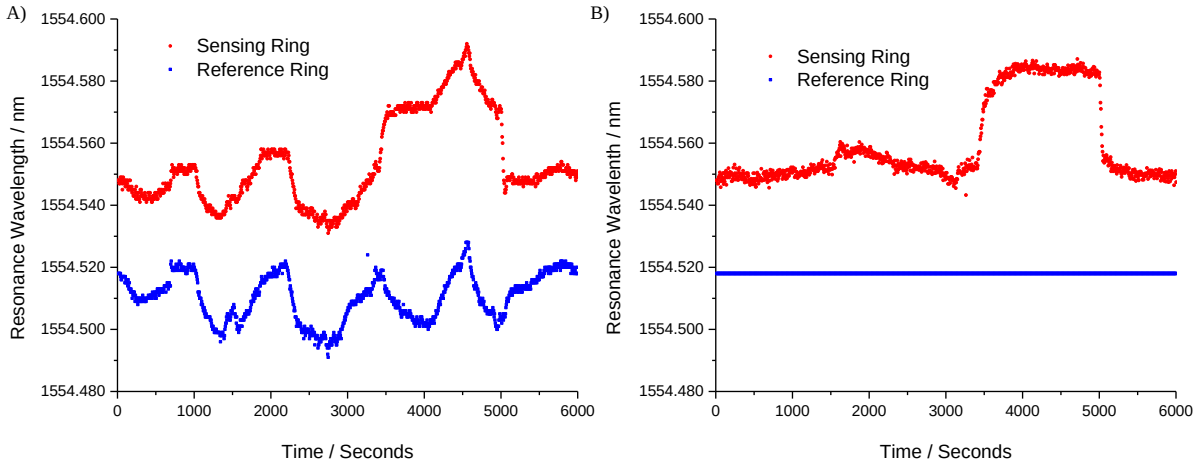

Figure 8.28: Compensation of temperature effects from the resonance shifts of the reference ring of a tandem ring resonator. A) The resonance wavelength of the sensing and reference peak shown over a 6000 s period. B) The temperature related resonance shifts have been subtracted from the sensing and reference rings using temperature sensitivities of 48.9 pm/°C and 62.1 pm/°C for the two rings respectively.[63]

The corrected resonance wavelength in Figure 8.28B is calculated by subtracting the weighted effects from the reference ring shifts.

$$\lambda_{sen,Corrected}(t) = \lambda_{sen}(t) - \Delta\lambda_{ref}(t)\left[\frac{\Delta\lambda}{\Delta T}(sen) \Big/ \frac{\Delta\lambda}{\Delta T}(ref)\right] \tag{8.27}$$

The cyclic reference resonance shifts were due to cycling of the ventilation and air conditioning in the room. Experimentally, the room temperature was simultaneously recorded using a USB temperature probe (OM-EL-USB Omega, Laval, QC) and showed the same periodicity as these fluctuations (Figure 8.29).

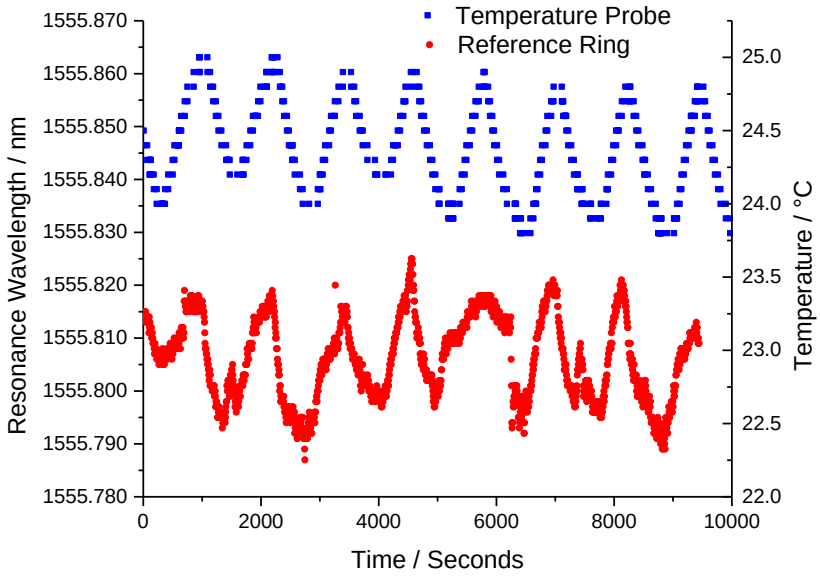

Figure 8.29: Correlation between the resonance shifts of the reference ring and changes in the ambient room temperature. The bottom red data shows the change in the reference ring resonance wavelength with the first 6000 seconds shown previously in Figure 8.28. The top blue data was recorded using a temperature probe and shows changes in the ambient room temperature during the SOI experiment. It can be seen that the periodicity in the temperature fluctuations is the same as was observed with the reference resonance wavelength.

While temperature compensation was necessary to correct for drift during long experiments, it was not required for most of the VOC sensing experiments performed using siloxane coated SOI devices described in Section 8.3.

8.3 Results

Experiments were initially performed using Mach-Zehnder (MZ) interferometers interrogated at a constant laser wavelength while the intensity was measured over time. This was the simplest method to interrogate MZ interferometers. The challenge with MZ interferometers is that they only show relative

changes in the refractive index between the two arms. If both the coating on the sensing arm and the protective overcoat on the reference arm interact with an analyte, then the experiment becomes very complicated to interpret. Microring resonators were later used to quantify and separate the analyte interactions with polymer coatings and from those with the protective overcoat.

8.3.1 Polymer Coated Mach-Zehnder Interferometers

An L = 8.1 mm Mach-Zehnder interferometer, similar to the one shown in Figure 8.5, was used for the following experiments. The typical sensitivity of the interferometers was $\Delta\phi/\Delta n$ = 3900 radians/RIU, as was shown previously in Figure 8.17. A sample spectrum of the L = 8.1 mm MZ interferometer is shown in Figure 8.30 where the interference fringes were spaced by $\Delta\lambda$ = 2.1 nm.

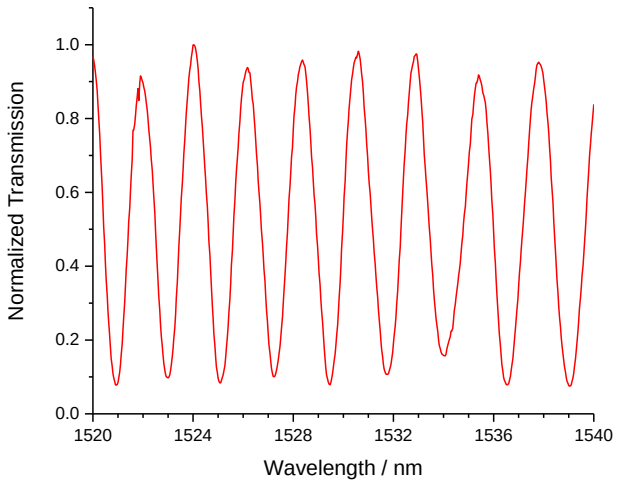

Figure 8.30: Transmission spectrum of a Mach-Zehnder interferometer with arm lengths of L = 8.1 mm. The sensing arm was exposed to air, while the reference ring was buried under a layer of SU-8. The spacing of the fringes was approximately $\Delta\lambda$ = 2.1 nm.

Polydimethylsiloxane (PDMS) films were prepared on the SOI chip by combining 1.1 g of polymer base with 110 μL of curing agent in 2-5 mL of hexanes. The solution was spin coated onto a clean SOI device at 3000 rpm to yield a coating that was approximately 3-10 μm thick. The PDMS-coated SOI device was then exposed to saturated m-xylene vapours with a partial pressure of P = 800 Pa where the balance was dry nitrogen (Praxair, Kingston, ON). The laser was set to a wavelength of λ = 1535 nm and the

transmission intensity was recorded as m-xylene diffused into the PDMS film. The transmission intensity was recorded as the interference fringes passed and the phase shift was extracted using equation(8.25) as is shown in Figure 8.31.

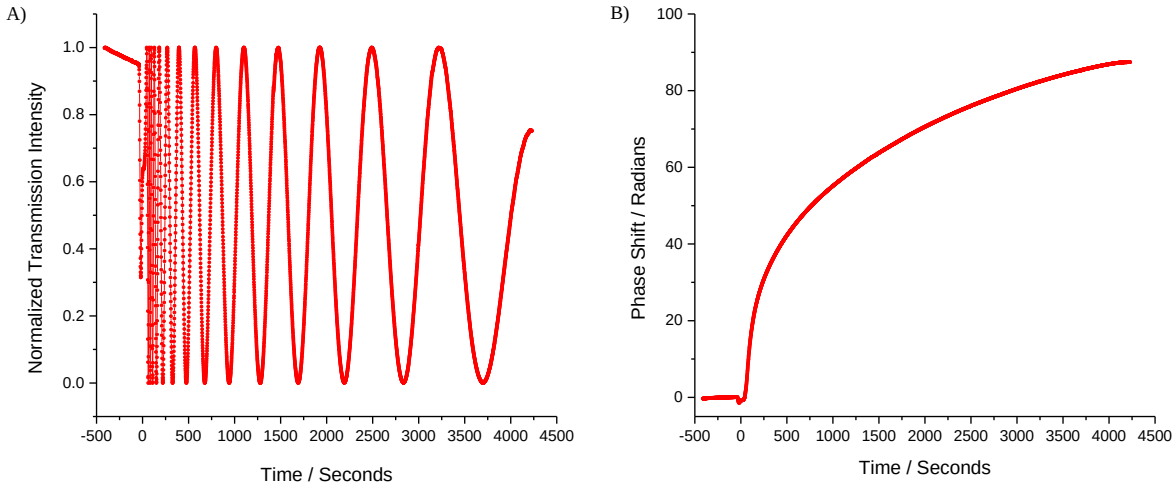

Figure 8.31: The transmission intensity of an *L* = 8.1 mm MZ interferometer showing the interference fringes passing and the extracted phase shift observed for a PDMS coated device exposed to saturated m-xylene vapour. A) The normalized interference fringes show the phase shift that occurred at λ = 1535 nm during the uptake of m-xylene (P = 800 Pa). B) The accumulated phase shift was calculated from the intensity changes shown in A).

The refractive index change during the uptake of m-xylene was calculated from the phase shift data in Figure 8.31 and the refractive index calibration in Figure 8.17. This refractive index change was then used to calculate the analyte concentration in the film using the equations previously discussed in Chapter 3.2. The initial refractive index of PDMS was assumed to be $n_{1550} = 1.3997$.[37] Experiments with SOI devices do not provide any thickness information about the film, and the actual film thickness was unknown, so $\Delta d/d$ was assumed to be 0 for the purpose of estimating the analyte concentration in the film. Due to this assumption, the concentration will be underestimated, as it did not account for the swelling of the material. Although, one would expect the same diffusion rates as long as the rates of refractive index change and swelling were identical. The data was fit to a two-rate diffusion model for the refractive index change at the film-substrate interface (the bottom of the film), based on equation (3.24).

$$X(t)_{uptake} = X_1\left[1-\frac{4}{\pi}\sum_{n=0}^{\infty}\frac{(-1)^n}{(2n+1)}\exp\left(-\frac{(2n+1)^2 D_1\pi^2(t-t_0)}{4d_1^{\,2}}\right)\right] + X_2\left[1-\frac{4}{\pi}\sum_{n=0}^{\infty}\frac{(-1)^n}{(2n+1)}\exp\left(-\frac{(2n+1)^2 D_2\pi^2(t-t_0)}{4d_2^{\,2}}\right)\right] \quad (8.28)$$

The concentration data and the fit to equation (8.28) are shown in Figure 8.32.

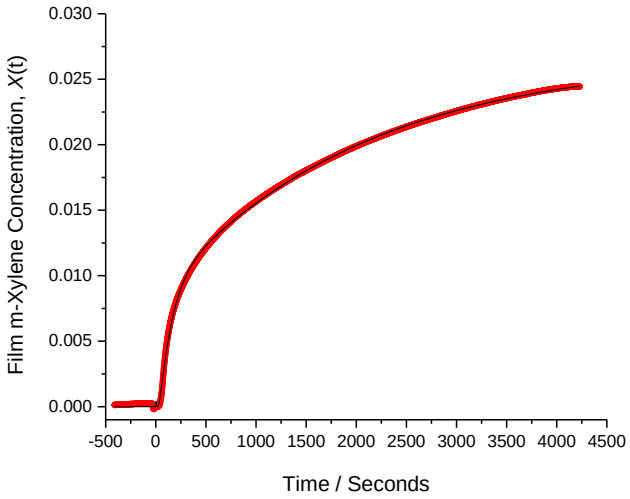

Figure 8.32: Approximated m-xylene concentration within a PDMS film during the uptake of saturated vapours (P = 800 Pa). The concentration was calculated from the refractive index changes related to Figure 8.31, assuming an initial refractive index of 1.3997 for the PDMS film[37] and that no film swelling occurred. The two-rate diffusion fit gave fit parameters of D_1 = 1.81×10^{-9} cm^2/s, D_2 = 7.04×10^{-11} cm^2/s, X_1 = 0.012 and X_2 = 0.014 with thicknesses of d_1= 8.3 µm and d_2 = 5.8 µm.

While a two-rate diffusion process can be used to account for simultaneous diffusion into PDMS and SU-8, there will be some complication with the competing affinity of these two materials. Two different thicknesses are used as fitting parameters for the SU-8 and PDMS layers. These extra fitting parameters influenced the extracted diffusion rates and inherently limited the accuracy of diffusion studies using this platform. The diffusion rates (D_1 = 5×10^{-8} cm^2/s and D_2 = 5×10^{-9} cm^2/s) previously reported using the refractometer in Chapter 7 are expected to be more accurate as they properly model the analyte concentration in the film by accounting for the film swelling during the uptake. The fit in Figure 8.32 is presented to demonstrate that the diffusion equations described in Chapter 3 are fully compatible with other refractive index sensing devices including MZ interferometers and ring resonators.

The PDMS coated MZ interferometer was also exposed to a range of different concentration of m-xylene vapours from 40 to 160 Pa and showed a linear phase response with concentration of $\Delta\phi/\Delta P$ = 0.057 rad/Pa (Figure 8.33).

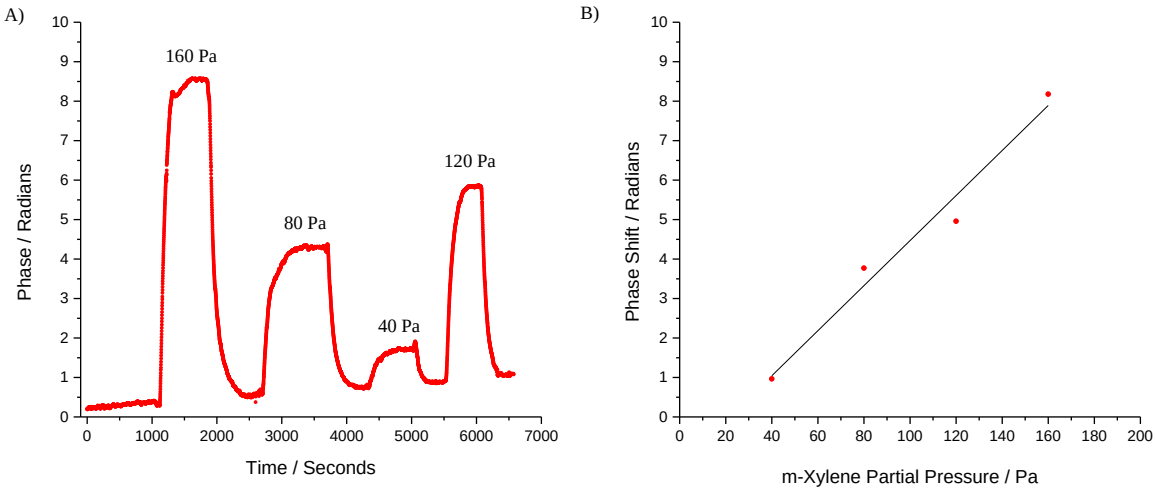

Figure 8.33: Phase-shift response of a PDMS coated MZ interferometer to m-xylene vapour concentrations between 40-160 Pa. A) The phase response was measured at a constant wavelength of λ = 1529.4 nm for the uptake and release of m-xylene vapours. Between each sample, the device was flushed with dry nitrogen to recover the device. B) The MZ interferometer shows a reasonably linear response with a sensitivity of $\Delta\phi/\Delta P$ = 0.057 rad/Pa.

As was previously discussed, MZ interferometers measure the refractive index difference between the two arms of the device. The uptake curves can become complicated when diffusion also occurs through the protective overcoat on the reference ring. The protective overcoat over the reference arms on the SOI devices was made from either SU-8 epoxy or silica. An uncoated SU-8 clad MZ interferometer was also exposed to saturated m-xylene vapours and showed a phase-shift as either m-xylene partitioned into the SU-8 or condensed on the surface of the sensing ring. When an uncoated silica clad interferometer was exposed to m-xylene vapours, only a small phase shift was observed. The phase-shifts observed with both the uncoated SU-8 and silica clad chips are shown in Figure 8.34 with the PDMS coated SU-8 clad results from Figure 8.31.

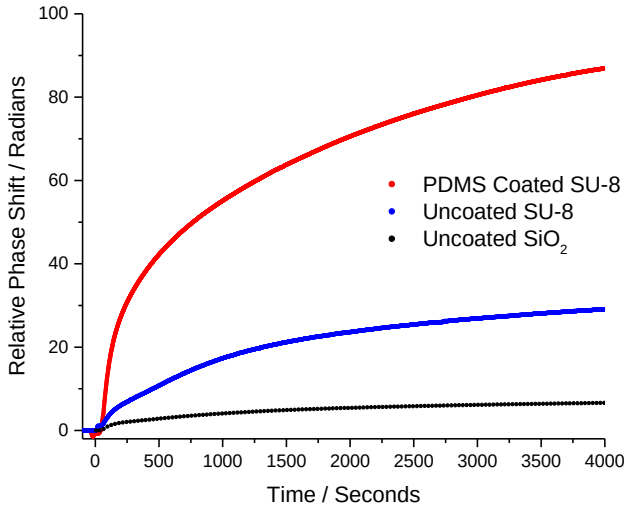

Figure 8.34: Comparison between the phase response of coated and uncoated Mach-Zehnder interferometers with saturated m-xylene vapour. The PDMS coated SU-8 clad chip showed the strongest phase response though approximately 25% of the phase shift was observed when the uncoated SU-8 chip was exposed to m-Xylene. The uncoated silica clad device showed a much smaller response and was artificially set negative for comparison.

The trouble with measuring interferometers at a single wavelength is there is no way to distinguish which direction the interferogram has shifted. From these experiments, one cannot determine if the relative refractive index increased in the reference or sensing arm of the interferometer. The fact that there is a substantial difference in the response between the uncoated SU-8 and silica clad chips suggests that the refractive index of SU-8 must change during the exposure to m-xylene vapour. The diffusion equations would not fit to either of the phase responses observed on the uncoated SU-8 or silica clad devices, suggesting that whatever occurred was not strictly diffusion controlled, which could be the result of solvent also condensing on the sensing ring. Finally, since the strongest signal was observed for the PDMS coated device, we can infer that PDMS also interacts with m-xylene and has likely a stronger affinity to m-xylene than the SU-8 protective overcoat.

In order to better explore the observed effects, the sensing arm and reference arm needed to be probed independently. Tandem ring resonators were used to independently study the effects of solvent vapour uptake into polymer coatings and the protective overcoats. The results from ring resonator experiments are described in the following section.

8.3.2 Polymer Coated Tandem Ring Resonators

In order to study the resonances of microring resonators, the laser needed to be stepped or scanned over a full spectral window. The data in the following section was collected using the laser step code that was described in Section 8.2.3.2 at a resolution of $\Delta\lambda$ = 0.005-0.01 nm. This method gave very poor time resolution with a 5 nm scan taking longer than 3.5 minutes, and was not suitable for any kinetic measurements. The higher resolution scanning code described in Section 8.2.3.3 was not developed until after all of the experiments were completed and was not available at the time of this study.

An uncoated SU-8 clad tandem microring resonator (Figure 8.11) was exposed to m-xylene vapours from 40-160 Pa and the response was measured simultaneously for both the sensing and reference rings. A strong response was observed with both the sensing and reference rings but the wavelength shifts were in opposite directions (Figure 8.35).

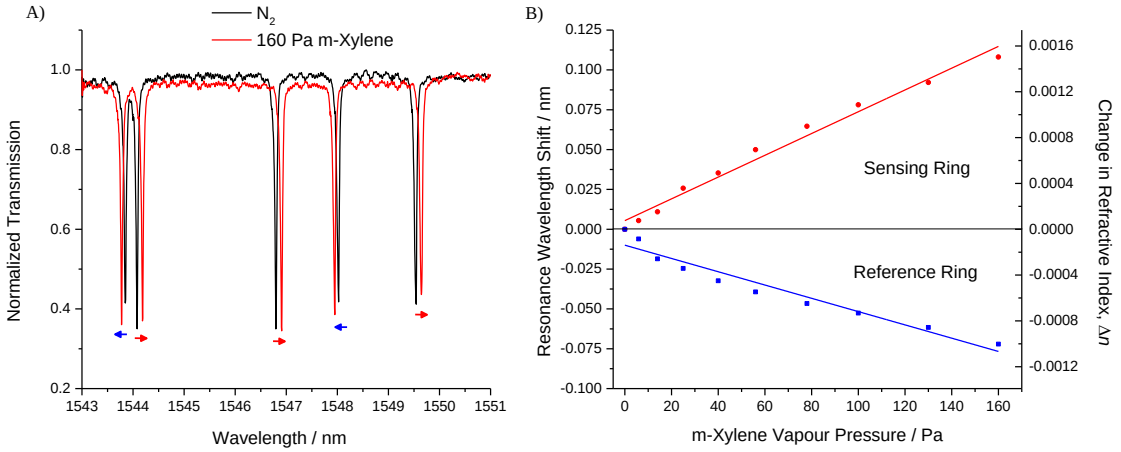

Figure 8.35: Uncoated tandem ring resonator spectrum and response when exposed to m-xylene vapour from 40-160 Pa. A) When the uncoated resonator was exposed to 160 Pa m-xylene vapour, the reference peaks shifted to shorter wavelength while the sensing rings shifted to longer wavelength. B) The observed trends of the sensing ring and reference ring are shown with linear fits from 40-160 Pa.

The increase in refractive index above the sensing ring can be explained by solvent condensation on the waveguide surface as the shifts were too large to be strictly related to the gas phase concentration. Note that the highest partial pressures corresponded to 20% of the saturation pressure of 800 Pa. In the case of the reference ring, the decrease in refractive index suggested that the SU-8 swelled when exposed to m-xylene.

When the uncoated silica clad tandem ring resonators were exposed to vapours of BTEX compounds only the sensing ring showed a response. In a few cases, small peak shifts were observed with the reference ring, but those appeared to correlate with temperature changes during the experiment (Figure 8.36A). The temperature induced resonances shifts were removed using the coefficients of $\delta\lambda/\delta T$ = 60.6 pm/K and $\delta\lambda/\delta T$ = 62.1 pm/K for the sensing and reference ring respectively.[63] The temperature compensated resonance shifts of the uncoated tandem ring resonator device with BTEX vapours are shown in Figure 8.36B.

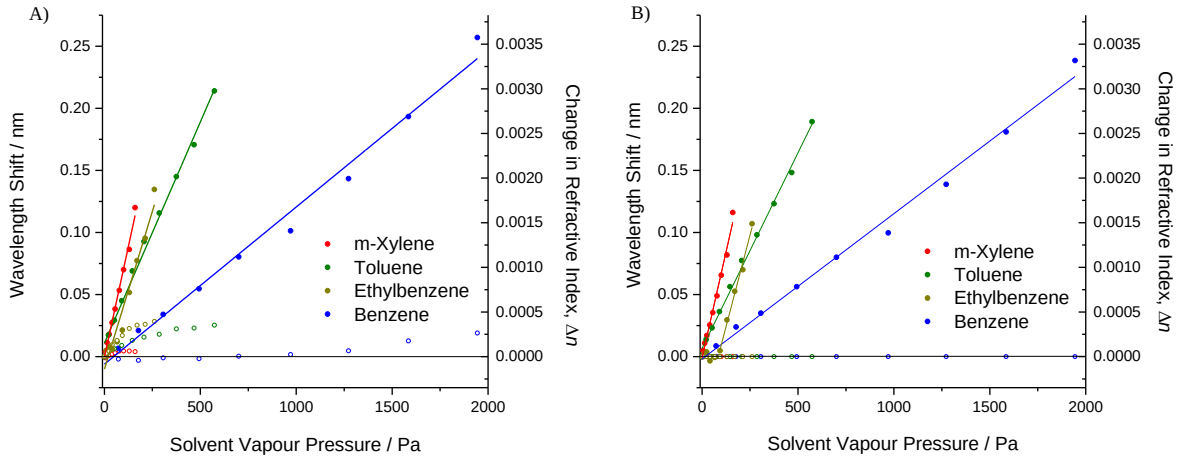

Figure 8.36: Raw and temperature compensated resonance wavelength shifts of uncoated silica clad tandem ring resonators exposed to BTEX vapours from 40-1900 Pa. A) The raw sensing peak shifts during exposure to BTEX vapours are shown with linear fits to illustrate the refractive index trends. The solid points show the resonance shift of the sensing ring and the hollow circles show the resonance shift of the reference ring. B) The resonance shifts of the reference ring were used to remove the temperature effects during exposure of the uncoated silica clad device to BTEX solvent vapours.

A poly(dimethyl-co-diphenyl)siloxane (PDMS-PDPS) copolymer film was prepared following the procedure detailed in Chapter 7.3.2 and spin coated onto an SU-8 clad tandem ring resonator. The resonance wavelength response of both the sensing and reference rings of the PDMS-PDPS coated tandem ring resonator are shown in Figure 8.37. The reference ring response was likely partially related to temperature fluctuations during the experiments, as there was no discernable trend to the partitioning of BTEX compounds into the SU-8 overcoat. For the toluene uptake experiment, there was a much stronger resonance shift observed with the reference ring than the sensing ring. This experiment was believed to be

an anomaly, and the observed response was probably due to temperature instability or problems with the gas dosing system during the experiment. The response of the PDMS-PDPS film to toluene should fall between that of m-xylene and benzene. This experiment would need to be repeated to achieve reliable data on the uptake of toluene into PDMS-PDPS films. The response of the film to ethylbenzene was comparable to that of m-xylene as would be expected as they are comparable in size and have the same molecular weight.

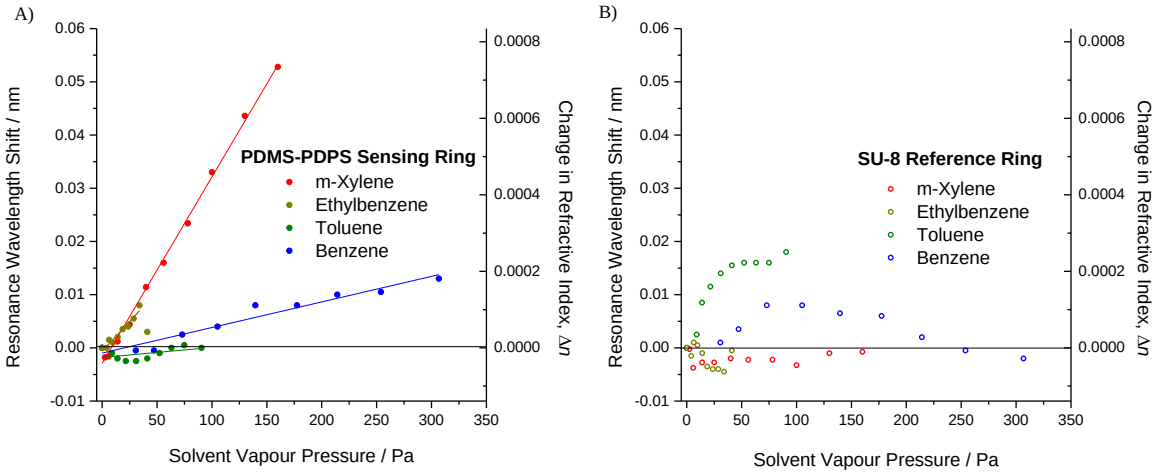

Figure 8.37: PDMS-PDPS coated tandem ring resonator response to BTEX vapours. A) The resonance shifts of the PDMS-PDPS coated sensing ring are shown during the uptake of BTEX compounds. B) The response of the buried reference ring under SU-8 photoresist did not show any discernable trend to BTEX compounds.

It is difficult to effectively compensate for temperature effects once the device is coated, as the temperature dependent resonance response of a coated and uncoated ring resonator will be different. For accurate temperature compensation, the temperature dependence needs to be experimentally determined for each polymer coated system.

Interestingly, the sensitivity of the uncoated SU-8 clad microring resonator was stronger to m-xylene than the PDMS-PDPS coated device (Figure 8.38). One may speculate that the shifts observed by the uncoated device were the result of m-xylene condensing directly onto the sensing ring (leading to a large increase in refractive index) and due to partitioning into the SU-8 covered reference ring (leading to a decrease in refractive index). Of course, a thin film of liquid m-xylene on the sensing ring would result

in a large refractive index change as the microring cladding changed from air to liquid m-xylene. For the PDMS-PDPS-coated device, the partitioning of m-xylene shows a much smaller change in refractive index as the refractive indices of the polymer film and m-xylene are comparable. Additionally, if the affinity of the PDMS-PDPS coating to m-xylene (and other non-polar compounds) is much stronger than SU-8, the polymer film may prevent diffusion into SU-8, explaining the negligible response of the SU-8 clad reference ring on the polymer coated devices.

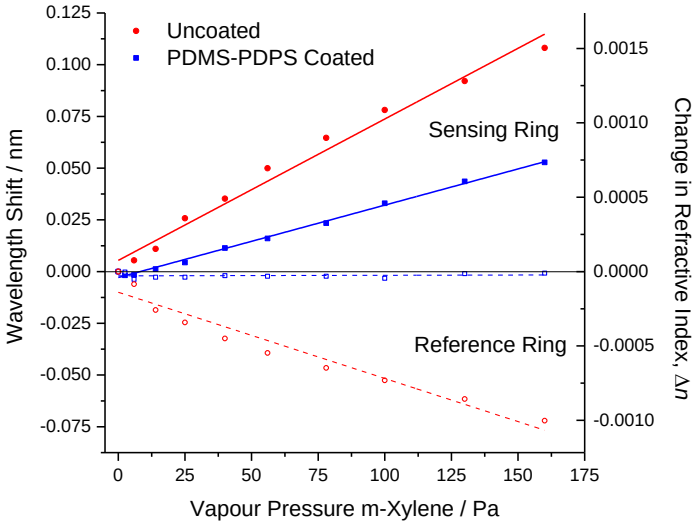

Figure 8.38: Comparison of the resonance shifts observed for the uncoated and PDMS-PDMS coated SU-8 clad tandem ring resonators exposed to saturated m-xylene vapour. The refractive index over the uncoated sensing ring increased (solid red circles) while the refractive index of the SU-8 cladding decreased (red hollow circles). This suggested that m-xylene condensed on the sensing ring and caused the SU-8 overcoat to swell. Once coated with PDMS-PDPS, the reference ring no longer showed any response to the m-xylene vapour (blue hollow squares) while the sensing ring showed a much weaker response (solid blue squares) corresponding to partitioning into the polymer film.

When cyclohexane vapours were exposed to the PDMS-PDPS coated device, similar trends were observed. As might be expected considering the results of cyclohexane partitioning into PDMS-PDPS films in Chapter 7, the PDMS-PDPS coated tandem ring resonator showed a decrease in refractive index upon exposure to cyclohexane vapours (Figure 8.39). Once again, the refractive index remained mostly constant over the reference ring as was observed for the uptake of m-xylene (Figure 8.38). The refractive index of the PDMS-PDPS film was measured as $n_{1550} = 1.4586$, while the indices of m-xylene and cyclohexane were

n_{1550} = 1.4769 and n_{1550} = 1.4147 respectively.[70] If the polymer film swelled during the uptake of cyclohexane, then a drop in refractive index should be expected.

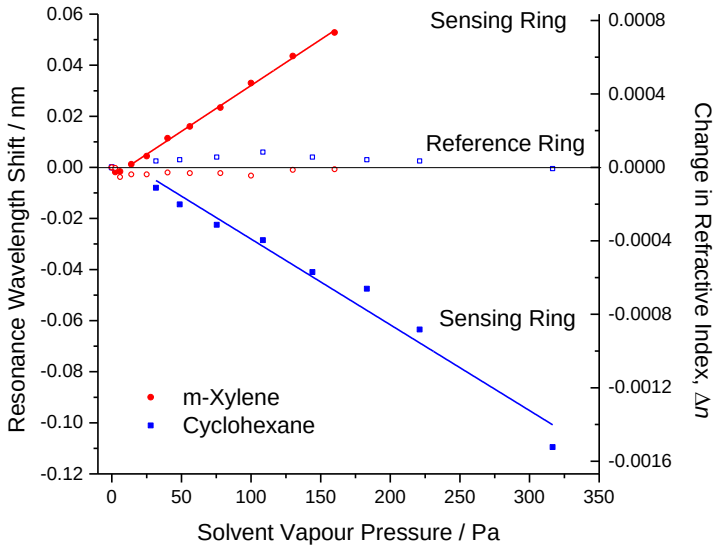

Figure 8.39: Uptake of m-xylene and cyclohexane vapour into a PDMS-PDPS coated SU-8 clad tandem ring resonator. The PDMS-PDPS film increased in refractive index when exposed to m-xylene (red circles) and decreased in refractive index when exposed to cyclohexane (blue squares). In both cases the reference peaks remained constant shown by the hollow circles and squares around Δλ = 0 nm.

When the PDMS-PDPS coated devices were exposed to methanol and isopropanol vapours, large resonance shifts were observed for the SU-8 clad reference ring as is shown in Figure 8.40. It was shown previously in Chapter 6, that liquid methanol could fully degrade SU-8 films that were not hard baked, so it is not surprising to see a strong affinity of SU-8 to methanol vapour. A smaller refractive index response was observed upon exposure to isopropanol which further agrees with our refractometer experiments in Chapter 6. In both of these experiments only minor changes were observed in the hydrophobic PDMS-PDPS coating.

When exposed to more complicated mixtures, such as the vapour from commercial gasoline, simultaneous responses in the PDMS-PDPS film and SU-8 layers were observed as some of the compounds partitioned into each layer (Figure 8.41). In this experiment, the refractive index of the PDMS-PDPS

coating decreased, probably from the presence of aliphatic and cyclic hydrocarbons. The SU-8 ring increased in refractive index possibly from trace alcohols, phenols or carboxylic acids in the gasoline.

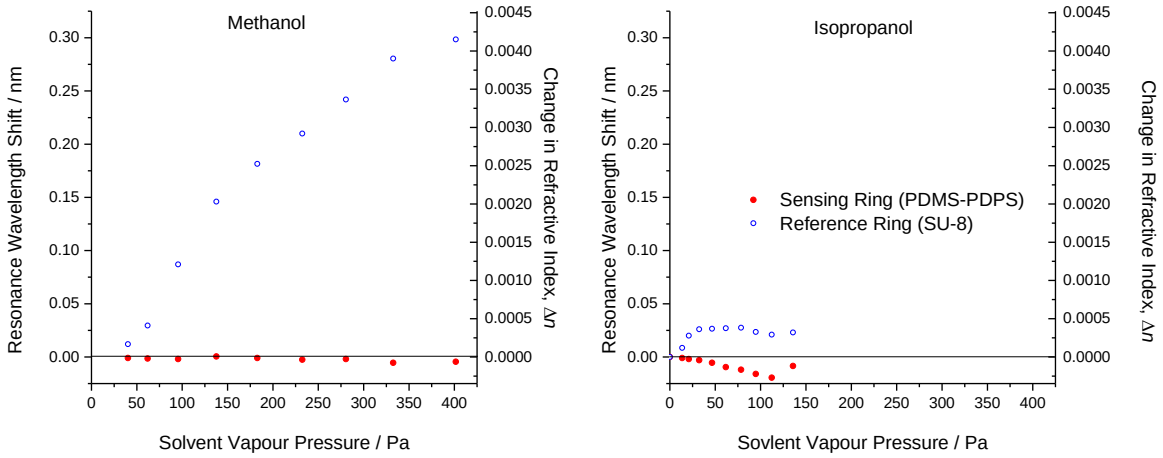

Figure 8.40: Uptake of methanol and isopropanol into the protective SU-8 overcoat over the reference ring on a PDMS-PDPS coated tandem ring resonator. Large resonance changes were observed as the SU-8 refractive index increased during exposure to methanol. Smaller changes were observed for partitioning of isopropanol into SU-8. In both cases only minor refractive index changes were observed in the hydrophobic PDMS-PDPS coating.

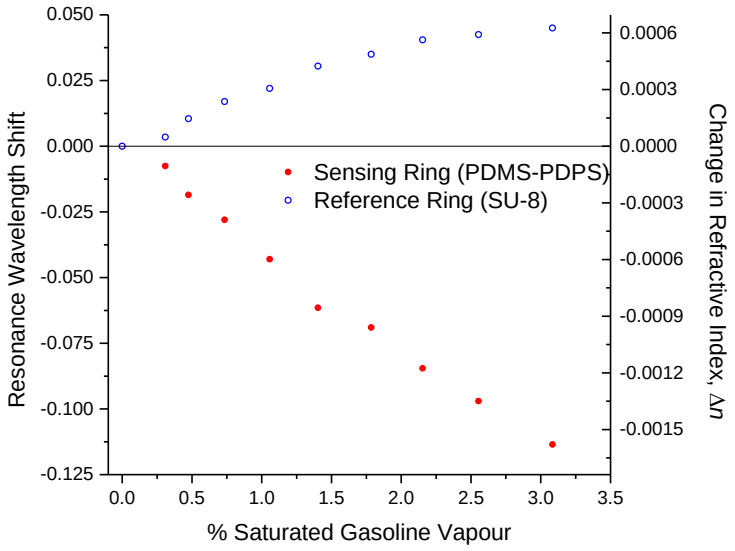

Figure 8.41: Uptake of gasoline vapour into PDMS-PDPS coated SU-8 clad tandem ring resonators. The refractive index decreased in the PDMS-PDPS coating which would be expected for aliphatic and cyclic hydrocarbons, while the refractive index of the SU-8 coating on the reference ring increased possibly due to the presence of trace alcohols, phenols and carboxylic acids in the gasoline.

Gasoline is a complex mixture of hydrocarbons and the combination of different types of molecules may have had combined synergistic or antagonistic effects on the changes to film refractive index and thickness. Many more experiments are needed to fully understand the effects of various mixtures in order to identify the source of the shifts observed in Figure 8.41

8.4 Discussion

The addition of PDPS to the PDMS films was expected to increase the affinity of the films to aromatic compounds. While the partition coefficient was enhanced, the film refractive index (n_{1550} = 1.4586) was initially closer to aromatic compounds, e.g. m-xylene (n_{1550} = 1.4769)[70], and consequently much smaller refractive index changes were observed during uptake. A higher refractive index sensitivity would be observed for the exposure of commercial PDMS to m-xylene as there is a larger refractive index contrast. The major challenge with the polymer coated SOI experiments was that film swelling could not be simultaneously measured. This resulted in major underestimation of the concentration of analytes within the film at equilibrium.

Attempts were made to calculate partition coefficients using only the refractive index changes observed within the PDMS-PDPS coatings, and initially, the swelling was assumed to be negligible ($\Delta d/d = 0$). This either resulted in an underestimate of the analyte concentrations within the film or resulted in "negative concentrations" when the film refractive index decreased (e.g. during the exposure to cyclohexane and hexanes). To better predict partition coefficients, a linear extrapolation was made to the swelling data from the refractometry experiments (Chapter 7). The fits were then used to estimate the swelling expected in each SOI experiment. The resulting partition coefficients assuming no film swelling and with extrapolated swelling parameters are presented in Table 8.1 and are compared with the values previously obtained through refractometry in Chapter 7. The partition coefficients were not calculated for the toluene experiment as the data did not seem reliable, and either had temperature effects or problems with the gas dosing system. The K_{fa} values calculated using the estimated swelling parameters showed a similar trend to the partition coefficients obtained in Chapter 7 from refractometry.

Table 8.1: Comparison of the partition coefficients of VOCs into PDMS-PDPS copolymer films from refractometry and microring resonator experiments. The first column shows the values reported in Chapter 7 from the interferometric refractometry studies of PDMS-PDPS films. The other two columns show estimated film-air partition coefficients assuming no swelling and using extrapolated swelling approximations from the refractometry data.

Solvent	K_{fa} (Chapter 7)	K_{fa} (No Swelling)	K_{fa} (Extrap. Swelling)
m-Xylene	9500 (1000)	156 (11)	9300 (1100)
Ethylbenzene	6000 (750)	84 (35)	3500 (660)
Benzene	1900 (100)	31 (5)	1200 (270)
Cyclohexane	1300 (300)	-190 (20)	660 (150)
Hexanes	500 (150)	-190 (16)	1700 (650)

The vapour pressures were much smaller for the SOI experiments than the refractometer experiments so the swelling parameter had to be extrapolated well below the pressures previously measured. This would be a large source of error and should explain the differences in the K_{fa} values observed for ethylbenzene, cyclohexane, and hexanes when compared to the refractometry experiments. The K_{fa} values calculated assuming no film swelling were drastically underestimated, as would be expected because the films swelled by as much as 10% in the presence of BTEX vapours. Additionally, it is impossible to determine partition coefficients when the film refractive index decreases without including swelling information.

These experiments have shown that it is possible to extract partition coefficients and estimate the analyte concentration within a film when the system has been well characterized and the film swelling can be inferred from past experiments. However, replicate experiments with a broader range of analyte concentration are still needed to achieve more reliable partition coefficients. Conducting experiments with a faster data sampling rate would also allow for measurements of diffusion constants for the uptake and release of VOCs into siloxane polymers.

8.5 Conclusions

The theory behind MZ interferometers and microring resonators was described in detail in this chapter. Experimental data was presented showing measurements of cavity quality factors and finesse. Typical quality factors of Q = 13 000-35 000 and cavity Finesse of F = 5-85 were observed for microring resonators. The full optical experimental setup was described including details about refractive index calibration and temperature compensation.

The development of data acquisition programs was also discussed and the benefits of each method were described in detail. The fixed wavelength method, used to analyze MZ interferometers, gave high time resolution measurements but was susceptible to intensity drift and refractive index changes due to chemical uptake within the protective coating over the reference arm. The laser stepping program had the most accurate spectral wavelength assignment but gave the worst time resolution. The final continuous scanning mode gave the ability to collect high-resolution spectra with a reasonable time resolution, although it was subject to wavelength jitter.

Initial experiments were conducted exposing uncoated and PDMS coated Mach-Zehnder interferometers to saturated m-xylene vapours, and the results suggested that m-xylene partitioned into the SU-8 overcoat. Two diffusion coefficients were extracted for the diffusion of m-xylene through PDMS of $D_1 = 1.81\times10^{-9}$ cm^2/s and $D_2 = 7.04\times10^{-11}$ cm^2/s. An uncoated pair of tandem ring resonators, with an SU-8 clad reference ring, was exposed to m-xylene vapours and wavelength shifts in opposite directions were observed for the sensing and reference ring. The results suggested that m-xylene condensed on the sensing ring and also partitioned into the SU-8 over the reference ring causing the epoxy to swell. The swelling of SU-8 from exposure to m-xylene did not agree with the previous refractometer experiments in Chapter 6, where SU-8 did not interact with m-xylene. The curing conditions and the formulation of SU-8 used in Chapter 6 were different from those used with the overcoat on the SOI devices and may been the reason for the different behaviour. The same SU-8 clad tandem ring resonators were coated with a PDMS-PDPS copolymer film and the affinities to BTEX compounds, cyclohexane and hexanes were assessed. The refractive index trends observed for BTEX compounds and cyclohexane were comparable to those

previously observed with refractometry. Using estimated swelling parameters from the refractometer data in Chapter 7, partition coefficients were calculated using the SOI refractive index data and yielded comparable results with previous experiments. When the polymer coated SOI devices were tested with vapours of polar compounds (methanol and isopropanol), the refractive index of the SU-8 overcoat increased substantially to methanol, and showed only a weak response to isopropanol. This agreed with the affinities observed in Chapter 6, where liquid methanol dissolved soft baked SU-8 epoxy films, and isopropanol did not interact strongly with the film.

Now that the polymer systems are better understood from our refractometry experiments and the data acquisition programs are more efficient, there is much more exciting work that could be performed with this platform. A future work section is included to suggest possible directions for future experiments and for the development of practical sensors based on the SOI platform.

8.6 Future Work

The experiments performed using polymer coated silicon-on-insulator interferometers and microring resonators were part of our initial study on refractive index changes in polymers. The understanding that was later gained through refractometry was essential for interpreting the results presented in this chapter. Knowing what has been learned in Chapters 6 and 7, there are a number of ways in which the study may be extended in the future. Some of these proposed experiments will be discussed in the following sections.

8.6.1 Experimental Improvements

A complication of the data analysis came from unwanted uptake into the SU-8 overcoat on some of the SOI devices. When the protective overcoat was made from silica, the devices were much less susceptible to the uptake of analytes over the reference arm or ring resonator. The silica-clad devices could be used to more accurately correct for temperature fluctuations during experiments. Using silica-clad tandem ring resonators, the polymer VOC sensing experiments could be repeated with a faster time resolution to allow for determination of the diffusion kinetics. Unfortunately, since the reference ring was

clad with SU-8 in the experiments in this chapter, it was impossible to distinguish between temperature effects and uptake within the protective overcoat. Also, in retrospect experiments should have been run with higher solvent vapour pressures so that they could be directly compared with the large-angle refractometry experiments in Chapter 7.4 and 7.5.

The development of a polymer sensor for VOC detection is currently restricted by a lack of selectivity of our materials to target analytes. Using a variety of different types of polymers would allow for distinguishing analytes through a differential response, and techniques like principal component analysis (PCA) or parallel factor analysis (PARAFAC) could be used to quantify mixtures of analytes.[71-73]

By exchanging the single channel photodiode with a linear diode array or an InGaAs camera, one could simultaneous detect light from multiple silicon photonic devices and thereby interrogate an entire sensor array simultaneously. Each device in these sensor arrays could be selectively coated with a unique polymer material using a micro-printer. The device could then be further packaged using fibre V-groove assemblies to permanently bond optical fibres to the silicon-on-insulator chips.

Finally, the large and expensive external cavity diode laser could be replaced with a smaller distributed feedback (DFB) laser that could be current-tuned over a desired wavelength range. By addressing all of these issues, a large step can be taken towards an all-photonic sensor array for a variety of VOCs– ultimately leading towards a practical sensor for monitoring the concentrations of VOCs or other contaminants in an environment.

8.6.2 Programing Improvements

The most efficient measurements are currently made using the continuous scanning program that was described in this thesis. Using this method, the jitter in the laser voltage ramp causes variability in the wavelength assignment. It would be better to control the laser wavelength directly by an external voltage or current ramp that could be used as master reference. This type of ramp could be generated as the result of a feedback loop to continually lock onto a single resonance as it shifts over time. The use of a feedback loop to lock to an optical resonator fringe has been previously reported by Drever[74], and has been used

successfully in our lab to lock the laser frequency of DFB lasers to Fabry-Perot cavity fringes and resonances of microsphere resonators.[69, 75]

While there have been attempts at running non-linear curve fits within the LabView™ code during experiments, it is not a very practical approach. Tracking of fringes directly from a feedback loop would be more robust and not require complicated fits to the data being collected. Future work is required to develop robust code to effectively interrogate the microring resonators and would be needed to complement the sensor experimental packaging previously described. Once the improvements are made to both of these areas, the development of a portable and remote sensor should be possible.

8.7 Acknowledgements

I would like the thank Dr. Dan-Xia Xu, Dr. Siegfried Janz, and members of their team at the National Research Council for designing, manufacturing, and providing all of the SOI devices used in this chapter. Their material and technical assistance was essential to this project. I would also like to thank Dr. Jack Barnes for the construction of the optical experimental setup at Queen's, and technical assistance will experiments and data analysis. I would like to acknowledge Ms. Jessica Litman and Dr. Helen Waechter for their guidance during the development of the LabView™ code. I would like to acknowledge Mr. Grant Ongo, who worked with me on the initial calibrations and VOC sensing experiments on the uncoated SOI devices. I would like to thank Mr. Hao Chen for the providing the data shown in Section 2.2.5 to illustrate the importance of temperature compensation. I would like to also acknowledge the work by Mr. Hao Chen, Dr. Sogol Borjian and Dr. Xiaowei Wu on the development of improved microfluidic designs and continued work on this setup. Finally, I would like to acknowledge CMC Microsystems for providing access to LabView™ through a Designer Subscription.

8.8 References

1. Densmore, A.; Xu, D.-X.; Waldron, P.; Janz, S.; Lapointe, J.; Mischki, T.; Lopinski, G.; Delage, A.; Cheben, P. Spotter-compatible SOI waveguide devices for biomolecular sensing, *Silicon Photonics III, Proceedings of SPIE 6898*, **2008**, 68981B, 1-8.

2. Carlborg, C. F.; Gylfason, K. B.; Kaźmierczak, A.; Dortu, F.; Bañuls Polo, M. J.; Maquieira Catala, A.; Kresbach, G. M.; Sohlström, H.; Moh, T.; Vivien, L.; Popplewell, J.; Ronan, G.; Barrios, C. A.; Stemme, G.; van der Wijngaart, W., A packaged optical slot-waveguide ring resonator sensor array for multiplex label-free assays in labs-on-chips. *Lab on a Chip* **2010,** *10*, 281-290.

3. *Silicon Photonics. The State of the Art*. Reed, G. T., Ed. John Wiley and Sons, Ltd., Hoboken, NJ, 2008.

4. Densmore, A.; Janz, S.; Ma, R.; Schmid, J. H.; Xu, D.-X.; Delâge, A.; Lapointe, J.; Vachon, M.; Cheben, P., Compact and low power thermo-optic switch using folded silicon waveguides. *Optics Express* **2009,** *17*, 10457-10465.

5. Edmiston, P. L.; Campbell, D. P.; Gottfried, D. S.; Baughman, J.; Timmers, M. M., Detection of vapor phase trinitrotoluene in the parts-per-trillion range using waveguide interferometry. *Sensors and Actuators B: Chemical* **2010,** *143*, 574-582.

6. Moss, D. J.; Morandotti, R.; Gaeta, A. L.; Lipson, M., New CMOS-compatible platforms based on silicon nitride and Hydex for nonlinear optics. *Nature Photonics* **2013,** *7*, 597-607.

7. Bååk, T., Silicon oxynitride; a material for GRIN optics. *Applied Optics* **1982,** *21*, 1069-1072.

8. Xu, D. X.; Densmore, A.; Delâge, A.; Waldron, P.; McKinnon, R.; Janz, S.; Lapointe, J.; Lopinski, G.; Mischki, T.; Post, E.; Cheben, P.; Schmid, J. H., Folded cavity SOI microring sensors for high sensitivity and real time measurement of biomolecular binding. *Optics Express* **2008,** *16*, 15137-15148.

9. Jellison, G. E., Optical functions of silicon determined by two-channel polarization modulation ellipsometry. *Optical Materials* **1992,** *1*, 41-47.

10. Politi, A.; Cryan, M. J.; Rarity, J. G.; Yu, S.; O'Brien, J. L., Silica-on-silicon waveguide quantum circuits. *Science* **2008,** *320*, 646-649.

11. Malitson, I. H., Interspecimen comparison of the refractive index of fused silica. *Journal of the Optical Society of America* **1965,** *55*, 1205-1209.

12. Yeniay, A.; Gao, R.; Takayama, K.; Gao, R.; Garito, A. F., Ultra-low-loss polymer waveguides. *Journal of Lightwave Technology* **2004,** *22*, 154-158.

13. Zhao, Y.-G.; Lu, W.-K.; Ma, Y.; Kim, S.-S.; Ho, S. T.; Marks, T. J., Polymer waveguides useful over a very wide wavelength range from the ultraviolet to infrared. *Applied Physics Letters* **2000,** *77*, 2961-2963.

14. Tien, M.-C.; Bauters, J. F.; Heck, M. J. R.; Spencer, D. T.; Blumenthal, D. J.; Bowers, J. E., Ultra-high quality factor planar Si3N4 ring resonators on Si substrates. *Optics Express* **2011,** *19*, 13551-13556.

15. Densmore, A.; Xu, D.-X.; Vachon, M.; Janz, S.; Ma, R.; Li, Y.; Lopinski, G.; Luebbert, C. C.; Liu, Q. Y.; Schmid, J. H.; Delage, A.; Cheben, P. Arrays of SOI photonic wire biosensors for label-free molecular detection, *Silicon Photonics V, Proceedings of SPIE 7606*, **2010**, 76060C, 1-8.

16. Jalali, B., Can silicon change photonics? *Physica Status Solidi A* **2008,** *205*, 213-224.

17. Transmission spectrum of silicon windows. ThorLabs, Inc., https://www.thorlabs.com (accessed Aug. 7, 2016).

18. Pan, H.; Assefa, S.; Green, W. M. J.; Kuchta, D. M.; Schow, C. L.; Rylyakov, A. V.; Lee, B. G.; Baks, C. W.; Shank, S. M.; Vlasov, Y. A., High-speed receiver based on waveguide germanium photodetector wire-bonded to 90nm SOI CMOS amplifier. *Optics Express* **2012,** *20*, 18145-18155.

19. Dangel, R.; Hofrichter, J.; Horst, F.; Jubin, D.; La Porta, A.; Meier, N.; Soganci, I. M.; Weiss, J.; Offrein, B. J., Polymer waveguides for electro-optical integration in data centers and high-performance computers. *Optics Express* **2015,** *23*, 4736-4750.

20. Densmore, A.; Xu, D.-X.; Waldron, P.; Janz, S.; Delâge, A.; Cheben, P.; Lapointe, J. Thin silicon waveguides for biological and chemical sensing, *Silicon Photonics II, Proceedings of SPIE 6477*, **2007**, 647718, 1-10.

21. Dell'Olio, F.; Passaro, V. M., Optical sensing by optimized silicon slot waveguides. *Optics Express* **2007,** *15*, 4977-4993.

22. Xia, J., Single-mode condition for silicon rib waveguides with large cross sections. *Optical Engineering* **2004,** *43*, 1953-1954.

23. Baehr-Jones, T.; Hochberg, M.; Walker, C.; Scherer, A., High-Q optical resonators in silicon-on-insulator-based slot waveguides. *Applied Physics Letters* **2005,** *86*, 081101, 1-3.

24. Gonzalo Wangüemert-Pérez, J.; Cheben, P.; Ortega-Moñux, A.; Alonso-Ramos, C.; Pérez-Galacho, D.; Halir, R.; Molina-Fernández, I.; Xu, D.-X.; Schmid, J. H., Evanescent field waveguide sensing with subwavelength grating structures in silicon-on-insulator. *Optics Letters* **2014,** *39*, 4442-4445.

25. Cheben, P.; Schmid, J. H.; Bock, P. J.; Lapointe, J.; Janz, S.; Xu, D.-X.; Densmore, A.; Delage, A.; Ma, R.; Halir, R.; Lamontagne, B.; Ortega-Monux, A.; Molina Fernandez, I.; Fedeli, J.-M.; Ibrahim, M.; Ye, W. N.; Hall, T. J. Subwavelength structures in SOI waveguides, *IEEE International Conference on Group IV Photonics*, London, UK, **2011**, 42-44.

26. Ctyroky, J.; Kwiecien, P.; Richter, I. Dispersion properties of subwavelength grating SOI waveguides, *Progress in Electromagnetics Research Symposium*, Stockholm, Sweden, **2013**, 1613-1617.

27. Nikkhah, H.; Hall, T. J., Subwavelength grating waveguides for integrated photonics. *Applied Physics A* **2016,** *122*, 368, 1-6.

28. Leonard, S. W.; van Driel, H. M.; Birner, A.; Gösele, U.; Villeneuve, P. R., Single-mode transmission in two-dimensional macroporous silicon photonic crystal waveguides. *Optics Letters* **2000,** *25*, 1550-1552.

29. Lee, M. R.; Fauchet, P. M., Nanoscale microcavity sensor for single particle detection. *Optics Letters* **2007,** *32*, 3284-3286.

30. Barrios, C. A., Optical slot-waveguide based biochemical sensors. *Sensors* **2009,** *9*, 4751-4765.

31. Yang, A. H. J.; Moore, S. D.; Schmidt, B. S.; Klug, M.; Lipson, M.; Erickson, D., Optical manipulation of nanoparticles and biomolecules in sub-wavelength slot waveguides. *Nature* **2009,** *457*, 71-75.

32. Yebo, N. A.; Lommens, P.; Hens, Z.; Baets, R., An integrated optic ethanol vapor sensor based on a silicon-on-insulator microring resonator coated with a porous ZnO film. *Optics Express* **2010,** *18*, 11859-11866.

33. Balik, C. M.; Xu, J. R., Simultaneous measurement of water diffusion, swelling, and calcium carbonate removal in a latex paint using FTIR–ATR. *Journal of Applied Polymer Science* **1994,** *52*, 975-983.

34. Linossier, I.; Gaillard, F.; Romand, M.; Feller, J. F., Measuring water diffusion in polymer films on the substrate by internal reflection fourier transform infrared spectroscopy. *Journal of Applied Polymer Science* **1997,** *66*, 2465-2473.

35. Schmitt, K.; Hoffmann, C., High-Refractive-Index Waveguide Platforms for Chemical and Biosensing. In *Optical Guided-wave Chemical and Biosensors I*, Zourob, M.; Lakhtakia, A., Eds. Springer-Verlag: Berlin, Germany, 2010; Vol. 7, pp 21-54.

36. Salzberg, C. D.; Villa, J. J., Infrared refractive indexes of silicon, germanium and modified selenium glass. *Journal of the Optical Society of America* **1957,** *47*, 244-246.

37. *Sylgard 184 Elastomer Product Information* Dow Corning, 2014, 11-3184B-01,

38. Densmore, A.; Xu, D.-X.; Waldron, P.; Janz, S.; Cheben, P.; Lapointe, J.; Delge, A.; Lamontagne, B.; Schmid, J. H.; Post, E., A silicon-on-insulator photonic wire based evanescent field sensor. *IEEE Photonics Technology Letters* **2006,** *18*, 2520-2522.

39. Bondarenko, O.; Fang, C.-Y.; Vallini, F.; Smalley, J. S. T.; Fainman, Y., Extremely compact hybrid III-V/SOI lasers: design and fabrication approaches. *Optics Express* **2015,** *23*, 2696-2712.

40. Daldosso, N.; Pavesi, L., Nanosilicon photonics. *Laser & Photonics Review* **2009,** *3*, 508-534.

41. Liu, J.; Sun, X.; Camacho-Aguilera, R.; Kimerling, L. C.; Michel, J., Ge-on-Si laser operating at room temperature. *Optics Letters* **2010,** *35*, 679-681.

42. Camacho-Aguilera, R. E.; Cai, Y.; Patel, N.; Bessette, J. T.; Romagnoli, M.; Kimerling, L. C.; Michel, J., An electrically pumped germanium laser. *Optics Express* **2012,** *20*, 11316-11320.

43. Lamponi, M.; Keyvaninia, S.; Jany, C.; Poingt, F.; Lelarge, F.; de Valicourt, G.; Roelkens, G.; Van Thourhout, D.; Messaoudene, S.; Fedeli, J.-M.; Duan, G. H., Low-threshold heterogeneously integrated InP/SOI lasers with a double adiabatic taper coupler. *IEEE Photonics Technology Letters* **2012,** *24*, 76-78.

44. Duan, G.-H.; Jany, C.; Le Liepvre, A.; Accard, A.; Lamponi, M.; Make, D.; Kaspar, P.; Levaufre, G.; Girard, N.; Lelarge, F.; Fedeli, J.-M.; Descos, A.; Ben Bakir, B.; Messaoudene, S.; Bordel, D.; Menezo, S.; de Valicourt, G.; Keyvaninia, S.; Roelkens, G.; Van Thourhout, D.; Thomson, D. J.; Gardes, F. Y.; Reed, G. T., Hybrid III--V on silicon lasers for photonic integrated circuits on silicon. *IEEE Journal of Selected Topics in Quantum Electronics* **2014,** *20*, 158-170.

45. Colace, L.; Sorianello, V.; Balbi, M.; Assanto, G., Germanium near infrared detector in silicon on insulator. *Applied Physics Letters* **2007,** *91*, 021107, 1-3.

46. Vivien, L.; Polzer, A.; Marris-Morini, D.; Osmond, J.; Hartmann, J. M.; Crozat, P.; Cassan, E.; Kopp, C.; Zimmermann, H.; Fédéli, J. M., Zero-bias 40Gbit/s germanium waveguide photodetector on silicon. *Optics Express* **2012,** *20*, 1096-1101.

47. Brouckaert, J.; Roelkens, G.; Van Thourhout, D.; Baets, R., Compact InAlAs-InGaAs metal-semiconductor-metal photodetectors integrated on silicon-on-insulator waveguides. *IEEE Photonics Technology Letters* **2007,** *19*, 1484-1486.

48. Park, H.; Fang, A. W.; Jones, R.; Cohen, O.; Raday, O.; Sysak, M. N.; Paniccia, M. J.; Bowers, J. E., A hybrid AlGaInAs-silicon evanescent waveguide photodetector. *Optics Express* **2007,** *15*, 6044-6052.

49. Gassenq, A.; Hattasan, N.; Cerutti, L.; Rodriguez, J. B.; Tournié, E.; Roelkens, G., Study of evanescently-coupled and grating-assisted GaInAsSb photodiodes integrated on a silicon photonic chip. *Optics Express* **2012,** *20*, 11665-11672.

50. Schmid, J. H.; Sinclair, W.; García, J.; Janz, S.; Lapointe, J.; Poitras, D.; Li, Y.; Mischki, T.; Lopinski, G.; Cheben, P.; Delâge, A.; Densmore, A.; Waldron, P.; Xu, D.-X., Silicon-on-insulator guided mode resonant grating for evanescent field molecular sensing. *Optics Express* **2009,** *17*, 18371-18380.

51. Alonso-Ramos, C.; Ortega-Moñux, A.; Molina-Fernández, I.; Cheben, P.; Zavargo-Peche, L.; Halir, R.; Janz, S.; Xu, D.-X.; Kim, N.; Lamontagne, B., Grating couplers for thick SOI rib waveguides. *Optical and Quantum Electronics* **2012,** *44*, 535-540.

52. Ulrich, R., Theory of the prism–film coupler by plane-wave analysis. *Journal of the Optical Society of America* **1970,** *60*, 1337-1350.

53. Janz, S.; Cheben, P.; Delage, A.; Densmore, A.; Xu, D.-X. Prism Coupled Silicon-on-Insulator Sensor. International Patent,WO2009021309, 2009.

54. Almeida, V. R.; Panepucci, R. R.; Lipson, M., Nanotaper for compact mode conversion. *Optics Letters* **2003,** *28*, 1302-1304.

55. Reed, G.; Knights, A., *Silicon Photonics: An Introduction*. John Wiley & Sons, Hoboken, NJ, 2004.

56. Cheben, P.; Bock, P. J.; Schmid, J. H.; Lapointe, J.; Janz, S.; Xu, D.-X.; Densmore, A.; Delâge, A.; Lamontagne, B.; Hall, T. J., Refractive index engineering with subwavelength gratings for efficient microphotonic couplers and planar waveguide multiplexers. *Optics Letters* **2010,** *35*, 2526-2528.

57. Cheben, P.; Schmid, J. H.; Wang, S.; Xu, D.-X.; Vachon, M.; Janz, S.; Lapointe, J.; Painchaud, Y.; Picard, M.-J., Broadband polarization independent nanophotonic coupler for silicon waveguides with ultra-high efficiency. *Optics Express* **2015,** *23*, 22553-22563.

58. Abeysinghe, D. C.; Ranatunga, V.; Banerjee, A.; Balagopal, A.; Klotzkin, D. J., Epoxyless fiber-to-submount bonding for active fiber optoelectronic and fiber backplane applications. *IEEE Journal of Selected Topics in Quantum Electronics* **2006,** *12*, 952-960.

59. Galan, J. V.; Sanchis, P.; Marti, J.; Marx, S.; Schroder, H.; Mukhopadhyay, B.; Tekin, T.; Selvaraja, S.; Bogaerts, W.; Dumon, P.; Zimmermann, L. CMOS compatible silicon etched V-grooves integrated with a SOI fiber coupling technique for enhancing fiber-to-chip alignment, *IEEE International Conference on Group IV Photonics*, San Francisco, CA, **2009**, 148-150.

60. Densmore, A.; Xu, D.-X.; Janz, S.; Waldron, P.; Mischki, T.; Lopinski, G.; Delâge, A.; Lapointe, J.; Cheben, P.; Lamontagne, B.; Schmid, J. H., Spiral-path high-sensitivity silicon photonic wire molecular sensor with temperature-independent response. *Optics Letters* **2008,** *33*, 596-598.

61. Densmore, A.; Vachon, M.; Xu, D.-X.; Janz, S.; Ma, R.; Li, Y.-H.; Lopinski, G.; Delâge, A.; Lapointe, J.; Luebbert, C. C.; Liu, Q. Y.; Cheben, P.; Schmid, J. H., Silicon photonic wire biosensor array for multiplexed real-time and label-free molecular detection. *Optics Letters* **2009,** *34*, 3598-3600.

62. Saleh, B. E. A.; Teich, M. C., *Fundamentals of Photonics*. 2nd Edition, John Wiley & Sons, Hoboken, NJ, 2007.

63. Xu, D.-X.; Vachon, M.; Densmore, A.; Ma, R.; Janz, S.; Delâge, A.; Lapointe, J.; Cheben, P.; Schmid, J. H.; Post, E.; Messaoudène, S.; Fédéli, J.-M., Real-time cancellation of temperature induced resonance shifts in SOI wire waveguide ring resonator label-free biosensor arrays. *Optics Express* **2010,** *18*, 22867-22879.

64. McKinnon, W. R.; Xu, D. X.; Storey, C.; Post, E.; Densmore, A.; Delâge, A.; Waldron, P.; Schmid, J. H.; Janz, S., Extracting coupling and loss coefficients from a ring resonator. *Optics Express* **2009,** *17*, 18971-18982.

65. Komma, J.; Schwarz, C.; Hofmann, G.; Heinert, D.; Nawrodt, R., Thermo-optic coefficient of silicon at 1550 nm and cryogenic temperatures. *Applied Physics Letters* **2012,** *101*, 041905, 1-4.

66. Middelmann, T.; Walkov, A.; Bartl, G.; Schödel, R., Thermal expansion coefficient of single-crystal silicon from 7 K to 293 K. *Physical Review B* **2015,** *92*, 174113, 1-7.

67. Burgoyne, F. Simple fabrication of microfluidic devices by replicating Scotch-tape masters. Chips and Tips Forum, Lab on a Chip, http://blogs.rsc.org/chipsandtips/2010/05/17/simple-fabrication-of-microfluidic-devices-by-replicating-scotch-tape-masters/ (accessed Aug. 7, 2016).

68. Shrirao, A. B.; Perez-Castillejos, R. Microfluidics labs using devices fabricated by soft-lithographic replication of scotch-tape molds *American Society for Engineering Education Northeast*, **2010**, 1-6.

69. Barnes, J. A.; Gagliardi, G.; Loock, H.-P., Absolute absorption cross-section measurement of a submonolayer film on a silica microresonator. *Optica* **2014,** *1*, 75-83.

70. Saunders, J. E.; Sanders, C.; Chen, H.; Loock, H.-P., Refractive indices of common solvents and solutions at 1550 nm. *Applied Optics* **2016,** *55*, 947-953.

71. Wold, S.; Esbensen, K.; Geladi, P., Principal component analysis. *Chemometrics and Intelligent Laboratory Systems* **1987,** *2*, 37-52.

72. Harshman, R. A.; Lundy, M. E., PARAFAC: Parallel factor analysis. *Computational Statistics & Data Analysis* **1994,** *18*, 39-72.

73. Bro, R., PARAFAC. Tutorial and applications. *Chemometrics and Intelligent Laboratory Systems* **1997,** *38*, 149-171.

74. Drever, R. W. P.; Hall, J. L.; Kowalski, F. V.; Hough, J.; Ford, G. M.; Munley, A. J.; Ward, H., Laser phase and frequency stabilization using an optical resonator. *Applied Physics B Photophysics and Laser Chemistry* **1983,** *31*, 97-105.

75. MacLean, A. G.; Schneider, L. T.; Freytag, A. I.; Gribble, A.; Barnes, J. A.; Loock, H.-P., Cavity-enhanced photoacoustic detection using acoustic and fiber-optic resonators. *Applied Physics B* **2015,** *119*, 11-19.

Chapter 9

Conclusions and Future Work

9.1 Thesis Summary

There is a large wealth of literature on the development of novel sensors for refractive index sensing applications. Great progress has been made on the construction of fibre-based interferometers and grating based sensors, and, more recently, significant progress has been made on the development of planar waveguide devices. Unfortunately, most sensors reported in the literature have only been demonstrated using sucrose test solutions or calibration standards. Often, calibrations of optical devices operating in the near-infrared are made using refractive indices reported at the sodium-D line (λ = 589 nm) which results in a great degree of error. Additionally, the strong focus on releasing the newest state-of-the-art sensors has led to poorly reported device resolutions in the literature. The device resolution is frequently reported based on the minimum resolution of the detectors, and does not account for any experimental noise, which could increase the actual resolution by orders of magnitude. There is also currently a major disconnect between groups designing new refractive index sensors and groups developing novel coatings for chemical sensing applications. This gap can be addressed by an increased focus on interdisciplinary collaborations between optics groups designing instruments and chemistry or chemical engineering groups designing novel materials.

In this thesis, a prism-based refractometer was used to study the refractive indices of both thick ($d > 100$ μm) and thin (10 μm $< d < 100$ μm) films of liquids and polymers. While this instrument was previously reported in the literature,[1] there were many challenges with reproducibility of the analysis techniques. Significant improvements were made to the experimental setup and analysis techniques in this thesis to improve the quality of the results obtained. Thick films were easily measured by fitting the angular reflection profiles to a piecewise function for the Fresnel reflection and total internal reflection. The critical angle was marked by the transition between the two functions and was used to determine the refractive

index with an accuracy of Δn = 1-7×10^{-4}. For thin films, the angular reflection also contained thin-film interference fringes within the Fresnel reflection region below the critical angle. In this thesis, a series of pre-processing techniques were applied to remove non-periodic noise prior to Fourier analysis. Fourier analysis of the filtered interferogram was used to simultaneously extract both the refractive index and thickness of thin films. Additionally, systematic methods were used to track the position of individual fringes near the critical angle which were used as limits for data analysis. Averaging the values from fits to different windows of the data helped reduce the analysis uncertainty and increase the reproducibility of the results. Comparison between thick and thin films of the same liquid solvents showed that the refractive index of measurements from Fourier analysis had similar accuracies. Comparison of thickness measurements using a stylus profilometer and white light scanning interferometric microscope yielded thicknesses that differed by < 7%. These differences were not due to instrumental inaccuracy, but were the result of variation across the films, as they were not necessarily measured at the same spot. We conservatively estimated the accuracy of the thickness measurements to be better than Δd < 3 -5%.

To date, there are very few studies of refractive indices in the near infrared, and values for most solvents were previously unavailable. The refractive indices of 29 common organic solvents were measured at λ = 1550 nm and were reported with uncertainties of Δn = 1 - 7×10^{-4}.[2] The measurements ranged from n_{1550} = 1.3164(2) for water to n_{1550} = 1.4846(2) for o-xylene. The measured refractive indices of water, methanol, acetonitrile, 1-propanol, and 1,4-dioxane differed only by Δn = 1- 3×10^{-4} from reported literature values. In the worst case, the refractive index of benzene differed by as much as Δn = 2×10^{-3} from two literature values. Series of aqueous solutions were prepared up to the solubility limit of sodium chloride (0-25% w/w) and sucrose (0-80% w/w). Binary aqueous mixtures were also prepared with ethylene glycol, glycerol, and dimethylsulfoxide over the full miscible range (0-100% w/w). The resulting measurements were fit with a 3rd order polynomial to establish a relationship between weight fraction and refractive index. From these measurements, calibration solutions can now be prepared for SOI micro-optical devices and other near-infrared sensors.

In this thesis, I have presented a model that can be used to calculate the concentration of an analyte partitioned into a film from experimentally obtained refractive index and thickness changes. This model is based on the Lorentz-Lorenz equation and assumes that polarizabilities are linearly additive by mole. This model is a major improvement from previous studies, where only a refractive index or thickness response was used to relate film changes to external analyte concentration. With this equation, we also developed Fickian diffusion models from solutions by Crank[3] for concentration changes within bulk films or at a film-substrate interface. It became apparent from studying the sensors literature, that there is a great deal of confusion surrounding diffusion models. This could translate into errors of a factor of 4 should the wrong coordinate system be used when developing models. Moreover, approximated models are commonly used to measure diffusion coefficients and require estimations of the saturated concentration within the film. This can result in errors as much as 20% from uncertainty in the asymptotic value. The model we present has a series of exponential terms that fits the data well when 10 terms are used. While adding additional exponential terms improves the fitting, it does not add any extra fitting parameters. Additionally, this model does not require the saturated concentration to be known, and this parameter is extracted during the fit. While this model agrees well with experimental data, parameters could still be added to account for surface roughness, absorption, scattering and birefringence.

Typically, SU-8 is thought of as being a chemically inert epoxy that is often used for microfluidics and as a protective overcoat on optical devices. A soft baked SU-8 film was exposed to water and other solvents, and the uptake of water was observed, resulting in a refractive index change of $\Delta n = 9\times10^{-4}$ and a film swelling of 0.7%. The concentrations of water in the bulk SU-8 film and at the film-substrate interface were calculated using the model previously derived. When ignoring the swelling, the uptake curves fit well to a Fickian diffusion model and yielded diffusion coefficients of $D_{FS} = 1.398\times10^{-8}$ cm^2/s and $D_{Bulk} = 1.642\times10^{-8}$ cm^2/s at the film-substrate interface and through the bulk film respectively. If the swelling was included with the bulk refractive index change, then the uptake fit to a sum of two diffusion processes of $D_1 = 5.67\times10^{-9}$ cm^2/s and $D_2 = 61.2\times10^{-9}$ cm^2/s. The two diffusion rates are believed to correspond to a fast process relating to restructuring at the surface of the SU-8 film, and a slower process

of the diffusion through the polymer film. The slow rate is only slightly higher than literature values previously reported of D = 1.25-3.00 $\times 10^{-9}$ cm^2/s through similar SU-8 materials. The differences in the results that we observed were likely due to differences in the formulation of SU-8 used for the study and differences in the curing conditions of the material. Notably, the other literature studies did not account for the effects from both refractive index and thickness changes during the uptake of water. When organic solvents were exposed to the SU-8 film, methanol, acetone, and acetonitrile caused rapid delamination as the polymer dissolved and lifted off the slide. If the film was optimized for chemical stability and was hard baked, then it may not have dissolved, but a strong affinity to these organic solvents would still likely have occurred.

Thin-film refractometry can also be used for systems with much larger refractive index and thickness changes. Siloxane polymers when exposed to vapours from VOCs showed refractive index changes as large as $\Delta n = 6\times10^{-3}$ with polymer swelling of close to 10%. Commercial polydimethylsiloxane (PDMS) films were exposed to a range of BTEX, cyclohexane, acetone, methanol, and isopropanol vapours. For most cases, a two-term diffusion model fit the data best. This may have been due to restructuring of the polymer at the surface of the film or may have been due to different domains in the polymer as a result of nanoparticle filler that was present in the PDMS kit. The fast diffusion process was found to be an order of magnitude slower than values previously reported in the literature. This might have been due to differences in the polymer composition, as other groups studied different brands of PDMS. It may also have been a result of the analysis procedure or the diffusion model that was used. However, the partition coefficients calculated from the saturated analyte concentrations within the films were in very close agreement with literature values. This suggested that the observed differences in diffusion coefficients were not the result of problems with our model. Copolymer films containing polydiphenylsiloxane (PDPS) were also exposed to BTEX and cyclohexane. The refractive index changes were much smaller as the polymer refractive index was closer to those of the BTEX compounds. Interestingly, because the PDMS-PDPS refractive index was much higher, a decrease in refractive index was observed for the uptake of cyclohexane. This difference in response indicated a behaviour that could be used to help identify analytes and increase the selectivity of

future devices. Even though the observed refractive index change was much smaller, the saturated analyte concentration in the PDMS-PDPS film was enhanced by 2-3 times. This resulted in higher partition coefficients for aromatic compounds, and indicated that changing the functional groups in a polymer could be a useful method of changing the selectivity.

Siloxane polymer coatings were also applied to SOI Mach-Zehnder interferometers and microring resonators to test sensing on compact platforms. The phase response of the PDMS coated MZ interferometers exposed to saturated m-xylene vapours was fit with our diffusion model for the concentration at the film-substrate interface and fit well to a 2-rate diffusion process of $D_1 = 1.81\times10^{-9}$ cm^2/s and $D_2 = 7.04\times10^{-11}$ cm^2/s. The uncoated chip showed a strong response to m-xylene and our experiments indicated that the SU-8 protective overcoat was taking up analytes. To explore these effects, tandem ring microresonators were used. When m-xylene was exposed to the tandem ring devices, an increase in refractive index over the sensing arm and a decrease over the reference arm was observed. This suggested that molecules condensed on the sensing arm and that the SU-8 swelled during the uptake of m-xylene. Once the chip was coated with a PDMS-PDPS copolymer film, the SU-8 no longer showed any response to most analytes. Similarly to the refractometry experiments, the uptake of m-xylene and cyclohexane resulted in resonance shifts in opposite directions. Additionally, when the PDMS-PDPS coated devices were exposed to methanol, a strong response was observed in the SU-8 over the reference ring. This strong affinity agreed with our previous experiments where methanol caused soft-baked films to delaminate. The refractive index changes observed in these experiments could not be directly correlated with the analyte concentrations within the film. For experiments where the refractive index of the film decreased, (e.g. cyclohexane) negative analyte concentrations in the film would be predicted – unless the swelling is explicitly included. When swelling parameters were estimated from the refractometry experiments, comparable partition coefficients could also be obtained using the SOI platform.

9.2 Overall Conclusions

In this thesis, I have presented an accurate model for calculating the analyte concentration in a film from refractive index and thickness changes occurring during chemical uptake. I have presented methods for reproducibly analysing data in order to study the behaviour of polymer films in the presence of a variety of different analytes. As a test case, we have shown that siloxane polymers are useful materials for the partitioning of non-polar and aromatic VOCs. Changing the functionality within polymers was also shown to increase the selectivity to different analytes. I have also shown that these materials can be applied to miniaturized refractive index sensors, e.g. SOI microring resonators and interferometers for sensing experiments. The film characterization techniques described in this thesis were essential for understanding the responses observed with the SOI devices. For example, the uptake of methanol into the SU-8 overcoat agreed with the refractometry experiments, and would have been difficult to explain without this additional information. Smaller refractive index changes were observed when BTEX compounds were exposed to the PDMS-PDPS copolymer films compared with the commercial PDMS films. This would have suggested that the copolymer had a lower affinity to BTEX compounds than the commercial PDMS film. Taking swelling into account, the PDMS-PDPS films showed significant enhancement of the partition coefficients to aromatic compounds. While the development of a field-deployable sensor for VOC detection is still in progress, I have laid much of the ground work for future students to be able to explore additional materials and polymers in order to find suitable materials for a "molecular-nose" sensor for VOCs.

9.3 Future Work

There are many other applications that could be explored using interferometric refractometry. This technique could be used to study the curing of coatings, paints, and adhesives. Some of this work is currently underway by colleagues in our group. Similarly, interferometric refractometry could be also used to study the degradation or corrosion of thin transparent films.

Currently, there are some limitations with the robustness of the refractometry setup. Switching to a cylindrical prism would allow for the focal points to be constantly centred on the prism. Additionally, this would reduce the refraction inside the prism as light would now hit the prism at normal incidence. If the optics before and after the prism are mounted on rotating arms, then the alignment of the refractometer would be greatly simplified. This would make the instrument easier to use and it would be much simpler to change between refractive index ranges.

For the SOI experiments, there are many different applications that could be investigated. For example, biomolecules could be tethered directly to the waveguides and SOI devices could be easily used for biosensing applications. Tetrasulfide functionalized mesoporous silicate materials can also be coated onto waveguides for aqueous sensing of lead and mercury ions. This work was started by Dr. Jenny Du[4] and is currently being studied using SOI microring resonators in our group.

For the polymer experiments, only two types of siloxane polymers were explored in this thesis. Tests should be performed on siloxane polymers with different functional groups including naphthyl, and fluorinated groups. Additionally, siloxanes terminated with ethers, esters, and hydroxyl groups could be used to increase the hydrophilicity of the polymers. Testing these materials against a full range of analytes would be essential to build a database with different responses. Other polymers could also be explored to widen the range of interactions including polystyrene, polyacrylates, polyacrylic acids, and polyisobutylene (butyl rubber). Once a large enough database has been constructed, efforts could begin on the construction of "molecular nose" sensor for VOCs. Arrays of SOI microring resonators could be individually coated with different polymer materials using micro-plotters. Integrating an array detector with the SOI devices would allow for simultaneous analysis of the full array of devices. Even though none of the coatings on their own are entirely selective, they will all show differential responses to a target analyte. Techniques like principal component analysis or parallel factor analysis could be used to disentangle the response and quantify the amounts of analytes present. Once all of this has been achieved, the SOI devices could be integrated with a miniaturized light source and packaged for environmental sensing applications.

9.4 References

1. Chen, W.; Saunders, J. E.; Barnes, J. A.; Yam, S. S.-H.; Loock, H.-P., Monitoring of vapor uptake by refractive index and thickness measurements in thin films. *Optics Letters* **2013,** *38*, 365-367.

2. Saunders, J. E.; Sanders, C.; Chen, H.; Loock, H.-P., Refractive indices of common solvents and solutions at 1550 nm. *Applied Optics* **2016,** *55*, 947-953.

3. Crank, J., *The Mathmatics of Diffusion*. First Edition, Oxford University Press, London, UK, 1956.

4. Du, J.; Cipot-Wechsler, J.; Lobez, J. M.; Loock, H.-P.; Crudden, C. M., Periodic mesoporous organosilica films: Key components of fiber-optic-based heavy-metal sensors. *Small* **2010,** *6*, 1168-1172.

Appendix 3.1

Rearrangement From Equation (3.17) to Equation (3.18)

This appendix details the rearrangement from equation (3.17) to equation (3.18) in a step by step process.

$$X_A = \frac{P_P\left(1+\left(\frac{X_A}{1-X_A}\right)\frac{M_A}{M_P}\right)-\left(\frac{{n_{mix}}^2-1}{{n_{mix}}^2+2}\right)\left(\frac{{n_P}^2+2}{{n_P}^2-1}\right)P_P\left(1+\frac{\Delta d}{d}\right)}{\left(\frac{M_A}{\rho_P}\right)\left(\frac{{n_{mix}}^2-1}{{n_{mix}}^2+2}\right)\left(1+\frac{\Delta d}{d}\right)-P_P\left(\frac{{n_{mix}}^2-1}{{n_{mix}}^2+2}\right)\left(\frac{{n_P}^2+2}{{n_P}^2-1}\right)\left(1+\frac{\Delta d}{d}\right)+\left(P_P-P_A\right)\left(1+\left(\frac{X_A}{1-X_A}\right)\frac{M_A}{M_P}\right)} \tag{A3.1}$$

The first step is to multiply X_A with the denominator and expand the terms.

$$X_A\left[\left(\frac{M_A}{\rho_P}\right)\left(\frac{{n_{mix}}^2-1}{{n_{mix}}^2+2}\right)\left(1+\frac{\Delta d}{d}\right)-P_P\left(\frac{{n_{mix}}^2-1}{{n_{mix}}^2+2}\right)\left(\frac{{n_P}^2+2}{{n_P}^2-1}\right)\left(1+\frac{\Delta d}{d}\right)+\left(P_P-P_A\right)\left(1+\left(\frac{X_A}{1-X_A}\right)\frac{M_A}{M_P}\right)\right] = P_P\left(1+\left(\frac{X_A}{1-X_A}\right)\frac{M_A}{M_P}\right)-P_P\left(\frac{{n_{mix}}^2-1}{{n_{mix}}^2+2}\right)\left(\frac{{n_P}^2+2}{{n_P}^2-1}\right)\left(1+\frac{\Delta d}{d}\right) \tag{A3.2}$$

$$X_A\left(\frac{M_A}{\rho_P}\right)\left(\frac{{n_{mix}}^2-1}{{n_{mix}}^2+2}\right)\left(1+\frac{\Delta d}{d}\right)-P_P X_A\left(\frac{{n_{mix}}^2-1}{{n_{mix}}^2+2}\right)\left(\frac{{n_P}^2+2}{{n_P}^2-1}\right)\left(1+\frac{\Delta d}{d}\right)+P_P X_A\left(1+\left(\frac{X_A}{1-X_A}\right)\frac{M_A}{M_P}\right) -P_A X_A\left(1+\left(\frac{X_A}{1-X_A}\right)\frac{M_A}{M_P}\right) = P_P\left(1+\left(\frac{X_A}{1-X_A}\right)\frac{M_A}{M_P}\right)-P_P\left(\frac{{n_{mix}}^2-1}{{n_{mix}}^2+2}\right)\left(\frac{{n_P}^2+2}{{n_P}^2-1}\right)\left(1+\frac{\Delta d}{d}\right) \tag{A3.3}$$

The terms can then be re-arranged so that it is possible to begin factoring out common terms.

$$X_A\left(\frac{M_A}{\rho_P}\right)\left(\frac{{n_{mix}}^2-1}{{n_{mix}}^2+2}\right)\left(1+\frac{\Delta d}{d}\right)+P_P\left(\frac{{n_{mix}}^2-1}{{n_{mix}}^2+2}\right)\left(\frac{{n_P}^2+2}{{n_P}^2-1}\right)\left(1+\frac{\Delta d}{d}\right)-P_P X_A\left(\frac{{n_{mix}}^2-1}{{n_{mix}}^2+2}\right)\left(\frac{{n_P}^2+2}{{n_P}^2-1}\right)\left(1+\frac{\Delta d}{d}\right) -P_A X_A\left(1+\left(\frac{X_A}{1-X_A}\right)\frac{M_A}{M_P}\right) = P_P\left(1+\left(\frac{X_A}{1-X_A}\right)\frac{M_A}{M_P}\right)-P_P X_A\left(1+\left(\frac{X_A}{1-X_A}\right)\frac{M_A}{M_P}\right) \tag{A3.4}$$

$$X_A\left(\frac{M_A}{\rho_P}\right)\left(\frac{{n_{mix}}^2-1}{{n_{mix}}^2+2}\right)\left(1+\frac{\Delta d}{d}\right)+\left(1-X_A\right)P_P\left(\frac{{n_{mix}}^2-1}{{n_{mix}}^2+2}\right)\left(\frac{{n_P}^2+2}{{n_P}^2-1}\right)\left(1+\frac{\Delta d}{d}\right) -P_A X_A\left(1+\left(\frac{X_A}{1-X_A}\right)\frac{M_A}{M_P}\right) = (1-X_A)P_P\left(1+\left(\frac{X_A}{1-X_A}\right)\frac{M_A}{M_P}\right) \tag{A3.5}$$

This equation can be further rearranged by dividing $(1 - X_A)$ from all the terms.

$$\left(\frac{X_A}{1-X_A}\right)\left(\frac{M_A}{\rho_P}\right)\left(\frac{{n_{mix}}^2-1}{{n_{mix}}^2+2}\right)\left(1+\frac{\Delta d}{d}\right)+P_P\left(\frac{{n_{mix}}^2-1}{{n_{mix}}^2+2}\right)\left(\frac{{n_P}^2+2}{{n_P}^2-1}\right)\left(1+\frac{\Delta d}{d}\right) -P_A\left(\frac{X_A}{1-X_A}\right)\left(1+\left(\frac{X_A}{1-X_A}\right)\frac{M_A}{M_P}\right) = P_P\left(1+\left(\frac{X_A}{1-X_A}\right)\frac{M_A}{M_P}\right) \tag{A3.6}$$

Re-arrangement of equation (A3.6) leads to the following relationship:

$$\left(\frac{X_A}{1-X_A}\right)\left(\frac{M_A}{\rho_P}\right)\left(\frac{{n_{mix}}^2-1}{{n_{mix}}^2+2}\right)\left(1+\frac{\Delta d}{d}\right)+P_P\left(\frac{{n_{mix}}^2-1}{{n_{mix}}^2+2}\right)\left(\frac{{n_P}^2+2}{{n_P}^2-1}\right)\left(1+\frac{\Delta d}{d}\right)$$
$$=P_P\left(1+\left(\frac{X_A}{1-X_A}\right)\frac{M_A}{M_P}\right)+P_A\left(\frac{X_A}{1-X_A}\right)\left(1+\left(\frac{X_A}{1-X_A}\right)\frac{M_A}{M_P}\right) \tag{A3.7}$$

This can be further simplified by consolidating terms on the right side of the equation.

$$\left(\frac{X_A}{1-X_A}\right)\left(\frac{M_A}{\rho_P}\right)\left(\frac{{n_{mix}}^2-1}{{n_{mix}}^2+2}\right)\left(1+\frac{\Delta d}{d}\right)+P_P\left(\frac{{n_{mix}}^2-1}{{n_{mix}}^2+2}\right)\left(\frac{{n_P}^2+2}{{n_P}^2-1}\right)\left(1+\frac{\Delta d}{d}\right)$$
$$=\left(P_P+P_A\left(\frac{X_A}{1-X_A}\right)\right)\left(1+\left(\frac{X_A}{1-X_A}\right)\frac{M_A}{M_P}\right) \tag{A3.8}$$

From the molar polarization equation (eqn. (3.2)) it is possible to derive an expression for $(\rho_P)^{-1}$.

$$\frac{1}{\rho_P}=\frac{P_P}{M_P}\left(\frac{{n_P}^2+2}{{n_P}^2-1}\right) \tag{A3.9}$$

Inserting equation (A3.9) into equation (A3.8) gives the following:

$$P_P\left(\frac{X_A}{1-X_A}\right)\left(\frac{M_A}{M_P}\right)\left(\frac{{n_{mix}}^2-1}{{n_{mix}}^2+2}\right)\left(\frac{{n_P}^2+2}{{n_P}^2-1}\right)\left(1+\frac{\Delta d}{d}\right)+P_P\left(\frac{{n_{mix}}^2-1}{{n_{mix}}^2+2}\right)\left(\frac{{n_P}^2+2}{{n_P}^2-1}\right)\left(1+\frac{\Delta d}{d}\right)$$
$$=\left(P_P+P_A\left(\frac{X_A}{1-X_A}\right)\right)\left(1+\left(\frac{X_A}{1-X_A}\right)\frac{M_A}{M_P}\right) \tag{A3.10}$$

This equation can be greatly simplified by consolidating the terms on the left side of the equation.

$$P_P\left(\frac{{n_{mix}}^2-1}{{n_{mix}}^2+2}\right)\left(\frac{{n_P}^2+2}{{n_P}^2-1}\right)\left(1+\frac{\Delta d}{d}\right)\left(1+\left(\frac{X_A}{1-X_A}\right)\frac{M_A}{M_P}\right)=\left(P_P+P_A\left(\frac{X_A}{1-X_A}\right)\right)\left(1+\left(\frac{X_A}{1-X_A}\right)\frac{M_A}{M_P}\right) \tag{A3.11}$$

Now both sides of the equation have a common factor of $\left(1+\left(\frac{X_A}{1-X_A}\right)\frac{M_A}{M_P}\right)$ that can be divided out.

$$P_P\left(\frac{{n_{mix}}^2-1}{{n_{mix}}^2+2}\right)\left(\frac{{n_P}^2+2}{{n_P}^2-1}\right)\left(1+\frac{\Delta d}{d}\right)=\left(P_P+P_A\left(\frac{X_A}{1-X_A}\right)\right) \tag{A3.12}$$

This equation is now straight forward to rearrange and solve for X_A.

$$P_P\left(\frac{{n_{mix}}^2-1}{{n_{mix}}^2+2}\right)\left(\frac{{n_P}^2+2}{{n_P}^2-1}\right)\left(1+\frac{\Delta d}{d}\right)-P_P=P_A\left(\frac{X_A}{1-X_A}\right) \tag{A3.13}$$

$$\left[P_P\left(\frac{{n_{mix}}^2-1}{{n_{mix}}^2+2}\right)\left(\frac{{n_P}^2+2}{{n_P}^2-1}\right)\left(1+\frac{\Delta d}{d}\right)-P_P\right]\left(1-X_A\right)=P_AX_A \tag{A3.14}$$

The $(1 - X_A)$ term can be multiplied through the left side of the equation.

$$P_P\left(\frac{{n_{mix}}^2-1}{{n_{mix}}^2+2}\right)\left(\frac{{n_P}^2+2}{{n_P}^2-1}\right)\left(1+\frac{\Delta d}{d}\right)-P_P+P_P X_A-P_P X_A\left(\frac{{n_{mix}}^2-1}{{n_{mix}}^2+2}\right)\left(\frac{{n_P}^2+2}{{n_P}^2-1}\right)\left(1+\frac{\Delta d}{d}\right)=P_A X_A \qquad \text{(A3.15)}$$

The terms can be rearranged so that all the terms containing X_A are on the same side of the equation.

$$P_P X_A-P_P X_A\left(\frac{{n_{mix}}^2-1}{{n_{mix}}^2+2}\right)\left(\frac{{n_P}^2+2}{{n_P}^2-1}\right)\left(1+\frac{\Delta d}{d}\right)-P_A X_A=P_P-P_P\left(\frac{{n_{mix}}^2-1}{{n_{mix}}^2+2}\right)\left(\frac{{n_P}^2+2}{{n_P}^2-1}\right)\left(1+\frac{\Delta d}{d}\right) \qquad \text{(A3.16)}$$

Factoring out X_A allows for the development of the final equation (eqn. (3.18)).

$$X_A\left(P_P-P_P\left(\frac{{n_{mix}}^2-1}{{n_{mix}}^2+2}\right)\left(\frac{{n_P}^2+2}{{n_P}^2-1}\right)\left(1+\frac{\Delta d}{d}\right)-P_A\right)=P_P-P_P\left(\frac{{n_{mix}}^2-1}{{n_{mix}}^2+2}\right)\left(\frac{{n_P}^2+2}{{n_P}^2-1}\right)\left(1+\frac{\Delta d}{d}\right) \qquad \text{(A3.17)}$$

$$X_A=\frac{P_P-P_P\left(\frac{{n_{mix}}^2-1}{{n_{mix}}^2+2}\right)\left(\frac{{n_P}^2+2}{{n_P}^2-1}\right)\left(1+\frac{\Delta d}{d}\right)}{P_P-P_P\left(\frac{{n_{mix}}^2-1}{{n_{mix}}^2+2}\right)\left(\frac{{n_P}^2+2}{{n_P}^2-1}\right)\left(1+\frac{\Delta d}{d}\right)-P_A} \qquad \text{(A3.18)}$$

Appendix 3.2

Error Functions

This appendix is provided as a short primer on error functions, more information can be found in statistics textbooks or by searching online. The error function is derived from statistics and is a useful method to describe diffusion processes. This function is available in most data processing software including Microsoft Excel. The error function is the integral of a normalized Gaussian function.[1]

$$\operatorname{erf}(x) = \frac{2}{\sqrt{\pi}} \int_0^x e^{-u^2} du \tag{A3.19}$$

A normalized Gaussian distribution is given with the related error function in Figure A3.1.

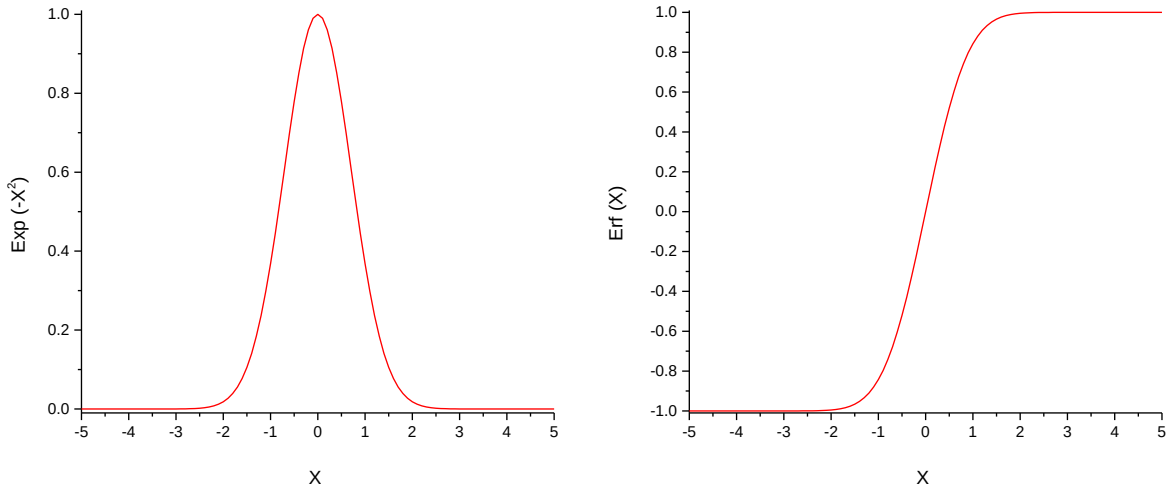

Figure A3.1: Sample plots of a normalized Gaussian function and the error function.The normalized Gaussian curve has an amplitude of 1 and is centred around *x* = 0. The error function is defined as the integral of the Gaussian function and is shown in the graph on the right. Another useful form of this function is called the complementary error function (erfc), and does not contain any negative values.

$$\operatorname{erfc}(x) = 1 - \operatorname{erf}(x) \tag{A3.20}$$

The integral of a Gaussian function from -∞ to ∞ is a well-known expression.[1]

$$\int_{-\infty}^{\infty} e^{-u^2} du = \sqrt{\pi} \tag{A3.21}$$

If we consider half of this relation, we can determine the following term.

$$\int_0^{\infty} e^{-u^2}\,du = \frac{\sqrt{\pi}}{2}$$
$$\frac{2}{\sqrt{\pi}}\int_0^{\infty} e^{-u^2}\,du = 1 \qquad \text{(A3.22)}$$

Combining this term with the original expression of the error function allows for the description of the complementary error function.[1]

$$\operatorname{erfc}(x) = \frac{2}{\sqrt{\pi}}\int_0^{\infty} e^{-u^2}\,du - \frac{2}{\sqrt{\pi}}\int_0^{x} e^{-u^2}\,du$$
$$\operatorname{erfc}(x) = \frac{2}{\sqrt{\pi}}\int_x^{\infty} e^{-u^2}\,du \qquad \text{(A3.23)}$$

The complementary error function is shown in Figure A3.2.

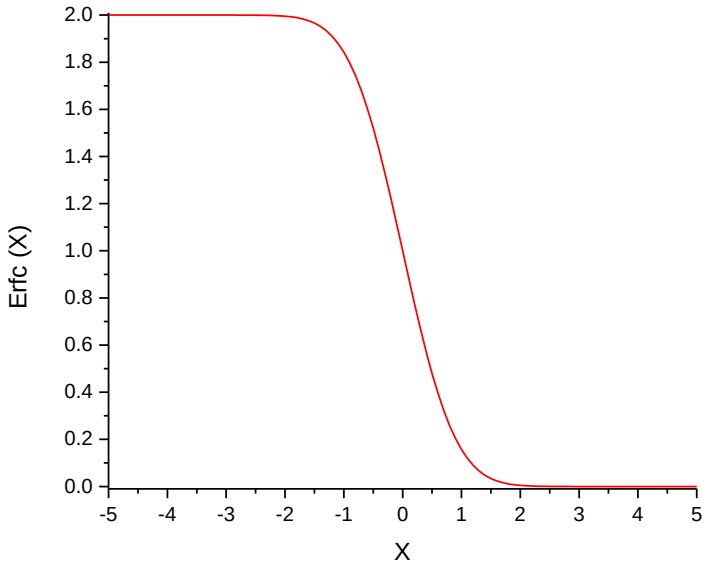

Figure A3.2: Plot of the complementary error function. The complementary error function ranges from y = 2 to y = 0 passing through y = 1 at x = 0.

1. Gautschi, W., Error Function and Fresnel Integrals. In *Handbook of Mathematical Functions, Graphs, and Mathematical Tables*, 10th Printing; Abramowitz, M.; Stegun, I. A., Eds. U.S. Department of Commerce, NIST: Washington, DC, 1972.

Appendix 5.1

Solvent Supplier and Purity Information

Table A5.1: Solvent supplier and purity information. All solvents studied were reagent grade or higher and obtained from major chemical suppliers. Where available, information on additives and impurities are listed with the grade.

Solvent	Grade	Purity	Supplier
De-ionized Water	Protocol De-ionized Water (100% v/v)	> 10 MΩ	Thermo-Fisher Scientific[1]
Methanol	HPLC Grade	99.9 %	Fisher Scientific[1]
Acetonitrile	HPLC Grade	99.97 %	Fisher Scientific[1]
Acetone	ACS Reagent Grade	> 99.5 %	ACP Chemicals[2]
100% Ethanol	Anhydrous	> 99%	Commercial Alcohols[3]
95% Ethanol	95% Ethanol, 5% Water	> 95%	Commercial Alcohols[3]
Formaldehyde Solution (37% w/w)	10-15% Methanol as Stabilizer, 48-53% Water	37.38%	Sigma Aldrich[4]
Isopropyl Alcohol (2-Propanol)	ACS Reagent Grade	> 99.5 %	ACP Chemicals[2]
Hexanes (Mixture of C_6H_{14} Isomers)	ACS Reagent Grade	> 98.5 %	ACP Chemicals[2]
1-Propanol	Anhydrous	99.7 %	Sigma Aldrich[4]
2-Butanol		> 99 %	Sigma Aldrich[4]
Tetrahydrofuran	Certified (0.025% Butylatedhydroxytoluene as stabilizer)	> 95%	Fisher Scientific[1]
1,4-Dioxane	Certified ACS Grade	99.9 %	Fisher Scientific[1]
Dichloromethane	ACS Reagent Grade	≥ 99.5 %	ACP Chemicals[2]

Solvent	Grade	Purity	Supplier
Cyclohexane	Puriss, ACS Reagent Grade	≥ 99.5 %	Sigma Aldrich[4]
N,N-Dimethylformamide	Certified ACS Grade	99.9 %	Fisher Scientific[1]
Ethylene Glycol	Reagent Plus	≥ 99 %	Sigma Aldrich[4]
N,N-Dimethylacetamide	OmniSolv	99.5%	BDH[5]
Chloroform	ACS Reagent Grade (0.75% Ethanol as Stabilizer)	> 99.8%	Fisher Scientific[1]
Glycerol	Reagent Plus	≥ 99.0 %	Sigma Aldrich[4]
Trichloroethylene	ACS Reagent Grade	> 99.5 %	Sigma Aldrich[4]
Dimethylsulfoxide	Certified ACS Grade	99.9 %	Fisher Scientific[1]
Ethylbenzene	Reagent Plus	99 %	Sigma Aldrich[4]
Toluene	ChromaSolv Plus for HPLC	≥ 99.9 %	Sigma Aldrich[4]
m-Xylene	Puriss	≥ 99.0 %	Sigma Aldrich[4]
o-Xylene	Reagent Grade	≥ 98.0 %	Sigma Aldrich[4]
p-Xylene	Reagent Plus	99 %	Sigma Aldrich[4]
Xylenes (Mixture of 3 isomers) + 4% Ethylbenzene	Certified ACS Grade	99.8 %	Fisher Scientific[1]
Benzene	ChromaSolv Plus for HPLC	≥ 99.9%	Sigma Aldrich[4]

1. Fisher Scientific, 112 Colonnade Road, Nepean, ON
2. ACP Chemicals, 421 Jane Street, Toronto, ON
3. Commercial Alcohols, 2 Chelsea Lane, Brampton, ON
4. Sigma Aldrich, 2149 Winston Park Drive, Oakville, ON
5. BDH via VWR Canada, 2360 Argentia Road, Mississauga, ON

Appendix 5.2

Experimental Refractive Indices of Aqueous Solutions.

The refractive indices are presented for aqueous solutions of sodium chloride, sucrose, dimethylsulfoxide, ethylene glycol, and glycerol. Sodium chloride and sucrose solutions were prepared to saturation. Dimethylsulfoxide, ethylene glycol and glycerol are all fully soluble in water and were measured over the full range. The precision error is indicated as the standard deviation from three measurements, or six measurements when the sample overlapped between two calibration ranges.

Table A5.2: Measured refractive indices, n_{1550}, of aqueous sodium chloride solutions.

Mass Fraction, *W*	Mole Fraction, *X*	*n*(1550 nm) at 298K	Mass Fraction, *W*	Mole Fraction, *X*	*n*(1550 nm) at 298K
0.0000	0.0000	1.3164(2)	0.0896	0.0295	1.3314(1)
0.0025	0.0008	1.3165(4)	0.0999	0.0331	1.3329(2)
0.0052	0.0016	1.3169(3)	0.1095	0.0365	1.3347(1)
0.0078	0.0024	1.3173(3)	0.1198	0.0403	1.3366(1)
0.0099	0.0031	1.3177(4)	0.1300	0.0441	1.3382(3)
0.0124	0.0039	1.3183(1)	0.1398	0.0477	1.3401(1)
0.0150	0.0047	1.3185(3)	0.1498	0.0515	1.3416(3)
0.0175	0.0055	1.3192(1)	0.1585	0.0549	1.3434(3)
0.0198	0.0062	1.3196(1)	0.1681	0.0586	1.3451(1)
0.0251	0.0079	1.3203(4)	0.1787	0.0629	1.3470(1)
0.0301	0.0095	1.3211(1)	0.1899	0.0674	1.3489(1)
0.0354	0.0112	1.3218(2)	0.1987	0.0710	1.3509(6)
0.0401	0.0127	1.3227(1)	0.2098	0.0756	1.3528(3)
0.0454	0.0144	1.3236(1)	0.2202	0.0801	1.3546(4)
0.0502	0.0160	1.3244(2)	0.2380	0.0878	1.3578(3)
0.0600	0.0193	1.3260(2)	0.2401	0.0887	1.3582(3)
0.0700	0.0227	1.3277(2)	0.2504	0.0933	1.3601(5)
0.0800	0.0261	1.3301(9)			

Table A5.3: **Measured refractive indices, n_{1550}, of aqueous sucrose solutions**. **Super-saturated solutions were prepared for mass fractions above W = 0.68 using a boiling water bath.**

Mass Fraction, W	Mole Fraction, X	n(1550 nm) at 298K	Mass Fraction, W	Mole Fraction, X	n(1550 nm) at 298K
0.0000	0.0000	1.3164(2)	0.3601	0.0288	1.3748(6)
0.0029	0.0002	1.3169(1)	0.3797	0.0312	1.3787(4)
0.0053	0.0003	1.3174(1)	0.4007	0.0340	1.3825(1)
0.0077	0.0004	1.3177(1)	0.4196	0.0366	1.3866(4)
0.0100	0.0005	1.3188(1)	0.4408	0.0398	1.3904(2)
0.0154	0.0008	1.3179(1)	0.4608	0.0430	1.3945(2)
0.0195	0.0010	1.3193(2)	0.4803	0.0464	1.3992(10)
0.0297	0.0016	1.3209(1)	0.5003	0.0501	1.4032(11)
0.0398	0.0022	1.3224(2)	0.5206	0.0541	1.4075(12)
0.0498	0.0028	1.3239(1)	0.5407	0.0583	1.4126(8)
0.0599	0.0033	1.3251(2)	0.5585	0.0624	1.4164(10)
0.0797	0.0045	1.3282(3)	0.5795	0.0676	1.4210(6)
0.1016	0.0059	1.3317(4)	0.6006	0.0733	1.4261(9)
0.1211	0.0072	1.3344(2)	0.6186	0.0786	1.4295(6)
0.1401	0.0085	1.3372(1)	0.6393	0.0853	1.4342(7)
0.1595	0.0099	1.3405(1)	0.6599	0.0927	1.4389(4)
0.1781	0.0113	1.3439(3)	0.6795	0.1004	1.4436(8)
0.1976	0.0128	1.3466(1)	0.6990	0.1089	1.4488(3)
0.2196	0.0146	1.3501(2)	0.7002	0.1095	1.4489(7)
0.2387	0.0162	1.3534(4)	0.7201	0.1193	1.4540(8)
0.2589	0.0181	1.3569(3)	0.7405	0.1306	1.4589(2)
0.2797	0.0200	1.3605(4)	0.7584	0.1418	1.4637(3)
0.2996	0.0220	1.3639(3)	0.7798	0.1571	1.4701(11)
0.3188	0.0240	1.3672(4)	0.7994	0.1734	1.4781(12)
0.3400	0.0264	1.3707(4)			

Table A5.4: Measured refractive indices, n_{1550}, of aqueous dimethylsulfoxide solutions.

Mass Fraction, *W*	Mole Fraction, *X*	*n*(1550 nm) at 298K	Mass Fraction, *W*	Mole Fraction, *X*	*n*(1550 nm) at 298K
0.0000	0.0000	1.3164(2)	0.5255	0.2034	1.3965(1)
0.0250	0.0059	1.3199(1)	0.5503	0.2200	1.4006(2)
0.0488	0.0117	1.3233(1)	0.5728	0.2362	1.4045(9)
0.0740	0.0181	1.3269(1)	0.5997	0.2568	1.4083(3)
0.1006	0.0251	1.3301(1)	0.6248	0.2774	1.4133(11)
0.1249	0.0319	1.3336(1)	0.6483	0.2983	1.4168(8)
0.1505	0.0392	1.3374(1)	0.6753	0.3241	1.4204(1)
0.1761	0.0470	1.3412(2)	0.7001	0.3499	1.4248(6)
0.2002	0.0546	1.3449(1)	0.7251	0.3782	1.4283(3)
0.2235	0.0622	1.3481(1)	0.7504	0.4094	1.4320(6)
0.2482	0.0708	1.3517(2)	0.7767	0.4450	1.4359(7)
0.2747	0.0803	1.3560(1)	0.8004	0.4804	1.4387(3)
0.2992	0.0896	1.3596(1)	0.8251	0.5210	1.4423(5)
0.3253	0.1000	1.3638(2)	0.8498	0.5662	1.4452(2)
0.3484	0.1097	1.3673(1)	0.8749	0.6172	1.4482(3)
0.3753	0.1217	1.3716(1)	0.9001	0.6750	1.4517(1)
0.3996	0.1331	1.3755(1)	0.9247	0.7391	1.4546(1)
0.4254	0.1458	1.3799(1)	0.9498	0.8135	1.4574(1)
0.4502	0.1588	1.3840(1)	0.9754	0.9015	1.4604(1)
0.4755	0.1729	1.3881(1)	1.0000	1.0000	1.4631(1)
0.5001	0.1874	1.3922(1)			

Table A5.5: Measured refractive indices, n_{1550}, of aqueous ethylene glycol solutions.

Mass Fraction, *W*	Mole Fraction, *X*	*n*(1550 nm) at 298K	Mass Fraction, *W*	Mole Fraction, *X*	*n*(1550 nm) at 298K
0.0000	0.0000	1.3164(2)	0.5264	0.2439	1.3699(5)
0.0241	0.0071	1.3183(5)	0.5499	0.2618	1.3725(7)
0.0458	0.0137	1.3210(6)	0.5750	0.2820	1.3755(3)
0.0727	0.0222	1.3237(9)	0.5996	0.3030	1.3781(1)
0.1004	0.0314	1.3266(3)	0.6260	0.3270	1.3809(1)
0.1239	0.0394	1.3282(10)	0.6505	0.3508	1.3833(3)
0.1495	0.0485	1.3307(7)	0.6749	0.3760	1.3857(2)
0.1757	0.0583	1.3338(5)	0.7002	0.4040	1.3884(1)
0.1984	0.0670	1.3356(9)	0.7261	0.4349	1.3912(1)
0.2258	0.0780	1.3387(8)	0.7504	0.4659	1.3935(1)
0.2507	0.0885	1.3416(3)	0.7766	0.5023	1.3963(2)
0.2741	0.0988	1.3426(12)	0.8007	0.5383	1.3987(1)
0.3004	0.1108	1.3465(7)	0.8250	0.5778	1.4010(2)
0.3249	0.1226	1.3487(8)	0.8520	0.6255	1.4034(2)
0.3498	0.1350	1.3509(6)	0.8753	0.6708	1.4056(3)
0.3755	0.1486	1.3539(9)	0.8995	0.7220	1.4082(1)
0.3989	0.1615	1.3566(6)	0.9251	0.7820	1.4107(2)
0.4258	0.1771	1.3597(3)	0.9501	0.8467	1.4131(3)
0.4507	0.1923	1.3623(3)	0.9750	0.9188	1.4152(1)
0.4747	0.2078	1.3647(5)	1.0000	1.0000	1.4174(2)
0.4999	0.2249	1.3672(7)			

Table A5.6: Measured refractive indices, n_{1550}, of aqueous glycerol solutions.

Mass Fraction, *W*	Mole Fraction, *X*	*n*(1550 nm) at 298K	Mass Fraction, *W*	Mole Fraction, *X*	*n*(1550 nm) at 298K
0.0000	0.0000	1.3164(2)	0.5279	0.1795	1.3862(1)
0.0239	0.0048	1.3188(3)	0.5447	0.1897	1.3886(1)
0.0491	0.0100	1.3222(4)	0.5766	0.2104	1.3933(1)
0.0747	0.0156	1.3251(6)	0.5982	0.2255	1.3967(4)
0.0968	0.0205	1.3275(4)	0.6262	0.2468	1.4007(4)
0.1284	0.0280	1.3317(2)	0.6521	0.2683	1.4045(5)
0.1504	0.0335	1.3342(3)	0.6757	0.2896	1.4076(6)
0.1757	0.0400	1.3378(1)	0.6992	0.3126	1.4115(7)
0.1983	0.0462	1.3407(5)	0.7153	0.3296	1.4154(5)
0.2231	0.0532	1.3437(6)	0.7516	0.3719	1.4193(7)
0.2525	0.0620	1.3475(3)	0.7768	0.4051	1.4232(5)
0.2748	0.0690	1.3505(4)	0.7996	0.4383	1.4271(4)
0.2993	0.0771	1.3540(4)	0.8278	0.4847	1.4316(4)
0.3284	0.0873	1.3576(3)	0.8538	0.5332	1.4354(7)
0.3503	0.0954	1.3607(2)	0.8795	0.5880	1.4394(5)
0.3764	0.1056	1.3642(3)	0.9021	0.6431	1.4429(4)
0.4002	0.1155	1.3674(4)	0.9288	0.7185	1.4465(4)
0.4288	0.1281	1.3717(1)	0.9505	0.7899	1.4496(4)
0.4495	0.1377	1.3749(1)	0.9749	0.8839	1.4529(1)
0.4739	0.1498	1.3783(1)	1.0000	1.0000	1.4569(1)
0.5017	0.1646	1.3821(1)			

Appendix 7.1:

Uncertainties of Solvent Vapour Concentrations in Flow Meter Experiments

Table A7.1: The uncertainties of BTEX vapour pressures with analyte mole fractions of X = 0.05-0.95. The two values in the error represent the lower and upper errors on the concentrations, i.e. 40 (-15, +35) implies that the pressure can range from 25 to 75 Pa. The saturated vapour pressures were used as provided by the chemical suppliers at 20°C.[1]

X Analyte	$P°$ Benzene (Pa)	$P°$ Toluene (Pa)	$P°$ Ethylbenzene (Pa)	$P°$ m-Xylene (Pa)
0.05	480 (-180, +440)	140 (-54, +130)	64 (-24, +58)	40 (-15, +35)
0.10	990 (-330, +500)	290 (-100, +150)	130 (-40, +70)	80 (-27, +41)
0.15	1500 (-400, +600)	440 (-130, +180)	200 (-60, +80)	120 (-40, +50)
0.20	2000 (-500, +800)	590 (-150, +230)	270 (-70, +100)	160 (-40, +60)
0.25	2500 (-700, +700)	740 (-200, +200)	340 (-90, +100)	200 (-60, +60)
0.30	3000 (-800, +900)	900 (-220, +270)	410 (-100, +120)	240 (-60, +70)
0.35	3500 (-900, +1000)	1030 (-250, +290)	470 (-120, +130)	280 (-70, +80)
0.40	4000 (-1000, +1100)	1180 (-280, +310)	540 (-130, +140)	320 (-80, +90)
0.45	4500 (-1000, +1200)	1320 (-300, +360)	600 (-140, +160)	360 (-80, +100)
0.50	5000 (-1000, +1400)	1470 (-300, +410)	670 (-140, +180)	400 (-80, +110)
0.55	5400 (-1100, +1500)	1610 (-330, +440)	730 (-150, +200)	440 (-90, +120)
0.60	6000 (-1200, +1500)	1750 (-360, +460)	800 (-160, +210)	480 (-100, +120)
0.65	6500 (-1300, +1600)	1910 (-380, +490)	870 (-180, +220)	520 (-100,+130)
0.70	6900 (-1400, +1700)	2040 (-410, +510)	920 (-190, +230)	560 (-110, +140)
0.75	7500 (-1500, +1800)	2200 (-440, +530)	1000 (-200, +240)	600 (-120, +140)
0.80	7900 (-1600, +1900)	2340 (-470, +570)	1060 (-210, +260)	640 (-130, +160)
0.85	8400 (-1700, +1500)	2490 (-500, +440)	1130 (-230, 200)	680 (-140, +120)
0.90	9000 (-1800, +1000)	2640 (-540, +290)	1200 (-240, 130)	720 (-150, +80)
0.95	9500 (-1900, +500)	2790 (-570, +140)	1270 (-260, +60)	760 (-155, +40)

Table A7.2: The uncertainties of cyclohexane, acetone, methanol and isopropanol vapour pressures with analyte mole fractions of X = 0.05-0.95. The two values in the error represent the lower and upper errors on the concentrations, i.e. 490 (-190, +450) implies that the pressure can range from 300 to 940 Pa. The saturated vapour pressures were used as provided by the chemical suppliers at 20°C.[1]

X Analyte	$P°$ Cyclohexane (Pa)	$P°$ Acetone (Pa)	$P°$ Methanol (Pa)	$P°$ Isopropanol (Pa)
0.05	490 (-190, +450)	1200 (-400,+1100)	630 (-240, 570)	210 (-80, +190)
0.10	1000 (-300, +500)	2400 (-800, +1200)	1300 (-400, +700)	440 (-150, +220)
0.15	1600 (-500, +600)	3700 (-1100, +1500)	2000 (-600, +800)	660 (-200, +270)
0.20	2100 (-500, +800)	5000 (-1200, +1900)	2600 (-700, +1000)	890 (-220, +350)
0.25	2600 (-700, +800)	6200 (-1700, +1800)	3300 (-900, +1000)	1100 (-300, +300)
0.30	3100 (-800, +900)	7500 (-1900, +2200)	4000 (-1000, +1200)	1300 (-300, +400)
0.35	3600 (-900, +1000)	8600 (-2100, +2400)	4600 (-1100, +1300)	1500 (-400, +400)
0.40	4100 (-1000, +1100)	9900 (-2400, +2600)	5300 (-1300, +1400)	1800 (-400 , +500)
0.45	4600 (-1000, +1300)	11100 (-2500, +3000)	5900 (-1300, +1600)	2000 (-400, +500)
0.50	5100 (-1100, +1400)	12300 (-2500 , +3400)	6500 (-1300. +1800)	2200 (-500, +600)
0.55	5600 (-1200, +1500)	13500 (-2800, +3600)	7200 (-1500, +1900)	2400 (-500, +700)
0.60	6100 (-1200, +1600)	14700 (-3000,+3800)	7800 (-1600, +2000)	2600 (-500, +700)
0.65	6700 (-1300, +1700)	15900 (-3200, +4100)	8500 (-1700, +2200)	2900 (-600, +700)
0.70	7100 (-1400, +1800)	17000 (-3400, +4300)	9100 (-1800, +2300)	3100 (-600, +800)
0.75	7700 (-1500, +1900)	18400 (-3700, +4500)	9800 (-2000, +2400)	3300 (-700, +800)
0.80	8200 (-1600, +2000)	19600 (-3900, +4800)	10400 (-2100, +2500)	3500 (-700, +900)
0.85	8700 (-1800, +1600)	20800 (-4200, +3700)	11100 (-2200, +2000)	3700 (-800, +700)
0.90	9200 (-1900, +1100)	22100 (-4500, +2400)	11800 (-2400, +1300)	4000 (-800, +400)
0.95	9800 (-2000, +500)	23400 (-4700, +1100)	12400 (-2500, +700)	4200 (-900, +200)

1. Sigma-Aldrich, Chemical Information and MSDS. Sigma-Aldrich Co. LLC, https://www.sigmaaldrich.com/canada-english.html (accessed Aug. 6, 2016).

Appendix 8.1:

Common GPIB Codes for the Ando AQ4320D Tuneable Laser

This appendix describes the GPIB codes used to control the laser with the manual stepping and continuous scanning modes as was discussed in Sections 8.2.3.2 and 8.2.3.3. For more details and other commands please refer to Chapter 6 of the Ando AQ4320D user manual.

Table A8.1: GPIB commands used to control the Ando AQ4320D laser when conducting manual stepping or continuous wavelength scans of microresonators and interferometers. **The example code shows the required syntax of the commands.**

General Code	Description	Example
IDN?	Inquires information about the device and connects to the laser.	IDN?
TPMW	Sets the laser power in mW (ranges from 0.01-10mW) Typically 0.5-1.0 mW has the most constant power with wavelength.	TPMW1.00 Sets laser power to 1.0 mW
TWL	Sets the laser to a specific wavelength in nanometers. Used with the manual stepping mode to control the wavelength. (Ranges from λ = 1520-1620 nm)	TWL1550.000 Sets the laser wavelength to 1550 nm
TSTAWL	Sets the start wavelength when running a laser sweep in a continuous scan mode.	TSTAWL1532.000 Sets the sweep start wavelength to 1532 nm
TSTPWL	Sets the stop wavelength when running a laser sweep in a continuous scan mode	TSTPWL1538.000 Sets the sweep stop wavelength to 1538 nm
TSWET	Sets the sweep time of a continuous laser sweep in seconds (ranges from t = 1-99999s)	TSWET20.0 Sets the time of the continuous sweep to 20 s.
TSGL	Command to start a single laser sweep over the previously specified wavelength window.	TSGL
TRET	Command to start a continuous loop of repeated laser sweeps over the previously specified wavelength window.	TRET
TSTP	Command to stop the laser scan, used as a Boolean condition when the program is ended.	TSTP

Appendix 8.2:

Front Panel of LabView™ Data Acquisition Code

This section shows the front panel of the custom LabView™ virtual instrument for data acquisition using the continuous scanning mode of the laser. A screenshot highlighting the different inputs and outputs is shown below in Figure A8.1.

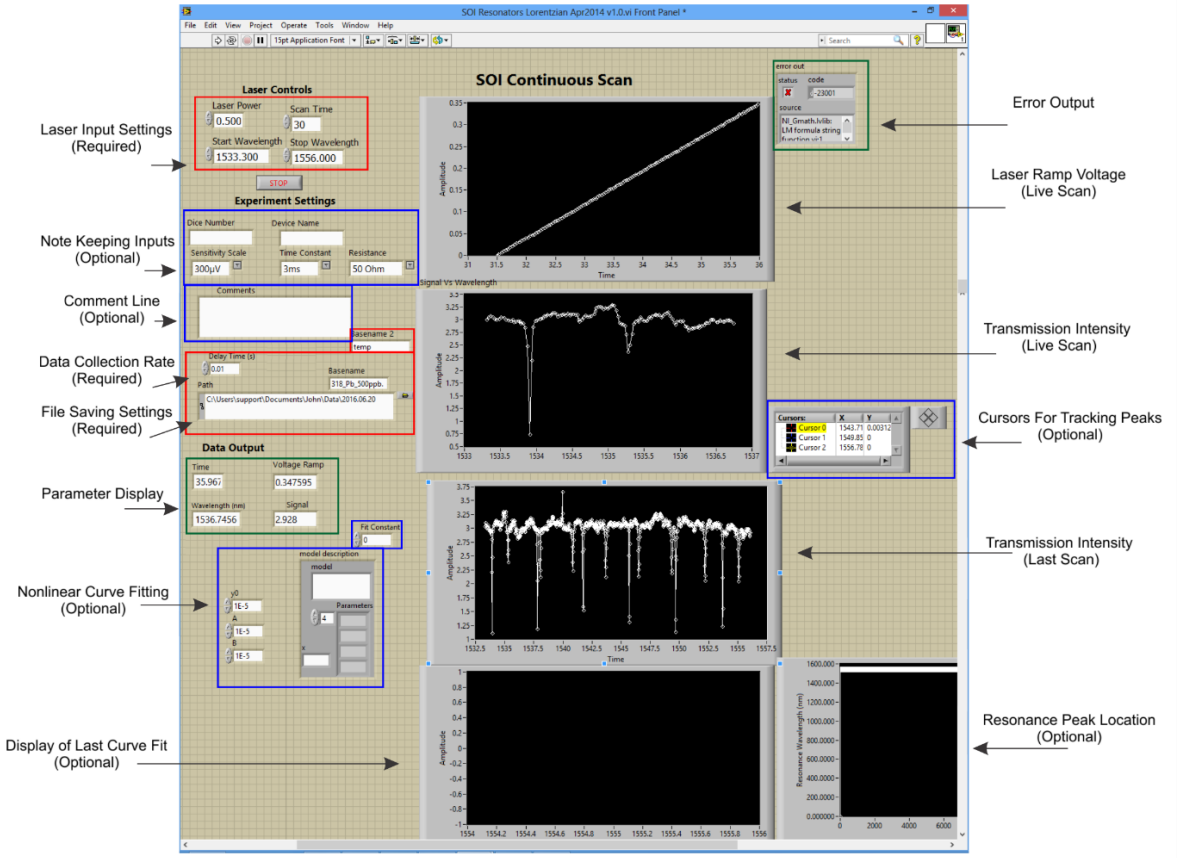

Figure A8.1: Screenshot of the front panel of the custom LabView™ virtual instrument for data acquisition.Required inputs are highlighted with red boxes, the optional inputs are highlighted with blue boxes and the output display properties are highlighted with green boxes. Each of these parameters are described below.

A8.2.1 Laser Input Settings

The laser input settings allow the user to specify the laser power, start wavelength, end wavelength and scan time parameters. These parameters were used to initialize the laser settings and were also used for on-the-fly wavelength assignments.

A8.2.2 Optional Note Keeping and Comment Inputs

The note keeping inputs allowed the user to save crucial experimental information in the header of the experimental data file. While these fields do not prohibit data from being collected, they may be essential parameters needed during data analysis. These inputs included a chip reference number (Dice Number), and information on the type of device under measurement (Device Name). This section also included fields for recording the lock-in amplifier sensitivity scale and time constant. Occasionally, a variable resistor was used at the lock-in amplifier signal input to convert the photodetector current into a voltage. When the resistor was not present, the built in lock-in amplifier resistance was set to 50 Ω. The final field was a comment line where the user could record detailed experimental information, for example, the type of material being studied, analyte concentration, etc.

A8.2.3 Data Collection Rate and File Saving Settings

This section contained required fields necessary for the program to execute. The data collection rate is the time delay between collecting data points in the program. This delay time should be at least 2-3 times slower than the lock-in amplifier time constant to avoid over-sampling data. For example, when the lock-in amplifier has a time constant of 3 ms, this rate could be set to 10 ms (0.010 s).

The file path field is used to select the folder to save the experimental data. To browse the computer, the user can click the folder button next to the field to select the appropriate folder. Two filename fields are also required, one for the actual data file (Basename) and a second that is used as a temporary file storing only the data of the last completed scan (Basename2).

A8.2.4 Parameter Display

The parameter display shows a live readout of the current experiment time, laser ramp voltage, assigned wavelength and transmission signal. These readouts are partly for coding troubleshooting but also allow the user to observe key experimental details. The graphical indicators, described later are more useful for assessing the progress of experiments.

A8.2.5 Cursors for Peak Tracking

The cursor box provides a series of indicators that the user can use to track resonance shifts in their experiments. The cursor must be first manually set to a wavelength in the range of the graph display, and then the user is able to drag it to the desired location. The user must use the first cursor to define the guess for the initial resonance location when the curve fitting algorithm is enabled. Each time, a laser scan is completed, the data will be fit and the second cursor will appear at the resonance wavelength of the previous scan. As long as this cursor is close to the original cursor, its position will be used for future fitting. Should an error occur, the fitting algorithm automatically reverts to the originally defined user cursor when conducting the next fit. Both of these cursors can still be used when the curve fitting algorithm is disabled to identify the location of features in the recorded spectrum

A8.2.6 Nonlinear Curve Fitting

The nonlinear curve fitting algorithm can be used to determine the resonance positions on the fly. To use this feature, a model equation must be entered. The correct syntax for a Lorentzian function is:

$$a1 + a2 / ((x - a3) \wedge 2 + a4)$$

Under the variable section, the four variables need to be entered as $a1$, $a2$, $a3$ and $a4$ respectively. Also, x must be entered in the box for the x variable. Here, $a1$ is the y-offset, $a2$ is related to the amplitude, $a3$ is the centre wavelength of the peak and $a4$ is related to the width of the peak. The wavelength range (in nm) that will be fit on either side of the resonance position is set in the field labeled fit constant (e.g. 0.1 would be 100pm). Finally, an approximate value for each parameter is needed to initialize the least squares fit. The resulting fit is plotted with the data in a graph on the screen. The centre resonance wavelength is stored in the memory and the change in resonance wavelength over time is plotted on a final graph.

A8.2.7 Error Display

This box displays any errors in the LabView™ code. When this box is not displayed on the front panel, any errors will cause the LabView™ VI to immediately stop running. This output dialogue shows

any errors and allows the LabView™ VI to continue to run should minor errors occur during an experiment, for example a curve fit that does not converge properly.

A8.2.8 Graph Displays

A series of graphical displays are provided to allow the user to assess and troubleshoot the progress of experiments. The top two graphs show a live feed of the laser ramp voltage and the transmission signal for the current laser scan. Once the scan is completed, it is saved in the temporary file and displayed on the third graph. This graph refreshes at the end of each laser scan to always show the last completed scan. Two cursors are located on the live transmission scan and are used to define the centre wavelength of a peak resonance when the peak fitting algorithm is enabled. When the fitting is enabled, the data within the fitting window specified by the fitting constant is plotted in the 4th graph with the resulting Lorentzian fit. The resonance wavelength is plotted with scan time in the final graph to show resonance shifts over time. Currently, the fit to the resonance wavelengths are not saved as the fitting algorithms in LabView™ are less robust than the algorithms used in post-experimental processing. Using LabView™ to call more powerful fitting programs like Igor Professional or Matlab should be considered in the future to increase the robustness of on-the-fly analysis.